

FLOW AND TURBULENCE IN SHARP OPEN-CHANNEL BENDS



THÈSE N° 2545 (2002)

PRÉSENTÉE A LA FACULTÉ DE L'ENVIRONNEMENT NATUREL,
ARCHITECTURAL ET CONSTRUIT

ÉCOLE POLYTECHNIQUE FÉDÉRALE DE LAUSANNE

POUR L'OBTENTION DU GRADE DE DOCTEUR ÈS SCIENCES

PAR

Koen BLANCKAERT

Burgerlijk Bouwkundig Ingenieur, Universiteit Gent, Belgique
Certificat de troisième cycle en Dynamique des Fluides, EPFL
Diplôme d'Études Approfondies de Mécanique, Université C. Bernard, Lyon I, France

Composition du jury :

Prof. P. Egger, président
Prof. W. H. Graf, directeur de thèse
Prof. H. J. de Vriend, rapporteur
Prof. W. H. Hager, rapporteur
Prof. P. A. Monkewitz, rapporteur
Prof. A. Schleiss, rapporteur
Prof. Y. Zech, rapporteur

Lausanne, EPFL
2002

*“ Wer dies Wasser und seine Geheimnisse verstünde,
so schien ihm,
der würde auch viel anderes verstehen,
viele Geheimnisse, alle Geheimnisse.”*

From *Siddharta* by Hermann Hesse

*Aan mijn ouders,
Aan Beril*

Acknowledgements

Towards the end of this PhD, I can look back on a period rich of experiences and satisfaction. Though writing a PhD is by definition an individual work, contributions by a lot of people are essential for its success.

My most respectful thanks are due to my supervisor, Prof. W.H. Graf, for having given me the opportunity to work in Lausanne. I especially want to acknowledge him for his confidence, the academic liberty he gave me, and for having introduced me in academia.

I am grateful to Prof. A.J. Odgaard (Iowa University, USA) for his decisive contributions in defining the subject and objectives of this PhD.

I had the chance to work with a brilliant man as Prof. H.J. de Vriend (Techn. Univ. Delft, The Netherlands), who – although not officially - is the co-supervisor of this PhD. His contributions were of fundamental importance for this dissertation. He co-authored papers III.2,3,4 and improved papers II.1 and III.1. My appreciation and thanks simply cannot be put into words.

The experimental part of this PhD relies on a high-tech instrument, the Acoustic Doppler Velocity Profiler, developed in our laboratory under the supervision of Dr. U. Lemmin. I am indebted to him for having given me the opportunity to use this instrument and for having accepted to co-author paper I.1. Thanks are due to R. Fontanellaz for his invaluable advice in conceiving and constructing the experimental infrastructure and to C. Perrinjacquet for keeping the computer resources operational.

Numerical simulations have been carried out in collaboration with Prof. S.S.Y. Wang and Prof. Y. Jia (Mississippi Univ, USA) that resulted in the joint paper IV.2. I am grateful to them for this fruitful collaboration.

I acknowledge Prof. I. Nezu (Kyoto Univ., Japan) and Dr. R. Booij (Techn. Univ. Delft, The Netherlands) for their willingness to review and improve parts of this dissertation.

I was honored by the acceptance of Prof. A. Schleiss (EPFL), Prof. P.A. Monkewitz (EPFL), Prof. W.H. Hager (ETH Zürich), Prof. Y. Zech (Univ. Louvain, Belgium) and Prof. H.J. de Vriend (Techn. Univ. Delft, The Netherlands) to serve on the doctoral committee.

My gratitude is due to the Swiss National Science Foundation for having funded this research during the period May 1998-January 2002.

Acknowledgements are also due to Dr. M. Altinakar, who is presently acting director of our laboratory, for his continuing support. Furthermore, I thank my colleagues P. Aviolat, M. Cellino, I. Fer, Y. Guan, D. Hurther, I. Istiarto, R. Jiang, A. Kurniawan, B. Özen, Z. Qu, I. Schoppe, W. Shen, L. Umlauf and B. Yulistiyanto for creating a fruitful working environment, as well as my friends for making life in Lausanne enjoyable.

Finally, my most heartfelt thanks go to my parents and my girlfriend Beril. I will never forget their faithful travels to Lausanne, their unconditional support and their love.

VERSION ABRÉGÉE

Summary

The sustainable development of rivers requires a knowledge on the three-dimensional mean flow field and the turbulence in complex morphologies. In a future, the computational capacity will be sufficient to simulate numerically the fine details of the flow. Our physical knowledge, however, is at present insufficient: the overwhelming majority of experimental research concerns straight-uniform flow and even complex numerical models are based on straight-uniform-flow knowledge. A sound understanding of the relevant physical processes will always be essential in complicated problems such as the river management, which concern a variety of different fields, and this irrespective of the available computational capacity.

This PhD investigates, mainly experimentally, the mean-flow field and the turbulence in open-channel bends; this situation is considered as a generic case for complex highly three-dimensional flow. The experimental investigation is rendered feasible by the availability of a powerful Acoustic Doppler Velocity Profiler (ADVP), developed in our laboratory. The principal objectives of this PhD are:

- To provide a high-quality data base on three-dimensional open-channel flow, including all three mean velocity components and all six Reynolds stresses on a fine grid.
- To document interesting features of the flow field and the turbulence, such as the multi-cellular pattern of secondary circulation, the curvature influence on the turbulence, etc.
- To gain insight in the relevant physical mechanisms and processes underlying these features.
- To apply the acquired knowledge in an engineering sense, mainly by evaluating, improving and developing numerical simulation techniques.

First, a limited series of experiments was conducted in a small laboratory flume, with the aim of testing the feasibility of the project. Subsequently, extended series of experiments have been designed in a large and optimized laboratory flume. The small-flume experiments yielded results beyond all expectations and form the core of this dissertation. The large-flume experiment are intended to confirm those results and to investigate newly emerged questions. Only few large-flume results are included in this dissertation; more large-flume results will be reported in literature in the future.

The structure of this dissertation follows the above-mentioned objectives.

In **PART I** “Instrumentation and experimental set-up”, the experimental set-up, the ADVP and the measuring strategy are presented. Furthermore, a method is proposed to improve acoustic turbulence measurements.

PART II “Experimental observations” provides high-quality data on the mean flow and the turbulence and documents the most interesting features:

- (i) The downstream velocity increases in outward direction and its vertical profiles are flatter (increased/decreased velocities in the lower/upper part of the flow depth) than in straight flow.
- (ii) A relatively small and weak outer-bank cell of secondary circulation exists besides the classical center-region cell (helical motion).
- (iii) The turbulence activity is reduced in the outer half of the cross-section in the investigated bend, as compared to a straight-uniform flow.
- (iv) Linear models that are commonly used to account for the effect of the secondary circulation in depth-integrated flow models are inaccurate for moderately to strongly curved flows.

PART III “Fundamental research” investigates the physical mechanisms and processes underlying these observations, mainly by making term-by-term evaluations of the relevant flow equations (momentum, vorticity, turbulent kinetic energy) and by considering the instantaneous flow behavior.

The distribution of the downstream velocity is dominated by both cells of secondary circulation, whereby the outer-bank cell has a protective effect on the stability of the outer bank by keeping the core of maximum velocity at distance.

The center-region cell is mainly generated by the vertical gradient of the centrifugal force, $(\partial/\partial z)(v_s^2/R)$: the non-uniform outward centrifugal force and the nearly-uniform inward pressure gradient, due to the super-elevation of the water surface, are on the average in equilibrium; their local non-equilibrium, however, gives rise to the center-region cell. There exists a strong negative feedback between the vertical profile of the downstream velocity, v_s , and the center-region cell: the center-region cell flattens the v_s -profiles, which on its turn leads to a reduction of $(\partial/\partial z)(v_s^2/R)$ and a weakening of the center-region cell. Linear models that are commonly used to account for the effect of the secondary circulation in depth-integrated flow models perform poorly because they neglect this feedback.

Similar outer-bank cells exist in straight turbulent flow as well as in curved laminar flow. In straight turbulent flow, they are induced by the anisotropy of turbulence whereas they come into existence in curved laminar flow when the curvature exceeds a critical value: the v_s -profiles flatten to such an extent that the gradient of the centrifugal force changes sign near the water surface, $(\partial/\partial z)(v_s^2/R) < 0$, provoking the generation of the outer-bank cell. In curved turbulent flow, both mechanisms have a comparable contribution to the generation of the outer-bank cell and strengthen each other, whence the outer-bank cell is stronger in a curved turbulent flow than in a curved laminar or a straight turbulent flow. The restitution of kinetic energy from the turbulence to the mean flow plays an important

role in the generation of the outer-bank cell, and the deficiency of standard k - ε turbulence closures to accurately simulate them is due to their inherent incapability to account for such kinetic-energy restitution.

The turbulence structure is fundamentally different than in a straight-uniform flow: for the same amount of turbulent kinetic energy, there is less shear in a curved flow. This change in turbulence structure is responsible for the observed reduced turbulence activity. An analysis of the instantaneous flow behavior suggests that the turbulence fluctuations can be decomposed into two fundamentally different parts: a wave-like oscillation of the pattern of circulation cells embedded in background turbulence.

PART IV “Applied research” tries to apply the acquired knowledge in an engineering sense. It proposes a non-linear model to account for the effect of the secondary circulation in depth-integrated flow models, that simulates the negative feedback between the downstream velocity profile and the center-region cell. Contrary to the commonly used linear models, this non-linear model agrees well with experimental data for strongly curved flow from both the small and the large-flume experiments. The model depends on the curvature ratio, the friction factor and the spanwise distribution of the downstream velocity, which can all be incorporated in a newly defined bend parameter, that allows an objective definition of weak, moderate and strong curvature. The linear model is found as the asymptotic solution for vanishing curvature. An evaluation for natural rivers has shown that differences between the linear model and the non-linear model are relevant.

Moreover, outer-bank cells have been successfully simulated by means of a non-linear k - ε turbulence closure.

As mentioned before, the small-flume experiments yielded results beyond all expectations. As a side-effect, the analysis of the large-flume experiments could not be accomplished within this dissertation and the work that is presently in progress is briefly described in **PART V** “Work in progress”.

Finally, **PART VI** summarizes the main conclusions of this dissertation.

Résumé

Le développement durable des rivières nécessite des connaissances sur l'écoulement moyen tridimensionnel ainsi que sur la turbulence dans des morphologies complexes. Tout laisse prévoir que la capacité des ordinateurs permettra dans un avenir de simuler numériquement même les fins détails de l'écoulement. A présent, cependant, des importantes lacunes existent dans la compréhension des écoulements complexes. La grande majorité des recherches portent sur les écoulements droits et uniformes, et la plupart des modèles numériques se fondent sur des connaissances acquises dans celles-ci. Une compréhension des processus physiques pertinents constituera toujours un élément essentiel dans des problèmes aussi complexes que la gestion des rivières, qui couvrent une multitude de disciplines, et ceci indépendamment de la capacité de calcul disponible.

Cette thèse de doctorat traite de l'écoulement moyen et de la turbulence dans les courbes des rivières, qui sont considérées comme cas génériques pour des écoulements complexes tridimensionnels. La majeure partie de cette thèse concerne une étude expérimentale, rendue possible grâce au Profileur Vélocimétrique Acoustique Doppler (PVAD), conçu et développé au sein de notre laboratoire. Les principaux objectifs de cette recherche doctorale sont de:

- fournir une base de données de haute qualité sur un écoulement tridimensionnel à surface libre, comprenant les trois composantes du vecteur de vitesse moyenne ainsi que les six composantes du tenseur de Reynolds sur un maillage fin.
- documenter des caractéristiques intéressantes de l'écoulement moyen et de la turbulence, telles que la configuration bi-cellulaire des courants secondaires, l'influence de la courbure sur la turbulence, etc.
- éclairer les mécanismes et processus physiques dirigeant ces observations.
- appliquer les résultats en ingénierie hydraulique, notamment en évaluant, améliorant et développant des techniques de simulation numériques.

D'abord, une série limitée d'expériences a été conçue dans un petit canal en laboratoire, avec le but d'évaluer la plausibilité des objectifs. Ensuite, une série étendue d'expériences a été faite dans un grand canal en laboratoire, optimisé pour cette recherche. Les résultats provenant du petit canal étaient au-delà de nos attentes, et forment le noyau de ce mémoire. Les expériences en grand canal ont pour but de confirmer ces résultats ainsi que d'examiner les nouvelles questions apparues. Ce mémoire comprend peu de résultats du grand canal; ils seront communiqués dans la littérature postérieurement.

La structure de ce mémoire suit les objectifs déclarés ci-dessus.

PARTIE I "Instrumentation et installations expérimentales" présente les installations expérimentales, le PVAD, ainsi que la stratégie de mesure. En outre, une méthode permettant d'améliorer les mesures de la turbulence à l'aide de systèmes acoustiques, comme le PVAD, est exposée.

PARTIE II “Observations expérimentales” fournit une base de données de haute qualité comprenant les champs de vitesses moyennes ainsi que turbulentes et documente les caractéristiques principales:

- (i) La vitesse longitudinale augmente vers la rive extérieure et ses profils verticaux sont aplatis (vitesses augmentées/réduites dans la partie inférieure/supérieure de la profondeur) comparé à l’écoulement droit uniforme.
- (ii) En plus de l’écoulement hélicoïdal classique, appelé cellule-de-centre, une autre cellule de circulation secondaire, plus faible et plus petite, avoisine la rive extérieure; elle est appelée cellule-de-rive.
- (iii) L’activité turbulente est réduite dans la partie extérieure de la courbe examinée, comparé au cas d’écoulement droit uniforme.
- (iv) Les modèles linéaires, couramment utilisés pour inclure les effets de la circulation secondaire dans les équations d’écoulement moyennées sur la profondeur, sont imprécis pour des courbures modérées ou fortes.

PARTIE III “Recherche fondamentale” essaie d’éclairer les mécanismes et processus physiques dirigeant ces observations, notamment en évaluant les termes individuels dans les équations pertinentes – quantité de mouvement, vorticité et énergie cinétique turbulente – ainsi qu’en examinant le comportement instantané de l’écoulement.

La répartition de la vitesse longitudinale est dominée par les cellules de circulation secondaire; la cellule-de-rive ayant un effet protecteur sur la stabilité de la rive en gardant le noyau de vitesses maximales à distance.

La cellule-de-centre est principalement due au gradient vertical de la force centrifuge, $(\partial/\partial z)(v_s^2/R)$: la force centrifuge à une répartition verticale, tandis que le gradient de pression, dû à la surélévation de la surface libre, est quasiment uniforme sur la profondeur. En moyenne, les deux s’équilibrent; cependant, leur déséquilibre local génère la cellule-de-centre. Une forte interaction non-linéaire existe entre le profil vertical de la vitesse longitudinale et la cellule-de-centre: la cellule-de-centre aplatit les profils de v_s , entraînant une réduction de $(\partial/\partial z)(v_s^2/R)$ et un affaiblissement de la cellule-de-centre. L’imprécision des modèles linéaires, couramment utilisés pour inclure les effets de la circulation secondaire dans les équations d’écoulement moyennées sur la profondeur, est due au fait que cette interaction non-linéaire est négligée.

Des cellules-de-rives semblables existent dans l’écoulement turbulent droit ainsi que dans l’écoulement laminaire courbe. Dans l’écoulement turbulent droit, elles sont générées par l’anisotropie de la turbulence, tandis qu’elles se manifestent soudainement dans l’écoulement laminaire courbe lorsque la courbure dépasse un seuil critique: l’aplatissement des profils de v_s devient tel que le signe du gradient de la force centrifuge est inversé près de la surface, $(\partial/\partial z)(v_s^2/R) < 0$, ce qui provoque la cellule-de-rive. Dans l’écoulement turbulent courbe, les deux mécanismes contribuent également à la génération de la cellule-de-rive. Puisqu’ils se soutiennent mutuellement, la cellule-de-rive est plus forte en écoulement turbulent courbe qu’en écoulement laminaire courbe ou turbulent droit. La restitution d’énergie cinétique de la turbulence vers l’écoulement moyen joue un rôle principal dans la génération de la cellule-de-rive. Le modèle de

turbulence $k-\varepsilon$ standard est intrinsèquement incapable de tenir compte d'une telle restitution d'énergie cinétique, ce qui explique son insuffisance pour simuler les cellules-de-rive.

Des différences fondamentales existent entre la structure de la turbulence en écoulement courbe et droit: pour une même quantité d'énergie cinétique turbulente, il y a moins de contraintes turbulentes de cisaillement en courbe. Cette différence peut expliquer la réduction observée de l'activité turbulente. Une analyse du comportement instantané de l'écoulement suggère que les fluctuations turbulentes de vitesses se décomposent en deux parties fondamentalement différentes: une oscillation des cellules de circulation secondaires à caractère d'ondes, noyée dans une turbulence de fond.

PARTIE IV "Recherche appliquée" essaie d'appliquer les résultats obtenus en ingénierie hydraulique. Un modèle non-linéaire est proposé pour inclure les effets de la circulation secondaire dans les équations d'écoulement moyennées sur la profondeur, qui tient compte de l'interaction entre le profil de v_s et la cellule-de-centre. Contrairement aux modèles linéaires couramment utilisés, le modèle non-linéaire simule bien les mesures faites pour des fortes courbures dans le petit et le grand canal. Il dépend du rapport entre la profondeur de l'écoulement et le rayon de courbure, du coefficient de frottement et de la répartition transversale de v_s . Ces trois paramètres peuvent être combinés dans un nouveau paramètre, nommé paramètre-de-courbe, qui permet de différencier objectivement entre des courbures faibles, modérées et fortes. Les modèles linéaires couramment utilisés correspondent à la solution asymptotique pour courbure tendant vers zéro. Une évaluation pour des rivières naturelles démontre que les différences entre les modèles linéaires et non-linéaires sont significatives.

En outre, les cellules-de-rives ont été simulées numériquement moyennant un modèle de turbulence $k-\varepsilon$ non-linéaire.

Comme mentionné auparavant, les résultats des expériences dans le petit canal étaient au-delà de nos attentes. Comme effet secondaire, l'analyse des expériences dans le grand canal n'a pas pu être accomplie dans le cadre de ce mémoire. La recherche en cours est brièvement exposée dans la **PARTIE V** "Recherche en cours".

PARTIE VI résume les principales conclusions de ce mémoire.

Samenvatting

De duurzame ontwikkeling van rivieren vereist een kennis van de driedimensionele gemiddelde stroming en de turbulentie in complexe morfologiën. Alles laat veronderstellen dat de rekencapaciteit van computers in een nabije toekomst zal volstaan om zelfs de fijne details van de stroming te berekenen. Onze fysische kennis is momenteel echter ontoereikend: de overgrote meerderheid experimenteel onderzoek betreft rechte uniforme stroming en zelfs de meest complexe numerieke modellen zijn gebaseerd op kennis vergaard voor rechte uniforme stroming. Inzicht in de relevante fysische processen zal altijd van primordiaal belang zijn in complexe multidisciplinaire problemen zoals rivierbeheer, en dit ongeacht de beschikbare rekencapaciteit.

Dit doctoraat onderzoekt, voornamelijk experimenteel, de gemiddelde stroming en de turbulentie in rivierbochten, deze situatie beschouwend als generiek geval voor complexe driedimensionele stroming. Dit experimenteel onderzoek was mogelijk dank zij de beschikbaarheid van een revolutionaire snelheidsmeter, de “Acoustic Doppler Velocity Profiler” (ADVP), die in ons laboratorium ontwikkeld werd. De hoofddoelen van dit doctoraat zijn:

- Het beschikbaar maken van hoogkwalitatieve meetgegevens betreffende een driedimensionele stroming met vrij oppervlak, inclusief de drie gemiddelde snelheidscomponenten en de zes turbulente spanningen, op een fijn rooster.
- Het documenteren van interessante eigenschappen van de gemiddelde stroming en de turbulentie, zoals de verschillende cellen van secundaire stroming en de invloed van kromming op de turbulentie, enz.
- Het verwerven van inzicht in de relevante fysische mechanismen and processen verantwoordelijk voor deze eigenschappen.
- Het toepassen van de verworven kennis in de ingenieurspraktijk, hoofdzakelijk d.m.v het beoordelen, verbeteren en ontwikkelen van methodes voor de numerieke berekening van stromingen.

Aanvankelijk werd een beperkte reeks experimenten uitgevoerd in een kleine laboratoriumgoot, met als doel de haalbaarheid van de doelstellingen te bevestigen. Vervolgens werd een uitgebreide reeks experimenten uitgevoerd in een grote geoptimaliseerde laboratoriumgoot. De resultaten in de kleine goot overtroffen alle verwachtingen en vormen de hoofdmoot van deze dissertatie. De experimenten in de grote goot hebben tot doel het bevestigen van de resultaten uit de kleine goot en het onderzoeken van nieuw opgedoken vragen. Deze dissertatie bevat maar enkele resultaten uit de grote goot; meer resultaten zullen te zijner tijd via de vakliteratuur verspreid worden.

De inhoud van deze dissertatie volgt in grote lijnen de bovenvermelde doelstellingen.

DEEL I “Instrumentatie en proefopstelling” presenteert de proefopstelling, de ADVP-snelheidsmeter alsook de meetstrategie. Daarnaast wordt een methode voorgesteld om acoustische turbulentiemetingen te verbeteren.

DEEL II “Experimentele waarnemingen” bevat een hoogkwalitatieve dataset betreffende de gemiddelde stroming en de turbulentie en documenteert daarnaast de meest interessante eigenschappen:

- (v) De stroomwaartse snelheidscomponent neemt naar de buitenoever toe en zijn snelheidsverdeling over de diepte is vlakker dan in rechte uniforme stroming (verlaagde/verhoogde snelheden in de bovenste/onderste helft van de waterdiepte).
- (vi) De secundaire stroming wordt gekenmerkt door een relatief kleine en zwakke buitenoever-cel naast de klassieke centrum-cel (de welbekende helicoïdale stroming).
- (vii) De turbulente activiteit is beduidend lager in de bestudeerde buitenbocht dan in rechte uniforme stroming.
- (viii) Lineaire modellen, die algemeen aangewend worden om rekening te houden met de invloed van secundaire stromingen in de dieptegemiddelde stromingsvergelijkingen, zijn onnauwkeuring voor gematigd tot sterk gekromde stroming.

DEEL III “Fundamenteel onderzoek” onderzoekt de fysische mechanismen en processen verantwoordelijk voor bovenvermelde waarnemingen, en dit voornamelijk door middel van termsgewijze evaluaties van de relevante stromingsvergelijkingen – impulsie, vorticitiet en turbulente kinetische energie – alsook door het bestuderen van het ogenblikkelijk stromingsgedrag.

De verdeling van de stroomwaartse snelheidscomponent wordt gedomineerd door beide cellen van secundaire stroming, waarbij de buitenoever-cel een beschermende invloed uitoefent op de stabiliteit van de buitenoever door het op afstand houden van de zone met de hoogste snelheden.

De centrum-cel wordt hoofdzakelijk veroorzaakt door de verticale gradient van de centrifugaalkracht, $(\partial/\partial z)(v_s^2/R)$: dieptegemiddeld zijn de niet-constante uitwaartse centrifugaalkracht en de quasi-constante inwaartse drukgradient, tengevolge van het dwarsverhang van het wateroppervlak, in evenwicht; hun lokale verschil leidt tot het ontstaan van de centrum-cel. Er bestaat een belangrijke niet-lineaire interactie tussen de verticale verdeling van de stroomwaartse snelheidscomponent v_s en de centrum-cel: de centrum-cel vervlakt de verticale verdeling van v_s , hetgeen leidt tot een vermindering van $(\partial/\partial z)(v_s^2/R)$ en een verzwakking van de centrum-cel. Lineaire modellen, die algemeen aangewend worden om rekening te houden met de invloed van secundaire stromingen in de dieptegemiddelde stromingsvergelijkingen, zijn onnauwkeuring omdat ze deze niet-lineaire interactie verwaarlozen.

Gelijkaardige buitenoever-cellen bestaan in rechte turbulente stroming alsook in gekromde laminaire stroming. In rechte turbulente stroming worden ze veroorzaakt door de anisotropie van de turbulentie, terwijl ze ontstaan wanneer de kromming een bepaalde grenswaarde overschrijdt in gekromde laminaire stroming: de verticale v_s -verdeling vervlakt dusdanig dat het teken van de gradient van de centrifugaalkracht omslaat nabij het wateroppervlak, $(\partial/\partial z)(v_s^2/R) < 0$, waardoor de buitenoever-cel ontstaat. In gekromde turbulente stroming dragen beide mechanismen in gelijkaardige mate bij tot het ontstaan van de buitenoever-cel. Bovendien versterken ze mekaar waardoor de buitenoever-cel in gekromde turbulente stroming sterker is dan in rechte turbulente en gekromde laminaire stroming. De teruggave van kinetische energie van de turbulentie aan de gemiddelde

stroming speelt een belangrijke rol in het ontstaan van de buitenoever-cel. Omdat het standaard $k-\varepsilon$ turbulentiemodel intrinsiek niet in staat is om deze in aanmerking te nemen, is het ongeschikt voor het berekenen van buitenoever-cellen.

De eigenschappen van de turbulentie in gekromde stroming verschillen fundamenteel van deze in rechte stroming: een zelfde hoeveelheid turbulente kinetische energie leidt tot minder turbulente schuifspanningen in gekromde stroming. Dit verschil verklaart waarom de turbulente activiteit in de bestudeerde bocht lager is dan in rechte stroming. Het ogenblikkelijk stromingsgedrag wijst erop dat de turbulente snelheidsfluctuaties kunnen opgesplitst worden in twee fundamenteel verschillende delen: een oscillatie van beide cellen van secundaire stroming met de eigenschappen van een golfbeweging ingebed in een ontwikkelde achtergrondturbulentie.

DEEL IV “Toegepast onderzoek” tracht de verworven kennis praktisch toe te passen. Het presenteert een niet-lineair model voor de invloed van secundaire stromingen in de dieptegemiddelde stromingsvergelijkingen dat rekening houdt met de interactie tussen de verticale v_s -verdeling en de centrum-cel. In tegenstelling tot de algemeen aangewende lineaire modellen geeft dit niet-lineaire model goede overeenstemming met de meetresultaten voor sterk gekromde stroming uit de kleine en de grote goot. Het niet-lineaire model hangt af van de verhouding waterdiepte/krommingsstraal, de wrijvingsfactor en de breedteverdeling van v_s , die allen kunnen gecombineerd worden in een nieuw gedefinieerde bochtparameter; deze laat toe een objectief onderscheid te maken tussen zwak, gematigd en sterk gekromde stroming. De lineaire modellen komen overeen met de asymptotische oplossing voor verwaarloosbare kromming. Een evaluatie voor natuurlijke rivieren toont aan dat de verschillen tussen lineaire en niet-lineaire modellen relevant zijn.

Bovendien zijn de buitenoever-cellen met succes numeriek berekend aan de hand van een niet-lineair $k-\varepsilon$ turbulentiemodel.

Zoals reeds vermeld overtroffen de resultaten uit de kleine goot alle verwachtingen. Dit had tot gevolg dat de analyse van de experimenten uit de grote goot niet kon afgewerkt worden binnen het kader van dit doctoraat. **DEEL V** “Onderzoek in uitvoering” beschrijft bondig het nog aan de gang zijnde onderzoek.

DEEL VI vat de belangrijkste conclusies van dit doctoraat samen.

Zusammenfassung

Die nachhaltige Entwicklung der Flüsse erfordert Kenntnis der drei-dimensionalen mittleren Strömung und der Turbulenz in komplexer Morphologie. In Zukunft wird die Rechenkapazität der Computer ausreichen um selbst die feinsten Details der Strömung simulieren zu können. Zur Zeit jedoch ist unser physikalisches Verständnis noch unzulänglich. Die überwältigende Mehrheit der experimentellen Forschung befasst sich mit der geraden uniformer Strömung, und die meist komplexen numerischen Modelle stützen sich auf das Wissen über diese Strömung. Das Verständnis der relevanten physikalischen Prozesse wird in komplexen interdisziplinären Problemen, als auch des Flussmanagements, stets unerlässlich bleiben. Dies ist unabhängig von der verfügbaren Rechenkapazität.

Diese Dissertation untersucht hauptsächlich experimentell die mittlere Strömung und die Turbulenz in Flusskrümmungen. Diese Situation wird als ein generischer Fall für komplexe drei-dimensionale Strömungen betrachtet. Die experimentelle Untersuchung war vor allem durch die Verfügbarkeit eines akustischen Doppler-Geschwindigkeitsmessinstrumentes (ADVP), welches an unserem Institut entwickelt wurde, durchführbar.

Die Hauptziele dieser Dissertation sind:

- Die Bereitstellung eines hochwertigen Datenbestandes über drei-dimensionale Freispiegelströmungen einschliesslich der drei Komponenten der mittleren Geschwindigkeit und der sechs Reynoldsschen Spannungen auf einem feinem Gitter.
- Die Dokumentation interessanter Merkmale der mittleren Strömung und der Turbulenz, wie zum Beispiel mehrere sekundäre Strömungszellen, der Einfluss der Krümmung auf die Turbulenz, usw.
- Das Verständnis relevanter physikalischer Mechanismen und Prozessen in solchen Strömungen.
- Die Anwendung dieser neuen Erkenntnisse im Ingenieursalltag, hauptsächlich durch Auswerten, Verbessern und Entwickeln der numerischen Simulationstechniken.

Gestartet wurde mit einer begrenzten Anzahl von Experimenten in einer kleinen Laborrinne mit dem Ziel die Durchführbarkeit dieses Projektes zu testen. Anschliessend wurde eine ausgedehnte Serie an Experimenten in einer grossen optimierten Laborrinne durchgeführt. Die Resultate der kleinen Laborrinne übertrafen alle Erwartungen und formen den Kern dieser Dissertation. Die Experimente mit der grossen Laborrinne waren zur Bestätigung dieser Ergebnisse und zur Klärung von neu auftauchenden Fragen gedacht. Nur eine kleine Anzahl der Resultate mit der grossen Laborrinne sind dieser Dissertation beigelegt; neue Ergebnisse werden in der Fachliteratur erscheinen.

Der Aufbau dieser Dissertation verfolgt die oben genannten Ziele.

In **Teil 1**, "Instrumentation und der Versuchsaufbau", werden der Versuchsaufbau, das ADVP und die Messmethoden vorgestellt. Ferner wird eine Methode zur Verbesserung akustischer Turbulenzmessungen vorgeschlagen.

Teil 2, “Experimentelle Beobachtungen”, stellt hochwertigen Daten über die mittlere Strömung und die Turbulenz zur Verfügung und dokumentiert somit die interessantesten Merkmale:

- (i) Die Längsgeschwindigkeit nimmt nach aussen hin zu und die vertikale Geschwindigkeitsverteilung wird flacher als in der geraden Strömung (erhöhte/verringerte Geschwindigkeiten im unteren/höheren Teil der Wassertiefe);
- (ii) Die Sekundärströmung wird durch eine relativ kleine und schwache Aussenuferzelle neben der klassischen Zentrumzelle (Helikoïdalströmung) gekennzeichnet.
- (iii) Die Turbulenzaktivität ist, im Vergleich zu geraden uniformen Strömung, geringer in der Aussenuferzelle der untersuchten gekrümmten Strömung.
- (iv) Lineare Modelle, die häufig angewendet werden um den Effekt der Sekundärströmung in tiefenintegrierten Strömungsmodellen zu berücksichtigen, sind ungenau für mässig bis stark gekrümmte Strömung.

Teil 3, “Grundlagenforschung”, untersucht die physikalischen Mechanismen und Prozesse in solchen Strömungen durch Auswertung der Terme in den relevanten Strömungsgleichungen - Impuls, Wirbelstärke, turbulente kinetische Energie - und durch Betrachtung des unmittelbaren Strömungsverhaltens.

Die Verteilung der Längsgeschwindigkeit wird durch die beiden Zellen der Sekundärströmung dominiert, wobei die Aussenuferzelle, durch das Fernhalten des Kerns der maximalen Geschwindigkeit, eine schützende Wirkung auf die Stabilität des Aussenufers hat.

Die Zentrumzelle wird hauptsächlich durch den vertikalen Gradienten der Zentrifugalkraft erzeugt, $(\partial/\partial z)(v_s^2/R)$: Die nicht gleichförmige nach Aussen gerichtete Zentrifugalkraft und der fast gleichförmige nach Innen gerichtete Druckgradient, beruhend auf der Querneigung des Wasserspiegels, sind im Durchschnitt im Gleichgewicht. Ihr lokales Ungleichgewicht führt zur Entstehung der Zentrumzelle. Es besteht eine starke negative Rückkoppelung zwischen dem vertikalen Profil der Längsgeschwindigkeit v_s und der Zentrumzelle: Die Zentrumzelle verflacht die v_s -Profile, welches zu einer Verminderung des Terms $(\partial/\partial z)(v_s^2/R)$ führt und damit zu einer Schwächung der Zentrumzelle. Lineare Modelle, die häufig benutzt werden um den Effekt der Sekundärströmung in tiefenintegrierten Strömungsmodellen zu berücksichtigen, sind ungenau wegen der Vernachlässigung dieser Rückkoppelung.

Ähnliche Aussenuferzellen gibt es in der geraden turbulenten wie auch in der gekrümmten laminaren Strömung. In der geraden turbulenten Strömung werden sie verursacht durch die Anisotropie der Turbulenz. In gekrümmten laminaren Strömungen entstehen sie, wenn die Krümmung einen kritischen Wert übersteigt: Die vertikale v_s -Profile verflachen derartig, dass das Vorzeichen des Gradienten der Zentrifugalkraft nahe der Wasseroberfläche umschlägt, $(\partial/\partial z)(v_s^2/R) < 0$, wodurch die Aussenuferzelle entsteht. In der gekrümmten turbulenten Strömung, tragen beide Mechanismen in vergleichbarem Maße zur Generation der Aussenuferzelle bei und verstärken sich gegenseitig. Dadurch ist die Aussenuferzelle stärker in einer gekrümmten turbulenten Strömung als in einer gekrümmten laminaren oder geraden turbulenten Strömung. Die Umformung von kinetischer turbulenter Energie in Energie der mittleren Strömung spielt eine wichtige

Rolle bei der Erzeugung der Aussenuferzelle. Da das standard $k-\varepsilon$ Turbulenzmodell nicht in der Lage ist diese Umformung zu berücksichtigen, ist es ungeeignet für die Simulation von Aussenuferzellen.

Die Struktur der Turbulenz in der gekrümmten Strömung ist wesentlich anders als in der geraden uniformen Strömung: Bei gleicher turbulenter kinetischer Energie existiert weniger Schubspannung in der gekrümmten Strömung. Dieser Unterschied erklärt die beobachtete verminderte Turbulenzaktivität in der untersuchten Strömung. Eine Analyse des unmittelbaren Strömungsverhaltens weist darauf hin, dass die Turbulenzschwankungen in zwei wesentliche, verschiedene Teile zerlegt werden können: Eine wellenähnliche Schwankung beider sekundären Strömungszellen, eingebettet in ausgebildete Hintergrundsturbulenz.

Teil IV, “Angewandte Forschung”, versucht das erlangte Wissen im Ingenieursalltag anzuwenden. Es präsentiert ein nicht-lineares Modell für den Effekt der Sekundärströmung in tiefenintegrierten Strömungsmodellen, dass die negative Rückkoppelung zwischen der Längsgeschwindigkeit und der Zentrumzelle berücksichtigt. Im Gegensatz zu den häufig benutzten linearen Modellen ergibt dieses nicht-lineare Modell eine gute Übereinstimmung mit den Messresultaten für stark gekrümmte Strömung aus der kleinen und grossen Rinne. Das Modell hängt vom Verhältnis Wassertiefe/Krümmungsradius, dem Reibungskoeffizienten, und der Breiteverteilung v_s ab, welche alle in einem neu definiertem Krümmungsparameter vereint werden können. Dies erlaubt eine objektive Definition von schwach, moderat und stark gekrümmter Strömung. Das lineare Modell entspricht dem asymptotischem Verhalten für infinitesimale Krümmung. Eine Untersuchung von natürlichen Flussströmungen hat gezeigt, dass Unterschiede zwischen linearen und nicht-linearen Modellen relevant sind.

Ausserdem sind die Aussenuferzellen erfolgreich mit einem nicht-linearen $k-\varepsilon$ Turbulenzmodell simuliert worden.

Wie vorher erwähnt, haben die Experimente in der kleinen Rinne alle Erwartungen übertroffen. Dies hatte zur Folge, dass eine Analyse der Experimente mit der grossen Rinne nicht im Rahmen dieser Dissertation diskutiert werden konnte. **Teil V**, “Laufende Forschung”, beschreibt die noch laufende Forschung.

Teil VI fasst die Hauptfolgerungen dieser Dissertation zusammen.

TABLE OF CONTENTS

Acknowledgements	i
Summary	iv
Résumé	vii
Samenvatting	x
Zusammenfassung	

PART 0 INTRODUCTION

0.1 Motivation and objectives	0.1
0.2 Outline of dissertation	0.4

PART I INSTRUMENTATION AND EXPERIMENTAL SET-UP

I.0 Introduction	
I.1 Acoustic Doppler Velocity Profiler (ADVP) and Experimental Set-up	I.1
1 Acoustic Doppler Velocity Profiler (ADVP)	I.1
2 Small-flume experiments	I.4
3 Large-flume experiments	I.5
I.2 Improving Acoustic Turbulence Measurements	I.11
1 Introduction	I.11
2 Principle of Acoustic Doppler Velocimetry (ADV)	I.12
3 Noise reduction by optimizing the ADV configuration	I.15
3.1 Principle of ADV optimization	I.15
3.2 ADVP instrument and experimental set-up	I.21
3.3 Experimental verification	I.22
4 Noise reduction by increasing the signal-to-noise ratio (SNR)	I.28
5 Conclusions	I.31

PART II EXPERIMENTAL OBSERVATIONS

II.0 Introduction	
II.1 Mean Flow and Turbulence in Open-Channel Bend	II.1
1 Introduction	II.1
2 Experimental installation	II.1
3 Experimental results	II.6
3.1 Time-averaged velocities	II.6
3.2 Turbulent normal stresses	II.8
3.3 Turbulent shear stresses	II.9
3.4 Mean-flow and turbulent kinetic energy	II.9
4 Discussion	II.10
5 Summary and Conclusions	II.11

II.2	Bend-Flow Simulation Using 2D Depth-Averaged Model	II.15
II.3	Experiments on Flow in a Strongly Curved Channel Bend	II.19
1	Introduction	II.19
2	Theoretical considerations	II.19
3	The experiments	II.21
4	Experimental results	II.23
4.1	Velocity distribution	II.23
4.2	Secondary circulation and velocity redistribution	II.23
5	Conclusions	II.24
II.4	Secondary Currents Measured in Sharp Open-Channel Bends	II.27
1	Introduction	II.27
2	The experiments	II.29
3	Experimental results and analysis	II.29
3.1	Centerline evolution of secondary circulation	II.29
3.2	Three-dimensional flow patterns	II.30
4	Conclusions	II.34
II.5	Conclusions	II.37

PART III ***FUNDAMENTAL RESEARCH***

III.0	Introduction	
III.1	Momentum Transport in Sharp Open-Channel Bends	III.1
1	Introduction	III.2
2	Analysis of experimental data	III.3
2.1	The experiment	III.3
2.2	Theoretical considerations	III.6
2.3	Downstream momentum equation	III.9
2.4	Depth-integrated downstream momentum equation	III.13
3	Theoretical model and mathematical analysis	III.14
3.1	Linear model	III.16
3.2	Non-linear model	III.17
4	Relevance to engineering practice	III.20
5	Conclusions	III.20
III.2	Secondary Flow in Sharp Open-Channel Bends	III.27
1	Introduction	III.28
2	Theoretical basis and previous work	III.30
2.1	Cross-stream motion and downstream vorticity	III.30
2.2	Current state of knowledge	III.32
2.3	Kinetic energy transfer between mean flow and turbulence	III.38

3	Present objectives	III.40
4	Analysis of experimental data	III.41
4.1	The experiment	III.41
4.2	Experimental results	III.43
4.3	Analysis of the centre-region cell	III.46
4.4	Analysis of the outer-bank cell	III.48
4.5	Kinetic energy transfer	III.52
5	Conclusions	III.54
III.3	Turbulence Characteristics in Sharp Open-Channel Bends	III.61
1	Introduction	III.61
2	The experiment	III.63
3	Experimental results	III.65
4	Analysis	III.68
4.1	Transport equation for k	III.68
4.2	Turbulence structure	III.73
4.3	Discussion	III.77
5	Influence of streamline curvature on turbulence structure	III.78
5.1	Theoretical considerations	III.78
5.2	Experimental observations	III.79
5.3	Discussion	III.81
6	The curvature Richardson number	III.83
7	Conclusions	III.84
III.4	Turbulence Structure in Sharp Open-Channel Bends	III.91
1	Introduction	III.91
2	The experiment	III.92
3	Experimental results	III.94
4	Analysis of velocity fluctuations and of turbulence structure	III.97
4.1	Width-coherent velocity fluctuations	III.97
4.2	Decomposition of the velocity fluctuations	III.98
4.3	Bulk-oscillation of the pattern of circulation cells	III.99
4.4	Decomposition of the turbulent stresses	III.100
4.5	Spectral analysis of the structure of turbulence	III.102
5	The influence of streamline curvature	III.106
6	Discussion and conclusions	III.109
III.5	Conclusions	III.113

PART IV *APPLIED RESEARCH*

IV.0 Introduction

IV.1 Non-Linear Modeling of Secondary Flow and Vertical Flow Structure in Open-Channel Bends

	IV.1
1 Introduction	IV.1
2 Mathematical framework	IV.3
3 Approaches of model closure	IV.6
4 The experiments	IV.7
5 Linear approach of closure	IV.10
6 Non-linear approach of closure	IV.13
6.1 Existing non-linear models	IV.13
6.2 Non-linear-model equations	IV.13
6.3 Validation	IV.15
6.4 Parameter reduction	IV.17
7 Linear vs. non-linear model	IV.20
8 Relevance of non-linear model and practical application	IV.22
8.1 Theoretical background	IV.23
8.2 Practical application	IV.24
9 Conclusions	IV.26
Annex 1 Derivation of linear and non-linear-model equations	IV.30
Annex 2 Transversal gradients in non-linear model	IV.32
Annex 3 Solution procedure of the non-linear closure submodel	IV.34

IV.2 Simulation of Secondary Flow in Curved Channels IV.35

1 Introduction	IV.35
2 The mathematical model	IV.36
3 Physical model data	IV.38
4 Comparison of measured with computed flow field	IV.39
5 Conclusions	IV.41

IV.3 Conclusions IV.43

PART V *WORK IN PROGRESS*

V.1 Experimental observations and fundamental research	V.1
V.2 Applied research	V.2

PART VI *CONCLUSIONS*

VI.1 Introduction and objectives	VI.1
VI.2 Conclusions	VI.1

Curriculum Vitae

PART 0

INTRODUCTION

0.1	Motivation and objectives	0.1
0.2	Outline of dissertation	0.4

0.1 Motivation and objectives

Rivers are the arteries of our planet: they shape our landscapes, irrigate our lands, supply us with drinking water and food and constitute important connecting links. But rivers also frequently cause devastation: they erode fertile land and endanger property, inundate vast areas of land and spread disease.

Mankind has always tempted to tame its rivers by exploiting its resources and seeking protection against its threats. In his book “L’Hydrauliques dans les Civilisations Anciennes”, P.L. Viollet¹ (2000) gives examples of human interventions in the river network that date back 5000 years. Although tempting for so long, mankind is still far from mastering its rivers, as is all-too-often tragically illustrated in all parts of the world. In his plenary lecture “Flood disasters: lessons from the past – worries for the future” at the 28th IAHR-congress in Graz (Austria), Berz² (1999) states: “Flood disasters account for about a third of all natural catastrophes throughout the world (by number and economic losses) and are responsible for more than half of the fatalities. Trend analyses reveal that major flood disasters and the losses generated by them have increased drastically in recent years”.

In a perpetual dynamic process, mankind has always tempted to adapt the river network to its requirements: with every intervention, mankind not only enhanced its understanding of the river system, but inadvertently also discovered new unresolved problems and additional requirements, leading to an ever-extending list of concerned disciplines: fluid dynamics, hydraulics, hydrology, erosion and sedimentation, geomorphology, geology, biology, chemistry, mathematics, etc. Recent nominations such as computational fluid dynamics, morpho-dynamics, eco-hydraulics, fluvial geomorphology, etc., readily indicate that these different disciplines, which cover a wide range of time and length-scales, are strongly interrelated. Due to their complexity, a sound understanding of the relevant physical mechanisms and processes will always be essential in river projects, and this irrespective of the available computational capacity.

This PhD can be situated in the discipline of **fluid dynamics applied to river flow**, i.e. it investigates the dynamics of the mean-flow field and the turbulence in the river environment, thereby always keeping in mind the interactions with other disciplines. For example: some details of the three-dimensional flow field are relevant for the geomorphologic development of the river, some characteristics of the turbulence are relevant for the water quality and the spreading and mixing of pollutants, or some flow and turbulence characteristics are relevant in mathematical simulation techniques. Moreover, there are mutual interactions with other related fields of fluid dynamics such as meteorology, aeronautics, turbo-machinery, etc.

1 Viollet, P.-L. (2000). “L’hydraulique dans les civilisations anciennes : 5000 ans d’histoire”. Presses de l’Ecole Nationale des Ponts et Chaussées, Paris.

2 Berz, G. (1999). “Flood disasters: lessons from the past – worries for the future”. 28th IAHR-congress, Post Congr. Vol.: General & Special Lectures, Graz Univ. Techn., Austria, 9-16.

Some recent evolutions in the river management are illustrative of this growing complexity. After WWII, river interventions mainly intended to improve navigation and flood control, to generate hydropower and to reclaim fertile soil on the river, which required knowledge on the mean-flow field and the river morphology. Huge experimental and mathematical research efforts were undertaken that led to a good understanding of the river behavior in simplified geometries. Numerous river canalization works were undertaken that imposed such a simplified geometry upon the river whereby the reclaimed land was used for urban development or industry, leading to a variety of new unresolved problems, such as devastating inundations of the reclaimed land, degradation of the chemical and biological river quality due to the imposed un-natural geometry and the over-drainage of waste water by the industry. These problems evoked the definition of new ecologically-related requirements and the present tendency to renaturalize rivers by letting them more freely shape their course in their alluvial plane, which is recognized as a rich biotope and as an important factor in flood defense systems by providing buffer capacity. The simultaneous satisfaction of the traditional technical requirements and the recent ecological requirements is often designated with the in-vogue term “**sustainable development**”. The design of river renaturalization works, flood protection schemes or navigation improvement works now require an understanding of the **three-dimensional flow field** and the river morphology in complicated geometries, whereas insight in the role of **turbulence** is essential in problems related to the chemical and biological quality of the river.

During the same time-span, also research methods have evolved: both the available computational capacity and the cost of experimental research have exploded, leading to a predominance of the former. At present, simulations of the three-dimensional flow field in complicated geometries are already feasible for flow domains of moderate size and within a prescribed morphology, and it is beyond doubt that simulating large flow domains and morphological interactions will become feasible in a future. The increased computational capacity and developments in fields like electronics, acoustics and optics enable to investigate experimentally the fine details of the flow field as well as the characteristics of turbulence. However, due to the enormous cost of high-tech experimental research, the overwhelming majority of investigations are limited to straight uniform flows and **hardly any experimental data exist on the three-dimensional flow field and the turbulence in complicated geometries.**

Contradictory, the recent explosion of computational capacity has often impoverished research: there is a tendency to credit blindly the results of numerical simulations, not in the least due to their colorful presentation including spectacular animations. It is all-too-often forgotten that due to the lack of research on turbulence in three-dimensional open-channel flows, mostly straightforward extensions of straight-uniform-flow turbulence models are adopted without sufficient validation, and that due to the lack of experimental data on the three-dimensional flow field in complicated geometries, numerical models are insufficiently validated to be a reliable tool for river development predictions. As mentioned before, a **sound understanding of the relevant physical mechanisms and processes** will always be essential in river projects, and this irrespective of the available computational capacity.

These critical remarks are at the basis of this PhD that, starting from detailed experimental measurements in a three-dimensional flow, investigates the mean-flow field and the turbulence as well as the underlying physical mechanisms and processes. Such an experimental investigation is rendered feasible by the availability of a powerful Acoustic Doppler Velocity Profiler (ADVP), developed in our laboratory (see chapters I.1-2). We have chosen to investigate the flow in an open-channel bend as a generic case of three-dimensional flow, because it contains all the complexities of a three-dimensional flow in a simple geometry. A definition sketch of a reach of an open-channel bend is given in Fig. 0.1; it indicates a multi-cellular pattern of secondary circulation (also called helical motion), which will play an important role in this dissertation.

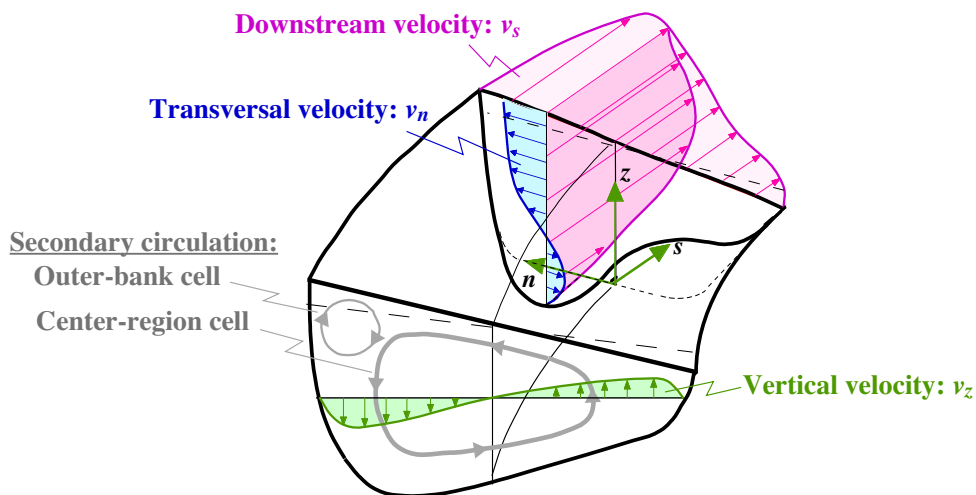


Fig. 0.1: Definition sketch of curved open-channel flow

The principal aims of this PhD are:

- To provide a high-quality data base on three-dimensional open-channel flow, including all three mean velocity components and all six Reynolds stresses on a fine grid.
- To document interesting features of the flow field and the turbulence, such as the multi-cellular pattern of secondary circulation, the curvature influence on the turbulence, etc.
- To gain insight in the relevant physical mechanisms and processes underlying these features.
- To apply the acquired knowledge in an engineering sense, mainly by evaluating, improving and developing numerical simulation techniques.

Accordingly, the core of this dissertation is structured into three parts, i.e. experimental observations, fundamental research and applied research, as illustrated by Fig. 0.2. Experimental observations on the mean flow field and the turbulence were first made in a small low-budget laboratory flume (see chapter I.1), which was mainly intended to test the feasibility of the project. These small-flume experiments yielded a wealth of high-quality data and documented some interesting flow features. Subsequently, fundamental research was done on the physical mechanisms and processes underlying these observations, mainly by making term-by-term evaluations of the flow equations based on the experimental data and by investigating the instantaneous flow behavior. With applied research is meant the evaluation, improvement and development of engineering methods,

mainly numerical simulation techniques. From this fundamental and applied research on the small-flume experiments, new questions emerged, that lead to the design of extended series of experiments in a new, larger and better equipped laboratory flume (chapter I.1). Obviously, the three parts are not independent but profit from mutual interactions. The contents of this dissertation are outlined more in detail in the following.

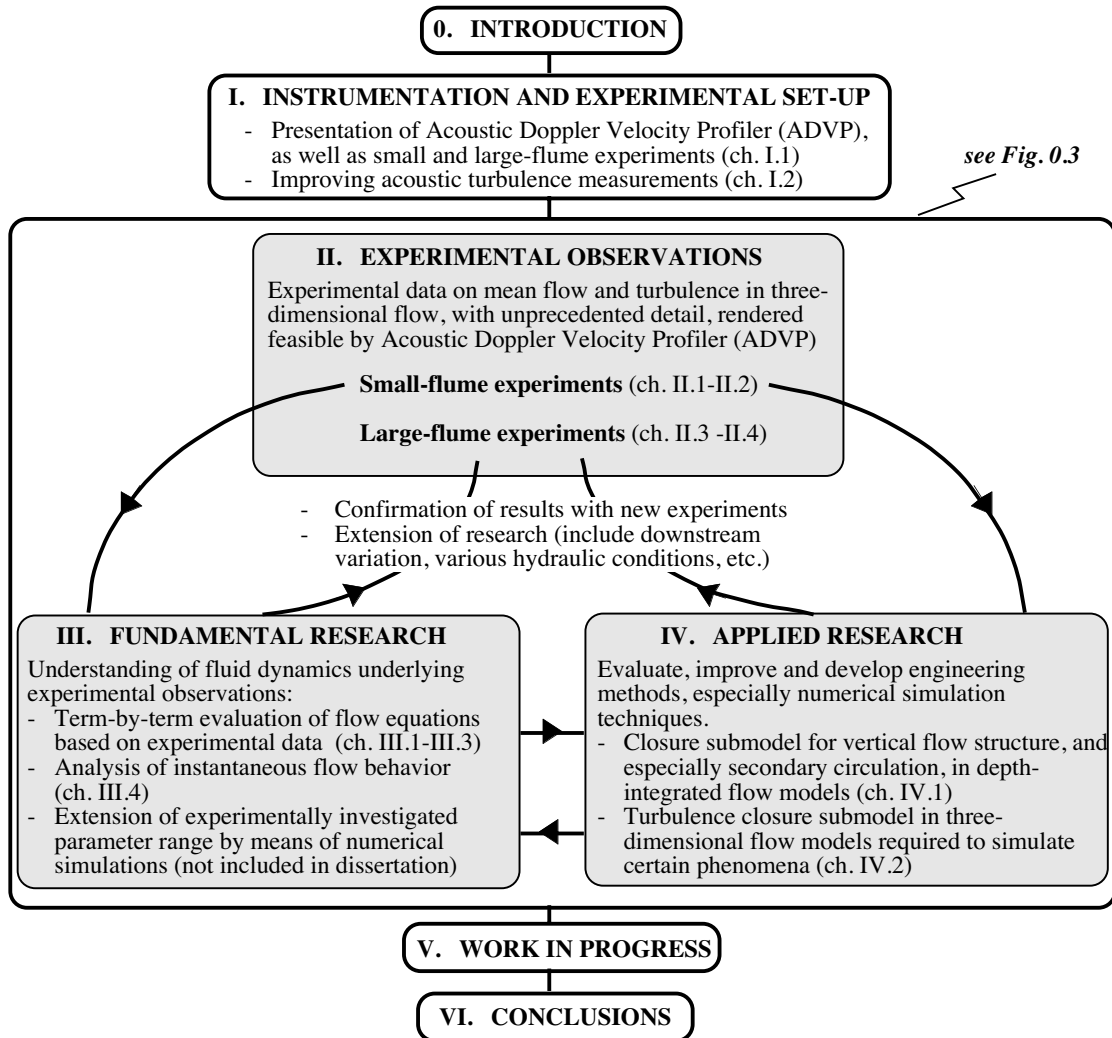


Fig. 0.2: Outline of dissertation

0.2 Outline of dissertation

As mentioned above and shown in Fig. 0.2, this **INTRODUCTION** will be followed by **PART I** “Instrumentation and experimental set-up” in which the Acoustic Doppler Velocity Profiler (ADVP) and the small and large-flume experiments, are presented (chapter I.1). Furthermore, some efficient ways to improve turbulence measurements by means of Acoustic Doppler Velocimetry (ADV) are proposed (chapter I.2).

Part I is followed by the core of this dissertation, structured into three parts: experimental observations, fundamental research and applied research, whose outline is schematized in the “organigramme”, Fig. 0.3, and described below.

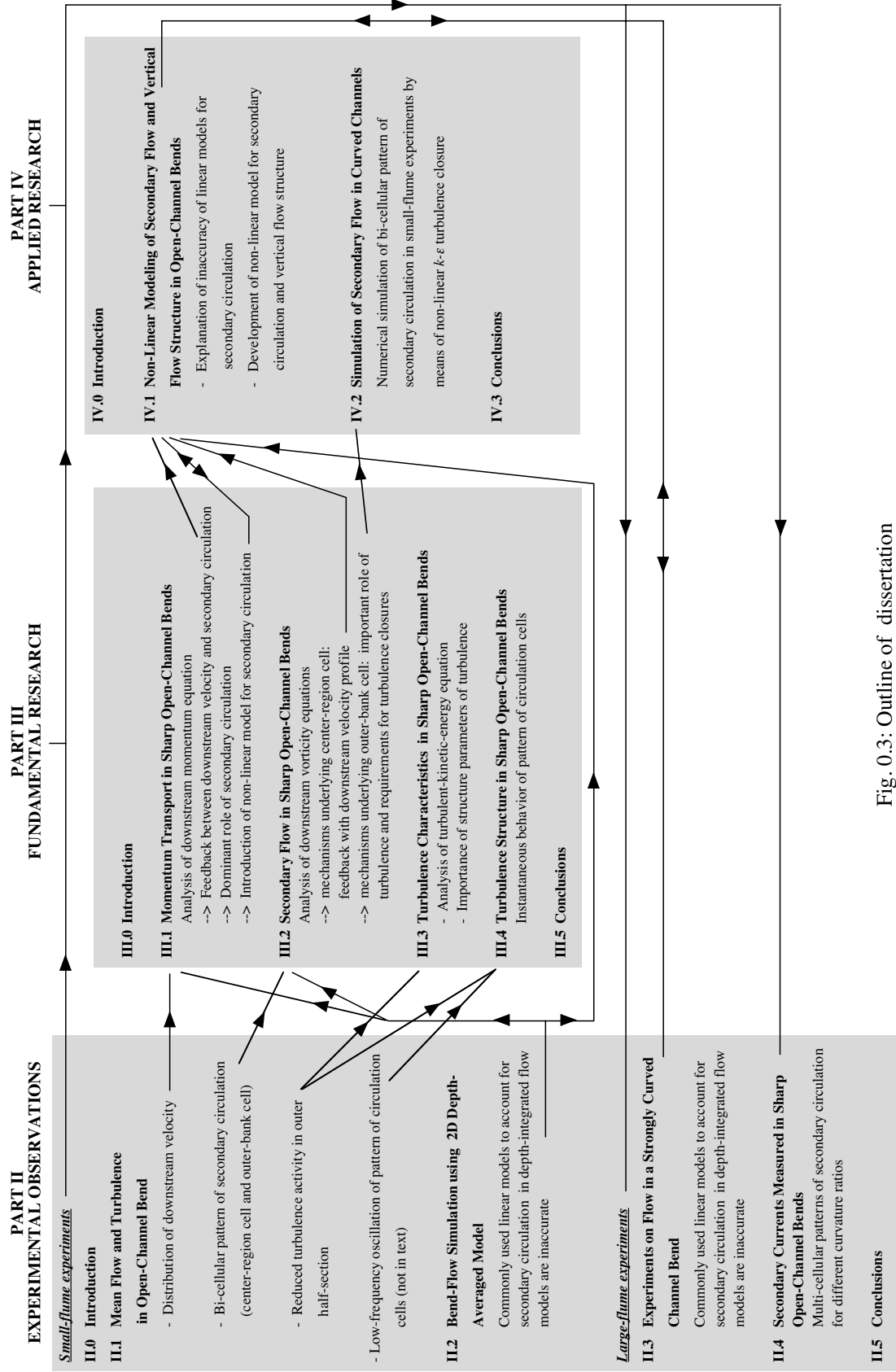


Fig. 0.3: Outline of dissertation

PART II “Experimental observations” presents experimental data and highlights some interesting observations. This dissertation, however, only presents data that will subsequently be analyzed in Parts III and IV. Chapter II.1 presents the working principle of the ADV, the data analysis techniques, and the principal data of the small-flume experiments, being the downstream velocity distribution, the pattern of secondary circulation cells, the distributions of the Reynolds stresses and the distributions of the mean flow as well as the turbulent kinetic energy. In chapter II.2 the linear models that are commonly used to account for the influence of the secondary circulation in the depth-integrated flow equations are compared to these experimental data and shown to be inaccurate. Chapter II.3 presents some data of the large-flume experiments, that confirm the inaccuracy of these linear models and that are subsequently used in chapter IV.1 to validate a proposed non-linear model. Chapter II.4 presents multi-cellular patterns of secondary circulation measured in the large-flume experiments for different degrees of curvature. Chapter II.5 summarizes the main conclusions of part II.

PART III “Fundamental research” analyzes the mechanisms and physical processes underlying the observations made in the small-flume experiments, chapters II.1-II.2 (see Fig. 0.3), mainly by making term-by-term evaluations of the relevant flow equations as well as by investigating the instantaneous behavior of the flow. The distribution of the downstream velocity, analyzed in chapter III.1, highlights the important role played by the secondary circulation. The analysis of the bi-cellular pattern of secondary circulation in chapter III.2 points to the important dynamical role of the turbulence. Finally, some observations on the turbulence, such as the reduced turbulence activity and the instantaneous behavior of the pattern of circulation cells are analyzed in chapters III.3 and III.4. Chapter III.5 summarizes the main conclusions.

PART IV “Applied research” aims to apply the acquired knowledge by evaluating, improving and developing engineering methods, and especially numerical simulation techniques. Chapter IV.1 proposes a non-linear-model to account for the influence of the secondary circulation in the depth-integrated flow equations that compares well with experimental data from the small and the large-flume experiments. Based on the results of chapter III.2, chapter IV.2 reports successful numerical simulations of the observed multi-cellular patterns of secondary circulation with a non-linear $k-\varepsilon$ turbulence closure.

This dissertation almost exclusively concerns the small-flume experiments, despite the fact that the overwhelming majority of data were gathered in the large-flume experiments. As mentioned in chapter I.1, the small-flume experiments were intended as a feasibility test of the project and measurements were only made in the outer half of one cross-section under one set of hydraulic conditions, whereas entire cross-sections all around the flume were measured under different hydraulic conditions and over different bottom configurations in the large-flume experiments. However, the small-flume experiments yielded results beyond all expectations that form the core of this dissertation. As a side

effect, the detailed analysis of the large-flume experiments has not yet been accomplished and a lot of work is still in progress, as indicated in the **PART V** “Work in progress”. The final **PART VI** of this dissertation summarized the principal **CONCLUSIONS**.

Note: This dissertation is mainly a compilation of published and submitted journal and congress papers as well as papers that are being prepared for submission. By making each one of them auto-consistent and intelligible, repetition of some parts (such as the presentation of the experimental setup) could not be avoided. A literature review of the various investigated topics is given in the relevant papers.

PART I

INSTRUMENTATION AND EXPERIMENTAL SET-UP

I.0	Introduction	
I.1	Acoustic Doppler Velocity Profiler (ADVP) and Experimental Set-up	I.1
I.2	Improving Acoustic Turbulence Measurements	I.11

I.0 Introduction

This PhD relies on a high-tech velocity meter, the Acoustic Doppler Velocity Profiler (ADVP), developed in our laboratory. This instrument as well as its different configurations adopted are briefly presented in **chapter I.1(1)**.

Experiments were made in two experimental infrastructures. First, a limited series of experiments was conducted in a small-flume, with the aim of testing the feasibility of the project. Subsequently, extended series of experiments were done in a large and optimized laboratory flume. Both experimental flumes, the hydraulic conditions, the measuring strategies and the measuring grids are presented in **chapter I.1(2-3)**.

In the framework of this PhD, some methods were developed that improve acoustic turbulence measurements. They are presented and illustrated in **chapter I.2**.

I.1 Acoustic Doppler Velocity Profiler (ADVP) and Experimental Set-up

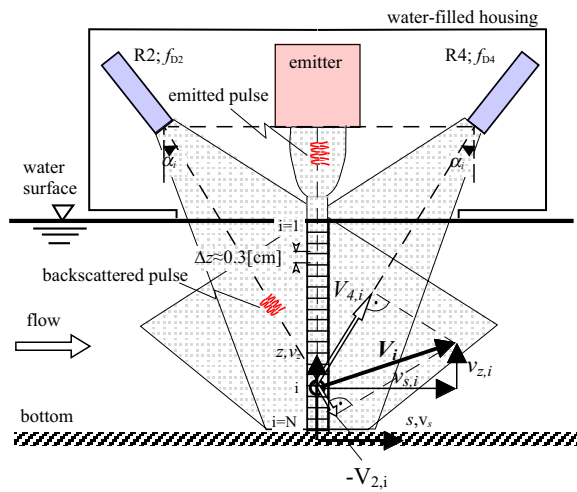
1 Acoustic Doppler Velocity Profiler (ADVP)

This PhD relies on the availability of a high-tech velocity meter, the Acoustic Doppler Velocity Profiler (ADVP), developed in our laboratory. The ADVP consists of a central emitter surrounded by four receivers (Fig. I.1), each of them simultaneously measuring a quasi-instantaneous velocity component along an entire water column. This gives sufficient information to obtain the mean velocity vector $\bar{v}(\bar{v}_s, \bar{v}_n, \bar{v}_z)$, the fluctuating velocity vector $\bar{v}'(v'_s, v'_n, v'_z)$, all Reynolds stresses $\overline{v'_j v'_k}$, and all higher-order turbulent correlations $\overline{v_j'^a v_k'^b}$ ($j, k = s, n, z$; a, b integer; the overbar denotes time-averaged values). The ADVP has important advantages over most commercially available velocity meters:

- It does not measure point-by-point, but it measures simultaneously profiles along an entire water column, which enables to do measurements much faster and on much denser grids than with point-by-point instruments. This characteristic allowed to investigate extensively the flow field and the turbulence in open-channel bends under different hydraulic conditions (see sections 2 and 3).
- Its profiling capacity furthermore enables to investigate the bulk behavior of large flow structures, such as cells of secondary circulation (see chapter III.4), or to investigate coherent flow structures (ejections, sweeps, etc.).
- It measures simultaneously four quasi-instantaneous velocity components, whereas three would be sufficient to derive the three-dimensional velocity field. However, the fourth component gives a redundant information that can be used to improve the quality of the velocity measurements and especially the resolution of the turbulence (see chapter I.2).

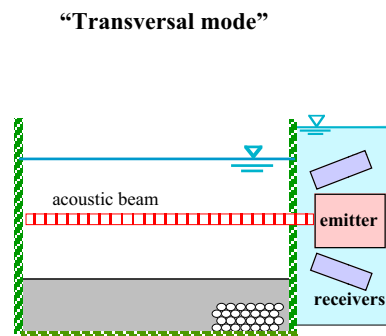
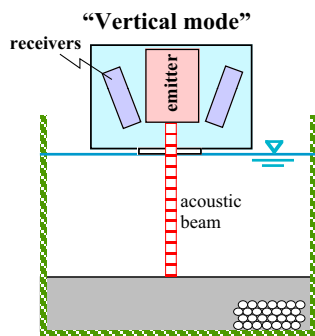
The ADVP is being developed in our laboratory and it is amply reported in literature (Lhermitte and Lemmin, 1994; Shen and Lemmin, 1996 and 1997; Lemmin and Rolland, 1997; Rolland and Lemmin, 1997; Hurther and Lemmin, 1998 and 2001)¹. Therefore, its working principle is only briefly explained in chapters I.2 and II.1.

¹ Lhermitte, R., & Lemmin, U. (1994). "Open-channel flow and turbulence measurement by high-resolution Doppler sonar." *J. Atm. Oc. Techn.*, AMS, 11(5), 1295-1308.
 Shen, C., & Lemmin, U. (1996). "A tristatic Doppler velocity profiler and its application to turbulent open-channel flow." *Advances in Turbulence VI*, P. A. Monkewitz and S. Gavrilakis, eds., Kluwer Academic Publications, Lausanne, 483-486.
 Shen, C., & Lemmin, U. (1997). "Ultrasonic scattering in highly turbulent clear water flow." *Ultrasonics*, 35, 57-64.
 Lemmin, U., & Rolland, T. (1997). "Acoustic velocity profiler for laboratory and field studies." *J. Hydr. Engng*, ASCE, 123(12), 1089-1098.
 Rolland, T., & Lemmin, U. (1997). "A two-component acoustic velocity profiler for use in turbulent open-channel flow." *J. Hydr. Res.*, IAHR, 35(4), 545-561.
 Hurther, D., & Lemmin, U. (1998). "A constant beamwidth transducer for three-dimensional Doppler profile measurements in open channel flow." *Meas. Sciences Techn.*, 9(10), 1706-1714.
 Hurther, D., & Lemmin, U. (2001). "A correction method for turbulence measurements with a 3-D acoustic Doppler velocity profiler." *J. Atm. Oc. Techn.*, AMS, Vol.18, 446-458.

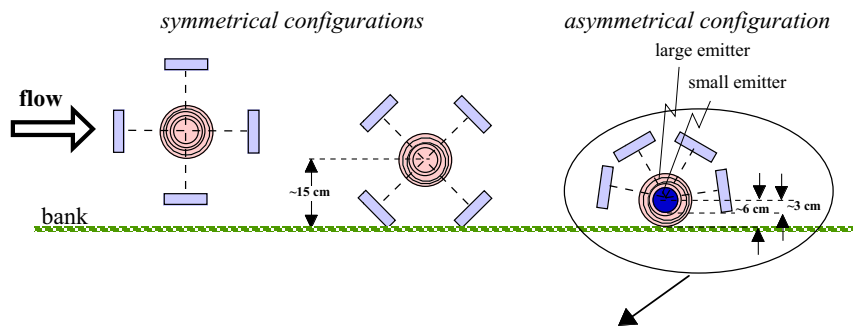


Advantages of ADVP

- Simultaneous all quasi-instantaneous velocity components
 - > all 3 mean velocity components
 - all 6 Reynolds stresses
 - all higher-order turbulent correlation
- Profiler: simultaneous entire water column
 - > saves time and enables to cover very fine grids
 - > enables to investigate bulk-behavior of large flow structures and instantaneous coherent flow structures
- High temporal and spatial resolution



Planview for "vertical mode"



Asymmetrical configuration

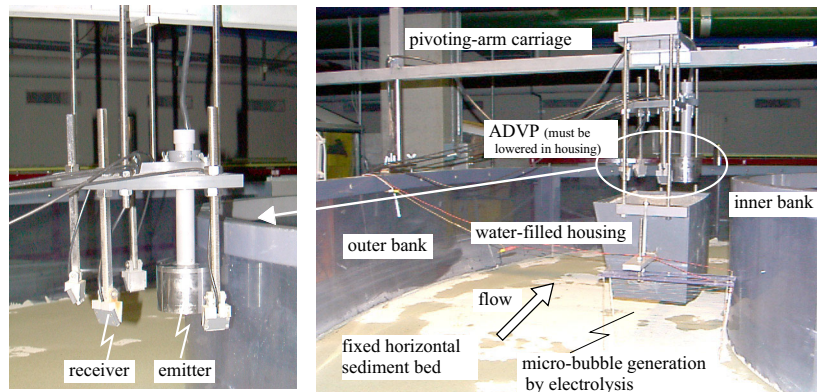


Fig. I.1: Acoustic Doppler Velocity Profiler (ADVP)

Within the framework of this PhD, the measuring technique has been improved, mainly by optimizing the geometrical configuration of the ADVP.

Previously, measurements were made along vertical water columns with the ADVP mounted in a water-filled housing that touches the water surface, whereby the four receivers were aligned in longitudinal and transversal direction in a symmetrical configuration, as indicated in Fig. I.1. Although it might seem like a trivial difference, a considerable improvement in turbulence measurements is obtained by aligning the four receivers symmetrically along the bisectors of the longitudinal and transversal planes (Fig. I.1), as theoretically explained and illustrated in chapter I.2.

This configuration does not allow to measure closer than about 15 cm to an obstacle, such as a vertical bank (or a bridge pier,...). Therefore, an asymmetrical configuration, with all four receivers at the same side of the emitter, has been developed that enables to measure as close as about 3 cm to an obstacle (Fig. I.1). Both configurations were applied in the large-flume experiments (see section 3).

Furthermore, in the small-flume experiments (see section 2), measurements of transversal water columns were made through the vertical Plexiglas bank of the flume, with the ADVP placed in a water-filled box attached to the bank (Fig. I.1). This configuration is completely non-intrusive (the “vertical configuration” somewhat perturbs the water surface) and allows to measure even closer to the bank. It has not been adopted in the large-flume experiments since the flume’s width of 1.3 m could not be covered.

Finally, acoustic measurements based on the Doppler principle are often hindered by a lack of scattering targets in the flow. Within the framework of this PhD a method has been developed to add scattering targets, in the form of micro air bubbles, to the flow by electrolysis. It is presented in chapter I.2.

A rich experience has been gained in the study of flow and turbulence in straight-uniform flow (Kironoto and Graf, 1994; Song et al., 1994; Cellino and Graf, 1999; Hurther, 2001)², but this PhD is its first application in a complex three-dimensional flow. Therefore, a first limited series of experiments in a small low-budget laboratory flume was mainly intended to test the ADVP in such flows, and especially to test its capabilities to measure accurately the very weak outer-bank cell of secondary circulation (see Fig. 0.1). These small-flume experiments yielded results beyond all expectations that form the core of this dissertation. They were followed by extended series of measurements in a new and large optimized flume. Both the small and the large-flume experiments are briefly presented in the following.

² Kironoto, B. A., & Graf, W. H. (1994). “Turbulence characteristics in rough uniform open-channel flow.” *Instn Civ. Engrs, Wat., Marit. et Energy*, Vol. 106, 333-344.
 Song, T., Graf, W. H., & Lemmin, U. (1994). “Uniform flow in open channels with movable gravel bed.” *J. Hydr. Res., ASCE*, 32(6), 861-876.
 Cellino, M., & Graf, W. H. (1999). “Sediment-laden flow in open-channels under noncapacity and capacity Conditions.” *J. Hydr. Engng, ASCE*, 125(5), 455-462.
 Hurther, D. (2001). “Sediment transport assessment in suspension flow based on coherent structure characteristics.” *Proc. JFK Student Paper Comp., 29th-IAHR congress, Beijing, China*, 73-82.

2 Small -flume experiments

The small laboratory flume, shown in Fig. I.2, is $B=0.4\text{m}$ wide and has a rectangular cross-section of 0.3m height with boundaries made out of Plexiglas. It consists of an inlet basin (I), followed by a 2m long straight inflow reach (II), a 120° bend with constant centerline radius of curvature, $R=2\text{m}$ (III), a sediment deposition basin (IV), a V-shaped weir (V) and an outlet basin (VI). The overall length of the flume is 6.2m along the centerline. The discharge is regulated by the automatically operated pump, PF, and valve, VF1. The supply (1) and restitution (2) pipes have a diameter of $\phi=200\text{mm}$ and water is recirculated through the laboratory sump (VII).

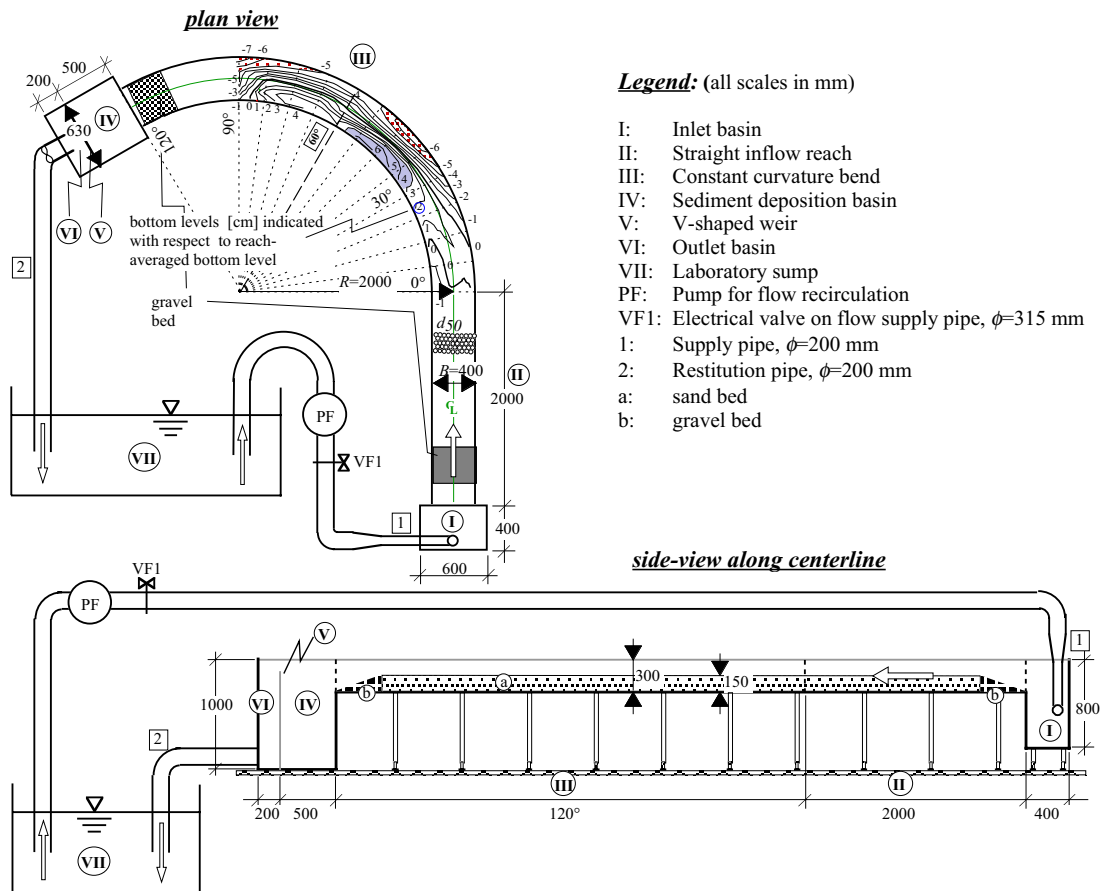
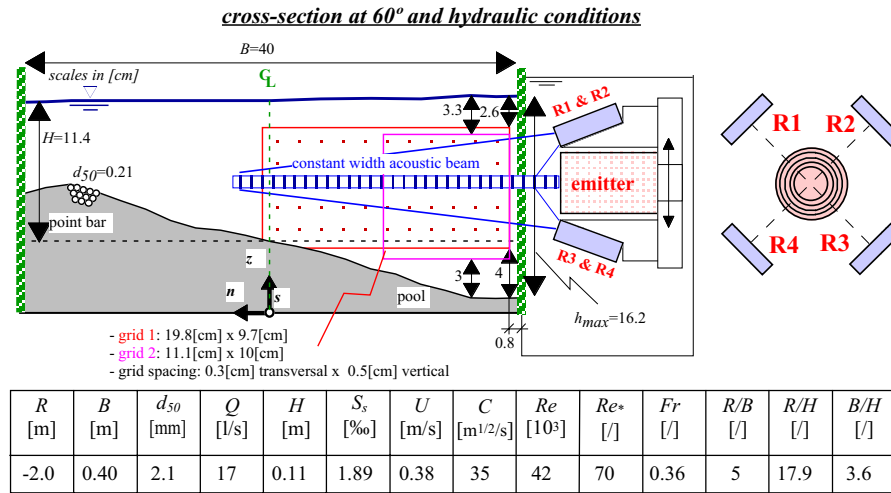


Fig. I.2: Small laboratory flume

As mentioned above, measurements were first done in this small low-budget flume with the aim of evaluating the capabilities of our ADVP to measure accurately the flow and the turbulence in an open-channel bend. The supreme test consists of attempting to measure the outer-bank cell of secondary circulation (see Fig. 0.1) characterized by very weak velocities of $O(1\text{ cm/s})$. Therefore, measurements were made on two overlapping grids in the outer half of one single cross-section at 60° in the bend under one hydraulic condition. Measurements were made along transversal water columns with the ADVP placed in a water-filled box attached to the outer bank. The small-flume experiments were done over the mobile-bottom topography shown in Fig. I.2, which, together with the water surface, was measured with a point gauge. The measuring section at 60° , the measuring grids, the ADVP-configuration and the hydraulic conditions are shown in Fig. I.3.



R : centerline radius of curvature (negative along the n -axis)
 B : channel width
 d_{50} : median grain size diameter of the bed material
 Q : flow discharge
 H : reach-averaged flow depth
 S_s : reach-averaged water-surface gradient on the centerline
 u_* : shear velocity

U : reach-averaged velocity
 C : Chezy friction factor: $C/\sqrt{g}=U/u_*$
 $Fr=U/(gH)^{1/2}$: reach-averaged Froude number
 $Re=UH/\nu$: reach-averaged flow Reynolds number
 $Re^*=u_*k_s/\nu$: reach-averaged particle Reynolds number
 ν : molecular viscosity
 k_s : Nikuradse equivalent sand roughness

Fig. I.3: Measuring section at 60°, measuring grids, ADVP-configuration and hydraulic conditions in small-flume experiments

These small-flume experiments were unexpectedly successful. The most relevant experimental data, including the outer-bank cell of secondary circulation, are presented in chapters II.1 and II.2 and subsequently analyzed in chapters III.1-4.

3 Large -flume experiments

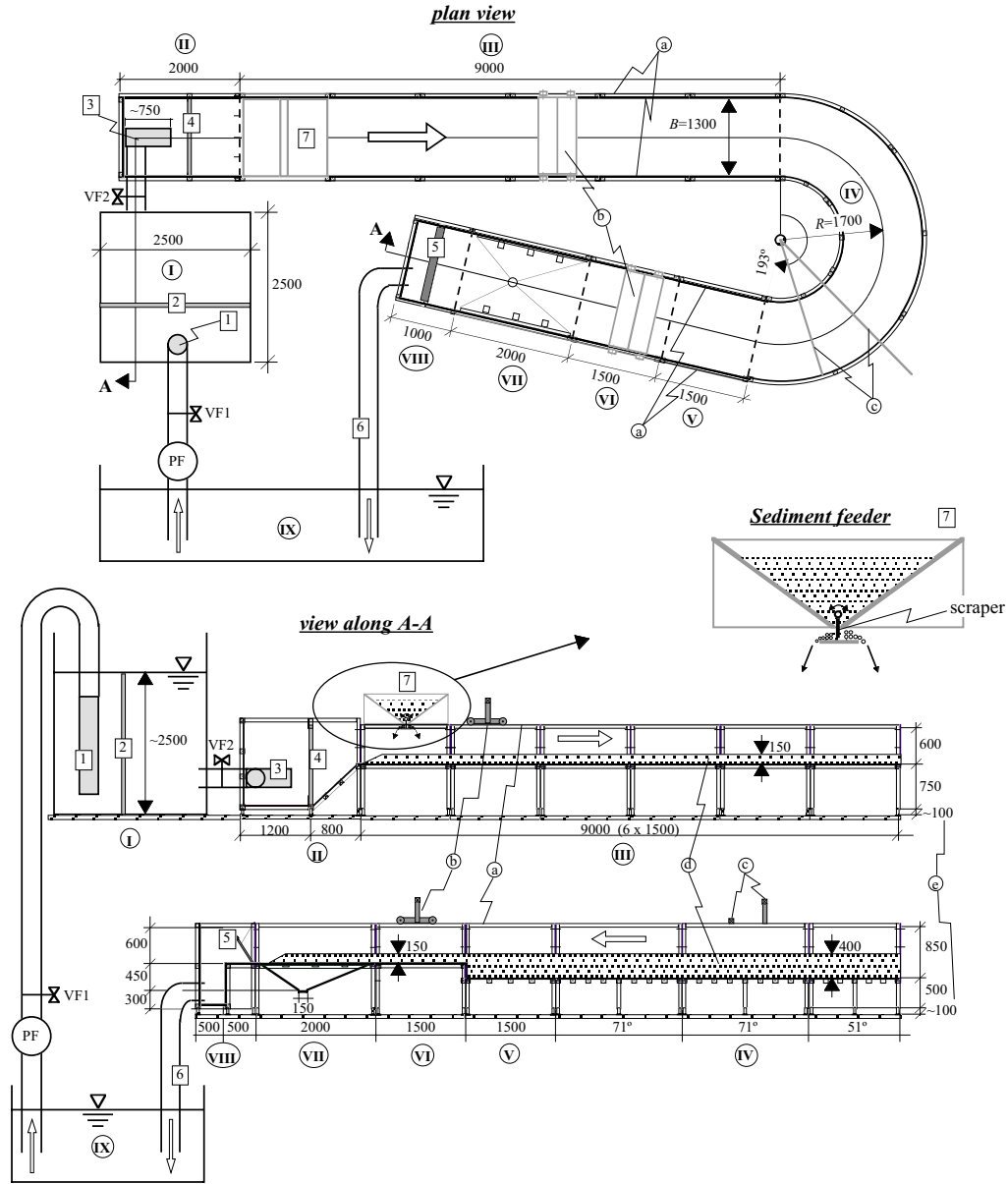
As mentioned above, the small-flume experiments have been followed by extended series of measurements in a new and larger optimized laboratory flume, shown in Fig. I.4, with the aim of:

- confirming the results of the small-flume experiments.
- extending the research by measuring entire cross-sections all along the flume under various hydraulic conditions and for different bottom configurations.
- Investigating new questions that emerged from the small-flume experiments.

The large flume's geometry is primarily determined by characteristics of the ADVP. Its positioning at the water surface (Fig. I.6) to measure vertical water columns imposes an optimal flow depth between $0.1\text{m} < H < 0.2\text{m}$. In order to have a reasonable aspect ratio, $B/H > 6$, a width of 1.3 m has been adopted. By considering a sharp bend, $R/B=1.31$, the curvature effects are more pronounced, hence better visible.

The large laboratory flume (Fig. I.4) has rectangular cross-sections with boundaries made out of Plexiglas. It consists of a 2m long inlet basin (II), followed by a 9m long straight inflow reach (III), a 193° bend with constant centerline radius of curvature, $R=1.7\text{m}$ (IV), a 3m long straight outflow reach (V, VI), a 2m long sediment deposition basin (VII) and a 2m long outflow basin (VIII). The overall length of the flume is 22.7m along the centerline. By covering the sediment deposition basin with a flat Plexiglas plate, the

length of the straight outflow reach can be extended to 5m. The depth of the sections in the straight inflow (III) and outflow (VI, VII) reaches is 0.6m. To allow the study of local bend scour, sections with a depth of 0.85m are foreseen in the bend (IV) and in the straight outflow reach just downstream of it (V). The entire flume is posed on adjustable feet (e) with a maximum height of about 0.1m.



Legend: (all scales in mm)

- | | |
|--|---|
| I: Constant discharge basin | 1: Perforated pipe, $\phi=315$ mm |
| II: Inlet basin | 2: Porous plate filter |
| III: Straight inflow reach (depth 600 mm) | 3: Perforated pipe, $\phi=315$ mm |
| IV: Constant curvature bend (depth 850 mm) | 4: Porous polyether filter 10 ppi, 10 mm thick |
| V: Straight outflow reach (depth 850 mm) | 5: Adjustable water level control weir |
| VI: Straight outflow reach (depth 600 mm) | 6: Restitution pipe, $\phi=315$ mm |
| VII: Sediment deposition basin / straight outflow reach (depth 600 mm) | 7: Sediment feeder |
| VIII: Outlet basin | a: Inclinal guiding rail for carriage |
| IX: Laboratory sump | b: Carriage for straight inflow and outflow reaches |
| PF: Pump for flow recirculation | c: Two pivoting-arm carriages for bendway |
| VF1: Electrical valve on flow supply pipe, $\phi=315$ mm | d: sediment bed |
| VF2: Manual valve on pipe, $\phi=315$ mm, to regulate water level in I | e: adjustable feet |

Fig. I.4: Large laboratory flume

The discharge in the flow recirculation system is regulated by the automatically operated pump, PF, and valve, VF1. The supply pipe has a diameter of $\phi=315\text{mm}$ and the maximum discharge is, $Q=250\text{l/s}$. Water is pumped from the laboratory sump into the constant discharge basin (I) in which the water level is regulated by the manual valve VF2. The porous plate filter (2) and the choice of a water level of about 2.5m ($\sim 15\text{m}^3$ stocking) in the constant discharge basin guarantee the elimination of discharge fluctuations and of air bubbles entrained by the pump. From the constant discharge basin (I), the water flows into the inlet basin (II) through a perforated pipe, $\phi=315\text{mm}$, symmetrically disposed on the flume axis. The inlet basin is connected with the actual test reach by a 45° inclined ramp, which together with the porous polyether filter (4) guarantee stable flow conditions at the entrance of the test reach. At the downstream end of the flume, the water level is controlled by a manually adjustable weir (5). The water flows back into the sump from the outlet basin (VIII) through a restitution pipe (6), $\phi=315\text{mm}$.

When conducting experiments with a mobile bottom, the sediment deposition basin (VII) is uncovered and sediment is continuously fed (7) into the flume near its entrance. Sediment falls from a funnel on a plate, and is moved into the flume by means of a back-and-forth moving scraper. The frequency of the scraper regulates the sediment discharge.

Measuring instruments can be mounted on the carriages (b) and (c). The carriage (b) for the straight flow reaches is guided by a rail (a), that can be given an inclination. The two bend carriages (c) pivot around a pile placed in the center of curvature of the bend. The flume bed is normally covered with a 0.15m thick layer of sand (which is deformed in mobile-bottom experiments) of nearly uniform diameter, $1.6\text{mm} < d < 2.2\text{mm}$.

Measurements of the bottom and the water surface topography are made by moving a set of 8 acoustic limnimeters, mounted on a carriage that covers the width of the flume, along the flume (Fig. I.5).



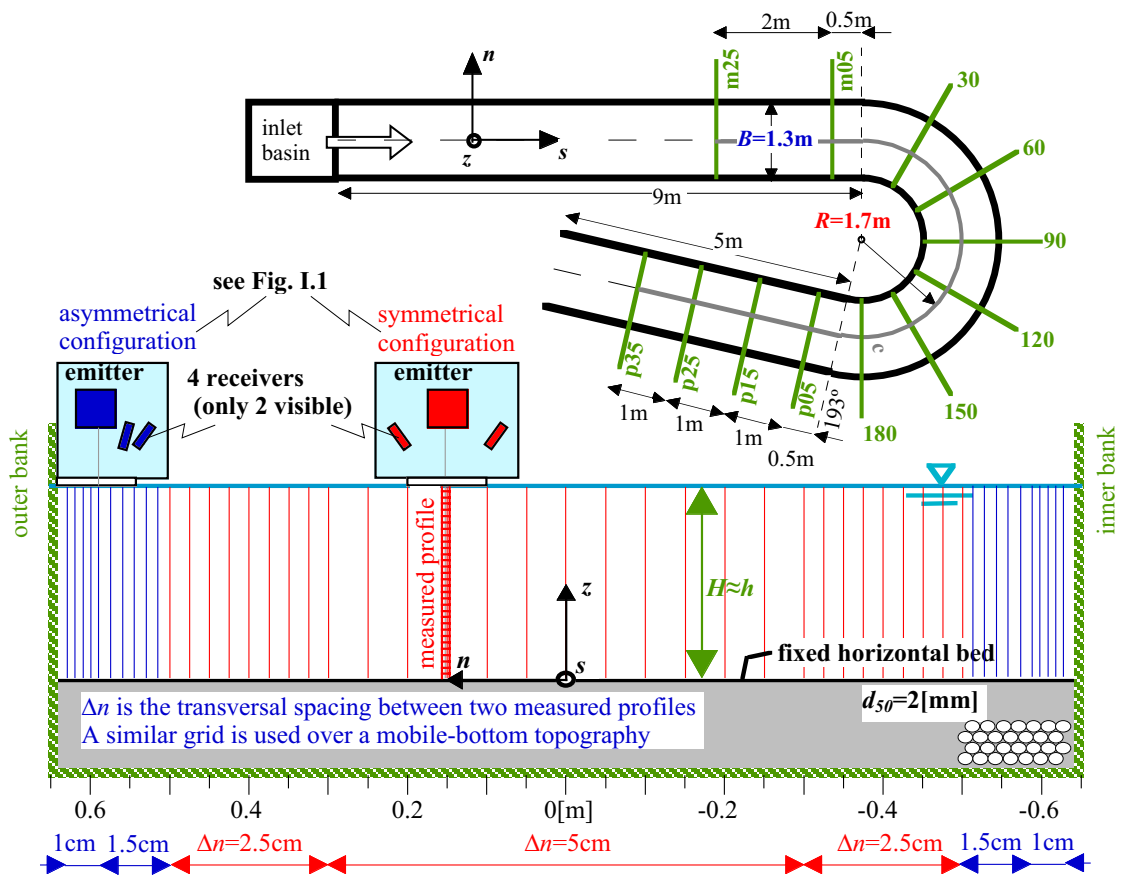
Fig. I.5: Acoustic limnimeters for measuring water-surface and bottom topography

Based on the small-flume experiments, which only considered one outer half-section under one hydraulic condition, a non-linear model for the vertical flow structure and the secondary circulation has been proposed (chapter IV.1) that indicates that the principal

parameters in a curved open-channel flow are the curvature ratio H/R and the spanwise distribution of the downstream velocity. On this basis, measurements in the large-flume were made:

- in entire cross-sections on the fine grid shown in Fig. I.6.
- all along the flume in order to track the downstream evolution of the flow field.
- for three different curvature ratios, H/R , corresponding to the hydraulic conditions indicated in Fig. I.6.
- over a horizontal bottom topography (maximum velocity at the inside) as well as a mobile-bottom topography (maximum velocity at the outside).

The measured sections, the measuring grids, the ADVP-configurations and the hydraulic conditions are indicated in Fig. I.6.



Horizontal-bottom experiments

legend: see Fig. I.3

name	Q [l/s]	H [m]	S_s [‰]	U [m/s]	C [√m/s]	Re [10 ³]	Fr [/]	R/B [/]	R/H [/]	B/H [/]
Q56	56	0.108	1.41	0.40	32	43	0.39	1.31	15.6	12.1
Q89	89	0.159	0.94	0.43	34	69	0.35	1.31	10.6	8.2
Q104	104	0.212	0.49	0.38	35	81	0.26	1.31	8	6.1

Mobile-bottom experiments

Experiments were performed under three hydraulic conditions similar to the ones in the horizontal-bottom experiments. This series of experiments has not yet been analyzed.


Fig. I.6: Measured sections, measuring grids, ADVP-configurations and hydraulic condition in large-flume experiments

First, the series of experiments over a horizontal bottom configuration was made (because its data treatment is less complicated). For each of the three curvature ratios, measurements were first of all made on the centerline, with a streamwise spacing of 0.5m in the straight inflow and outflow reaches and of 15° in the bend. These measurements gave valuable information on the downstream evolution of the mean-flow field and the turbulence. These centerline measurements allowed to identify the cross-section in the bend characterized by the strongest secondary circulation, which was subsequently measured in detail on the fine grid shown in Fig. I.6. For comparison, also the reference cross-section in the straight inlet reach 2.5m upstream of the bend was measured in the same detail. For the middle value of the three curvature ratios investigated, the twelve cross-sections along the flume indicated in Fig. I.6 were measured in detail. The measuring strategy in the subsequent series of experiments over a mobile-bottom configuration is completely similar.

As mentioned before, the small-flume experiments yielded results beyond all expectations and they form the core of this dissertation. As a side effect, the large-flume experiments were somewhat postponed and their detailed analysis is not yet accomplished. This dissertation presents large-flume data in chapters II.3, II.4 and IV.1. More large-flume results will be communicated in literature.

I.2 Improving Acoustic Turbulence Measurements

By K. Blanckaert¹ and U. Lemmin²,

 *Submitted for publication to Journal of Hydraulic Engineering, ASCE)*

Abstract

Although three-receiver Acoustic Doppler Velocimeters (ADV) can accurately measure the three-dimensional mean flow field, their turbulence measurements suffer from parasitical noise contributions. By adding a fourth receiver and optimizing the transducer configuration, the turbulence results can be considerably improved. Redundant information is obtained for all velocity components which theoretically allows to achieve noise-free turbulence measurements. Experiments show that the parasitical noise contribution is not completely eliminated but reduced by an order of magnitude and the useful low-noise frequency range extended by one. Furthermore, the noise levels of the different components can be directly estimated from the redundant information which allows (i) to check the quality of the measurements and the system; (ii) to estimate the accuracy of the turbulence measurements; (iii) to optimally choose the measuring frequency. Good turbulence results with a four-receiver ADV require a sufficiently high acoustic scattering level of the fluid. A simple, low cost and non-polluting technique to enhance the acoustic scattering level by generating micro hydrogen bubbles in the flow is presented and its efficiency is demonstrated.

Keywords

Acoustic Doppler Velocimetry, turbulence measurements, Doppler effect, noise reduction

1 Introduction

Recently, Acoustic Doppler Velocimeters (ADV) have become popular in the field of fluid dynamics. They are applied to study the three-dimensional flow field and turbulence in laboratory applications, as well as in rivers, lakes and the ocean.

ADVs are able to accurately measure the time-averaged flow field. Rolland (1994) and Lemmin and Rolland (1997) suggest an accuracy that is typically better than 4%. High resolution ADV measurements of turbulence are only possible with pulse-to-pulse coherent instruments (Lhermitte and Lemmin, 1994), however, and are known to suffer from parasitical noise contributions. Authors such as Garbini et al. (1982), Lhermitte and Lemmin (1994), and Voulgaris and Trowbridge (1998) have worked on the identification of the different noise sources which have been summarized by Hurther and Lemmin (2001). The noise problem is not specific to the ADV, since all measuring techniques suffer from it.

¹ Res. Assoc., Lab. d'Hydraulique Environnementale, Ecole Polytechnique Fédérale, CH-1015 Lausanne, Switzerland.

² Res. Assoc., Lab. d'Hydraulique Environnementale, Ecole Polytechnique Fédérale, CH-1015 Lausanne, Switzerland.

Hurther and Lemmin (2001) have proposed a direct correction method, referred to as the HL method in this paper by which most of the noise in turbulence measurements with four-receiver ADV instruments can be eliminated. The additional receiver (most ADV only have three receivers) gives redundant information on the vertical velocity component which provides for an estimate of the noise level. This noise level is subsequently subtracted from the longitudinal and transversal components. Their method is uniquely based on the measurements and does not depend on flow or instrument characteristics. They compared profiles of the turbulent normal stresses, the turbulent kinetic energy, the turbulent shear stresses and terms in the energy balance equation measured in a straight, uniform flow with semi-theoretical models in order to demonstrate the effectiveness of the correction method.

This paper refines and complements the HL method. It proposes and illustrates a simpler but better performing method to eliminate the noise on turbulence measurements. By optimizing the ADV geometry, redundant information can be obtained for all three velocity components, instead of only for the vertical component. From this information the (theoretically) noise-free turbulence characteristics can be readily obtained.

ADV instruments are known to perform poorly in clear water characterized by a low acoustic scattering level that is often found in laboratory flumes, the deep ocean or lakes, etc. This paper describes a simple, low cost, non-polluting technique to supply acoustic targets to the flow in the form of micro hydrogen bubbles generated by electrolysis.

First, the principle of Acoustic Doppler Velocimetry will be briefly recalled. Next, the noise reduction method is presented and subsequently validated by measurements done with an Acoustic Doppler Velocity Profiler (ADVP). The ADVP and the experimental conditions are also presented. Finally, the technique used to enhance the acoustic scattering level is described.

The presentation and illustration of the noise reduction by geometrical optimization of the ADV configuration and the description of the acoustic target supply technique do not require an in depth treatment of the underlying acoustics and statistics. For more details on these subjects, reference is made to Hurther and Lemmin (2001).

2 Principle of Acoustic Doppler Velocimetry (ADV)

The principle of Acoustic Doppler Velocimetry (ADV) is illustrated in Fig. 1. An ADV basically consists of two fixed transducers, an emitter and a receiver. The emitter generates an acoustic wave of frequency f_e and wavelength $\lambda_e = c/f_e$ (c is the speed of sound) that propagates through the fluid, is scattered by acoustic targets (see later) moving with the fluid velocity \vec{v} , and finally is detected by the receiver. Due to the target velocity \vec{v} , the wavelength λ_r and the corresponding frequency $f_r = c/\lambda_r$ of the scattered acoustic wave differ from those of the emitted one; the Doppler frequency is defined as the frequency shift of the acoustic wave, induced by the moving target, i.e. $f_D = f_r - f_e$. Fig. 1 summarizes the relation between the Doppler frequency and the projections of the fluid velocity \vec{v} along the emitter and receiver axes, v_e and v_r , respectively: $f_D = f_e/c(v_e + v_r)$.

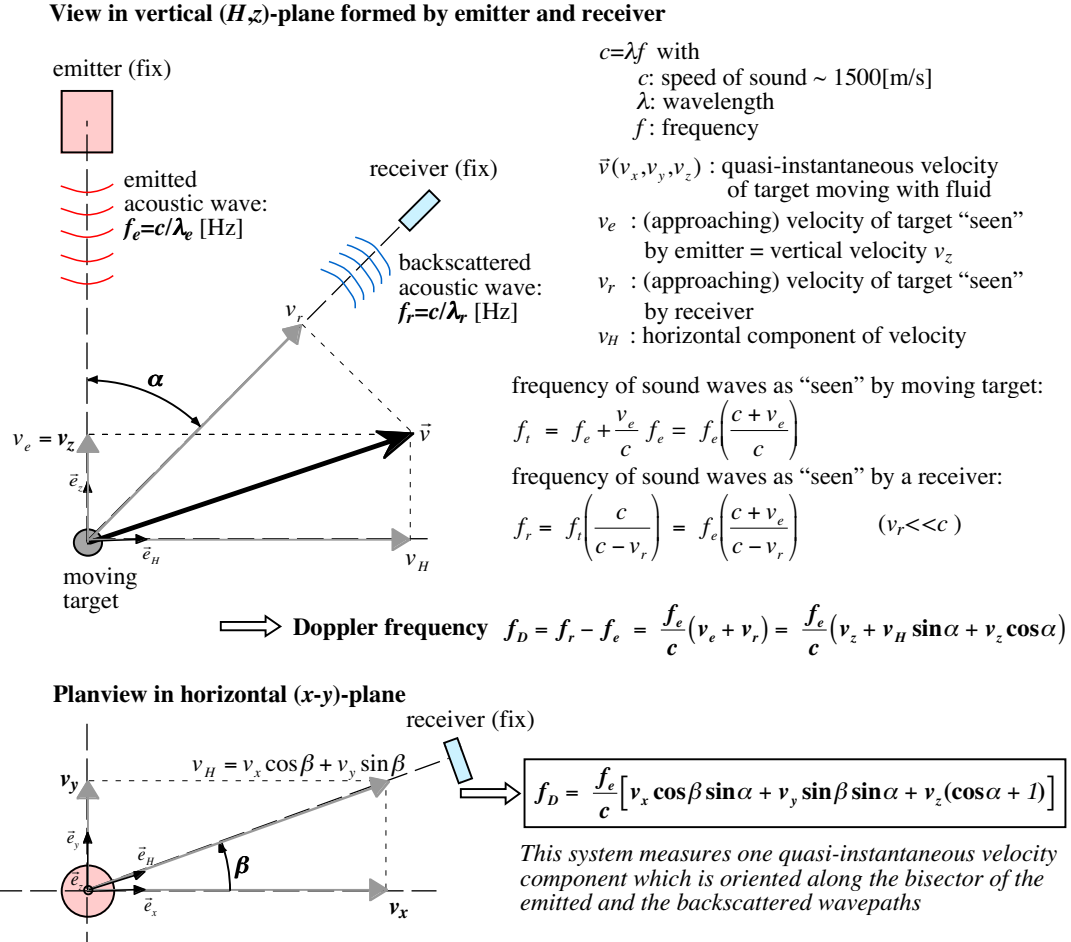


Fig. 1: Principle of Acoustic Doppler Velocimetry (ADV)

In this paper we will adopt a Cartesian reference system (x, y, z) . Furthermore, we will consider ADV configurations with one vertically pointing emitter and receivers inclined at an angle α with respect to the vertical, positioned in a vertical plane placed at an angle β with respect to the (x, z) -plane; the extension to other configurations is straightforward. In this configuration, the measured Doppler frequency f_D relates to the target velocity $\vec{v}(v_x, v_y, v_z)$ as (Fig. 1):

$$f_D = \frac{f_e}{c} [v_x \cos \beta \sin \alpha + v_y \sin \beta \sin \alpha + v_z (\cos \alpha + 1)] \quad (1)$$

It is easy to show that the right-hand side corresponds to the projection of the velocity \vec{v} along the bisector of the emitted and scattered wave paths. The univocal determination of the three-dimensional velocity vector $\vec{v}(v_x, v_y, v_z)$ requires at least three independent estimates of the Doppler frequency which is commonly obtained by surrounding the emitter with three receivers:

$$\begin{bmatrix} v_x(t) \\ v_y(t) \\ v_z(t) \end{bmatrix} = \frac{c}{f_e} \begin{bmatrix} \cos \beta_1 \sin \alpha & \sin \beta_1 \sin \alpha & \cos \alpha + 1 \\ \cos \beta_2 \sin \alpha & \sin \beta_2 \sin \alpha & \cos \alpha + 1 \\ \cos \beta_3 \sin \alpha & \sin \beta_3 \sin \alpha & \cos \alpha + 1 \end{bmatrix}^{-1} \begin{bmatrix} f_{D1}(t) \\ f_{D2}(t) \\ f_{D3}(t) \end{bmatrix} \quad \text{or} \quad \vec{v}(t) = \frac{c}{f_e} \mathbf{G}^{-1} \vec{f}_D(t) \quad (2)$$

Three-dimensional ADV instruments typically have a sampling frequency of O(20Hz). They measure time series of the quasi-instantaneous velocity, $\vec{v}(t)$. From these data the time-averaged velocity $\bar{\vec{v}}(\bar{v}_x, \bar{v}_y, \bar{v}_z)$, the fluctuating velocity $\vec{v}'(t) = \vec{v}(t) - \bar{\vec{v}}$, the Reynolds stresses, $\overline{v'_i v'_j}$, as well as higher-order turbulence correlations, $\overline{v'_j{}^a v'_k{}^b}$ ($i, j, k = x, y, z$ and a, b integer) can be derived; the overbar denotes time-averaged values. Obviously, $\bar{\vec{v}} = (c/f_e)\mathbf{G}^{-1}\bar{\vec{f}}_D$ and $\vec{v}'(t) = (c/f_e)\mathbf{G}^{-1}\vec{f}'_D(t)$, where:

$$\vec{f}_D(t) = \bar{\vec{f}}_D + \vec{f}'_D(t) \quad (3)$$

Acoustic velocity measurements are often affected by parasitical noise since the measured Doppler frequencies $\tilde{f}_{D,i}$ ($i=1$ to 3) contain a noise contribution σ_i besides the true Doppler frequency $f_{D,i}$ related to the fluid velocity:

$$\tilde{f}_{D,i}(t) = f_{D,i}(t) + \sigma_i(t) = \bar{f}_{D,i} + [f'_{D,i}(t) + \sigma_i(t)] = \bar{f}_{D,i} + \tilde{f}'_{D,i}(t) \quad (4)$$

With good approximation, this noise has the following characteristics, as experimentally verified by Hurther and Lemmin (2001):

- Its energy content is uniformly distributed over the investigated frequency domain (white noise).
- It is unbiased: $\bar{\sigma}_i = 0$. Therefore, it does not affect the estimates of the time-averaged velocity $\bar{\vec{v}}$.
- It is statistically independent of the corresponding true Doppler frequency: $\overline{\sigma_i f_{D,i}} = 0$.
- The noise of the different receivers is statistically independent: $\overline{\sigma_i \sigma_j} = 0$ if $i \neq j$.

The main problem of acoustic velocity measurements in fluid mechanics, and especially turbulence measurements, is that the energy content of the noise, $\overline{\sigma_i^2} > 0$, biases the estimates of the Reynolds stresses, since (Figs. 2 and 3):

$$\overline{\tilde{f}_{D,i}{}'^2} = \overline{f'_{D,i}{}'^2} + \overline{\sigma_i^2} \quad (6)$$

If the different receivers are identical and ideal, which is commonly assumed, their noise has the same energy content:

$$\overline{\sigma_i^2} = \overline{\sigma_j^2} = \overline{\sigma^2} \quad (7)$$

Garbini et al. (1982), Lhermitte and Lemmin (1994), and Voulgaris and Trowbridge (1998) have identified different noise sources which have been summarized in Hurther and Lemmin (2001).

This paper proposes efficient ways to improve turbulence measurements with an ADV by reducing the noise contribution. In the next section an optimized ADV configuration with four instead of three receivers is proposed that eliminates the major part of the noise contribution. Thereafter, a simple technique is presented that enables to considerably increase the signal-to-noise ratio (SNR).

3 Noise reduction by optimizing the ADV configuration

3.1 Principle of ADV optimization

3.1.1 Three-receiver ADV

As mentioned above, an emitter surrounded by at least three receivers is required to measure the three-dimensional velocity field. Most commercially available ADV instruments consist of a central emitter symmetrically surrounded by three receivers at 60° angles, as indicated in Fig. 2.

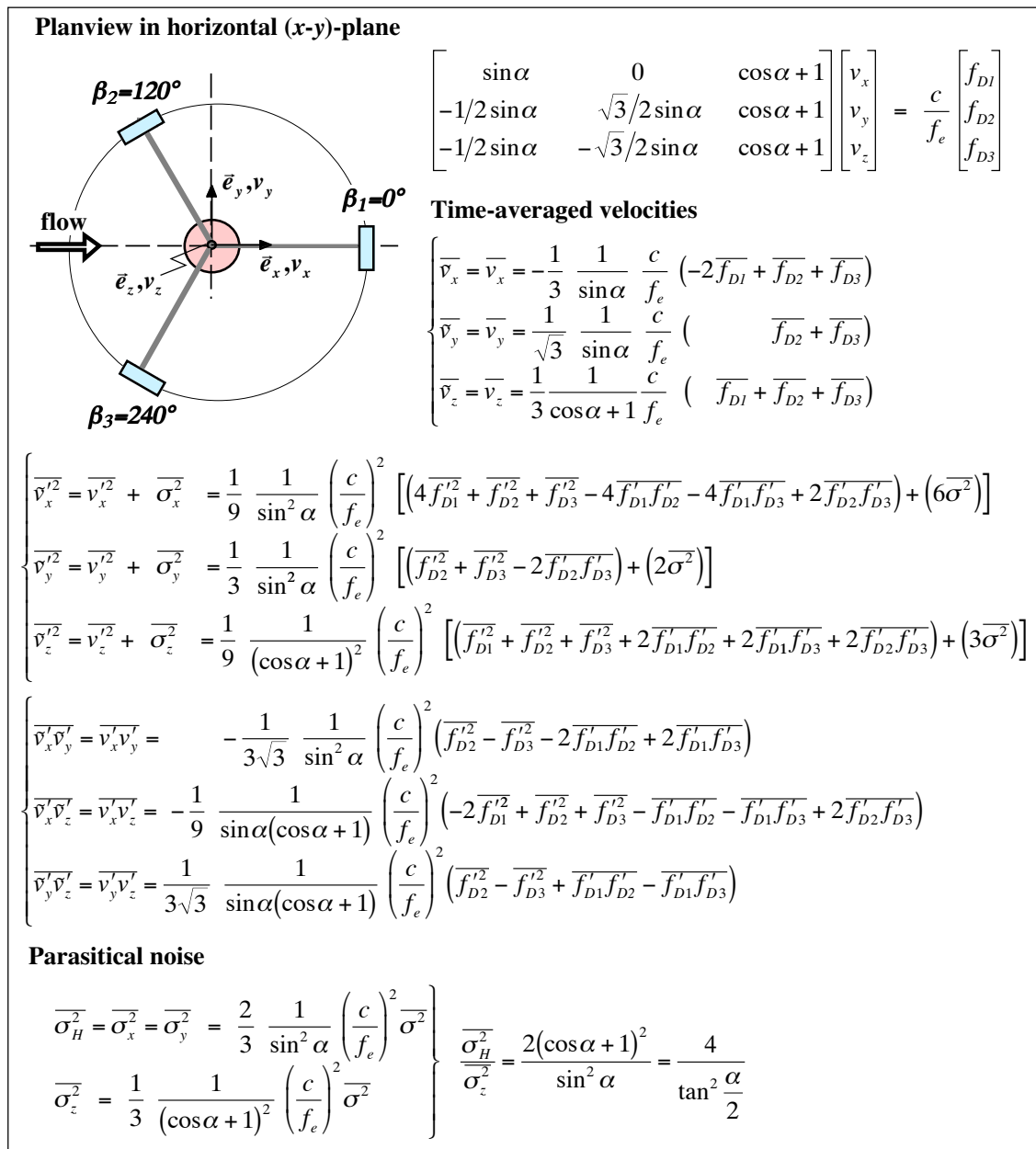


Fig. 2: Acoustic Doppler Velocimeter configuration with three receivers

For this ADV configuration, Fig. 2 also reports the relations between the measured Doppler frequencies and the time averaged velocities, the turbulent normal stresses and the turbulent shear stresses. As mentioned before, the noise is unbiased, $\overline{\sigma_i} = 0$, and does not influence the estimates of the time-averaged velocities. Since $\overline{\sigma_i \sigma_j} = 0$, noise-free estimates of the turbulent shear stresses are obtained if $\overline{\sigma_i^2} = \overline{\sigma_j^2} = \overline{\sigma^2}$ (Eq. 7). The estimates of the turbulent normal stresses, however, are affected by noise. The noise level of the two horizontal components is equal and it is typically an order of magnitude larger than that of the vertical component ($\alpha \sim 45^\circ$ for most commercial instruments and $15^\circ < \alpha < 60^\circ$ for the ADVP presented below).

The noise contribution can only be removed by indirectly estimating it from semi-theoretical models for the different noise sources, as proposed by Lhermitte and Lemmin (1994), Zedel et al. (1996) and Voulgaris and Trowbridge (1998). These estimates depend on characteristics of the flow and the ADV instrument and are not very accurate. Since the noise contribution cannot be correctly determined, the accuracy of the turbulence measurements cannot be estimated either. The parasitical noise contributions can be reduced, but not eliminated by increasing the SNR, as will be illustrated later.

3.1.2 *Four-receiver ADV*

Although most ADV work with three receivers, an ADV Profiler (ADVP) consisting of a central emitter symmetrically surrounded at 90° angles by four receivers has been developed in our laboratory. It will be presented below. Hurther and Lemmin (2001) reported that the parasitical noise contribution can almost be entirely eliminated with the fourth-receiver configuration.

Fig. 3 shows the configuration of the four-receiver ADVP, as adopted by Hurther and Lemmin (2001). The ADVP is composed of two so-called tristatic systems, oriented along longitudinal and transversal directions. The longitudinal system measures the longitudinal and the vertical velocity components, v_x and v_{z1} . The transversal system measures the transversal and the vertical components, v_y and v_{z2} , according to the relations given in Fig. 3. This configuration thus gives a redundancy of the vertical velocity component, since v_{z1} and v_{z2} are simultaneously measured.

Similar to the three-receiver configuration, the estimates of the turbulent shear stresses are free of noise if $\overline{\sigma_i^2} = \overline{\sigma_j^2} = \overline{\sigma^2}$ (Eq. 7), whereas the estimates of turbulent normal stresses are noise polluted (Fig. 3).

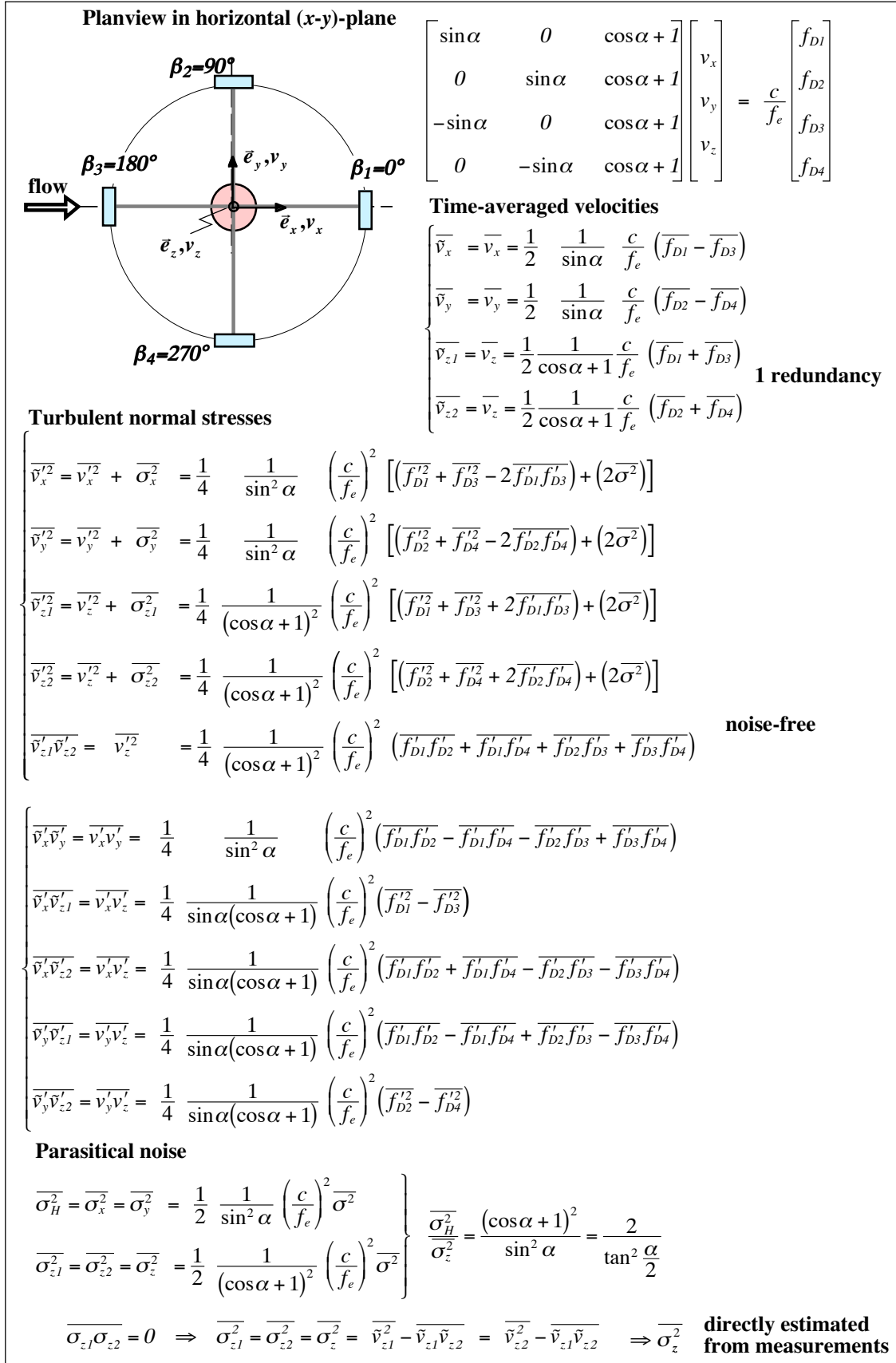


Fig. 3: Acoustic Doppler Velocimeter configuration with four receivers

Hurther and Lemmin (2001) have proposed the HL method which makes use of the redundancy of the vertical velocity component to eliminate the parasitical noise and which we will briefly summarize. The estimate of the vertical turbulent normal stress from only one of the measured vertical velocities contains noise, $\overline{v'_{zj}{}^2} = \overline{v_z'^2} + \overline{\sigma_{zj}^2}$ ($j=1,2$), whereas an estimate based on two redundant simultaneously measured vertical velocities is (theoretically) noise free, $\overline{v'_{z1}v'_{z2}} = \overline{v_z'^2}$ (see Fig. 3). From the difference between the two estimates, the noise level of the vertical component can be determined:

$$\overline{\sigma_z^2} \approx \begin{cases} \overline{\sigma_{z1}^2} = \overline{v'_{z1}{}^2} - \overline{v'_{z1}v'_{z2}} \\ \overline{\sigma_{z2}^2} = \overline{v'_{z2}{}^2} - \overline{v'_{z1}v'_{z2}} \end{cases} \quad (8)$$

The horizontal turbulent normal stresses can now be corrected by extracting the parasitical noise, which is geometrically related to the vertical noise level (see Fig. 3):

$$\overline{v'_{j,HL}{}^2} = \overline{v_j'^2} - \frac{2}{\tan^2 \alpha/2} \overline{\sigma_z^2} \quad (j=x,y) \quad (9)$$

The method proposed in this paper, based on an optimization of the ADVP configuration, will show that the best result is obtained by taking $\overline{\sigma_z^2} = 0.5(\overline{\sigma_{z1}^2} + \overline{\sigma_{z2}^2})$. Hurther and Lemmin (2001) have reported successful applications of this noise correction method by which all Reynolds stresses are obtained free of noise. Advantages of this method are:

- The quality of the measurements and the system can be assessed by comparing the two redundant vertical velocities and the corresponding noise levels $\overline{\sigma_{z1}^2}$ and $\overline{\sigma_{z2}^2}$.
- It enables an estimate of the accuracy of the turbulence quantities, since the noise level can be estimated.

Unfortunately, this correction method still has some disadvantages:

- It is based on the essential assumption that $\overline{\sigma_i^2} = \overline{\sigma_j^2} = \overline{\sigma^2}$ ($i,j = 1$ to 4, Eq. 7) which cannot be verified from the measurements.
- The noise level of the horizontal components is obtained by multiplying the experimentally estimated noise level of the vertical component with a geometrical factor of $2/\tan^2(\alpha/2)$. For the measurements reported below, the angle α varied from 50° at the water surface to 25° at the bottom, resulting in values of this geometrical factor as high as 40 near the bottom. Therefore this approach is rather sensitive to error propagation.

3.1.3 Four-receiver ADV with optimized geometry

The optimized four-receiver geometry is obtained by simply rotating the previously discussed four-receiver ADVP configuration over 45° . In this way the transducer planes are aligned along the bisectors of the longitudinal and transversal planes, as illustrated in Fig. 4. Although this might appear to be a trivial difference, due to the enhanced symmetry of this configuration redundancies now exist for all three velocity components instead of only for the vertical component. This allows to readily obtain all turbulent normal stresses free of noise, without having to first estimate the noise levels of the HL method, as indicated in Fig. 4:

$$\overline{v_i'^2} = \overline{v'_{i1}v'_{i2}} \quad (i=x,y,z) \quad (10)$$

This procedure is thus more efficient than the HL method. Note that each of the three turbulent shear stresses can now be obtained in four different ways; only the average of these four possibilities is indicated in Fig. 4.

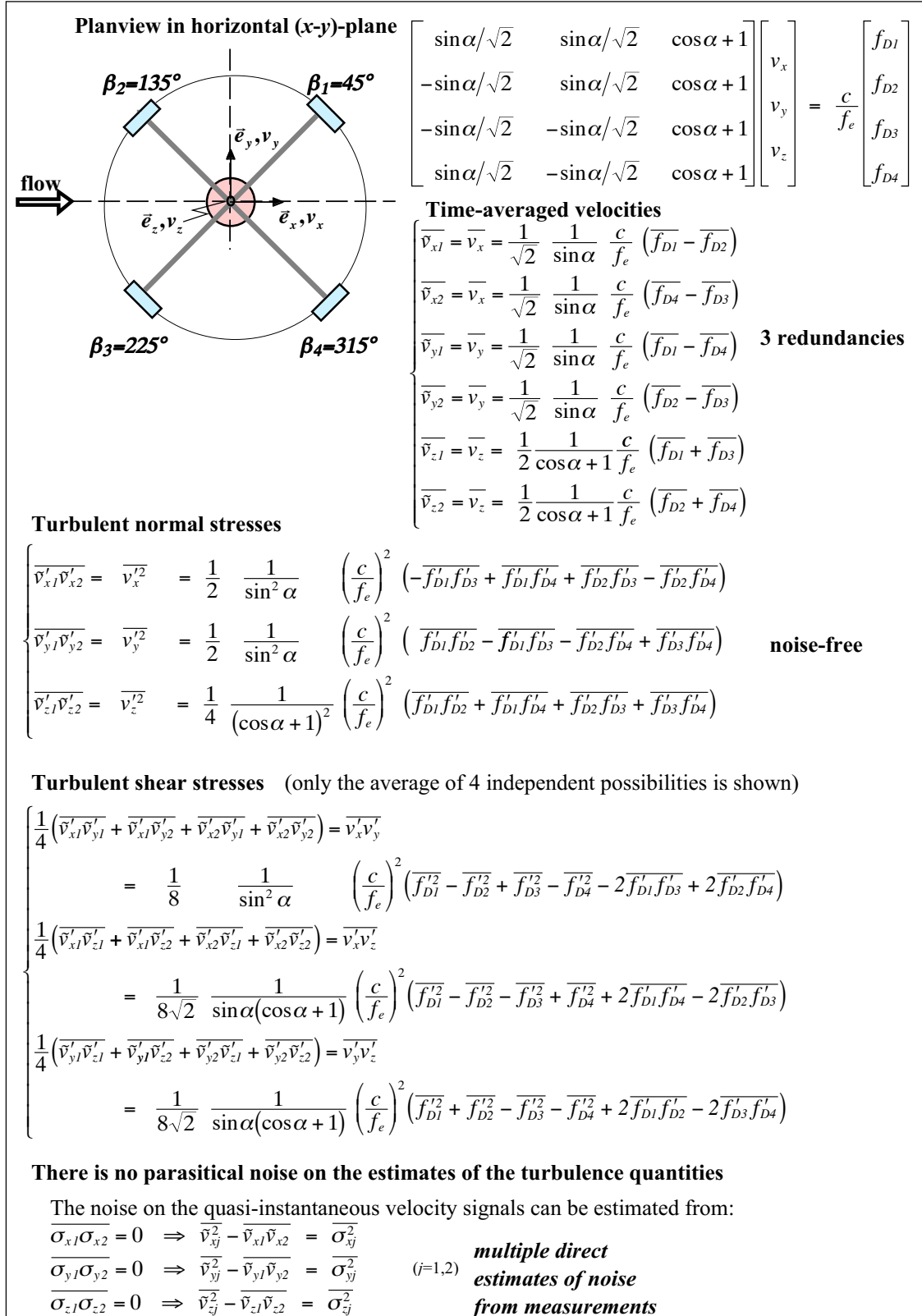


Fig. 4: Optimized Acoustic Doppler Velocimeter configuration with four receivers

Further advantages of this configuration are:

- The quality of the measurements can be evaluated by comparing the redundant information for all time-averaged velocities and all Reynolds stresses.
- It provides for an estimate of the accuracy of the turbulence quantities, since the noise levels of all turbulent normal stresses can be estimated: $\overline{\sigma_{ij}^2} = \overline{v_{ij}^{\prime 2}} - \overline{v_{i1}^{\prime} v_{i2}^{\prime}}$ ($i=x,y,z$ and $j=1,2$).
- The quality of the ADV system can be assessed by experimentally verifying that the noise of the different receivers has the same energy content $\overline{\sigma_i^2} = \overline{\sigma_j^2} = \overline{\sigma^2}$ ($j=1$ to 4 , cf. Eq. 7). This is non-trivial, and an essential condition to obtain noise-free turbulence measurements. According to the relations in Fig. 4:

$$\left. \begin{aligned} \overline{\sigma_{x1}^2} &= 2/\sin^2 \alpha \left(\overline{\sigma_1^2} + \overline{\sigma_4^2} \right) & \overline{\sigma_{x2}^2} &= 2/\sin^2 \alpha \left(\overline{\sigma_2^2} + \overline{\sigma_3^2} \right) \\ \overline{\sigma_{y1}^2} &= 2/\sin^2 \alpha \left(\overline{\sigma_1^2} + \overline{\sigma_3^2} \right) & \overline{\sigma_{y2}^2} &= 2/\sin^2 \alpha \left(\overline{\sigma_2^2} + \overline{\sigma_4^2} \right) \\ \overline{\sigma_{z1}^2} &= 1/(\cos \alpha + 1)^2 \left(\overline{\sigma_1^2} + \overline{\sigma_2^2} \right) & \overline{\sigma_{z2}^2} &= 1/(\cos \alpha + 1)^2 \left(\overline{\sigma_3^2} + \overline{\sigma_4^2} \right) \end{aligned} \right\} \quad (11)$$

which can be transposed into:

$$\left. \begin{aligned} \Sigma_\sigma &= \frac{1}{3} \left[\overline{\sigma_{x1}^2} + \overline{\sigma_{x2}^2} + \overline{\sigma_{y1}^2} + \overline{\sigma_{y2}^2} + \frac{2}{\tan^2 \alpha/2} \left(\overline{\sigma_{z1}^2} + \overline{\sigma_{z2}^2} \right) \right] \\ \overline{\sigma_1^2} &= \frac{\sin^2 \alpha}{4} \left(\overline{\sigma_{x1}^2} + \overline{\sigma_{y1}^2} + \frac{2}{\tan^2 \alpha/2} \overline{\sigma_{z1}^2} - \Sigma_\sigma \right) \\ \overline{\sigma_2^2} &= \frac{\sin^2 \alpha}{4} \left(-\overline{\sigma_{x1}^2} - \overline{\sigma_{y1}^2} + \frac{2}{\tan^2 \alpha/2} \overline{\sigma_{z1}^2} + \Sigma_\sigma \right) \\ \overline{\sigma_3^2} &= \frac{\sin^2 \alpha}{4} \left(-\overline{\sigma_{x1}^2} + \overline{\sigma_{y1}^2} - \frac{2}{\tan^2 \alpha/2} \overline{\sigma_{z1}^2} + \Sigma_\sigma \right) \\ \overline{\sigma_4^2} &= \frac{\sin^2 \alpha}{4} \left(\overline{\sigma_{x1}^2} - \overline{\sigma_{y1}^2} - \frac{2}{\tan^2 \alpha/2} \overline{\sigma_{z1}^2} + \Sigma_\sigma \right) \end{aligned} \right\} \quad (12)$$

An illustration will be given in the result section below. Note that the assumption of equality of the noise of the four receivers implies that the noise of the different turbulent normal stresses is equal:

$$\overline{\sigma_{x1}^2} = \overline{\sigma_{x2}^2} = \overline{\sigma_{y1}^2} = \overline{\sigma_{y2}^2} = \frac{2}{\tan^2 \alpha/2} \overline{\sigma_{z1}^2} = \frac{2}{\tan^2 \alpha/2} \overline{\sigma_{z2}^2} \quad (13)$$

Table 1 summarizes the noise characteristics of ADV instruments with three receivers, four receivers and four receivers with optimized geometry.

3 receivers	4 receivers	4 receivers optimized
$\overline{v_x'v_y'}, \overline{v_x'v_z'}, \overline{v_y'v_z'}$: noise-free	$\overline{v_x'v_y'}, \overline{v_x'v_z'}, \overline{v_y'v_z'}, \overline{v_z'^2}$: noise-free	$\overline{v_x'v_y'}, \overline{v_x'v_z'}, \overline{v_y'v_z'}$: noise-free
$\overline{v_x'^2}, \overline{v_y'^2}, \overline{v_z'^2}$: noisy	$\overline{v_x'^2}, \overline{v_y'^2}$: noisy	$\overline{v_x'^2}, \overline{v_y'^2}, \overline{v_z'^2}$: noise-free
<i>no noise correction</i>	<i>noise correction:</i> <i>estimation of noise from $\overline{v_z'^2}$</i> <i>and subsequent subtraction</i> <i>of noise from $\overline{v_x'^2}, \overline{v_y'^2}$</i>	<i>multiple noise estimations</i> <i>enable check of system</i> <i>and data quality</i>

Table 1: Summary of noise characteristics of ADV configurations

3.2 ADVP instrument and experimental set-up

The importance of the parasitical noise contributions, the HL method and the above proposed noise elimination by geometrical optimization will be illustrated below based on measurements carried out with an Acoustic Doppler Velocity Profiler (ADVP), developed and built in our laboratory.

The ADVP consists of a central emitter surrounded by four receivers, as illustrated in Fig. 5. This instrument is completely non-intrusive. The transducers are placed in a separate water-filled housing that is in contact with the water surface. Contrary to most commercially available ADV instruments, the ADVP does not measure a profile point-wise but it simultaneously provides the quasi-instantaneous velocities along an entire water column. The emitter is focalized and has a constant beam diameter of $\sim 0.7\text{cm}$ (Hurther and Lemmin, 1998). The water column is divided into intervals of height $\sim 0.3\text{cm}$, resulting in a continuous string of identical measuring volumes. Acoustic wave pulses are generated by the emitter with a frequency, called “pulse-repetition-frequency” (*prf*). From a number of NPP (number of pulse-pairs) scattered acoustic pulses, one quasi-instantaneous Doppler frequency can be estimated by the pulse-pair algorithm for each volume. The measuring frequency, given by prf/NPP , is a parameter of the ADVP, since both *prf* and NPP can be chosen.

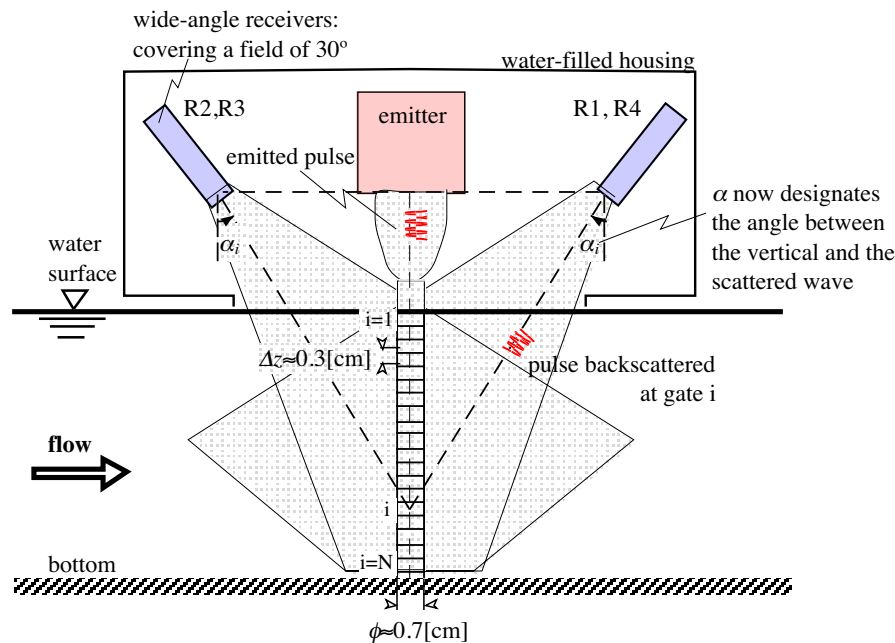


Fig. 5: Four-receiver Acoustic Doppler Velocity Profiler (ADVP). Receivers R1 and R3 are in one plane and R2 and R4 in a plane perpendicular to it (see Fig. 4)

Different aspects of the ADVP development have been reported in the literature (Lhermitte and Lemmin, 1994; Shen and Lemmin, 1996 and 1997; Lemmin and Rolland, 1997; Rolland and Lemmin, 1997; Hurther and Lemmin, 1998 and 2001). The instrument system has been successfully applied in various studies on straight, uniform and non-uniform clear water flows over rigid as well as movable bottom configurations (Song et al., 1994; Song and Graf, 1996), straight, uniform suspension flow (Cellino and Graf, 1999), coherent flow structures in straight, uniform flow (Hurther, 2001), highly three-

dimensional flow around cylinders over a flat rigid as well as scoured movable bottom configuration (Graf and Yulistiyanto, 1998 and Graf and Istiarto, 2002) or highly three-dimensional curved flow (Blanckaert, 2001; Blanckaert and Graf, 2001), testifying to its versatility and reliability.

The present measurements were made in a straight, uniform flow over a mobile rough granular bottom in a 16.8m long and 0.6m wide open-channel laboratory flume. A vertical profile was measured at the centerline of the cross-section 8m downstream of the flume's entrance where the boundary layer is fully developed. The hydraulic conditions are summarized in Table 2:

Q [l/s]	H [m]	S_b [‰]	U [m/s]	u^* [m/s]	Re [10 ³]	Fr [/]	B/H [/]
65	0.175	1.5	0.62	0.035	108	0.47	3.4

Q : flow discharge

H : flow depth

S_b : bottom slope

U : depth-averaged velocity

The median grain size diameter of the immobile bed material was 6 mm, that of the moving bedload material was 2.5 to 3 mm

u^* : shear velocity estimated from the profile of $\overline{v'_x v'_z}$

$Re=UH/\nu$: flow Reynolds number

$Fr=U/(gH)^{1/2}$: Froude number

B : channel width

Table 2: Hydraulic conditions

A *prf* of 1000 Hz was adopted for the present ADV measurements and Doppler frequencies were estimated with NPP=16 and 32, yielding measuring frequencies of 62.5 Hz and 31.25 Hz, respectively. The measurement duration was 600s. The angle α decreased from 50° at the water surface to 25° at the bottom (Fig. 5).

3.3 Experimental verification

3.3.1 Validation of the noise correction methods

The noise characteristics of turbulence measurements with both the standard as well as the optimized four-receiver configuration are illustrated in Fig. 6. It shows vertical profiles of the longitudinal turbulent normal stress, estimated:

- from only one of the velocity measurements, $\overline{v'^2_{x1}}$ and $\overline{v'^2_{x2}}$ (curves 1 and 2).
- by applying the HL method for the elimination of noise (subscript HL; curves 3 and 4).
- from both redundant velocity measurements, $\overline{v'_{x1} v'_{x2}}$ (curve 5).

Furthermore, curve 6 represents the vertical profile of the noise contribution, $0.5(\overline{v'^2_{x1}} + \overline{v'^2_{x2}}) - \overline{v'_{x1} v'_{x2}}$ and curve 7 is the semi-theoretical expression for the longitudinal turbulent normal stress proposed by Nezu and Nakagawa (1993). NPP=32 was chosen in these measurements, yielding a measuring frequency of 31.25 Hz.

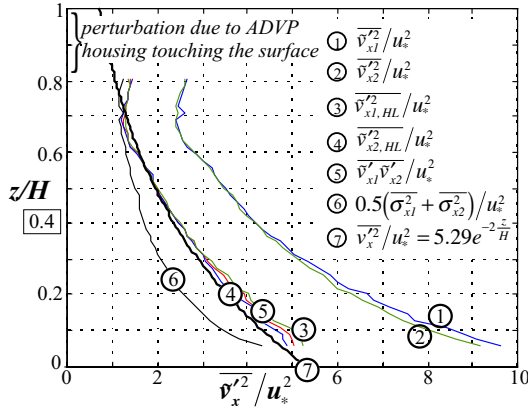


Fig. 6: Estimates of longitudinal turbulent normal stress

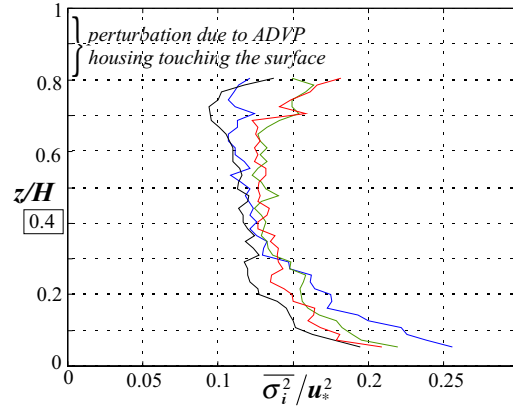


Fig. 7: Estimates of noise levels of four receivers ($i=1$ to 4)

These results show the importance of the parasitical noise contribution. For this specific example with a high acoustic scattering level, the parasitical noise increases towards the bottom and accounts on the average for about 74% of the true value, $\overline{v'_{x1} v'_{x2}}$. As mentioned above, no accurate methods for the reduction of this parasitical noise exist for measurements done with three-receiver ADV instruments.

The longitudinal velocity obtained with the standard four-receiver ADVP configuration is identical to the average of the two redundant longitudinal velocities obtained with the optimized configuration, $\overline{v_{x,HL}} \equiv 0.5(\overline{v_{x1}} + \overline{v_{x2}})$. Two estimates of the longitudinal turbulent normal stress are obtained by applying the HL method which correspond to: $\overline{v'^2_{xj,HL}} = \overline{v'^2_{x,HL}} - \tan^{-2}(\alpha/2) \overline{\sigma_{zj}^2}$ ($j=1,2$). It is straightforward to demonstrate that the noise-free profile obtained with the optimized ADVP configuration coincides with the average of both estimates with the HL method:

$$\overline{v'_{x1} v'_{x2}} \equiv \overline{v'^2_{x,HL}} - \frac{0.5}{\tan^2 \alpha/2} (\overline{\sigma_{z1}^2} + \overline{\sigma_{z2}^2}) \quad (14)$$

The turbulence results obtained with the optimized ADVP configuration thus confirm and refine the HL method. Being directly calculated, they eliminate the ambiguity on the estimate of the noise level for the vertical component by the HL method. Both estimates with the HL method as well as the noise free profile obtained with the optimized ADVP configuration agree fairly well with the semi-theoretical curve proposed by Nezu and Nakagawa (1993).

As mentioned above, a major advantage of the optimized four-receiver ADVP configuration is that it allows a better assessment of the quality of the measurements and the system. Whereas only $\overline{\sigma_{z1}^2}$ and $\overline{\sigma_{z2}^2}$ can be experimentally estimated with the HL method, $\overline{\sigma_{x1}^2}$, $\overline{\sigma_{x2}^2}$, $\overline{\sigma_{y1}^2}$ and $\overline{\sigma_{y2}^2}$ can now also be experimentally obtained with the optimized receiver configuration. According to Eq. 12, this enables to experimentally verify the equality of the noise levels of the four receivers, $\overline{\sigma_i^2} = \overline{\sigma_j^2} = \overline{\sigma^2}$ ($j=1$ to 4, cf. Eq. 7), which is an important and essential condition to obtain noise-free turbulence measurements. Fig. 7 shows that the noise levels of the four receivers are all nearly identical. They are rather constant over most of the water column but increase near the

bottom ($z/H < 0.2$). This increase is mainly due to strong vertical gradient of the horizontal velocity component in this layer.

A better insight into the noise characteristics and in the functioning of the correction methods is obtained by analyzing the power spectral density of the signals. Fig. 8 presents the (co)spectra and the cumulative (co)spectra of $\overline{v'_{x1}{}^2}$, $\overline{v'_{x1}v'_{x2}}$ and $\overline{\sigma_{x1}^2}$ for the point at $z/H=0.4$ indicated in Figs. 6 and 7. They are based on Doppler frequencies estimated with NPP=16, yielding a measuring frequency of 62.5 Hz and a Nyquist frequency (maximum frequency for which the power spectral density can be estimated) of 31.25 Hz. The spectrum of $\overline{\sigma_{x1}^2}$ is close to that of white noise, in agreement with the above assumption (cf. Eq. 5). In the low frequency range, $f < 1$ Hz, the energy content of the noise is small compared to the energy content of the true fluctuations and the difference between the spectra of $\overline{v'_{x1}{}^2}$ and $\overline{v'_{x1}v'_{x2}}$ is small. With increasing frequency the SNR decreases and the spectrum of $\overline{v'_{x1}v'_{x2}}$ starts to deviate considerably from that of $\overline{v'_{x1}{}^2}$. Finally, in the high frequency range, $f > 10$ Hz, the energy content of the noise is an order of magnitude greater than that of the true velocity fluctuations.

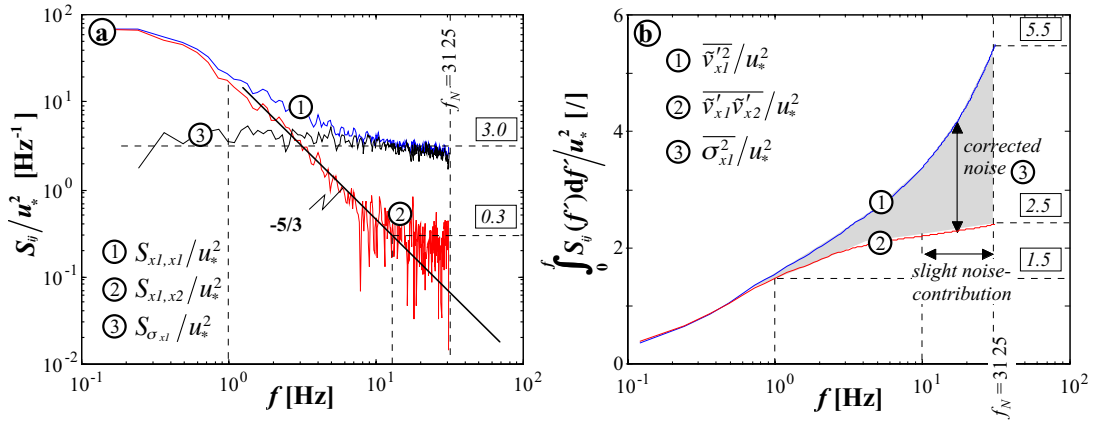


Fig. 8: Normalized power (co)spectra (a) and cumulative power (co)spectra (b) of $\overline{v'_{x1}{}^2}$, $\overline{v'_{x1}v'_{x2}}$ and $\overline{\sigma_{x1}^2}$

According to Kolmogoroff's concept (Kolmogoroff, 1941), the power spectrum should contain a low-frequency production range, followed by an inertial subrange, and a high-frequency viscous range. The inertial subrange is characterized by a $-5/3$ slope in a log-log presentation and covers a rather broad intermediate frequency range. In this inertial subrange, turbulence production and dissipation are in equilibrium and the turbulent kinetic energy is merely transferred from larger to smaller eddies in the so-called energy cascade. In the viscous range, the slope of the power spectrum becomes steeper than $-5/3$ due to dissipation.

Nezu and Nakagawa (1993) present an expression for the velocity power spectrum in the production and inertial subranges that has originally been proposed by von Karman:

$$\frac{S(k_w)}{L_x} = \frac{2}{\pi} \left[1 + \left(\frac{k_w}{k_0} \right)^2 \right]^{-5/6} \quad (15)$$

k_w is the wave-number, L_x and $1/k_0$ are both macroscales of turbulence. By applying Taylor's frozen-turbulence hypothesis (Nezu and Nakagawa, 1993):

$$S(k_w) = \left(\frac{v_x}{2\pi}\right)S(f) \quad \text{and} \quad k_w = \left(\frac{2\pi}{v_x}\right)f \quad (16)$$

an equivalent expression for the power spectrum in the frequency space is obtained:

$$\frac{S(f)}{T_x} = \frac{2}{\pi} \left[1 + \left(\frac{f}{f_0}\right)^2 \right]^{-5/6} \quad (17)$$

where $T_x = (2\pi/v_x)L_x$ and $f_0 = (v_x/2\pi)k_0$. Integration of this expression with respect to f indicates that the corresponding cumulative spectrum should have a typical “S” shape in a semilog representation.

Fig. 8a shows that the slope of the spectrum of $\overline{v'_{x1}{}^2}$ remains flatter than $-5/3$. Furthermore, in the high frequency range, it does not steepen, but instead flattens and finally becomes almost horizontal when the $\overline{v'_{x1}{}^2}$ signal mainly consists of white noise. The corresponding cumulative spectrum (Fig. 8b) does not show the typical “S” shape, but “explodes” at the high frequency end. The spectrum and the cumulative spectrum of $\overline{v'_{x1}v'_{x2}}$ (Figs. 8a,b) agree much better with the Kolmogoroff concept. The spectrum shows a $-5/3$ slope in the frequency range $1 \text{ Hz} < f < 10 \text{ Hz}$, and only starts to flatten for $f > 10 \text{ Hz}$. Correspondingly, the cumulative spectrum has an “S” shape for $f < 10 \text{ Hz}$ and only starts to deviate slightly for $f > 10 \text{ Hz}$.

Fig. 8a, and especially Fig. 8b, show that a considerable improvement is obtained by estimating the turbulent normal stress $\overline{v_x'^2}$ from the redundant velocity information as $\overline{v'_{x1}v'_{x2}}$ instead of from only one velocity information as $\overline{v'_{x1}{}^2}$. Although the estimate $\overline{v'_{x1}v'_{x2}}$ should theoretically be free of parasitical noise, Figs. 8a and b indicate a remaining noise contribution in the high frequency range. However, this noise level is about one order of magnitude smaller than the original noise level of $\overline{v'_{x1}{}^2}$. As a result, the useful frequency range where noise contributions are small has been extended by about an order of magnitude by applying the noise correction method.

In the example given in Figs. 8a,b, a parasitical noise contribution remains for $f > 10 \text{ Hz}$. This limiting frequency depends on the SNR and thus on the acoustic scattering level of the fluid. This will be further discussed below.

The above results indicate that by simply optimizing the ADV configuration with four receivers, the parasitical noise on turbulence measurements can largely be eliminated. Obviously, the turbulence characteristics can be obtained in any other reference system by applying a coordinate transformation.

3.3.2 Discussion of results

In the following, we will focus on two important points that are rarely discussed in the literature:

(i) *What measuring frequency should be chosen in ADV turbulence measurements ?*

As mentioned before, the measuring frequency of the ADVP is given by prf/NPP . Here, the measurements will be treated with $NPP=16$, yielding a measuring frequency of 62.5 Hz.

The cospectra and the cumulative cospectra of the three almost noise free turbulent normal stresses, estimated as $\overline{v'_{x1}v'_{x2}}$, $\overline{v'_{y1}v'_{y2}}$ and $\overline{v'_{z1}v'_{z2}}$ are given in Figs. 9a,b. The cospectrum of $\overline{v'_{z1}v'_{z2}}$ clearly shows a zone with a $-5/3$ -slope and does not contain any parasitical noise tail. Its slope even gets steeper in the high frequency range. The corresponding cumulative cospectrum has a typical “S” shape. The cospectra of $\overline{v'_{x1}v'_{x2}}$ and $\overline{v'_{y1}v'_{y2}}$ also show a zone with a $-5/3$ slope but they contain a remaining high frequency noise tail for $f > 10$ Hz. This noise tail is clearly discernible in the cumulative cospectra, that have the typical shape for $f < 10$ Hz, but start to deviate for $f > 10$ Hz.

The reason that the vertical turbulent normal stress $\overline{v'_{z1}v'_{z2}}$ has better noise characteristics than the horizontal ones $\overline{v'_{x1}v'_{x2}}$ and $\overline{v'_{y1}v'_{y2}}$ is purely geometrical. The horizontal velocity components are calculated from the difference between measured Doppler frequencies, whereas the vertical ones are obtained from their sum (cf. Fig. 4), which is less sensitive to error propagation.

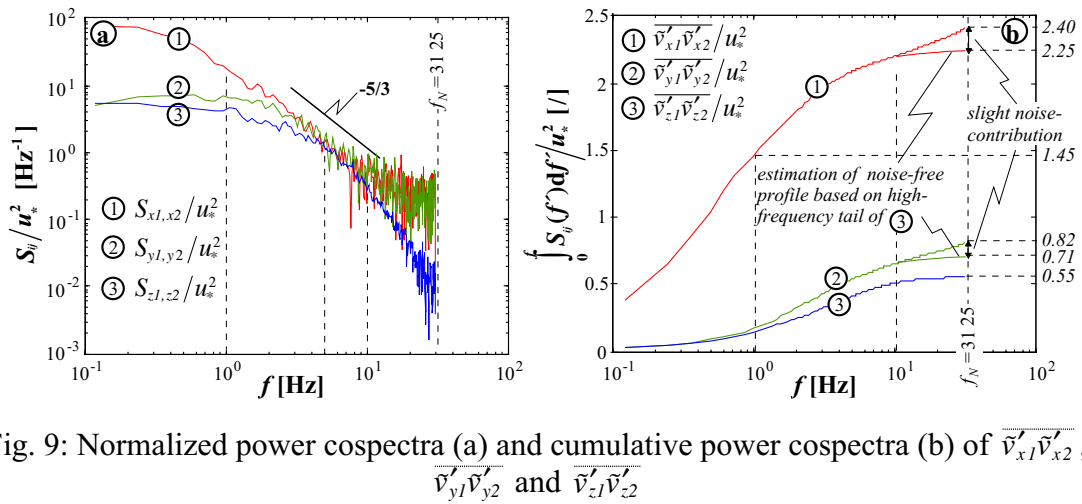


Fig. 9: Normalized power cospectra (a) and cumulative power cospectra (b) of $\overline{v'_{x1}v'_{x2}}$, $\overline{v'_{y1}v'_{y2}}$ and $\overline{v'_{z1}v'_{z2}}$

With a measuring frequency of 62.5 Hz, $\overline{v_x'^2}$ and $\overline{v_y'^2}$ are clearly overestimated. Fig. 9b further indicates that increasing the measuring frequency would result in an important deterioration of the estimates, since the parasitical noise tail tends to “explode”. Taking too low a measuring frequency instead can result in considerable underestimates, since most of the energy is contained in the inertial subrange. For example, when estimating the longitudinal turbulent normal stress as $\overline{v_{x1}'^2}$, the low noise range is limited to $f < 1$ Hz (Fig. 8), which would lead to an underestimate of about 35% (cf. Fig. 9b). Figs. 9 a,b

demonstrate that good estimates are obtained by choosing the “cut-off” measuring frequency in the flat part of the cumulative (co)spectrum before the noise tail becomes important. For the considered example, good estimates are obtained with a measuring frequency of 31.25 Hz (NPP=32, corresponding to a Nyquist frequency of 15.6 Hz).

Obviously, the choice of the optimal measuring frequency is case- and instrument-dependent and is based on the knowledge of the noise levels. If the SNR level is too low, the flat part in the cumulative spectrum is not reached as is the case in Fig. 8b for $\overline{v_{xI}^2}$, and accurate estimates of the turbulent normal stresses are not possible. The next section presents and illustrates a technique to increase the SNR.

(ii) *What is the influence of a relatively low measuring frequency on the turbulence results ?*

Obviously, the accuracy of ADV turbulence measurements depends on:

- The characteristic lengthscales of the flow,
- The acoustic scattering level of the fluid,
- The measuring frequency
- The characteristics of the ADV

The effect of most of these aspects can only be roughly estimated. In the above example, good turbulence results are obtained with a measuring frequency of 31.25 Hz in a flow with a relatively high acoustic scattering level. The accuracy estimates indicated in Fig. 9b correspond to the accuracy estimate of O(10%) given by Hurther and Lemmin (2001).

Typically, the measuring frequency with ADV instruments is O(20 Hz), and the corresponding Nyquist frequency (maximum frequency for which the power spectral density can be estimated) is O(10 Hz). Taylor has defined a microscale of turbulence as $\lambda = \sqrt{15 \nu \overline{v_x^2}} / \varepsilon$ with ε the dissipation rate, which is a characteristic scale for the small turbulent eddies that dissipate energy. Using Taylor’s frozen turbulence hypothesis, Eq. 16, the corresponding frequencies can be estimated as $f_\lambda = (\overline{v_x} / 2\pi) / \lambda$. In the spectral space, these small eddies are found at the high frequency end of the $-5/3$ -slope region. As mentioned above, this inertial subrange is followed by a viscous range where the slope is steeper than $-5/3$ due to dissipation. Nezu and Nakagawa (1993) propose different methods to experimentally estimate λ , all of which resulted in $f_\lambda = O(10 \text{ Hz})$ for the investigated flow. This complies with Fig. 9a, where the slope of the spectrum at $f_N = 31.25$ Hz is already steeper than $-5/3$. The presented ADVP measurements thus cover the entire inertial subrange and even the beginning of the viscous range. In general, the extent of the inertial subrange in the frequency domain depends on the specific flow conditions, and especially on the Reynolds number of the flow. Often, ADV measurements of turbulence are limited to the low-frequency part of the inertial subrange. The influence of the non-captured high frequency contributions on the interpretation of the turbulence results will now be discussed.

Figs. 9a and b show the cospectra and cumulative cospectra of the three “noise-corrected” turbulent normal stresses, estimated as $\overline{v'_{x1}v'_{x2}}$, $\overline{v'_{y1}v'_{y2}}$ and $\overline{v'_{z1}v'_{z2}}$. In the low frequency range, $f < 1$ Hz, the energy content of the longitudinal fluctuations is larger than that of the transversal fluctuation, and the vertical fluctuations contain the least energy (Fig. 9a). With increasing frequency, the power spectral densities converge and they nearly coincide at about 5 Hz. Physically, this signifies that the turbulence tends towards isotropy and nearly reaches it at about 5 Hz. For $f > 10$ Hz, the power spectral densities diverge again since the remaining parasitical noise of the vertical fluctuations is smaller than that of the other two components (see above). This behavior is not physical, however, since turbulence is known to converge progressively towards isotropy with increasing frequency.

Turbulence anisotropy plays an important physical role. First of all, it is the anisotropy of the turbulent normal stresses that gives rise to the turbulent shear stresses, as can easily be demonstrated by a representation of the turbulent stresses on a Mohr circle. As a result, the turbulent shear stresses will mainly be generated in the low frequency range. According to Tchen (1953) and Nikora (1999), the velocity cospectra have a $-7/3$ slope in the inertial subrange, indicating the rapid decay of shear stress generation with increasing frequency. This implies that an accurate estimate of the turbulent shear stresses can be obtained with a lower measuring frequency than the turbulent normal stresses and that the accuracy of the turbulent shear stresses will be better than that of the turbulent normal stresses.

Secondly, turbulence anisotropy interacts dynamically with the mean flow field. The anisotropy $\overline{v_y'^2} - \overline{v_z'^2}$ is responsible for the generation of near bank cells of secondary circulation in straight, open-channel flow (Nezu and Nakagawa, 1993). Blanckaert and de Vriend (2002) have shown that it also plays a dominant role in the generation of a secondary circulation cell near the outer bank in open-channel bends. Similar to the turbulent shear stresses, the turbulence anisotropy is mainly generated in the low frequency range. It can be resolved with a lower measuring frequency than the turbulent normal stresses and its estimate is more accurate. Note that the high frequency, nearly isotropic turbulence does not play an important dynamical role. It accounts for the dissipation of energy and does not interact with the mean flow field.

4 Noise reduction by increasing the signal-to-noise ratio (SNR)

As explained above, acoustic measurements based on the Doppler principle require the scattering of acoustic waves on acoustic targets moving with the fluid. Shen and Lemmin (1997) have shown that the acoustic targets for the ADVP are turbulence induced air bubble microstructures with a mean size of about 750 μm , which are ideal flow tracers since they follow the fluid motion with negligible inertial lag. The size of the ideal flow tracers depends on the frequency of the emitted acoustic wave and is thus instrument dependent. Most commercial ADV instruments operate at a higher frequency than our ADVP, which emits 1 MHz-pulses, and require smaller targets.

ADV instruments are known to perform poorly in (very) clear water characterized by a low acoustic scattering level, as is often found in laboratory applications or in naturally clean water areas such as the deep ocean, deep lakes, arctic water, etc. The successful application of ADV measurements in such cases requires an artificial supply of neutral acoustic targets to the water in order to increase the SNR. Note that this is particularly important for three-receiver ADV configurations where no accurate noise reduction techniques can be applied. The aim of this section is to describe a simple, low cost, non-polluting technique of supplying acoustic targets to the water that has proven to be successful in measurements with the ADVP and with a commercial Nortek NDV (not shown).

The technique, illustrated in Fig. 10, consists of generating hydrogen bubbles of the correct size in the fluid by means of electrolysis. The cathodic and anodic electrodes are formed by an array of horizontal stainless steel wires with a diameter of $100\ \mu\text{m}$ that cover the entire water depth with a vertical spacing of about $1\ \text{cm}$. The spacing between the two electrodes is about $2\ \text{cm}$ and they are placed about $15\ \text{cm}$ upstream of the measured vertical water column. This distance is about 1500 times the wire diameter, which is sufficient to avoid any perturbation in the turbulence characteristics. The horizontal span of both electrodes has to be adequate to assure that the measured water column is outside the wake of the vertical insulating stems which carry the wires. A constant tension of $0(5\ \text{V})$ was sufficient to obtain a high acoustic scattering level with this configuration. The bubble generation is initially not efficient when the stainless steel wires are still clean. After some minutes, a surface reaction takes place on the wires and the bubble generation becomes efficient. Note that a similar supply of hydrogen bubbles to the flow has been commonly used in the past to measure velocities by means of the so-called hydrogen bubble technique.

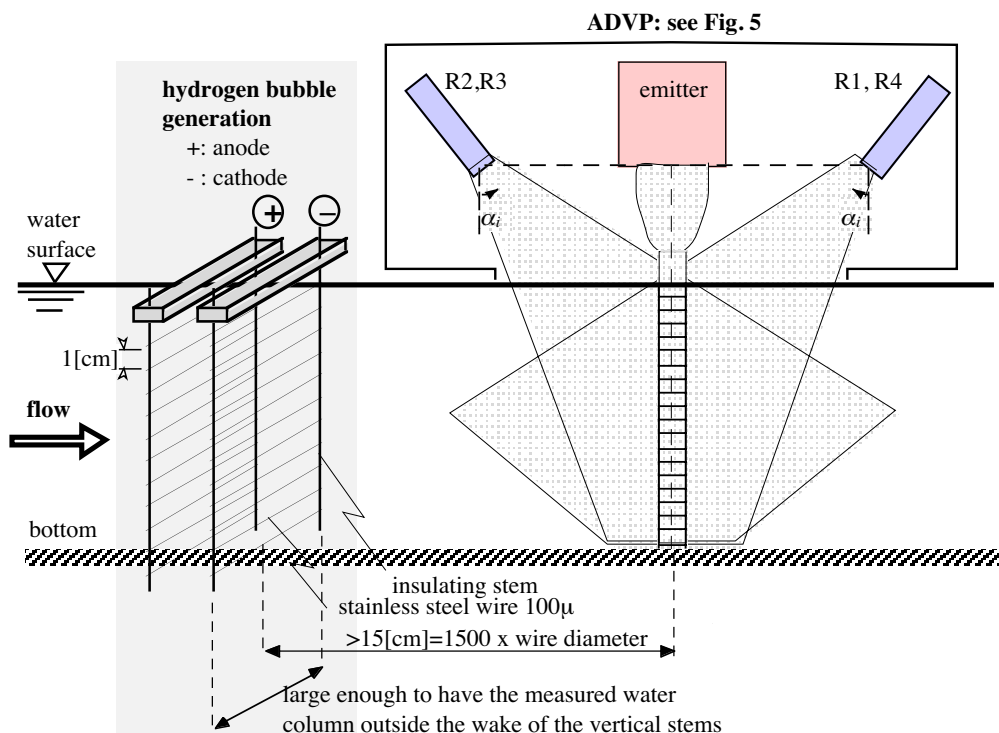


Fig. 10: Application of acoustic target supply by hydrogen bubble generation

The measurements with the optimized four-receiver ADVP configuration presented in the previous section were carried out with a supply of acoustic targets by this technique. They will now be compared to measurements without bubble injection under identical flow conditions (both treated with $NPP=16$ corresponding to $f_N=31.25$ Hz).

Vertical profiles of the longitudinal turbulent normal stress, estimated as $\overline{v'_{x1}{}^2}$ and $\overline{v'_{x1}v'_{x2}}$, are shown in Fig. 11. They indicate that the measurements with a low acoustic scattering level contain considerably more noise. Even the estimate of $\overline{v'_{x1}v'_{x2}}$, which in theory should be noise free, still contains a rather important noise contribution. The noise correction methods presented and illustrated in the previous section thus require a sufficiently high SNR. Note that the turbulence results should be independent of the acoustic scattering level under the condition that it is sufficiently high.

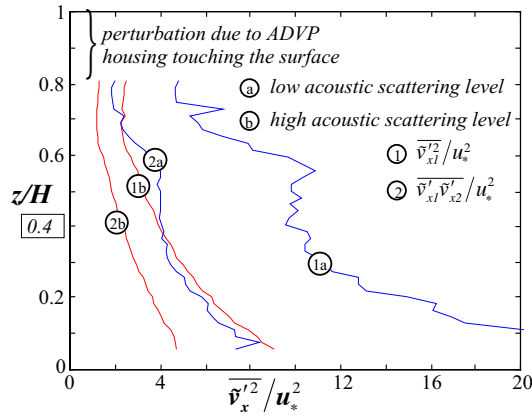


Fig. 11: Estimates of longitudinal turbulent normal stress with low and high acoustic scattering level

The corresponding (co)spectra and cumulative (co)spectra of $\overline{v'_{x1}{}^2}$ and $\overline{v'_{x1}v'_{x2}}$, for the level at $z/H=0.4$, confirm these findings. The noise contribution to $\overline{v'_{x1}{}^2}$ in the measurements with a low acoustic scattering level is higher than in those with a supply of acoustic targets. In both cases it remains nearly constant over the frequency range. The cospectrum and cumulative cospectrum of $\overline{v'_{x1}v'_{x2}}$ for the measurements with a supply of acoustic targets show the typical $-5/3$ -slope and “S” shape, respectively, and appear to be of good quality. Their counterparts for the measurements with low acoustic scattering level indicate that the remaining noise in $\overline{v'_{x1}v'_{x2}}$ mainly affects the frequency range above 1 Hz.

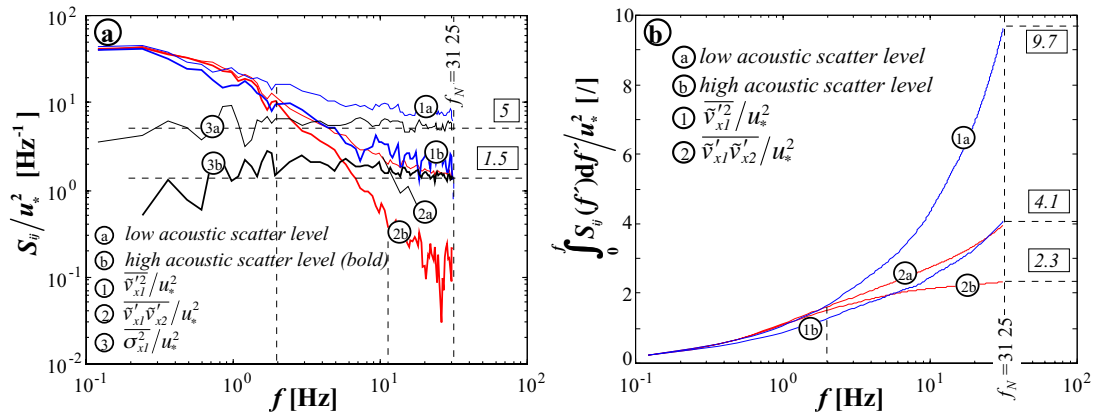


Fig. 12: Normalized power (co)spectra (a) and cumulative power (co) spectra (b) of $\overline{v'_{x1}{}^2}$, $\overline{v'_{x1}v'_{x2}}$ and σ_{x1}^2 for high and low acoustic scattering level

Even though the measurements with low acoustic scattering level yield low quality turbulence results that are polluted by noise, they still give good estimates of the time-averaged velocities, as shown in Fig. 13. Nearly identical profiles of the time-averaged longitudinal velocity are obtained for low and high acoustic scattering levels. This confirms that the noise is unbiased, $\overline{\sigma_i} = 0$. Hence it does not affect the estimates of the time-averaged velocity.

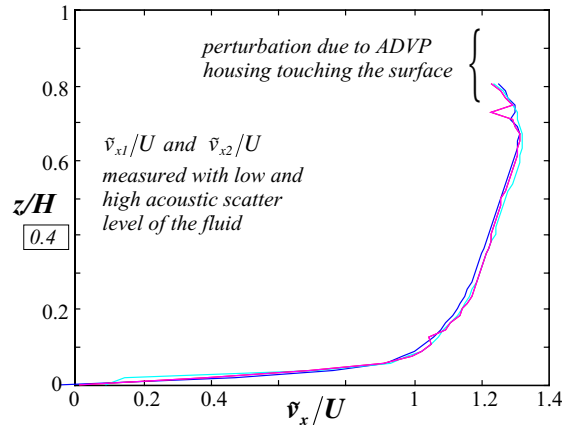


Fig. 13: \bar{v}_{x1}/U and \bar{v}_{x2}/U measured with low and high acoustic scattering level

It can be concluded that accurate measurements of the time-averaged velocities can be obtained even with low acoustic scattering levels, but that accurate turbulence measurements require a high acoustic scattering level which can be improved by supplying suitable acoustic targets to the flow.

5 Conclusions

This paper proposes efficient ways to reduce the parasitical noise contribution in pulse-to-pulse coherent Acoustic Doppler Velocimetry (ADV) thereby improving turbulence measurements with such instruments. Although the three-dimensional mean flow field can be accurately measured with three-receiver ADV instruments, turbulence measurements with these instruments suffer from parasitical noise contributions that cannot be accurately estimated and eliminated. To overcome this problem, Hurther and Lemmin (2001) propose the HL method, based on an ADV configuration with four instead of three receivers. Due to the fourth receiver, a redundancy of the vertical velocity component exists that allows to estimate the noise level and subsequently extract it from the longitudinal and transversal velocity components.

In the present investigation, this four-receiver ADV system has been optimized by turning the receiver plains by 45° with respect to the direction of the mean flow. This reorientation has several advantages:

- It provides for redundant information on all three velocity components which theoretically allows to directly obtain all turbulent stresses free of noise. This avoids the potential of error propagation which may result from the application of the HL method.
- The quality of the measurements can be checked with this configuration because the noise levels of all three velocity components can be directly estimated from the measurements. Furthermore, from this information the noise level of each receiver can be individually determined providing a continuous check on the performance of the instrument. This is a great advantage over the previous four-receiver ADVP which did not allow this detailed system check.

The parasitical noise is not completely eliminated by the proposed method. It is, however, reduced by about an order of magnitude when compared to the uncorrected results where the uncorrected results represent the level that can be obtained with three-receiver instruments. Therefore, the useful frequency range characterized by low noise levels is also extended by about an order of magnitude.

The knowledge of the noise levels through the calculation of noise spectra allows to estimate the accuracy of the turbulence measurements. We have demonstrated that cumulative power spectra are particularly well suited for the determination of the noise effects and their elimination due to their particular shape in turbulent flow. They allow:

- to investigate the quality of the data. Power spectra become always noisy at the high frequency end and the amplitude of the variation makes it often difficult to determine the mean spectral slope in that range (Fig. 8a). Cumulative power spectra are smooth and therefore indicate more clearly the trend at the high frequency end (Fig. 8b). We have demonstrated that the noise effect strongly modifies this part of the cumulative spectra and this makes it easy to detect noise contributions.
- to provide for an optimal choice of the measuring frequency. The presence of an inertial subrange in a power spectrum is in itself not yet a proof that the turbulence is well resolved in the measurements. The extent of the inertial subrange in the frequency domain depends on the specific flow conditions. Thus a cumulative spectrum should always reach past the “straight line” section and well into the high frequency curving part (Fig. 9). This is a good indication that a high enough sampling frequency has been chosen. However, it has to be realized that increasing the sampling frequency in an effort to extend the observations to higher frequencies may deteriorate the turbulence estimates. It risks to push the Nyquist frequency into a spectral region where only white noise is found (Fig. 9).

ADV instruments typically operate at a measuring frequency of O(20Hz). This may not always be sufficient to cover the full inertial subrange. It was demonstrated that turbulence is nearly isotropic above 10 Hz in the open-channel laboratory flow we have investigated. In this particular case the non-captured high frequency range does not significantly contribute to the turbulent normal stresses with the contribution being estimated at less than 10% (Fig. 9). This corresponds to the estimated system accuracy.

The contributions of the high frequency range to the turbulent shear stresses and the turbulent isotropy are even smaller. ADV instruments can thus resolve the low frequency part of the turbulence spectrum that interacts dynamically with the mean flow and that is important for the understanding of typical hydraulic processes. The non-captured, high frequency contribution mainly relates to the nearly-isotropic energy dissipation. ADV instruments can thus be successfully applied in many turbulence investigations provided that the noise contribution is correctly eliminated. However, in all these efforts it has to be remembered that the actual velocity sampling frequency is virtually restricted to what the acoustic targets can provide.

Successful acoustic turbulence measurements with all ADV require sufficiently high acoustic scattering levels. Estimates of time-averaged velocities, on the other hand, are less sensitive and may still be possible at low acoustic scattering levels if measurements are taken over a sufficiently long time. Low scattering levels are often encountered in clear water, as is found in laboratory flumes, deep oceans, lake etc. Little can be done about this in a “natural” flow environment of deep oceans, lakes and some rivers. For laboratory studies, it is frequently suggested to “seed” the flow using small, almost neutrally buoyant particles as seeding material in order to increase the signal-to-noise ratio. Although this may be a solution in some cases, it is difficult, rather costly and may cause an undesirable pollution of the installation.

A simple low cost and non-polluting technique to supply acoustic targets to the fluid has been described here which proved to be successful in our laboratory measurements. It consists of generating micro-hydrogen bubbles of an optimum size in the fluid by means of electrolysis. It is illustrated that very noisy turbulence measurements are obtained with low acoustic scattering levels and that a significant improvement in the quality of the results is possible by supplying sufficient micro-hydrogen bubbles as acoustic targets.

The principal conclusion of this paper is that accurate turbulence measurements can be obtained with Acoustic Doppler Velocimeters by adopting an optimized four-receiver configuration of the instrument and by assuring a sufficiently high acoustic scattering level. Although uniquely illustrated by means of ADV measurements which have the further advantage to allow non-intrusive profiling, the concepts outlined herewith can invariantly be applied to improve turbulence measurements with other ADV instruments.

Acknowledgements

This research is being sponsored by the Swiss National Science Foundation under grants Nr.2100-052257.97/1 and 2000-059392.99/2. The first author gratefully acknowledges his PhD supervisor, Prof. W.H. Graf, for his support and Prof. H.J. de Vriend for many fruitful discussions during his stay at the EPFL.

APPENDIX I. REFERENCES

- Blanckaert, K. (2001). "Discussion on: Bend-flow simulation using 2D depth-averaged model." *J. Hydr. Eng.*, 127(2), 167-170.
- Blanckaert, K. & de Vriend, H. J. (2002). "Secondary flow in sharp open-channel bends." (*submitted for publication*).
- Blanckaert, K. & Graf, W. H. (2001). "Experiments on flow in a strongly curved channel bend." *Proc. 29th IAHR Congress*, Vol. D1, Beijing, China, 371-377.
- Cellino, M. & Graf, W. H. (1999). "Sediment-Laden flow in open-channels under noncapacity and capacity conditions." *J. Hydr. Eng.*, 125(5), 455-462.
- Garbini, J. L., Forster, F. K. & Jorgensen, J. E. (1982). "Measurement of fluid turbulence based on pulsed ultrasound techniques. Part I. Analysis." *J. Fluid Mech.*, 118, 445-470.
- Graf, W. H. & Yulistiyanto, B. (1998). "Experiments on flow around a cylinder; the velocity and vorticity fields." *J. Hydr. Res., IAHR*, 36(4), 637-653.
- Graf, W. H. & Istiarto, I. (2002). "Flow pattern in the scour hole around a cylinder." *J. Hydr. Res., IAHR*, 40(1), 13-20.
- Hurther, D. (2001). "Sediment transport assessment in suspension flow based on coherent structure characteristics." *Proc. JFK Student Paper Comp., 29th IAHR Congress*, Beijing, China, 73-82.
- Hurther, D. & Lemmin, U. (1998). "A constant beamwidth transducer for three-dimensional Doppler profile measurements in open channel flow." *Meas. Sciences Techn.*, 9(10), 1706-1714.
- Hurther, D. & Lemmin, U. (2001). "A correction method for turbulence measurements with a 3-D acoustic Doppler velocity profiler." *J. Atm. Oc. Techn.*, Vol.18, 446-458.
- Kolmogoroff, A. N. (1941). "The local structure of turbulence in incompressible viscous fluid for very large Reynolds numbers." *C. R. Acad. Sci. U.R.S.S.*, 30(301).
- Lemmin, U. & Rolland, T. (1997). "Acoustic velocity profiler for laboratory and field studies." *J. Hydr. Eng.*, 123(12), 1089-1098.
- Lhermitte, R. & Lemmin, U. (1994). "Open-channel flow and turbulence measurement by high-resolution Doppler sonar." *J. Atm. Oc. Techn.*, 11(5), 1295-1308.
- Nezu, I. & Nakagawa, H. (1993). *Turbulence in open-channel flows*, IAHR-monograph, Balkema.
- Nikora, V. (1999). "Origin of the "-1" Spectral law in wall-bounded turbulence." *Physical Review Letters*, 83(4), 734-736.
- Rolland, T. (1994). "Développement d'une instrumentation Doppler ultrasonore adaptée à l'étude hydraulique de la turbulence dans les canaux." PhD thesis no 1281, EPFL, Lausanne, Switzerland.
- Rolland, T. & Lemmin, U. (1997). "A two-component acoustic velocity profiler for use in turbulent open-channel flow." *J. Hydr. Res.*, 35(4), 545-561.
- Shen, C., & Lemmin, U. (1996). "A tristatic Doppler velocity profiler and its application to turbulent open-channel flow." *Advances in Turbulence VI*, P. A. Monkewitz and S. Gavrilakis, eds., Kluwer Academic Publications, Lausanne, 483-486.

- Shen, C. & Lemmin, U. (1997). "Ultrasonic scattering in highly turbulent clear water flow." *Ultrasonics*, 35, 57-64.
- Shen, C. & Lemmin, U. (1998). "A new method for probing the turbulence scalar spectrum by ultrasonic scanning." *Experiments in Fluids*, 24, 90-92.
- Song, T. & Graf, W. H. (1996). "Velocity and turbulence distribution in unsteady open-channels flows." *J. Hydr. Engng, ASCE*, 122(3), 141-154.
- Song, T., Graf, W. H. & Lemmin, U. (1994). "Uniform flow in open channels with movable gravel bed." *J. Hydr. Res., ASCE*, 32(6), 861-876.
- Tchen, C.M. (1953). "On the spectrum of energy in turbulent shear flow." *J. Res. Natl. Bur. Stand.*, 50(1), 51-62.
- Voulgaris, G. & Trowbridge, J. H. (1998). "Evaluation of the Acoustic Doppler Velocimeter (ADV) for turbulence measurements." *J. Atm. Oc. Techn.*, 15, 272-289.
- Zedel, L., Hay, A. E., Cabrera, R. & Lohrmann, A. (1996). "Performance of a single beam pulse-to-pulse coherent Doppler profiler." *J. Oceanic Eng., IEEE*, 21(3), 290-297.

APPENDIX II. NOTATION

ADV	=	Acoustic Doppler Velocimeter / Velocimetry
ADVP	=	Acoustic Doppler Velocity Profiler
B	=	flume width
$Fr=U/\sqrt{gH}$	=	Froude number
H	=	flow depth
L_x	=	macro lengthscale of turbulence in the wavenumber space
NPP	=	number of pulse-pairs
Q	=	discharge
$Re=UH/\nu$	=	Reynolds number of reach-averaged flow
S_b	=	downstream bottom slope
S_{ij}	=	cospectrum of components i and j
SNR	=	signal-to-noise ratio
T_x	=	macro timescale of turbulence in the frequency space
U	=	$Q/(BH)$ = globally-averaged velocity
c	=	speed of sound in the fluid
f	=	frequency
k	=	wavenumber
prf	=	pulse-repetition-frequency
v_j	=	velocity component along i -direction
x,y,z	=	longitudinal, transversal and vertical reference axes

symbols

α	=	angle between vertical and scattered wave
β	=	angle between longitudinal axis and vertical (emitter-receiver) plane
λ	=	wavelength
ν	=	molecular viscosity of water; $\nu=1.004 \times 10^{-6} \text{ m}^2/\text{s}$ at 20°
σ	=	noise contribution on a receiver or a velocity component
arrow	=	vector quantity

overbar	=	time-averaged values
prime	=	fluctuating part of a quantity (with zero time-averaged value)
tilde	=	measured value of a quantity that estimates its true value
O(.)	=	order of magnitude of .

subscripts

<i>D</i>	=	Doppler
<i>H</i>	=	horizontal component or projection in the horizontal (<i>x,y</i>)-plane
<i>HL</i>	=	reference to Hurther and Lemmin (2001)
<i>N</i>	=	Nyquist
<i>e</i>	=	emitter
<i>r</i>	=	receiver

PART II

EXPERIMENTAL OBSERVATIONS

II.0	Introduction	
II.1	Mean Flow and Turbulence in Open-Channel Bend	II.1
II.2	Bend-Flow Simulation Using 2D Depth-Averaged Model	II.15
II.3	Experiments on Flow in a Strongly Curved Channel Bend	II.19
II.4	Secondary Currents Measured in Sharp Open-Channel Bends	II.27
II.5	Conclusions	II.37

II.0 Introduction

An Acoustic Doppler Velocity Profiler (ADVP), developed in our laboratory, has been used to measure in detail the three-dimensional flow field and the turbulence in open-channel bends. A limited series of experiments in a small low-budget flume, done with the aim of testing the capabilities of the ADVP, was followed by extended series of experiments in a large optimized flume. This dissertation mainly considers the small-flume experiments, which yielded results beyond all expectations, and only includes few large-flume results.

This part II presents the most relevant experimental data and observations that are subsequently analyzed in parts III and IV. It consists of four papers with the following contents:

- **chapter II.1** explains the working principle of the ADVP and the data-analysis techniques. Furthermore, it presents distributions of all three mean velocity components and all six Reynolds stresses as well as the mean flow and turbulent kinetic energy measured in the small-flume experiments.
- **chapter II.2** compares distributions of the downstream velocity and the secondary circulation measured in the small-flume experiments with predictions according to linear models, which are commonly used to account for the vertical dimension of the flow field in depth-integrated flow models. Chapter IV.1 will explain these linear models in detail.
- Similar to the previous paper, **chapter II.3** compares distributions of the downstream velocity and the secondary circulation measured in the large-flume experiments with linear model predictions.
- **chapter II.4** presents three-dimensional patterns of the downstream velocity and the multi-cellular secondary circulation measured in the large-flume experiments.

At the end of Part II, the main **conclusions** are summarized.

Some other small-flume data have been presented in a paper that is not included in this dissertation:

Blanckaert, K., and Graf, W. H. (1999) "Experiments on flow in open-channel bends." *Proc. 28th Congr. IAHR.*, Techn. Univ.Graz, Graz, Austria, CD-ROM.

II.1 MEAN FLOW AND TURBULENCE IN OPEN-CHANNEL BEND

By Koen Blanckaert¹ and Walter H. Graf,² Member, ASCE

ABSTRACT: Flow over a developed bottom topography in a bend has been investigated experimentally. The measuring section is in the outer-bank half of the cross section at 60° into the bend. Spatial distributions of the mean velocities, turbulent stresses, and mean-flow and turbulent kinetic energy are presented. The cross-sectional motion contains two cells of circulation: besides the classical helical motion (center-region cell), a weaker counterrotating cell (outer-bank cell) is observed in the corner formed by the outer bank and the water surface. The downstream velocity in the outer half-section is higher than the one in straight uniform flow; the core of maximum velocities is found close to the separation between both circulation cells, well below the water surface. The turbulence structure in a bend is different from that in a straight flow, most notably in a reduction of the turbulent activity toward the outer bank. Both the outer-bank cell and reduced turbulent activity have a protective effect on the outer bank and the adjacent bottom and thus influence the stability of the flow perimeter and the bend morphology.

INTRODUCTION

Most natural rivers meander and tend to erode the outer banks in their successive bends. Important engineering efforts are undertaken on rivers of all scales to stabilize the banklines. This is an essential component of projects to improve navigability; increase flood capacity and decrease floodplain destruction; avoid massive loss of fertile soil (Odgaard 1984); and reduce dredging requirements of the river. Recently, there has been an increased interest in the modeling of the erosional behavior of the outer bank (see the discussion section). However, little is known about the characteristics of the mean flow and turbulence near the outer bank, where the flow pattern is highly three-dimensional (3D).

A large amount of research on flow in bends has been performed in the last decades, but most of the experimental investigations concentrated on the central portion of the flow and often did not cover the outer-bank region in detail. Moreover, in most investigations a fixed rectangular section with a smooth bed was imposed on the flow. This is different from the rough turbulent flow over a typical developed bed topography, as found in nature. Furthermore, in most experimental investigations, not all of the three velocity and six turbulent stress components were measured, and the measuring grids were rather coarse. A literature review of experimental research on flow in open-channel bends is given in Table 1.

More recently, environmental problems such as the spreading and mixing of pollutants or the transport in suspension of polluted sediments have become of major concern in river management. These phenomena are closely related to the turbulence structure of the flow.

The scarcity of reliable experimental data on the 3D flow pattern and turbulence structure, particularly in bends, is responsible for the lack of insight into the physical mechanisms, such as those related to outer-bank erosion and the mixing of pollutants. Furthermore, this lack hampers the verification of investigations by means of numerical simulations.

In this study, detailed measurements were made of a rough turbulent flow in equilibrium with its developed bottom topography. Special attention was given to the complex flow

region near the fixed vertical outer bank. Nonintrusive measurements were made on a fine grid with an acoustic Doppler velocity profiler (ADVP), which simultaneously measures instantaneous profiles of all velocity components. This enables one to evaluate the three mean velocity components, v_j ($j = s, n, z$), along the downstream, transversal, and vertical axes, respectively [Figs. 1 (a and c)], as well as the six turbulent stress components, $-\rho v_j' v_k'$ ($j, k = s, n, z$).

This paper aims at improving our understanding of the flow and turbulence in bends and their relationship to boundary erosion and spreading (mixing) of pollutants. Furthermore, due to the detailed measurements on a fine grid, we want to provide a useful data set for verification of numerical simulations of the flow field. The paper gives a description of the experimental facility, hydraulic parameters, ADVP, and data-treatment procedures. Spatial distributions of the mean downstream velocity, mean cross-sectional motion, turbulent normal and shear stresses, and mean-flow and turbulent kinetic energy are presented and analyzed. The importance of the observed flow and turbulence distributions with respect to the stability of the outer bank and the adjacent bottom are discussed.

EXPERIMENTAL INSTALLATION

Experiments were performed in a $B = 0.4$ m wide laboratory flume with fixed vertical sidewalls made of plexiglass, consisting of a 2 m long straight approach section followed by a 120° bend with a constant radius of curvature of $R = -2$ m [Fig. 1(a); R is negative along the n -axis]. Initially, a horizontal bottom of nearly uniform sand, $d_{50} = 2.1$ mm, was installed. Subsequently, a discharge corresponding to clear-water scour conditions was established. As a result, the bottom in the straight approach channel remained stable, but a typical bar-pool bottom topography developed in the bend. Ultimately, this topography stabilized and there was no active sediment transport along the flume. The resulting developed bottom topography is shown in Fig. 1(a). The transversal bottom slope increases from $\sim 0^\circ$ at the bend entry to a maximum value of $\sim 24^\circ$ at 45° into the bend and subsequently shows an oscillating behavior [Fig. 1(b)]. A number of analytical models for the flow and the bottom topography have been proposed that qualitatively predict such a behavior (de Vriend and Struikema 1984; Odgaard 1986). A comparison of different models can be found in Parker and Johansson (1989). A superelevation of the water surface [Fig. 1(b)] develops from the bend entry onto $\sim 45^\circ$ into the bend. Subsequently it remains nearly constant (the fluctuations are within the measuring accuracy) at $\sim 0.65^\circ$, yielding a difference of $\Delta z_s = 4.5$ mm = $1.5(B/R)(U^2/g)$ in water surface elevation between the two banks.

The hydraulic conditions of the flow over this bottom to-

¹Res. Assoc., Lab. de Recherches Hydrauliques, Ecole Polytechnique Fédérale, CH-1015 Lausanne, Switzerland.

²Prof., Lab. de Recherches Hydrauliques, Ecole Polytechnique Fédérale, CH-1015 Lausanne, Switzerland.

Note. Discussion open until March 1, 2002. To extend the closing date one month, a written request must be filed with the ASCE Manager of Journals. The manuscript for this paper was submitted for review and possible publication on April 4, 2000; revised May 16, 2001. This paper is part of the *Journal of Hydraulic Engineering*, Vol. 127, No. 10, October, 2001. ©ASCE, ISSN 0733-9429/01/0010-0835-0847/\$8.00 + \$.50 per page. Paper No. 22307.

II.2

TABLE 1. Literature Review of Experimental Research on Flow in Open-Channel Bends

Literature	Cross section and channel bed	Planform	Flow regime	Size of measuring grid (approximately)	Number of vertical profiles in outer-bank region	Flow and turbulence measurements
Rozovskii (1957)	Rectangular: smooth bed	Single bend, 180°	Transition	$H/7 \times B/8$	2	v_s, v_n
	rough bed		Rough turbulent	$H/7 \times B/8$	2	
	Triangular		Transition	$H/7 \times B/4$	1	
Götz (1975)	Rectangular smooth bed	Single bend, 180°	Transition	$H/5 \times B/10$ (denser near banks and bottom)	2, 3, 4, 5 (for aspect ratios of 20, 10, 4.6, 2.9)	v_s, v_n
de Vriend (1979)	Rectangular smooth bed	Single bend, 180°	Transition	$H/10 \times B/10$	3	v_s, v_n
de Vriend (1981)	Rectangular rough bed	Single bend, 180°	Rough turbulent	$H/10 \times B/10$	3	v_s, v_n
Siebert (1982)	Rectangular smooth bed	Single bend, 180°	Transition	$H/5 \times B/4$	3	v_s, v_n v'_s, v'_n, v'_z
				$z/H = 0.09, 0.66 \times B/3$	2	
Dietrich and Smith (1983)	Natural topography; sand bottom	Meander, field study	Rough turbulent	$H/6 \times B/13$	<10	v_s, v_n
Steffler (1984)	Rectangular smooth bed	Single bend, 270°	Transition	$H/10 \times B/10$ (denser near bottom)	2	$v_s, v_n, \overline{v_s^2}, \overline{v_n^2}$
Anwar (1986)	Natural topography; sand bottom	Single bend, 35°; field study	Rough turbulent	$H/4 \times B/15$	<7	$\frac{v_s, \overline{v_s^2}}{v'_s, v'_n, v'_z}$
Odgaard and Bergs (1988)	Natural bed topography, fixed inclined banks; sand bottom	Single bend, 180°	Transition	$H/10 \times B/8$	1	v_s, v_n
Muto (1997)	Rectangular smooth bed	Meander	Transition	$H/10 \times B/10$	5	$v_s, \overline{v'_z v'_z}$
Tominaga et al. (1999)	Rectangular smooth bed + different configuration with vegetation	Single bend, 60°	Transition	$H/10 \times B/18$ (bend outlet section)	6	v_s, v_n, v_z
				$H/5 \times B/18$ (other sections)		
Present study	Natural bed topography, fixed vertical banks; sand bottom	Single bend, 120°	Rough turbulent	$H/22 \times B/33$	65	$v_s, \overline{v'_z v'_z}$

Note: H = averaged water depth; B = channel width; z = distance above bed; outer-bank region = region extending $2H$ from outer bank; v_j ($j = s, n, z$): mean velocities; $\overline{v'_j v'_k}$ ($j, k = s, n, z$): turbulent correlations.

pography are listed in Table 2. $Q = 17$ L/s is the discharge, $H = 0.11$ m is the reach-averaged flow depth, $U = Q/(BH) = 0.38$ m/s is the reach-averaged velocity, and $S_b = 1.89\%$ is the reach-averaged water-surface gradient on the centerline. From these basic hydraulic parameters, the following reach-averaged quantities can be derived.

The boundary-shear stress estimated from this water-surface gradient as $\tau \approx \rho g R_b S_b = 1.35$ N/m² — where $R_b = 0.07$ m is the hydraulic radius of the cross section — corresponds well to the critical shear stress for the sediment according to Shields' diagram. The Chézy friction factor can be estimated by $C = 21.1 (R_b/d_{50})^{1/6} = 38$ m^{1/2}/s [Strickler (1923), pp. 11–15] or by $C = U/(R_b S_b)^{1/2} = 33$ m^{1/2}/s. Throughout the study, a value of $C = 35$ m^{1/2}/s is therefore adopted further on. The flow Reynolds numbers, $R = UH/\nu = 42,000$ and $R_* = u_* k_s/\nu \approx 70$ (with $u_* = (\sqrt{g/C})U$, $k_s \approx d_{50}$ is the Nikuradse equivalent sand roughness, and ν is the molecular kinematic viscosity), show that the flow is rough turbulent, and the Froude number, $F = U/\sqrt{gH} = 0.36$, indicates a subcritical flow.

The parameters $R/B = 5$ and $R/H = 17.9$ correspond to a rather tight bend. With an aspect ratio of $B/H = 3.6$, the flume is much narrower than typical natural open-channel bends. In a wide bend with a developed bed topography, however, often the shallow point bar is wide and the flow is concentrated over the deepest part of the section near the outer bank, where an important transversal bottom slope exists [Odgaard (1984), Fig. 20; Dietrich (1987), Fig. 8.2]. It is expected that the flow over the deepest outer half-section in the reported experiment is representative of the flow over the deepest part in wider natural bends.

Three-dimensional velocity measurements were made at one single section, located at 60° from the bend entrance, being in

the reach with the least downstream bottom variation, where only the half-section at the outer bank was investigated. The data were analyzed in a reference system with the s -axis pointing downstream along the channel centerline, the transversal n -axis pointing to the inner bank, and the vertical z -axis directed upward from the horizontal (s, n)-plane [Figs. 1(a and c)]. The ADVP developed in our laboratory (Lemmin and Roland 1997) was used. The nonintrusive measurements were made by measuring through the outer bank (plexiglass), with the ADVP mounted in a water-filled box attached to the outer bank [Figs. 1(a and c)].

The ADVP consists of a central emitter, symmetrically surrounded by four wide-angle receivers, R1 to R4 (Fig. 2). The central transducer periodically emits acoustic pulses. Imagine that it emits an acoustic pulse at the time $t = 0$ (Fig. 2). While progressing along the water column, the acoustic pulse is backscattered on targets moving with the water. The backscattered echo is recorded by the four receivers, R1 to R4. An echo recorded after a time t_i has traversed a flight path of length ct_i ($c \approx 1,500$ m/s is the speed of sound in water). From elementary geometry it follows from what position along the water column, $i = 1, \dots, N$ (Fig. 2), the backscattered echo originated. By continuously recording the backscattered signal, the entire water column is covered.

By dividing the arrival time, t_i , in intervals of Δt (which can be chosen), discrete measuring points are defined along the water column (with a spacing of about $c\Delta t/2$). After a time $T = \text{prf}^{-1}$ (pulse repetition frequency), long enough to have the backscattered echo recorded from the entire water column and long enough for parasitical echoes to have died out, the central transducer can emit the next acoustic pulse (Fig. 2). The signals recorded by the receivers from NPP (number pulse

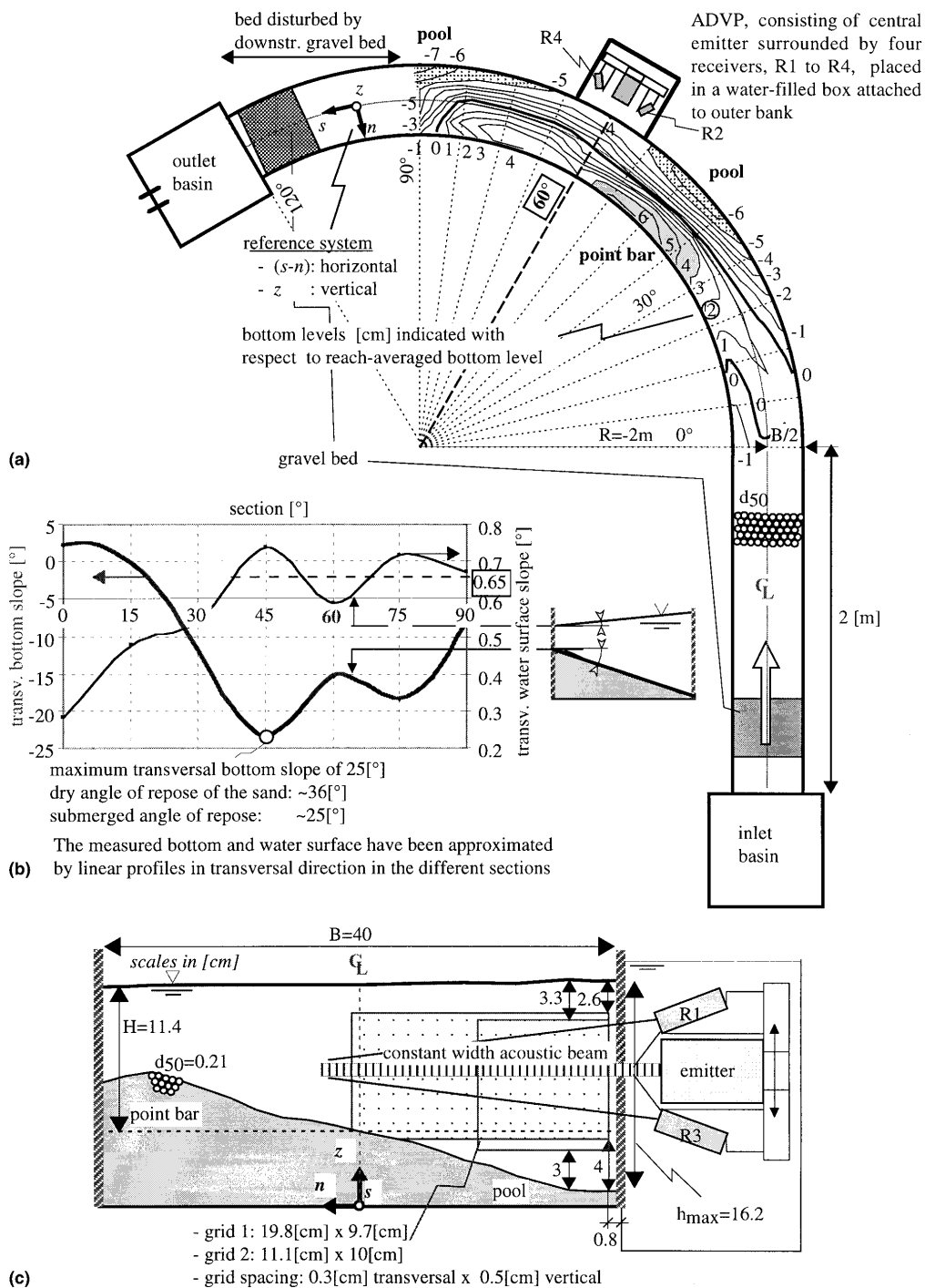


FIG. 1. (a) Experimental Setup, Bottom Topography, and Reference System; (b) Transversal Bottom and Water Surface Slope along Flume; (c) Measurement Section at 60° , Acoustic Doppler Velocity Profiler (ADVP), and Reference System

TABLE 2. Hydraulic Conditions

R	B	d ₅₀	Q	H	S _s	U	u*	C	R	R*	F	R/B	R/H	B/H
(m)	(m)	(mm)	(L/s)	(m)	[%e]	(m/s)	(m/s)	(m ^{1/2} /s)	(10 ³)	(/)	(/)	(/)	(/)	(/)
2.0	0.40	2.1	17	0.11	1.89	0.38	0.034	35	42	70	0.36	5	17.9	3.6

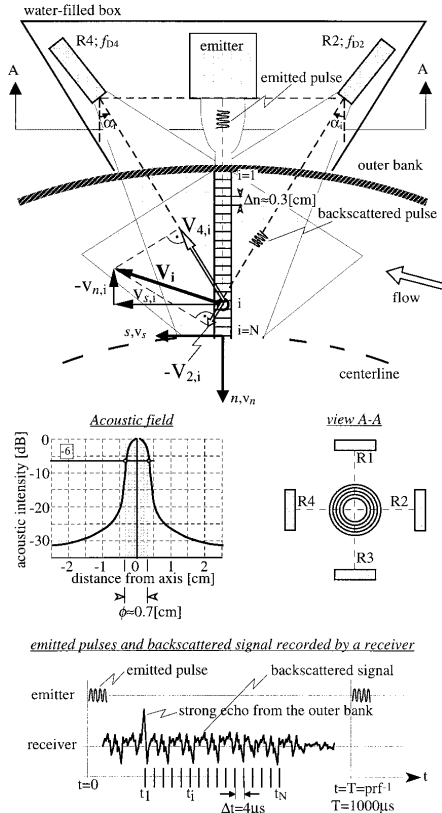


FIG. 2. Acoustic Doppler Velocity Profiler

pairs) consecutive acoustic pulses are used to estimate one quasi-instantaneous Doppler frequency, $f_{Dr,i}(t)$ ($r = 1, \dots, 4$), in each of the measuring points ($i = 1, \dots, N$, Fig. 2), which corresponds with one quasi-instantaneous velocity, $v_{j,i}(t)$ ($j = s, n, z$; $i = 1, \dots, N$) (see below).

In the reported experiment, $T = 1,400 \mu\text{s}$, and for most analysis the data were treated with $\text{NPP} = 16$, thus giving a sampling frequency of $f = (T \times \text{NPP})^{-1} = 44.6 \text{ Hz}$ for the quasi-instantaneous velocities. The sampling period was 180 s, and measuring points were defined every $\Delta n = 3 \text{ mm}$ along the water column ($\Delta t = 4 \mu\text{s}$). By using a central emitter consisting of five annular piezoelectrical transducers, a focalized acoustic field with a constant beamwidth over the entire water column can be generated. The intensity of the acoustic field is maximum on the axis of the emitter, decreasing in a Gaussian way with distance perpendicular to the axis. The intensity isoline of -6 dB is situated at about 0.35 cm from the axis, from which the diameter of the measuring volume can be estimated as $\phi \approx 0.7 \text{ cm}$ (Hurther and Lemmin 1998) (Fig. 2). The zone where the acoustic field is focalized is limited and depends on the electronic configuration of the ADVP. In the presented experiments, measurements were made with focalized zones of 25 and 15 cm long [corresponding to measuring

grids 1 and 2; see Fig. 1(c)]. Due to this limitation, the entire channel width could not be covered and the measurements are limited to the outer half-section.

In the following, the derivation of the velocity field from the Doppler frequencies is given for the horizontal plane formed by the two receivers R2 and R3; the vertical plane formed by the two receivers R1 and R3 is similar (Fig. 2). The Doppler frequencies $f_{D2,i}(t)$ and $f_{D4,i}(t)$, resulting from the signal recorded by R2 and R4, relate to the velocity components lying along the axes of the emitter and the receiver, $v_{n,i}(t)$ and $v_{2,i}(t)$, respectively $v_{n,i}(t)$ and $v_{4,i}(t)$ [Lemmin and Rolland (1997), eq. (1)] as

$$f_{D2,i}(t) = \frac{f_e}{c} (-v_{n,i}(t) + v_{2,i}(t)) \quad (1a)$$

and

$$f_{D4,i}(t) = \frac{f_e}{c} (-v_{n,i}(t) + v_{4,i}(t)) \quad (1b)$$

where $f_e = 1 \text{ MHz}$ is the frequency of the emitter and c is the speed of sound in water. By substitution of the geometrical relations (α_i defined in Fig. 2)

$$v_{2,i}(t) = v_{s,i}(t) \sin(-\alpha_i) - v_{n,i}(t) \cos(-\alpha_i) \quad (2a)$$

$$v_{4,i}(t) = v_{s,i}(t) \sin(\alpha_i) - v_{n,i}(t) \cos(\alpha_i) \quad (2b)$$

a system of equations for the velocity components ($v_{s,i}$, $v_{n,i}$) is obtained

$$\frac{f_e}{c} [-v_{s,i}(t) \sin \alpha_i - v_{n,i}(t) (\cos \alpha_i + 1)] = f_{D2,i}(t) \quad (3a)$$

$$\frac{f_e}{c} [v_{s,i}(t) \sin \alpha_i - v_{n,i}(t) (\cos \alpha_i + 1)] = f_{D4,i}(t) \quad (3b)$$

that has the solutions

$$v_{s,i}(t) = \frac{f_{D4,i}(t) - f_{D2,i}(t)}{2 \sin \alpha_i} \cdot \frac{c}{f_e} \quad (4a)$$

$$v_{n,i}(t) = \frac{-f_{D4,i}(t) + f_{D2,i}(t)}{2(\cos \alpha_i + 1)} \cdot \frac{c}{f_e} = \frac{-f_{D4,i}(t) + f_{D2,i}(t)}{4 \cos^2 \alpha_i / 2} \cdot \frac{c}{f_e} \quad (4b)$$

The index $i = 1, \dots, N$, indicating the measuring point, is dropped from there on. From these instantaneous velocities, $v_j(t)$ ($j = s, n, z$), it is straightforward to derive the mean velocities, \bar{v}_j , the velocity fluctuations, $v'_j(t) = v_j(t) - \bar{v}_j$, and turbulent correlations, $\overline{v'_j v'_k}$ ($j, k = s, n, z$) (the overbar denotes time-averaged values; for simplicity of notation it is omitted on the mean velocities). In both orthogonal planes formed by the receivers, a simultaneous and independent measurement of the transversal velocity component, $v_n(t)$, exists. This is of importance since it permits an evaluation and correction for the experimental noise (Hurther and Lemmin 2001). Furthermore, comparison of both measurements gives an idea about the accuracy of the ADVP.

The above describes how the ADVP measures the flow over an entire water column, which is oriented along the n -axis with the present ADVP configuration [Figs. 1(c) and 2]. Measurements were made in two overlapping grids [Fig. 1(c)] by manually displacing the ADVP in a vertical direction. Only the results from the larger grid are shown in the following; results from the smaller grid are similar. The grid spacing for the

larger grid was 0.5 cm vertically ($\sim H/22$) and 0.3 cm transversally ($\sim B/133$), resulting in 1,360 measuring points. The regions near the water surface and the bottom [indicated in Fig. 1(c)] could not be measured with the adopted configuration of the ADVP (see below).

The ADVP sometimes produces results in a limited number of measuring points that fall far outside the usual scatter. There are two reasons for these clearly erroneous measurements. (1) As explained in the section on the ADVP, the velocity in point i (Fig. 2) on the transversal profile is derived from the backscattered signal recorded at arrival time t_i . It sometimes happens that multiple-scattered parasitical echos reach the receiver at exactly the same arrival time, thus perturbing the measurement in point i . This effect is very local and only influences a couple of points on the profiles. By carefully choosing the ADVP configuration, this problem is strongly reduced and these parasitical echos only occur occasionally. (2) In the reported experiment, the regions close to the water surface and to the bottom far away from the bank contained some clearly erroneous points. This is while the flypath of the backscattered signal passes near the water surface or the bottom for points far away from the bank. The influence of this surface and bottom proximity gave perturbations in some of the measuring points.

A goal of this research is to analyze experimentally the various terms in the flow equations (momentum, vorticity, and energy equations) and to derive the mixing coefficients. This requires the evaluation of derivatives of the measured quan-

ties (such as derivatives of mean velocities or turbulent stresses), which is difficult to do from the raw data because of the experimental scatter. Therefore, analytical surfaces have been fitted to the experimental data using 2D smoothing splines with weight functions [de Boor (1978), chapters 14 and 17]. Thanks to the weight functions, the measured data can be extended outside the measuring grid by imposing physical boundary conditions (such as the no-slip condition on rigid boundaries and no shear parallel to the water surface). The fitted surface is found as a compromise between smoothness of the analytical surface [see de Boor (1978) for a mathematical description] and proximity to the measured data, defined as

$$\sum_{\text{grid}} w(n, z)(x_{\text{exp}}(n, z) - x_{\text{fit}}(n, z))^2 < \text{tolerance} \quad (5)$$

in which w is the weight function, x_{exp} are the experimental values of the concerned variable, and x_{fit} the approximation by surface fitting to them. The choice of a compromise between both criteria is subjective and has to be made separately for each fitted quantity. Care has been taken not to introduce systematic errors. This means that $x_{\text{exp}} - x_{\text{fit}}$ should have a random distribution over the measuring grid with frequent sign changes along both the n - and z -directions. Thanks to the fine measuring grid, this analytical surface fitting could be done with a high precision.

This surface fitting is illustrated for the normalized transversal turbulent normal stress, $\overline{v_n'^2}/u_{*,60}^2$ [this variable is treated further on in Fig. 5(c)]. Figs. 3(a and b) show a spatial view

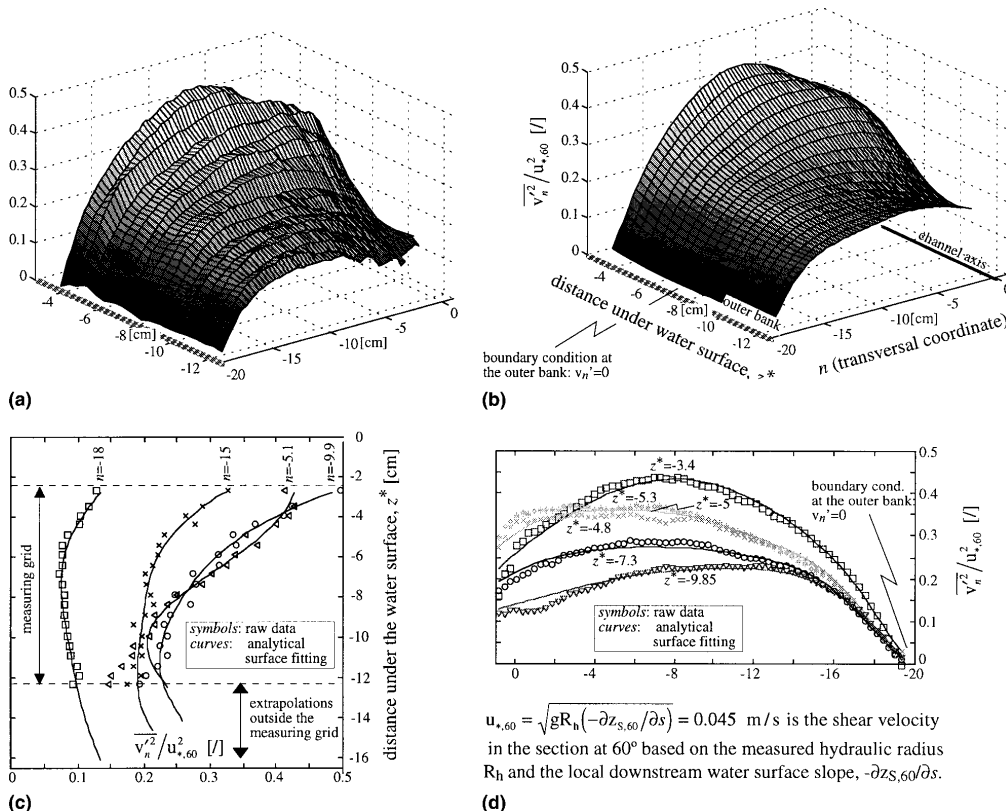


FIG. 3. Surface Plots of Measured (a) and Surface-Fitted (b) Normalized Transversal Turbulent Normal Stress $\overline{v_n'^2}/u_{*,60}^2$; Vertical (c) and Transversal (d) Profiles of Measured and Surface-Fitted $\overline{v_n'^2}/u_{*,60}^2$

II.6

of the raw data and the surface-fitted ones. Fig. 3(c) shows vertical profiles of the raw and the fitted data at some characteristic locations [close to the outer bank, in the outer-bank cell, at the separation between both cells, and in the center-region cell; see Fig. 4(b)]. Similarly, Fig. 3(d) shows some transversal profiles distributed over the measuring grid. At the outer bank, the physical boundary condition, $v_n^2 = 0$, has been imposed [Figs. 3(b and d)]. The fitted surface closely follows the raw data and conserves all its characteristic features, but smooths the scatter. The analytically fitted surfaces are used for most analysis of the data and for their further presentation in this paper.

The accuracy of the measurements has been evaluated indirectly by

1. Comparing the results of the measurements made on the two overlapping grids with different configurations of the ADVP
2. Comparing the two simultaneous and independent measurements of the transversal velocity component, $v_n(t)$
3. Evaluating a coefficient of determination of the surface fitting procedure, defined as [Lancaster and Salkauskas (1986), p. 55]

$$R^2 = 1 - \frac{\sum (x_{\text{exp}} - x_{\text{fit}})^2}{\sum (x_{\text{exp}} - \langle\langle x_{\text{exp}} \rangle\rangle)^2} \quad (6)$$

in which $\langle\langle x_{\text{exp}} \rangle\rangle$ is the average value over the measuring grid of x_{exp} . The summation is done over the measuring grid; clearly erroneous data (explained before) have been

omitted. This coefficient gives an idea about the scatter on the data. This scatter includes systematic errors due to inaccuracy of the ADVP alignment as well as random scatter inherent to experimental measurements.

An estimation of the accuracy and the coefficient of determination of the surface-fitting procedure are reported in Figs. 4–6. Overall, a high accuracy was obtained. The accuracy of the mean velocities was slightly better than that of the turbulent normal stresses, followed by the turbulent shear stresses. In general, the uncertainty increased somewhat with distance from the bank. Close to fixed boundaries (in the region of about 20% of the water depth), the measurements of the turbulent stresses are not very reliable, which is mainly due to the large gradient in the mean velocity that exists in the measuring volumes. Care should be taken with the interpretation of boundary shear stresses, which can only be estimated after bridging this region through extrapolation. The mean velocity measurements remain accurate close to the fixed boundaries. A detailed analysis of the precision and accuracy of measurements made with the ADVP is presented by Hurther and Lemmin (2001).

EXPERIMENTAL RESULTS

Time-Averaged Velocities

The distribution of the normalized downstream velocity component, v_s/U , in the half-section investigated is presented in Fig. 4(a). Over the larger part of the measured region, its depth-averaged value is almost constant at $U_s/U \approx 1.35$ [Fig.

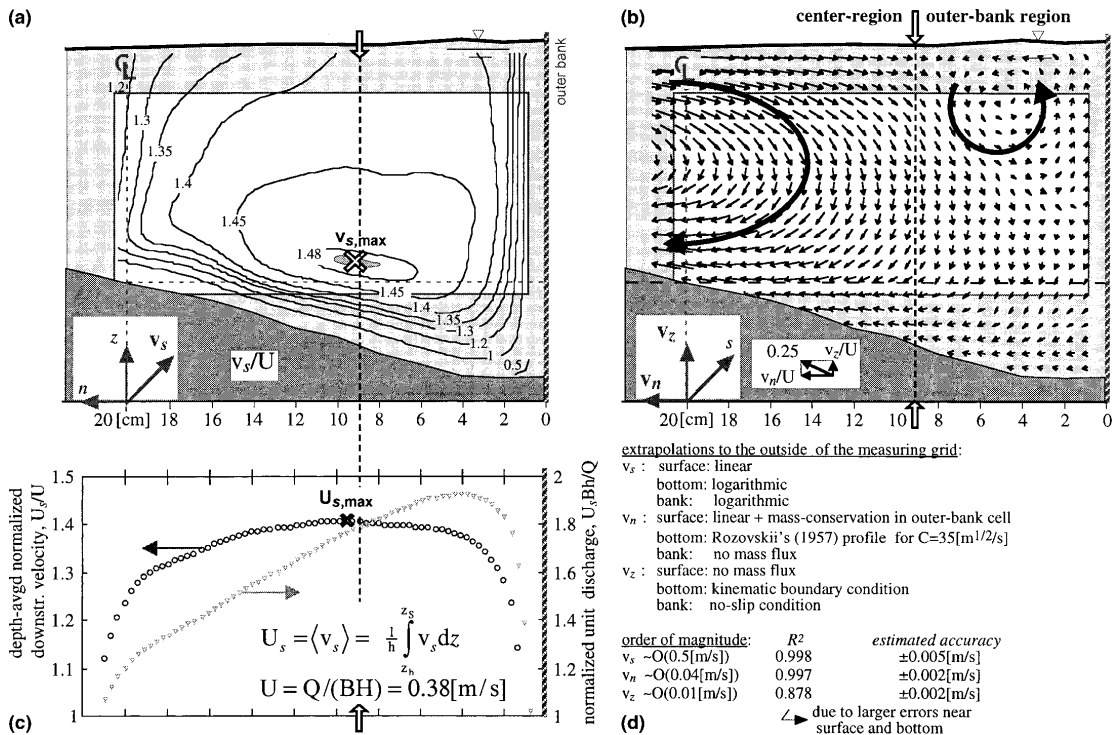


FIG. 4. (a) Isocontours of Normalized Downstream Velocity, v_s/U ; (b) Vector Representation of Normalized Cross-Sectional Motion, $\sqrt{v_n^2 + v_s^2}/U$; (c) Normalized Depth-Averaged Downstream Velocity, U_s/U , and Normalized Unit Discharge, U_s*Bh/Q ; (d) Extrapolations Outside Measuring Grid and Estimation of Accuracy

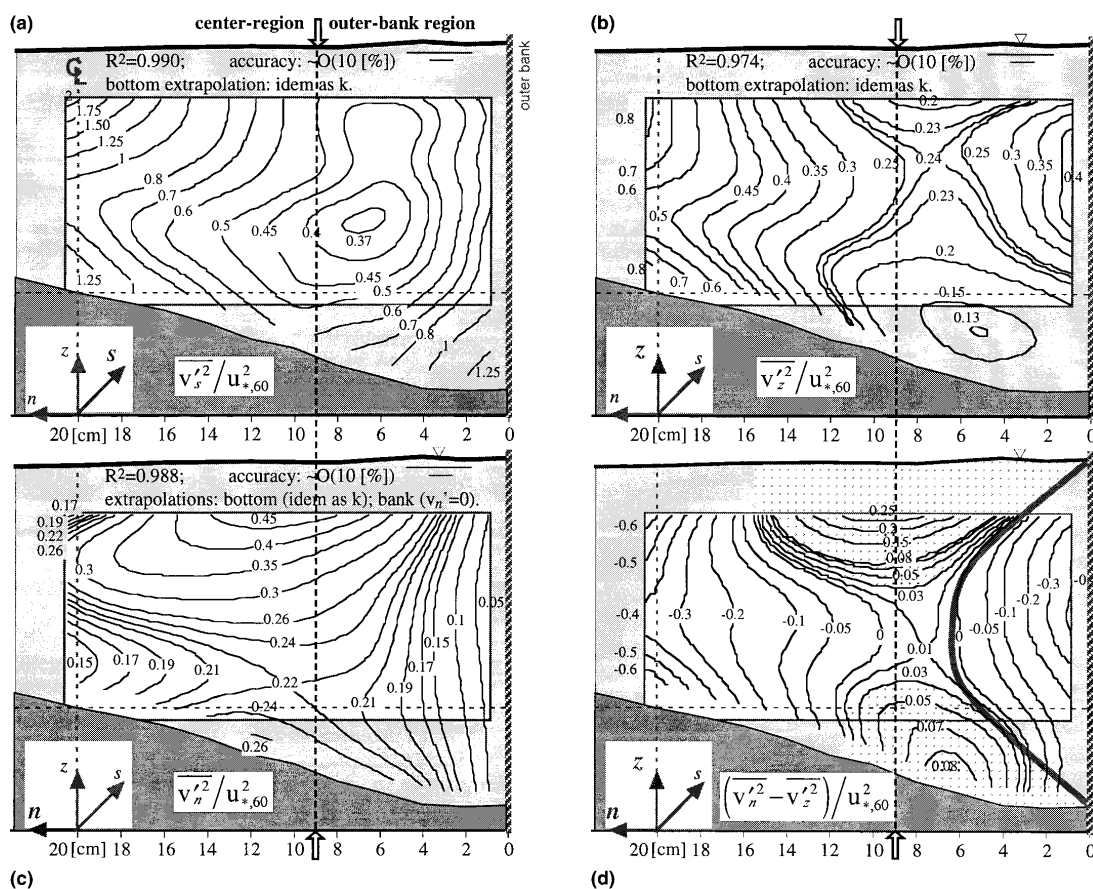


FIG. 5. Isocontours of Normalized (a) Downstream Turbulent Intensity $\overline{v_s'^2}/u_{*,60}^2$; (b) Vertical Turbulent Intensity $\overline{v_z'^2}/u_{*,60}^2$; (c) Transversal Turbulent Intensity $\overline{v_n'^2}/u_{*,60}^2$; (d) Cross-Sectional Turbulent Anisotropy $(\overline{v_n'^2} - \overline{v_z'^2})/u_{*,60}^2$

4(c)], thus being higher than the reach-averaged velocity, $U = 0.38$ m/s. The distribution of the normalized unit discharge, $(U_s h)/Q$ [Fig. 4(c); h is the local flow depth], shows that the flow is concentrated over the deeper outer part of the section. Integration of this profile shows that about 80% of the discharge flows through the investigated half-section. Whereas the maximum velocity over the flow depth in straight uniform flow is usually found near the water surface, in our bend experiment the core of maximum velocity, $v_{s,max} \approx 1.5U$, was observed in the lower part of the flow depth and close to the outer bank [Fig. 4(a), X].

The vectorial representation of the normalized cross-sectional motion, $\sqrt{\overline{v_n'^2} + \overline{v_z'^2}}/U$, in the half-section investigated is shown in Fig. 4(b). A circulation cell—named center-region cell—with outward velocities near the water surface and inward velocities near the bottom is observed in the center region. This cell represents the classical helical motion characteristic of flow in bends. It consists of cross-sectional velocities of $\sqrt{\overline{v_n'^2} + \overline{v_z'^2}}/U = O(0.1)$ on the average. A region characterized by weaker cross-sectional velocities is noticed close to the outer bank. In the upper part of this outer-bank region an additional circulation cell—named outer-bank cell—with a rotation sense opposite to the center-region cell is noticed. It

consists of cross-sectional velocities of $\sqrt{\overline{v_n'^2} + \overline{v_z'^2}}/U = O(0.03)$ on the average. These observations can be summarized as

$$\sqrt{\overline{v_n'^2} + \overline{v_z'^2}}_{\text{outer-bank cell}} < \sqrt{\overline{v_n'^2} + \overline{v_z'^2}}_{\text{center-region cell}} \ll U \quad (7a)$$

$$O(0.01) \text{ m/s} < O(0.04) \text{ m/s} \ll 0.38 \text{ m/s} \quad (7b)$$

and

$$U = 0.38 \text{ m/s} < v_s = O(1.35U) = O(0.5) \text{ m/s} \quad (8)$$

Contrary to the center-region cell, the outer-bank cell has not always been observed in previous experiments on flow in channel bends. Possibly it is not well documented because in most previous investigations the measuring grid was too coarse (Table 1) and the accuracy too low to measure these small velocities, $O(0.01)$ m/s. Furthermore, the outer-bank cell has an intermittent behavior and thus is difficult to visualize experimentally. It is only after time-averaging the measured data over long periods that it becomes discernible (Blanckaert and Graf 1999a). The effects of this outer-bank cell on the stability of the outer bank are discussed in the discussion section.

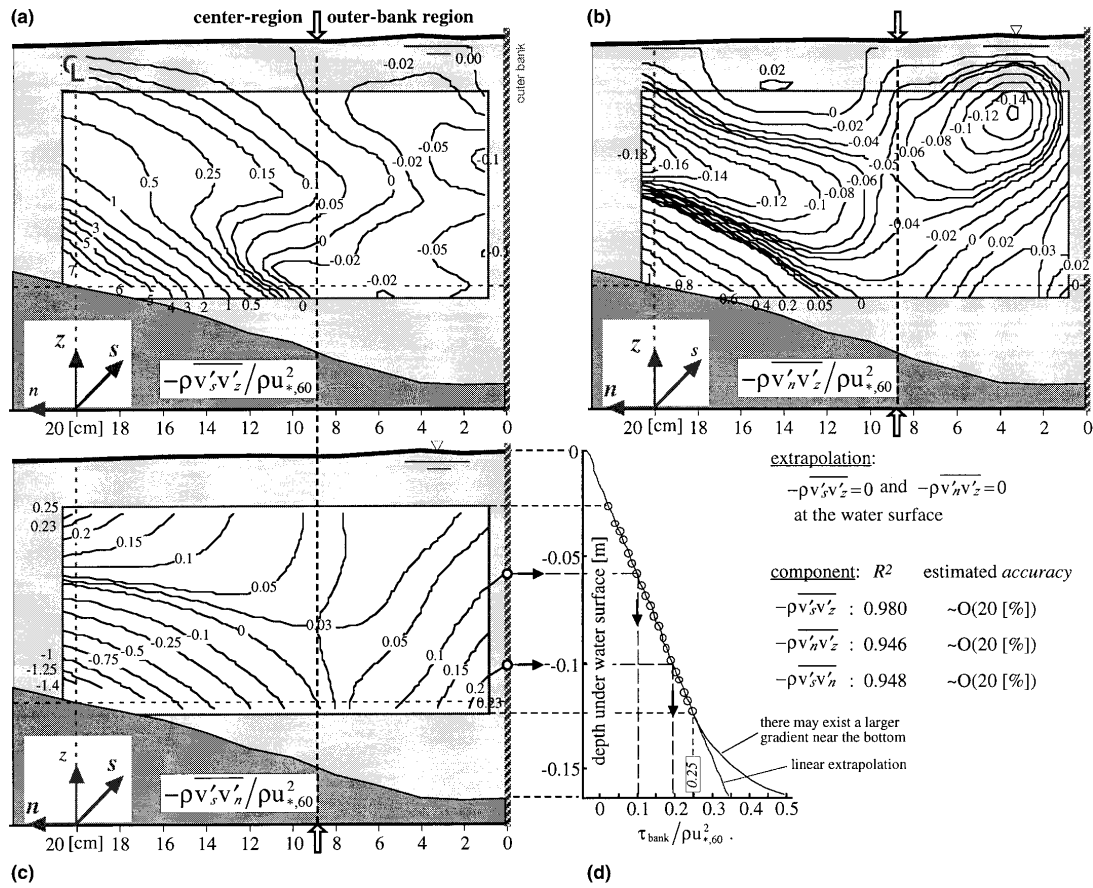


FIG. 6. Isocontours of Normalized Reynolds Shear Stresses (a) $-\rho \overline{v'_s v'_z} / \rho u_{*60}^2$ and (b) $-\rho \overline{v'_n v'_z} / \rho u_{*60}^2$; (c) Isocontours of Normalized Reynolds Shear Stress $-\rho \overline{v'_s v'_n} / \rho u_{*60}^2$ and Normalized Bank Shear Stress $\tau_{bank} / \rho u_{*60}^2$; (d) Extrapolations Outside Measuring Grid and Estimation of Accuracy

Turbulent Normal Stresses

Figs. 5(a–c) show the distribution in the investigated half-section of the turbulent normal stress components, $\overline{v_i'^2}$ ($i = s, n, z$), normalized by u_{*60}^2 . The characteristic shear velocity in the measuring section, u_{*60} , is defined as $u_{*60} = \sqrt{gR_n(-\partial z_{s,60}/\partial s)}$, where $-\partial z_{s,60}/\partial s$ is the local downstream water-surface gradient at the centerline in the section at 60° . In the present experiment, the downstream water surface slope was 2.89‰ and the hydraulic radius was $R_n = 0.07$ m, giving $u_{*60} = 0.045$ m/s.

The spatial distribution of the dominant component $\overline{v_s'^2}$ [Fig. 5(a)] shows an outward decrease from the centerline to minimum values at about the separation between the outer-bank region and the center region; subsequently it increases strongly in the outer-bank shear layer. The spatial distribution of the vertical component $\overline{v_z'^2}$ [Fig. 5(b)] is similar, with the exception that vertical fluctuations are damped near the bottom and near the water surface due to their geometrical constraints. Contrary to $\overline{v_s'^2}$ and $\overline{v_z'^2}$, the transversal component $\overline{v_n'^2}$ [Fig. 5(c)] has its highest values at about the separation between the center region and the outer-bank region and decreases toward the bank and the shallower inner half-section. (A spectral analysis of the fluctuating velocities has confirmed that the inward increase of $\overline{v_s'^2}$ and $\overline{v_z'^2}$ is not due to an increase of ex-

perimental noise but has a physical reason.) When averaged over the entire measuring grid — indicated by $\langle \langle \rangle \rangle$ — the ratios of the cross-sectional normal stress components to the one downstream are

$$\langle \langle \overline{v_n'^2} / \overline{v_s'^2} \rangle \rangle = 0.34 < \langle \langle \overline{v_z'^2} / \overline{v_s'^2} \rangle \rangle = 0.47 \quad (9)$$

This shows that the downstream fluctuations (s) are dominant and that the intensity of the transversal fluctuations (n) is smaller than that of the vertical fluctuations (z). Both ratios have a pronounced spatial distribution in the measured half-section. In a bidimensional straight uniform flow, however, they approach constant values [Nezu and Nakagawa (1993), p. 54], such as

$$\begin{aligned} \langle \langle \overline{v_n'^2} / \overline{v_s'^2} \rangle \rangle_{\text{straight}} &\cong \overline{v_n'^2} / \overline{v_s'^2} |_{\text{straight}} = 0.51 \\ > \langle \langle \overline{v_z'^2} / \overline{v_s'^2} \rangle \rangle_{\text{straight}} &\cong \overline{v_z'^2} / \overline{v_s'^2} |_{\text{straight}} = 0.31 \end{aligned} \quad (10)$$

where the intensity of the transversal fluctuations is larger than that of the vertical fluctuations. Such differences show that turbulence has a complex 3D structure in a bend, which is different from that in a straight uniform flow.

Near the flow boundaries, the fluctuations perpendicular to the boundary are hindered by geometrical constraints. This becomes obvious when considering the distribution of the an-

isotropy of the cross-sectional turbulence, $\overline{v_n'^2} - \overline{v_z'^2}$, as shown normalized by $u_{*0.60}^2$ in Fig. 5(d). In the regions near the bottom and the water surface, the vertical fluctuations are hindered and $\overline{v_n'^2} > \overline{v_z'^2}$, whereas in the region near the outer bank the transversal fluctuations are hindered and $\overline{v_n'^2} < \overline{v_z'^2}$. On a line formed by the diagonals pointing away from the upper and lower corners of the flow domain [dark line in Fig. 5(d)], the transversal and vertical fluctuations are equally hindered by the outer bank, respectively the water surface and the bottom, resulting in isotropic cross-sectional turbulent normal stresses, $\overline{v_n'^2} = \overline{v_z'^2}$.

Similar patterns of $\overline{v_n'^2} - \overline{v_z'^2}$ have been measured in experimental investigations on cross-sectional circulation cells near vertical banks in straight uniform flow [Nezu et al. (1985), Fig. 15 for airflow in a duct; Tominaga et al. (1989), Fig. 11(b) for open-channel flow]. The latter showed this term to be responsible for the generation of these near-bank circulation cells.

Turbulent Shear Stresses

Fig. 6(a) shows the distribution of the normalized turbulent shear stress, $-\rho \overline{v_s' v_z'} / \rho u_{*0.60}^2$, in the investigated half-section. It is mainly generated by the downstream component of the bottom shear stress, $\tau_{b,s}$. In the outer-bank region, this turbulent shear stress assumes small negative values on the measuring grid: $-0.1 < -\rho \overline{v_s' v_z'} / \rho u_{*0.60}^2 < 0$. The measured values increase toward the center region of the channel, where the nearly parallel isolines with the bottom indicate the close relation of this turbulent shear stress with friction on the bottom. In the center region, where mainly a downflow occurs [Fig. 4(b)], this turbulent shear stress remains low in the upper part of the flow depth and increases sharply — and nearly linearly — in the lower part of the flow depth, attaining values as high as $-\rho \overline{v_s' v_z'} / \rho u_{*0.60}^2 = 7$. As mentioned before, measurements close to the bottom ($\sim 20\%$ of the flow depth) are not very reliable, and care should be taken with their interpretation. However, close to the bottom $-\rho \overline{v_s' v_z'} / \rho u_{*0.60}^2$ has to decrease from its maximum value to the value of the normalized downstream bottom shear stress, which can be estimated as $\tau_{b,s} / \rho u_{*0.60}^2 \sim \rho g (U_s/C)^2 / \rho u_{*0.60}^2 \sim g(1.35U/C)^2 / u_{*0.60}^2 \sim 1$ [Fig. 4(c)]. Nezu et al. [(1985), Fig. 13], have measured similar vertical profiles of this turbulent shear stress in the downflow region of a cross-sectional circulation cell existing near a vertical bank for the case of an air flow in a straight duct. In the outer-bank region, where mainly a downflow occurs also, an important vertical gradient might exist close to the bottom, outside the measuring grid.

Fig. 6(b) shows the distribution of the normalized cross-sectional turbulent shear stress, $-\rho \overline{v_n' v_z'} / \rho u_{*0.60}^2$, in the investigated half-section. This turbulent shear stress seems to be correlated with the circulation cells [Fig. 4(b)] as it increases toward maximum negative values in the eyes of the cells. In both circulation cells rotating in opposite sense, this turbulent shear stress has the same sign. In the eye of the weaker outer-bank cell, the value is only slightly lower than near the eye of the center-region cell. This turbulent shear stress is of the same order of magnitude as both $-\rho \overline{v_s' v_z'} / \rho u_{*0.60}^2$ and $-\rho \overline{v_s' v_n'} / \rho u_{*0.60}^2$. In the region affected by bottom friction, it is mainly generated by the transversal component of the bottom shear stress, which is inward directed near the bottom and thus assumes positive values. In that bottom region, the pattern of isolines is similar to that of the shear stress $-\rho \overline{v_s' v_z'}$.

Fig. 6(c) shows the distribution of the normalized turbulent shear stress, $-\rho \overline{v_n' v_s'} / \rho u_{*0.60}^2$, in the investigated half-section. In the outer-bank region, a triangular region affected

by bank friction, increasing in lateral extent from the surface to the bottom, is discernible. The transversal distribution of $-\rho \overline{v_n' v_s'}$ in this region is nearly linear, with a comparable gradient at all elevations above the (s, n) -plane. A similar linear distribution in transversal direction of $-\rho \overline{v_n' v_s'}$ has been measured by Nezu et al. [(1985), Fig. 14] near vertical banks in a straight uniform airflow in a duct. Extrapolation of the linear profiles onto the outer bank (thus bridging the region close to the bank where the measurements are not very reliable — see before) gives an idea about the bank-shear stress, τ_{bank} . A triangular vertical distribution results [Fig. 6(d)], increasing from about $\tau_{\text{bank}} = 0$ at the water surface toward $\tau_{\text{bank}} = 0.25u_{*0.60}^2$ at the lower edge of the measuring grid at $z/h = 0.2$ (h is the local flow depth). Similar to the $-\rho \overline{v_s' v_z'}$ -profiles in the center region, the vertical gradient might increase more than linearly near the bottom, $z/h < 0.2$. In the center region, a region affected by transversal shear on the inclined bottom can be discerned. The isolines have a pattern similar to those of the shear stress $-\rho \overline{v_s' v_z'}$.

Mean-Flow and Turbulent Kinetic Energy

Figs. 7(a and b) show the normalized distributions over the investigated half-section of the mean-flow kinetic energy, $K/(1/2U^2)$, and the turbulent kinetic energy, $k/(1/2u_{*0.60}^2)$, per unit mass, defined as

$$K = \frac{1}{2} (v_s^2 + v_n^2 + v_z^2) \quad \text{and} \quad k = \frac{1}{2} (\overline{v_s'^2} + \overline{v_n'^2} + \overline{v_z'^2}) \quad (11)$$

The composition of the total kinetic energy, averaged over the entire measuring grid, $\langle\langle K + k \rangle\rangle$, is summarized in Table 3.

The downstream velocity v_s dominates; integrated over the flow field it contains 98.7% of the total kinetic energy. The kinetic energy content of the cross-sectional motion, being 0.4% of the total kinetic energy, is smaller than that of the turbulence, being 0.9% of the total kinetic energy, $\langle\langle K + k \rangle\rangle$. The distributions of K and k are very similar to those of their dominant components, v_s^2 [Fig. 4(a)] and $v_s'^2$ [Fig. 5(a)], respectively.

The distributions of K and k are more or less opposite [Figs. 7(a and b)]. The position of the maximum of K nearly coincides with that of the minimum of k , and positive/negative gradients of K correspond to negative/positive gradients of k . Fig. 7(c) shows the normalized depth-averaged mean-flow and turbulent kinetic energy, $\langle K \rangle / (1/2U^2)$ and $\langle k \rangle / (1/2u_{*0.60}^2)$, respectively, and the ratio $\langle k \rangle / \langle K \rangle$; $\langle K \rangle / (1/2U^2) \approx 1.9$ is nearly constant in the outer-bank region, but decreases toward the shallower inner half-section. The turbulent kinetic energy $\langle k \rangle / (1/2u_{*0.60}^2)$ decreases from the outer bank to a minimum value of $\langle k \rangle / (1/2u_{*0.60}^2) \approx 0.9$ at some distance from the bank and then increases toward the centerline. Similar to $\langle k \rangle / (1/2u_{*0.60}^2)$, the ratio $\langle k \rangle / \langle K \rangle$ has a minimum value at some distance from the bank and is smaller than $\langle k \rangle / \langle K \rangle < 0.01$ in the outer-bank region. Toward the shallower inner half-section, the ratio increases to values of $\langle k \rangle / \langle K \rangle \approx 0.02$.

In straight uniform flow, the ratio $\langle k \rangle / \langle K \rangle$ depends uniquely on the friction coefficient, increasing with the bottom roughness. Assuming a logarithmic downstream velocity profile [for example, de Vriend (1977)]

$$v_{\text{straight}} = U_s f_s \left(\frac{z}{h} \right) = U_s \left[1 + \frac{\sqrt{g}}{\kappa C} \left(1 + \ln \frac{z}{h} \right) \right] \quad (12)$$

and an exponentially decreasing turbulent kinetic energy from the bottom toward the water surface [Nezu and Nakagawa (1993), p. 54]

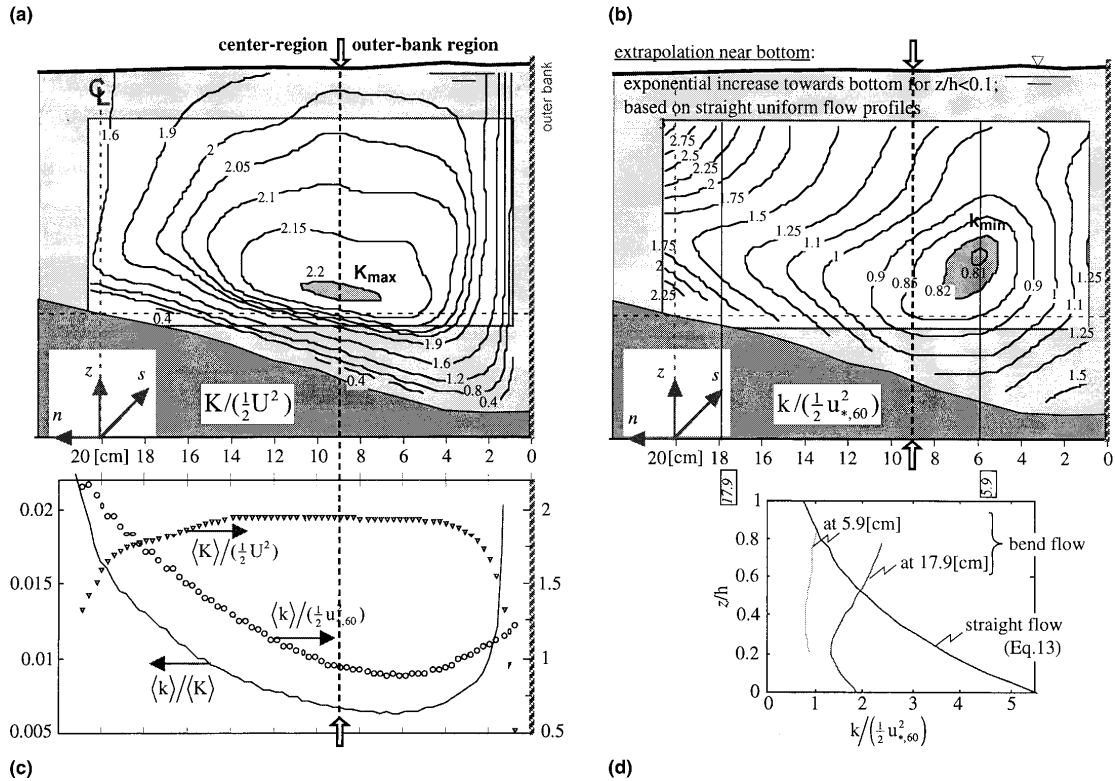


FIG. 7. Isocontours of Normalized (a) Mean Flow Kinetic Energy $K/(1/2U^2)$; (b) Turbulent Kinetic Energy $k/(1/2u_{*60}^2)$; (c) Depth-Averaged Normalized Mean Flow and Turbulent Kinetic Energy, $\langle K \rangle / (1/2U^2)$ and $\langle k \rangle / (1/2u_{*60}^2)$, and Ratio $\langle k \rangle / \langle K \rangle$; (d) Vertical Profiles of $k/(1/2u_{*60}^2)$ in Straight Flow and Bend Flow (Measured)

TABLE 3. Composition of Total Kinetic Energy, Averaged over Entire Measuring Grid

$(10^{-4} \text{ m}^2/\text{s}^2)$	$(10^{-4} \text{ m}^2/\text{s}^2)$
$\frac{1}{2} \langle \langle v_x^2 \rangle \rangle = 1.316.5$ [Fig. 4(a)]	$\frac{1}{2} \langle \langle v_x^2 \rangle \rangle = 6.75$ [Fig. 5(a)]
$\frac{1}{2} \langle \langle v_y^2 \rangle \rangle = 4.69$ [Fig. 4(b)]	$\frac{1}{2} \langle \langle v_y^2 \rangle \rangle = 2.3$ [Fig. 5(b)]
$\frac{1}{2} \langle \langle v_z^2 \rangle \rangle = 0.86$ [Fig. 4(b)]	$\frac{1}{2} \langle \langle v_z^2 \rangle \rangle = 3.15$ [Fig. 5(c)]
$\langle \langle K \rangle \rangle = 1.322$ [Fig. 7(a)]	$\langle \langle k \rangle \rangle = 12.2$ [Fig. 7(b)]

$$k_{\text{straight}} = 4.78u_{*60}^2 e^{-2(z/h)} \quad (13)$$

it is found by integration of (12) and (13) over the flow depth that

$$\left. \frac{\langle k \rangle}{\langle K \rangle} \right|_{\text{straight}} = \frac{\langle k_{\text{straight}} \rangle}{\frac{1}{2} \langle v_{\text{straight}}^2 \rangle} = \frac{4.133}{\langle f_s^2 \rangle} \cdot \left(\frac{u_{*60}}{U_s} \right)^2 = \frac{4.133}{\langle f_s^2 \rangle} \cdot \frac{g}{C^2} \approx 4.1 \frac{g}{C^2} \quad (14)$$

For the earlier estimated bottom roughness, $C \approx 35 \text{ m}^{1/2}/\text{s}$, a ratio of $\langle k \rangle / \langle K \rangle \approx 0.03$ would be expected, which is nearly the case toward the inner half-section but is higher than the observed value, $\langle k \rangle / \langle K \rangle < 0.01$, in the outer-bank region.

In Fig. 7(d), the vertical profile of $k_{\text{straight}}/(1/2u_{*60}^2)$ as found in straight uniform flow — according to (13) and based on $u_{*60} = U\sqrt{g/C}$ with $C \approx 35 \text{ m}^{1/2}/\text{s}$ — is compared with the vertical profiles of $k/(1/2u_{*60}^2)$ measured at 5.9 and 17.9 cm from the outer bank. Whereas the straight flow profile decreases exponentially from the bottom toward the water surface, the measured profiles decrease from the bottom to a minimum value and then increase toward a maximum value near the water surface [see also Fig. 7(b)]. Muto [(1997), Figs. 4.10, 23, 36, 49, 57] and Tamai and Ikeya [(1985), Fig. 3(d)] have measured similar profiles in a meandering channel.

DISCUSSION

The most important features observed in our experiment are the existence of an outer-bank cell of secondary circulation [Fig. 4(b)] and the reduced level of turbulent activity in the region near the outer bank [Fig. 7(c)]. Their influence on the stability of the outer bank and the adjacent bottom will be discussed.

As already mentioned in the introduction, bankline stabilization is a major task in river management. Some recent papers witness the increased interest in the erosional behavior of the channel banks and their modeling. Thorne (1982) has recognized two dominant processes of bank erosion and retreat: basal erosion and geotechnical bank failure. Basal erosion steepens the bank and intermittently causes mass bank failure. Duan et al. (1999) presented a detailed model of bank retreat through basal erosion, driven by the bank shear stress. A

depth-averaged flow model, extended with semiempirical information on the vertical flow structure, is used. The bank shear stress contains contributions from the downstream energy slope (accounting for downstream changes in the near-bank velocity and near-bank bottom shear stress) and from the transversal momentum exchange by the cross-sectional flow (circulation cells). Darby and Thorne (1996) have proposed a model for prediction of the probability of geotechnical bank failure and for the amount of collapsed bank material. Nagata et al. (2000) proposed a model that accounts for bank retreat through basal erosion followed by intermittent geotechnical bank failure. They divide the intermittent process of bank erosion into four steps: bed scouring at the side bank; bank collapse due to instability of the scoured bank; deposition of the collapsed bank materials at the front of the bank; and transportation of the deposited materials. They used a depth-averaged flow model and described the intermittent sediment transport near the bank with a nonequilibrium model.

These recent models use simplified representations of the flow: 3D flow patterns, such as the outer-bank cell, and turbulence are not accounted for. In our experiment, both the outer-bank cell and the reduced level of turbulent activity have a protective effect on the outer bank and the adjacent bottom.

The outer-bank cell acts as a stabilizing buffer region between the center-region cell and the outer bank [Fig. 4(b)]. The outward increase of the downstream velocity, v_x , does not extend into the outer-bank region, and the core of maximum velocity, $v_{x,\max}$, is found at the separation between the center region and the outer-bank region and well below the water surface [Figs. 4(a and b), X]. By keeping the core of maximum velocity at a distance, the outer-bank cell has a protective effect on the outer bank and the adjacent bottom. Blanckaert and Graf (1999b) have given a more rigorous proof of this protective effect, by means of an experimental analysis of the depth-averaged momentum equation.

The reduced turbulent activity results in a reduced bank shear stress. Extrapolation of the linear $-\rho v'_s v'_n$ -profiles [Fig. 6(c)] toward the outer bank yields a triangular vertical distribution of the outer-bank shear stress, increasing from about $\tau_{\text{bank}} = 0$ at the water surface toward a maximum of about $\tau_{\text{bank}} = 0.35\rho u_{*,60}^2$ at the toe of the bank. This value is considerably lower than the shear stress on a vertical bank in a straight uniform flow, being of the order of $\tau_{\text{bank}} \approx \rho u_{*,60}^2$. This is in contrast to the expectation that the increase of velocity in the outer half-section results in an increase of bank shear stress, $\tau_{\text{bank}} > \rho u_{*,60}^2$.

The strength of the outer-bank cell and the reduction in turbulent activity are expected to increase with tightness of the bend. Both mechanisms could explain why the bend tightness in a meandering river does not grow infinitely but seems to adopt a maximum value. Since turbulence is an important factor in the generation of the outer-bank cell, we can conclude that the erodibility of the outer bank and adjacent bottom and thus the morphologic evolution of a bend do not only depend on the mean flow distribution, but that turbulence also plays a major role. Furthermore, such phenomena as the spreading and mixing of pollutants or the transport in suspension of polluted sediments are also closely related to the turbulence structure of the flow. A general conclusion from this experiment is that it is of engineering importance to predict the turbulence characteristics accurately.

SUMMARY AND CONCLUSIONS

It should be emphasized that our experimental results come from measurements in one single section, being at 60° into the bend, under one set of hydraulic (F , C) and geometric (R/B , B/H) conditions. The experimental research is presently enlarged by measuring in different sections and under various

hydraulic conditions in a larger flume (Blanckaert and Graf 2001).

With an ADVP, 3D measurements of the flow were made in an outer half-section of an open-channel bend for a rough turbulent flow over a developed bottom topography (Figs. 1 and 2). The ADVP measures the three components of the mean velocity, $\bar{V} = (v_s, v_n, v_z)$, as well as the six turbulent stresses, $-\rho v'_j v'_k$, ($j, k = s, n, z$), on a fine grid.

1. In the outer half-section, the downstream velocity is higher than the straight-flow velocity [Figs. 3(a and c)]. The core of maximum velocity is found at the separation between the center region and the outer-bank region, well below the water surface [Figs. 3(a and b)].
2. The pattern of cross-sectional velocities contains two circulation cells [Fig. 3(b)]. Besides a center-region cell—the classical helical cell—a weaker counterrotating cell is observed in the corner formed by the outer bank and the water surface.
3. The downstream and vertical turbulent normal stresses show an outward decrease from the centerline and increase again in the outer-bank shear layer; the transversal turbulent normal stress has an opposite behavior [Figs. 5(a–c)]. Turbulence in a bend is structurally different from turbulence in a straight flow, as appears from the ratios of the turbulent normal stresses. Fluctuations perpendicular to the boundaries are damped [Fig. 5(d)].
4. The turbulent shear stress components $-\rho v'_s v'_z$ and $-\rho v'_n v'_z$ are low in the outer-bank region, resulting in an outer-bank shear stress that is smaller than the one in a straight flow [Figs. 6(a, c, d)]. This is in contradiction to the expected increase of the outer-bank shear stress in bends. The turbulent shear stress component $-\rho v'_n v'_z$ is related to the circulation cells, as it increases to maximum values in the eyes of both cells [Fig. 6(b)].
5. Averaged over the entire measuring grid, the downstream velocity contains 98.7% of the kinetic energy, and turbulence (0.9%) contains more kinetic energy than the cross-sectional velocities (0.4%). The mean and turbulent kinetic energy have opposite distribution patterns [Figs. 7(a and b)].
6. Averaged over the depth, the ratio of turbulent to mean kinetic energy $\langle k \rangle / \langle K \rangle$ decreases outward from the centerline, only to increase again in the outer-bank shear layer [Fig. 7(c)]. In most of the outer-bank region, turbulence is reduced, as appears from the ratio $\langle k \rangle / \langle K \rangle$, which is significantly smaller than in straight channel flow.
7. Both the outer-bank cell and the reduced turbulent activity have a protective effect on the outer bank and the adjacent bottom: the outer-bank cell keeps the core of maximum velocity away from the bank [Figs. 3(a and b)], whereas the reduced turbulence results in a reduced outer-bank shear stress. Hence, the morphologic evolution of bends depends not only on the mean flow but also on the turbulence.

A detailed analysis of the data herewith presented will be communicated in a forthcoming paper.

ACKNOWLEDGMENTS

This research is being sponsored by the Swiss National Science Foundation under Grant No. 2100-052257.97/1. D. Hurther and U. Lemmin are acknowledged for their help with the ADVP instrument. H. J. de Vriend and A. J. Odgaard are thanked for fruitful discussions during their stay at the Ecole Polytechnique Fédérale.

REFERENCES

- Anwar, H. O. (1986). "Turbulent structure in a river bed." *J. Hydr. Engrg.*, ASCE, 112(8), 657–669.
- Blanckaert, K., and Graf, W. H. (1999a). "Experiments on flow in open-channel bends." *Proc., 28th Congr. Int. Assoc. Hydr. Res.*, Technical University of Graz, Austria (CD-ROM).
- Blanckaert, K., and Graf, W. H. (1999b). "Outer-bank cell of secondary circulation and boundary shear stress in open-channel bends." *Proc., Symp. on River, Coastal and Estuarine Morphodynamics*, University of Genova, Italy, Vol. 1, 533–543.
- Blanckaert, K., and Graf, W. H. (2001). "Experiments on flow in a strongly curved channel bend." *Proc., 29th Congr. Int. Assoc. Hydr. Res. and Engrg.*, Chinese Hydraulic Engineering Society, Beijing, China (in press).
- Darby, S. E., and Thorne, C. R. (1996). "Development and testing of riverbank-stability analysis." *J. Hydr. Engrg.*, ASCE, 122(8), 443–454.
- de Boor, C. (1978). *A practical guide to splines*, Springer, New York.
- de Vriend, H. J. (1977). "A mathematical model of steady flow in curved shallow channels." *J. Hydr. Res.*, Delft, The Netherlands, 15(1), 37–54.
- de Vriend, H. J. (1979). "Flow measurements in a curved rectangular channel." *Rep. No. 9-79*, Lab. Fluid Mech., Dept. of Civ. Engrg., Delft University of Technology, The Netherlands.
- de Vriend, H. J. (1981). "Flow measurements in a curved rectangular channel. II: Rough bottom." *Rep. No. 5-81*, Lab. Fluid Mech., Dept. of Civ. Engrg., Delft University of Technology, The Netherlands.
- de Vriend, H. J., and Struikma, N. (1984). "Flow and bed deformation in river bends." *River meandering*, C. M. Elliot, ed., ASCE, New York, 810–828.
- Dietrich, W. E. (1987). "Mechanics of flow and sediment transport in river bends." *River channels: Environment and process*, K. Richards, ed., Institute of British Geography, Oxford, U.K.
- Dietrich, W. E., and Smith, J. D. (1983). "Influence of the point bar on flow through curved channels." *Water Resour. Res.*, 19(5), 1173–1192.
- Duan, G., Jia, Y., and Wang, S. (1999). "Simulation of meandering channel migration processes with the enhanced CCHE2D." *Proc., 28th Congr. Int. Assoc. Hydr. Res.*, Technical University of Graz, Austria (CD-ROM).
- Götz, W. (1975). "Sekundärströmungen in aufeinander folgenden Gerinnkrümmungen." *Rep. No. 163*, Theodor-Rehbock Flussbaulaboratorium, Karlsruhe, Germany.
- Hurthler, D., and Lemmin, U. (1998). "A constant beamwidth transducer for three-dimensional Doppler profile measurements in open channel flow." *Measurement Science and Technology*, 9(10), 1706–1714.
- Hurthler, D., and Lemmin, U. (2001). "A correction method for turbulence measurements with a 3-D acoustic Doppler velocity profiler." *J. Atm. Oc. Techn.*, Vol. 18, 446–458.
- Lancaster, P., and Salkauskas, K. (1986). *Curve and surface fitting: An introduction*, Academic Press, London.
- Lemmin, U., and Rolland, T. (1997). "Acoustic velocity profiler for laboratory and field studies." *J. Hydr. Engrg.*, ASCE, 123(12), 1089–1098.
- Muto, Y. (1997). "Turbulent flow in two-stage meandering channels." PhD thesis, University of Bradford, U.K.
- Nagata, N., Hosoda, T., and Muramoto, Y. (2000). "Numerical analysis of river channel processes with bank erosion." *J. Hydr. Engrg.*, ASCE, 126(4), 243–252.
- Nezu, I., and Nakagawa, H. (1993). *Turbulence in open-channel flows*, Balkema, Rotterdam, The Netherlands.
- Nezu, I., Nakagawa, H., and Tominaga, A. (1985). "Secondary currents in a straight channel flow and the relation to its aspect ratio." *Turbulent shear flows 4*, L. J. S. Bradbury et al., eds., Springer, Berlin, 246–260.
- Odgaard, A. J. (1984). "Bank erosion contribution to stream sediment load." *IIHR Rep. No. 280*, Iowa Institute of Hydraulic Research, Iowa City.
- Odgaard, A. J. (1986). "Meander flow model. I: Development." *J. Hydr. Engrg.*, ASCE, 112(12), 1117–1136.
- Odgaard, A. J., and Bergs, M. A. (1988). "Flow processes in a curved alluvial channel." *Water Resour. Res.*, 24(1), 45–56.
- Parker, G., and Johannesson, H. (1989). "Observations on several recent theories of resonance and overdeepening in meandering channels." *River meandering*, S. Ikeda and G. Parker, eds., *Water Resour. Monograph 12*, American Geophysical Union, Washington, D.C., 379–415.
- Rozovskii, I. L. (1957). *Flow of water in bends of open channels*, Academy of Sciences of the Ukrainian SSR, Kiev, 1957; Israel Program for Scientific Translations, Jerusalem, 1961.
- Shiono, K., and Muto, Y. (1998). "Complex flow mechanisms in compound meandering channels with overbank flow." *J. Fluid Mech.*, Vol. 376, 221–261.
- Siebert, W. (1982). "Strömungscharakteristiken in einem Kanal mit 180°-Krümmungen." *Rep. No. 168*, Theodor-Rehbock Flussbaulaboratorium, Karlsruhe, Germany.
- Steffler, P. M. (1984). "Turbulent flow in a curved rectangular channel." PhD thesis, University of Alberta, Canada.
- Strickler, A. (1923). "Beiträge zur Frage der Geschwindigkeitsformeln." *Rep. No. 16*, Amt. f. Wasserwirtschaft, Bern, Switzerland.
- Tamai, N., and Ikeya, T. (1985). "Three-dimensional flow over alternating point bars in a meandering channel." *J. Hydrosoci. Hydr. Engrg.*, 3(1), 1–13.
- Thorne, C. R. (1982). "Processes and mechanisms of river bank erosion." *Gravel-bed rivers*, R. D. Hey, J. C. Bathurst, et al., eds., Wiley, New York, 227–259.
- Tominaga, A., Ezaki, K., Nezu, I., and Nakagawa, H. (1989). "Three-dimensional turbulent structure in straight channel flows." *J. Hydr. Res.*, Delft, The Netherlands, 27(1), 149–173.
- Tominaga, A., Nagao, M., and Nezu, I. (1999). "Flow structure and momentum transport processes in curved open-channels with vegetation." *Proc., 28th Congr. Int. Assoc. Hydr. Res.*, Technical University of Graz, Austria (CD-ROM).

NOTATION

The following symbols are used in this paper:

- ADVP = acoustic Doppler velocity profiler;
 B = channel width;
 C = Chézy roughness coefficient;
 c = celerity of sound in water, $c = 1,500$ m/s at 20°;
 d_{50} = mean diameter of sand bottom;
 F = Froude number = U/\sqrt{gH} ;
 f_s = normalized vertical profiles of downstream velocity component, v_s ;
 f_{Dr} = Doppler signal recorded by receiver r , $r = 1, 2, 3, 4$;
 f_e = frequency of emitter, = 1 MHz;
 g = gravitational acceleration;
 H = reach-averaged flow depth;
 h = local flow depth;
 K = mean flow kinetic energy per unit mass;
 k = turbulent kinetic energy per unit mass;
 k_s = Nikuradse equivalent sand roughness;
 N = number of measuring points on profile;
NPP = number of pair-pulses;
 n = transversal reference axis;
 n^* = distance from outer bank;
prf = pulse repetition frequency;
 Q = discharge;
 R = radius of curvature of channel centerline;
 R^2 = coefficient of determination of surface fitting;
 R_h = hydraulic radius of cross section;
 Rr = Receiver r , $r = 1, 2, 3, 4$;
 $R = UH/\nu$ = Reynolds number;
 $R_* = u_* k_s/\nu$ = particle Reynolds number;
 S_s = reach-averaged water surface gradient on centerline;
 s = downstream reference axis;
 t = time;
 $U = Q/(BH)$ = reach-averaged velocity;
 U_s = depth-averaged downstream velocity;
 $u_* = U\sqrt{g/C}$ = friction velocity;
 V_r = velocity component along axis of receiver r , $r = 1, 2, 3, 4$;
 v_j = time-averaged velocity component, $j = s, n, z$;
 $v_j(t)$ = instantaneous velocity component, $j = s, n, z$;
 $v_j'(t)$ = instantaneous velocity fluctuation, $j = s, n, z$;
 $\overline{v_j' v_k'}$ = time-averaged correlation of velocity fluctuations, $j, k = s, n, z$;
 x_{exp} = experimental data;
 x_{fit} = approximation by surface fitting to x_{exp} ;
 z = vertical reference axis; elevation above horizontal (s, n)-plane;
 z^* = distance under water surface;
 α_i = angle defined in Fig. 2;
 Δn = height of measuring volumes;

κ = von Karman constant;
 ν = molecular viscosity of water; $\nu = 1.004 \times 10^{-6}$
 m^2/s at 20° ;
 ρ = density of water; $\rho = 998.2 \text{ kg}/\text{m}^3$ at 20° ;
 τ = shear stress at flow boundary (bottom or bank);
 ϕ = diameter of measuring volumes;
 overbar = time-averaged values;
 $\langle \cdot \rangle$ = values averaged over local flow depth;
 $\langle\langle \cdot \rangle\rangle$ = values averaged over the measuring grid; and
 $O(\cdot)$ = order of magnitude of.

Subscripts

b = bottom;
 bank = values at outer bank;
 max = maximum magnitude over measuring grid of
 variable;
 S = water surface;
 straight = corresponding value in straight uniform flow;
 and
 60 = value in the section at 60° .

II.2 BEND-FLOW SIMULATION USING 2D DEPTH-AVERAGED MODEL^a

Discussion by K. Blanckaert⁵

The authors are to be commended for presenting a simple model that is accessible for practicing engineers, for simulating the flow in a channel bend. The authors' main conclusion — that dispersion stresses contribute to the transverse convection of momentum and should be considered in bend flow simulations — is in agreement with the conclusions of Kalkwijk and de Vriend (1980) and Johannesson and Parker (1989).

In the following, some experimental results obtained by the discussor will be presented which hopefully will add to the understanding of some simplifications adopted in the authors' model.

The discussor performed velocity measurements in a curved flow over a mobile-bed topography. Our laboratory flume is $B = 0.4$ m wide and consists of a 2 m long straight approach section, followed by a 120° bend with a constant radius of curvature of $R_c = 2$ m (Fig. 16). The hydraulic conditions of

^aOctober 1999, Vol. 125, No. 10, by H. C. Lien, T. Y. Hsieh, J. C. Yang, and K. C. Yeh (Paper 17977).

⁵Res. Asst., Lab. de Recherches Hydrauliques, Ecole Polytechnique Fédérale, CH-1015 Lausanne, Switzerland.

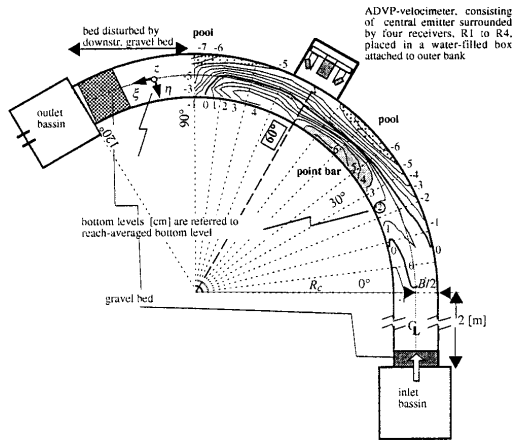


FIG. 16. Experimental Setup, Bottom Topography, and Velocimeter

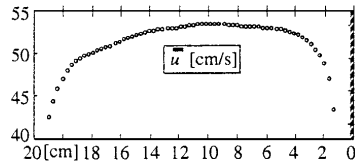


FIG. 17. Depth-Averaged Streamwise Velocity, \bar{u} (cm/s)

the flow are as follows: $Q = 17$ l/s is the discharge; $d = 0.11$ m is the reach-averaged flow depth; $U = Q/(Bd) = 0.38$ m/s is the reach-averaged velocity; $S_b = 1.89\%$ is the reach-averaged water-surface gradient on the centerline; $c = 35$ m^{1/2}/s is the Chezy friction factor; $R = Ud/\nu = 42,000$ is the Reynolds number; and $F = U/\sqrt{gd} = 0.36$ is the Froude number. The parameters $R_c/B = 5$ and $R_c/d = 17.9$ correspond to a rather tight bend. The mean diameter of the sand bed is $d_{50} = 2.1$ mm. 3D velocity measurements were made at one single section, located at 60° from the bend entrance; there, only the half-section at the outer bank was investigated (Figs. 17–20). Fig. 17 shows our measured depth-averaged velocity, \bar{u} , whereas Fig. 18 shows our measured distributions of the streamwise, transversal, and vertical velocity components, \bar{u} , \bar{v} and \bar{w} . Figs. 19(a and b) show the analytical streamwise and transversal [excluding the net transversal mass transport, $\bar{v}_m(\zeta)$] velocity distributions according to (14), based on our measured depth-averaged velocity, \bar{u} ; the Chezy frictional factor, $c = 35$ m^{1/2}/s, and the radius of lines parallel to the banks. Fig. 19(c) shows the vertical velocity component, computed by substituting the analytical transversal velocity in the continuity equation for axisymmetric flow. Fig. 20 shows the dispersion stresses, $DSXY_{exp}$, based on our measured velocity distribution, and $DSXY_{an}$, based on the analytical distributions [Figs. 19(a and b)]. A description of the experimental setup, the velocimeter, the data treatment, a presentation of the data on the mean velocities and the Reynolds stresses, and an analysis of the data can be found in Blanckaert and Graf (1999; in preparation, 2000a,b).

The authors compute the dispersion stresses from the analytical streamwise and transversal velocity profiles proposed by de Vriend (1977), who defines those velocity profiles in the directions parallel and perpendicular to the depth-averaged flow and uses the radius of curvature of the local depth-averaged streamline. In the authors' model, however, the velocity

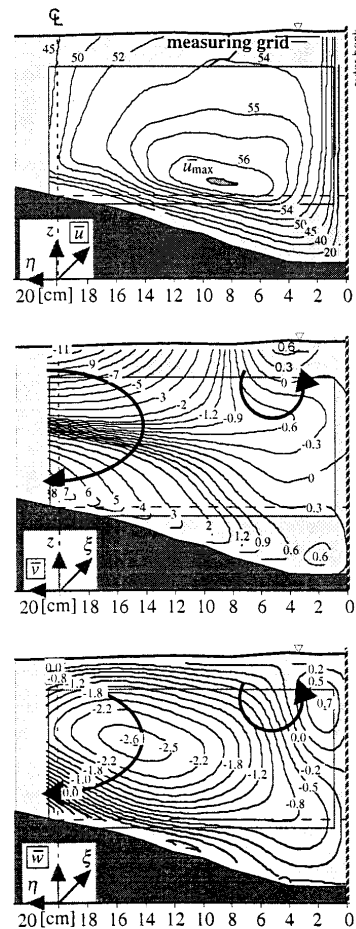


FIG. 18. Isocontours of Measured Streamwise, Transversal, and Vertical Velocities, \bar{u} , \bar{v} , \bar{w} (cm/s)

profiles parallel and perpendicular to the ξ - and η -axis are required. The authors' (14) is an approximation, proposed by Kalkwijk and de Vriend (1980, equations 12 and 18) for small curvatures, that consists in retaining the profile parallel to the depth-averaged flow in the ξ -direction and adding the net transversal mass transport, $\bar{v}_m(\zeta)$, to the profile perpendicular to the depth-averaged flow. Furthermore, they approximate the radius of curvature of the local depth-averaged streamline by the one of the channel centerline R_c . This approximation results in a discontinuous behavior of \bar{v} , $DSXY$, and all terms depending on \bar{v} at the bend entry and exit in the authors' test cases (Figs. 10–15). This discontinuous behavior could have been avoided by applying de Vriend's analytical profiles in the directions parallel and perpendicular to the local depth-averaged flow, based on the radius of curvature of the local depth-averaged streamline, followed by a transformation of these expressions in the ξ - and η -directions. This procedure has been followed successfully by Yulistiyanto et al. (1998) to simulate the flow around a cylinder by means of a depth-averaged model including dispersion stresses.

The analytical velocity profiles [(14)] can only be resolved from the simplified flow equations, in which the interaction between the streamwise velocity and the secondary flow is

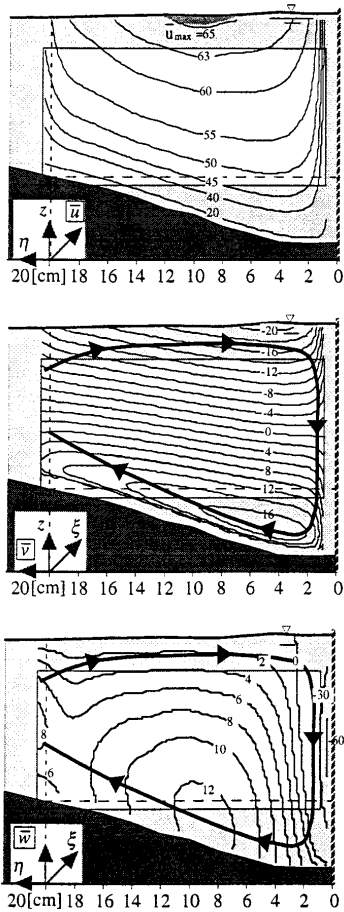


FIG. 19. Isocontours of Analytical Streamwise, Transversal, and Vertical Velocities, \bar{u} , \bar{v} , \bar{w} (cm/s)

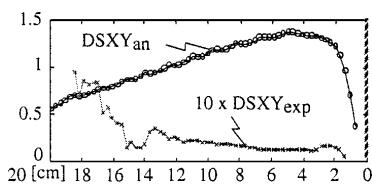


FIG. 20. Measured and Analytical Dispersion Stress, DSXY (N/m)

neglected. Momentum transport by the secondary flow, however, causes a flattening of the streamwise velocity profiles (de Vriend 1981a), which in turn results in a decrease of the strength of the secondary flow (de Vriend 1981b; pp. 26–27) and thus a decrease of the dispersion stress, DSXY. This interaction between the streamwise velocity and the secondary flow increases with the bend tightness, R, B . Consequently, the dispersion stress, DSXY, calculated with the analytical velocity profiles [(14)] can only represent the momentum convection for mildly curved bends. For strongly curved bends in

which an important interaction between the streamwise and the secondary flow exists, such as the authors' second test case, the dispersion stress does not reliably model the momentum convection, and a fully 3D model should be used. This is illustrated by our experimental results in Figs. 18–20. Whereas the analytical streamwise velocity profiles have their maximum at the water surface, our measured profiles showed an important flattening with the maximum well below the water surface [Figs. 18(a) and 19(a)]. Furthermore, our measured transversal velocities are weaker than the predicted analytical ones [Figs. 18(b) and 19(b)]. These differences are amplified in the dispersion stress, DSXY (Fig. 20). Near the centerline, the dispersion stress based on our measured velocities, $DSXY_{exp}$, is an order of magnitude smaller than the dispersion stress, $DSXY_{an}$, based on the analytical velocity distributions; in the region covered by the outer-bank cell, the measured dispersion stress almost vanishes. It should be remarked that there is some uncertainty on $DSXY_{exp}$ due to the extrapolation of our velocity profiles outside the measuring grid near the bottom and the water surface [Fig. 18(a)]. However, this uncertainty cannot be responsible for the difference of an order of magnitude between $DSXY_{exp}$ and $DSXY_{an}$. A more detailed analysis of the interaction between the streamwise velocity and the secondary flow is presented in Blanckaert and Graf (2000b).

The authors use the analytical profiles of de Vriend over the whole cross-section to compute the dispersion stress, resulting in $DSXY \geq 0$ (Fig. 20). Johannesson and Parker (1989) have shown that, to account correctly for the effect of the transverse momentum flux, this dispersion stress must satisfy two conditions: (1) DSXY should be positive in the central region of the cross section; and (2) it should decay to zero toward the impervious banks. For their simulation of the strongly curved flow, the authors impose free-slip boundary conditions at the banks. Johannesson and Parker (1989; p. 1022) have shown that this is equivalent to generating a fictitious momentum flux at the banks that just balances out the redistribution and prevents it from being felt. Fig. 15 illustrates this transversal momentum flux through the banks. For their simulation of the mildly curved flow, the authors impose the no-slip condition at the banks, $\bar{u} = 0$, resulting in $DSXY = 0$. However, Johannesson and Parker (1989; p. 1031) pretend that this procedure does not correctly model the dispersion stresses, but only represents them as higher-order contributions to the momentum balance. This is confirmed by the results of Kalkwijk and de Vriend (1980; p. 339), who find a better agreement with experimental data when the dispersion stress is multiplied by a factor of 1.5. Fig. 19 shows that using de Vriend's profiles with the bank boundary condition, $\bar{u} = 0$, does not yield a realistic pattern of secondary flow for the discussor's experiment, with notable shortcomings near the banks: (1) the analytical transversal velocity attains its maximum value very near the bank and drops sharply to zero in a thin layer near the bank [Figs. 18 and 19(b)]; and (2) over most of the outer half-section, upflow occurs $\bar{w} > 0$, resulting — due to continuity — in a much too large downflow, $\bar{w} < 0$, concentrated in a thin layer near the outer bank [Figs. 18 and 19(c)]. Dispersion stresses based on such an unrealistic pattern of secondary flow cannot be expected to model correctly the transversal momentum convection and will notably fail to account correctly for the influence of the impervious banks. Ikeda et al. (1990) have presented analytical solutions for \bar{u} and \bar{v} that are valid over the whole cross section, including the bank boundary layers. Dispersion terms based on their profiles should model more correctly the transversal momentum convection and the influence of the impervious banks.

The authors have tested their model for two cases. The first concerns a mildly curved flow, $R_c/B = 8.3$, for which de

II.18

Vriend's assumptions seem to be justified. The second case concerns a strongly curved flow, $R_c/B = 1$, in which the dispersion stresses contribute significantly to the momentum balance. The discussor's experimental data show that the authors' model of momentum convection by dispersion stresses is unreliable for strong curvatures. Our measured flow field is highly three-dimensional, as shown by the important interaction between the streamwise velocity and the secondary flow and by the appearance of an outer-bank cell of circulation [Figs. 18(b and c)]. In the discussor's opinion, only fully 3D simulations can be reliable for strongly curved flows. Unfortunately, no channel bends with a curvature of $R_c/B \sim 3$, which is typical for natural bends, were tested by the authors.

The above remarks and our experimental result are aimed to show that care should be taken when applying the authors' model to bends of moderate or strong curvature.

APPENDIX. REFERENCES

- Blanckaert, K., and Graf, W. H. (1999). "Outer-bank cell of secondary circulation and boundary shear stress in open-channel bends." *RCEM Symp.*, Vol. 1, Genova, Italy, 533–543.
- de Vriend, H. J. (1981a). "Velocity redistribution in curved rectangular channels." *J. Fluid Mech.*, 107, 423–439.
- de Vriend, H. J. (1981b). "Steady flow in shallow channel bends." *Rep. No. 81-3*, Dept. of Civ. Engrg., Delft University of Technology, Delft, The Netherlands.
- Ikeda, S., Yamasaka, M., and Kennedy, J. F. (1990). "Three-dimensional fully developed shallow-water flow in mildly curved bends." *Fluid dynamics research 6*, North-Holland, 155–173.
- Johannesson, H., and Parker, G. (1989). "Velocity redistribution in meandering rivers." *J. Hydr. Engrg.*, ASCE, 115(8), 1019–1039.
- Yulistiyanto, B., Zech, Y., and Graf, W. H. (1998). "Free-surface flow around cylinder: shallow-water modeling with diffusion-dispersion." *J. Hydr. Engrg.*, ASCE, 124(4), 419–429.

II.3 Experiments on Flow in a Strongly Curved Channel Bend

K. BLANCKAERT and W.H. GRAF

Proceedings XXIX IAHR congress, Theme D, Vol. I, 371-377, Beijing, China, Sept 2001

ABSTRACT

The secondary circulation in open-channel bends largely determines the bed topography. It is often described by the “Rozovskii model” in depth-integrated flow models. Our experimental results indicate that the “Rozovskii model” has a tendency to overpredict the strength of the secondary circulation and its effect on the velocity distribution for the case of strongly curved open-channel flow. Both also decrease with increasing curvature ratio; this is in contrast with the unique dependence on the Chezy coefficient predicted by the “Rozovskii model”.

KEYWORDS

strongly curved flow, open-channel bend, secondary circulation, experiments

INTRODUCTION

The most characteristic feature of curved flow is the helical flow pattern, also known as secondary circulation. It advects flow momentum and redistributes transversally the velocity and the boundary shear stress over the bend. Furthermore, the direction of the bottom shear stress, and thus also of the sediment transport, directly depends on the strength of the secondary circulation. As a consequence, the evolution of the secondary circulation will largely determine the resulting bed topography with its characteristic bar-pool formation.

Since fully-3D flow models are not yet feasible for engineering problems concerned with the river morphology, most often 2D depth-integrated flow models are used. By depth-integrating the flow equations, all information on the secondary circulation is lost. However, as mentioned above, it is essential to account for the effect of the secondary circulation and this can only be done by providing it as input to the model. This input is mostly based on simplified expressions for the velocity profiles, which have been proposed by Rozovskii (1957).

In this paper, experimental data is presented that illustrates the shortcomings of this approach for strongly curved flows. Blanckaert (2001) presents a model for the velocity profiles in strongly curved flows that explains the features observed in the here reported experiments.

THEORETICAL CONSIDERATIONS

The distribution of the depth-averaged downstream velocity, U_s , is governed by the depth-integrated downstream momentum equation. Assuming a hydrostatic pressure, this equation is (Dietrich and Whiting, 1989):

$$\frac{\tau_{bs}}{\rho} = \underbrace{-\frac{1}{1+n/R}gh\frac{\partial z_s}{\partial s}}_G - \left[\underbrace{\frac{1}{1+n/R}\frac{\partial}{\partial s}(\langle v_s^2 \rangle h)}_{C1} + \underbrace{\frac{\partial}{\partial n}(\langle v_s v_n \rangle h)}_{C2} + \underbrace{\frac{2}{1+n/R}\frac{\langle v_s v_n \rangle h}{R}}_{C3} \right] + \underbrace{\frac{\partial}{\partial n}(\langle \tau_{ns}/\rho \rangle h)}_{T1} + \underbrace{\frac{2}{1+n/R}\frac{\langle \tau_{ns}/\rho \rangle h}{R}}_{T2} \quad (1)$$

where τ_{bs} is the downstream component of the bottom shear stress, ρ is the water density, g is the gravitational acceleration, h is the local flow depth, R is the centreline radius of curvature, $(1+n/R)$ is a metric factor, z_s is the elevation of the water surface above the horizontal reference plane (s,n) (for which the flume-average bottom level is chosen), τ_{ns} is a component of the Reynolds tensor and v_j ($j=s,n,z$) are the time-averaged velocity components along the reference axes. The s -axis follows the channel centreline, the n -axis is perpendicular to it and points towards the outer bank and the vertical z -axis is positive in upward direction (Fig.1a). The brackets, $\langle \rangle$, indicate depth-averaged values.

In a 2D straight uniform flow, the bottom shear stress τ_{bs}/ρ is in equilibrium with the energy expenditure G in all points (s,n) of the flume, and the momentum equation reduces to $\tau_{bs}/\rho=G$. In a 3D flow, the velocities are non-uniformly distributed and the other terms have to be considered. The terms T1 and T2 are shear stresses which are mainly generated by transversal velocity gradients; they are usually of minor importance. The terms C1, C2 and C3 represent advective transport of momentum. C1 is due to downstream variation of the flow field and drops out when the flow is completely adapted to the curvature ($\partial/\partial s=0$). The non-uniform velocity distribution over the channel width is mainly due to the terms C2 and C3. These are redistribution terms that nearly cancel when integrated over the cross-section. They represent the effect of the advective transport of downstream momentum, ρv_s , by the transversal velocities, v_n , which after depth-integration yields: $\rho h \langle v_s v_n \rangle$. By decomposing the velocity components v_j ($j=s,n$) in a depth-averaged value, $\langle v_j \rangle = U_j$, and its local deviations, v_j^* :

$$v_j = \langle v_j \rangle + v_j^* = U_j + v_j^* \quad \text{where} \quad \langle v_j^* \rangle = 0 \quad (2)$$

the velocity redistribution term can be decomposed as:

$$\langle v_s v_n \rangle = \langle (U_s + v_s^*)(U_n + v_n^*) \rangle = U_s U_n + \langle v_s^* v_n^* \rangle \quad (3)$$

The first term, $U_s U_n$, represents a redistribution of downstream velocity U_s by the transversal velocity U_n ; it can be resolved by depth-integrated flow models. The second term, $\langle v_s^* v_n^* \rangle$, represents the velocity redistribution by the secondary flow; since it depends on the vertical distributions of v_s^* and v_n^* , it is an unknown in the depth-integrated momentum equation and has to be modelled. Often, this term is modelled using vertical profiles of v_s^* and v_n^* that are derived from a simplified set of the 3D Navier-Stokes equations, proposed by Rozovskii (1957). de Vriend (1977) gives the following solution of these simplified equations, which will be called the ‘‘Rozovskii model’’ further on:

$$v_s^* = v_s - U_s = U_s (f_s - 1) = U_s \frac{\sqrt{g}}{\kappa C} (1 + \ln \eta) \quad (4)$$

$$v_n^* = U_s \frac{h}{R} f_n = -U_s \frac{h}{R} \frac{1}{\kappa^2} \left[2 \int_{\eta_0}^{\eta} \frac{\ln \eta'}{1 - \eta'} d\eta' + \frac{\sqrt{g}}{\kappa C} \int_{\eta_0}^{\eta} \frac{\ln^2 \eta'}{1 - \eta'} d\eta' + \left(1 - \frac{\sqrt{g}}{\kappa C} \right) f_s(\eta) \right] \quad (5)$$

where f_s and f_n are the normalised profiles of v_s , and v_n^* , C is the Chezy friction coefficient, κ is the von Karman constant, $\eta=z/h$ is the normalised vertical co-ordinate and η_0 is the near-bottom level where $f_s(\eta_0)=0$. According to the ‘‘Rozovskii model’’, the secondary circulation, v_n^* , increases linearly with increasing curvature ratio, h/R , for a given downstream velocity, U_s . $\langle f_s f_n \rangle$ represents the velocity redistribution term $\langle v_s^* v_n^* \rangle$ normalised by $U_s^2 h/R$:

$$\langle v_s^* v_n^* \rangle = \langle (v_s - U_s) v_n^* \rangle = U_s^2 \frac{h}{R} \langle (f_s - 1) f_n \rangle = U_s^2 \frac{h}{R} \langle f_s f_n \rangle \quad (6)$$

where $\langle f_n \rangle = 0$. $\langle f_s f_n \rangle$ is called the *velocity-redistribution coefficient* further on, while $\langle f_n^2 \rangle$ shall be interpreted as the normalised *strength of the secondary circulation*. According to the expressions, eq.4 and eq.5, both f_s and f_n , - and thus also $\langle f_n^2 \rangle$ and $\langle f_s f_n \rangle$ - are unique functions of the Chezy friction coefficient, C , and do not depend on the curvature parameter, h/R . $\langle f_n^2 \rangle$ and $\langle f_s f_n \rangle$ calculated from the ‘‘Rozovskii model’’ as a function of C are shown in Fig.3.

In this paper, predictions of $\langle f_n^2 \rangle$ and $\langle f_s f_n \rangle$ based on ‘‘Rozovskii model’’ (eq.4 and eq.5 and shown in Fig.3) will be compared with experimental data for a strongly curved open-channel bend (Fig.4 and Fig.5). The experimental normalised velocity profiles are calculated from the measured distributions of $v_s(\eta)$ and $v_n(\eta)$ according to eq.2, eq.4 and eq.5 as:

$$f_s(\eta) = v_s(\eta) / U_s \quad (7)$$

$$f_n(\eta) = v_n^*(\eta) / \left(U_s \frac{H}{R} \right) = (v_n(\eta) - U_n) / \left(U_s \frac{H}{R} \right) \quad (8)$$

where the flume-averaged water depth, H , will be used as an approximation for the local water depth, h .

THE EXPERIMENTS (FIG.1)

Experiments were performed in a 1.3m wide laboratory flume, consisting of a 9m long straight inflow, followed by a 193° bend with a constant radius of curvature of $R=1.7m$ on the centreline, and a 5m long straight outflow. The horizontal bed was covered by a sand with diameters in the range $1.6mm < d < 2.2mm$, which has been fixed by spraying a layer of paint on it, thus preserving the roughness of the sediments. The vertical banks were made of Plexiglas. A ratio $R/B=1.31$ was chosen, which corresponds to a very strongly curved bend; a bend is considered strongly curved when $R/B < 2$ to 3.

The investigated hydraulic parameters are tabulated in Fig.1c. The main parameter of interest is the curvature ratio H/R , which was varied by testing three different values of the flume-averaged water depth, $H=10.8, 15.9$ and 21.2 [cm], yielding a curvature ratio of, $H/R=0.064, 0.094$ and 0.125 . In the paper, the experiments will be named after their discharge: Q56, Q89 and Q104 [l/s]. In all three experiments, a similar flume-averaged velocity was chosen, $U=0.4, 0.43$ and 0.38 [m/s], corresponding to different Fr-numbers, $Fr=U/(gH)^{1/2}=0.39, 0.35, 0.26$ (A literature review has shown us that the flow field in a channel bend is rather insensitive to the Froude number). The flume-averaged water surface gradient and energy gradient were, $S_s=-\partial Z_s/\partial s=1.41, 0.94, 0.49$ [%] and $E_s=-\partial(Z_s + \langle \langle U_s \rangle \rangle / 2g) / \partial s = 1.46, 1.01, 0.54$ [%], where Z_s is the sectional-

averaged water surface elevation and $\langle\langle U_s \rangle\rangle$ is sectional-averaged downstream velocity. The shear velocities were, $u_*=(gHS_s)^{1/2}=3.9, 4.0$ and $3.3[\text{cm/s}]$ giving Chezy coefficients, $C=g^{1/2}U/u_*=32, 34$ and $35[\text{m}^{1/2}/\text{s}]$ and the channel aspect ratios were, $B/H=12.1, 8.2$ and 6.1 .

By moving a set of 8 acoustic limnimeters - mounted on a carriage that covers the width of the channel - along the channel, a detailed description of the water surface topography was obtained.

Velocity measurements were made with an Acoustic Doppler Velocity Profiler (ADVP), developed in our laboratory (Lemmin and Rolland, 1997). It measures simultaneously and quasi-instantaneously profiles of the three velocity components, from which the three time-averaged velocity components, $\vec{v} = \vec{v}(v_s, v_n, v_z)$, as well as the six turbulent stresses, $-\rho v'_i v'_j$ ($i, j = s, n, z$), and higher order turbulent correlations can be computed. With the ADVP placed in a water-filled box on the water surface (Fig.1b), velocity profiles covering the flow depth were obtained. The measuring volumes were cylinders of $(\pi 0.7^2/4) \times (0.3) = 0.12[\text{cm}^3]$. The sampling frequency was 31.25 Hz and the sampling time was 200s. Detailed information on the ADVP and estimations of the accuracy of the measurements can be found elsewhere (Hurther and Lemmin, 2000).

Velocity profiles were measured on the centerline, with a streamwise spacing of 0.5m in the straight inflow and outflow reaches and of 15° in the bend. In this paper, mainly these centreline measurements are exploited. Only the calculation of the coefficient α_s (see further, Fig.2) required detailed measurements of the 3D-velocities in cross-sections. These detailed cross-sectional measurements were made in the section with the strongest secondary circulation – at 135° for Q56, at 90° for Q89 and at 75° for Q104, as determined from the centerline measurements (Fig.4) – as well as in the reference section m25 (Fig.1a). In these sections, 29 vertical profiles were measured, with a transversal spacing that decreases towards the banks (Fig.1b). For the Q89-experiment sections all along the flume (sections m25, m05, $30^\circ, 60^\circ, 90^\circ, 120^\circ, 150^\circ, 180^\circ, p05, p15, p25, p35$, Fig.1a) have been measured in detail on the same fine grid.

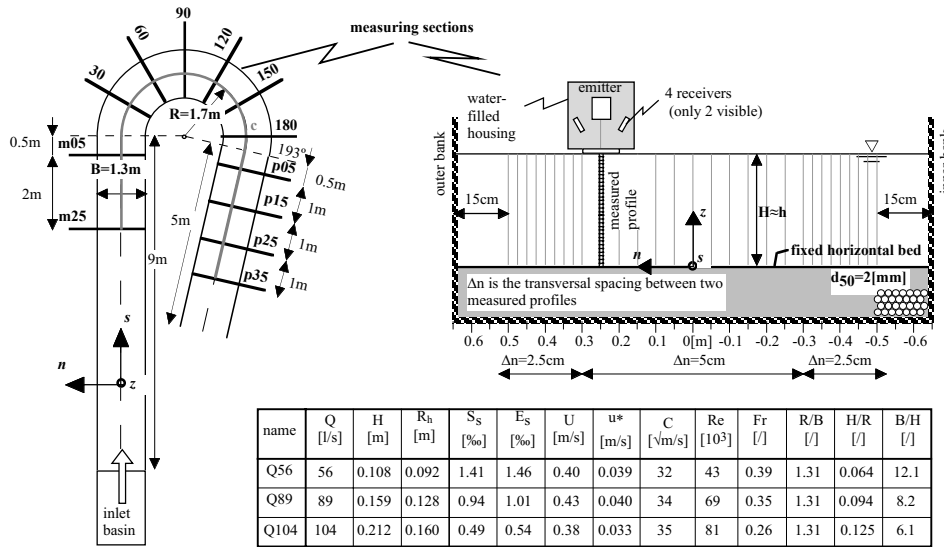


Fig.1: (a) Laboratory flume and measuring sections; (b) Measuring grid in sections and ADVP; (c) Hydraulic parameters.

EXPERIMENTAL RESULTS

VELOCITY DISTRIBUTION

Modelling the secondary flow in strongly curved channel bends (Blanckaert, 2001), a strong interdependence between the transversal non-uniformity of the downstream velocity distribution, $\partial U_s/\partial n$, and the strength of the secondary circulation, $\langle f_n^2 \rangle$, was elaborated. The transversal non-uniformity of the velocity distribution is well reflected by its centreline value, $\partial U_s/\partial n$ at $n=0$. After normalisation by U_s/R at $n=0$, a dimensionless parameter, α_s , can be evaluated such as:

$$\alpha_s = \frac{\partial U_s / \partial n}{U_s / R} \quad \text{at } n=0 \quad (9)$$

For the Q89-experiment, the distribution of $U_s(s,n)$ along the flume has been evaluated and the resulting α_s -values are shown in Fig.2. There one observes that α_s decreases from $\alpha_s=0$ in the straight inflow to $\alpha_s=-1$ at about 30° into the bend. α_s subsequently increases to a value of $\alpha_s \approx 0.3$ at 180° . At the bend exit, it increases to $\alpha_s=1$ and then shows a decreasing tendency in the straight outflow. Furthermore, the two experimental points for the Q56 and Q104-experiments (see Fig.2) suggest a similar evolution.

For flow over a horizontal bed, the velocity distributions are often approximated by a “free-vortex” distribution near the bend entry and by a “forced-vortex” distribution near the bend exit (de Vriend, 1981, p29-30, p213; Steffler, 1984, p30-33). In the adopted reference system, the “free-vortex” distribution is defined by, $U_s(n)=U_s(n=0)(1+n/R)^{-1}$, giving $\alpha_s=(\partial U_s/\partial n)/(U_s/R)=-1$, whereas the “forced-vortex” distribution is defined by, $U_s(n)=U_s(n=0)(1+n/R)$, giving $\alpha_s=(\partial U_s/\partial n)/(U_s/R)=1$. Our experimental data thus confirm these approximations, as used in the literature. The two types of vortices are schematically illustrated in Fig.2.

SECONDARY CIRCULATION AND VELOCITY REDISTRIBUTION

Fig.4 shows the centreline evolution of the *strength of the secondary circulation*, $\langle f_n^2 \rangle$, for the three experiments. After being negligible in the straight inflow, the strength of the secondary circulation starts to increase almost linearly at the bend entry. Then a zone of almost constant maximum strength is attained, extending from about 90° - 135° for Q56, 75° - 120° for Q89 and 75° - 105° for Q104. Subsequently, the strength decreases and it is reduced to less than 50% of its maximum value at the bend exit. In the straight outflow, it further decreases to attain negligible values only relatively far downstream of the bend. Similar observations have been reported (de Vriend, 1981, figs.65,69,73; Odgaard and Bergs, 1988, Fig.9) and explained (de Vriend, 1981, p.216; Yeh and Kennedy, 1993, p.782) before. It is often assumed that the strength of the secondary circulation attains an equilibrium value in long bends, eventually after initially attaining higher values. In none of our experiments, such an equilibrium value was observed, since the strength still decreased considerably at the bend exit.

The “Rozovskii model” predicts the strength of the secondary circulation, $\langle f_n^2 \rangle$, as a function of C , but independent of the curvature ratio, H/R . This is in contradiction with our experimental observation where the strength of the secondary circulation decreases with an increasing curvature ratio. The maximum observed values on the centreline decrease with the curvature ratio from about $\langle f_n^2 \rangle \approx 10$ for Q56 ($H/R=0.064$), to $\langle f_n^2 \rangle \approx 5.5$ for Q89 ($H/R=0.094$) and $\langle f_n^2 \rangle \approx 4$ for Q104 ($H/R=0.125$). The average values over the entire bend reach (0 - 193°) decrease from $\langle f_n^2 \rangle \approx 6.9$ for Q56, to $\langle f_n^2 \rangle \approx 3.0$ for Q89 and $\langle f_n^2 \rangle \approx 2.2$ for Q104. With the only exception of the

maximum value attained for Q56, these values are also lower than the value of $\langle f_n^2 \rangle \approx 9$ predicted by the “Rozovskii model” (Fig.3). This behaviour has already been remarked and physically explained by de Vriend (1981, Fig.5c). He shows a similar result computed with a fully 3D flow model, which however was for the case of laminar flow.

Fig.5 shows, for the same three experiments, the centreline evolution of the *velocity-redistribution coefficient*, $\langle f_s f_n \rangle$. For all cases, this coefficient is negligible in the straight inflow. At the bend entry it increases and attains maximum values at about 60° in the bend. After reaching these maximum values, it drops to nearly zero values at the bend exit. In the straight outflow the term is positive for the experiments Q56 and Q89, whereas it is slightly negative for Q104. Similar to $\langle f_n^2 \rangle$, the centreline evolution of $\langle f_s f_n \rangle$ does not attain an equilibrium value in the bend.

The “Rozovskii model” predicts the coefficient $\langle f_s f_n \rangle$ as a function of C , but independent of the curvature ratio, H/R . Our experimental observations suggest that $\langle f_s f_n \rangle$ decreases with increasing curvature ratio. The average values over the entire bend reach (0-193°) decreased from $\langle f_s f_n \rangle \approx 0.156$ for Q56 ($H/R=0.064$), to $\langle f_s f_n \rangle \approx 0.152$ for Q89 ($H/R=0.094$) and $\langle f_s f_n \rangle \approx 0.075$ for Q104 ($H/R=0.125$). The maximum values on the centreline were $\langle f_s f_n \rangle \approx 0.25$ for Q56, $\langle f_s f_n \rangle \approx 0.29$ for Q89 and $\langle f_s f_n \rangle \approx 0.20$ for Q104. In all cases, these values are lower than the value of $\langle f_s f_n \rangle \approx 0.44$ predicted by the “Rozovskii model” (Fig.3). An even stronger over-prediction by the “Rozovskii model” has been observed for the case of flow in an open-channel bend over a developed bar-pool topography (Blanckaert, 2001).

Blanckaert (2001) presents a model for the downstream velocity and the secondary circulation that explains the observed centreline evolution of $\langle f_n^2 \rangle$ and $\langle f_s f_n \rangle$ and the discrepancies with the “Rozovskii model”.

CONCLUSION

The secondary circulation in open-channel bends largely determines the bed topography. Depth-integrated flow models, used in engineering practice, cannot resolve the secondary circulation and information on it has to be provided as input to these models. The effect of the secondary circulation on the velocity distribution is accounted for by the velocity-redistribution coefficient, $\langle f_s f_n \rangle$, in the depth-integrated flow models, while the strength of the secondary circulation is defined as, $\langle f_n^2 \rangle$. Both are often described according to the “Rozovskii model”, which gives analytical expressions for the normalised profile of the downstream velocity, f_s , as well as for the normalised profile of the secondary circulation, f_n . This paper reports on an experimental investigation on strongly curved open-channel flow (Fig.1), used to evaluate the “Rozovskii model”.

The strength of the secondary circulation, $\langle f_n^2 \rangle$ (see Fig.4), and the velocity-redistribution coefficient, $\langle f_s f_n \rangle$ (see Fig.5), increase at the bend entry. After reaching a maximum value, they decrease and do not attain an equilibrium value in the bend. $\langle f_n^2 \rangle$ (see Fig.4) and $\langle f_s f_n \rangle$ (see Fig.5) are over-predicted by the “Rozovskii model” (see Fig.3). Furthermore, $\langle f_n^2 \rangle$ and $\langle f_s f_n \rangle$ show a

decrease with increasing curvature ratio, H/R , which is in contradiction with the unique dependence on the Chezy coefficient C predicted by the “Rozovskii model”. It can be concluded that the “Rozovskii model” does not correctly represent the secondary circulation and its effect on the velocity distribution for strongly curved open-channel flows.

Blanckaert (2001) presents a model for the flow in strongly curved channel bends that explains and predicts the behaviour observed in the reported experiments. This model depends on the transversal non-uniformity of the downstream velocity, which has been parametrised by the normalised transversal velocity gradient on the centreline, $\alpha_s = (\partial U_s / \partial n) / (U_s / R)$. In the reported experiments (see Fig.2), α_s decreases from $\alpha_s = 0$ in the straight inflow to $\alpha_s = -1$ just downstream of the bend entry. In the bend, α_s increases slightly, only to increase strongly near the bend exit to values of $\alpha_s = 1$.

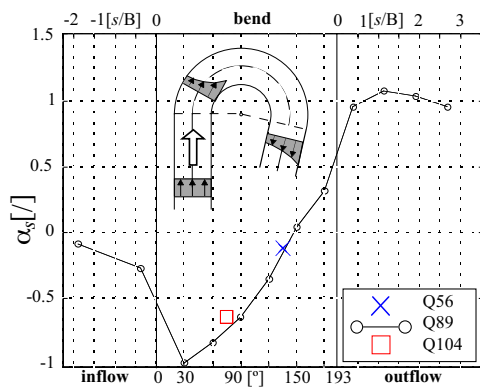


Fig.2: Centreline evolution of normalised transversal gradient of downstream velocity, $\alpha_s = (\partial U_s / \partial n) / (U_s / R)$ at $n=0$.

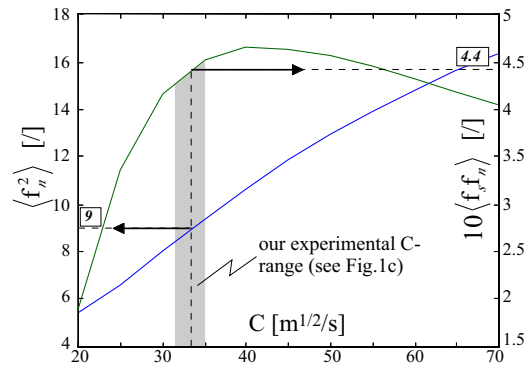


Fig.3: Strength of secondary circulation, $\langle f_n^2 \rangle$, and velocity-redistr. coeff., $\langle f_{s,n} \rangle$, as function of Chezy coefficient according to "Rozovskii model".

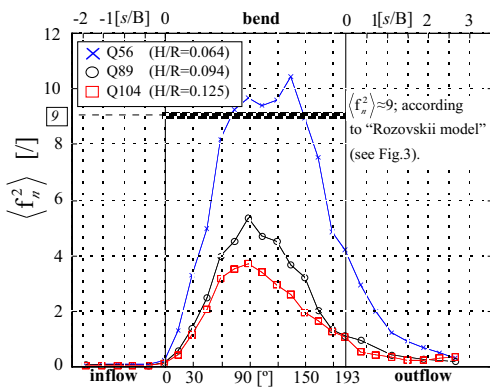


Fig.4: Centreline evolution of strength of secondary circulation, $\langle f_n^2 \rangle$.

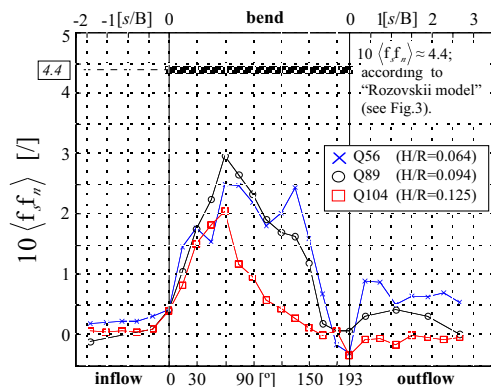


Fig.5: Centreline evolution of velocity-redistribution coefficient, $\langle f_{s,n} \rangle$.

ACKNOWLEDGEMENTS

This research is being sponsored by the Swiss National Science Foundation under grant Nr.2100-052257.97/1. D. Hurther and U. Lemmin are acknowledged for help with the ADVP instrument.

REFERENCES

- Blanckaert, K. (2001). "discussion on: Bend-flow simulation using 2D depth-averaged model, by." *J. Hydr. Eng.*, ASCE, Vol.127(No.2), (scheduled for publication)
- Blanckaert, K. (2001). "A model for flow in strongly curved channel bends" XXIX IAHR-congress, Beijing, China (submitted for publication)
- de Vriend, H. J. (1977). "A mathematical model of steady flow in curved shallow channels." *J. Hydr. Res.*, IAHR, 15(1), 37-54.
- de Vriend, H. J. (1981). "Steady flow in shallow channel bends." Rep. No. 81-3, Comm. on Hydraulics, Dept. Civ. Eng., Delft Univ. Techn., Delft.
- Dietrich, W.E. and Whiting, P. (1989). Boundary shear stress and sediment transport in river meanders of sand and gravel. *River Meandering* Eds. S. Ikeda and G. Parker. Washington, AGU. 1-50
- Hurther, D. and Lemmin, U. (2000). "A correction method for turbulence measurements with a 3-D acoustic Doppler velocity profiler." *J. Atm. Oc. Techn.*, AMS, accepted for publication,
- Lemmin, U. and Rolland, T. (1997). "Acoustic velocity profiler for laboratory and field studies." *J. Hydr. Eng.*, ASCE, 123(12), 1089-1098.
- Odgaard, J. A. and Bergs, M. A. (1988). "Flow processes in a curved alluvial channel." *Wat. Resourc. Res.*, AGU, 24(1), 45-56.
- Rozovskii, I. L. (1957). *Flow of Water in Bends of Open Channels*. Ac. Sc. Ukr. SSR, Isr. Progr. Sc. Transl., Jerusalem, 1961.
- Steffler, P. M. (1984). "Turbulent flow in a curved rectangular channel." *Ph.D.*, The University of Alberta, Alberta.
- Yeh, K. C. and Kennedy, J. F. (1993). "Moment model of nonuniform channel-bend flow. I: Fixed beds." *J. Hydr. Eng.*, ASCE, 119(7), 776-795.

II.4 Secondary currents measured in sharp open-channel bends

K. Blanckaert

Laboratoire d'Hydraulique Environnementale, Ecole Polytechnique Fédérale de Lausanne, Switzerland

Proc. River Flow 2002, Vol. I, p. 117-125, Sept. 4-6, 2002, Louvain-la Neuve, Belgium

River Flow 2002, Bousmar & Zech (eds.)

© Swets & Zeitlinger, Lisse, ISBN 90 5809 509 6

ABSTRACT: The importance of secondary currents in open-channel bends has long been recognized. They redistribute the flow, the boundary shear stress and the sediment transport, and hence affect the river morphology. Furthermore, they are an important contributor to the mixing and spreading of suspended matter, pollutants and heat. Besides the classical center-region cell (helical motion), a relatively weak outer-bank cell of secondary circulation often occurs, which plays a major role with respect to bank erosion processes. Despite their importance both circulation cells still bear secrets. Especially the outer-bank cell is poorly understood: its conditions of occurrence are not known and its numerical simulation is not yet satisfactory. This paper presents detailed patterns of bi-cellular secondary currents and downstream velocity measured in a sharp laboratory bend with a horizontal bottom. Three hydraulic conditions are investigated, corresponding to three values of the ratio between the flow depth and the centerline radius of curvature.

1 INTRODUCTION

Secondary currents play an important role in three-dimensional open-channel flows. By advecting flow momentum, they redistribute the velocity, the boundary shear stress and the sediment transport, and shape the river morphology. Furthermore, they enhance the mixing and spreading of suspended matter, pollutants and heat. Hence, an accurate representation of the secondary circulation is a prerequisite to successful flow simulations.

The classical helical motion, termed here center-region cell, has been amply investigated and is relatively well understood. Its outward/inward velocities in the upper/lower part of the water column are commonly explained as resulting from the interplay between the centrifugal force, the pressure gradient due to the tilting of the water surface, and the bottom friction.

De Vriend (1981a) already noticed an important feedback between the center-region cell and the downstream velocity distribution. The center-region cell flattens the downstream velocity profile, by increasing/decreasing the velocities in the lower/upper part of the water column, which reduces the centrifugal forcing and weakens the center-region cell. Based on the above mentioned interplay between the centrifugal force, the pressure gradient and the

bottom friction, Blanckaert (2001) and Blanckaert & Graf (2001c, 2002) have proposed a non-linear model for the center-region cell and the downstream velocity profile that accounts for this feedback. This model agrees fairly well with experimental data for moderately and strongly curved flow. For very strong curvatures, however, Blanckaert & de Vriend (2002) show that the mechanics underlying the center-region are more complex and require a fully three-dimensional flow description. Experimental data on center-region cells in moderately to strongly curved flows are scarce.

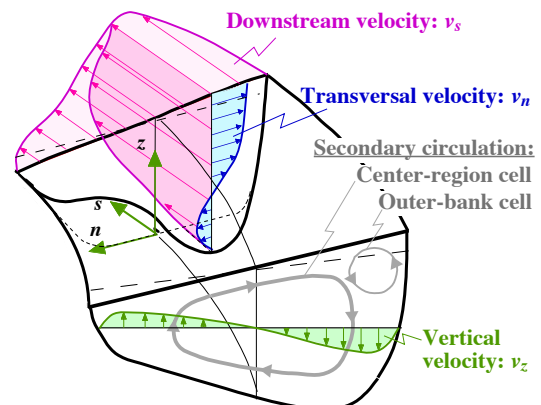


Figure 1. Definition sketch of curved open-channel flow and secondary circulation.

Near the outer bank of channel bends, often an additional counter-rotating circulation cell, termed outer-bank cell, occurs. Although relatively weak, it is of major importance with respect to bank erosion processes. Both cells of secondary circulation are schematically indicated in Figure 1.

Outer-bank cells have since long been observed in laboratory flows (Mockmore 1943, Einstein & Harder 1954, Rozovskii 1957, etc.) as well as in natural flows (Bathurst et al. 1979, Dietrich & Smith 1983, de Vriend & Geldof 1983, etc.). Nevertheless, they are still poorly understood, which is mainly due to a lack of detailed experimental data. Important questions that remain unanswered are:

- What are the relevant mechanisms with respect to the generation of the outer-bank cell ?
- Under what conditions do these mechanisms lead to the formation of an outer-bank cell ?
- How can outer-bank cells be simulated numerically ?
- How do outer-bank cells behave as a function of the hydraulic parameters ?
- What role do outer-bank cells play in bank erosion processes and river meandering ?

Blanckaert & Graf (2001a) experimentally investigated an outer-bank cell existing over a natural bottom topography in a laboratory flume. They present distributions of all three mean velocity components as well as all six Reynolds stresses on a fine grid. Subsequently, Blanckaert & Graf (1999) have analyzed the influence of this outer-bank cell on the boundary shear stress and the bank stability. Blanckaert & de Vriend (2002) have investigated the mechanisms underlying this outer-bank cell which led to their successful simulation by Jia et al. (2001) with a non-linear $k-\epsilon$ turbulence closure. Although these investigations yielded valuable in-

formation, they are restricted to one highly non-uniform flow over a varying natural bottom topography in a relatively narrow flume.

Christensen et. al. (1999) have simulated numerically the outer-bank cell for the case of axisymmetric flow (infinitely long bend, often called fully-developed flow) with a standard $k-\epsilon$ turbulence model as well as with a second-order Reynolds stress turbulence model. They investigated its behavior as a function of the ratio H/R (H being the flow depth and R the radius of curvature at the centerline) and the bottom topography. The main drawback of these investigations is the lack of validation with experimental data.

The key to a better understanding is the availability of high-resolution experimental data on both circulation cells including all three mean velocity components. Such data are at present scarce, in particular for the outer-bank cell. Most previous experimental investigations of the circulation cells were restricted to measurements of the downstream and the transversal velocity components on relatively coarse grids in the center of the cross-section and with a relatively low accuracy (Blanckaert and Graf, 2001a).

The main goal of this paper is to present high-quality experimental data on both cells of secondary circulation. Experiments over a horizontal bottom topography, adopted to facilitate interpretation, have been conducted under different hydraulic conditions. Sharp bends were investigated, with the aim of obtaining pronounced outer-bank cells. This paper reports some preliminary results: the measured distributions of the downstream velocity and bi-cellular patterns of secondary circulation are presented and discussed.

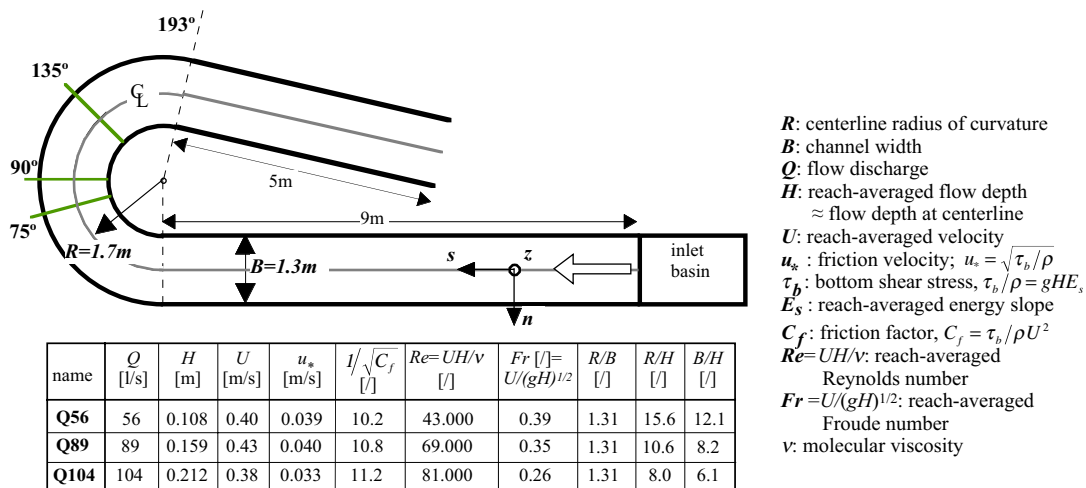


Figure 2. Laboratory flume and hydraulic conditions.

2 THE EXPERIMENTS

Experiments were conducted in the laboratory flume shown in Figure 2. It consists of a 9 m long straight entry reach, followed by a 193° bend with constant centerline radius of curvature, $R=1.7$ m, and a 5 m long straight exit reach. The vertical side-walls are made of Plexiglas and the horizontal bottom is covered with a nearly uniform sand, $1.6 \text{ mm} < d < 2.2 \text{ mm}$, that was fixed by spraying a paint on it, thus preserving its roughness.

Experiments were done for three values of the curvature ratio, H/R . They will be named after their discharge Q . The hydraulic conditions are tabulated in Figure 2. The parameters $R/B = 1.31$ and $R/H = 8$ to 15.6 corresponds to sharp bends. These values were chosen with the aim of obtaining pronounced, hence well visible, outer-bank cells. The aspect ratio, $B/H = 6.1$ to 12.1, corresponds to flows that are narrower than usual in natural lowland rivers, but do occur in mountain rivers and man-made channels.

Non-intrusive three-dimensional measurements of the mean flow field and the turbulence were made with an Acoustic Doppler Velocity Profiler (ADVP), developed in our laboratory (see Fig. 3). This instrument measures simultaneously the quasi-instantaneous velocity components at a high spatial and temporal resolution. From the measured data, the mean velocity field, $\bar{v}(v_s, v_n, v_z)$, can be derived, as well as the fluctuating velocity field, $\bar{v}'(v'_s, v'_n, v'_z)$, and the turbulent stress tensor, $\bar{v}'_j v'_k$ ($j, k = s, n, z$). Whereas most commercial velocity meters measure point-by-point, our ADVP measures simultaneously all the velocities along its main axis. This profiling capacity allows to do measurements much faster and to cover much denser grids than with conventional instruments.

The non-intrusive measurements were made with the ADVP placed in a water-filled housing that touches the water surface (Fig. 3). In this configuration, vertical profiles were measured that were divided into discrete cylindrical measuring volumes of size $(\pi \cdot 0.7^2 / 4) \times (0.3) = 0.12 \text{ cm}^3$. The sampling frequency was 31.25 Hz and the acquisition time was 200 s. The accuracy on the mean velocities is typically better than 4 %. More information on the working principle of the ADVP, its experimental accuracy and its comparison with other velocity meters can be found in Lemmin & Rolland (1997), Hurther & Lemmin (1998, 2001), Blanckaert & Graf (2001a) and Blanckaert & Lemmin (2002).

3 EXPERIMENTAL RESULTS AND ANALYSIS

3.1 Centerline evolution of secondary circulation

For each of the three hydraulic conditions, measurements were first of all done along the centerline of the flume with a spacing of 0.5 m in the straight reaches and 15° in the bend. These measurements aimed at investigating the downstream evolution of the secondary circulation and identifying the cross-section characterized by the strongest secondary circulation.

In order to define the strength of the secondary circulation, let's first decompose the velocity component as:

$$v_s = U_s f_s \quad (1)$$

$$v_n = U_n f_s + v_n^* = U_n f_s + U_s \frac{H}{R} f_n \quad (2)$$

v_s and v_n are the downstream and transversal velocity components; U_s and U_n their depth-averaged values; v_n^* is the transversal component of the sec-

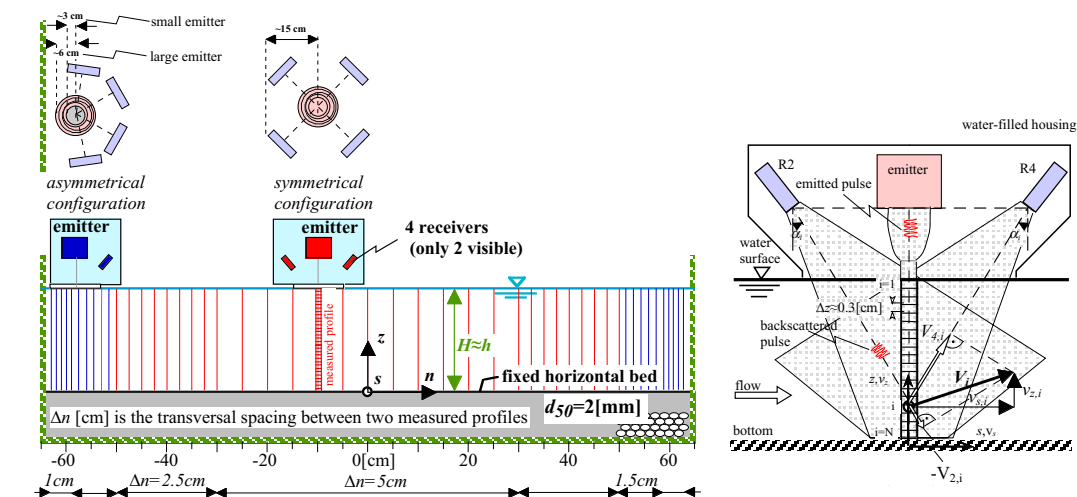


Figure 3. Acoustic Doppler Velocity Profiler (ADVP) configurations and measuring grid.

ondary circulation; f_s and f_n are the normalized profiles of v_s and v_n^* , respectively. Since the strength of the secondary circulation is expected to increase with curvature, H/R has been included in the normalization of v_n^* . At the centerline, where the vertical velocity component is negligible, the strength of the secondary circulation is now defined by:

$$\langle f_n^2 \rangle = \frac{1}{h} \int_{z_b}^{z_s} f_n^2 dz \quad (3)$$

$h = z_s - z_b$ is the flow depth where z_s and z_b are the elevations of the water surface and the bottom, respectively.

Figure 4 shows the measured evolution of $\langle f_n^2 \rangle$ along the centerline for the three experiments. The secondary circulation comes into existence at the bend entry and increases nearly linearly in the beginning of the bend. About halfway in the bend, a zone of almost constant maximum strength exists, which extends from about 90° - 135° for Q56, 75° - 120° for Q89 and 75° - 105° for Q104. Subsequently, the secondary circulation weakens considerably and at the bend exit its strength is reduced to less than 50% of its maximum value. In the straight outflow, it further decreases to attain negligible values at the end of the flume. Similar findings have been reported before by de Vriend (1981a) and Odgaard & Bergs (1988).

It is often assumed that the secondary circulation attains an equilibrium strength in long bends, eventually after an initial overshoot. In none of our experiments, such an equilibrium value was observed, since the strength still decreased considerably at the bend exit. De Vriend (1981a) and Yeh & Kennedy (1993) have qualitatively explained the mechanisms underlying this behavior of the secondary circulation. Blanckaert (2001) and Blanckaert & Graf (2001c, 2002) have proposed a non-linear model for the secondary circulation that agrees well with the presented experimental findings.

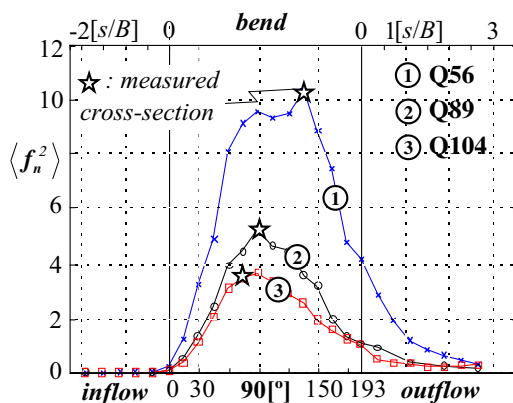


Figure 4. Measured centerline evolution of strength of secondary circulation, $\langle f_n^2 \rangle$.

3.2 Three-dimensional flow patterns

Subsequently, the three-dimensional flow patterns were measured in the cross-section characterized by the strongest secondary circulation. According to Figure 4, these cross-sections are situated at 135° , 90° and 75° for the Q56, Q89 and Q104-experiments, respectively.

The measurements were made on the fine grid shown in Figure 3, containing 48 verticals with a transversal spacing that progressively decreases towards the banks. These measuring grids cover about 1700, 2500 and 3400 measuring points for the three experiments, respectively. Close to the banks, a spacing of 1 cm was required to obtain a high-resolution image of the cells of secondary circulation. Furthermore, an adapted asymmetrical configuration of the ADVP (see Figure 3) was developed that enabled to measure onto 2/3 cm from the inner/outer bank. To improve the legibility of the figures, the experimental scatter has been eliminated by fitting analytical surfaces to the raw data, using two-dimensional smoothing splines with weight functions (de Boor, 1978).

Figure 6 (see further) presents isolines of the downstream velocity normalized with the overall mean velocity, v_s/U . Blanckaert & Graf (2001b) have presented the evolution of the spanwise distribution of U_s/U in the same experiments. Near the bend entry, it approaches a “potential-vortex” distribution with the core of maximum velocities at the inner bank. Advective momentum transport by the secondary circulation causes the core of maximum velocities to shift gradually towards the outer bank. Near the bend exit, the core of maximum velocities is found at the outer bank and U_s/U approaches a “forced-vortex” distribution.

This gradual outward shifting of the core of maximum velocities is clearly discernable in Figure 6. In the cross-section at 135° in the Q56-experiment, the core of maximum velocities has reached the centerline. At 90° in the Q89-experiment, it is found in the inner bend at about 45 cm from the inner bank and at 75° in the Q104-experiment, it has shifted only about 30 cm from the inner bank. The role of the secondary circulation is revealed by the inclination of the v_s -isolines, which is caused by the outward/inward secondary velocities in the upper/lower part of the water column. As a result, the maximum velocities in the inner bend are not found at the water surface, as in straight uniform open-channel flow, but in the lower part of the water column.

Figure 5 shows the normalized profiles of v_s , averaged over the width of the cross-section. In the near-bottom zone, $z/H < 0.1$, the profiles are logarithmic (Fig. 5a) and allow an estimation of the local friction velocity and friction factor in the considered cross-section. The local values of the friction velocity are considerably higher than their flume-averaged counterparts: $u_{*,135}=4.6$ cm/s $>$ $u_*=3.9$ cm/s for the Q56-experiment, $u_{*,90}=4.9$ cm/s $>$ $u_*=4.0$ cm/s for the Q89-experiment and $u_{*,75}=4.8$ cm/s $>$ $u_*=3.3$ cm/s for the Q104-experiment, and the corresponding local friction factor of $1/\sqrt{C_f} \approx 8.4$ is lower than the flume-averaged one of 10.2 to 11.2 (cf. Fig. 2). These values indicate that the investigated cross-sections, where the secondary circulation is at maximum strength, are characterized by enhanced friction losses.

In the introduction, it was mentioned that a feedback mechanism between the center-region cell and the downstream velocity leads to a flattening of the v_s -profiles. This is illustrated in Figure 5b, where the measured width-averaged profiles are compared to a logarithmic profile for the local friction factor $1/\sqrt{C_f} \approx 8.4$. The profiles are rather similar for the three experiments and are considerable flatter than the logarithmic profile. Furthermore, the locus of maximum velocity is found in the lower part of the water column. It is remarkable, however, that near the spanwise location of the ‘eye’ of the center-region cell, the maximum downstream velocities are found at the water surface.

Figure 6 also presents normalized streamlines of the secondary circulation, $100\psi/(UH)$. For axisymmetric curved flow ($\partial/\partial s=0$, infinitely long bend), the relation between the secondary circulation and the streamfunction ψ is given by:

$$v_n = v_n^* = -\frac{1}{1+n/R} \frac{\partial \psi}{\partial z} \quad (4)$$

$$v_z = \frac{1}{1+n/R} \frac{\partial \psi}{\partial n} \quad (5)$$

$$\psi = -(1+n/R) \int_{z_b}^* v_n^* dz = \int_n^{B/2} (1+n/R) v_z dn \quad (6)$$

$1+n/R$ is a metric factor accounting for the divergence of the transversal co-ordinate axes. Figure 6 is based on the average of both expressions in Equation 6.

In developing curved flow, as is the case in the experiments, the above definitions are only approximate. Inserting the velocities according to Equations (1) and (2) in the continuity equation yields:

$$\frac{\partial U_s f_s}{\partial s} + \frac{\partial}{\partial n} [(1+n/R) U_n f_n] + \frac{\partial}{\partial n} [(1+n/R) v_n^*] + \frac{\partial}{\partial z} [(1+n/R) v_z] = 0 \quad (7)$$

By definition of ψ , Equations (4) and (5), the second line is identically zero. Although the terms on the first line tend to balance each other, their sum does not equal to zero, as can be seen from the depth-integrated continuity equation:

$$\frac{\partial U_s h}{\partial s} + \frac{\partial}{\partial n} [(1+n/R) U_n h] = 0 \quad (8)$$

If f_s and h vary less than U_s and U_n , the first line in Equation (7) is close to zero and the secondary circulation can with good approximation be represented by its streamfunction ψ .

The ψ -patterns in Figure 6 clearly reveal the existence of a bi-cellular secondary circulation for all three experiments. They are rather smooth, except for some irregularities near the inner bank, where the three-dimensional flow pattern is very complex. The outer-bank cells are noticeable in the corner formed by the outer bank and the water surface. They seem to widen with increasing curvature ratio. For the Q56-experiment, the outer-bank cell covers a width of about $3/4 H$, for Q89 its width increases to about H and for Q104 it covers already twice the flow depth. Note that the figures are distorted: the vertical scale equals twice the horizontal one. Correspondingly, the center-region cell narrows and occupies the remaining part of the cross-section. The ‘eye’ of the center-region cell is not found near the axis of the flume, but seems to coincide with the

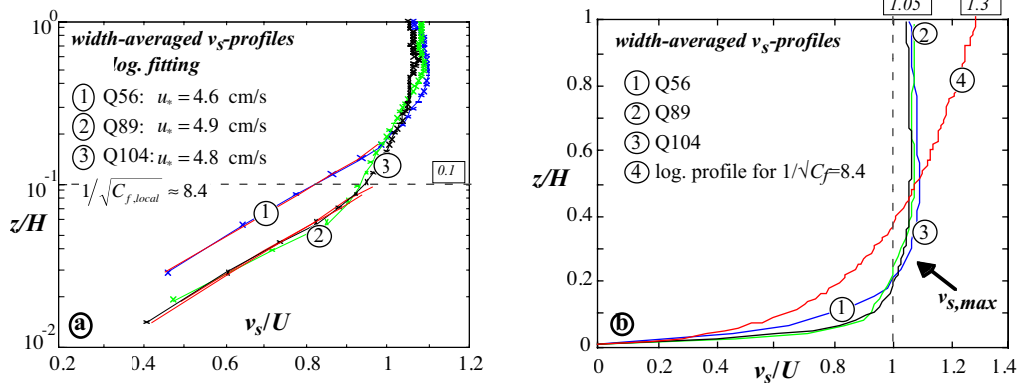


Fig. 5: Profiles of the normalized downstream velocity, v_s/U , averaged over the width of the cross-section.

spanwise location of the core of maximum downstream velocities.

Table 1 summarizes the information on the strength of both circulation cells. On the basis of linear perturbation theory, one might expect the strength of the center-region cell to increase linearly with the curvature ratio H/R . When adopting the linear model proposed by de Vriend (1977), a ψ -profile results that increases from zero values at the bottom and the water surface to a maximum value at about mid-depth that depends on the friction factor. For the considered experiments, this value is $[100\psi/(UH)_{max}]/(H/R) \approx 150$. Our measurements show that the maximum ψ -values in center-region cell hardly vary between the three experiments, and they decrease considerably when normalized with H/R . The maximum value in the Q56-experiment is comparable to the linear model prediction, whereas the values in the Q89 and Q104-experiments are considerably smaller. This indicates that the efficiency of the curved flow to generate secondary circulation reduces with increasing curvature.

Note that $[100\psi/(UH)_{max}]/(H/R)$ and $\sqrt{\langle f_n^2 \rangle}$ are both measures of the normalized strength of the center-region cell. The experimental data indicate that they are equivalent, since their ratio is nearly constant (cf. Table 1). This confirms that the streamfunction approach is adapted to investigate the secondary currents.

As aforementioned, de Vriend (1981a) already noticed that this reduced efficiency of secondary circulation generation is due to a negative feedback between the downstream velocity profile and the center-region cell. As illustrated in Figure 5, the downstream velocity profile is flattened by the center-region cell. This decreases the centrifugal forcing and weakens the center-region cell. Blanckaert (2001) and Blanckaert & Graf (2001c, 2002) have proposed a non-linear model for the secondary circulation that captures and explains this reduced efficiency of secondary circulation generation with increasing curvature. Similar to the linear models, it calculates the center-region cell from a simplified transversal momentum equation that expresses the

interplay between the centrifugal force, the pressure gradient due to the superelevation of the water surface, and the bottom friction. However, contrary to the linear models that adopt a straight-uniform-flow v_s -profile, they calculate the flattened v_s -profiles from a simplified downstream momentum equation that accounts for advective momentum transport by the center-region cell.

The solution of this non-linear model for the strength of the center-region cell is shown in Fig. 7, normalized by the linear-model solution. It is expressed as a function of one single parameter, called bend parameter β , that accounts for the curvature ratio H/R , the friction factor C_f , and the spanwise distribution of the downstream velocity. For vanishing curvature, this non-linear model reduces to the linear model. The non-linear model predicts a reduction of the strength of the center-region cell of about 0.6 for the Q56 and Q89-experiments and about 0.45 for the Q104-experiments (cf. Fig. 7), which should be compared with the experimental values of 0.97, 0.70 and 0.57, respectively (cf. Table 1, derived from ψ). For the Q89 and Q104-experiments, the agreement is reasonably well. Blanckaert & Graf (2002) have shown that the remaining differences are largely due to the neglect of inertia in the non-linear model. For the Q56, hardly any reduction was observed in the experiment, and this despite the pronounced curvature. Note that the bend parameter allows to distinguish objectively between weak, moderate and strong curvatures (see Fig. 7). According to this criterium, the considered flows are strongly curved.

Similar near-bank circulation cells exist in straight uniform open-channel flow and their strength is characterized by maximum magnitudes of $100\psi/(UH) \approx 0.2$ to 0.4 (Tominaga et al. 1989, Nezu & Nakagawa 1993). Outer-bank cells in bends are thought to be stronger than near-bank cells in straight flow. Christensen et al. (1999) have simulated the outer-bank cell for axisymmetric flow (infinitely long bend) with a second-order Reynolds stress turbulence model. They found it even to occur in wide channels of weak curvature and to strengthen with H/R .

Table 1. Strength of the circulation cells

name	section	H/R	center-region cell				outer-bank cell		$\frac{\psi_{center\ region}}{\psi_{outer\ bank}}$
			$100\psi/(UH)_{max}$	$\frac{100\psi/(UH)_{max}}{H/R}$	$\sqrt{\langle f_n^2 \rangle}$	$\frac{\psi/(UH)_{max}}{H/R}$	$100\psi/(UH)_{max}$	$\frac{100\psi/(UH)_{max}}{H/R}$	
Q56	135°	0.064	9.2	145	3.2	2.2	-0.3	-5	-31
Q89	90°	0.094	9.6	102	2.3	2.2	-0.9	-10	-11
Q104	75°	0.125	10.3	83	1.9	2.3	-2.7	-22	-3.8

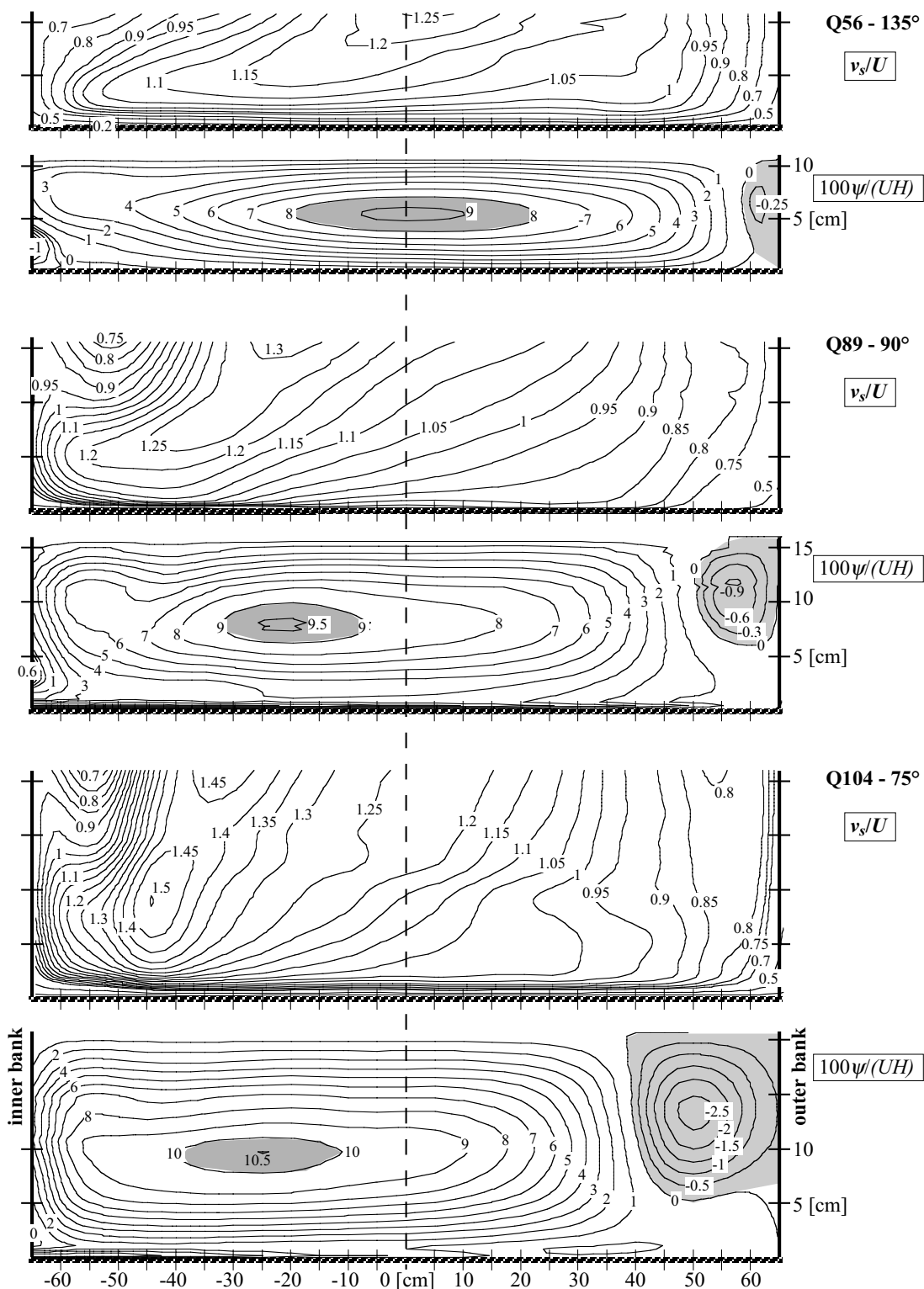


Figure 6. Isolines of downstream velocity, v_s/U , and streamfunction of secondary circulation, $100\psi/(UH)$.

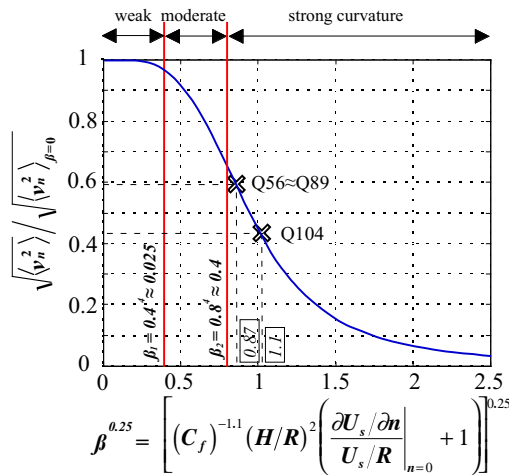


Figure 7. Non-linear model solution for strength of center-region cell, normalized by linear model solution.

The experimental results confirm this strengthening, which occurs at a more than linear rate. For $H/R=0.064$ in the Q56-experiment, the outer bank cell is weak with maximum magnitudes of about $100\psi/(UH)=0.3$ (cf. Table 1). For $H/R=0.094$, the maximum magnitude is tripled to about 0.9 and for $H/R=0.125$ it is tripled again to 2.7. This is in contrast with the behavior of the center-region cell, as is clearly indicated by the ratio of the strengths of both cells. Whereas the center-region cell is about 31 times stronger than the outer-bank cell for $H/R=0.064$, this ratio drops to 3.8 for $H/R=0.125$. In their simulation for axisymmetric curved flow, Christensen et al. (1999) found a small ratio of about 5 for a weak curvature of $H/R=0.0074$.

It is surprising that the outer-bank cell in the Q56-experiment is not stronger than the near-bank cells in straight flow, despite the high curvature ratio, and that its relative strength in all three experiments is smaller than in the weakly curved flow simulated by Christensen et al. (1999). Possible, the outer-bank cell is crushed against the outer bank and weakened by the center-region cell, which is at maximum strength in the measured section. With increasing curvature ratio, the center-region cell gets relatively weaker (cf. Fig. 7) and the outer-bank cell can better develop. Moreover Blanckaert & de Vriend (2002) claim that the outer-bank cell is generated by two mechanisms that positively interact, whence the outer-bank cell strengthens around the bend.

So the size and strength of the outer-bank cell are expected to vary in an opposite way to the center-region cell along the bend, and thus increase. This explains why Christensen et al. (1999) found such an important relative strength of the outer-bank cell in his weakly curved axisymmetric flow.

It is interesting to mention some results obtained for the case of strongly curved laminar flow, which is characterized by a similar bi-cellular pattern of secondary circulation. Cheng et al. (1976), de Vriend (1981b) and Winters (1987) have done numerical simulations for the case of axisymmetric flow and obtained an outer-bank cell that was only slightly weaker than the center-region cell. In an experimental investigation, Hille et al. (1985) found that the outer-bank cell is much weaker than the center-region cell in most of the bend, and only picks up beyond 120° .

4 CONCLUSIONS

Secondary currents are a characteristic feature of flow in open-channel bends. Besides the classical helical motion, termed here center-region cell, often a weaker and smaller outer-bank cell occurs near the outer bank. It plays an important role in bank erosion processes and in meander formation.

In spite of their importance, secondary currents still bear a lot of questions, which is largely due to a lack of detailed experimental data. Most previous investigations considered weakly curved flow and were restricted to the center-region cell.

This paper presents detailed data on the downstream velocity distribution and on both circulation cells based on measurements of all three mean velocity components on a fine grid. Three strongly curved flows were investigated, parameterized by different values of the ratio between the flow depth and the centerline radius of curvature, H/R .

The strength of the secondary circulation does not increase towards an equilibrium value along the bend, as is often assumed. It increases quickly upon entering the bend, reaches a maximum and subsequently decreases rather strongly in the second part of the bend. Three-dimensional patterns of the downstream velocity and the secondary circulation are presented in the cross-section of maximum secondary circulation.

The effect of the secondary circulation is clearly visible in the distribution of the downstream velocity v_s . The locus of maximum velocity shifts in outward direction and the vertical profiles are flattened (increased/decreased velocities in the lower/upper part of the water column). An estimation of the friction velocity and the friction factor from the logarithmic near-bottom part of the v_s -profile reveals that the cross-section of maximum secondary circulation is characterized by enhanced energy losses.

For all three experiments, a bi-cellular pattern of secondary currents exists. The secondary circulation is represented by its streamfunction ψ . The strength of the center-region cell does not increase linearly with the curvature ratio H/R , as could be expected on the basis of linear perturbation theory, but hardly varies between the three experiments. This relative weakening of the center-region cell is due to the flattening of the v_s -profiles and the corresponding centrifugal forcing. The measured evolution with increasing curvature agrees fairly well with predictions based on a non-linear model that takes due account of the negative feedback between the v_s -profile and the center-region cell.

The outer-bank cell seems to widen and strengthen more than linearly with H/R . However, it is weaker than could be expected on the basis of the similar near-bank cells in straight uniform flow or in axisymmetric curved turbulent flow. Possible, it is crushed against the outer bank and weakened by the center-region cell, which attains its maximum strength in the investigated sections. Furthermore, the outer-bank cell is expected to strengthen upon proceeding through the bend.

A more detailed analysis of the flow field, and especially the bi-cellular pattern of secondary circulation will be reported in forthcoming papers.

ACKNOWLEDGEMENTS

This research is being sponsored by the Swiss National Science Foundation under grants Nr.2100-052257.97/1 and 2000-059392.99/2. The author gratefully acknowledges his PhD supervisor, prof. W.H. Graf, for his support and Prof. de Vriend for fruitful discussion during his stay at EPFL.

REFERENCES

- Bathurst, J.C., Thorne, C.R. & Hey, R.D. 1979. Secondary flow and shear stress at river bends. *J. Hydr. Div.* 105(10): 1277-1295.
- Blanckaert, K. 2001. A model for flow in strongly curved channel bends. *Proc. 29th-IAHR Congr., J.F. Kennedy Student Paper Comp.* Beijing: Tsinghua Univ. Press.
- Blanckaert, K., & de Vriend, H.J. 2002. Secondary flow in sharp open-channel bends. (*submitted for publication*)
- Blanckaert, K. & Graf, W.H. 1999. Outer-bank cell of secondary circulation and boundary shear stress in open-channel bends. *Proc. 1st-RCEM symp.*, Genova: Univ. Genova.
- Blanckaert, K. & Graf, W.H. 2001a. Mean flow and turbulence in open channel bend. *J. Hydr. Engng.* 127(10): 835-847.
- Blanckaert, K. & Graf, W.H. 2001b. Experiments on flow in a strongly curved channel bend. *Proc. 29th-IAH Congr., Theme D, Vol. I*, Beijing: Tsinghua Univ. Press
- Blanckaert, K. & Graf, W.H. 2001c. Non-linear model for secondary circulation and transversal bottom slope in sharp bends. *Proc. 2th-RCEM-congr.* Obihiro..
- Blanckaert, K. & Graf, W. H. 2002. Secondary circulation and vertical flow structure in open-channel bends. I. Presentation and analysis of a non-linear model. (*submitted for publication*).
- Blanckaert, K. & Lemmin, U. 2002. Improving acoustic turbulence measurements. (*submitted for publication*).
- Cheng, K.C., Lin, R.C. & OU, J.W. 1976. Fully developed laminar flow in curved rectangular channels. *J. Fluids Engng:* 41-48.
- Christensen, B., Gislason, K. & Fredsoe, J. 1999. Secondary turbulent flow in an infinite bend. *Proc. 1st-RCEM symp.*, Genova: Univ. Genova.
- de Boor, C. 1978. *A Practical Guide to Splines*. Springer: Berlin.
- de Vriend, H.J. 1977. A mathematical model of steady flow in curved shallow channels. *J. Hydr. Res.* 15(1): 37-54.
- de Vriend, H.J. 1981a. Steady flow in shallow channel bends. *Report No. 81-3*, Dept. Civ. Eng., Delft Univ. Techn., Delft.
- de Vriend, H.J. 1981b. Velocity redistribution in curved rectangular channels. *J. Fluid Mech* 107: 423-439.
- de Vriend, H.J. & Geldof, H.J. 1983. Main flow velocity in short and sharply curved river bends. *Report No. 83-6*, Dept. Civ. Eng., Delft.
- Dietrich, W.E. & Smith, J.D. 1983. Influence of the point bar on flow through curved channels. *Water Resour. Res.*, 19(5): 1173-1192.
- Einstein, H.A. & Harder, J.A. 1954. Velocity distribution and the boundary layer at channel bends. *Trans. AGU*, 35(1): 114-120.
- Hille, P., Vehrenkamp, R. & Schulz-Dubois, E.O. 1985. The development and structure of primary and secondary flow in a curved square duct. *J. Fluid Mech.* 151: 219-241.
- Hurther, D. & Lemmin, U. 1998. A constant beamwidth transducer for three-dimensional Doppler profile measurements in open channel flow. *Meas. Sc. Techn.* 9(10): 1706-1714.
- Hurther, D. & Lemmin, U. 2001. A correction method for turbulence measurements with a 3-D acoustic Doppler velocity profiler. *J. Atm. Oc. Techn.*, 18: 446-458.
- Jia, Y., Blanckaert, K. and Wang, S.S.. 2001. Numerical simulation of secondary currents in curved channels. *Proc. 8th FMTM-congress*, Tokyo.
- Lemmin, U. & Rolland, T. 1997. Acoustic velocity profiler for laboratory and field studies. *J. Hydr. Engng.* 123(12): 1089-1098.
- Mockmore, C.A. 1943. Flow around bends in stable channels. *Transactions ASCE* 109: 593-628 (incl. discussions).
- Nezu, I. & Nakagawa, H. 1993. *Turbulence in open-channel flows*. Rotterdam: Balkema.
- Odgaard, J.A., & Bergs, M.A. 1988. Flow processes in a curved alluvial channel. *Water Resour. Res.* 24(1): 45-56.
- Rozovskii, I.L. 1957. *Flow of Water in Bends of Open Channels*. Jerusalem: Isr. Progr. Sc. Transl.
- Tominaga, A., Ezaki, K., Nezu, I. & Nakagawa, H. 1989. Three-dimensional turbulent structure in straight channel flows. *J. Hydr. Res.* 27(1): 149-173.
- Yeh, K.C. & Kennedy, J.F. 1993. Moment model of nonuniform channel-bend flow. I: Fixed beds. *J. Hydr. Engng.* 119(7): 776-795.
- Winters, K.H. 1987. A bifurcation study of laminar flow in a curved tube of rectangular cross-section. *J. Fluid Mech.* 180: 343-369.

PART II

EXPERIMENTAL OBSERVATIONS

II.5 Conclusions

The experiments testify to the ability of our Acoustic Doppler Velocity Profiler (ADVP) to measure accurately the mean flow field, including both cells of secondary circulation, and the turbulence in complex three-dimensional flows, such as occurring in open-channel bends.

The **small-flume experiments** yielded some interesting observations on the mean-flow field and the turbulence that will be further investigated in parts III and IV:

- The downstream velocity increases from the centerline towards the outer bank, and the core of maximum velocity is found at the separation of both cells of secondary circulation. Furthermore, the downstream velocity profiles are not monotonically increasing towards the water surface, as in a straight uniform open-channel flow, but have maximum values in the lower part of the water column.
- Besides the classical center-region cell (helical motion), a weaker counter-rotating outer-bank cell of secondary circulation exists in the corner formed by the outer bank and the water surface. Although relatively small and weak, this outer-bank cell is important since it has a protective effect on the stability of the outer bank by keeping the core of maximum velocity at distance.
- The Reynolds stresses have pronounced spatial distributions that considerably differ from their counterparts in straight uniform open-channel flow. Most interestingly, the turbulence activity, represented by the ratio of turbulent to mean-flow kinetic energy, is reduced in the outer half of the cross-section in the investigated bend.

The **large-flume experiments** confirmed the existence of a multi-cellular pattern of secondary circulation. The center-region cell strengthens only slightly with increasing curvature, whereas both the size and the strength of the outer-bank cell are considerably enhanced.

Furthermore, the small and large-flume experiments show that linear models, which are commonly used to account for the effect of the secondary circulation in depth-integrated flow models, do not comply with the observed behavior: they are over-estimative and do neither reproduce the observed weakening of the secondary circulation with increasing curvature, nor its observed downstream evolution. The reasons responsible for their failure are investigated in part III and a non-linear model that reproduces the observations of the small and large-flume experiments is proposed in chapter IV.1.

PART III

FUNDAMENTAL RESEARCH

III.0	Introduction	
III.1	Momentum Transport in Sharp Open-Channel Bends	III.1
III.2	Secondary Flow in Sharp Open-Channel Bends	III.27
III.3	Turbulence Characteristics in Sharp Open-Channel Bends	III.61
III.4	Turbulence Structure in Sharp Open-Channel Bends	III.91
III.5	Conclusions	III.113

III.0 Introduction

The physical mechanisms and processes underlying the experimental observations reported in part II are investigated, mainly by making term-by-term evaluations of the relevant flow equations based on the experimental data. Since the ADV-measurements give the distributions of all three mean velocity components and all six Reynolds stresses on a fine grid, most of the terms in the flow equations can be evaluated. To eliminate scatter, the raw data are first smoothed following the procedure outlined and illustrated in chapter II.1. These term-by-term evaluations of the flow equations indicate what terms and corresponding physical mechanisms play an important role. They are applied in:

- **chapter III.1** on the downstream momentum equation in order to explain the downstream velocity distribution reported in chapter II.1. A similar analysis limited to the depth-integrated downstream momentum equation has been presented in a paper that is not included in this dissertation:

Blanckaert K. and Graf, W. H. (1999b). "Outer-bank cell of secondary circulation and boundary shear stress in open-channel bends." *Proc. symp. River, Coastal and Estuarine Morphodynamics*, Univ. Genova, Genova, Italy, Vol. I, 533-543.

- **chapter III.2** on the downstream vorticity equation in order to explain the bi-cellular pattern of secondary circulation reported in chapter II.1.
- **chapter III.3** on the turbulent kinetic energy equation in order to explain the lower than expected turbulence activity in the outer bend reported in chapter II.1.

Chapter III.4 further analyses the turbulence structure observed in the small-flume experiments, by investigating the instantaneous flow behavior, in order to explain an observed coherence in the bulk-behavior of the pattern of circulation cells.

Part III ends with a summary of the main **conclusions**.

Note that this part on fundamental research makes uniquely use of the small-flume experiments. Based on these results, the large-flume experiments have been designed, and their analysis will be reported in the future.

III.1 Momentum Transport in Sharp Open-Channel Bends

By Koen Blanckaert¹ and Walter H. Graf², life member, ASCE

(tentatively approved for publication in Journal of Hydraulic Engineering, ASCE)



Abstract

Flow in open-channel bends is characterized by cross-stream circulation, which redistributes the velocity and the boundary shear stress and thereby shapes the characteristic bottom topography. Besides a center-region cell - the classical helical motion – a weaker counter-rotating outer-bank cell often exists. In spite of its engineering importance, the mechanisms underlying the distributions of the velocity and the boundary shear stress in open-channel bends, and especially the role of both circulation cells, are not yet fully understood.

In order to investigate these mechanisms, an evaluation is made of the various terms in the momentum equations based on the measured data, which gave the following results. The outer-bank cell forms a buffer layer that protects the outer bank from influences of the center-region cell and keeps the core of maximum velocity at distance from the bank. Advective momentum transport by the center-region cell is a dominant mechanism; it significantly contributes to the observed outward shift of the downstream velocity and the bottom shear stress and to the flattening of the vertical profiles of the velocity.

This important advective momentum redistribution has to be included in the depth-integrated flow models often used in engineering practice. Commonly used linear models overpredict the effects of the center-region cell. Based on the results of the analysis of experimental data, these models are extended by accounting for the feedback between the center-region cell and the downstream velocity. The thus obtained non-linear model clearly reveals the mechanisms of the center-region cell and its advective momentum transport. An analysis of non-linear model results confirms and complements the analysis of experimental data. A true quasi-three-dimensional flow model is obtained by coupling this non-linear model to depth-integrated flow models, thus providing an engineering tool for morphodynamical investigations.

Keywords

Open-channel flow, channel bend, advection, secondary circulation, laboratory experiments, velocity distribution, turbulence, quasi-three-dimensional model

¹ Res. Assoc., Lab. d'Hydraulique Environnementale, Ecole Polytechnique Fédérale, CH-1015 Lausanne, Switzerland.

² Prof., Lab. d'Hydraulique Environnementale, Ecole Polytechnique Fédérale, CH-1015 Lausanne, Switzerland.

1 Introduction

The velocity distribution in open-channel bends is characterized by the existence of a cross-stream circulation (also called helical flow or secondary flow; Boussinesq, 1868; Thomson, 1876), which redistributes the velocity, influences the sediment transport and shapes the characteristic bar-pool bottom topography around the bend. Accurate predictions of the velocity distribution and the bottom topography are essential to problems related to river restoration, navigability, water quality and structures such as bridge piers and abutments. In spite of its practical importance, the mechanisms underlying the distributions of the velocity and the boundary shear stress in open-channel bends are not yet fully understood. This paper reports on an investigation of these mechanisms, but especially on the role of the cross-stream circulation, by means of a combined experimental and mathematical analysis.

Insight into this role – and into the flow dynamics in general – is hampered by the scarcity of experimental data, due to the difficulty of measuring the weak cross-stream velocities and the various Reynolds stress components (see Table 1 in Blanckaert and Graf, 2001a). The presented experimental analysis is based on a detailed dataset (Blanckaert and Graf, 2001a) that includes distributions of all mean velocity components and all Reynolds stresses on a fine grid in the outer half of one cross-section of a strongly curved laboratory flume. From these data, the terms in the downstream momentum equation, as well as in its depth-integrated form, are evaluated, which gives indications on the relative importance of the different mechanisms underlying the observed distribution of the velocity and the boundary shear stress. This experimental analysis will confirm and help to clarify the dominant role played by the cross-stream circulation cells. In addition, this experimental evaluation of terms in the momentum equations can also be used to validate numerical models.

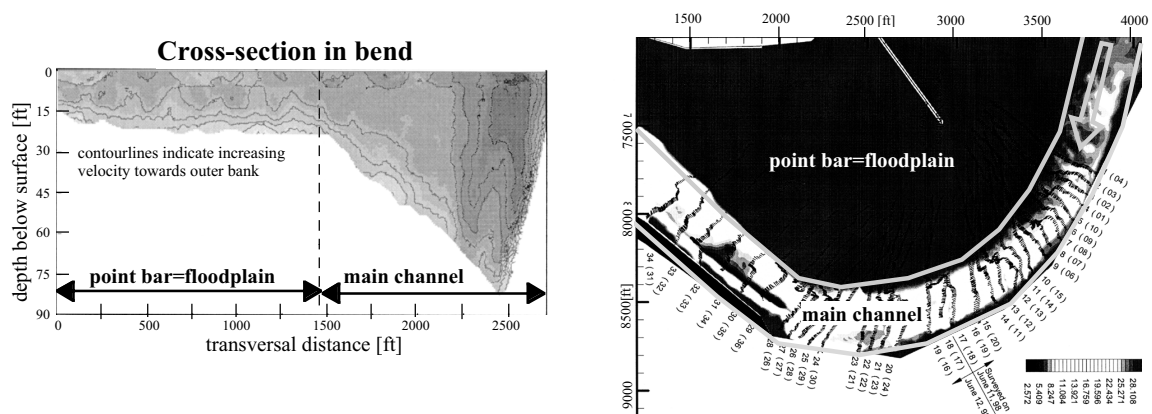


Figure 1: Victoria bend.

A practical relevance of our research is illustrated with the case of the Victoria bend in the lower Mississippi River between Arkansas and Mississippi (Fig. 1). This is a rather sharp bend where barges often experience navigational problems. It has an opening angle of about 108° , a radius of curvature of about $R=1280\text{m}$ and a ratio of radius of curvature to channel width that varies between $1 < R/B < 3$, depending on the flow stage. This bend has been under investigation to improve the navigability by modifying the flow field and the channel bed topography. Jia and Wang (2000) have carried out a three-dimensional

numerical simulation of the flow field in this bend, assuming a fixed channel bed. The solution of the problem, however, would require a three-dimensional simulation with a movable bed. In a large area like the Victoria bend, such simulations are not yet practically feasible, due to limitations in computer power. Simulations of a movable bed are therefore still based on the depth-integrated flow equations. However, when integrating the flow equations over the depth all information on the cross-stream circulation is lost. To remedy this shortcoming, the depth-integrated flow equations have to be extended with a (semi-)analytical model for the cross-stream circulation.

The commonly used models (Rozovskii, 1957; Engelund, 1974; de Vriend, 1977, etc) – termed linear models - are known to be insufficient and to overestimate the role of the cross-stream circulation (de Vriend, 1981a; Yeh & Kennedy, 1993; Blanckaert, 2001a; Blanckaert & Graf, 2001b). Moreover, they do not clearly reveal the mechanisms underlying the cross-stream circulation, mainly because they neglect its feedback with the downstream velocity. Based on the results of the here-presented experimental analysis, we have extended the linear models by including this feedback. The obtained non-linear model agrees well with experimental data (Blanckaert, 2001b & 2002b; Blanckaert & Graf, 2001c), even for strongly curved flow. A mathematical analysis of this non-linear model is performed in order to confirm and complement the results of the foregoing analysis of experimental data.

The first part of our paper concerns the analysis based on the experimental data. The relevant experimental data are presented, the underlying theory is developed and the downstream momentum equation and its depth-integrated form are analyzed using the data. The second part focuses on the modeling of the cross-stream circulation in the depth-integrated flow equations. The insufficiency of the linear models is illustrated, the outline and solution of the non-linear model are briefly presented, and a mathematical analysis is performed. Finally, the engineering potential of the non-linear model for the numerical investigation of morphodynamical river problems is discussed.

2 Analysis of Experimental Data

2.1 The Experiment

The experimental set-up, the ADV velocity meter, the data processing, the measuring grid, the experimental accuracy and the observed distributions of the mean velocities and the turbulent stresses have been presented in detail by Blanckaert (2002b) and Blanckaert and Graf (2001a). Only features of particular importance for the presented analysis are reported hereafter.

Flow measurements were performed in a curved laboratory flume with a mobile-bed topography (Fig. 2). The laboratory flume consisted of a 2 m long straight approach reach, followed by a 120° bend with a constant radius of curvature of $R=2$ m. The flow conditions are tabulated in Fig. 2. The parameters $R/B=5$, $R/H=17.9$ and $B/H=3.6$

III.4

correspond to a rather sharp bend being much narrower than typical natural open-channel bends. These ratios do occur in man-made channels and mountain rivers. Moreover, in wide bends with a developed bed topography, the shallow point bar is usually wide and the flow is concentrated most of the time in the deep part near the outer bank, where an important transverse bottom slope exists (Fig. 1; also see Odgaard, 1984, and Dietrich, 1987). It is therefore expected that the flow in the deep outer half of the cross-section of the flume is representative of the flow in the deepest part of wider natural bends.

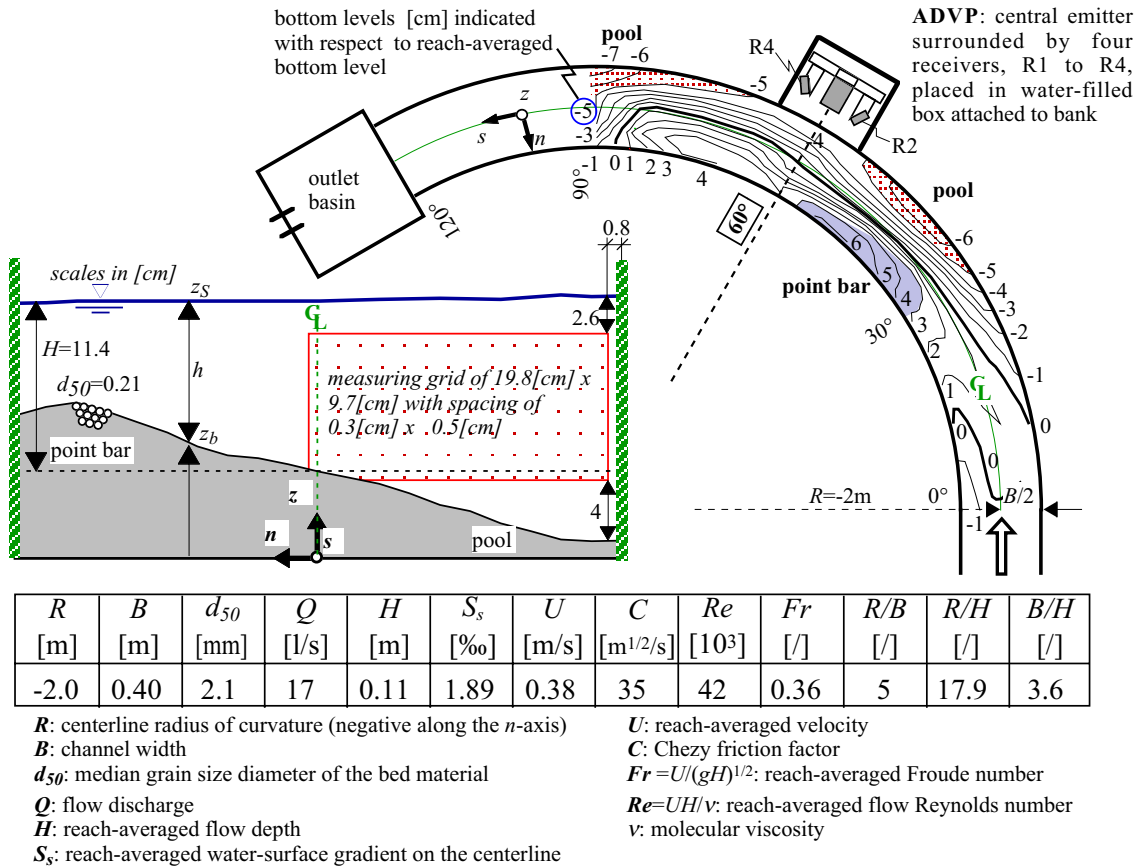


Fig. 2: Experimental set-up, bottom topography, reference system, measurement section at 60° and hydraulic conditions.

Velocity measurements were made with an Acoustic Doppler Velocity Profiler (ADVP) on a fine grid in one cross-section at 60° from the bend entrance (Fig. 2). Even though only the outer-half of the cross-section was measured, about 80% of the total discharge was captured. The data are represented and analyzed in a cylindrical co-ordinate system with the s -axis along the channel centerline, the n -axis perpendicular to it and pointing towards the center of curvature, and the z -axis pointing vertically upwards from the horizontal (s, n)-plane. The ADVP measures profiles of the three quasi-instantaneous velocity components $v_j(t)$, simultaneously along the acoustic beam. Thus the mean velocity vector $\bar{\mathbf{v}} = (v_s, v_n, v_z)$, as well as the fluctuating velocity vector $\bar{\mathbf{v}}' = (v'_s, v'_n, v'_z)$ and all Reynolds stresses $\overline{v'_i v'_j}$ ($i, j = s, n, z$), can be evaluated.

The vectorial representation of the cross-stream motion (v_n, v_z) , normalized by the overall mean velocity $U = Q/(BH)$, is shown in Fig. 3b. Besides the classical helical motion – called here *center-region cell* – a weaker counter-rotating cell of cross-stream circulation – called *outer-bank cell* – exists in the corner formed by the water surface and the outer bank. This outer-bank cell is occasionally reported in the literature (see Mockmore, 1943; Shukry, 1949; Einstein and Harder, 1954; etc.), but is as yet not fully understood, nor precisely measured. The part of the cross-section covered by the center-region cell and the outer-bank cell will be denoted by *center region* and *outer-bank region*, respectively.

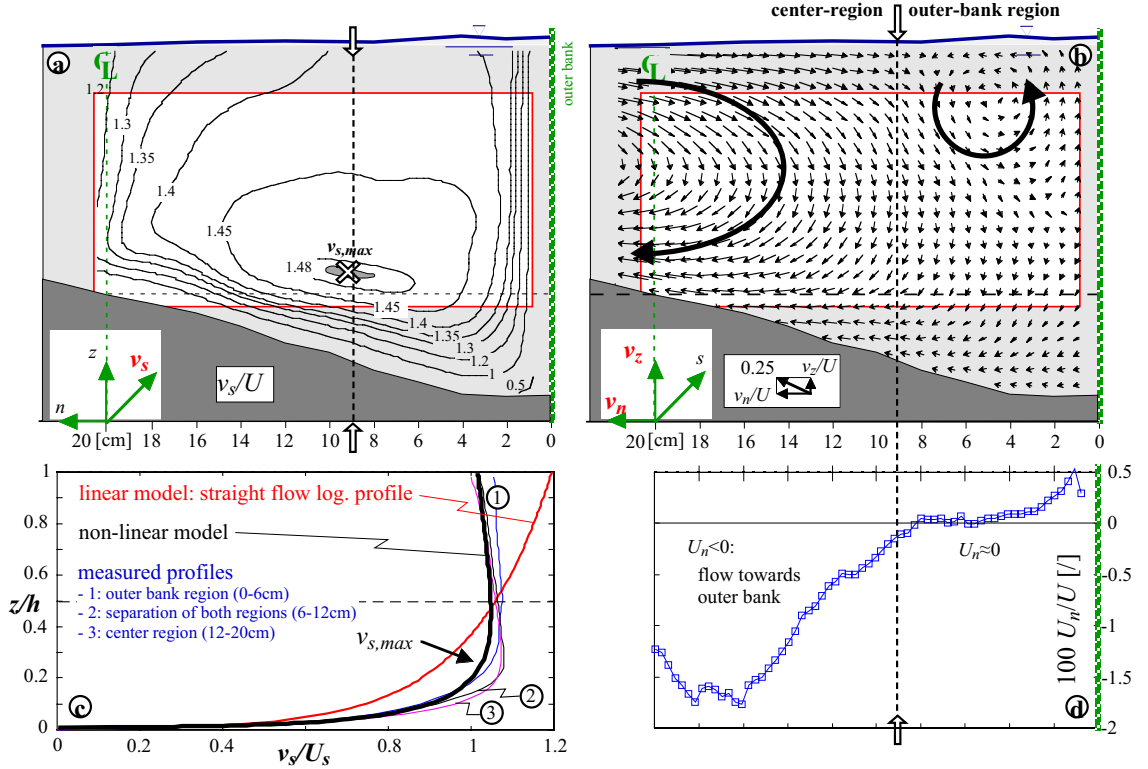


Fig. 3: (a) Isolines of downstream velocity, v_s/U ; (b) Vector representation of cross-stream motion, $(v_n, v_z)/U$; (c) Vertical profiles of measured and simulated downstream velocity, v_s/U_s ; (d) Depth-averaged transversal velocity, U_n/U .

The velocity components v_j ($j=s, n$) can be decomposed into a depth-averaged value $\langle v_j \rangle = U_j$ and local deviations from it, v_j^* :

$$v_j = \langle v_j \rangle + v_j^* = U_j + v_j^* \quad \text{in which } \langle v_j^* \rangle = 0 \text{ by definition} \quad (1)$$

v_n^* therefore refers to the transversal component of the cross-stream circulation. The depth-averaged transversal velocity $U_n = \langle v_n \rangle$ (Fig. 3d) – sometimes called cross-flow – is directed towards the outer bank in the center region and reaches maximum values of about 2% of U . It decreases in the outward direction and is negligible in the outer-bank region. U_n is mainly induced by downstream variations in the bottom topography and its direction corresponds with the deepening of the bed downstream of the measuring section (Fig. 2). Odgaard and Bergs (1988) have shown that over a typical bar-pool topography U_n alternates between positive and negative values along the bend. Contrary to the transversal component of the cross-stream circulation, v_n^* , U_n vanishes in fully-developed curved flow, which is defined by $\partial/\partial s=0$.

III.6

The distribution of the normalized downstream velocity component, v_s/U , in the half-section investigated is presented in Figs. 3a,c. Fig. 3c compares some of the observed vertical profiles with a logarithmic profile for the experimental Chezy friction factor of $C=35 \text{ m}^{1/2}/\text{s}$. The shown profiles are averages of the profiles measured in the outer-bank region (0-6 cm from outer bank), in the transition zone between both regions (6-12cm) and in the center region (12-20cm). The profiles observed in these three regions are rather similar, but differ significantly from the logarithmic profile. In the upper part of the water column the velocity is up to 20% smaller, in the lower part it is up to 20% larger, even to the extent that the maximum velocities are located in the lower part of the water column. The downstream velocity increases in outward direction: it is larger than the overall mean velocity in the outer-half of the cross-section and has to be smaller in the inner half due to mass conservation. The core of maximum velocity (⊗ in Fig. 3a) is found close to the bottom and near the separation of the two circulation cells. This observation already indicates the importance of the circulation cells with respect to the v_s -distribution.

A further indication of this importance follows from the case of *laminar* bend flow, which has been investigated numerically by Cheng et al. (1976), de Vriend (1981b) and Winters (1987) and experimentally by Hille et al. (1985). They reported that in the case of weak curvature only the center-region cell exists. With increasing curvature, the center-region cell gets stronger and the core of maximum downstream velocity shifts to the outward direction, to be ultimately found close to the outer bank. Further increasing the curvature, an outer-bank cell suddenly comes into existence and the core of maximum downstream velocity is found further from the outer bank at the separation between the two circulation cells. This behavior, which is in agreement with our experimental observations (Figs. 3a,c), suggests the outer-bank cell to have a positive effect on the stability of the outer bank. Although the flow mechanisms in laminar flow differ from those in turbulent flow, the observations also suggest that the downstream velocity distribution be strongly influenced by the cross-stream circulation cells.

In the following sections, we will analyze the turbulent flow data, in order to understand the mechanisms that underlie the observed distribution of the downstream velocity v_s and the downstream bottom shear stress, τ_{bs} , with special attention to the role of the cross-stream circulation cells.

2.2 Theoretical Considerations

The momentum equations in cylindrical co-ordinates are given by Batchelor (1970, p.598). Its downstream component, which governs the distribution of the downstream velocity, v_s , reads:

$$\begin{aligned} \frac{\partial v_s}{\partial t} = & - \left[\frac{1}{1+n/R} v_s \frac{\partial v_s}{\partial s} + v_n \frac{\partial v_s}{\partial n} + v_z \frac{\partial v_s}{\partial z} + \frac{1}{1+n/R} \frac{v_s v_n}{R} \right] \\ & - \frac{1}{1+n/R} g \frac{\partial z_s}{\partial s} - \left(\frac{1}{1+n/R} \frac{\partial \overline{v_s'^2}}{\partial s} + \frac{\partial \overline{v_s' v_n'}}{\partial n} + \frac{\partial \overline{v_s' v_z'}}{\partial z} + \frac{2}{1+n/R} \frac{\overline{v_s' v_n'}}{R} \right) \end{aligned} \quad (2)$$

Using the mass-conservation equation, the first term in the right-hand part of Eq. (2) can be transformed to:

$$\left[\frac{1}{1+n/R} \frac{\partial v_s^2}{\partial s} + \frac{\partial v_s v_n}{\partial n} + \frac{\partial v_s v_z}{\partial z} + \frac{2}{1+n/R} \frac{v_s v_n}{R} \right] = \text{div}(v_s \vec{v}) + \frac{1}{1+n/R} \frac{v_s v_n}{R} \quad (3)$$

Integration of Eqs. (2) and (3) over the flow depth yields the depth-integrated downstream momentum equation. It governs the distribution of the downstream component of the bottom shear stress vector τ_{bs} and is given as (see Dietrich and Whiting, 1989):

$$\begin{aligned} \frac{\tau_{bs}}{\rho} = & -\frac{1}{1+n/R} gh \frac{\partial z_s}{\partial s} - \left[\frac{1}{1+n/R} \frac{\partial}{\partial s} (\langle v_s^2 \rangle h) + \frac{\partial}{\partial n} (\langle v_s v_n \rangle h) + \frac{2}{1+n/R} \frac{\langle v_s v_n \rangle h}{R} \right] \\ & - \frac{1}{1+n/R} \frac{\partial}{\partial s} (\langle \overline{v_s'^2} \rangle h) - \frac{\partial}{\partial n} (\langle \overline{v_s' v_n'} \rangle h) - \frac{2}{1+n/R} \frac{\langle \overline{v_s' v_n'} \rangle h}{R} \end{aligned} \quad (4)$$

The bottom shear-stress term in the left-hand-side of Eq. (4) results mainly from the depth-integration of the term $\partial \overline{v_s' v_z'} / \partial z$ in Eq. (2). Since no pressure measurements were made, a hydrostatic pressure distribution is assumed in the above equations, $p = \rho g(z_s - z)$; $h = z_s - z_b$ is the local flow depth, where z_s and z_b are the water surface and bottom elevation above the horizontal (s, n) -plane. $(1+n/R)$ is a metric factor accounting for the divergence of the n -coordinate lines; the brackets $\langle \rangle$ indicate depth-averaged values. Being irrelevant in turbulent flow, molecular diffusion terms have been omitted. Our experiment concerns steady flow ($\partial v_s / \partial t = 0$), but the unsteady term is retained in Eq. (2) to facilitate interpretation: positive/negative terms in the right-hand-side tend to increase/decrease the local downstream velocity, v_s .

Open-channel flow is driven by gravity, via the terms containing $g \partial z_s / \partial s$ in Eqs. (2) and (4), and resisted by friction at the flow boundaries, generating momentum fluxes by the Reynolds stresses, $\overline{v_s'^2}$, $\overline{v_s' v_n'}$ and $\overline{v_s' v_z'}$. Advective transport of flow momentum is represented by the terms in square brackets in the momentum equations, Eqs. (2) and (3), and in its depth-integrated form, Eq. (4). It does not generate or dissipate flow momentum, but just redistributes it over the cross-section. This distributive property is characteristic of divergence-type terms (cf. Eq. (3)), as can be demonstrated applying the divergence theorem. This already indicates that the advective momentum transport may play an important role in the distributions of v_s and τ_{bs} .

Besides the $\partial / \partial s$ -term related to the downstream non-uniformity of the flow field, the advective momentum transport according to Eqs. (2) and (4) is associated with the cross-stream motion (v_n, v_z) . A distinction can be made between the translatory and the circulatory parts of this motion, sometimes also called ‘cross-flow’ and ‘identifiable downstream vortices’ (Bradshaw, 1987). The decomposition of the transversal velocity in Eq. (1) roughly corresponds to this distinction, $U_n = \langle v_n \rangle$ being the cross-flow and v_n^* being the transversal component of the cross-stream circulation. Applying this velocity decomposition to the advective momentum transport terms in the momentum equations, Eqs. (2) and (4), (terms in square brackets only) gives:

$$\left[\left(\frac{1}{1+n/R} v_s \frac{\partial v_s}{\partial s} + U_n \frac{\partial v_s}{\partial n} + \frac{1}{1+n/R} \frac{v_s U_n}{R} \right) + \left(v_n^* \frac{\partial v_s}{\partial n} + \frac{1}{1+n/R} \frac{v_s v_n^*}{R} + v_z \frac{\partial v_s}{\partial z} \right) \right] \quad (5)$$

and

$$\left[\left(\frac{1}{1+n/R} \frac{\partial}{\partial s} (\langle v_s^2 \rangle h) + \frac{\partial}{\partial n} (U_s U_n h) + \frac{2}{1+n/R} \frac{U_s U_n h}{R} \right) + \left(\frac{\partial}{\partial n} (\langle v_s^* v_n^* \rangle h) + \frac{2}{1+n/R} \frac{\langle v_s^* v_n^* \rangle h}{R} \right) \right] \quad (6)$$

When a straight channel is followed by a bend, the flow field and the bottom topography gradually adapt to the imposed curvature. The cross-stream circulation (v_n^*, v_z) comes into existence and a bar-pool bottom topography develops around the bend (Fig. 2). This varying bottom topography gives rise to a cross-flow, U_n (Fig. 3d). Both this topography-induced cross-flow and the cross-stream circulation advect momentum and lead to a redistribution of the velocity and the boundary shear stress over the cross-section. The former is represented by the first group of terms in brackets in Eqs. (5) and (6), whereas the latter is represented by the second group in either equation. Flow in this adaptation zone is called *developing* curved flow. Obviously, the flow in our experiment belongs to this category: the bottom topography varies in downstream direction (Fig. 2) and a non-zero cross-flow exists (Fig. 3d). Ultimately, the flow field and the transversal bottom slope become completely adapted to the curvature and no longer vary in the downstream direction. Hence $\partial/\partial s=0$ (except for the driving gravity term) and, by implication, $U_n=0$. In this so-called *fully-developed* curved flow (also called uniform or axisymmetric curved flow), the first group of terms in brackets in Eqs. (5) and (6) vanishes and the distribution of the velocity and the boundary shear stress over the cross-section is uniquely due to advective momentum transport by the cross-stream circulation (v_n^*, v_z). According to Dietrich and Whiting (1989), the $\partial/\partial s$ -term and the U_n -terms in the first group of the depth-integrated equation (6) also tend to balance each other in developing curved flow. In our further considerations, attention will be focused on the second group of terms in either of the above equations, representing advective momentum transport by the cross-stream circulation.

The aim of our experimental research is to understand the mechanisms underlying the redistribution of the velocity and the boundary shear stress in a bend and especially the influence of the advective momentum transport by the cross-stream circulation. To that end, the different terms in the downstream momentum equation and its depth-integrated form are evaluated on the basis of the measured data. Only the terms related to downstream variations in the flow field – terms containing $\partial/\partial s$, except for the gravity term - could not be evaluated from our measurements in a single section. To evaluate the terms in the depth-integrated equations (4) and (6), the measured data were extrapolated outside the measuring grid towards the water surface and the bottom (Figs. 2 and 3). The measured distributions of the mean velocities and the turbulent stresses, their accuracy and their extrapolation are reported by Blanckaert and Graf (2001a). Due to the products and derivatives in the terms, experimental errors tend to be accumulated and amplified, hence these evaluations are bound to be rather inaccurate. Interpretations should therefore be limited to order-of-magnitude considerations. Yet, this is sufficient to identify the relevant mechanisms and to investigate the role of the advective momentum transport by the cross-stream circulation.

Distributions of the most important terms in the downstream momentum equation, Eq. (2) and (5), as well as in its depth-integrated form, Eqs. (4) and (6), are shown in Figs. 4 and 5, respectively. All terms are normalized by – and thus compared with – the value in the centerline ($n=0$) of the driving gravity term:

$$-g \frac{\partial z_{s,60}}{\partial s} = \frac{u_{*,60}^2}{R_h} = 0.028 \text{ m/s}^2 \quad \text{in the downstream momentum equation (7a)}$$

$$-g R_h \frac{\partial z_{s,60}}{\partial s} = u_{*,60}^2 = 0.002 \text{ m}^2/\text{s}^2 \quad \text{in the depth-integrated equation (7b)}$$

in which R_h is the hydraulic radius of the cross-section. In either of these equations, the characteristic shear velocity in the measuring section, $u_{*,60}$, is defined as $u_{*,60} = \sqrt{g R_h (-\partial z_{s,60}/\partial s)}$. As $-\partial z_{s,60}/\partial s = 0.0029$ and $R_h = 0.07$ m, the shear velocity amounts $u_{*,60} = 0.045$ m/s.

2.3 Downstream Momentum Equation

In summary, the most important terms in the following form of the downstream momentum equation will now be analyzed one by one (see Fig. 4):

$$\begin{aligned}
 \underbrace{0 = \frac{\partial v_s}{\partial t}}_{\text{steady flow}} = & \underbrace{\left[\frac{1}{1+n/R} v_s \frac{\partial v_s}{\partial s} + U_n \frac{\partial v_s}{\partial n} + \frac{1}{1+n/R} \frac{v_s U_n}{R} \right]}_{\substack{\text{non-uniformity} \\ \text{(not measured)}}} + \underbrace{\left[v_n^* \frac{\partial v_s}{\partial n} + \frac{1}{1+n/R} \frac{v_s v_n^*}{R} + v_z \frac{\partial v_s}{\partial z} \right]}_{\substack{\text{advective momentum transport} \\ \text{by cross-stream circulation} \\ \text{(see Fig.4c)} + \text{(see Fig.4d)}}} \\
 & - \underbrace{\frac{1}{1+n/R} g \frac{\partial z_s}{\partial s}}_{\substack{\text{gravity} \\ \text{(not shown)}}} - \underbrace{\left[\frac{1}{1+n/R} \frac{\partial \overline{v_s'^2}}{\partial s} + \frac{\partial \overline{v_s' v_z'}}{\partial z} + \frac{\partial \overline{v_s' v_n'}}{\partial n} + \frac{2}{1+n/R} \frac{\overline{v_s' v_n'}}{R} \right]}_{\substack{\text{non-uniformity} \\ \text{(not measured)} \text{ (see Fig.4a)+} \\ \text{turbulent momentum transport} \\ \text{(see Fig.4b)}}} \quad (8)
 \end{aligned}$$

The normalized gravity term, $-[(1+n/R)^{-1} g \partial z_s / \partial s] / (u_{*,60}^2 / R_h)$, is constant over the depth and is by definition $O(1)$. It varies like the metric factor $-(1+n/R)^{-1}$ over the width, decreasing nearly linearly from a value of 1.1 at the inner bank ($n/R=-0.1$) to a value of 0.9 at the outer bank ($n/R=0.1$).

In two-dimensional straight uniform flow, Eq. (8) reduces to the balance between the driving gravity term $-(1+n/R)^{-1} g \partial z_s / \partial s$ and the resisting Reynolds stress term $-(\partial \overline{v_s' v_z'} / \partial z)$, both of which are constant throughout the water column and have a constant ratio of -1. The Reynolds stress term can be expressed by introducing the eddy viscosity concept, $-\overline{v_s' v_z'} = \nu_t \partial v_s / \partial z$. The resulting equation can be solved for v_s , to yield vertical profiles that are completely determined by the prescribed eddy viscosity (a parabolic eddy viscosity, for instance, yields logarithmic v_s -profiles). Far from the sidewalls, the horizontal distribution of v_s (and U_s) is identical to that of the gravity term.

In our experiment on curved flow, the vertical v_s -profiles have an a-typical shape, with the maximum velocity occurring in the lower part of the water column (Fig. 3c). Furthermore, the transversal distribution of v_s (and of U_s) differs from that of the gravity

term (cf. Fig. 3a). This measured v_s -distribution will be explained by evaluating the different terms in the downstream momentum equation, Eq. (8). Besides the gravity term, all other terms have pronounced distributions and show a different behavior in the center region and in the outer-bank region. These two regions will therefore be analyzed separately.

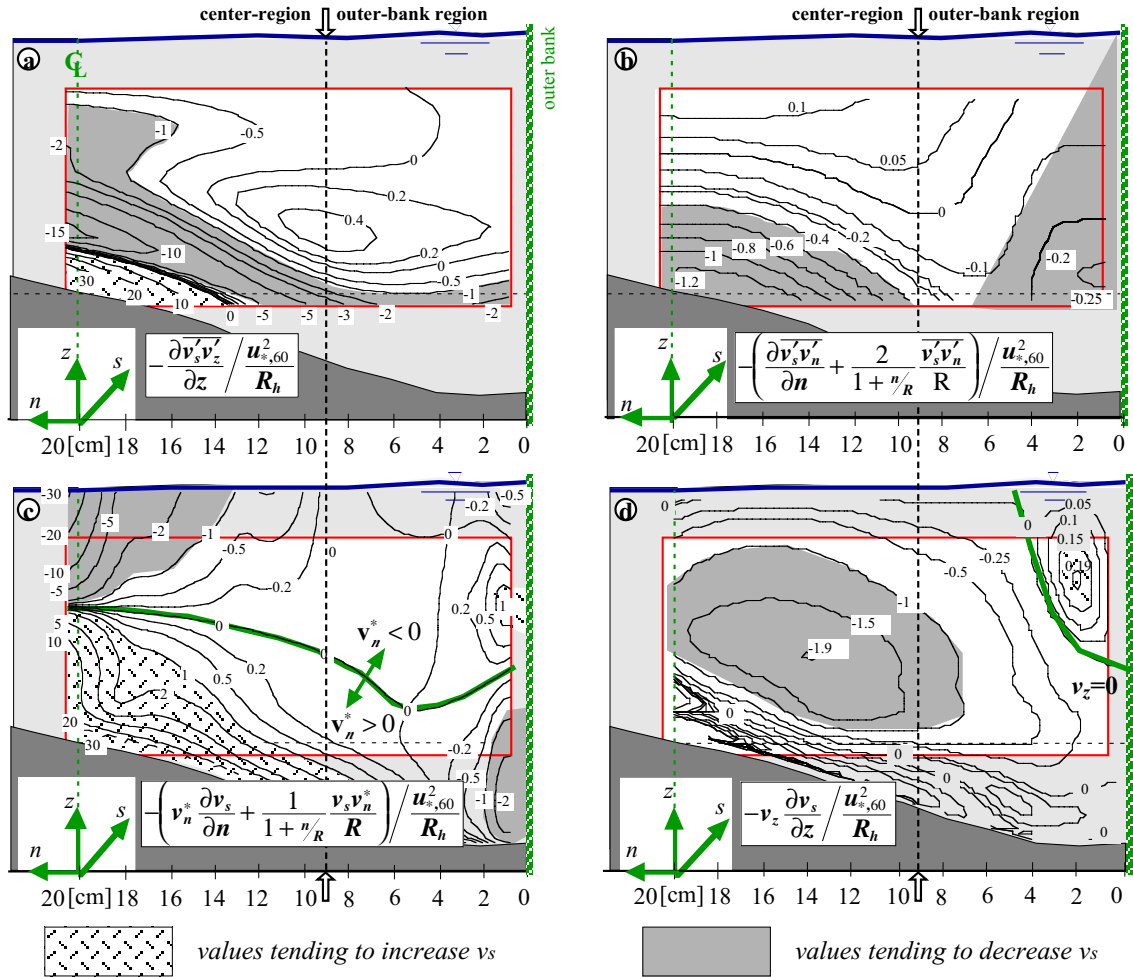


Fig.4: Distribution of normalized terms in downstream momentum equation, Eq. (8).

2.3.1 Center Region

As mentioned above, Eq. (8) reduces in straight uniform flow ($v_n=v_z=0$) to the balance between the gravity term and the remaining Reynolds stress term, whose ratio is exactly equal to -1 . Averaged over the flow depth, the ratio of the two terms is still $O(-1)$ in our experiment on curved flow, since it can be estimated as:

$$-\frac{R_h}{u_{*,60}^2} \frac{1}{h} \int_{z_b}^z \frac{\partial \overline{v'_s v'_z}}{\partial z} dz = \frac{R_h}{u_{*,60}^2} \frac{\overline{v'_s v'_z}(z_b)}{h} \sim -\frac{\tau_{b,s}}{\rho u_{*,60}^2} \frac{R_h}{h} \sim -\frac{g(U_s/C)^2}{u_{*,60}^2} \frac{R_h}{h} \sim -\frac{g(1.35U/C)^2}{u_{*,60}^2} \frac{R_h}{h} = O(-1)$$

in which use is made of the experimental result $U_s \sim 1.35U$ (Blanckaert and Graf, 2001a). However, the normalized Reynolds stress term $-(\partial \overline{v'_s v'_z} / \partial z) / (u_{*,60}^2 / R_h)$, shown in Fig. 4a,

now has a pronounced vertical distribution. In the center region, it shows negative values $O(-1)$ near the surface, then strongly decreases to values $O(-10)$ in the lower part of the water column and subsequently increases strongly up to values $O(20)$ close to the bottom. The observed behavior should be interpreted with caution, however, since the turbulence data are less reliable in the lower 20% of the water column (Blanckaert and Graf, 2001a).

Obviously, the advective momentum transport by the cross-stream circulation, $\left[v_n^* (\partial v_s / \partial n) + (1 + n/R)^{-1} (v_s v_n^* / R) + v_z (\partial v_s / \partial z) \right] / (u_{*,60}^2 / R_h)$, vanishes in straight uniform flow, since $v_n^* = v_z = 0$. Yet, it is the dominant mechanism in the center region of the curved flow and reaches values that are an order of magnitude larger than the driving gravity term. The terms related to the transversal component v_n^* (Fig. 4c) increase from high negative values near the water surface to high positive values near the bottom, reaching normalized magnitudes up to 30 times the driving gravity term. Note that these high values are driven by the steep spanwise velocity gradient $\partial v_s / \partial n$ in the narrow flume, and may be larger than typical values in wide bends. The combination of terms is maximum near the centerline and decreases towards the edge of the center-region cell. As compared to straight flow, it tends to flatten the v_s -profile by decreasing the velocity in the upper part of the water column and increasing it in the lower part, in line with our observations. Averaged over the flow depth, however, the group of terms is of the same order of magnitude as the gravity term, i.e. $O(1)$, and causes an overall increase of the velocities in the outer half-section. The term related to the vertical component v_z (Fig. 4d) is generally smaller than that related to v_n^* . However, at about mid-depth towards the edge of the center-region cell, it attains maximum normalized values $O(-2)$, whence it is the dominant term in the momentum equation in that part of the cross-section.

The Reynolds stress terms generated by friction on the inclined bottom, $\left[\partial \overline{v_s' v_n'} / \partial n + 2(1 + n/R)^{-1} (\overline{v_s' v_n'} / R) \right] / (u_{*,60}^2 / R_h)$ (see Fig. 4b), as well as momentum advection by the cross-flow, $\left[U_n (\partial v_s / \partial n) + (1 + n/R)^{-1} (v_s U_n / R) \right] / (u_{*,60}^2 / R_h)$ (not shown), play a minor role.

In steady flow, all terms in the right-hand-side of Eq. (8) should add up to zero. Even when taking the experimental inaccuracy into account, the sum of the investigated terms significantly deviates from zero: it is negative in the upper part of the cross-section and positive in the lower part. This non-zero sum is probably compensated by the non-uniformity term $-(1+n/R)^{-1} v_s \partial v_s / \partial s$, which was not measured. If this is the case, there should be an ongoing flattening of the v_s -profiles in downstream direction, which is characteristic of accelerating flow (Graf and Altinakar, 1998, p.49). This is in agreement with the further deepening of the outer half-section downstream of the measuring section (Fig. 2) and with the observed outward cross-flow $U_n < 0$ (Fig. 3d).

In summary, in the center region the advective momentum transport by the secondary circulation, and especially by its transversal component, is the dominant mechanism underlying the v_s -distribution. It tends to flatten the v_s -profiles and causes an outward increase of v_s .

2.3.2 Outer-Bank Region

The outer-bank region is hydrodynamically less active than the center region, since all the terms in the momentum equation are smaller and show less variation (Fig. 4a-d).

The gravity term in the outer-bank region is almost balanced by the friction at the bottom and the outer bank. This friction gives rise to the $\overline{v'_s v'_z}$ - and the $\overline{v'_s v'_n}$ -Reynolds stress components, respectively. In the part of the outer-bank region covered by the measuring grid, the Reynolds stress $\overline{v'_s v'_z}$ is positive, but remains negligibly small (Fig. 6 in Blanckaert and Graf, 2001a). Correspondingly, the $\overline{v'_s v'_z}$ -turbulent transport term (Fig. 4a) is small: $0 < -(\partial \overline{v'_s v'_z} / \partial z) / (u_{*,60}^2 / R_h) < 1$. Towards the bottom, the Reynolds stress has to increase to the bottom value of $O(-1)$, which induces the negative values of $-(\partial \overline{v'_s v'_z} / \partial z) / (u_{*,60}^2 / R_h) < -1$ near the lower bound of the measuring grid.

In a triangular region affected by friction at the outer bank, the $\overline{v'_s v'_n}$ -turbulent transport terms (Fig. 4b) reach normalized values $O(-0.25)$. This indicates that the outer bank friction is smaller than the bottom friction, i.e. its absolute value is smaller than $O(1)$, although strong gradients may exist near the bottom outside the measuring grid. These smaller values of the turbulent transport terms related to $-\overline{v'_s v'_n}$ and $-\overline{v'_s v'_z}$ are in agreement with the reduced turbulence activity observed in the outer-bank region (Fig. 7c in Blanckaert and Graf, 2001a).

The advective momentum transport by the cross-stream circulation $-(v_n^*, v_z)$ -terms - is of the same order of magnitude as the gravity term, so an order of magnitude smaller than in the center region. The transversal component v_n^* (Fig. 4c) is dominant near the outer bank, where it conveys low-momentum fluid away from the bank near the water surface and near the bottom and high-momentum fluid towards the bank near the lower edge of the outer-bank cell. The outer-bank cell has also been observed by Bathurst et al. (1979) in a field study. They claim that the high-momentum fluid it conveys towards the bank at its lower edge locally increases the near-bank velocity and thus endangers bank stability. In our experiment, this mechanism is weak and no local increase of v_s is noticed. The magnitude of the vertical advection term (Fig. 4d) increases with the distance from the bank. With the exception of the corner formed by the water surface and the outer bank, it is negative, reaching values $O(-0.5)$, so tending to decrease the downstream velocity adjacent to the outer bank. This indicates a protective effect on the stability of the outer bank.

In summary, in the outer-bank region, the $\overline{v'_s v'_z}$ -term and the advective transport term are smaller than in the center-region. Furthermore, friction at the outer-bank is smaller than the bottom friction in the center-region. By creating a hydrodynamically quiet zone between the center-region cell and the outer bank, the outer-bank cell protects the outer bank.

2.4 Depth-Integrated Downstream Momentum Equation

Combining Eqs. (4) and (6), the following depth-integrated downstream momentum equation is investigated:

$$\begin{aligned}
 \underbrace{\frac{\tau_{bs}}{\rho}}_{\substack{\text{downstream} \\ \text{bottom shear stress} \\ \text{(not measured)}}} = & \underbrace{-\frac{1}{1+n/R} gh \frac{\partial z_s}{\partial s}}_{\substack{\text{gravity} \\ \text{(see Fig.5, curve a)}}} - \underbrace{\left[\frac{1}{1+n/R} \frac{\partial}{\partial s} (\langle v_s^2 \rangle h) \right]}_{\substack{\text{non-uniformity} \\ \text{(not measured)}}} + \underbrace{\frac{\partial}{\partial n} (U_s U_n h) + \frac{2}{1+n/R} \frac{U_s U_n h}{R}}_{\substack{\text{advective momentum} \\ \text{transport by cross-flow} \\ \text{(not shown)}}} \\
 + & \underbrace{\left[\frac{\partial}{\partial n} (\langle v_s^* v_n^* \rangle h) + \frac{2}{1+n/R} \frac{\langle v_s^* v_n^* \rangle h}{R} \right]}_{\substack{\text{advective momentum transport} \\ \text{by cross-stream circulation} \\ \text{(see Fig.5, curve b)}}} - \underbrace{\frac{1}{1+n/R} \frac{\partial}{\partial s} (\langle \overline{v_s'^2} \rangle h)}_{\substack{\text{non-uniformity} \\ \text{(not measured)}}} - \underbrace{\frac{\partial}{\partial n} (\langle \overline{v_s' v_n'} \rangle h)}_{\substack{\text{turbulent momentum transport} \\ \text{(see Fig.5, curve c)}}} - \underbrace{\frac{2}{1+n/R} \frac{\langle \overline{v_s' v_n'} \rangle h}{R}}_{\substack{\text{turbulent momentum transport} \\ \text{(see Fig.5, curve c)}}} \quad (9)
 \end{aligned}$$

A detailed analysis of this equation, which describes the mechanisms that contribute to the downstream bottom shear stress τ_{bs} , is given in Blanckaert and Graf (1999). As mentioned before, the downstream non-uniformity term on the first line and the advective momentum transport term associated with the cross-flow nearly balance each other. Therefore, they are ignored in this analysis (cf. Dietrich and Whiting, 1989). Fig. 5 (based on Fig. 4a in Blanckaert and Graf, 1999) shows only the most important terms, normalized by $u_{*,60}^2$ (cf. Eq. (7b)).

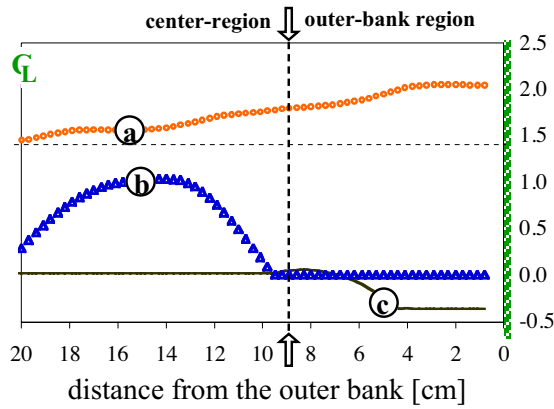


Fig. 5: Terms in the depth-integrated downstream momentum equation, Eq. (9), normalized by $u_{*,60}^2$. (a) gravity; (b) advective momentum transport by cross-stream circulation; (c) turbulent momentum transport.

In our experiment, the measured downstream water surface slope in the measuring section is nearly constant over the width. The transverse bottom slope gives rise to an almost linear outward increase of the gravity term, $-\left[(1+n/R)^{-1} gh (\partial z_s / \partial s) \right] / u_{*,60}^2$ (curve a), from a value of 1.1 at the inner bank ($h = 0.07$ m), via 1.6 in the centerline ($h = 0.11$ m), to a value of 2.1 at the outer bank ($h = 0.16$ m). According to Eq. (9), this outward increase of the gravity term provokes a contribution to τ_{bs} with a similar width-distribution: values smaller than average in the inner part of the half-section and larger than average in the outer part.

The terms $\left[\frac{\partial (\langle v_s^* v_n^* \rangle h)}{\partial n} + 2(1+n/R)^{-1} \frac{\langle v_s^* v_n^* \rangle h}{R} \right] / u_{*,60}^2$ (curve b) behave differently in the center region and in the outer-bank region. In the center region, the normalized value of

the group increases from about zero near the centerline to a maximum $O(1)$ somewhat further outwards, and then decreases again to zero at the edge of the outer cell. Throughout the outer-bank region, the value is negligible. Since these terms are redistribution terms and must cancel out when integrating over the entire width, they have to be negative in the inner half-section of the channel, where no measurements are available. These advective transport terms will therefore decrease the downstream bottom shear stress (and also the downstream velocity) in the inner half-section and increase it in the part of the outer half-section covered by the center-region cell. Due to the negligible values in the outer-bank region, this outward increase does not continue in the outer-bank region. This is consistent with the observation that the core of maximum velocity occurs near the edge of the outer-bank region (cf. Figs. 3a,c).

The outward increase of the downstream bottom shear stress, which is typical of flow in alluvial open-channel bends, is thus explained by the combined influence of the sloping bottom (gravity term) and the cross-stream circulation (advective momentum redistribution). In our experiment, the normalized gravity term increases by about 0.5 from the centerline to the outer bank, whereas the advective momentum transport terms show a variation of about 1.0. This indicates that their effects on the redistribution of the bottom shear stress and the depth-averaged downstream velocity will be comparable in magnitude. This agrees with findings by Johannesson and Parker (1989b).

In the outer-bank region, the terms related to the friction at the outer bank are negative: $-\left[\partial(\langle \vec{v}_s \vec{v}_n \rangle h) / \partial n + 2(1 + \eta/R)^{-1} \langle \vec{v}_s \vec{v}_n \rangle h / R\right] / u_{*60}^2 = O(-0.5)$ (curve c). They balance part of the driving gravity term and thus reduce the downstream bottom shear stress. In the center region, these terms are negligible.

In summary, gravity and advective momentum transport by the center-region cell have a contribution of comparable magnitude to the outward increase of the downstream bottom shear stress and velocity. Note that over a horizontal bottom, only the advective momentum transport contributes. Due to the negligible advective momentum transport in the outer-bank region, the maximum downstream velocity occurs at the inner edge of the outer-bank region. This confirms the conclusion from the analysis of the momentum equation, Eq. (8): the outer-bank cell protects the outer bank.

3 Theoretical model and mathematical analysis

The analysis so far has revealed the importance of the advective momentum transport by both the center-region cell and the outer-bank cell with respect to the distribution of v_s and τ_{bs} . In engineering practice, flow models are often based on the depth-integrated momentum equations (like Eq. (9)). Only the depth-averaged velocities, U_j ($j=s,n$), can be solved from these equations, in which the advective momentum transport $\langle v_s^* v_n^* \rangle$ by the cross-stream circulation appears as an unknown that needs to be modeled in terms of these depth-averaged velocities. Even in recently reported depth-integrated flow simulations, these important terms are still often neglected (Ye & McCorquodale, 1997; Jia & Wang, 1999; Duan et al., 2001; Kassem & Chaudhry, 2002; the latter three do however account for the effect of the cross-stream circulation in the sediment transport

calculations). Depth-integrated flow simulation including these terms have been reported by Yulistiyanto et al. (1998) and Lien et al. (1999).

The mechanisms underlying the *outer-bank cell* are complicated and it can only be simulated using the fully three-dimensional flow equations with complicated turbulence closures (Section 9.2.6 in de Vriend, 1981a; Christensen et al., 1999; Jia et al., 2001). Since a simplified conceptual model for the outer-bank cell is hard to develop, the mathematical analysis will focus only on the center-region cell, which was shown above to be of major importance for the outward increase of the velocity and the bottom shear stress, as well as for the deformation of the vertical velocity profiles.

Conceptual models have been developed that account for the effects of the *center-region cell*. They typically follow a two-step approach:

- (i) A model is developed for the case of fully-developed curved flow ($\partial/\partial s=0$ and $U_n=0$) and limited to the central part of the center-region cell where $v_z \ll v_n^*$, $n \approx 0$ and $h \approx H$.
- (ii) The solution is subsequently extended to include for inertia effects (developing curved flow) and to cover the entire flow width.

Hereafter, attention will be limited to the first step. Commonly-used models – termed linear models - are simple, but known to overestimate the effects of the center-region cell, especially for moderately to strongly curved flows. These models neglect the feedback between the downstream velocity and the center-region cell and do not clearly reveal the mechanisms underlying the center-region cell. We have extended and improved these linear models, mainly by incorporating advective momentum transport by the center-region cell, which was identified by the experimental analysis as the dominant mechanism. The so obtained non-linear model clearly reveals the mechanisms underlying the center-region cell and its feedback with the downstream velocity. Furthermore, it agrees well with experimental data for strongly curved flows. Some aspects of this non-linear model have already been presented by Blanckaert (2001b) and Blanckaert and Graf (2001c) and a detailed presentation is reported by Blanckaert (2002b).

Hereafter, the linear model is briefly outlined and the principle of the non-linear model and its general solution are briefly presented. This paper mainly aims at presenting the results of a mathematical analysis of the non-linear model, that intended to:

- confirm the conclusion of the foregoing analysis that advective momentum transport, $\langle v_s^* v_n^* \rangle$, significantly contributes to the deformation of the v_s -profiles. As mentioned before, the accuracy of the terms in the momentum equations evaluated from measured data is rather low and terms related to downstream variations of the flow field could not be evaluated. Furthermore, the laboratory flume was much narrower than typical open channels and some questions remain on the role of the high but poorly reliable values of the shear stress term close to the bottom.
- gain insight into the behavior of the advective momentum transport $\langle v_s^* v_n^* \rangle$. The analysis so far is limited to an experiment under one hydraulic condition. The mathematical analysis enables investigating the behavior of the advective momentum transport as a function of the hydraulic parameters.
- establish a model for the advective momentum transport by the center-region cell that can be usefully coupled to the depth-integrated flow equations.

3.1 Linear Model

The advective momentum transport $\langle v_s^* v_n^* \rangle$ by the center-region cell is usually modeled by assuming the downstream velocity v_s to have the same vertical profile as in straight uniform flow. The profile of the transversal component of the cross-stream circulation v_n^* in the central part of the center-region cell is subsequently found from a simplified transversal momentum equation for steady fully-developed curved flow, as proposed by Rozovskii (1957):

$$-\frac{v_s^2}{R} = -g \frac{\partial z_s}{\partial n} + \frac{d}{dz} \left(v_t \frac{dv_n^*}{dz} \right) \quad (10)$$

where an eddy viscosity model is used to describe the turbulent momentum flux as $-\overline{v_n' v_z'} = v_t dv_n^*/dz$. According to this equation, the horizontal component of the cross-stream circulation, v_n^* , results from the local imbalance between the centrifugal force, $-v_s^2/R$, and the transverse pressure gradient, $-g\partial z_s/\partial n$. From the computed profiles of v_s and v_n^* , the advective momentum transport by the center-region cell and the strength of the center-region cell can easily be derived as:

$$\langle v_s^* v_n^* \rangle = U_s^2 \frac{H}{R} \text{fnct}_{sn}(C) \quad \text{and} \quad \sqrt{\langle v_n^{*2} \rangle} = U_s \frac{H}{R} \text{fnct}_{mn}(C) \quad (11)$$

Models of this type, which are essentially based on a perturbation approach, yield solutions that are linearly proportional to the curvature ratio, H/R . This approach has been proposed by Rozovskii (1957) and is commonly used in combination with a depth-integrated flow model (Yulistiyanto et al., 1998, Lien et al., 1999). Similar linear models have been proposed by Engelund (1974), Kikkawa et al. (1976), de Vriend (1977), Falcon and Kennedy (1983) and Johannesson and Parker (1989a). All of them are based on vertical profiles of the downstream velocity, v_s , and the eddy viscosity, v_t , derived from straight uniform flow. Kalkwijk and de Vriend (1980) and Ikeda et al. (1990) proposed basically similar models that are valid over the entire cross-section.

The distributions of the downstream velocity, v_s , the cross-stream circulation, v_n^* , and the advective momentum transport, $\langle v_s^* v_n^* \rangle h$, according to the above linear model deviate significantly from the measured distributions (for a detailed comparison see Blanckaert, 2001a). Table 1 indicates that the linear model overestimates the advective momentum transport by the center-region cell, $\langle v_s^* v_n^* \rangle h$, by about an order of magnitude on the centerline in the investigated flow. The observed center-region cell may be weakened by the narrow cross-section and the pronounced transversal bottom slope, but these effects cannot account for the observed discrepancy of an order of magnitude in $\langle v_s^* v_n^* \rangle h$.

<i>Measured</i>	<i>Linear model</i>	<i>Non-linear model</i>
-0.5 to -1	-5	-0.5

Table 1: Advective momentum transport $\langle v_s^* v_n^* \rangle h / (u_{*60}^2 R_h)$ in central part of center-region cell.

It is well known that the overestimation of the linear model is due to the adoption of a straight-flow v_s -profile, thereby neglecting the feedback between the v_s -profile and the center-region cell. De Vriend (1981a) already qualitatively described this negative feedback mechanism as follows: advective momentum transport by the center-region cell deforms the vertical v_s -profile (cf. Fig. 3c), which weakens the center-region cell, leads to a reduction of the advective momentum transport $\langle v_s^* v_n^* \rangle$, and hence reduces the deformation of the v_s -profile.

3.2 Non-Linear Model

The foregoing rationale leads to the conclusion, that the effects of the center-region cell in moderately to strongly curved flow can only be modeled when taking due account of the deformation of the downstream velocity profiles and the feedback between the downstream velocity and the center-region cell.

According to our analysis of experimental data, both mechanism are dominated by those terms in the downstream momentum equation representing advective momentum transport by the center-region cell. By incorporating these terms in the linear model formulation, we have developed the so-called non-linear model. Some aspects of this model have already been presented by Blanckaert (2001b) and Blanckaert and Graf (2001c) and a detailed presentation is reported by Blanckaert (2002b). Hereafter, the outline of the non-linear model and its general solution are briefly presented and subsequently the main results of a mathematical analysis of the model are reported. The aim of this section is to illustrate how the theoretical conceptual model has been used to confirm and complement the results of the analysis of experimental data.

3.2.1 Outline and general solution of the non-linear model

The transversal component of the center-region cell v_n^* is described by the same momentum equation as in the linear model, namely Eq. (10). Instead of using a straight-uniform-flow v_s -profile, the v_s -profile is now computed from the following simplified downstream momentum equation (cf. Eq. 8):

$$\left[v_n^* \frac{\partial v_s}{\partial n} + \frac{v_n^* v_s}{R} \right] = -g \frac{\partial z_s}{\partial s} + \frac{\partial}{\partial z} \left(v_t \frac{\partial v_s}{\partial z} \right) \quad \text{at } n=0 \quad (12)$$

where an eddy viscosity model is used to describe the turbulent momentum flux as $-\overline{v'_s v'_z} = v_t dv_s/dz$. Recall that this equation is applied for the case of fully developed flow near the central part of the center-region cell. The left-hand part of this equation accounts for advective momentum transport by the center-region cell. Our foregoing analysis of the experimental data identified these terms as the main responsables for the deformation of the v_s -profiles. They furthermore account for the coupling of the downstream velocity and the center-region cell. By neglecting them, Eq. (12) reduces to its straight-uniform-flow form, which was at the basis of the preceding linear model.

To solve equations (10) and (12) for v_s and v_n^* , they need some further elaboration. Similar to straight uniform flow, a parabolic eddy viscosity is adopted,

$$v_t = \kappa \sqrt{\|\vec{\tau}_b / \rho\|} h \frac{z}{h} \left(1 - \frac{z}{h} \right) \quad (13)$$

whose magnitude is proportional to the norm of the bottom shear-stress vector. The transverse gradient of the downstream velocity in Eq. (12) shall be parameterized by

$$\frac{\partial v_s}{\partial n} = \alpha_s \frac{v_s}{R} \quad \text{near } n=0 \quad (14)$$

which means that v_s in the vicinity of the centerline is described as a power-law function of n . Thus, Eq. (12) reduces from a partial to an ordinary differential equation,

$$(1 + \alpha_s) \frac{v_n^* v_s}{R} = -g \frac{\partial z_s}{\partial s} + \frac{d}{dz} \left(v_t \frac{dv_s}{dz} \right) \quad (15)$$

The left-hand-side vanishes for $\alpha_s = -1$. This corresponds to a "potential-vortex" spanwise velocity distribution, and can be seen as a reasonably lower bound for α_s (Blanckaert, 2001b). For flows over a natural bar-pool bottom topography, values are typically $\alpha_s \gg 0$.

The solution of the non-linear model generally depends on the three parameters H/R , C and α_s . Surprisingly, when represented as a function of the combined parameter $\beta = \left[(\sqrt{g}/C)^{-2.2} (H/R)^2 (\alpha_s + 1) \right]^{0.25}$ - termed bend parameter - the general solution only shows slight scatter around single curves. The general solutions for the advective momentum transport $\langle v_s^* v_n^* \rangle$ and the strength of the center-region cell $\sqrt{\langle v_n^{*2} \rangle}$, normalized by the corresponding linear model solutions are shown in Fig.6b. They can be written as:

$$\begin{aligned} \langle v_s^* v_n^* \rangle &= \langle v_s^* v_n^* \rangle_{\text{linear}} \text{fnc}_{sn}(\beta) \stackrel{\text{Eq.(11)}}{=} U_s^2 \frac{H}{R} \text{fnc}_{sn}(C) \text{fnc}_{sn}(\beta) \\ \sqrt{\langle v_n^{*2} \rangle} &= \sqrt{\langle v_n^{*2} \rangle}_{\text{linear}} \text{fnc}_{nn}(\beta) \stackrel{\text{Eq.(11)}}{=} U_s \frac{H}{R} \text{fnc}_{nn}(C) \text{fnc}_{nn}(\beta) \end{aligned} \quad (16)$$

Fig 6a illustrates the deformation of the v_s -profiles with increasing bend parameter β , for the experimental Chezy friction factor of $C=35 \text{ m}^{1/2}/\text{s}$.

Although the numerical solution of the non-linear model is quite cumbersome, its general solution is hardly more complicated than the linear-model solution and can be represented by single curves as a function of one additional parameter. Validations of this non-linear model solution with experimental data for moderately to strongly curved flow are reported by Blanckaert (2001b) and Blanckaert and Graf (2001c).

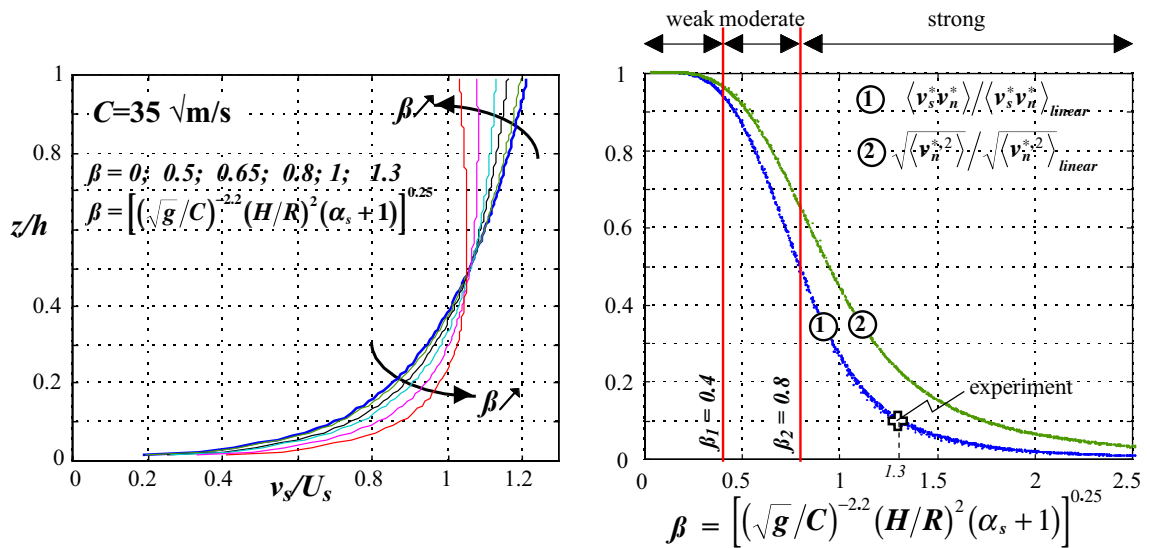


Fig. 6: Solutions of the non-linear model: (a) deformation of the v_s -profiles with increasing bend parameter β for $C=35 \text{ m}^{1/2}/\text{s}$; (b) strength of the center-region cell $\sqrt{\langle v_n^{*2} \rangle}$ and its advective momentum transport $\langle v_s^* v_n^* \rangle$ as a function of the bend parameter.

3.2.2 Analysis of the non-linear model

The non-linear model enables to confirm and complement the results of the previous "analysis of experimental data". As mentioned before, this paper only briefly mentions the main results, while an in-depth presentation and analysis are reported in Blanckaert (2002b).

Fig. 6b shows that the non-linear model reduces to the linear model for vanishing curvature ratio, $H/R \downarrow 0$, i.e. the linear model is an asymptotic solution of the non-linear model. The non-linear model thus confirms and quantifies the over-estimative character of the linear model. Moreover, it provides an objective criterion to distinguish between weak, moderate and sharp curvatures. Weak curvatures correspond to the validity range of the linear model, given by $\beta < 0.4$. Without stretching the low β range by taking the parameter combination $\left[(\sqrt{g}/C)^{-2.2} (H/R)^2 (\alpha_s + 1) \right]$ to the power 0.25, this region would not be noticeable. Moderate bend curvatures correspond to the β region where the ratio of non-linear to linear model decreases strongly and nearly linearly, and strong curvature corresponds to the region where the advective momentum transport is reduced to less than half its linear model value. Whereas previous (rather arbitrary) definitions of strongly curved flow were based on purely geometrical parameter like H/R or B/R , the definition based on the bend parameter β also includes the channel roughness and the flow distribution. The non-linear model clearly indicates that the center-region cell becomes self-limiting for sharp bends. This idea is not completely new, but the non-linear model establishes this phenomenon clearly and quantifies it.

The non-linear model captures well the negative feedback between the downstream velocity and the center-region cell. With increasing bend parameter, the v_s -profiles flatten (Fig. 6a) and the strength of the center-region cell, $\sqrt{\langle v_n^{*2} \rangle}$, as well as its advective momentum transport, $\langle v_s^* v_n^* \rangle$, weaken (Fig. 6b). The simulated v_s -profile agrees rather well with the measured profile (Fig. 3c). Moreover, whereas the linear model overestimated $\langle v_s^* v_n^* \rangle$ by an order of magnitude (cf. Table 1), the non-linear model prediction – based on the experimental values $C = 35 \text{ m}^{1/2}/\text{s}$, $H/R = 0.057$ and $\alpha_s = 3.6$, - agrees fairly well with the measured $\langle v_s^* v_n^* \rangle$ (Fig. 6b).

Whereas the influence of the parameters C and H/R was only qualitatively known before, the non-linear model now provides a quantification. Furthermore, the non-linear model identifies and quantifies the influence of the spanwise velocity distribution on the feedback between the downstream velocity and the center-region cell. This influence was not known before.

Finally, the non-linear model confirms the result of the analysis of experimental data that the advective transport of momentum by the center-region cell is the dominant mechanism with respect to the downstream velocity distribution, since good results are obtained by adopting a very basic eddy viscosity turbulence closure.

4 Relevance to Engineering Practice

An analysis of our experimental data showed the important role of advective momentum transport by the cross-stream circulation in the redistribution of the downstream velocity and bottom shear stress. River engineering problems concerning morphology are often studied using models that are based upon the depth-integrated flow equations, extended with a (semi)-analytical description of the cross-stream circulation.

As of to date, linear models being used for the cross-stream circulation are simple but rather inaccurate, especially for moderate to strong curvatures. The above presented non-linear model is particularly well suited for improving the description of the cross-stream circulation. By accounting for the feedback between the downstream velocity and the cross-stream circulation, it gives accurate results even for moderate to strong curvatures, and is computationally hardly more expensive than the linear models. To incorporate it in the depth-integrated flow equations, it suffices to multiply the existing linear-model implementation by the correction factors defined in Fig. 6b, representing the ratio of the non-linear to the linear model as a function of the unique bend parameter β .

Contrary to the linear model, the non-linear model describes the effect of the cross-stream circulation in a dynamical way, i.e. it depends on the to-be-computed depth-averaged flow field. The depth-averaged flow equations require input on the relationship between $\langle v_s^* v_n^* \rangle$ and the depth-averaged velocity, but it produces values of H/R , α_s and C , whereas the non-linear model requires input on $\beta = \left[(\sqrt{g}/C)^{-2.2} (H/R)^2 (\alpha_s + 1) \right]^{0.25}$, but gives the relationship between $\langle v_s^* v_n^* \rangle$ and the depth-averaged velocity. So, the 3-D flow field can be described with a combination of a 2-D depth-integrated model and a model describing the vertical structure of the flow, thus yielding a real quasi-three-dimensional flow model.

This dynamical coupling between the depth-integrated flow equations and the non-linear model is presently being done, and first results indicate that it is computationally efficient enough to be used in morphological computations.

Note, that the non-linear model describes the advective momentum transport by the center-region cell, but it cannot account for the outer-bank cell. Our analysis indicates that the outer bank cell has a stabilizing effect on the outer bank. Discarding the effect of the outer-bank cell is therefore not dramatic: it will only lead to conservative estimates of the boundary shear stress in the outer-bank area.

5 Conclusions

The hydromechanics of flow in a sharp open-channel bend was analyzed on the basis of experimental data and by means of a theoretical model. Attention was paid to the role of both cells of cross-stream circulation: the classical helical motion – termed here center-region cell - and the weaker counter-rotating outer-bank cell. The conclusions to be drawn from this work can be summarized as follows:

- Evaluation of the different terms in the downstream momentum equation (Eq. (8) and Fig. 4) and its depth-integrated form (Eq. (9) and Fig. 5) on the basis of the experimental data showed a different hydrodynamical behavior in the center region and in the outer bank region (corresponding to either circulation cell). Advective momentum transport by the center-region cell is the dominant mechanism behind the velocity redistribution in the center region; it significantly contributes to the observed outward increase of the downstream velocity and to the flattening of its vertical profile. By creating a hydrodynamically quiet zone between the center-region cell and the outer bank, the outer-bank cell protects the outer bank from influences of the center-region cell and keeps the core of maximum downstream velocity away from the bank.
- Based on the results of the experimental analysis, we have developed a conceptual theoretical model – termed non-linear model - for advective momentum transport by the center-region cell. Contrary to the previous linear models, it takes due account of the feedback between the downstream velocity profile and the center-region cell, and agrees much better with experimental data. In this paper, the analysis of experimental data is complemented by a mathematical analysis of this non-linear model. The non-linear model quantifies the overestimation by the linear model, as well as the influence of the Chezy friction factor C and the curvature ratio H/R , which were previously only qualitatively understood. It identifies the spanwise velocity distribution as an important parameter and quantifies it. It confirms and quantifies the idea that the center-region cell becomes self-limited for strong curvature and allows to distinguish objectively between weak, moderate and strong curvatures. Finally, by yielding good results with a basic eddy viscosity turbulence closure, it confirms the result of the analysis of experimental data that the advective momentum transport is the dominant mechanism with respect to the velocity distribution.
- Since the advective momentum transport by the cross-stream circulation strongly influences the downstream velocity distribution, it has to be included in the depth-integrated flow models that are often used in engineering practice. The linear models that are used to date are known to yield poor results for moderate to strong curvatures. The non-linear model is particularly well suited to improve the description of the effects of the center-region cell at low computational cost. It suffices to multiply the linear model implementation by a correction factor – non-linear-model / linear model (Fig. 6b) – that depends on a unique, newly defined bend parameter. Tests have indicated that the dynamical coupling between the depth-integrated flow equations and the non-linear model is computationally efficient enough to be used in morphological computations.

Even though the experimental data were limited to the outer-half of one single cross-section under one set of hydraulic and geometric conditions, they yielded valuable information on the mechanisms underlying the velocity distribution, which resulted in the development of a conceptual theoretical model for the dominant center-region cell. The experimental research is presently extended by measuring entire cross-sections all along a large optimized laboratory flume under different hydraulic and geometric conditions. Some results of these experiments have already been reported by Blanckaert and Graf (2001b) and Blanckaert (2002a,b).

Acknowledgements

This research is being sponsored by the Swiss National Science Foundation under grants Nr.2100-052257.97/1 and 2000-059392.99/2. Profs. H.J. de Vriend and A.J. Odgaard are thanked for the fruitful discussions during their stays at EPFL.

APPENDIX I. REFERENCES

- Batchelor, G. K. (1970). *An introduction to fluid dynamics*, Cambr. Univ. Press, Cambridge, UK.
- Bathurst, J. C., Thorne, C. R., and Hey, R. D. (1979). "Secondary flow and shear stress at river bends." *J. Hydr. Div.*, ASCE, Vol.105(HY10), 1277-1295.
- Blanckaert, K. (2001a). "discussion on: Bend-flow simulation using 2D depth-averaged model, by Lien H.C. et al." *J. Hydr. Engng.*, ASCE, Vol. 127(2), 167-170.
- Blanckaert, K. (2001b) "A model for flow in strongly curved channel bends." *Proc. 29th-IAHR Congr.*, Beijing, China.
- Blanckaert K. (2002a). "Secondary currents measured in sharp open-channel bends." *Proc. River Flow 2002*, Louvain, Belgium.
- Blanckaert K. (2002b). "Flow and turbulence in sharp open-channel bends." *PhD-thesis Nr 2545*, Ecole Polytechnique Fédérale Lausanne, Switzerland.
- Blanckaert, K., and Graf, W. H. (1999). "Outer-bank cell of secondary circulation and boundary shear stress in open-channel bends." *Proc. 1st RCEM symp.*, Genova, Italy, Vol.I, 533-543.
- Blanckaert, K., and Graf, W. H. (2001a). "Mean flow and turbulence in an open-channel bend." *J. Hydr. Engng.*, ASCE, Vol. 127 (10), 835-847.
- Blanckaert, K., and Graf, W. H. (2001b). "Experiments on flow in a strongly curved channel bend." *Proc. 29th IAHR Congr.*, Beijing, China.
- Blanckaert, K., and Graf, W. H. (2001c) "Non-linear model for secondary circulation and transversal bottom slope in sharp bends." *Proc. 2th RCEM-congr.*, Obihiro, Japan.
- Boussinesq, J. (1868). "Mémoire sur l'influence de frottement dans les mouvements réguliers des fluides; XII - Essai sur le mouvement permanent d'un liquide dans un canal horizontal à axe circulaire." *J. Math. pures et appl.*, série 2 (Tome XIII), 413.
- Bradshaw, P. (1987). "Turbulent secondary flows." *Annual Rev. Fluid Mechanics*, 53-74.
- Cheng, K. C., Lin, R.-C., and Ou, J.-W. (1976). "Fully developed laminar flow in curved rectangular channels." *J. Fluids Engng.*, ASME, March 1976, 41-48.
- Christensen, B., Gislason, K., and Fredsoe, J. (1999). "Secondary turbulent flow in an infinite bend." *Proc. 1st RCEM symp.*, Genova, Italy, 543-552.
- de Vriend, H. J. (1977). "A mathematical model of steady flow in curved shallow channels." *J. Hydr. Res.*, IAHR, Vol.15(1), 37-54.

- de Vriend, H. J. (1981a). "Steady flow in shallow channel bends." *Report No. 81-3*, Lab. Fl. Mech., Dept. Civ. Eng., Delft Univ. Techn., Delft, The Netherlands.
- de Vriend, H. J. (1981b). "Velocity redistribution in curved rectangular channels." *J. Fluid Mech.*, Cambr. Univ. Press, Vol.107, 423-439.
- Dietrich, W. E. (1987). "Mechanics of flow and sediment transport in river bends." *River Channels: environment and process*, K. Richards, ed., Inst. Brit. Geogr. spec. publ., Oxford, 179-227.
- Dietrich, W. E., and Whiting, P. (1989). "Boundary shear stress and sediment transport in river meanders of sand and gravel." in *River meandering*, Ikeda, S. and Parker, G., eds., AGU, Washington, USA, 1-50.
- Duan, J. G., Wang, S.S.Y. and Jia, Y. (2001). "The application of the enhanced CCHE2D model to study the alluvial channel migration processes." *J. Hydr. Res.*, IAHR, Vol.39(5), 469-480.
- Einstein, H.A. and Harder, J.A. (1954). "Velocity distribution and the boundary layer at channel bends.", *Transactions AGU*, Vol. 35(1), 114-120.
- Engelund, F. (1974). "Flow and bed topography in channel bends." *J. Hydr. Div.*, ASCE, 100(11), 1631-1648.
- Falcon Ascanio, M. & Kennedy, J. F. (1983). "Flow in alluvial-river curves." *J. Fluid Mech.*, 133, 1-16.
- Graf, W. H., and Altinakar, M. (1998). *Fluvial hydraulics*, Wiley, Chichester, UK.
- Hille, P., Vehrenkamp, R., and Schulz-Dubois, E. O. (1985). "The development and structure of primary and secondary flow in a curved square duct." *J. Fluid Mech.*, Cambr. Univ. Press, Vol.151, 219-241.
- Ikeda, S., Yamasaka, M., and Kennedy, J. F. (1990). "Three-dimensional fully developed shallow-water flow in mildly curved bends." *Fluid dynamics research 6*, JSFM, Noth-Holland, 155-173.
- Jia, Y., Blanckaert, K., and Wang, S.S.Y. (2001). "Numerical simulation of secondary currents in curved channels." *8th FMTM-congr.*, Tokyo, Japan.
- Jia, Y. and Wang, S.S.Y. (1999). "Numerical model for channel flow and morphological change studies." *J. Hydr. Engng*, ASCE, 125(9), 924-933.
- Jia, Y. and Wang, S.S.Y. (2000). "Numerical simulation of the channel flow with submerged weirs in Victoria Bendway, Mississippi River". Report to U.S. Army Corps of Engineer Research and Development Center.
- Johannesson, H. & Parker, G. (1989a). "Secondary flow in mildly sinuous channel." *J. Hydr. Engng*, ASCE, 115(3), 289-308.
- Johannesson, H., and Parker, G. (1989b). "Velocity redistribution in meandering rivers." *J. Hydr. Engng.*, ASCE, Vol.115(8), 1019-1039.
- Kalkwijk, J.P.Th. and De Vriend, H.J., 1980. Computation of the flow in shallow river bends. *J. Hydr. Res.*, Vol.18(4), 327-342.

- Kassem, A.A. and Chaudhry M.H. (2002). "Numerical modeling of bed evolution in channel bends." *J. Hydr. Engng, ASCE*, 128(5), 507-514.
- Kikkawa, H., Ikeda, S. & Kitagawa, A. (1976). "Flow and bed topography in curved open channels." *J. Hydr. Div., ASCE*, Vol. 102(9), 1327-1342.
- Lien, H. C., Hsieh, T. Y., Yang, Y. C., and Yeh, K. C. (1999). "Bend-flow simulation using 2D depth-averaged model." *J. Hydr. Engng., ASCE*, Vol.125(10), 1097-1108.
- Mockmore, C.A. (1943). "Flow around bends in stable channels." *Transactions, ASCE*, Vol. 109, 593-628 (incl. discussions).
- Odgaard, A. J. (1984). "Bank erosion contribution to stream sediment load." *IIHR Report No. 280*, Iowa Institute of Hydraulic Research, Iowa.
- Odgaard, J. A., and Bergs, M. A. (1988). "Flow processes in a curved alluvial channel." *Water Resour. Res.*, AGU, Vol.24(1), 45-56.
- Rozovskii, I. L. (1957). *Flow of water in bends of open channels*, Ac. Sc. Ukr. SSR, Isr. Progr. Sc. Transl., Jerusalem, Israel.
- Shukry, A. (1949). "Flow around bends in an open flume". *Proc. ASCE*, 6, p.713.
- Thomson, W. (1876). "On the origin of windings of rivers in alluvial plains, with remarks on the flow of water round bends in pipes." *Proc. Royal Soc. London*, 25, 5-8.
- Winters, K. H. (1987). "A bifurcation study of laminar flow in a curved tube of rectangular cross-section." *J. Fluid Mech.*, Cambr. Univ. Press, Vol.180, 343-369.
- Ye, J., and McCorquodale, J. A. (1997). "Depth-averaged hydrodynamic model in curvilinear collocated grid." *J. Hydr. Engng, ASCE*, 123(5), 380-388.
- Yeh, K. C., and Kennedy, J. F. (1993). "Moment model of nonuniform channel-bend flow. I: Fixed beds." *J. Hydr. Engng., ASCE*, Vol.119(7), 776-795.
- Yulistiyanto, B., Zech, Y., and Graf, W. H. (1998). "Flow around a cylinder: shallow-water modeling with diffusion-dispersion." *J. Hydr. Engng., ASCE*, Vol.124(4), 419-429.

APPENDIX II. NOTATION

<i>ADVP</i>	=	Acoustic Doppler Velocity Profiler
<i>B</i>	=	channel width
<i>C</i>	=	Chezy roughness coefficient
<i>d₅₀</i>	=	mean diameter of the sand bottom
$Fr=U/\sqrt{gH}$	=	Froude number
<i>g</i>	=	gravitational acceleration
<i>H</i>	=	reach-averaged flow depth
<i>h</i>	=	local flow depth
<i>n</i>	=	transversal reference axis
<i>p</i>	=	pressure
<i>Q</i>	=	discharge

R	=	radius of curvature of the channel centerline
R_h	=	hydraulic radius of the cross-section
$Re=UH/\nu$	=	Reynolds number of reach-averaged flow
S	=	water surface slope
s	=	downstream reference axis
t	=	time
U	=	$Q/(BH)$ = reach-averaged velocity
U_j	=	depth-averaged velocity component, $j=s,n$
$u^*=U\sqrt{g/C}$	=	friction velocity
v_j	=	time-averaged velocity component, $j=s,n,z$
$v_j(t)$	=	instantaneous velocity component, $j=s,n,z$
$v'_j(t)$	=	instantaneous velocity fluctuation, $j=s,n,z$
v_j^*	=	local deviations from the depth-averaged velocity, $j=s,n$
$\overline{v'_j v'_k}$	=	time-averaged correlation of the velocity fluctuations, $j,k=s,n,z$
z	=	vertical reference axis; elevation above the horizontal (s,n)-plane

symbols

α_s	=	normalized transversal velocity gradient, $(\partial v_s / \partial n) / (v_s / R)$
β	=	$\left[(\sqrt{g/C})^{-2.2} (H/R)^2 (\alpha_s + 1) \right]^{0.25}$: bend parameter
κ	=	Karman constant
ρ	=	density of water; $\rho=998.2 \text{ kg/m}^3$ at 20°
ν	=	molecular viscosity of water; $\nu=1.004 \times 10^{-6} \text{ m}^2/\text{s}$ at 20°
ν_t	=	eddy viscosity
τ	=	shear stress at the flow boundary (bottom or bank)
arrow	=	vectorial quantity
overbar	=	time-averaged values
$\langle . \rangle$	=	values averaged over the local flow depth
$O(.)$	=	order of magnitude of .
$ \dots $	=	absolute value of

subscripts

b	=	bottom
max	=	maximum magnitude over the measuring grid of a variable
S	=	water surface
60	=	value in the section at 60°

III.2 Secondary Flow in Sharp Open-Channel Bends

K. Blanckaert¹ and H.J. de Vriend²

(submitted for publication to J. Fluid Mech., Cambridge Univ. Press)



Abstract

Secondary currents are a characteristic feature of flow in open-channel bends. They advect flow momentum, redistribute the velocities, the boundary shear stresses and the sediment transport and shape the channel morphology. Their accurate prediction is a prerequisite for successful numerical simulations. Besides the classical helical motion (centre-region cell), often a weaker and smaller counter-rotating circulation cell (outer-bank cell) is observed near the outer bank. It plays an important role with respect to bank erosion processes. Rather similar bi-cellular patterns of secondary circulation occur in curved duct flow. The mechanisms underlying the circulation cells, and especially the outer-bank cell, are still poorly understood, and their numerical simulation still poses problems, which is largely due to a lack of detailed experimental data. The reported research provides detailed experimental data on both circulation cells. Furthermore, the underlying dynamics are investigated by simultaneously analysing the vorticity equation and the kinetic energy transfer between the mean flow and the turbulence. This shows that turbulence plays a minor role in the generation of the centre-region cell, which is mainly due to the centrifugal force. By accounting for the important negative feedback between the downstream velocity profile and the centre-region cell, accurate predictions of the centre-region cell can be obtained for moderate curvatures from a simplified vorticity balance that can be incorporated in depth-integrated flow models. For strong curvatures, however, a fully three-dimensional flow description is required. Due to the non-monotonic velocity profiles, the centrifugal force favours the outer-bank cell. Terms related to the anisotropy of the cross-stream turbulence, induced by boundary proximity, are of the same order of magnitude and include contributions that enhance the outer-bank cell. Both mechanisms strengthen each other. Furthermore, the occurrence of the outer-bank cell is not a matter of flow instability, as in the case of the similar outer-bank cell in curved laminar flow, but it also appears for weak curvatures. The outer-bank cell is enhanced by kinetic energy input from turbulence, and at the same time suppressed by turbulent dissipation. Although the kinetic energy transfer from turbulence to the mean flow is small compared to the total energy losses, it is essential for the generation of the outer-bank cell. Turbulence models based on a linear stress-strain relationship are inherently unable to account for it, which explains their inability to simulate turbulence-generated circulation cells.

Keywords

open-channel hydraulics, bend flow, laboratory experiments, outer-bank cell, secondary circulation, turbulence, downstream vorticity.

¹ Res. Assoc., Lab. d'Hydraulique Environnementale, Ecole Polytechnique Fédérale, CH-1015 Lausanne, Switzerland.

² Professor, Delft University of Technology, POB 5048, 2600 GA Delft, The Netherlands

1 Introduction

Curved open-channel flow is characterized by the existence of cross-stream circulation cells (secondary flow). By advecting flow momentum, these determine the spatial distributions of the velocities and the boundary shear stresses (Blanckaert & Graf 2002), and thereby shape the bottom topography.

Besides the classical helical motion (called hereafter centre-region cell) that covers a large part of the cross-section (called hereafter centre region), often a weaker counter-rotating cell is observed near the outer bank. Although relatively small and weak, this outer-bank cell is important, as it tends to protect steep outer banks against erosion (Blanckaert & Graf 1999, 2002). Figure 1 illustrates both circulation cells in a reach of an open-channel bend. Rather similar bi-cellular patterns of cross-stream circulation occur in curved duct flow; nonetheless important differences are known to exist between open-channel flow and duct flow (Nezu & Nakagawa 1993).

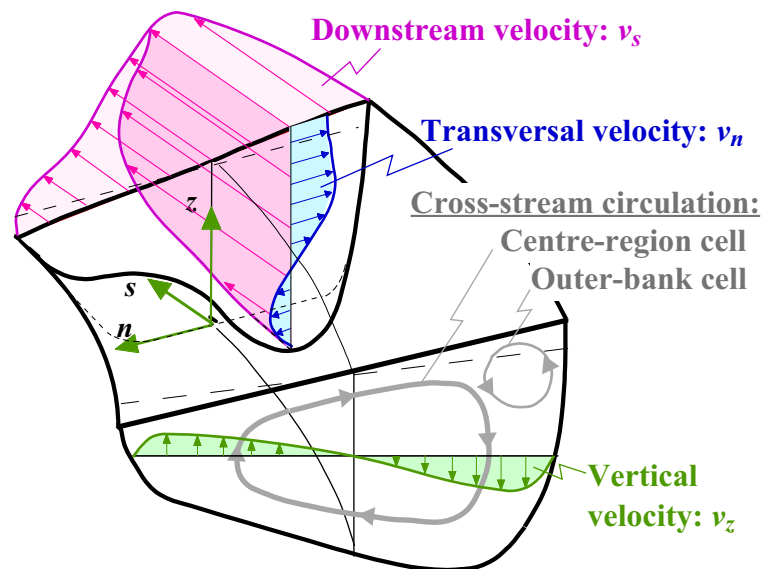


Figure 1: Definition sketch of curved open-channel flow and cross-stream circulation.

Detailed experiments on both circulation cells are scarce (Booij 1985, Booij & Tukker 1996, Blanckaert & Graf 2001a, Blanckaert 2002a,b), because they require accurate high-resolution measurements of the transversal and vertical velocity components on a fine grid. Most experimental investigations of the circulation cells are restricted to measurements of the downstream and the transversal velocity components on relatively coarse grids and with a relatively low accuracy (Blanckaert & Graf 2001a). This explains why, in spite of the fact that the occurrence of the second cell has been reported in the literature long ago (e.g. Mockmore 1943), they usually concentrate on the centre-region cell far from the banks.

The mechanisms underlying the two circulation cells are revealed by the downstream vorticity equation, which shows that the centrifugal force and the cross-stream turbulent stresses play a dominant role. So far, the experimental confirmation of this finding used to be hampered by the scarcity of experimental data on these cross-stream turbulent stresses.

A better insight into the mechanisms underlying the circulation cells will improve their numerical modelling and hence the modelling of the flow field in general. The centre-region cell is often explained as resulting from the local imbalance between the driving centrifugal force and the transverse pressure gradient (e.g. Rozovskii 1957, Engelund 1974) and it is usually modelled according to this simplified concept in the quasi-three-dimensional flow models that are often used in engineering practice (Lien et al. 1999). It is not clear to what extent this basic description captures all relevant mechanisms. Turbulence is known to be important to the generation of the outer-bank cell. However, there is little insight into the dynamics of the turbulence in the vicinity of that cell, and even the conditions of occurrence of the outer-bank cell are hardly known. The centre-region cell seems to be reproduced rather well by the fully-three-dimensional flow equations with standard turbulence closure, but more sophisticated turbulence closure models seem to be needed to reproduce the outer-bank cell (de Vriend 1981a, Christensen, Gislason & Fredsoe 1999, Jia, Blanckaert & Wang 2001). A better description of turbulence will be shown to be the key to better numerical simulations of the double-cell pattern.

The experimental research presented herein aims at getting a more detailed picture of the double-cell pattern in an open-channel bend, so as to gain insight into its dynamics and especially into the role of turbulence, and to find guidance for numerical modelling. Where previous investigations on cross-stream circulation cells only considered the vorticity equation (e.g. Perkins 1970, Demuren & Rodi 1984, Bradshaw 1987, Nezu & Nakagawa 1993), the present work simultaneously analyses the vorticity equation and the kinetic energy transfer between mean flow and turbulence. The experimental data are based on simultaneous high-resolution measurements of the three velocity components on a fine grid in one cross-section of a bend in a laboratory flume. This makes it possible to evaluate all three mean velocity components, as well as all turbulent stress components. Based on these results, the relevant terms in the vorticity equation and the kinetic energy transfer between the mean flow and the turbulence can be evaluated.

In the first part of this paper, a theoretical framework of analysis is given and the current state of knowledge on the cross-stream circulation is reviewed. The importance of considering the kinetic energy transfer between mean flow and turbulence is shown and the objectives of the analysis are formulated. Subsequently, the experiment is presented and an analysis of the mechanisms underlying the two circulation cells is made, on the basis of the experimental data and making use of the downstream vorticity equation and the kinetic energy equation. Special attention is paid to the implications for numerical modelling.

2 Theoretical basis and previous work

2.1 Cross-stream motion and downstream vorticity

A cylindrical co-ordinate system is adopted, with the curvilinear s -axis pointing downstream along the channel axis, the transversal n -axis pointing left and the vertical z -axis pointing upward from the horizontal (s,n) -plane (also see figures 1 and 3). The transformation of the flow equations from a Cartesian to a cylindrical co-ordinate system is given by Batchelor (1970, p.598).

The cross-stream motion, (v_n, v_z) , is governed by the transversal and vertical momentum equations for incompressible flow (Schlichting & Gersten 2000):

$$\begin{aligned} \frac{\partial v_n}{\partial t} = & - \left(\frac{1}{1+n/R} v_s \frac{\partial v_n}{\partial s} + v_n \frac{\partial v_n}{\partial n} + v_z \frac{\partial v_n}{\partial z} - \frac{1}{1+n/R} \frac{v_s^2}{R} \right) \\ & - \frac{1}{\rho} \frac{\partial p}{\partial n} - \left(\frac{1}{1+n/R} \frac{\partial \bar{v}'_s \bar{v}'_n}{\partial s} + \frac{\partial \bar{v}'^2}{\partial n} + \frac{\partial \bar{v}'_n \bar{v}'_z}{\partial z} + \frac{1}{1+n/R} \frac{\bar{v}'^2 - \bar{v}'_s^2}{R} \right) \\ & + v \left(\nabla^2 v_n - \frac{1}{(1+n/R)^2} \frac{1}{R} \frac{\partial v_s}{\partial s} - \frac{1}{1+n/R} \frac{\partial}{\partial s} \left(\frac{1}{1+n/R} \frac{1}{R} v_s \right) - \frac{1}{(1+n/R)^2} \frac{1}{R^2} v_n \right) \end{aligned} \quad (1)$$

$$\begin{aligned} \frac{\partial v_z}{\partial t} = & - \left(\frac{1}{1+n/R} v_s \frac{\partial v_z}{\partial s} + v_n \frac{\partial v_z}{\partial n} + v_z \frac{\partial v_z}{\partial z} \right) \\ & - g - \frac{1}{\rho} \frac{\partial p}{\partial z} - \left(\frac{1}{1+n/R} \frac{\partial \bar{v}'_s \bar{v}'_z}{\partial s} + \frac{\partial \bar{v}'_n \bar{v}'_z}{\partial n} + \frac{\partial \bar{v}'^2}{\partial z} + \frac{1}{1+n/R} \frac{\bar{v}'_n \bar{v}'_z}{R} \right) + v \nabla^2 v_z \end{aligned} \quad (2)$$

in which $(1+n/R)$ is a metric factor accounting for the divergence of the n -coordinate lines, R being the radius of curvature of the channel axis; p is the pressure; t is time; g is the gravitational acceleration; $\bar{v} = (v_s, v_n, v_z)$ and $\bar{v}' = (v'_s, v'_n, v'_z)$ are the mean and fluctuating velocity components; $-\rho \bar{v}'_j \bar{v}'_k$ ($j, k = s, n, z$) are the turbulent stresses; v is the molecular kinematic viscosity; ∇^2 is the Laplace-operator.

The transversal momentum equation (1) is dominated by the centrifugal-force and pressure-gradient terms, which nearly balance each other: $(1+n/R)^{-1}(v_s^2/R) - \rho^{-1} \partial p / \partial n \approx 0$. The vertical momentum equation (2) is dominated by the hydrostatic balance, $g + \rho^{-1} \partial p / \partial z \approx 0$. This keeps these equations from clearly revealing the dynamics of the cross-stream motion. For clarity's sake, a distinction will be made between the translatory and the circulatory parts of the cross-stream motion, which Bradshaw (1987) names cross-flow and identifiable downstream vortices, respectively. The translatory part is mainly pressure-induced, whereas the circulatory part is independent of the pressure field. The downstream component of the vorticity vector

$$\omega_s = \frac{\partial v_z}{\partial n} - \frac{\partial v_n}{\partial z} \quad (3)$$

has the advantage of representing the cross-stream circulation by a scalar, instead of a vector field. Therefore, the downstream vorticity balance is a good basis for analysis. The corresponding equation is obtained by cross-differentiation of equations (1) and (2), thus eliminating the pressure,

$$\begin{aligned}
\frac{\partial \omega_s}{\partial t} = & - \left(\frac{1}{1+n/R} v_s \frac{\partial \omega_s}{\partial s} + v_n \frac{\partial \omega_s}{\partial n} + v_z \frac{\partial \omega_s}{\partial z} \right) \\
& + \frac{1}{1+n/R} \omega_s \frac{\partial v_s}{\partial s} + \left[\omega_n \frac{\partial v_s}{\partial n} + \omega_z \frac{\partial v_s}{\partial z} + \frac{1}{1+n/R} \frac{v_n \omega_s}{R} - \frac{1}{1+n/R} \frac{v_s \omega_n}{R} \right] - \frac{1}{1+n/R} \frac{\partial}{\partial z} \left(\frac{v_s'^2}{R} \right) \\
& + \frac{\partial^2}{\partial z \partial n} (\overline{v_n'^2} - \overline{v_z'^2}) + \frac{1}{1+n/R} \frac{1}{R} \frac{\partial \overline{v_n'^2}}{\partial z} + \left\{ \frac{1}{1+n/R} \frac{\partial^2}{\partial z^2} - \frac{\partial}{\partial n} \left(\frac{1}{1+n/R} \frac{\partial}{\partial n} \right) \right\} [(1+n/R) \overline{v_n' v_z'}] \\
& + \frac{\partial}{\partial z} \left(\frac{1}{1+n/R} \frac{\partial \overline{v_s' v_n'}}{\partial s} \right) - \frac{\partial}{\partial n} \left(\frac{1}{1+n/R} \frac{\partial \overline{v_s' v_z'}}{\partial s} \right) \\
& + v \left(\nabla^2 \omega_s + \frac{2}{(1+n/R)^2} \frac{1}{R} \frac{\partial \omega_n}{\partial s} - \frac{1}{(1+n/R)^2} \frac{1}{R^2} \omega_s \right) \tag{4}
\end{aligned}$$

in which the n - and z -components of the vorticity vector are defined as:

$$\omega_n = \frac{\partial v_s}{\partial z} - \frac{1}{1+n/R} \frac{\partial v_z}{\partial s} \quad \text{and} \quad \omega_z = \frac{1}{1+n/R} \frac{\partial v_n}{\partial s} - \frac{\partial v_s}{\partial n} - \frac{1}{1+n/R} \frac{v_s}{R} \tag{5}$$

Without pretending mathematical rigour, this equation can be interpreted as follows in physical terms (e.g. Perkins 1970, Demuren & Rodi 1984, Bradshaw 1987, Nezu & Nakagawa 1993). The terms $v_n \partial \omega_s / \partial n + v_z \partial \omega_s / \partial z$ in the right-hand-side of the first line represent the advective transport of downstream vorticity by the cross-stream motion (v_n, v_z). This mechanism does not generate or dissipate ω_s , but redistributes it over the cross-section. The $\omega_s \partial v_s / \partial s$ -term in the second line represents amplification of ω_s due to vortex stretching. The terms in square brackets in the second line represent skewing-induced vorticity redistribution by quasi-inviscid deflection of existing mean vorticity $\bar{\omega}(\omega_s, \omega_n, \omega_z)$. Skewing-induced vorticity corresponds to Prandtl's circulation of the first kind (Prandtl 1942, p.130-134). By substitution of the definitions (3) and (5), these terms can be transformed into:

$$- \frac{1}{1+n/R} \frac{\partial}{\partial z} \left(\frac{v_s^2}{R} \right) + \frac{1}{1+n/R} \frac{v_n \omega_s}{R} + \left[\frac{1}{1+n/R} \frac{\partial v_n}{\partial s} \frac{\partial v_s}{\partial z} - \frac{\partial v_z}{\partial s} \frac{\partial}{\partial n} \left(\frac{1}{1+n/R} v_s \right) \right] \tag{6}$$

showing terms accounting for downstream non-uniformities (the $\partial/\partial s$ -terms in square brackets), a curvature-induced term with $v_n \omega_s / R$, and a term associated with the centrifugal force, $-v_s^2 / R$. Apparently, skewing-induced vorticity mainly results from the centrifugal force.

Apart from the mean centrifugal force, the second line of equation (4) also includes a turbulence-related centrifugal force term. The third line in equation (4) represents the influence of the cross-stream turbulent stress components, $\overline{v_n'^2}$, $\overline{v_z'^2}$ and $\overline{v_n' v_z'}$, on the

vorticity field. Globally, vorticity is dissipated by these turbulent stresses. In certain regions of the flow domain, however, they can generate mean vorticity (see below).

The terms in the fourth line of equation (4), as well as the $\partial/\partial s$ -terms in the first and second line relate to the downstream non-uniformity of the flow. They vanish for axisymmetric curved flow (defined by $\partial/\partial s = 0$), whence they are not characteristic of the aspects of curved flow considered herein. The last line represents the dissipation by the molecular viscosity. In the next section, the physical meaning of the various terms/mechanisms in the downstream vorticity equation will be analysed for axisymmetric curved flow (also see figure 2 below).

2.2 Current state of knowledge

The centre-region cell and the outer-bank cell are caused by different mechanisms. They will therefore be treated separately.

2.2.1 Centre-region cell

The centre-region cell has amply been investigated in the past, with Boussinesq (1868) and Thomson (1876) as pioneers. Its formation is usually explained as follows (see figure 2(a)). The centrifugal force $-v_s^2/R$ in a bend tends to move the fluid particles in outward direction and leads to a set-up (superelevation) of the water surface against the outer bank. This superelevation generates an inward directed pressure gradient $-\rho^{-1}\partial p/\partial n$ that globally balances the centrifugal force. Whereas this pressure gradient is constant over the depth (assuming hydrostaticity), the centrifugal force has a pronounced vertical structure. It is the local imbalance between the two that drives the centre-region cell. In the central part of the centre-region cell, where the vertical velocity is negligible, this mechanism can be represented by the simplified transversal momentum equation (cf. equation (1)),

$$0 = \frac{1}{1 + \eta/R} \frac{v_s^2}{R} - \frac{1}{\rho} \frac{\partial p}{\partial n} - \frac{\partial \overline{v_n' v_z'}}{\partial z} + \nu \nabla^2 v_n \quad (7)$$

or by the equivalent simplified downstream vorticity equation (cf. equations (4) through (6)),

$$0 = -\frac{1}{1 + \eta/R} \frac{\partial}{\partial z} \left(\frac{v_s^2}{R} \right) + \frac{\partial^2 \overline{v_n' v_z'}}{\partial z^2} + \nu \nabla^2 \omega_s \quad (8)$$

Equation (8) expresses the balance between the vorticity generation by the centrifugal force term and the vorticity dissipation by the turbulent shear stress $\overline{v_n' v_z'}$ and the molecular viscosity. The mechanism is similar in laminar and turbulent curved flow. In turbulent flow, the vertical profile of the transversal velocity in the central part of the centre-region cell can be solved from either of the above equations, by modelling the turbulent shear stress with an eddy-viscosity model and assuming vertical profiles for the downstream velocity and the eddy viscosity.

Without loss of generality, the downstream velocity can be written as the product of its depth-averaged value, U_s , and a given vertical profile function, typically the straight-

uniform-flow profile. If the eddy viscosity is taken proportional to $U_s H$, with H denoting the water depth in the channel axis, the above equations show that the strength of the centre-region cell must be proportional to H/R . In fact, the cross-stream velocity is treated here as a first-order perturbation to the downstream velocity, ignoring higher-order feedback. This is why such models are called linear. Linear models for the centre-region cell have been proposed among others by Rozovskii (1957), Engelund (1974), Kikkawa, Ikeda & Kitagawa (1976), de Vriend (1977), Falcon Ascanio & Kennedy (1983) and Johannesson & Parker (1989). Kalkwijk & de Vriend (1980) and Ikeda, Yamasaka & Kennedy (1990) proposed basically similar models that are valid all over the cross-section.

These linear models only give good results for very mildly curved bends, but overestimate the strength of the centre-region cell for moderately to strongly curved bends. Experimental data for strongly curved flow that illustrate this deficiency of linear models have been reported for flow over a horizontal bottom (de Vriend 1981a, Booij & Tukker 1996, Blanckaert & Graf 2001b), as well as for flow over a developed bottom topography (Blanckaert 2001a). It is a consequence of neglecting the feedback between the downstream velocity and the centre-region cell, i.e. the assumption of a straight-flow v_s -profile in equations (7) and (8) (cf. de Vriend 1981a). Advective momentum transport by the centre-region cell deforms the v_s -profiles, by decreasing the velocities in the upper part of the water column and increasing them in the lower part (Blanckaert & Graf 2002). For strong curvatures, the maximum velocity even occurs in the lower part of the water column, as is also the case in the experiment presented herein (cf. figures 4(a,c)). This deformation of the v_s -profile reduces the vertical gradient of the centrifugal force, $(\partial/\partial z)(v_s^2/|R|)$, which, according to equation (8), is the driving mechanism for the cross-stream circulation.

Yeh & Kennedy (1993) gave another description of this feedback mechanism, based on the principle of conservation of moment-of-momentum. This conservation law, however, can formally be derived from the mass and momentum balances, whence it should not add any new information. Blanckaert (2001b, 2002b) and Blanckaert & Graf (2001c) propose a non-linear model that accounts for this feedback. Similar to the linear models, a vertical profile of the eddy viscosity is assumed. However, instead of prescribing a straight-flow v_s -profile, they calculate the deformed v_s -profile from a simplified downstream momentum equation that accounts for advective momentum redistribution by the centre-region cell. This deformed v_s -profile is subsequently inserted into equation (7), yielding the vertical profile of the transversal velocity in the central part of the centre-region cell. This model compares rather well with experimental data for moderately to strongly curved flow over a horizontal bed (Blanckaert 2001b, 2002b), as well as over a developed bed topography (Blanckaert & Graf 2002).

Although this comparison with data is promising, it is not clear to what extent the non-linear model captures all relevant mechanisms underlying the formation of the centre-region cell. Especially the effects of the neglected advective transport terms in equations (7) and (8) and the rather basic modelling of turbulence need further investigation.

2.2.2 *Outer-bank cell*

Outer-bank cells have often been observed in curved turbulent flow and are known to play an important role with respect to the stability of the outer bank (Bathurs, Thorne & Hey 1979, de Vriend 1981a,b, Christensen et al. 1999, Blanckaert & Graf 1999, 2002). Despite this importance, little is known about the underlying mechanisms and the conditions under which these cells occur. This is to be attributed to the difficulty of accurately measuring the low velocities and the turbulent stresses involved (further see Blanckaert and Graf 2001a). Both skewing-induced and turbulence-induced vorticity generation must be expected to play a role. Similar cells have been observed in curved laminar flow and in straight turbulent flow, which can be seen as asymptotic cases, each showing one of the vorticity-generating mechanisms in isolation. In curved laminar flow, vorticity is exclusively skewing-induced (centrifugal force), whereas in straight turbulent flow it is exclusively turbulence-induced. Before considering curved turbulent flow, the literature on either of these asymptotic cases will be reviewed.

2.2.2.1 Curved laminar flow

The control parameter of outer-bank cell formation in curved laminar flow is the Dean number, defined as the product of the Reynolds number and the square root of a curvature ratio, e.g. $De = Re.(H/R)^{0.5}$, or $De = Re.(B/R)^{0.5}$. Numerical investigations have been done by Cheng, Lin & Ou (1976), de Vriend (1981b) and Winters (1987) for the case of axisymmetric curved flow ($\partial/\partial s = 0$). They show that, when increasing the Dean number, the outer-bank cell suddenly comes into existence at one critical value of De and suddenly disappears again at another critical value. Both critical Dean numbers depend on the curvature ratio, H/R , and the aspect ratio, B/H . As described before for the centre-region cell, the v_s -profiles in curved flow are stronger deformed as the curvature increases, and the driving centrifugal term $(\partial/\partial z)(v_s^2/|R|)$ in the vorticity equation correspondingly decreases. The outer-bank cell comes into existence when the v_s -profiles are so strongly deformed that the driving term changes sign in the upper part of the water column (see figure 2(a)). Physically, the Dean number can be interpreted as the ratio between the centrifugal term, which favours the outer-cell formation, and the molecular dissipation, which opposes it. For the curved flows investigated in these numerical models, the outer-bank cell was only slightly weaker than the centre-region cell. These numerical results have been confirmed by an experimental investigation of the flow in a 180° curved duct by Hille, Vehrenkamp & Schulz-Dubois (1985). However, they found the outer-bank cell to be much weaker than the centre-region cell in most of the bend, and only to pick up beyond 120°. All investigations indicate an outward shift of the core of maximum velocity with increasing Dean number within the single-cell range. When the outer-bank cell exists, the core of maximum velocity is found further away from the outer bank, near the separation point between the two cells. Apparently, the outer-bank cell keeps the downstream velocity maximum away from a steep outer bank, thus providing a natural protection for it.

Downstream vorticity equation (4/6) for axisymmetric curved flow:

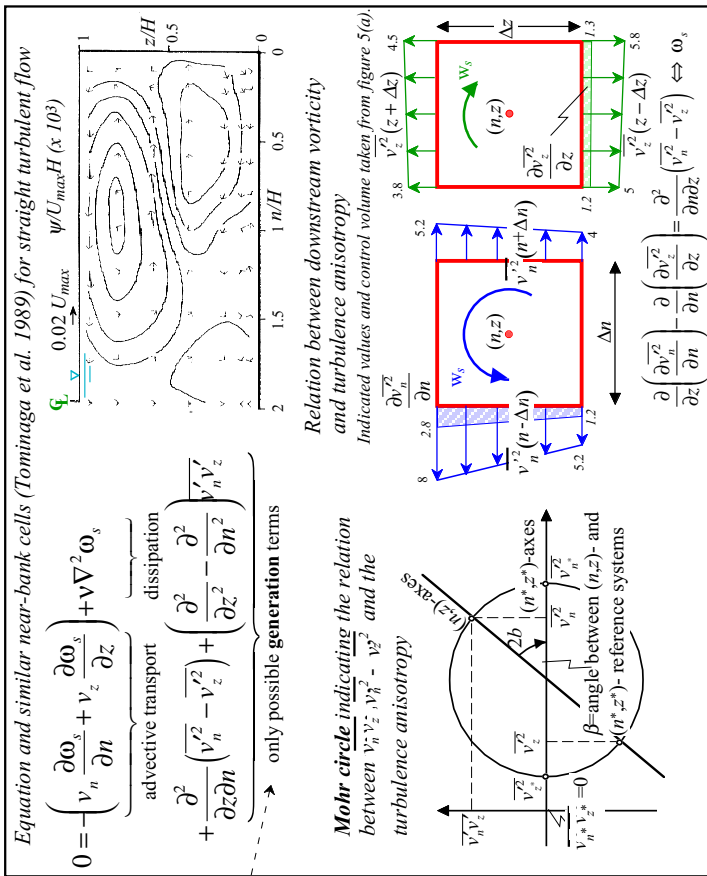
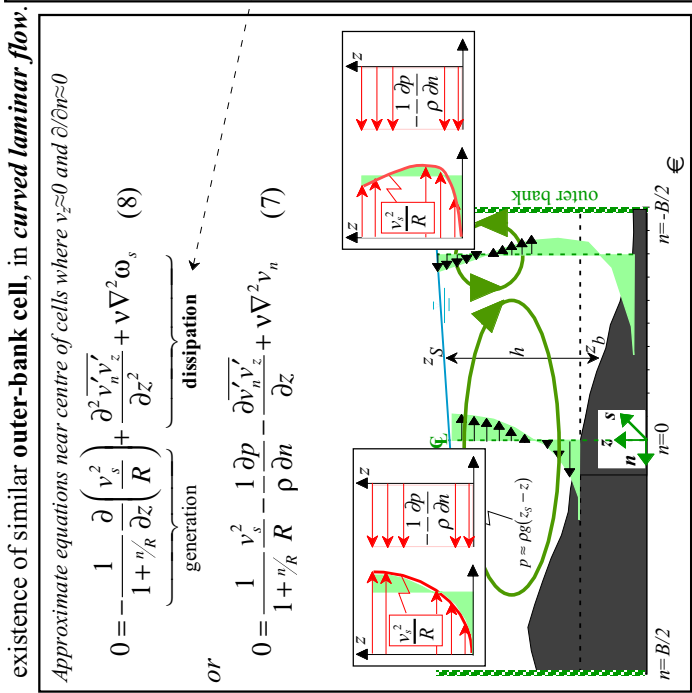
$$0 = - \left(v_n \frac{\partial \omega_s}{\partial n} + v_z \frac{\partial \omega_s}{\partial z} \right) + \frac{1}{1 + \eta/R} \frac{\partial \omega_s}{\partial z} + \frac{1}{1 + \eta/R} \frac{\partial}{\partial z} \left(\frac{v_s^2}{R} + \frac{v_z^2}{R} \right) + \frac{\partial^2}{\partial z^2} (v_n^2 - v_z^2) + \frac{1}{1 + \eta/R} \frac{\partial}{\partial z} \left(\frac{v_n^2}{R} - \frac{v_z^2}{R} \right) + \frac{1}{1 + \eta/R} \frac{\partial}{\partial n} \left(\frac{v_n^2}{R} - \frac{v_z^2}{R} \right) + v \nabla^2 \omega_s - \frac{1}{(1 + \eta/R)^2} \frac{\partial}{\partial n} \left(\frac{v_n^2}{R} - \frac{v_z^2}{R} \right) \omega_s$$

Centrifugal term:

- main mechanism for generation of **centre-region cell**
- unique vorticity generation mechanism, responsible for existence of similar **outer-bank cell**, in **curved laminar flow**.

Cross-stream turbulence terms:

- unique vorticity generation mechanism, responsible for existence of similar **near-bank cells**, in **straight turbulent flow**.



How do both terms behave and interact in curved turbulent flow ?

a b Figure 2: Physical meaning of terms in the downstream vorticity equation (4/6). (a) Centrifugal term; (b) Cross-stream turbulence terms.

2.2.2.2 Straight turbulent flow

The near-bank cells in straight uniform open-channel flow, as well as the corresponding downstream vorticity equation, are shown in figure 2(b). Prandtl (1942) suggested that these near-bank circulation cells be caused by turbulence, and Einstein & Li (1958) showed with a rigorous analysis that gradients of turbulent stresses generate the corresponding downstream vorticity. Ever since, the role of the cross-stream turbulence, $\overline{v_n'^2} - \overline{v_z'^2}$ and $\overline{v_n'v_z'}$, in the downstream vorticity equation (4) has been investigated extensively, in experiments as well as in numerical models.

Due to the difficulty to accurately measure the turbulent stresses, most experiments have been carried out in air flow (closed conduits) and did not include measurements of $\overline{v_n'v_z'}$ (except Perkins 1970). Demuren & Rodi (1984) summarize the experimental findings of Brundett & Baines (1964), Gessner & Jones (1965), Perkins (1970) and Gessner (1973) as follows. The dominant terms in the downstream vorticity equation include $\overline{v_n'^2} - \overline{v_z'^2}$ and $\overline{v_n'v_z'}$, which are almost equal and of opposite sign. The difference is of the same order of magnitude as the advective terms $v_n \partial \omega_s / \partial n + v_z \partial \omega_s / \partial z$ and drives the near-bank cells. Nezu & Nakagawa (1984) and Nezu, Nakagawa & Tominaga (1985) analysed the downstream vorticity equation in airflow experiments in rectangular ducts, whereas Tominaga et al. (1989) investigated it for open-channel flow experiments with different boundary roughnesses, aspect ratios and sidewall inclinations. They could not measure the turbulent shear stress $\overline{v_n'v_z'}$ and suggest that $\overline{v_n'^2} - \overline{v_z'^2}$ be the source term for the cross-stream circulation, and $\overline{v_n'v_z'}$ a dissipating sink term, as summarized by Nezu & Nakagawa (1993). Bradshaw (1987), on the other hand, states that the relative contributions of $\overline{v_n'^2} - \overline{v_z'^2}$ and $\overline{v_n'v_z'}$ only depends on the orientation of the n - and z -axis. This is illustrated by representing the cross-stream turbulence on a Mohr circle (figure 2(b)). When choosing the (n^*, z^*) -coordinates along the principal axes of the turbulent stress tensor, the cross-stream turbulent shear stress vanishes, i.e. $\overline{v_{n^*}'v_{z^*}'} = 0$, and the difference between the normal stresses, $\overline{v_{n^*}'^2} - \overline{v_{z^*}'^2}$, is maximum. If this quantity differs from zero, the cross-stream turbulence is anisotropic. Figure 2(b) also illustrates how such anisotropic turbulence contributes to the vorticity balance by exerting a torque on the fluid (also see Perkins 1970). The vorticity equation does not indicate, however, whether the cross-stream turbulence terms generate or dissipate mean downstream vorticity ω_s . For the case of straight uniform flow, they must contribute to the generation of ω_s since the vorticity equation does not contain other generation terms. Turbulence-generated vorticity corresponds to circulation of Prandtl's second kind (Prandtl 1942, p.130-134).

Nezu & Nakagawa (1993) highlighted the importance of the water surface, by comparing the turbulence-generated cross-stream circulation cells in open channels with those in curved ducts. Furthermore, they schematise in a very detailed and complete way the interactions between the cross-stream circulation, the cross-stream turbulence, the distributions of the mean flow and the boundary shear stress, the boundary properties, the channel geometry, etc.

Naot & Rodi (1982) and Demuren & Rodi (1984) claim that the turbulence-generated near-bank cells in straight turbulent flow cannot be simulated with linear eddy viscosity models, i.e. models assuming a linear stress-strain relationship. They succeed in simulating them with an Algebraic Stress Model. Speziale (1987) attributes this failure of linear eddy viscosity models (such as the linear $k-\varepsilon$ model) to their inability to represent correctly the turbulent normal stresses and proposes non-linear turbulence models ($k-\varepsilon$ and $k-l$ models) that are able to simulate the near-bank cells. Indeed, Colombini (1993) succeeds in simulating these cells with such a non-linear turbulence model. Kawahara & Tamai (1988) demonstrate mathematically that linear eddy viscosity models cannot simulate turbulence-induced cross-stream circulation.

Based on these experimental and numerical investigations and theoretical considerations, the following hypothesis concerning the formation of near-bank circulation cells in straight turbulent flow can be formulated. The advective transport redistributes vorticity over the cross-section, but is fundamentally unable to generate or dissipate vorticity. Hence, the cross-stream turbulent stresses, $\overline{v_n'^2} - \overline{v_z'^2}$ and $\overline{v_n'v_z'}$, have to account for both the generation and the dissipation of vorticity. Physically speaking, no distinction can be made between the role of the turbulent normal stresses $\overline{v_n'^2} - \overline{v_z'^2}$ and the role of the turbulent shear stress $\overline{v_n'v_z'}$, since their relative magnitudes uniquely depend on the orientation of the n - and z -axis. Locally, the difference between the terms including $\overline{v_n'^2} - \overline{v_z'^2}$ and $\overline{v_n'v_z'}$ is balanced by the advective transport terms. However, the mechanisms behind turbulence-generated vorticity and the physical explanation why linear turbulence models are unable to simulate the near-bank cells, whilst more complicated models are, require further investigation. These issues will be addressed further on in the paper.

2.2.2.3 Curved turbulent flow

The bi-cellular pattern of cross-stream circulation has often been observed in curved turbulent flow, in laboratory experiments (Mockmore 1943, Einstein & Harder 1954, Rozovskii 1957, Götz 1975, Choudhary & Narasimhan 1977, Siebert 1982, Booij 1985, Booij & Tukker 1996, Shiono & Muto 1998, Tominaga, Nagao & Nezu 1999), as well as in the field (Bathurst et al. 1979, Dietrich & Smith 1983, de Vriend & Geldof 1983). Yet, little is known about the mechanisms underlying it, nor about the conditions of its occurrence. Götz (1975) suggests a dependence on the aspect ratio, whereas Bathurst et al. (1979) suggest that the outer-bank cell occurs near steep banks, but not near shelving banks. In order to arrive at a quantitative criterion of occurrence, de Vriend (1981a) assumes the mechanisms to be the same as in curved laminar flow, where the outer-bank cell is generated by the centrifugal force only. He assumes the cross-stream turbulent stresses to act in a similar (dissipative) way as the molecular stresses in laminar flow, replacing the molecular viscosity in the Dean number by the depth-averaged turbulent eddy viscosity that is often used in straight uniform flow:

$$\langle v_t \rangle = 0.067 u_* H = 0.067 \sqrt{\frac{\tau_b}{\rho}} H = 0.067 \sqrt{C_f} UH = \frac{\kappa}{6} \sqrt{C_f} UH \quad (9)$$

Thus the turbulent Dean number becomes

$$De_t = \frac{6}{\kappa} \sqrt{C_f} \sqrt{\frac{H}{R}} \quad (10)$$

The curvature ratio H/R represents the driving centrifugal force whereas the friction factor C_f represents the opposing turbulent dissipation. From observations of the outer-bank cell in mildly curved bends, however, combined with the inability to simulate this pattern with fully three-dimensional numerical models with a linear turbulence closure, de Vriend concludes that the outer-bank cell cannot be explained from the centrifugal force only. Because the observed outer-bank cells in bends are stronger than in straight flows, they cannot be exclusively turbulence-generated, either. This led to the hypothesis that the outer-bank cell in curved turbulent flow is generated by the combined action of the centrifugal force (vortex-skewing) and turbulence. Christensen et al. (1999) carried out numerical simulations of the outer-bank cell with a linear $k-\varepsilon$ closure and with a Reynolds Stress Model. From the differences between the results they conclude that the outer-bank cell is not uniquely skewing-induced, but that turbulent vorticity-generation plays an important role. Jia et al. (2001) successfully simulated the outer-bank cell observed in the present experiment with a non-linear $k-\varepsilon$ closure.

From this literature review, it can be concluded that the isolated behaviour of the centrifugal term and the cross-stream turbulence terms is relatively well understood (figure 2). The insight into the physics of curved-flow turbulence and its interaction with the centrifugal force, however, needs further development.

2.3 Kinetic energy transfer between mean flow and turbulence

The above considerations on the downstream vorticity equation have shown that downstream vorticity is generated by the centrifugal force (skewing), and redistributed over the cross-section by the advective transport terms. To maintain the vorticity balance, there must be dissipation by the turbulent stresses. For the case of the near-bank cells in straight uniform flow, however, turbulent stresses are also responsible for the generation of vorticity. It is not a priori clear from the vorticity equation whether locally the turbulent stresses altogether tend to increase or decrease the mean vorticity.

By definition, the mean cross-stream motion (v_n, v_z) contains mean-flow kinetic energy, $(v_n^2 + v_z^2)/2$, whereas the cross-stream turbulent stresses correspond to cross-stream velocity fluctuations (v'_n, v'_z) and thus contain turbulent kinetic energy, $(\overline{v_n'^2} + \overline{v_z'^2})/2$. Hence, the exclusively turbulence-induced near-bank circulation cells in straight uniform flow require a transfer of kinetic energy from the turbulence to the mean flow.

Previous investigations on cross-stream circulation cells were limited to the vorticity equation (e.g. Perkins 1970, Demuren & Rodi 1984, Bradshaw 1987, Nezu & Nakagawa 1993), but further insight may be gained from looking into the transfer of kinetic energy between the mean flow and the turbulence. Terms representing this kinetic energy transfer appear with opposite signs in the dynamic equations for the mean-flow and the turbulent

kinetic energy. In the turbulent kinetic energy equation, they appear as (Hinze 1975, chapter 1-13):

$$\mathcal{P} = - \left[\left(\overline{v_s'^2} - \frac{2}{3} k \right) e_{ss} + \left(\overline{v_n'^2} - \frac{2}{3} k \right) e_{nn} + \left(\overline{v_z'^2} - \frac{2}{3} k \right) e_{zz} + 2 \overline{v_s'v_n'} e_{sn} + 2 \overline{v_s'v_z'} e_{sz} + 2 \overline{v_n'v_z'} e_{nz} \right] \quad (11)$$

in which the turbulent kinetic energy, k , and the strain rates, e_{jk} ($j,k=s,n,z$), are defined as (Batchelor 1970, p.600):

$$k = \frac{1}{2} (\overline{v_s'^2} + \overline{v_n'^2} + \overline{v_z'^2}) \quad (12)$$

$$e_{ss} = \frac{1}{1+n/R} \frac{\partial v_s}{\partial s} + \frac{1}{1+n/R} \frac{v_n}{R}, \quad e_{nn} = \frac{\partial v_n}{\partial n}, \quad e_{sn} = \frac{1}{2} \left(\frac{1}{1+n/R} \frac{\partial v_n}{\partial s} + \frac{\partial v_s}{\partial n} - \frac{1}{1+n/R} \frac{v_s}{R} \right)$$

$$e_{sz} = \frac{1}{2} \left(\frac{1}{1+n/R} \frac{\partial v_z}{\partial s} + \frac{\partial v_s}{\partial z} \right), \quad e_{nz} = \frac{1}{2} \left(\frac{\partial v_z}{\partial n} + \frac{\partial v_n}{\partial z} \right), \quad e_{zz} = \frac{\partial v_z}{\partial z} \quad (13)$$

Equation (11) indicates that the energy fluxes per unit mass take place through work done by the turbulent stresses as the mean flow deforms. The sum of these energy fluxes is (mostly) positive, i.e. from mean flow to turbulence; it is commonly called the production or generation \mathcal{P} of turbulent kinetic energy. Especially the sign of the kinetic energy transfer via the cross-stream turbulent stresses, $\overline{v_n'^2}$, $\overline{v_z'^2}$ and $\overline{v_n'v_z'}$, is expected to be important with respect to the turbulence-induced vorticity.

A comparison of these terms related to the cross-stream turbulence with the terms primarily related to boundary friction (the $\overline{v_s'v_z'}$ - and $\overline{v_s'v_n'}$ -terms) must give indications on their importance with respect to the total energy loss (equivalent to the total turbulence production) in a bend. This will be discussed later on in the paper.

Insight into the kinetic energy fluxes between mean flow and turbulence has important consequences for the numerical modelling of turbulence. Often, mixing coefficients are used to model the turbulent stresses. They are defined as the ratio between the deviatoric turbulent stresses $-(\overline{v_j'v_k'} - 2/3 \delta_{jk} k)$ and the corresponding strain rates e_{jk} :

$$v_{jk} = v_{kj} = - \frac{\overline{v_j'v_k'} - 2/3 \delta_{jk} k}{2e_{jk}} \quad (j,k=s,n,z) \text{ and } \delta_{jk} \text{ is the Kronecker symbol} \quad (14)$$

Note that these six mixing coefficients do not have the frame-indifferent characteristics of the Reynolds stress tensor $\overline{v_j'v_k'}$ or the strain rate tensor e_{jk} . Applying the definition of the mixing coefficients, the production of turbulent kinetic energy, equation (11), can be rewritten as:

$$\mathcal{P} = 2(v_{ss} e_{ss}^2 + v_{nn} e_{nn}^2 + v_{zz} e_{zz}^2 + 2v_{sn} e_{sn}^2 + 2v_{sz} e_{sz}^2 + 2v_{nz} e_{nz}^2) \quad (15)$$

The sign of the mixing coefficient v_{jk} indicates the sense of the corresponding kinetic energy flux. Applying a scalar eddy viscosity for turbulence closure implies that $v_{ss}=v_{nn}=v_{zz}=v_{sn}=v_{sz}=v_{nz}=v_t > 0$ and that all kinetic energy fluxes are definitely positive:

$$\mathcal{P} = 2\nu_t (e_{ss}^2 + e_{nn}^2 + e_{zz}^2 + 2e_{sn}^2 + 2e_{sz}^2 + 2e_{nz}^2) > 0 \quad (16)$$

This implies that kinetic energy is always transferred from the mean flow to the turbulence. By implication, when using a linear eddy viscosity concept the cross-stream turbulence terms in the downstream vorticity equation (4) are always dissipative. This means that this concept is not applicable to flows in which turbulence somehow contributes to the mean kinetic energy.

3 Present objectives

From the above review of the current state of knowledge it can be concluded that the mechanisms underlying the centre-region cell and the outer-bank cell are not yet fully understood. Research so far was mostly restricted to the downstream vorticity equation. Here we will carry out a simultaneous analysis of the downstream vorticity dynamics (cf. equations (4/6) and figure 6) and the kinetic energy transfer between mean flow and turbulence (cf. equation (11) and figures 7-8). This analysis will be based on the data resulting from the experiment described hereafter. It will concern the following questions:

- What are the relevant mechanisms behind the generation of the centre-region cell? Does the simplified vorticity equation (8), which is often used to model the centre-region cell, capture all relevant mechanisms? What are the roles of advective transport and turbulence?
- Can the hypothesis of de Vriend (1981a) and Christensen et al. (1999) that the outer-bank cell formation is associated with both skewing-induced and turbulence-induced vorticity be confirmed or rejected? What is the interaction between the two mechanisms?
- What is the role of the cross-stream turbulence terms, $\overline{v_n'^2} - \overline{v_z'^2}$ and $\overline{v_n'v_z'}$, in the generation of turbulence-induced vorticity? The availability of data on all turbulent stress components must enable investigating this role in further depth.
- To what extent does the cross-stream turbulence dissipate or generate vorticity? A simultaneous analysis of the downstream vorticity dynamics and the transfer of kinetic energy between mean flow and turbulence must give further insight at this point.
- What aspects are essential to the numerical modelling of strongly curved open-channel flow, and especially of the outer-bank cell?

Furthermore, this paper presents a detailed data set on strongly curved turbulent flow with a double pattern of cross-stream circulation cells.

4 Analysis of experimental data

4.1 The experiment

A separate paper (Blanckaert & Graf 2001a) has been dedicated to the presentation of the experimental set-up, the instrumentation, the measuring grids, the estimation of the experimental accuracy, the data treatment procedures and the distributions of the mean velocity components and the turbulent stress components. Here only features that are of particular relevance to the present analysis are repeated.

Flow measurements were performed in a laboratory flume of 0.4 m wide, consisting of a 2 m long straight approach reach, followed by a 120° bend to the left of constant curvature (radius 2 m). The initially horizontal sand bottom was deformed by the flow, via a process of so-called clear-water scour. Ultimately, the sediment transport vanished throughout and a bottom topography in static equilibrium with the flow was obtained (figure 3).

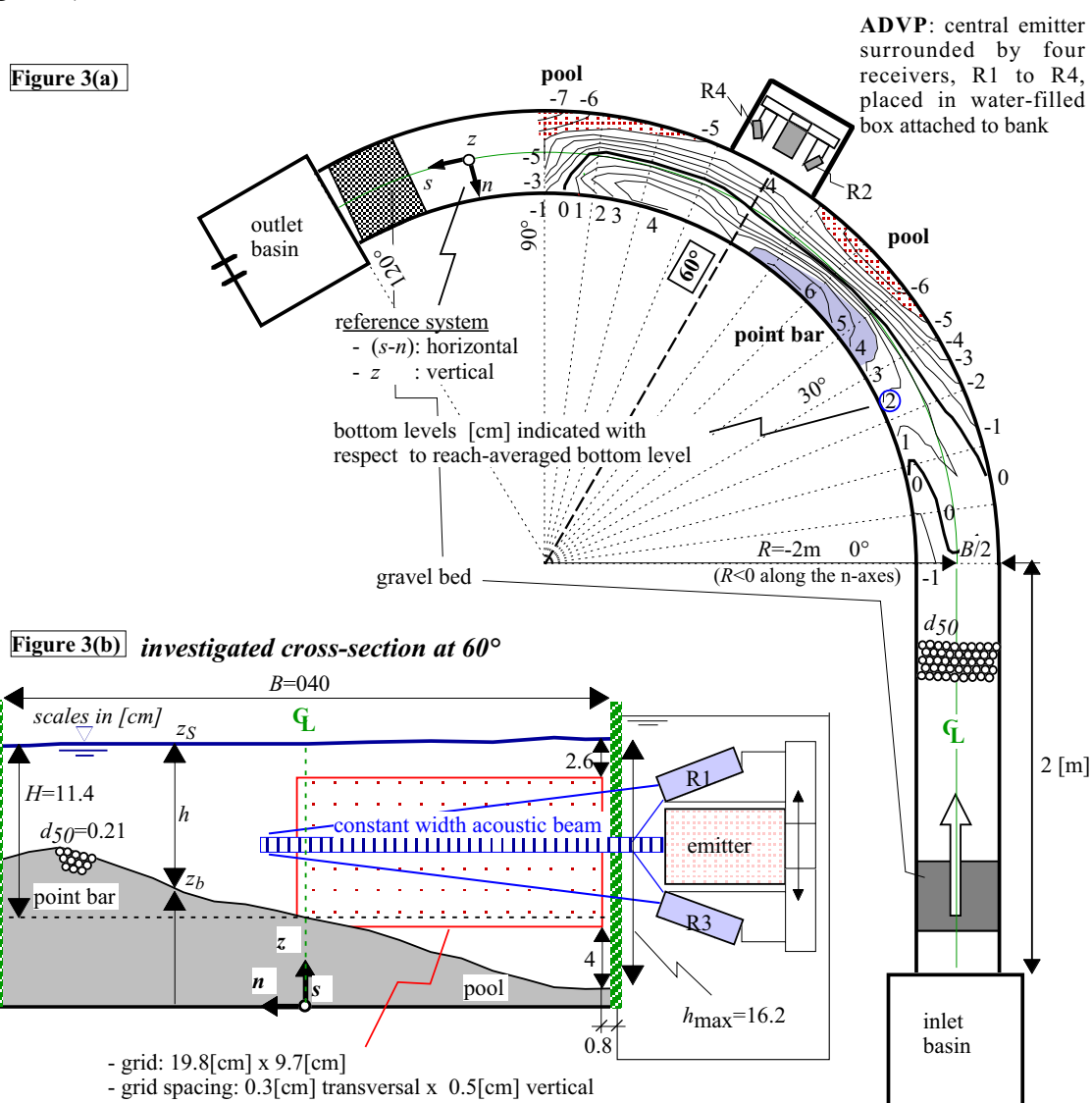


Figure 3: (a) Experimental set-up, bottom topography and reference system; (b) Measuring section at 60° and Acoustic Doppler Velocity Profiler (ADVP) set-up.

R [m]	B [m]	d_{50} [mm]	Q [l/s]	H [m]	S_s [‰]	U [m/s]	C_f [/]	Re [10 ³]	Re^* [/]	Fr [/]	R/B [/]	R/H [/]	B/H [/]
-2.0	0.40	2.1	17	0.11	1.89	0.38	0.008	42	70	0.36	5	17.9	3.6

R : centreline radius of curvature (negative along the n -axis)	C_f : friction factor (estimated by Blanckaert & Graf 2001a)
B : channel width	τ_b : bottom shear stress, $\tau_b/\rho = u_*^2 = C_f U^2$
d_{50} : median grain size diameter of the bed material	$Fr = U/(gH)^{1/2}$: overall Froude number
Q : flow discharge	$Re = UH/\nu$: overall flow Reynolds number
H : overall flow depth \approx depth at centreline	$Re^* = u_* k_s/\nu$: overall particle Reynolds number
S_s : overall water-surface slope at the centreline	ν : molecular viscosity
U : reach-averaged velocity	k_s : Nikuradse equivalent sand roughness

Table 1: Hydraulic conditions

Table 1 shows the hydraulic conditions. Clearly, this concerns a rather sharp bend, as is indicated by the parameter values $R/B = 5$ and $R/H = 17.9$ (B is the channel width, H is the reach-averaged water depth, which can be confounded with the depth at the channel axis in the investigated cross-section at 60°). With an aspect ratio $B/H = 3.6$, the flume is much narrower than typical natural open-channel bends. Yet, these ratios do occur in mountain rivers and man-made channels. Moreover, in a wide bend with a fully-developed bottom topography, the shallow point bar is usually wide and most of the time the flow is concentrated in the deepest part of the cross-section, where a significant transversal bottom slope exists (figure 20 in Odgaard 1984, figure 8.2 in Dietrich 1987). The flow in the deepest part of the cross-section in the experiment is considered to be representative of the flow in the deeper part of wider natural bends.

Non-intrusive velocity measurements, using an Acoustic Doppler Velocity Profiler (ADVP), were made in the outer half of the cross-section located at 60° from the bend entrance. The ADVP was mounted in a water-filled box attached to the outer bank. The measuring section, the measuring grid and the ADVP-configuration are shown in figure 3(b).

The ADVP simultaneously measures profiles along its main axis of the three quasi-instantaneous velocity components $v_j(t)$, from which the mean-velocity components v_j and the turbulent stress components $\overline{v_j v_k}$ ($j, k = s, n, z$) can be derived. By traversing the ADVP vertically, radial profiles covering about half the channel width were taken every $\Delta z = 0.5$ cm. Detailed information on the working principle of the ADVP, its experimental accuracy and its comparison with other velocity meters can be found in Lemmin & Rolland (1997), Hurther & Lemmin (1998, 2001), Blanckaert & Graf (2001a) and Blanckaert & Lemmin (2002). The accuracy of the mean-velocity measurements is typically better than 4%, the accuracy of the turbulent normal stresses is estimated as better than 10% and the accuracy of the turbulent shear stresses is slightly better than that of the turbulent normal stresses. In the lower 20% of the water column, however, the accuracy of the turbulence measurements is reduced, due to the important mean-velocity gradients in the measuring volume (effect of spatial averaging).

The present analysis requires the evaluation of the various terms in the vorticity equation (4/6), as well as the kinetic energy fluxes between mean flow and turbulence (equation (11)). These equations include derivatives of the measured quantities, which are difficult to evaluate directly from the raw data, because of the experimental scatter. Therefore, the experimental data have first been smoothed using two-dimensional splines with weight

functions (de Boor 1978, Ch.14, 17). Nonetheless, the results are rather inaccurate and interpretations should therefore be restricted to order-of-magnitude considerations. Thanks to the weight functions, the measured data can be extended outside the measuring grid by imposing physical boundary conditions (such as the no-slip condition at rigid boundaries, no shear parallel to the water surface, etc.). Wherever this has been done, it is indicated in the relevant figures. For further information on the smoothing technique (including an example), the extrapolations outside the measuring grid and the estimated accuracy, reference is made to Blanckaert & Graf (2001a).

4.2 Experimental results

The vectorial representation of the measured cross-stream velocity field, (v_m, v_z) , normalised by the overall mean velocity $U = Q/(BH)$, is shown in figure 4(d). The centre-region cell reflects the ‘classical’ helical motion that is characteristic of flow in bends. The magnitude of the velocities involved is typically 10% of U . A region with weaker cross-stream velocities is found close to the outer bank. In the upper part of this outer-bank region an additional circulation cell can be observed, with a sense of rotation opposite to the one of the centre-region cell. The velocities in this region are typically 3 % of U .

The circulatory part of the cross-stream motion is expressed in the downstream vorticity, ω_s , which is shown in figure 4(e). The centre-region cell and the outer-bank cell, separated by the $\omega_s=0$ -contour, are clearly visible in the vorticity field. The vorticity increases towards the ‘eye’ of either cell and reaches maximum magnitudes of about $0.9 U/H$ near the eye of the centre-region cell and $-0.22 U/H$ near the eye of the outer-bank cell. Close to the outer-bank, ω_s assumes positive values, which represent the boundary layer near the bank, rather than an identifiable vortex.

The distribution of the normalized downstream velocity component, v_s/U , is given in figure 4(a). Its depth-averaged value is nearly constant over most of the measuring area: $U_s/U \approx 1.35$ (figure 4(b)), which means that the depth-averaged velocity there is well above the overall mean velocity. The same figure shows that the distribution of the normalized unit discharge, $U_s Bh/Q$, with h denoting the local water depth, is concentrated in the deep outer part of the cross-section. Integration of this profile shows that about 80% of the discharge passes through the investigated outer half of the cross-section. The core of maximum velocity, marked by \otimes in figures 4(a-b), is found near the transition between the two circulation cells. Figure 4(c) compares some measured v_s/U_s -profiles with a logarithmic profile for a friction factor $C_f = 0.008$, which corresponds to the value estimated by Blanckaert & Graf (2001a) in the experiment. The profiles shown are averaged over the outer-bank region (0-6 cm from the outer bank), the transition zone (6-12 cm) and the centre region (12-20 cm). The profiles in these three regions are rather similar: the measured velocities are well below the logarithmic profile in the upper part of the water column and well above it in the lower part. This deformation of the v_s/U_s -profiles is substantial, to the extent that the velocity maximum is found in the lower part of the water column. By analysing the downstream momentum equation on the basis of the measured data, Blanckaert & Graf (2002) show that this redistribution of the downstream velocity is mainly due to advective momentum transport by the two cross-stream circulation cells.

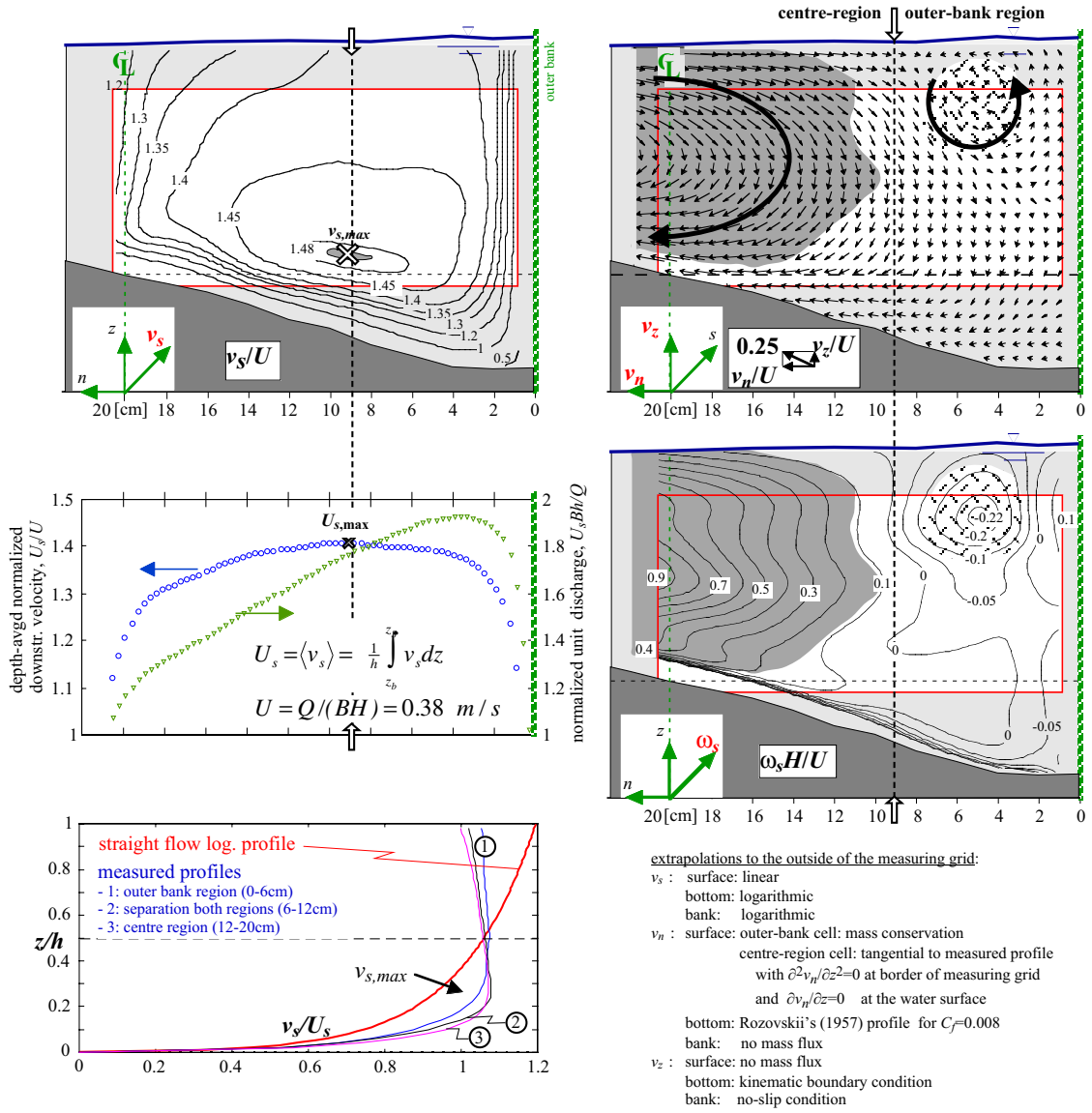


Figure 4(a): Isolines of normalized downstream velocity, v_s/U .

Figure 4(b): Normalized depth-averaged downstream velocity, U_s/U , Normalized unit discharge, $(U_s Bh)/Q$.

Figure 4(c): Vertical profiles of measured downstream velocity, v_s/U_s .

Figure 4(d): Vector representation of normalized cross-sectional motion, $(v_n, v_z)/U$.

Figure 4(e): Isolines of normalized downstream vorticity, $\omega_s H/U$.

Figure 4(f): Extrapolation outside of measuring grid and estimation of accuracy.

Figures 5(a-b) show the distributions of the turbulence properties $\overline{v_n'^2} - \overline{v_z'^2}$ and $\overline{v_n' v_z'}$, which play an important role in the vorticity equation. They have been normalized by the characteristic shear velocity in the measuring section, $u_{*,60}$, which is defined as $u_{*,60} = \sqrt{gR_h(-\partial z_{s,60}/\partial s)}$, in which $-\partial z_{s,60}/\partial s$ is the downstream water-surface gradient in the centreline and R_h is the hydraulic radius. In the experiment, this shear velocity amounted to 0.045 m/s. Near the flow boundaries, the velocity fluctuations perpendicular to the boundary are hindered by geometrical constraints. Near the bottom and near the

water surface, this concerns the vertical fluctuations, so there $\overline{v_n'^2} > \overline{v_z'^2}$. In the region near the outer bank, the transversal fluctuations are hindered and $\overline{v_n'^2} < \overline{v_z'^2}$. The damping of the fluctuations by the water surface is only slightly weaker than that by the outer bank, and the line where $\overline{v_n'^2} = \overline{v_z'^2}$, drawn in figure 5(a), only slightly deviates from the bisector of the upper right corner of the flow domain. There, the pattern of $\overline{v_n'^2} - \overline{v_z'^2}$ is nearly anti-symmetrical about this line. Similar patterns of $\overline{v_n'^2} - \overline{v_z'^2}$ have been observed in experiments with straight uniform flow (Nezu et al. 1985, for airflow in a duct, Tominaga et al. 1989, for open-channel flow). Nezu & Nakayama (1998, 1999) have shown that the damping by the water surface depends on the Froude number. For low Froude numbers, like in the present experiment, the water surface almost completely dampens the nearby vertical fluctuations, whereas this damping gets less as the Froude number increases.

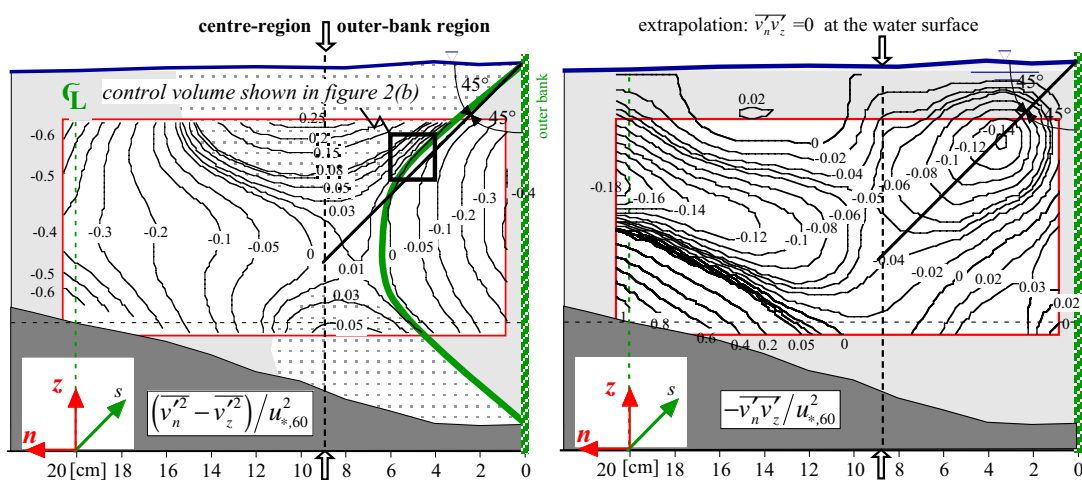


Figure 5: Isolines of normalized (a) turbulent normal stress difference, $(\overline{v_n'^2} - \overline{v_z'^2}) / u_{*,60}^2$; (b) turbulent shear stress, $-\overline{v_n'v_z'} / u_{*,60}^2$.

The turbulent shear stress $\overline{v_n'v_z'}$ seems to be correlated with the circulation cells. Even though the cells have a different sense of rotation, this turbulent shear stress does not change sign. Near the ‘eye’ of the weaker outer-bank cell, the absolute value is only slightly less than near the ‘eye’ of the centre-region cell. The pattern of $\overline{v_n'v_z'}$ is nearly symmetrical about the bisector of the upper right corner of the flow domain, which again indicates a similar influence of the water surface and the outer bank on the turbulent stresses. A similar near-corner pattern of $\overline{v_n'v_z'}$ has been measured by Nezu & Nakagawa (1984) in the case of air-flow in a duct. It is to be expected that the influence of the water surface on $\overline{v_n'v_z'}$ also depends on the Froude number. In the region dominated by bottom friction, this stress component is primarily associated with the transversal component of the bottom shear stress. It is positive there, since the bottom shear stress is directed towards the centre of curvature, so in the positive n -direction.

4.3 Analysis of the centre-region cell

4.3.1 Observations (Figures 4(e), 6 and 7)

As mentioned before, there is an important feedback between the downstream velocity and the centre-region cell. Skewing of existing mean vorticity by the centrifugal force, $-v_s^2/R$, is the principal generation mechanism of the centre-region cell. Integrated over the water depth, the centrifugal term in the vorticity equation (4/6) is always positive, which complies with the sense of rotation of the centre-region cell. In curved flow, advective momentum transport by the centre-region cell deforms the vertical v_s -profiles by decreasing v_s in the upper part of the water column and increasing it in the lower part. This is why the velocity maximum in the present experiments is found in the lower part of the water column (figure 4(c)). As a consequence, the centrifugal term $-(\partial/\partial z)(v_s^2/R)$ in the vorticity equation is negative in a significant part of the water column (figure 6(a)), opposite to the observed sense of rotation of the centre-region cell.

The advective transport terms in the vorticity equation, $v_n \partial \omega_s / \partial n + v_z \partial \omega_s / \partial z$, are of the same order of magnitude as the centrifugal term. They redistribute the vorticity over the cross-section. The positive values in the upper part of the water column (figure 6(b)) compensate for the negative centrifugal term (figure 6(a)). This explains why the centre-region cell extends over the entire water depth, instead of splitting into two cells on top of each other. The advective transport is generally dominated by the transversal contribution, $v_n \partial \omega_s / \partial n$. The vertical contribution, which is not shown separately in figure 6, is usually much smaller.

The role of the turbulent stress $\overline{v'_n v'_z}$ on the centre-region cell is complex. The $\overline{v'_n v'_z}$ -terms are of leading order in the vorticity equation (figure 6(d), cf. equation (8)). Close to the bottom, $\overline{v'_n v'_z}$ is associated with the transversal component of the bottom shear stress. Hence, the $\overline{v'_n v'_z}$ -term in the vorticity equation opposes the observed vorticity in this layer, and mean-flow vorticity is dissipated into turbulence there (figure 7(b)). Just above that near-bottom layer, but still in the lower part of the water column, the $\overline{v'_n v'_z}$ -term favours the observed vorticity. Analysis of the energy equation shows that a weak kinetic energy flux from turbulence to the mean flow occurs via $\overline{v'_n v'_z}$. In this zone, the centrifugal and $\overline{v'_n v'_z}$ -terms compliant with the existing vorticity are mainly balanced by the opposed advective transport term. As mentioned before, the turbulence measurements in the lower 20% of the water column are less accurate and should therefore be interpreted with care. In most of the upper part of the water column, the $\overline{v'_n v'_z}$ -term opposes the observed vorticity and mean-flow kinetic energy is transferred to turbulence.

The $\overline{v_n'^2} - \overline{v_z'^2}$ -terms in the vorticity equation are smaller than the other terms, but they are not negligible (cf. figure 6(c)). In the upper part of the water column, their sign is opposite to that of the observed (positive) vorticity. In the lower part of the water column, the sign of these terms complies with the observed vorticity.

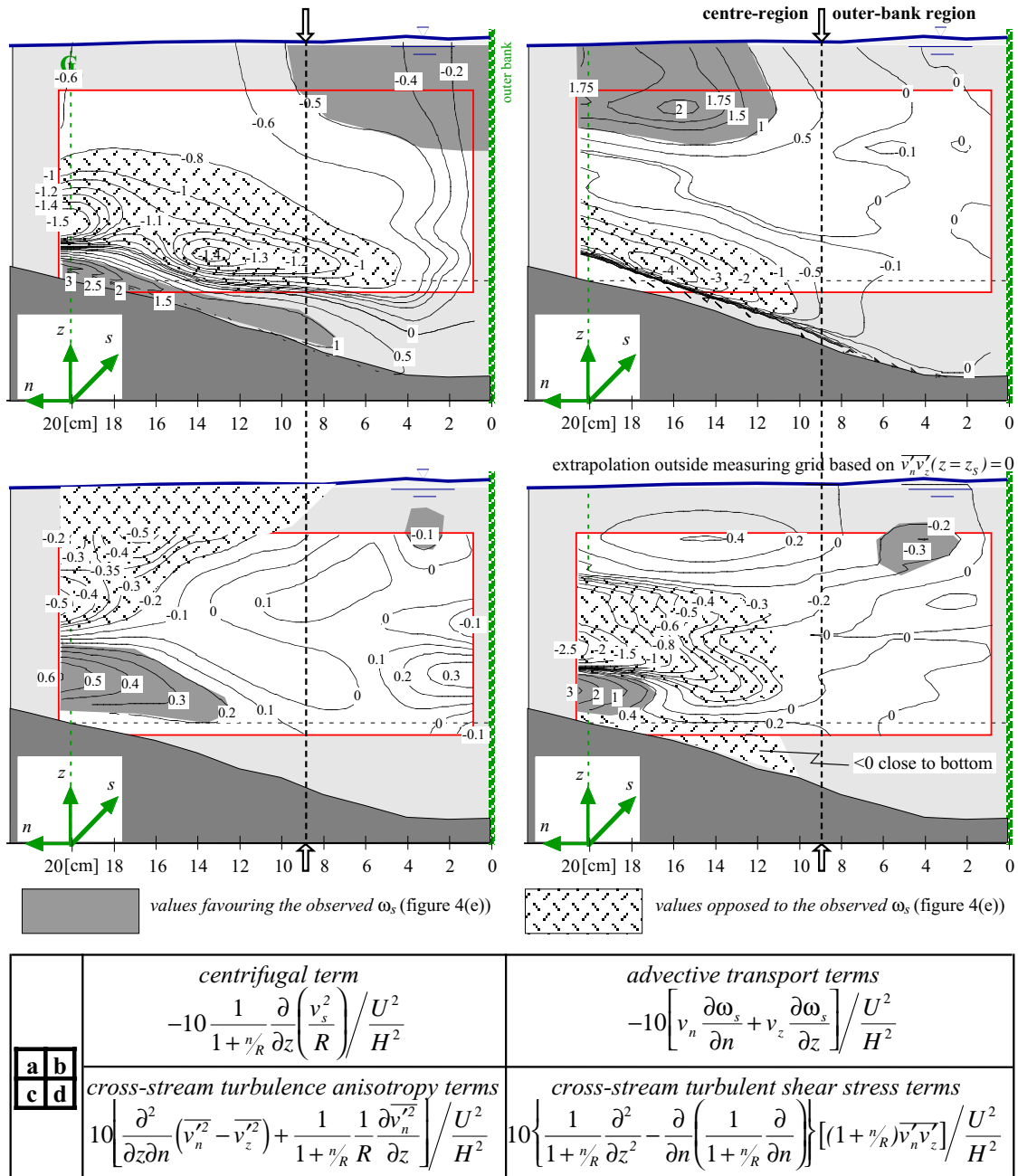


Figure 6: Isolines of normalized terms in downstream vorticity equations (4/6), multiplied by 10

4.3.2 Modelling implications

For mild to moderate curvatures, the simplified vorticity equation (8) is an adequate approximation of the downstream vorticity balance in the central part of the centre-region cell. Blanckaert (2001b, 2002b) and Blanckaert & Graf (2001c) have proposed a non-linear model for the centre-region cell based on equation (8), but coupled to a simplified downstream momentum equation that accounts for the deformation of the v_s -profile. By combining this model with a two-dimensional depth-averaged flow model, it should be possible to reproduce the velocity field in moderately curved flows with a reasonable

accuracy. However, for curvatures that are so strong that the velocity maximum is found in the lower part of the water column, like in the present experiment, it is essential to include the advective momentum transport terms into the transversal momentum equation. An accurate simulation of the centre-region cell, and of the flow field in general, now requires the use of the fully three-dimensional flow equations.

Turbulence is not purely dissipative, but restitution of kinetic energy from turbulence to the mean flow occurs in certain regions of the flow, accompanied by mean vorticity generation. The turbulence-generated vorticity away from the banks, however, is relatively weak, so that a fully three-dimensional numerical model with a linear turbulence closure must be good enough to describe the centre-region cell, even in the case of strong curvature.

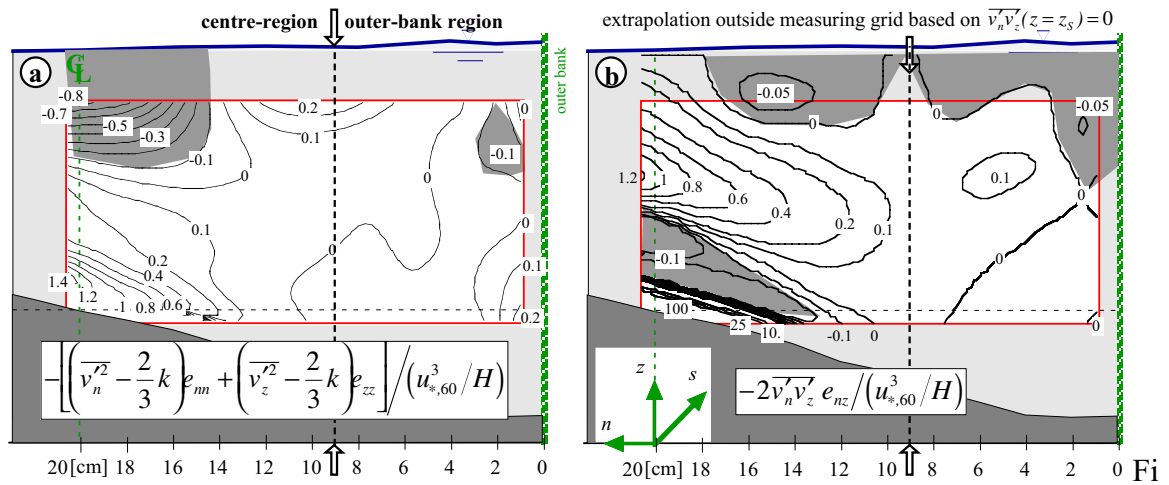


Figure 7: Isolines of the normalized kinetic energy fluxes between the mean flow and the turbulence via the cross-stream turbulent stresses (cf. equation (11)).

4.4 Analysis of the outer-bank cell

4.4.1 Observations

Except for the centrifugal term, all terms in the downstream vorticity equation (4/6) (cf. figure 6) and all kinetic energy fluxes between mean flow and turbulence (cf. equation (11) and figure (7)) are smaller in the outer-bank region than in the central region. The profiles of the downstream velocity in the outer-bank region are similar to those in the central region. The velocity maximum is located in the lower half of the water column and $\partial v_s / \partial z$ is slightly negative above that point. This implies that the sign of the centrifugal term in the vorticity equation complies with the sense of rotation of the outer-bank cell. Note that this is the only mechanism that drives the outer-bank cell in laminar bend flow.

In turbulent bend flow, cross-stream turbulence plays an important role. As was shown before, the normal stress difference $\overline{v_n^2} - \overline{v_z^2}$ in the region occupied by the outer-bank cell is nearly anti-symmetrical and the shear stress $\overline{v_n^T v_z^T}$ is nearly symmetrical about the

bisector of the top right corner of the flow domain. If these distributions were perfectly anti-symmetrical and symmetrical, respectively, like in a corner flow, anti-symmetrical patterns of the corresponding terms in the vorticity equation would result in either case (as is easily demonstrated by interchanging the n - and z -indices). Figures 6(c-d) show the distributions of the $\overline{v_n'^2} - \overline{v_z'^2}$ - and the $\overline{v_n'v_z'}$ -terms in the vorticity equation (4), respectively. In the flow domain covered by the outer-bank cell, either of them assumes positive and negative values of the same order of magnitude as the centrifugal term. The negative values, which comply with the sense of rotation of the outer-bank cell, seem to be found near the eye of the cell, but this observation is not conclusive due to the limited accuracy of the evaluations.

In the flow domain covered by the outer-bank cell, the advective transport of vorticity is negligible (figure 6(b)). The kinetic energy transfer between mean flow and turbulence via the cross-stream turbulent stresses $\overline{v_n'^2}$, $\overline{v_z'^2}$ and $\overline{v_n'v_z'}$ is an order of magnitude smaller than in the centre region (figures 7). It includes positive and negative contributions, which indicates that mean-flow energy in the outer-bank cell is produced as well as dissipated by cross-stream turbulent stresses.

4.4.2 Interpretation and modelling implications

The above observations lead to the following answers to the questions formulated in the “Present objectives”.

The hypothesis of de Vriend (1981a) and Christensen et al. (1999) that both skew-induced and turbulence-induced vorticity generation contribute to the generation of the outer-bank cell can be confirmed. Skew-induced generation seems to be dominant: all over the region occupied by the outer-bank cell, the sign of the centrifugal term complies with its rotation sense. The cross-stream turbulence terms contain favourable as well as opposing contributions, whereby the former seem to occur mainly near the ‘eye’ of the outer-bank cell.

The turbulence-induced vorticity generation seems to be quite similar to that in straight turbulent flow. Slight asymmetries may be relevant to the resulting vorticity pattern. This indicates the importance of accurately modelling the boundary conditions in numerical simulations. Nezu & Nakayama (1998, 1999), for example, have investigated the dependence of the boundary condition at the water surface on the Froude number.

In steady flow, all terms in the right-hand-side of equations (4/6) should add up to zero. Even when taking the experimental inaccuracy into account, the sum of the investigated terms seems to be negative in the flow region occupied by the outer-bank cell. This non-zero sum is presumably compensated by the non-uniformity term, $-(1+n/R)^{-1}v_s\partial\omega_s/\partial s$, which was not measured. This would mean that the outer-bank cell further strengthens in downstream direction, indicating that the two vorticity-generating mechanisms strengthen each other. For axisymmetric flow ($\partial/\partial s=0$), it is hypothesized that the downstream vorticity balance be maintained by an increase of the dissipation by the cross-stream turbulence.

For the present case of a channel with vertical sidewalls and a straight inflow reach followed by a constant-curvature bend, this positive feedback can be explained as follows. In the straight inflow reach, near-bank circulation cells are induced by the cross-stream turbulence. By advecting flow momentum, they deform the v_s -profiles, yielding a negative velocity gradient $\partial v_s/\partial z$ in the upper part of the water column. Upon entering the bend, this negative gradient gives rise to a centrifugal force that enhances the outer-bank cell, hence the deformation of the v_s -profile, etc. This positive feedback between the cell and the centrifugal force tends to intensify the outer-bank cell along the bend. This is in line with the observed strengthening of the outer-bank cell along the bend in curved laminar flow (Hille et al. 1985) and also explains why the near-bank cell in turbulent curved flow is stronger than in straight flow. Such an interaction between the two mechanisms has already been suggested by de Vriend (1981a). The experimental results indicate that outer-bank cells even occur in weakly curved flow and that the conditions of occurrence are not related to an instability phenomenon, like in curved laminar flow. This also supports the above interpretation.

De Vriend (1981a) and Christensen et al. (1999) furthermore claim that turbulence anisotropy be the mechanism responsible for the turbulence-induced vorticity and that it cannot be accounted for by a standard linear turbulence closure. Our observations show that the cross-stream turbulent stresses $\overline{v_n'^2} - \overline{v_z'^2}$ and $\overline{v_n'v_z'}$ have a similar role and contribute to the generation as well as the dissipation of mean-flow vorticity. As was shown before (figure 2(b)), the combination of these stresses represents the cross-stream turbulence anisotropy. Hence it can be concluded that turbulence anisotropy is indeed the physical cause of turbulence-induced vorticity. Also the kinetic energy fluxes via these turbulent stresses are of comparable (small) magnitude and generate as well as dissipate mean-flow energy of the outer-bank cell.

Speziale (1987) demonstrates that linear turbulence models are unable to correctly represent the turbulent normal stresses. He remarks that the near-bank circulation cells in straight flow cannot be resolved by them and postulates that a necessary condition for turbulence models to reproduce turbulence-generated circulation cells is that the downstream velocity field should give rise to a non-zero difference between the turbulent normal stresses: $\overline{v_n'^2} - \overline{v_z'^2} \neq 0$. He attributes the failure of linear turbulence models, among which the linear k - ϵ model, to the inability to satisfy this condition. Based on our simultaneous analysis of the vorticity dynamics and the kinetic energy transfer between mean flow and turbulence, this hypothesis can be refined and complemented.

Although linear turbulence models are unable to correctly represent the turbulent normal stresses, there is no physical reason why they should yield a zero cross-stream turbulence anisotropy:

$$\overline{v_n'^2} - \overline{v_z'^2} = -2v_t \left(\frac{\partial v_{n^*}}{\partial n^*} - \frac{\partial v_{z^*}}{\partial z^*} \right) \neq 0 \quad (17)$$

Consider for example a point in the central part of the centre-region cell, where $v_z \approx 0$. Obviously, $\partial v_n/\partial z \neq 0$ and, when using a linear eddy viscosity model, $\overline{v_n'v_z'} = -v_t (\partial v_n/\partial z + \partial v_z/\partial n) \neq 0$. According to figure 2(b), this implies that $\overline{v_n'^2} - \overline{v_z'^2} \neq 0$,

so a non-zero turbulence anisotropy. As a consequence, the inability of these models to correctly represent the turbulent normal stresses does not explain why they should not predict turbulence-generated cross-stream circulation cells (be it incorrect ones). Nonetheless, they apparently don't, which can be clarified as follows.

In the case of straight uniform flow considered by Speziale, linear turbulence models do not reproduce the near-bank circulation cells, i.e. $(v_n, v_z) = 0$. Consequently, $\overline{v_n'^2} - \overline{v_z'^2} = -2v_t(\partial v_n / \partial n - \partial v_z / \partial z) = 0$. This heuristic observation, however, does not prove that it is impossible for these models to simulate turbulence-generated circulation. Introducing a perturbation to the flow, $(\hat{v}_n, \hat{v}_z) \neq 0$, such that $\hat{\omega}_s \neq 0$ and $\overline{\hat{v}_n'^2} - \overline{\hat{v}_z'^2} = -2v_t(\partial \hat{v}_n / \partial n - \partial \hat{v}_z / \partial z) \neq 0$, will generally give rise to generation and/or dissipation of mean-flow vorticity. The numerical model shows that the perturbation dampens out, whence the turbulent stresses must be dissipative. Elaboration of the downstream vorticity equation with a constant eddy viscosity easily leads to the same conclusion.

In fact, when using a linear turbulence closure, the kinetic energy fluxes are always directed from the mean flow to turbulence (equation (16)). The analysis of our experimental data indicates that, in the region of the outer-bank cell, the (weak) kinetic energy fluxes due to the cross-stream turbulent stresses are directed both from the mean flow to turbulence and inversely. Hence, the cross-stream turbulent stresses contribute to the generation as well as the dissipation of the outer-bank cell. Clearly, this phenomenon cannot be reproduced by linear closure models with a scalar eddy viscosity. Kinetic energy fluxes from turbulence to mean flow have been observed in various other experiments in open-channel bends (Booij 1985, Anwar 1986, Booij & Tukker 1996, Shiono & Muto 1998 for the case of overbank flow in a meander).

The above analysis shows that, in addition to Speziale's (1987) necessary condition, there is a second necessary condition for turbulence models to reproduce turbulence-generated vorticity. The turbulence model may not be purely dissipative, but must be able to represent fluxes of kinetic energy from turbulence to the mean flow. This is confirmed by the results of Kawahara & Tamai (1988), who demonstrate theoretically that linear eddy viscosity models cannot represent turbulence-induced vorticity. Their demonstration is based on the presumption of a positive eddy viscosity. In a linear closure model, fluxes of kinetic energy from turbulence to the mean flow would imply negative mixing coefficients (cf. equation (15)).

Non-linear turbulence models, based on a non-linear relationship between the turbulent stresses and the strain rates, seem to satisfy both necessary conditions. At least, they correctly predict the near-bank cells in turbulent straight flow (Speziale 1987, Colombini 1993), as well as the outer-bank cell in the present experiment (Jia et al. 2001). Higher-order turbulence models, such as Algebraic Stress Models or Reynolds Stress Models, also seem to satisfy both conditions. Naot & Rodi (1982) and Demuren & Rodi (1984) simulated the near-bank cells in turbulent straight flow with an Algebraic Stress Model, and Christensen et al. (1999) simulated outer-bank cells in turbulent curved flow with a Reynolds Stress Model, even for weak curvature. They have also succeeded in simulating the outer-bank cell in a bend with a standard linear $k - \varepsilon$ model, but only for very strong

curvature ratios ($R/H < 16$). With the k - ϵ model, turbulence is dissipative and a very strong skewing-induced vorticity generation is needed to obtain the outer-bank cell. This is in line with the above conclusions.

The above results indicate that the vorticity pattern cannot be explained by uniquely considering the vorticity equation (4/6), as has been done in previous investigations, but that the kinetic energy transfer plays an essential role. Other observations seem to confirm this. Our measurements show that the influence of the water surface and the outer bank on the cross-stream turbulence, $\overline{v_n'^2} - \overline{v_z'^2}$ and $\overline{v_n'v_z'}$ (cf. figure 5), is nearly identical. The distributions of the corresponding cross-stream turbulence terms in the downstream vorticity equation will thus be nearly identical in a corner formed by two fixed boundaries and in one formed by a water surface and a fixed boundary. However, Tominaga et al. (1989) and Nezu & Nakagawa (1993) have shown that the resulting vorticity patterns are significantly different for the case of straight uniform flow. Whereas two identical counter-rotating circulation cells exist in a corner formed by two fixed boundaries, the circulation cell near the water surface is dominant over the counter-rotating one near the bank in an open-channel corner. These different vorticity patterns can be explained by differences in the kinetic energy fluxes. Near the water surface, the kinetic energy fluxes are smaller than near the fixed boundary, where the mean velocity gradients are more pronounced due to the no-slip condition.

The results of the present analysis of the outer-bank cell can be summarised as follows. The proximity of flow boundaries modifies the turbulence characteristics, which, in their turn, influence the downstream vorticity field, and thus the cross-stream motion (v_n, v_z). In the case of a bend with a vertical outer wall, this results in the formation of an outer-bank cell. By advecting momentum, the cross-stream motion causes a redistribution of the velocity and the boundary shear stress. An accurate description of the effects of boundary proximity on the turbulence characteristics, and especially on the kinetic energy transfer, is therefore a prerequisite to the accurate modelling of the flow field in the vicinity of the outer bank.

4.5 Kinetic energy transfer

Our analysis shows that the correct modelling of the kinetic energy fluxes between mean flow and turbulence, which add up to the total production of turbulent kinetic energy (cf. equation (11)), is the key to accurate simulation of the cross-stream circulation cells, especially the one near the outer bank. In order to estimate how this production of turbulent kinetic energy is composed, the contributions of the cross-stream turbulent stress components, $\overline{v_n'^2}$, $\overline{v_z'^2}$ and $\overline{v_n'v_z'}$ (cf. figure 7), will be compared with the main contributions related to friction at the flow boundaries.

In two-dimensional straight uniform flow, turbulence is produced by bottom friction and represented by the kinetic energy flux $-2\overline{v_s'v_z'} e_{sz}$, with the strain rate e_{sz} defined according to equation (13). Assuming a triangular distribution of $-\overline{v_s'v_z'}$, between 0 at the water

surface and u_*^2 at the bottom, and assuming a logarithmic vertical profile of v_s , this can be elaborated to

$$-2\overline{v'_s v'_z} e_{sz} = \frac{1}{\kappa} \frac{u_*^3}{H} \left(\frac{H}{z} - 1 \right) \quad \text{or} \quad \frac{-2\overline{v'_s v'_z} e_{sz}}{u_*^3/H} = \frac{1}{\kappa} \left(\frac{H}{z} - 1 \right) \quad (18)$$

This function is shown in figure 8(c). The measured distribution of this component $-2\overline{v'_s v'_z} e_{sz} / (u_{*,60}^3/H)$ in the present experiment is shown in figure 8(a). In the central region, kinetic energy is transferred from turbulence to the mean flow in the part of the water column where $\partial v_s / \partial z < 0$, since $-2\overline{v'_s v'_z} e_{sz} / (u_{*,60}^3/H) < 0$. Considerable magnitudes of this quantity are found in this region: $-2\overline{v'_s v'_z} e_{sz} / (u_{*,60}^3/H) = O(-50)$. Near the bottom mean flow kinetic energy is dissipated into turbulence, with transfer rates that strongly increase towards the bottom and reach values of $-2\overline{v'_s v'_z} e_{sz} / (u_{*,60}^3/H) = O(300)$. This measured order of magnitude agrees with that from the straight-flow profile in figure 8(c). In the part of the outer-bank region that is covered by the measuring grid, this component of the kinetic energy transfer is relatively small.

Close to the bottom, the kinetic energy transfer component $-2\overline{v'_n v'_z} e_{nz} / (u_{*,60}^3/H)$ (figure 7(b)) is associated with the transversal component of the bottom friction. Its maximum near-bottom values in the central region are of a similar order of magnitude as those associated with the downstream component of the bottom friction, $-2\overline{v'_n v'_z} e_{nz} / (u_{*,60}^3/H) = O(100)$.

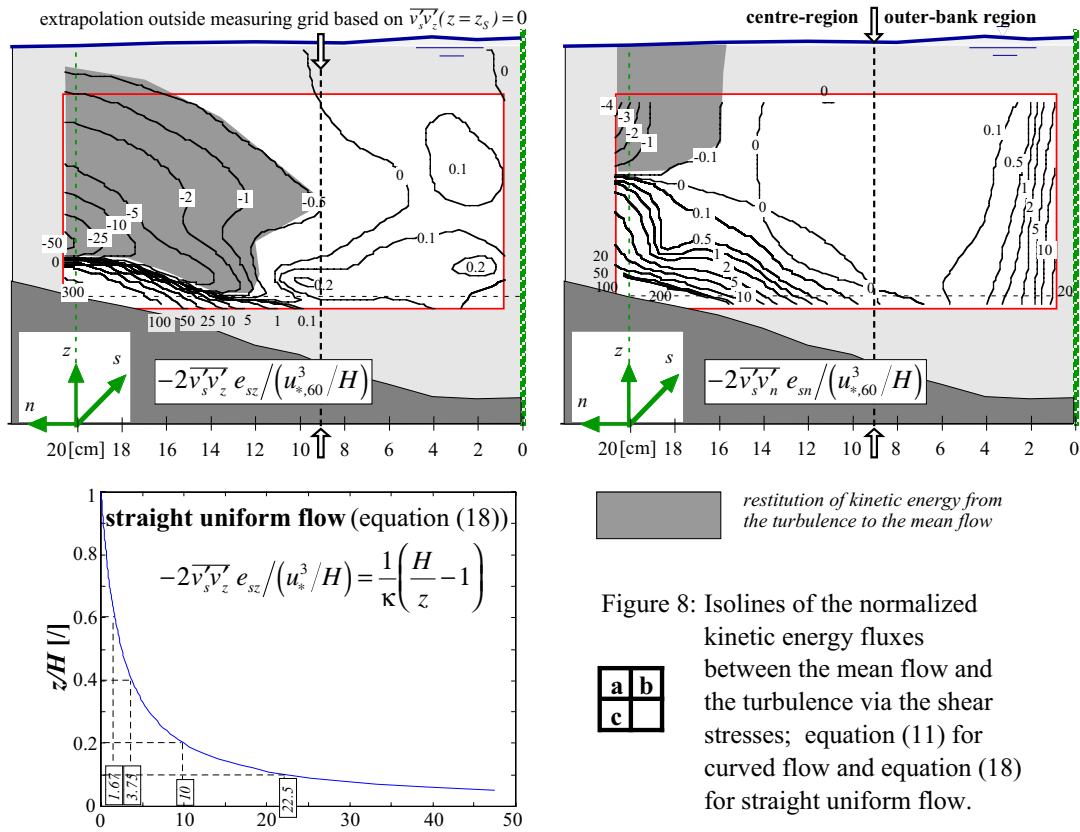


Figure 8: Isolines of the normalized kinetic energy fluxes between the mean flow and the turbulence via the shear stresses; equation (11) for curved flow and equation (18) for straight uniform flow.

In the central region, the pattern of $-2\overline{v_s v_n} e_{sn} / (u_{*,60}^3 / H)$ (figure 8(b)), is similar to that of $-2\overline{v_s v_z} e_{sz} / (u_{*,60}^3 / H)$ (figure 8(a)). In the upper part of the water column, where $\partial v_s / \partial z < 0$, it is negative, whereas it is positive in the lower part and strongly increases near the bottom, up to values $O(100)$. The latter was to be expected, since $-\overline{v_s v_n}$ represents downstream friction on the vertical projection of the inclined bottom. The strong increase of this term towards the outer bank is obviously associated with the bank friction. Yet, the turbulence production by the bank shear stress only reaches values of $-2\overline{v_s v_n} e_{sn} / (u_{*,60}^3 / H) = O(20)$, which is significantly smaller than the turbulence production by the bottom shear stress. This indicates that the bank shear stress is considerably smaller than the bottom shear stress, which is in agreement with the observed smaller turbulence activity in the outer-bank region (Blanckaert & Graf 2001a).

Mean flow kinetic energy is thus mainly transferred to turbulence in the boundary layers, especially near the bottom. The normalized kinetic energy flux related to boundary friction reaches values $O(100)$. Except for $-2\overline{v_s v_z} e_{sz} / (u_{*,60}^3 / H) = O(-50)$, the normalized kinetic energy fluxes in the centre region are at least one order of magnitude smaller, viz. $O(1 \text{ to } 10)$, over most of the water column. In the outer-bank region outside the area dominated by the sidewall-friction, they are at least another order of magnitude smaller, viz. $O(0.1)$. So the kinetic energy transfer via the cross-stream turbulent stresses in the regions covered by the two circulation cells represents a negligible part of the total kinetic energy transfer between mean flow and turbulence. Hence it is irrelevant to the total energy expenditure in a bend. Nonetheless, these small kinetic energy fluxes play an essential role in the formation of the circulation cells, hence the distribution of the downstream velocity and the boundary shear stress. In the centre-region cell, the dissipation of mean flow kinetic energy into turbulence balances the driving centrifugal force in most of the water column. The outer-bank cell partly originates from turbulent kinetic energy restitution and at the same time it is dissipated into turbulence via the cross-stream turbulent stresses.

5 Conclusions

Previous investigations of strongly curved turbulent flow, in which only the downstream vorticity equation was considered, have not produced a clear picture of the physics underlying the two cross-stream circulation cells. The present analysis, based on high-quality three-dimensional flow measurements, considers the combination of the downstream vorticity balance and the kinetic energy transfer between mean flow and turbulence. This leads to a better physical understanding, especially of the role of turbulence. Furthermore, it gives guidance to the numerical modelling of flow in sharply curved open-channel bends.

The **centre-region cell** is often explained as resulting from the balance between the driving centrifugal term $-(\partial/\partial z)(v_s^2/R)$ and the dissipating shear stress term $\partial^2 \overline{v_n v_z} / \partial z^2$ in the downstream vorticity equation. It is therefore often modelled using the corresponding simplified vorticity equation (8).

There is an important feedback between the centre-region cell and the downstream velocity, the distribution of which is determined to a large extent by the advective momentum transport by the cross-stream circulation cells. This decreases the velocities in the upper part of the water column, while increasing them in the lower part. The strength of the centre-region cell is determined by the vertical profile of the centrifugal force, which depends critically on the vertical profile of the downstream velocity. This leads to a negative feedback between the downstream velocity profile and the centre-region cell, and thus a considerably weaker centre-region cell than expected on the basis of the classical first-order perturbation approach. In the case of mild to moderate curvature, the simplified vorticity equation is nonetheless an adequate approximation of the downstream vorticity balance in the central region of the cross-section, but it has to be combined with a downstream momentum equation that takes due account of the advective redistribution phenomenon.

In the case of strong curvature, like in the present experiment, the deformation of the downstream velocity profiles due to advection is so strong, that the velocity maximum is found in the lower part of the water column and the vertical derivative of the velocity is negative above that point. This means that the centrifugal term in equation (8) changes sign at the point of maximum velocity. Under these conditions, equation (8) would predict two opposite centre-region cells on top of each other. The existence of a single centre-region cell that covers the entire water column is to be attributed to advective transport of vorticity, which compensates for the negative centrifugal term. Furthermore, the effect of the turbulent stress $\overline{v_n'v_z'}$ is not exclusively dissipative, in the lower part of the water column it also contributes to the generation of the centre-region cell. The accurate simulation of the centre-region cell for these strong curvatures requires the use of fully three-dimensional momentum equations, including the advective transport terms.

The linear turbulence closure (turbulent stress components linearly proportional to the corresponding strain rate components) that is often used in three-dimensional numerical models cannot account for the turbulence-generated vorticity, since it excludes the transfer of kinetic energy from turbulence to the mean flow. The contribution of turbulence-generated vorticity in the centre region is moderate, however, so fully three-dimensional numerical models with a linear turbulence closure are likely to yield reasonably accurate predictions of the centre-region cell, even in the case of strong curvature.

For the **outer-bank cell**, the analysis confirms the hypothesis formulated in the literature that both the centrifugal force and the cross-stream turbulent stresses contribute to the generation of this cell. Like in the central region, the maximum downstream velocity in the region near the outer bank is found in the lower part of the water column and the velocity gradient $\partial v_s/\partial z$ is negative in most of the water column. Hence the sign of the centrifugal term in the vorticity equation complies with the sense of rotation of the outer-bank cell, which means that the centrifugal force enhances this circulation. Terms related to the cross-stream turbulent stresses are of the same order of magnitude as the centrifugal term and include contributions that enhance the outer-bank cell. These turbulent stress terms represent the anisotropy of the cross-stream turbulence due to the proximity of boundaries. Cross-stream advective transport of vorticity seems to be negligible in the outer-bank region. In the outer-bank cell, vorticity generation by the centrifugal term and

by the cross-stream turbulence strengthen each other. The experimental results indicate that an outer-bank cell will also occur in the case of weak curvature, and that its occurrence is not caused by flow instability, like in the laminar flow case.

Linear turbulence closure models are unable to represent the turbulence-generated part of the outer-bank cell, although they may well produce anisotropy of the cross-stream turbulence. When described with such a linear turbulence model, the cross-stream turbulent stresses always dissipate mean flow vorticity, since the kinetic energy transfer can only be from mean flow to turbulence. The experimental results indicate that kinetic energy is transferred in either direction, so also from turbulence to the mean flow. As a consequence, the outer-bank cell is enhanced by kinetic energy input from turbulence, and at the same time suppressed by turbulent dissipation. Turbulence closures that include the possibility of kinetic energy transfer between turbulence and mean flow in either direction are therefore required to accurately reproduce the outer-bank cell. The kinetic energy transfer from turbulence to the mean flow is small compared to the total production of turbulent kinetic energy, which is mainly due to boundary friction. Nonetheless, it plays an essential role in the dynamics of the outer-bank cell.

Even though the experimental data were limited to the outer-half of one single cross-section under one set of hydraulic and geometric conditions, they yielded valuable information on the mechanisms underlying both cross-stream circulation cells and gave guidance to improve their numerical simulation. The experimental research is presently extended by measuring entire cross-sections all along a large optimised laboratory flume under different hydraulic and geometric conditions. Some measurements of similar bi-cellular patterns of cross-stream circulation have already been reported by Blanckaert (2002a).

Acknowledgements

This research is being sponsored by the Swiss National Science Foundation under grants Nr.2100-052257.97/1 and 2000-059392.99/2. The first author gratefully acknowledges his PhD supervisor, Prof. W.H. Graf, for his support and Dr. R. Booij and Prof. I. Nezu for reviewing a first draft of the manuscript.

The data used in this paper can be obtained from the first author.

REFERENCES

- Anwar, H. O. (1986). "Turbulent structure in a river bend." *J. Hydr. Engng*, ASCE, 112(8), 657-669.
- Batchelor, G. K. (1970). *An Introduction to Fluid Dynamics*, Cambridge University Press, Cambridge.
- Bathurst, J. C., Thorne, C. R. & Hey, R. D. (1979). "Secondary flow and shear stress at river bends." *J. Hydr. Div.*, ASCE, 105(10), 1277-1295.
- Blanckaert, K. (2001a). "discussion on: Bend-flow simulation using 2D depth-averaged model, by Lien H.C. et al." *J. Hydr. Engng.*, ASCE, 127(2), 167-170.
- Blanckaert, K. (2001b). "A model for flow in strongly curved channel bends." *Proc. 29th-IAHR congr.*, J.F. Kennedy Student Paper Comp, Beijing, China, 42-50.
- Blanckaert, K. (2002a). "Secondary currents measured in sharp open-channel bends." *Proc. River Flow 2002*, Louvain, Belgium.
- Blanckaert K. (2002b). "Flow and turbulence in sharp open-channel bends." *PhD-thesis Nr 2545*, Ecole Polytechnique Fédérale Lausanne, Switzerland.
- Blanckaert, K. & Graf, W. H. (1999). "Outer-bank cell of secondary circulation and boundary shear stress in open-channel bends." *1st-RCEM symp.*, Genova, Italy, Vol.1, 533-543.
- Blanckaert, K. & Graf, W. H. (2001a). "Mean flow and turbulence in open-channel bend." *J. Hydr. Engng*, ASCE, 127(10), 835-847.
- Blanckaert, K. & Graf, W. H. (2001b). "Experiments on flow in a strongly curved channel bend." *Proc. 29th-IAH congr.*, Theme D, Vol. I, 7 Beijing, China, 371-377.
- Blanckaert, K. & Graf, W. H. (2001c) "Non-linear model for secondary circulation and transversal bottom slope in sharp bends." *Proc. 2th-RCEM-congr.*, Obihiro, Japan, 791-800.
- Blanckaert, K. & Graf, W. H. (2002). "Momentum transport in sharp open-channel bends." (*tentatively approved for publication in J. Hydr. Engng.*, ASCE).
- Blanckaert, K. & Lemmin, U. (2002). "Improving acoustic turbulence measurements." (*submitted for publication*).
- Booij, R. (1985). "Eddy viscosity in channel bends." *Int. Symp. Refined Flow Mod. Turb. Meas.*, Iowa, E21,1-10.
- Booij, R. & Tukker, J. (1996). "3-Dimensional laser-Doppler measurements in a curved flume." In: *Developments in laser techniques and applications to fluid mechanics*, Springer, Berlin, 98-114.
- Boussinesq, J. (1868). "Mémoire sur l'influence de frottement dans les mouvements réguliers des fluides; XII - Essai sur le mouvement permanent d'un liquide dans un canal horizontal à axe circulaire." *J. Math. pures et appl.*, série 2 (Tome XIII), 413.
- Bradshaw, P. (1987). "Turbulent secondary flows." *Annual Review Fluid Mechanics*, 53-74.
- Brundett, E. & Baines, W. D. (1964). "The production and diffusion of vorticity in duct flow." *J. Fluid Mech.*, 19, 375-394.

- Cheng, K. C., Lin, R.-C. & Ou, J.-W. (1976). "Fully developed laminar flow in curved rectangular channels." *J. Fluids Engng*, ASME, 41-48.
- Choudhary, U. K. & Narasimhan, S. (1977). "Flow in 180° open channel rigid boundary bends." *J. Hydr. Div.*, ASCE, 103(6), 651-657.
- Christensen, B., Gislason, K. & Fredsoe, J. (1999). "Secondary turbulent flow in an infinite bend." *1st-RCEM symp.*, Genova, Italy, Vol.1, 543-553.
- Colombini, M. (1993). "Turbulence-driven secondary flows and formation of sand ridges." *J. Fluid Mech.*, 254, 701-719.
- de Boor, C. (1978). *A Practical Guide to Splines*, Springer, Berlin.
- de Vriend, H. J. (1977). "A mathematical model of steady flow in curved shallow channels." *J. Hydr. Res.*, IAHR, 15(1), 37-54.
- de Vriend, H. J. (1981a). "Steady flow in shallow channel bends." Report No. 81-3, Lab. Fl. Mech., Dept. Civ. Eng., Delft Univ. Techn., Delft.
- de Vriend, H. J. (1981b). "Velocity redistribution in curved rectangular channels." *J. Fluid Mech*, 107, 423-439.
- de Vriend, H. J. & Geldof, H. J. (1983). "Main flow velocity in short and sharply curved river bends." Report No. 83-6, Lab. Fl. Mech., Dept. Civ. Eng., Delft Univ. Techn., Delft.
- Demuren, A. O. & Rodi, W. (1984). "Calculation of turbulence-driven secondary motion in non-circular ducts." *J. Fluid Mech.*, 140, 189-222.
- Dietrich, W. E. (1987). "Mechanics of flow and sediment transport in river bends." *River Channels: environment and process*, K. Richards, ed., Inst. Brit. Geogr. spec. publ., Oxford, 179-227.
- Dietrich, W. E. & Smith, J. D. (1983). "Influence of the point bar on flow through curved channels." *Water Resour. Res.*, AGU, 19(5), 1173-1192.
- Einstein, H. A. & Harder, J. A. (1954). "Velocity distribution and the boundary layer at channel bends." *Trans.*, AGU, 35(1), 114-120.
- Einstein, H. A. & Li, H. (1958). "Secondary currents in straight channels." *Trans. AGU*, 39, 1085-1088.
- Engelund, F. (1974). "Flow and bed topography in channel bends." *J. Hydr. Div.*, ASCE, 100(11), 1631-1648.
- Falcon Ascanio, M. & Kennedy, J. F. (1983). "Flow in alluvial-river curves." *J. Fluid Mech.*, 133, 1-16.
- Gessner, F. B. (1973). "The origin of secondary flow in turbulent flow along a corner." *J. Fluid Mech.*, 58, 1-25.
- Gessner, F. B. & Jones, J. B. (1965). "On some aspects of fully developed turbulent flow in a rectangular channel." *J. Fluid Mech.*, 23, 689-713.
- Götz, W. (1975). "Sekundärströmungen in aufeinander folgenden Gerinnekrümmungen." *Mitteilungen No. 163*, Theodor-Rehbock Flussbaulaboratorium, Karlsruhe.

- Hille, P., Vehrenkamp, R. & Schulz-Dubois, E. O. (1985). "The development and structure of primary and secondary flow in a curved square duct." *J. Fluid Mech.*, 151, 219-241.
- Hinze, J. O. (1975). *Turbulence*, McGraw-Hill, New York.
- Hurther, D. & Lemmin, U. (1998). "A constant beamwidth transducer for three-dimensional Doppler profile measurements in open channel flow." *Meas. Sc. Techn.*, IOP, 9(10), 1706-1714.
- Hurther, D. & Lemmin, U. (2001). "A correction method for turbulence measurements with a 3-D acoustic Doppler velocity profiler." *J. Atm. Oc. Techn.*, AMS, 18, 446-458.
- Ikeda, S., Yamasaka, M. & Kennedy, J. F. (1990). "Three-dimensional fully developed shallow-water flow in mildly curved bends." *Fluid Dynamics Research 6*, JSFM, ed., Noth-Holland, 155-173.
- Jia, Y., Blanckaert, K. & Wang, S. S. Y. (2001). "Numerical simulation of secondary currents in curved channels." *8th FMTM-congress*, Tokyo, Japan.
- Johannesson, H. & Parker, G. (1989). "Secondary flow in mildly sinuous channel." *J. Hydr. Engng*, ASCE, 115(3), 289-308.
- Kalkwijk, J.P.Th. & de Vriend, H.J. (1980). "Computation of the flow in shallow river bends". *J. Hydr. Res.*, IAHR, 18(4), 327-342.
- Kawahara, Y. & Tamai, N. (1988). "Note on turbulence modeling for secondary flows in passages of non-circular cross-section." *Proc. Japanese Soc. Civ. Engng.*, 399/II-10, 247-250 (*in Japanese*).
- Kikkawa, H., Ikeda, S. & Kitagawa, A. (1976). "Flow and bed topography in curved open channels." *J. Hydr. Div.*, ASCE, 102(9), 1327-1342.
- Lemmin, U. & Rolland, T. (1997). "Acoustic velocity profiler for laboratory and field studies." *J. Hydr. Engng*, 123(12), 1089-1098.
- Lien, H. C., Hsieh, T. Y., Yang, Y. C., and Yeh, K. C. (1999). "Bend-flow simulation using 2D depth-averaged model." *J. Hydr. Engng.*, ASCE, Vol.125(10), 1097-1108.
- Mockmore, C.A. (1943). "Flow around bends in stable channels." *Transactions*, ASCE, Vol. 109, 593-628 (incl. discussions).
- Naot, D. & Rodi, W. (1982). "Calculation of secondary currents in channel flow." *J. Hydr. Div.*, ASCE, 108(8), 948-968.
- Nezu, I. & Nakagawa, H. (1984). "Cellular secondary currents in straight conduit." *J. Hydr. Engng*, ASCE, 110(2), 173-193.
- Nezu, I., Nakagawa, H. & Tominaga, A. (1985). "Secondary currents in a straight channel flow and the relation to its aspect ratio." *Turbulent Shear Flows 4*, L. J. S. Bradbury et al., eds., Springer, Berlin, 246-260.
- Nezu, I. & Nakagawa, H. (1993). *Turbulence in open-channel flows*, IAHR-monograph, Balkema.
- Nezu, I., & Nakayama, T. (1998). "Mutual-interaction between bursts and boils very near the free-surface of open-channel flows." *Environmental Hydraulics*, J. H. L. Lee et al., eds., Balkema, 297-303.

- Nezu, I., & Nakayama, T. (1999). "Numerical calculation of steep open-channel flows by considering effects of surface-wave fluctuations." *Hydraulic Modeling*, V. P. Singh et al., eds., Water Resources Publications, Colorado, 3-16.
- Odgaard, A. J. (1984). "Bank erosion contribution to stream sediment load." *IIHR Report No. 280*, Iowa Institute of Hydraulic Research, Iowa.
- Perkins, H. J. (1970). "The formation of streamwise vorticity in turbulent flow." *J. Fluid Mech.*, 44(4), 721-740.
- Prandtl, L. (1942). *Führer durch die Strömungslehre*, Vieweg, Braunschweig.
- Rozovskii, I. L. (1957). *Flow of Water in Bends of Open Channels*, Ac. Sc. Ukr. SSR, Isr. Progr. Sc. Transl., Jerusalem, 1961.
- Schlichting, H. & Gersten, K. (2000). *Boundary-Layer Theory*, 8th ed, Springer, Berlin.
- Shiono, K. & Muto, Y. (1998). "Complex flow mechanisms in compound meandering channels with overbank flow." *J. Fluid Mech.*, 376, 221-261.
- Siebert, W. (1982). "Strömungscharakteristiken in einem Kanal mit 180°-Krümmungen." *Mitteilungen No. 168*, Theodor-Rehbock Flussbaulaboratorium, Karlsruhe.
- Speziale, C. G. (1987). "On nonlinear K-l and K-e models of turbulence." *J. Fluid Mech.*, 178, 459-475.
- Thomson, W. (1876). "On the origin of windings of rivers in alluvial plains, with remarks on the flow of water round bends in pipes." *Proc. Royal Soc. London*, 25, 5-8.
- Tominaga, A., Ezaki, K., Nezu, I. & Nakagawa, H. (1989). "Three-dimensional turbulent structure in straight channel flows." *J. Hydr. Res., IAHR*, 27(1), 149-173.
- Tominaga, A., Nagao, M. & Nezu, I. (1999). "Flow structure and momentum transport processes in curved open-channels with vegetation." *28th-IAHR-congr.*, Graz, Austria.
- Winters, K. H. (1987). "A bifurcation study of laminar flow in a curved tube of rectangular cross-section." *J. Fluid Mech.*, 180, 343-369.
- Yeh, K. C. & Kennedy, J. F. (1993). "Moment model of nonuniform channel-bend flow. I: Fixed beds." *J. Hydr. Engng*, ASCE, 119(7), 776-795.

III.3 Turbulence Characteristics in Sharp Open-Channel Bends

K. Blanckaert¹ and H.J. de Vriend²

(in preparation for submission to Water Resources Research, Am. Geoph. Un.)

Abstract

In spite of its importance, little is known about the turbulence characteristics in open-channel bends. This paper reports on an experimental investigation of turbulence in one cross-section of an open-channel bend, in which the flow is characterized by a bi-cellular pattern of cross-stream circulation and a strongly reduced turbulence activity in the outer bend, as compared to straight uniform shear flow. Measured distributions are given of the turbulent kinetic energy, its production, the mixing coefficients, some parameters characterizing the turbulence structure, and the fourth-order correlations of the turbulent velocity fluctuations. Furthermore, the transport equation for the turbulent kinetic energy is evaluated term by term, on the basis of the measured data. This shows that the turbulence structure is the main cause of the observed reduction of turbulence activity. The departures of the measured turbulence structure from its equivalent for straight uniform shear flow are correlated with a curvature-flux-Richardson number, R_f , which parameterizes the streamline curvature. Such a correlation may be useful to improve simple turbulence closure models for curved open-channel flow. Since the cross-stream circulation depends on the same parameter, R_f is an important scaling parameter in this type of flow.

Keywords

Open-channel bend, curved flow, turbulence, turbulence structure, turbulent kinetic energy, experiment, turbulence closure, mixing coefficient

1 Introduction

Turbulence plays an important role in open-channel flows. It is to a large extent responsible for the spreading and mixing of suspended matter, pollutants and heat, and for the transport of sediment. It also has a strong interaction with the mean velocity field and the boundary shear stress. Turbulence plays an important role in the formation of cross-stream circulation cells (cf. Blanckaert and de Vriend, 2002a), which in their turn influence the distribution of the velocity and the boundary shear stress (cf. Blanckaert and Graf, 2002). This interaction is reflected by the sensitivity of flow models to the turbulence closure.

¹ Res. Assoc., Lab. d'Hydraulique Environnementale, Ecole Polytechnique Fédérale, CH-1015 Lausanne, Switzerland.

² Professor, Delft University of Technology, POB 5048, 2600 GA Delft, The Netherlands.

Open-channel bends are ubiquitous in alluvial lowland rivers, but they also occur in mountain rivers and in manmade channels. They influence the conveyance capacity of the channel, may lead to undesired erosion/deposition and enhanced mixing, and they provide a place for the intake of relatively clear water. From an ecological point of view, meander migration is an important agent in floodplain rejuvenation. Many good reasons, therefore, to investigate curved open-channel flow.

In spite of the relevance of both turbulence and bends, little is known about the turbulence characteristics in open-channel bends. The study of environmental problems, such as the spreading and mixing of pollutants and heat, suffers from an almost complete lack of experimental data on the mixing process. Numerical simulations of the flow in open-channel bends frequently use extensions of turbulence closures that were developed for rectilinear shear flow. They often give poor results, due to the different turbulence structure. The lack of experimental data, especially from simultaneous high-resolution measurements of all three velocity components, hampers the development of improved turbulence models.

The main goal of this paper is to present detailed experimental data on the turbulence characteristics in an open-channel bend, including distributions of the turbulent kinetic energy (tke), the production of turbulent kinetic energy, the mixing coefficients, parameters characterizing the turbulence structure, and fourth-order turbulence correlations. These experimental data are measured in one cross-section of a bend, in which the flow is characterized by the existence of a bi-cellular pattern of cross-stream circulation and by a strong reduction of the turbulence activity in the outer bend as compared to straight uniform shear flow.

A second goal of this paper is to analyze the mechanisms that lead to the reduction of the turbulence activity in the outer bend, via a term-by-term evaluation of the transport equation for the turbulent kinetic energy on the basis of the measured data. Special attention will be given to the terms representing the production of tke and to those representing its advective transport by the cross-stream motion. The turbulence structure is shown to implicitly play an important role in the tke-equation. A further analysis of the turbulence structure is reported in a complementary paper (Blanckaert and de Vriend, 2002b).

A third goal of this paper is to find indications on how turbulence closure models can be improved. The observed turbulence structure is shown to be correlated with the so-called curvature-flux-Richardson number, R_f , which parameterizes the effect of the streamline curvature. This correlation may be used to improve the capabilities of simple semi-empirical turbulence closures. Blanckaert (2001b) and Blanckaert and Graf (2001c) have shown that the cross-stream circulation strongly depends on the same curvature-flux-Richardson number. This number must therefore be an important parameter in curved open-channel flow.

2 The experiment

Flow measurements were performed in a laboratory bend with a natural bottom topography: the initially horizontal sand bed was deformed by the flow corresponding to clear-water-scour conditions (critical shear stress for sediment transport in straight uniform flow), ultimately leading to the stable topography shown in Fig. 1. The laboratory flume is $B=0.4$ m wide and consists of a 2 m long straight approach reach, followed by a 120° bend with a constant radius of curvature of $R = -2$ m (R is negative if the curvature vector is directed along the n -axis). The hydraulic conditions of the flow are shown in Table 1.

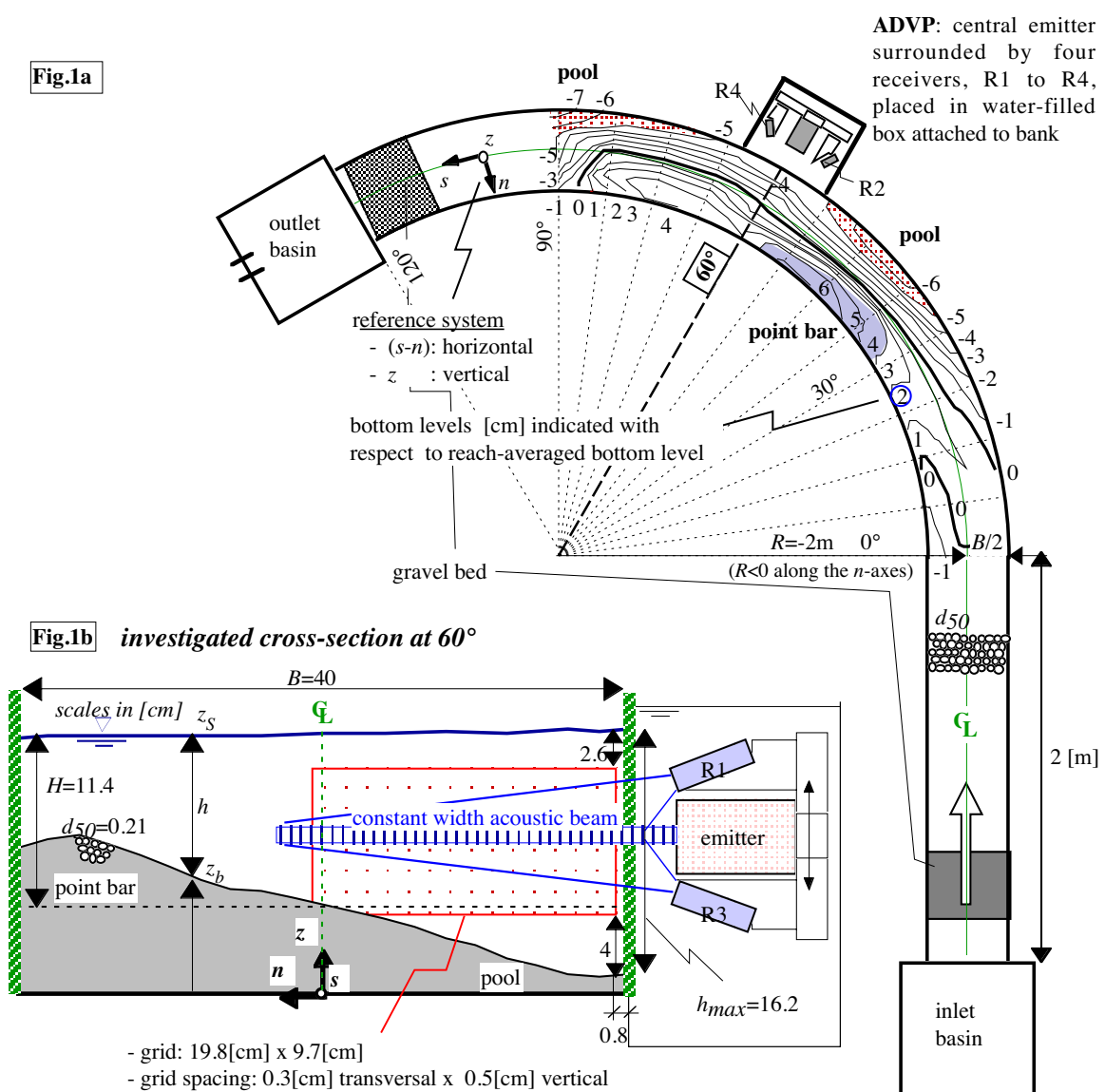


Fig. 1: (a) Experimental set-up, bottom topography and reference system; (b) Measuring section at 60° , Acoustic Doppler Velocity Profiler (ADVP) configuration

R [m]	B [m]	d_{50} [mm]	Q [l/s]	H [m]	S_s [‰]	U [m/s]	C [m ^{1/2} /s]	Re [10 ³]	Re^* [/]	Fr [/]	R/B [/]	R/H [/]	B/H [/]
-2.0	0.40	2.1	17	0.11	1.89	0.38	35	42	70	0.36	5	17.9	3.6

R : centerline radius of curvature (negative along the n -axis)

B : channel width

d_{50} : median grain size diameter of bed material

Q : flow discharge

H : reach-averaged flow depth \approx flow depth at centerline
in section at 60°

S_s : reach-averaged water-surface gradient at centerline

u^* : friction velocity

U : reach-averaged velocity

C : Chezy friction factor; $C\sqrt{g}=U/u^*$

$Fr = U/(gH)^{1/2}$: reach-averaged Froude number

$Re = UH/\nu$: reach-averaged flow Reynolds number

$Re^* = u^*k_s/\nu$: reach-averaged particle Reynolds number

ν : molecular viscosity

k_s : Nikuradse equivalent sand roughness

Table 1: Hydraulic conditions

The parameters $R/B = 5$ and $R/H = 17.9$, and hence the aspect ratio $B/H = 3.6$, correspond to a bend that is rather sharp and significantly narrower than usual in natural lowland rivers. These ratios do occur, however, in mountain rivers and man-made channels. Moreover, the flow in a wide bend with a mobile-bottom topography is concentrated most of the time in the deepest part of the cross-section near the outer bank, where a significant transversal bottom slope exists (Fig.1; Odgaard, 1984; Dietrich, 1987). The aspect ratio there is significantly smaller than in a straight reach of the same channel. The flow in the outer bend in the present experiment is thought to be representative of the flow in the deepest part of natural channel bends. By considering a relatively sharp bend, the curvature effects are more pronounced, hence better visible.

Velocity measurements were made on a fine grid in the outer half of the cross-section at 60° from the bend entrance, using an Acoustic Doppler Velocity Profiler (ADVP). The measured data are represented and analyzed in a co-ordinate system with the s -axis along the channel centerline, the n -axis perpendicular to it and pointing to the left and the z -axis vertically upwards, perpendicular to the horizontal (s,n)-plane. The measuring section, the reference system, the measuring grid and the ADVP-configuration are shown in Fig.1b. The ADVP measures the three instantaneous velocity components $v_j(t)$ simultaneously in a horizontal line perpendicular to the channel wall. This provides sufficient information to derive the mean velocity vector $\bar{v} = (v_s, v_n, v_z)$, as well as the fluctuating velocity vector $\bar{v}' = (v'_s, v'_n, v'_z)$ and all turbulent correlations $\overline{v_i'^a v_j'^b}$ ($i,j = s,n,z$; a and b are integers). To eliminate the experimental scatter, analytical surfaces have been fitted to the raw experimental data, using two-dimensional smoothing splines with weight functions (de Boor, 1978). This procedure allows for a more precise evaluation of the differential-terms in the transport equation for tke. Furthermore, thanks to the weight functions, the measured data can be extended outside the measuring grid by imposing physical boundary conditions (such as the no-slip condition on rigid boundaries, no shear parallel to the water surface, etc.). Yet, these experimental evaluations are rather inaccurate and interpretations should be limited to order-of-magnitude considerations. Detailed information on the experimental set-up, the ADVP, the data treatment procedures, the measuring grid and the extrapolations outside the measuring grid, estimations of the experimental accuracy and presentations of the distributions of the mean velocities and the turbulent stresses $\overline{v_i' v_j'}$ has been reported before (Blanckaert and Graf, 2001a). Only the measured data that are of particular relevance to this paper, viz. the mean and turbulent kinetic energy distributions, will be given here .

3 Experimental results

The flow field in the investigated cross-section at 60° is characterized by a bi-cellular pattern of cross-stream motion (v_n, v_z) , which is shown in Fig.2. A circulation cell – termed center-region cell - with outward velocities near the water surface and inward velocities near the bottom is observed in the center region. This cell represents the classical helical motion characteristic of flow in bends. The cross-stream velocities involved are typically 10% of the mean downstream velocity. A region of considerably weaker cross-stream velocities is observed close to the outer bank. In the upper part of this outer-bank region an additional circulation cell – termed outer-bank cell – is found, with a sense of rotation opposite to that of the center-region cell. The cross-stream velocities involved are typically 3% of the mean downstream velocity. The mechanisms leading to these two circulation cells have been analyzed by Blanckaert and de Vriend (2002a).

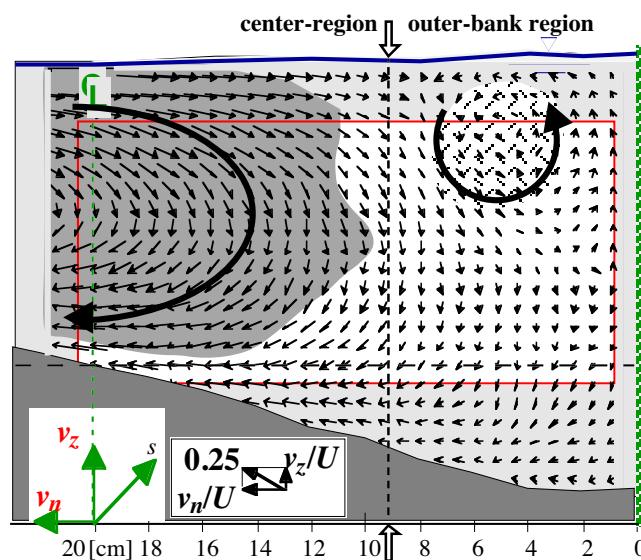


Fig. 2: Vector representation of normalized cross-stream motion, $(v_n, v_z)/U$.

Figs. 3a,b show the normalized distributions over the investigated part of the cross-section of the mean-flow kinetic energy, $K/(1/2U^2)$, and the turbulent kinetic energy, $k/(1/2u_{*,60}^2)$, per unit mass, in which K and k are defined as:

$$K = \frac{1}{2}(v_s^2 + v_n^2 + v_z^2) \approx \frac{1}{2}v_s^2 \quad \text{and} \quad k = \frac{1}{2}(\overline{v_s'^2} + \overline{v_n'^2} + \overline{v_z'^2}) \quad (1)$$

respectively. The characteristic shear velocity in the measuring section, $u_{*,60} = \sqrt{gR_h(-\partial z_{s,60}/\partial s)} = 0.045$ m/s, is based on the downstream water-surface gradient at the centerline, $-\partial z_{s,60}/\partial s = 2.89$ ‰, and the hydraulic radius, $R_h = 0.07$ m, in the section at 60° . The contribution of the different components to k and to K have been reported by Blanckaert and Graf (2001a).

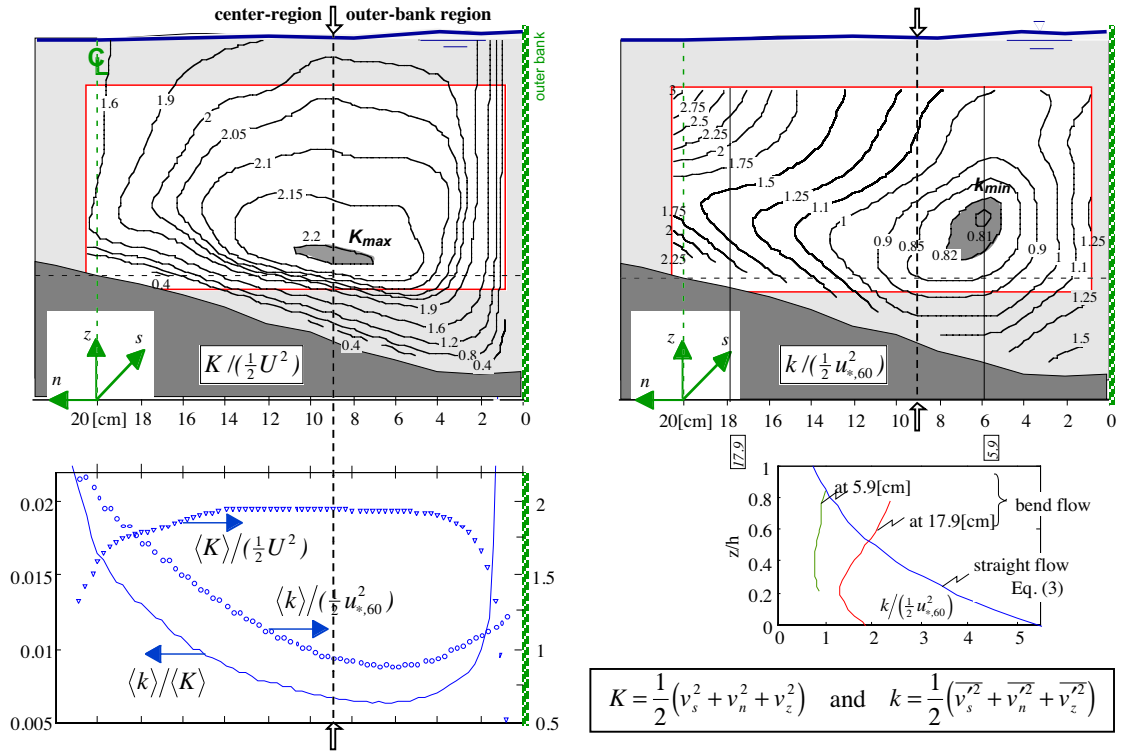


Fig.3a: Isolines of normalized mean-flow kinetic energy, $K / (\frac{1}{2} U^2)$.



Fig.3b: Isolines of normalized turbulent kinetic energy, $k / (\frac{1}{2} u_{*60}^2)$.

Fig.3c: Depth-averaged normalized mean flow and turbulent kinetic energy, $\langle K \rangle / (\frac{1}{2} U^2)$ and $\langle k \rangle / (\frac{1}{2} u_{*60}^2)$, and ratio, $\langle k \rangle / \langle K \rangle$.

Fig.3d: Vertical profiles of $k / (\frac{1}{2} u_{*60}^2)$ in straight flow and bend flow (measured).

In a straight uniform flow, the vertical profiles of $K_{straight} = v_{s, straight}^2 / 2$ typically increase from zero at the bottom to a maximum value near the water surface, whereas the vertical profiles of k typically decrease monotonically from the bottom towards the water surface. Assuming a logarithmic downstream velocity profile and an exponentially decreasing turbulent kinetic energy from the bottom towards the water surface (Nezu and Nakagawa, 1993, p.54):

$$v_{s, straight} = U_s \left[1 + \frac{\sqrt{g}}{\kappa C} \left(1 + \ln \frac{z}{h} \right) \right] = U_s f_s \quad \text{and} \quad k_{straight} = 4.78 u_*^2 e^{-2 \frac{z}{h}} \quad (2), (3)$$

($U_s = \langle v_s \rangle$ is the local depth-averaged downstream velocity), it is found by integration of equations (2) and (3) over the flow depth h that $\langle k \rangle / \langle K \rangle$ uniquely depends on the Chezy friction coefficient:

$$\left. \frac{\langle k \rangle}{\langle K \rangle} \right|_{straight} = \frac{\langle k_{straight} \rangle}{\frac{1}{2} \langle v_{s, straight}^2 \rangle} = \frac{4.133}{\langle f_s^2 \rangle} \left(\frac{u_*}{U_s} \right)^2 = \frac{4.133}{\langle f_s^2 \rangle} \cdot \frac{g}{C^2} \approx 4.1 \frac{g}{C^2} \quad (4)$$

For $C \approx 35 \text{ m}^{1/2}/\text{s}$, $\langle k \rangle / \langle K \rangle$ would assume a value of about 0.03.

In our experiment, the distributions of K and k show a much more complex behavior. The vertical profiles of $K/(1/2U^2) \approx (v_s/U)^2$ (Fig. 3a) do not increase from the bottom to the surface but have their maximum in the lower part of the water column. K increases in outward direction, to reach a maximum of about $1.1 U^2$ at the separation between the two circulation cells. Fig. 3c shows that the depth-averaged value, $\langle K \rangle$, increases strongly near the centerline and is nearly constant at about $0.95 U^2$ in most of the outer half of the cross-section. Since the total mean flow kinetic energy content of the cross-section will not be very different from that in the corresponding straight channel flow, $\langle K \rangle$ has to be much smaller in the inner part of the cross-section. This means that the mean flow kinetic energy is concentrated in the outer bend. The mechanism leading to this K -distribution has been analyzed by Blanckaert and Graf (2002).

The measured distribution of k (Fig. 3b) exhibits an opposite pattern, in the water column as well as over the width. The position of the core of minimum k -values nearly coincides with that of maximum K -values, and positive/negative gradients of k correspond to negative/positive gradients of K . In Fig. 3d, the vertical profile of $k_{straight}/(1/2u_{*,60}^2)$ for straight uniform flow - according to Eq. (3) and based on $u_* = U\sqrt{g/C}$ with $C \approx 35 \text{ m}^{1/2}/\text{s}$ - is compared with the vertical profiles of $k/(1/2u_{*,60}^2)$ measured at 5.9 cm and 17.9 cm from the outer bank. In contrast to straight uniform flow, the measured profiles decrease from the bottom to a minimum and then increase towards a maximum near the water surface (Fig. 3b). Similar vertical k -profiles have been measured in channel bends and meanders by Booij (1985), Tamai and Ikeya (1985), Anwar (1986), Muto (1997) and Sudo et al. (2001). The depth-averaged value $\langle k \rangle/(1/2u_{*,60}^2)$ decreases from a centerline value of 2.2 to minimum values of about 1 in the outer-bank region, only to increase in the region affected by bank friction.

While the ratio $\langle k \rangle/\langle K \rangle$ would be constant (about 0.03) over the width in straight uniform flow, the opposite patterns of K and k result in a pronounced variation of $\langle k \rangle/\langle K \rangle$ over the width in our experiment. Towards the centerline, $\langle k \rangle/\langle K \rangle$ is of the expected order of magnitude, but it then strongly decreases, down to 0.01 in most of the outer bend, only to increase strongly in the region affected by bank friction. Since the cross-sectional mean must be not far from 0.03, high $\langle k \rangle/\langle K \rangle$ -values must exist in the inner half-section. Thus, as compared to straight uniform flow, the turbulence activity is rather strongly reduced in the outer bend, and enhanced correspondingly in the inner bend.

As stated in the ‘‘Introduction’’, knowledge of the turbulence characteristics and insight into the role of turbulence are of practical relevance. In the next section, a term-by-term evaluation of the transport equation for k is made on the basis of the measured data, in order to gain insight into the mechanisms leading to the observed distributions of k and $\langle k \rangle/\langle K \rangle$.

4 Analysis

4.1 Transport equation for k

The distribution of k is governed by the *transport equation for k* (Hinze, 1975; see Batchelor, 1970, for the transformation to the curvilinear co-ordinate system):

$$\underbrace{0 = \frac{\partial k}{\partial t}}_{\text{steady flow}} = - \underbrace{\left(\frac{1}{1+n/R} v_s \frac{\partial k}{\partial s} \right)}_{\text{non-uniformity}} + \underbrace{\left(v_n \frac{\partial k}{\partial n} + v_z \frac{\partial k}{\partial z} \right)}_{\text{advective } k\text{-transport by cross-stream motion}}$$

$$- \underbrace{\left[\frac{1}{1+n/R} \frac{\partial}{\partial s} \left(\left(\frac{p'}{\rho} + k_t \right) v'_s \right) \right]}_{\text{non-uniformity}} + \underbrace{\left[\frac{1}{1+n/R} \frac{\partial}{\partial n} \left((1+n/R) \left(\frac{p'}{\rho} + k_t \right) v'_n \right) + \frac{\partial}{\partial z} \left(\left(\frac{p'}{\rho} + k_t \right) v'_z \right) \right]}_{\text{pressure-gradient work + turbulent } k\text{-transport}}$$

$$- \underbrace{\left[\left(\overline{v_s'^2} - \frac{2}{3} k \right) e_{ss} + \left(\overline{v_n'^2} - \frac{2}{3} k \right) e_{nn} + \left(\overline{v_z'^2} - \frac{2}{3} k \right) e_{zz} + 2 \overline{v_s' v_n'} e_{sn} + 2 \overline{v_s' v_z'} e_{sz} + 2 \overline{v_n' v_z'} e_{nz} \right]}_{\mathcal{P} = \text{production of } k = \text{exchange of kinetic energy between mean flow and turbulence}}$$

$$\underbrace{-\mathcal{E}(v)}_{\text{viscous dissipation of } k} \tag{5}$$

where k_t denotes the instantaneous turbulent kinetic energy and $e_{ss} + e_{nn} + e_{zz} = 0$:

$$k_t = \frac{1}{2} (v_s'^2 + v_n'^2 + v_z'^2) \tag{6}$$

Since they are not relevant for our experimental analysis, all terms containing the molecular viscosity ν are regrouped in $\mathcal{E}(v)$. Besides the viscous dissipation of turbulence it also contains some viscous diffusion (see Hinze, 1975), which is assumed to be negligibly small, given the high Reynolds number in these experiments. In Eq. (5), t denotes time, $(1+n/R)$ is a metric factor accounting for the divergence of the radial co-ordinate axes, p' are the turbulent pressure fluctuations and e_{ij} ($i, j = s, n, z$) are the strain rates.

The bracketed terms in the third line of Eq. (5), denoted by \mathcal{P} , are found with the opposite sign in the transport equation for the mean flow kinetic energy, K (Hinze, 1975). They represent the exchange of kinetic energy between mean flow and turbulence, which occurs through work of deformation of the mean motion by the turbulent stresses. Although negative contributions may exist in some regions of the flow domain (also see Fig. 4c), the sum is globally positive and it is commonly called the production of k . Globally speaking, \mathcal{P} is balanced by the viscous dissipation $\mathcal{E}(v)$. Locally, \mathcal{P} and $\mathcal{E}(v)$ do not balance and their difference is due to the transport terms in the first and second lines

of Eq. (5). These terms do not generate or dissipate energy, but merely redistribute it from one point in the flow to another (Tennekes and Lumley, 1972). The terms in the first line represent the advective transport of k by the cross-stream motion (v_n, v_z) and due to the flow non-uniformity ($\partial/\partial s$), whereas the terms in the second line represent turbulent diffusion of k and work done by the pressure-gradient. Our experiment concerns steady flow ($\partial k/\partial t=0$), but the unsteady term is retained in Eq. (5) to facilitate interpretation: positive/negative terms in the right-hand-side correspond to terms that tend to increase/decrease the local k .

The various terms in Eq. (5) are evaluated, as far as possible, from our experimental data, in order to gain insight into the mechanisms underlying to the observed k -distribution. By definition, the terms related to downstream variations in the flow field ($\partial/\partial s$ -terms; including those appearing implicitly in the strain rates e_{ss} , e_{sn} and e_{sz}) cannot be evaluated from velocity measurements in a single cross-section. The terms related to the pressure fluctuations could not be evaluated since the pressure was not measured.

In *straight uniform flow*, there is no advective transport of tke, whence Eq. (5) reduces to

$$0 = -\frac{\partial}{\partial z} \left(\overline{\left(\frac{p'}{\rho} + k_t \right) v'_z} \right) - 2\overline{v'_s v'_z} e_{sz} - \varepsilon(v) \quad (7)$$

Assuming a triangular distribution of $-\overline{v'_s v'_z}$ with values 0 at the water surface and u_*^2 at the bottom, and assuming a logarithmic vertical profile of the downstream velocity v_s (Eq. 2), one can easily derive that

$$\mathcal{P}_{straight} = -2\overline{v'_s v'_z} e_{sz} = \frac{1}{\kappa} \frac{u_*^3}{H} \left(\frac{H}{z} - 1 \right) \quad \text{or} \quad \frac{-2\overline{v'_s v'_z} e_{sz}}{u_*^3/H} = \frac{1}{\kappa} \left(\frac{H}{z} - 1 \right) \quad (8)$$

This function is shown in Fig. 4a. The k -production is maximum at the bottom and rapidly decreases towards the water surface. Clearly, bottom friction is the principal source of tke. This justifies normalizing the evaluated terms in the k -equation by $u_{*,60}^3/H = 0.0008 \text{ m}^2/\text{s}^3$. The tke is redistributed over the flow depth by the first terms in Eq. (7) and dissipated by the last term.

Intuitively, one would expect the observed k -pattern in our *curved-flow experiment* to be redistributed (advective transport) by the cross-stream motion (v_n, v_z). This is difficult to demonstrate, since the k -distribution strongly interacts with the cross-stream motion. In order to have an idea of its influence, we start from a fictitious k -distribution, as would exist in the absence of cross-stream motion, with high k -values near the flow boundaries and a rapid decrease away from those boundaries. Such a distribution, inspired by Eq. (3), is proportional with the bottom shear stress $\tau_b/\rho = u_*^2$, which in the absence of advective momentum transport and neglecting influences from the banks, can be obtained from the simplified depth-integrated downstream momentum equation (Blanckaert and Graf, 2002):

$$\frac{\tau_b}{\rho} = -\frac{1}{1 + n/R} gh \frac{\partial z_s}{\partial s} \quad (9)$$

$\partial z_s/\partial s$ is nearly constant over the width of the bend; however, the physical water surface slope, $(1+n/R)^{-1} \partial z_s/\partial s$, is larger in the inner bend than in the outer bend due to the metric factor $1+n/R$ ($n/R >/< 0$ in outer/inner bend). This is the so-called potential-vortex effect that impels the locus of high velocity towards the inner bank. Over a natural bottom topography, however, the influence of the local flow depth h is dominant and $\tau_b/\rho = u_*^2$ increases in outward direction. The fictitious k -distribution shown in Fig. 4b is obtained by inserting the measured values of $\partial z_s/\partial s$ and h in Eq. (9) and Eq. (3). To account in a simple way for turbulence generation by bank friction, the fictitious k -pattern is taken symmetrical about the bisectors of the lower corners of the flow domain.,

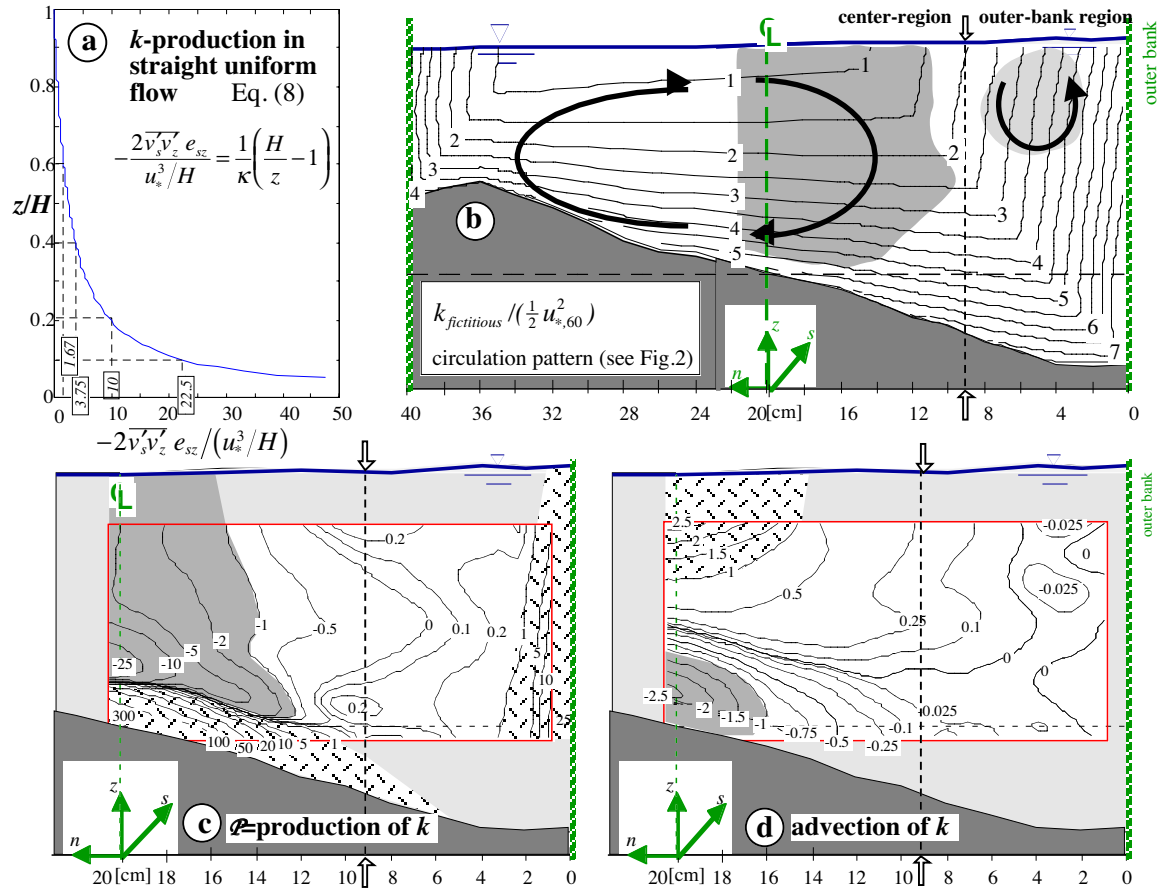


Fig. 4: (a) Normalized production of k in straight uniform flow; (b) Fictitious k -distribution and schematic pattern of cross-stream motion (v_n, v_z); (c) Normalized production of k measured in the experiment; (d) Normalized advective transport of k measured in the experiment.

We now let the measured (v_n, v_z)-pattern act upon this fictitious k -distribution (Fig. 4b). The center-region cell advects the clockwise:

- the high near-bottom k -values are concentrated in the inner bend;
- the high k -values near the inner bank spread out near the water surface in the inner bend;

- the low k -values near the water-surface shift towards the downward flow outer part of the center-region cell and give rise to a core of low k -values further down in the water column;
- the relatively low k -values originating from the region of downward flow between the two cells concentrate near the bottom in the outer bend.

Similarly, the outer-bank cell advects tke counter-clockwise:

- the high k -values near the outer-bank shift towards the water-surface near the outer-bank;
- the low values near the water surface shift towards the region where the outer-bank cell goes downwards and contributes to the core of low k -values;
- the relatively low k -values in the lower half of the outer-bank cell are advected toward the outer bank.

Qualitatively, the above description agrees well with the measured distribution of k (see Fig. 3b).

However, the measured distribution of the advective k -transport by the cross-stream motion (Fig. 4d) does not clearly show the above described redistribution. In the center-region, the measured advective k -transport (Fig.4d) is negative near the bottom and thus tends to decrease the observed k , whereas it is positive near the water surface and tends to increase the observed k . Averaged over the flow depth, the positive and the negative contributions nearly cancel. In the outer-bank region, the measured advective k -transport is negligible. The measured advective k -transport can still explain the deformation of the vertical k -profiles as compared to the straight-uniform flow profiles, but does not explain anymore the observed width-distribution of k , and especially the reduced values in the outer-bank region.

This seemingly contradiction is due to the non-linearity of the k -dynamics. Similar to the fictitious k -distribution, a fictitious \mathcal{P} -distribution can be assumed that would exist in the absence of cross-stream motion. Proportional to the local (shear) velocity, it would increase in outward direction and have the same vertical profiles as in straight uniform flow (Eq. 8). Under the influence of the cross-stream motion, the fictitious k -distribution gradually modifies as described above, which results in a gradual redistribution of \mathcal{P} and of the advective k -transport terms themselves.

The measured distribution of the production \mathcal{P} (see Fig.4c) strongly deviates from the fictitious distribution, over the flow depth as well as over the channel width. Whereas the fictitious \mathcal{P} -distribution increased in outward direction, the measured \mathcal{P} -distribution decreases in outward direction. In the center-region, \mathcal{P} (Fig.4c) is mainly due to bottom friction and the measured \mathcal{P} -values are of the same order of magnitude as the typical near-bottom values in straight uniform flow (Fig.4b); care should be taken, however, with the interpretation of the near-bottom values since turbulence measurements near the bottom are not very reliable (Blanckaert and Graf, 2001a). Contrary to the straight-uniform flow profiles, negative values of \mathcal{P} are observed over most of the flow depth, indicating a restitution of kinetic energy from the turbulence to the mean flow. These negative values, which reach normalized magnitudes as large as $O(-25)$, are almost entirely due to the

$\overline{v'_s v'_z} e_{sz}$ -contribution (Blanckaert and de Vriend, 2002a, Fig.7c). Obviously, as compared to a situation with uniquely production of turbulent kinetic energy, $\mathcal{P} > 0$, the existence of zones with $\mathcal{P} < 0$ tends to reduce k . In the outer-bank region, \mathcal{P} has a lower magnitude than in the center-region, which is mainly due to the negligible values of the turbulent shear stress $\overline{v'_s v'_z}$ (Blanckaert and Graf, 2001a, Fig.6a) and of the corresponding $\overline{v'_s v'_z} e_{sz}$ -contribution (Blanckaert and de Vriend, 2002a, Fig.7c) on the measuring grid. Values increase to $O(20)$ in the region affected by friction on the outer bank, indicating that the outer-bank friction is smaller than the bottom friction $O(300)$ in the center-region, which is in agreement with the measured distributions of $\overline{v'_s v'_n}$ and $\overline{v'_s v'_z}$ (Blanckaert and Graf, 2001a, Fig.6). This small outer-bank friction is explained partially by the smoothness of the outer-bank as compared to the rough sand bottom and partially by the reduced turbulence activity in the outer-bank region.

The turbulent diffusion in transversal direction (not shown) is found to be relatively small, with normalized magnitudes less than $O(0.1)$. The accuracy of the evaluated vertical diffusion terms (not shown) is poor. As expected, the terms are positive near the bottom, with relatively high normalized values of $O(50)$, and negative over most of the water column. By no means, these terms can explain the observed transversal distribution of k .

The above analysis leads to the following hypothesis about the mechanisms responsible of the observed distribution of k . In the absence of cross-stream motion, the fictitious production \mathcal{P} increases in outward direction and leads to an outward increasing fictitious k -distribution as shown in Fig.4b. The advective k -transport by the cross-stream motion is at the origin of the redistribution of k , and causes increasing values in the inner half of the cross-section and decreasing values in the outer half. As k gets redistributed, the advective k -transport becomes less efficient and ultimately, it does not explain the observed width-distribution of k anymore. However, as k becomes redistributed also the production terms \mathcal{P} are modified (the values of the turbulent stresses $\overline{v'_i v'_j}$ obviously depend on the available turbulent kinetic energy k). Whereas the initial fictitious \mathcal{P} increases in outward direction, the final modified \mathcal{P} -distribution decreases in outward direction. It can be concluded that this final \mathcal{P} -distribution is the major responsible for the similar measured outward decrease of k . Especially the low values of the $\overline{v'_s v'_z} e_{sz}$ -contribution in the outer-bank region might be important for the reduced k values.

Obviously there is a strong feedback between the reduced levels of k and the low values of the production term \mathcal{P} in the outer-bank region. From the distributions of k and of \mathcal{P} , however, it is not clear to what extent the reduced k is due to the low \mathcal{P} -values, or rather gives rise to those low values. This feedback problem will be investigated by means of some typical turbulence characteristics in Section 4.2 and discussed in Section 4.3.

4.2 Turbulence structure

In the previous chapter, the causal relation between k and \mathcal{P} did not become clear. We will therefore take a closer look at the turbulence-structure parameters a_I and v_{jk} (the mixing coefficients). The role of these turbulence-structure parameters in the k - \mathcal{P} relationship and the k -distribution will be discussed Section 4.3. A rather extensive presentation of the mixing coefficients is given, since they are also important with respect to spreading and mixing of matter, pollutants and heat.

4.2.1 Structure parameter a_I

An important turbulence-structure parameter is a_I , defined as (Schwarz and Bradshaw, 1994; Piquet, 1999):

$$a_I = \sqrt{\overline{v'_s v'_z}^2 + \overline{v'_n v'_z}^2} / 2k \quad (10)$$

According to Schwarz and Bradshaw (1994), it can be regarded as a first indicator of the efficiency of turbulent eddies in producing shear, given the amount of tke. The parameter a_I is known to be largest in two-dimensional flow and smaller in three-dimensional flows. These smaller values of a_I in various types of three-dimensional flows are shown and physically explained by Schwarz and Bradshaw (1994) and Piquet (1999). To our knowledge, values of a_I for three-dimensional open-channel flow have not been reported before.

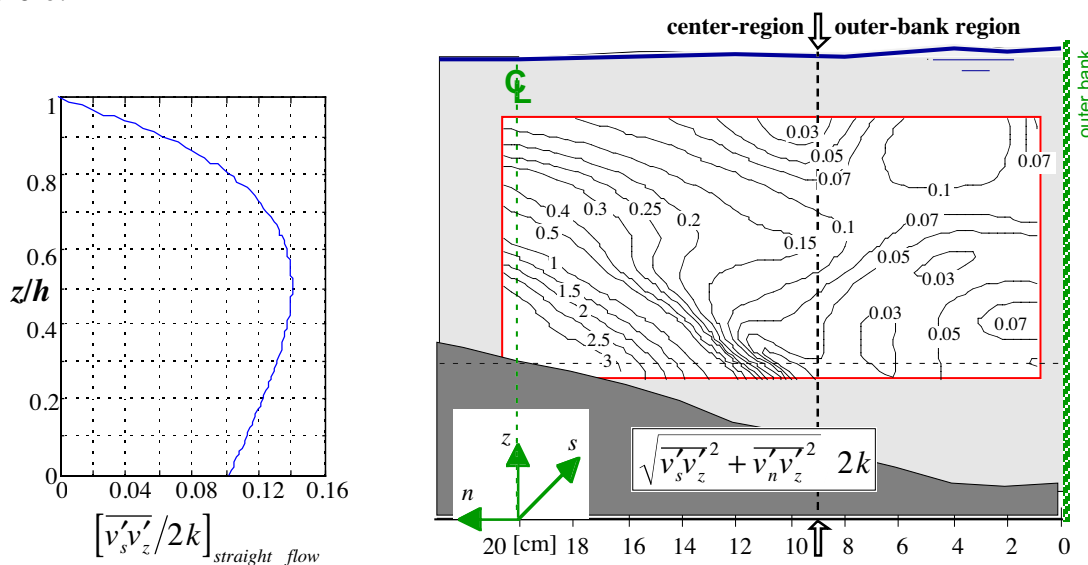


Fig. 5: Turbulence structure parameter $a_I = \sqrt{\overline{v'_s v'_z}^2 + \overline{v'_n v'_z}^2} / 2k$; (a) theoretical profile in straight uniform flow; (b) measured distribution in curved flow.

The vertical profile of a_I for straight uniform open-channel flow is shown in Fig. 5a. It is based on a triangular profile of $-\overline{v'_s v'_z}$ that increases from 0 at the water surface to u_*^2 at the bottom, under the assumption that $\overline{v'_n v'_z} = 0$ and that Eq. (3) holds for k . The a_I -profile increases from 0 at the water surface, reaches a maximum of about 0.14 around mid-depth and subsequently decreases to about 0.1 at the bottom. The experimental distribution of a_I for our curved open-channel flow is shown in Fig. 5b. In the center region, values are

high, $O(1)$. The estimation of the near-bottom values, however, is not very accurate (Blanckaert and Graf, 2001a), whence the values may be overestimated. Outward from the centerline, a strong reduction of a_l is observed: $a_l = O(0.1)$ near the separation of the two circulation cells and even less in the outer-bank region. This strong outward decrease of a_l corresponds with a similar outward decrease of $\overline{v'_s v'_z}$ (Blanckaert and Graf, 2001a). Apparently, the efficiency of shear production decreases towards the outer bend.

4.2.2 Mixing coefficients

The mixing coefficients v_{jk} also tell something about the turbulence structure. Similar to the definition of the eddy viscosity, they are defined as the ratio between the deviatoric turbulent stresses $-(\overline{v'_j v'_k} - 2/3 \delta_{jk} k)$ and the corresponding strain rates e_{jk} :

$$v_{jk} = v_{kj} = -\frac{\overline{v'_j v'_k} - 2/3 \delta_{jk} k}{2e_{jk}} \quad (j,k=s,n,z) \quad (11)$$

in which δ_{jk} is the Kronecker delta. Note that these six mixing coefficients do not have the frame-indifferent characteristics of the Reynolds stress tensor $\overline{v'_j v'_k}$ or the strain rate tensor e_{jk} . Applying the definition of the mixing coefficients, the terms representing production of turbulent kinetic energy in Eq. (5) can be rewritten as:

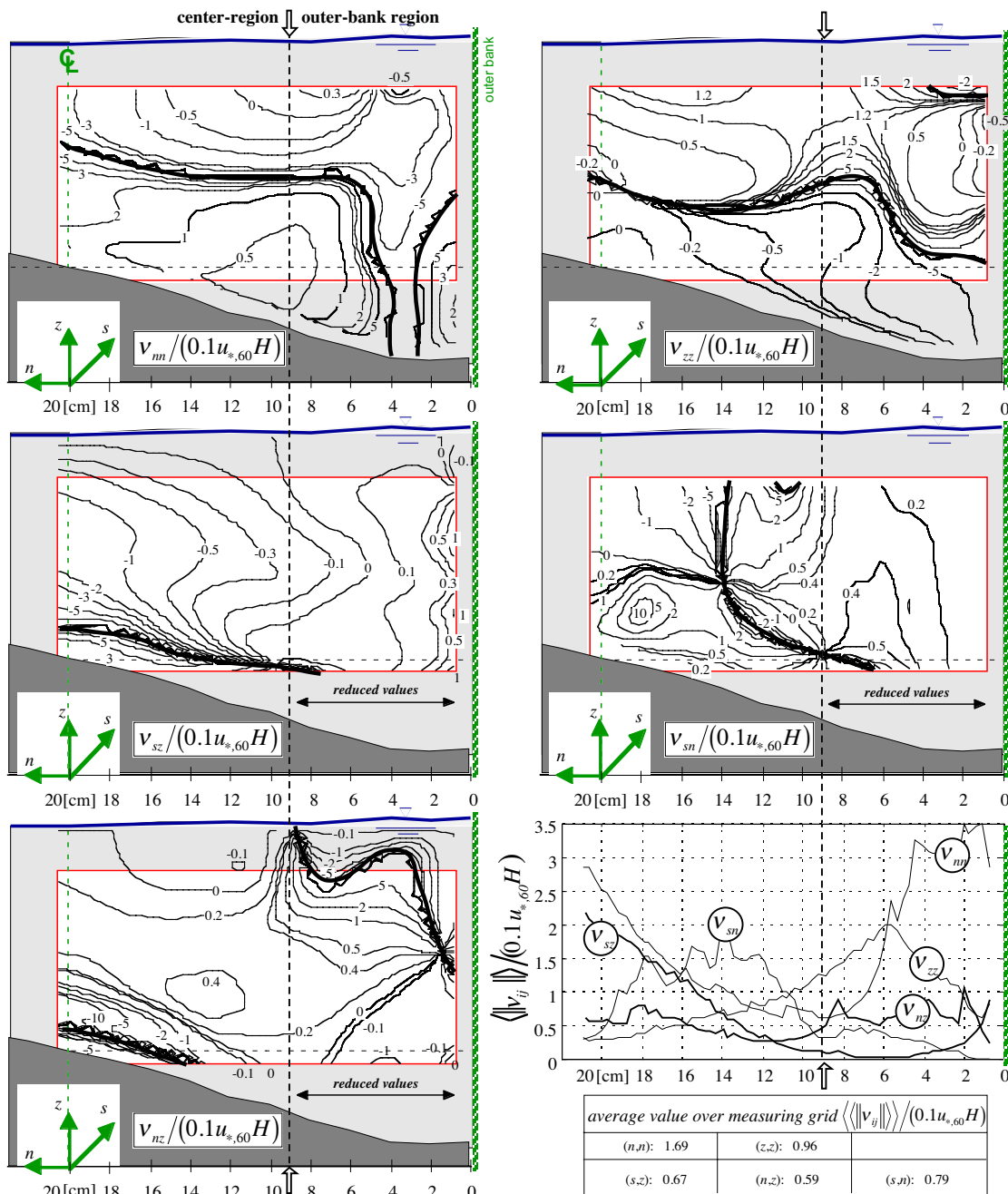
$$\mathcal{P} = 2(v_{ss} e_{ss}^2 + v_{nn} e_{nn}^2 + v_{zz} e_{zz}^2 + 2v_{sn} e_{sn}^2 + 2v_{sz} e_{sz}^2 + 2v_{nz} e_{nz}^2) \quad (12a)$$

According to Eqs. (11) and (12a), the mixing coefficients can be regarded as indicators of the efficiency of the strain rates in producing turbulence. The sign of the mixing coefficient v_{jk} corresponds to the sign of the energy exchange term $-(\overline{v'_j v'_k} - 2/3 \delta_{jk} k)e_{jk}$ in \mathcal{P} : $v_{jk} > 0$ corresponds to production of tke, whereas $v_{jk} < 0$ corresponds to a restitution of kinetic energy from the turbulence to the mean flow via the corresponding turbulent stress $\overline{v'_j v'_k}$. Applying a scalar eddy viscosity for turbulence closure implies that $v_{ss} = v_{nn} = v_{zz} = v_{sn} = v_{sz} = v_{nz} = v_t > 0$ and that \mathcal{P} is definitely positive:

$$\mathcal{P} = 2v_t (e_{ss}^2 + e_{nn}^2 + e_{zz}^2 + 2e_{sn}^2 + 2e_{sz}^2 + 2e_{nz}^2) > 0 \quad (12b)$$

The mixing coefficients are particularly important with respect to environmental problems such as the spreading and mixing of matter, pollutants and heat. Those phenomena are described by an advection-diffusion equation, in which the six diffusion coefficients (Rutherford, 1994, p. 33) are commonly taken proportional (multiplied by a Prandtl or Schmidt number) to the mixing coefficients.

In a straight uniform flow, often a scalar eddy viscosity, v_t , is assumed. A possible approach is to prescribe this quantity algebraically, for instance by a parabolic distribution over the water column. One such distribution, corresponding with the logarithmic velocity profile in straight uniform flow, equals zero at the water surface and at the bottom, and has a depth-averaged value $\langle v_t \rangle = 0.067 u_* h$. This is why the experimental mixing coefficients shown in Fig. 6 are normalized by $0.1 u_* h$. Note that the contributions due to the non-uniformity of the flow field ($\partial/\partial s$ -contributions) in the strain rates e_{sn} and e_{sz} could not be evaluated from the data available.



a **b**
c **d**
e **f**

Fig. 6a-e: Isolines of the normalized mixing coefficients (Eq.11).

Fig. 6f: Width-distribution of the depth-averaged mixing coefficients

The distributions of all mixing coefficients shown in Figs. 6a-e contain positive as well as negative values. Near the bottom, mainly positive are found, whereas negative values occur mainly in the upper part of the water column. These negative values, $v_{jk} < 0$, correspond to a restitution of kinetic energy from the turbulence to the mean flow via the turbulent stress $\overline{v'_j v'_k}$. Obviously, the existence of zones with negative mixing coefficients tends to reduce k with respect to the situation in which there is only production of turbulent kinetic energy ($v_{jk} > 0$). Negative values of the mixing coefficients v_{jk} - or of the

corresponding kinetic energy exchange $-(\overline{v'_j v'_k} - 2/3 \delta_{jk} k) e_{jk}$ - have been reported before (Booij, 1985; Anwar, 1986; Booij and Tukker, 1996; Shiono and Muto, 1998). Blanckaert and de Vriend (2002a) have shown that this restitution of kinetic energy from the turbulence to the mean flow plays an important role in the generation of the outer-bank cell of cross-stream circulation in the here-considered experiment.

Looking at the distribution over the water column, the magnitude of the experimental mixing coefficients has a tendency to be minimal near the bottom and near the water surface and to have a maximum somewhere halfway the water column. Qualitatively, this is in agreement with the parabolic profile used in straight uniform flow.

As stated before, the magnitudes of the mixing coefficients are very important to the modeling of spreading and mixing of matter, pollutants and heat. However, experimental data on these mixing coefficients are scarce. The present data show that the coefficient $\|v_{mn}\|$ (Fig. 6a) is maximum near the centerline, decreases towards a minimum near the separator between the two circulation cells and increases again towards the outer bank. The coefficient $\|v_{zz}\|$ (Fig. 6b) shows the opposite behavior and has its maximum in the separation zone between the two cells. As mentioned before, the (s,n) and the (s,z) contributions are dominant in the production of tke. The magnitude of the corresponding mixing coefficients $\|v_{sz}\|$ and $\|v_{sn}\|$ (Figs. 6c and 6d, respectively) strongly decreases in the outward direction, from $O(1 \text{ to } 5)$ in the center region to $O(0.1 \text{ to } 0.5)$ in the outer-bank region. $\|v_{nz}\|$ (Fig. 6e) behaves similarly, except that it assumes high values near the center of the outer-bank cell. This outward decrease of the mixing coefficients related to the turbulent shear stresses is in agreement with the outward decrease of the coefficient a_1 (Fig. 5b) and confirms the observation that the efficiency of shear stress production for a given turbulent kinetic energy is reduced in curved flow.

Fig. 6f shows the lateral distribution in the outer bend of the mixing coefficients, $\langle\langle \|v_{jk}\| \rangle\rangle$, being the depth-averaged absolute values evaluated within the measuring grid and excluding the asymptotic values where the strain tends to zero. These lateral distributions confirm the behavior observed in the three-dimensional distributions. Note the strong decrease of $\langle\langle \|v_{sz}\| \rangle\rangle$ in outward direction, with very low values in the outer-bank region. $\langle\langle \|v_{sn}\| \rangle\rangle$ reaches similar small values in the outer-bank region. The normalized average values over the entire measuring grid, $\langle\langle\langle \|v_{jk}\| \rangle\rangle\rangle$, are shown in the table below Fig. 6f. For the (s,z) -component, a value of 0.67 is found, which coincides with the typical average value in straight uniform flow (see before). The normalized values for the (s,n) and the (n,z) -component are of similar magnitude. The dominant component is (n,n) , with a normalized value of 1.69 that should be compared with the values of 1.5 (laboratory channels) to 6 (irregular waterways) reported by Graf and Altinakar (1998). It is remarkable that the components related to the turbulent normal stresses are larger than those related to the turbulent shear stresses. This confirms, once again, that the efficiency of shear stress production, given the turbulent kinetic energy, is reduced in curved flow.

4.3 Discussion

The analysis of the transport equation for k indicated that the reduced turbulence activity in the outer-bank region cannot be explained solely from the advective redistribution of k by the cross-stream motion. This phenomenon is primarily due to an outward decrease of the k -production. The parameter a_i and the mixing coefficients v_{jk} (chapter 4.2) indicate that the turbulence structure in our curved flow experiment is significantly different from that in straight uniform flow. Given the same amount of turbulent kinetic energy k , the turbulent shear stresses $\overline{v_j v_k}$ ($j \neq k$) turn out to be significantly smaller in the curved flow.

The observed decrease of the turbulence activity in the outer-bank region can be explained from these findings as follows. Suppose we start from the turbulence structure in straight uniform flow. If less turbulent shear stress is produced while the k -level remains the same, this leads to a reduced production of k (see Eq. 5), and less production obviously results in lower k -levels. The lower k -levels, in their turn, lead to smaller turbulent stresses $\overline{v_j v_k}$ and thus also to a smaller production \mathcal{P} . Ultimately, this feedback mechanism will lead to a reduced k -level as compared to that for straight uniform flow.

In a complementary paper, Blanckaert and de Vriend (2002b) have further analyzed the turbulence structure of the same flow field. They found that the velocity fluctuations are a-typically coherent over the width and therefore decomposed them into slow coherent fluctuations and a background signal. The slow fluctuations represent a bulk-oscillation of the pattern of circulation cells. A spectral analysis shows that the slow fluctuations have the characteristics of a wave-like motion (low efficiency of shear generation) whereas the background signal has the characteristics of developed turbulence. This physically explains why the total velocity fluctuations lead to less shear stress production than if all of it were developed turbulence.

As a consequence, in order to simulate accurately the k -distribution, it is not sufficient for turbulence closures to incorporate the transport equation for k (Eq. 5), they also need to accurately describe the turbulence structure, i.e. the distribution of the turbulence among the different turbulent stresses. Factors that influence the turbulence structure are the cross-stream motion, downstream and transversal pressure gradients, accelerations and decelerations along streamlines, the curvature of the streamlines, the relative bottom roughness d_{50}/h , etc. Turbulence closures that use a transport equation for each of the turbulent stresses – such as Reynolds Stress Models – can account for all these factors. Such models are computationally expensive, whence lower-order turbulence closures are the most commonly used in practice, at the moment. The commonly used two-equation closures, however, do not account for the factors mentioned above. The k - ε model, for instance, which is often used for open-channel flows, contains the transport equation for k , but distributes the deviatoric turbulent stresses $-(\overline{v_j v_k} - 2/3 \delta_{jk} k)$ in proportion to the strain rates e_{jk} ; the scalar eddy viscosity ν_t being the factor of proportionality (see Eqs. 11 and 12a,b). It cannot accurately represent the turbulence structure, since ν_t cannot account for the observed behavior of the mixing coefficients:

- (i) ν_t is strictly positive, whereas the experimental mixing coefficients have positive as well as negative values.
- (ii) ν_t is a scalar, whereas the six experimental mixing coefficients have different magnitudes and different distributions.
- (iii) The scalar ν_t cannot account for the different behavior of the mixing coefficients related to the turbulent normal stresses and those related to the turbulent shear stresses, and especially the outward reduction of the latter.

All factors influencing the turbulence structure in our experiment directly or indirectly result from the main flow curvature. In the following, it will be attempted to find a qualitative correlation between the changes in the turbulence structure and a curvature parameter. Such a correlation might be useful to make semi-empirical extensions to existing turbulence closures, in order to improve their capabilities in curved open-channel flow.

5 Influence of streamline curvature on turbulence structure

5.1 Theoretical considerations

The structure of turbulence is known to be very sensitive to the streamline curvature: its influence is an order of magnitude larger than predicted by straightforward extensions of calculation methods for simple shear layers (Bradshaw, 1973). Bradshaw (1969) has established a formal analogy between the influence of streamline curvature and the influence of buoyancy. The analysis usually applied to derive buoyancy parameters from the equations of motion can be used to formally derive analogous curvature parameters. Whilst buoyancy leads to a density stratification of the flow, curvature leads to a pressure stratification of the flow.

The influence of streamline curvature on the turbulence structure has been investigated theoretically and numerically (Irwin and Smith, 1975; Gibson and Rodi, 1981; Leschziner and Rodi, 1981; Rodi and Scheuerer, 1983; Cheng and Farokhi, 1992), as well as experimentally (So and Mellor, 1973; Holloway and Tavoularis, 1992) for two-dimensional shear flows. Bradshaw (1973) has written an extensive survey report on the influence of streamline curvature, whereas Gibson and Rodi (1981) demonstrated its influence briefly and elegantly from the transport equations for the turbulent stresses in a two-dimensional flow. Both define a curvature-flux-Richardson number as :

$$R_f = \left(-2\overline{v_s'v_n'} \frac{v_s}{r_{sn}} \right) / \left(\frac{-\overline{v_s'v_n'}}{r_{sn}} \frac{\partial r_{sn} v_s}{\partial n} \right) = \frac{2v_s}{r_{sn}} / \left(\frac{1}{r_{sn}} \frac{\partial r_{sn} v_s}{\partial n} \right) \quad (13)$$

where r_{sn} is the local radius of streamline curvature. R_f is interpreted as the ratio of the curvature-induced production of $(-\overline{v_n'^2})$ to the total $\overline{v_s'^2}$ -production. In these two-dimensional flows, turbulence is damped if $R_f > 0$ and enhanced if $R_f < 0$. Furthermore, the distribution of the turbulent kinetic energy among the turbulent normal stresses is altered: $\overline{v_n'^2} / \overline{v_s'^2}$ decreases as $R_f > 0$ and increases as $R_f < 0$.

Our experiment concerns a more complex three-dimensional flow field, with the strong cross-stream motion as the main complicating factor. In the following, we will present experimental data suggesting that a correlation between the turbulence structure and the curvature-flux-Richardson number also exist in our three-dimensional curved flow.

5.2 Experimental observations

Fig. 7a,b show the experimental distributions of R_f and its depth-averaged value, $\langle R_f \rangle$, respectively. The streamline curvature in the (s,n) -plane, r_{sn} , is defined as:

$$\frac{1}{r_{sn}} = \frac{1}{r'_{sn}} + \frac{1}{1 + n/R} \frac{1}{R} \quad R \text{ being the centerline curvature and} \quad (14)$$

$$\frac{1}{r'_{sn}} \approx \frac{d^2 n}{ds^2} = \frac{d}{ds} \left(\frac{v_n}{v_s} \right) = \frac{1}{v_s^2} \left(v_s \frac{dv_n}{ds} - v_n \frac{dv_s}{ds} \right) = \frac{1}{v_s^2} \left[\left(v_n \frac{\partial v_n}{\partial n} + v_z \frac{\partial v_n}{\partial z} \right) - \frac{v_n}{v_s} \left(v_n \frac{\partial v_s}{\partial n} + v_z \frac{\partial v_s}{\partial z} \right) \right] \quad (15)$$

based on $\frac{dv_i}{ds} = \frac{\partial v_i}{\partial s} + \frac{\partial v_i}{\partial n} \frac{v_n}{v_s} + \frac{\partial v_i}{\partial z} \frac{v_z}{v_s}$ ($i=s,n$) and the assumption $\frac{\partial v_i}{\partial s} \approx 0$ (16)

R_f and $\langle R_f \rangle$ are positive and increase in the outward direction, from small values near the centerline to maximum values $O(2)$. In the outer-bank shear layer, where R_f and $\langle R_f \rangle$ are negative, the influence of the bank proximity dominates the influence of the streamline curvature. R_f is rather uniformly distributed over most of the flow depth but decreases strongly close to the bottom.

Fig. 7b compares the transversal distributions of $\langle R_f \rangle$ and of $\langle k \rangle / \langle K \rangle$. The latter has been presented in Section 3. There seems to be a rather strong correlation between the two. Near the centerline, where $\langle R_f \rangle \sim 0$, $\langle k \rangle / \langle K \rangle$ approaches its straight-uniform-flow value (cf. Eq. 4). The outward decrease of $\langle k \rangle / \langle K \rangle$ is accompanied by increasing values of $\langle R_f \rangle > 0$; the location of the maximum $\langle R_f \rangle$ coincides with that of the minimum $\langle k \rangle / \langle K \rangle$. In the outer-bank shear layer, $\langle R_f \rangle$ is negative and $\langle k \rangle / \langle K \rangle$ strongly increases, due to friction at the outer bank.

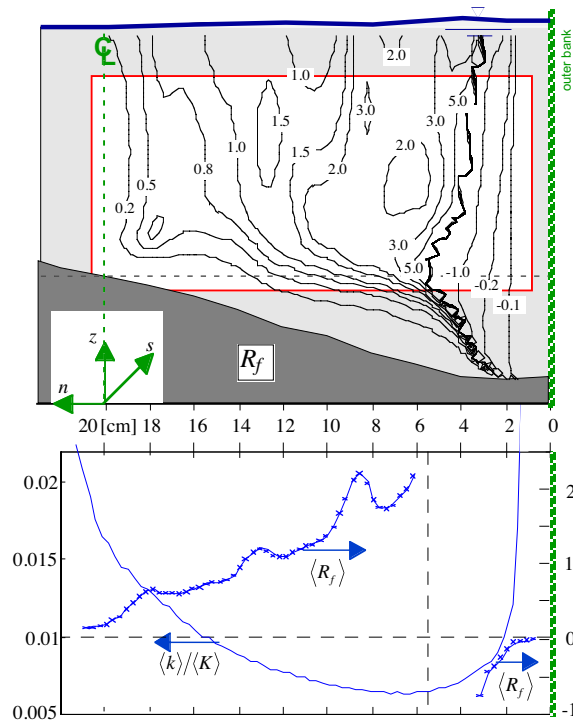


Fig.7: (a) Flux-curvature-Richardson number, R_f ; (b) Depth-avgd. flux-curvature-Richardson number $\langle R_f \rangle$, and ratio $\langle k \rangle / \langle K \rangle$ (cf. Fig. 3c).

Figs. 8a,b show the distributions of $\overline{v_n'^2}/\overline{v_s'^2}$ and $\overline{v_z'^2}/\overline{v_s'^2}$, representative of the distribution of the turbulent kinetic energy k among the turbulent normal stresses. Distributions of all the turbulent stresses have been presented in Blanckaert and Graf (2001a). $\overline{v_s'^2}$ and $\overline{v_z'^2}$ have rather similar distributions, be it that the vertical fluctuations are damped near the bottom and near the water surface, resulting in smaller values of $\overline{v_z'^2}/\overline{v_s'^2}$. This quantity is distributed rather uniformly over the width, as appears from the nearly horizontal isolines. The ratio $\overline{v_n'^2}/\overline{v_s'^2}$ is nearly uniform over the water column, but has a pronounced transversal distribution, which is due to the almost opposite behavior of $\overline{v_s'^2}$ and $\overline{v_n'^2}$. $\overline{v_n'^2}/\overline{v_s'^2}$ is small near the centerline and increases outwards, to reach maximum values near the separator of the two circulation cells. Due to the bank proximity, it decreases close to the outer bank. The values of these ratios averaged over the entire measuring grid, $\langle \langle \rangle \rangle$, are:

$$\langle \langle \overline{v_n'^2}/\overline{v_s'^2} \rangle \rangle = 0.34 < \langle \langle \overline{v_z'^2}/\overline{v_s'^2} \rangle \rangle = 0.47 \quad (17a)$$

showing that the downstream normal stresses are dominant (both numbers are less than 1), and that the intensity of the transversal fluctuations is smaller than that of the vertical fluctuations. These experimental ratios should be compared to their counterparts in straight uniform flow. According to Nezu and Nakagawa (1993), these ratios are nearly constant in straight uniform flow:

$$\langle \langle \overline{v_n'^2}/\overline{v_s'^2} \rangle \rangle_{straight} = \overline{v_n'^2}/\overline{v_s'^2}|_{straight} = 0.51 > \langle \langle \overline{v_z'^2}/\overline{v_s'^2} \rangle \rangle_{straight} = \overline{v_z'^2}/\overline{v_s'^2}|_{straight} = 0.31 \quad (17b)$$

where the intensity of the transversal fluctuations is larger than that of the vertical fluctuations. As compared to straight uniform flow, the ratio $\overline{v_n'^2}/\overline{v_s'^2}$ is smaller in the curved flow experiment and $\overline{v_z'^2}/\overline{v_s'^2}$ is larger.

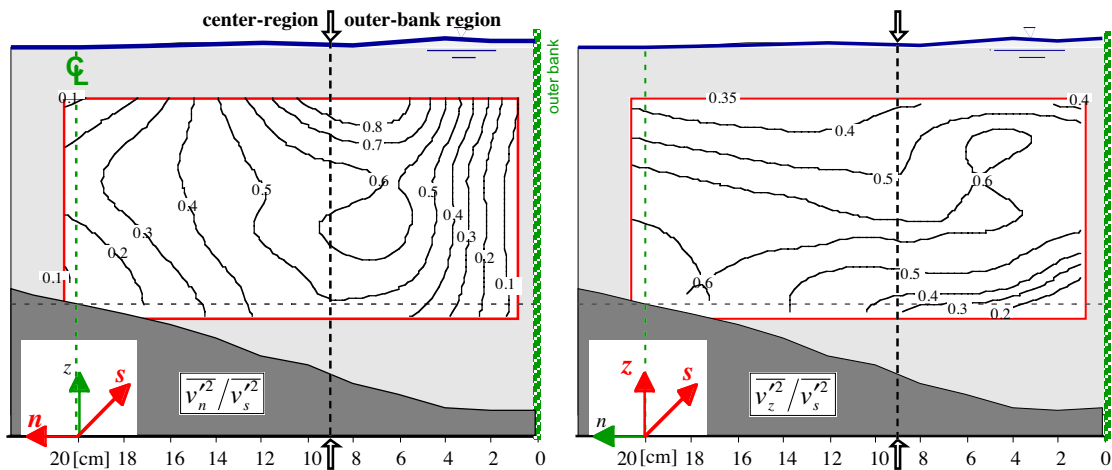


Fig. 8: Ratios of the turbulent normal stresses: (a) $\overline{v_n'^2}/\overline{v_s'^2}$; (b) $\overline{v_z'^2}/\overline{v_s'^2}$.

In line with the expectations from the theoretical considerations on 2D flows, our observations indicate that the curvature has a stabilizing effect for $\langle R_f \rangle > 0$ and leads to smaller values of the ratio $\overline{v_n'^2}/\overline{v_s'^2}$, that seem to be compensated by larger values of $\overline{v_z'^2}/\overline{v_s'^2}$. The stabilizing curvature seems to affect the transversal structure of the flow field (R_f and $\overline{v_n'^2}/\overline{v_s'^2}$ -distributions), but much less the vertical structure. Apparently, the influence of streamline curvature on this highly three-dimensional flow field mainly acts in the horizontal (s,n)-planes. Further evidence is given by the distributions of the fourth-order turbulence moments presented below.

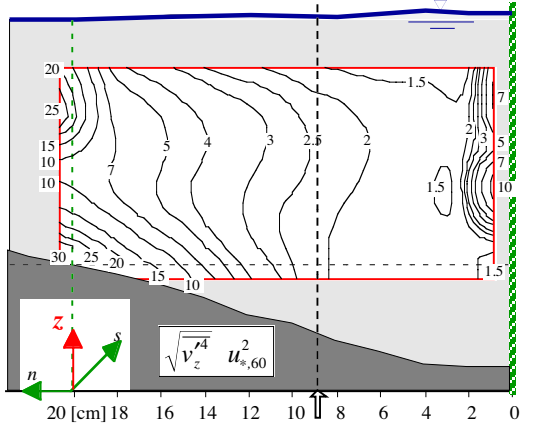
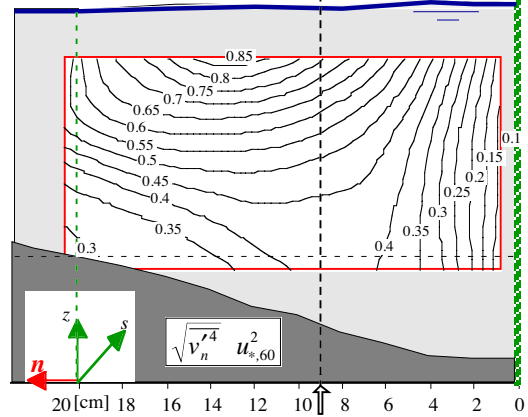
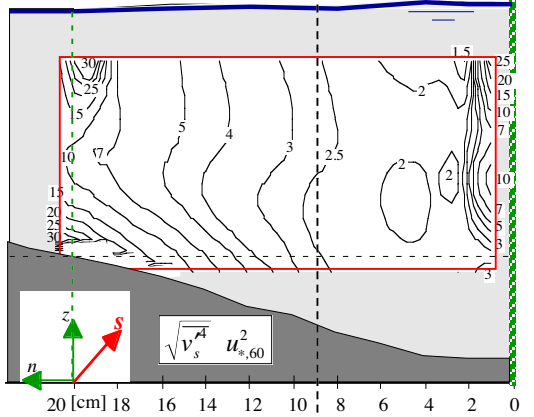
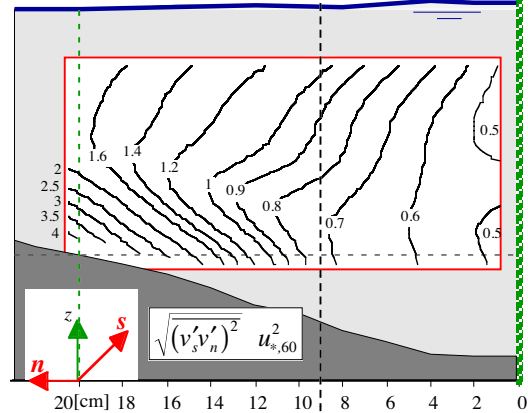
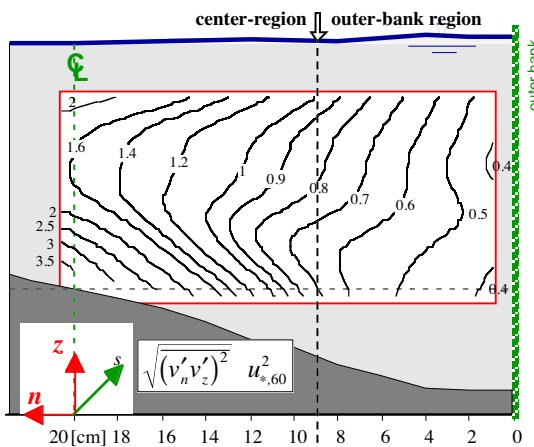
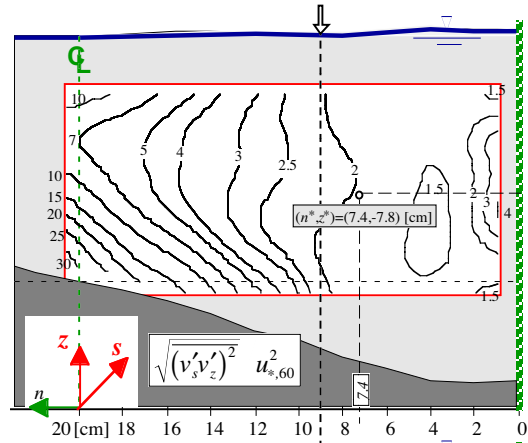
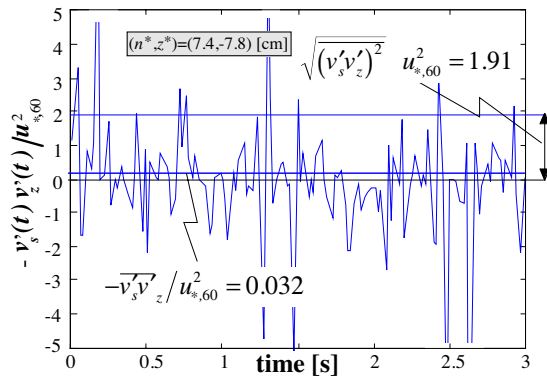
If it comes to the spreading and mixing of matter, pollutants and heat, sediment transport and erosion of alluvial boundaries, the instantaneous values of the quantities $v_j'(t)v_k'(t)$ are at least as important as their time-averaged values $\overline{v_j'v_k'}$, being the turbulent stresses. In regions of low turbulent stress, considerable positive and negative instantaneous values can be reached. This is illustrated for the turbulent shear stress $\overline{v_s'v_z'}$ at $(n^*, z^*) = (7.4, -7.8)$ cm, in Fig. 9a (n^* and z^* denote the distance from the outer bank and the distance below the water surface). The magnitude of these instantaneous values is characterized by the square root of the relevant fourth-order turbulent moment, $\sqrt{\overline{(v_j'v_k')^2}}$. These are shown in Figs. 9b-g, normalized by $u_{*,60}^2$. With the exception of the (n,n) -component, all components are almost uniformly distributed over the water column and decrease rather strongly in the outward direction. These higher-order turbulence characteristics also suggest that the streamline curvature imposes a transversal stratification onto the flow field and damps the turbulence in the outer bend.

5.3 Discussion

The above experimental observations suggest that in the present curved-flow experiments there is a correlation between the modified turbulence structure and the curvature-flux-Richardson number R_f . Such a correlation might be of use in developing semi-empirical extensions to turbulence closure models, such as the k - ε model.

Such extensions have been proposed for a variety of two-dimensional shear flows, characterized by streamline curvature in the plane of main shear (Irwin and Smith 1975; Leschziner and Rodi, 1981; Rodi and Scheuerer, 1983; Cheng and Farokhi, 1992; Holloway and Tavoularis, 1992). They are based on modeled versions of the simplified transport equations for the turbulent stresses, in which advective transport by the cross-stream motion is neglected. Although the advective transport by the cross-stream motion is important in bends, the extension to the k - ε model proposed by Leschziner and Rodi (1981) has been applied by Demuren and Rodi (1986) and by Ye and McCorquodale (1998) to simulate flow and pollutant dispersion in curved channels. The eddy-viscosity in this model is given by

$$v_t = c_\mu \cdot \frac{k^2}{\varepsilon} \quad \text{with} \quad c_\mu = \frac{0.09}{1 + 0.57 \frac{k^2}{\varepsilon^2} \left(\frac{\partial v_s}{\partial n} + \frac{v_s}{r_{sn}} \right) \frac{v_s}{r_{sn}}} = \frac{0.09}{1 + 0.57 \frac{k^2}{\varepsilon^2} \left(\frac{\partial v_s}{\partial n} \right)^2 \cdot \frac{2R_f}{(2 - R_f)^2}} \quad (18)$$



a b
c d
e f
g

Fig.9a: Time-series of $v'_s(t)v'_z(t)/u_{*,60}^2$ at the point $(n^*, z^*) = (7.4, -7.8)$ [cm].

Fig.9b-g: Isolines of the normalized fourth-order turbulent correlations

$$\sqrt{\overline{(v'_i v'_j)^2}} / u_{*,60}^2$$

in which the deviation from 1 in the denominator of the expression for c_μ is the extension. c_μ reduces to its standard value 0.09 for $R_f = 0$. The extension is only applied for the horizontal diffusion terms, and not for the vertical one. Demuren and Rodi (1986) simulated the flow and pollutant dispersion in three cases of meandering channels with rectangular cross-section. They only apply the curvature extension in the advection-diffusion equation for the pollutant. Ye and McCorquodale (1998) simulated the flow field in a single bend and the flow and pollutant dispersion in a meander, both with a horizontal bottom and smooth boundaries. They also applied the curvature extension to the flow field and found a significant effect on the intensity of the cross-stream motion, (v_n, v_z) , which in its turn transmits the effect to the downstream velocity, v_s .

Both simulations concerned channels with a flat bottom. In alluvial channel bends, a mobile-bottom topography develops with important transversal bottom slopes, especially near the outer bank, which causes the velocity distribution to be more skewed in outward direction than in the case of a flat bottom (Johannesson and Parker, 1989):

$$\left. \frac{\partial v_s}{\partial n} \right|_{\text{mobile-bed topography}} > \left. \frac{\partial v_s}{\partial n} \right|_{\text{flat bed}} \quad (19)$$

As a consequence, curvature effects are expected to be stronger over a mobile-bottom topography than over a flat bottom, since $\partial v_s / \partial n$ is the main component in the curvature-flux-Richardson number R_f . Furthermore, most of these numerical simulations were done for the case of a series of meanders. In such a configuration, the flow and turbulence fields are mainly a result of the geometrically imposed periodicity, with fluid elements alternating between inner and outer banks in successive bends. Hence the curvature effects are difficult to isolate.

Although such semi-empirical extensions are unable to correctly represent the turbulence structure in highly three-dimensional flow with a significant cross-stream motion, they can be useful to improve the capabilities of the standard models. Such semi-empirical models that do not correctly represent the underlying physics have to be based on a large amount of experimental data. By lack of experimental data for curved open-channel flow, Demuren and Rodi (1986) and Ye and McCorquodale (1998) incorporated the semi-empirical extension derived for two-dimensional flows in their simulations. The present experimental data must provide a basis for further improvement and testing of semi-empirical extensions for open-channel flows.

6 The curvature-Richardson number

The present paper mainly concerns the turbulence characteristics in an open-channel bend. It shows that differences in turbulence characteristics as compared to straight uniform flow can be attributed to the effect of the cross-stream motion and especially to the modified turbulence structure. There seems to be a correlation between the observed turbulence characteristics and a curvature-flux-Richardson number, R_f , that parameterizes the curvature of the streamlines.

Blanckaert (2001b) and Blanckaert and Graf (2001c) have proposed a mathematical model for the cross-stream circulation (often called secondary circulation) that, contrary to the commonly-used models, compares favorably with experimental data for strongly curved open-channel flows. Whilst the commonly used models for the cross-stream circulation uniquely depend on the Chezy friction coefficient, the proposed model also depends on the curvature ratio H/R , on the Froude number and especially on the normalized transversal gradient of the downstream velocity, parameterized by α_s+1 , which is defined as:

$$\alpha_s + 1 = \frac{\partial v_s / \partial n}{v_s / R} + 1 \quad (20)$$

It is easily shown from Eqs. (13) and (20) that

$$R_f = \frac{2}{\alpha_s + 1} \quad (21)$$

The proposed model predicts a rather strong decrease of the cross-stream circulation with increasing values of α_s+1 .

The cross-stream motion and the turbulence are the main agents responsible for the redistribution of the mean flow field and the boundary shear stresses in the bend, and for the spreading and mixing of matter, pollutants and heat. Since they both seem to depend on the curvature-flux-Richardson number, R_f must be an important parameter in curved open-channel flow.

7 Conclusions

This paper reports on an experimental investigation of turbulence characteristics in a sharp open-channel bend. This fills a gap in the availability of turbulence data that has hampered the modeling of such flows, so far.

In the outer half of one cross-section of a laboratory open-channel bend, three-dimensional velocity measurements were made with an Acoustic Doppler Velocity Profiler (ADVP) on a fine grid. This instrument takes simultaneous high-resolution measurements of all three velocity components, from which the mean velocity vector can be derived, as well as the fluctuating velocity vector, all six turbulent stress components and all higher-order turbulent velocity correlations. The flow in the investigated cross-section is characterized by the existence of a bi-cellular pattern of cross-stream circulation and by a rather strongly reduced turbulence activity in the outer bend.

The observed distributions of all six turbulent stress have been reported elsewhere (Blanckaert and Graf, 2001a). In the present paper, distributions of various other turbulence characteristics are given, such as the turbulent kinetic energy, the ratio between the depth-averaged turbulent kinetic energy and the depth-averaged mean flow

kinetic energy, the turbulence-structure parameter a_1 , the mixing coefficients, the ratios between the turbulent normal stresses, and the square root of the fourth-order turbulent correlations.

An analysis of the mechanisms leading to the reduced turbulence activity in the outer bend was made, via a term-by-term evaluation of the transport equation for the turbulent kinetic energy k on the basis of the measured data. Special attention was given to the terms representing the production of turbulent kinetic energy and to the terms representing its advective transport by the cross-stream motion. The rather speculative result can be summarized as follows. Initially, the cross-stream motion redistributes k over the cross-section and thereby modifies the distribution of the production terms \mathcal{P} and the turbulence structure. The final k -distribution is such that the influence of the cross-stream motion almost vanishes and that mainly the modified \mathcal{P} -distribution is responsible for the observed reduction of k towards the outer bank.

The relationship between the turbulent kinetic energy and its production is complex and characterized by a feedback-mechanism. It is shown to depend mainly on the turbulence structure, represented by the structure parameter a_1 and the mixing coefficients. The turbulence structure in our experiment is found to differ significantly from that in straight uniform flow. Both a_1 and the mixing coefficients indicate that the efficiency of shear stress production for a given amount of turbulent kinetic energy is less in curved-channel flow than in straight uniform flow, and that it decreases towards the outer bank. This modified turbulence structure explains the observed reduction of turbulence activity in the outer bend.

All departures from the turbulence structure in straight uniform flow are directly or indirectly due to the imposed streamline curvature. For two-dimensional curved shear layer flows, Bradshaw (1969) has established a formal analogy between streamline curvature and buoyancy, which leads to the definition of a curvature-flux-Richardson number, R_f . The turbulence structure in our highly three-dimensional flow appears to be correlated rather strongly to R_f and the departures from straight uniform flow qualitatively agree with predictions by the models developed for two-dimensional curved flow: turbulence is damped for $R_f > 0$ and the ratio $\overline{v_n'^2} / \overline{v_s'^2}$ is decreased. The influence of the streamline curvature acts primarily in the horizontal and imposes a kind of transversal stratification to the turbulence structure. The latter is further confirmed by the distributions of the fourth-order turbulent correlations.

Consequently, it is not sufficient for turbulence closures to incorporate the transport equation for the turbulent kinetic energy: they also have to represent the turbulence structure. Two-equation turbulence models, such as the commonly used k - ε -model, are inherently unable to do so. Semi-empirical extensions to two-equation turbulence closures based on the curvature-flux-Richardson R_f number have been proposed for two-dimensional curved flows. A similar approach may be used to improve the capabilities of two-equation turbulence closures for three-dimensional curved flows, but this requires more experimental data, with a larger spatial coverage and for a wider range of hydraulic and geometric conditions.

Finally, Blanckaert (2001b) and Blanckaert and Graf (2001c) have shown that the cross-stream circulation also depends strongly on R_f . Apparently, the curvature-flux-Richardson number is an important parameter in curved open-channel flow.

It should be emphasized that our experimental data originate from a single cross-section at 60° from the bend entrance, under one set of hydraulic (Fr , C) and geometric (R/B , B/H) conditions. The experimental program is presently extended to more cross-sections and a wider range of hydraulic conditions in a larger flume (Blanckaert and Graf, 2001b).

Acknowledgements

This research is being sponsored by the Swiss National Science Foundation under grants Nr.2100-052257.97/1 and 2000-059392.99/2. The first author acknowledges his PhD supervisor W.H. Graf.

APPENDIX I. REFERENCES

- Anwar, H. O. (1986). "Turbulent structure in a river bend." *J. Hydr. Engng*, ASCE, 112(8), 657-669.
- Batchelor, G. K. (1970). *An Introduction to Fluid Dynamics*, Cambridge University Press.
- Blanckaert, K. (2001a). "discussion on: Bend-flow simulation using 2D depth-averaged model, by Lien H.C. et al." *J. Hydr. Engng.*, ASCE, 127(2), 167-170.
- Blanckaert, K. (2001b) "A model for flow in strongly curved channel bends." *Proc. 29th-IAHR Congr.*, J.F. Kennedy Student Paper Comp, Beijing, China, 42-50.
- Blanckaert, K., and de Vriend, H. J. (2002a). "Secondary flow in sharp open-channel bends." (*submitted for publication*).
- Blanckaert, K., and de Vriend, H. J. (2002b). "Turbulence structure in sharp open-channel bends." (*submitted for publication*).
- Blanckaert, K. & Graf, W. H. (2001a). "Experiments on flow in an open-channel bend. Mean flow and turbulence." *J. Hydr. Engng*, ASCE, 127(10), 835-847.
- Blanckaert, K. & Graf, W. H. (2001b). "Experiments on flow in a strongly curved channel bend." *Proc. 29th-IAH Congr.*, Theme D, Vol. I, 7 Beijing, China, .371-377.
- Blanckaert, K. & Graf, W. H. (2001c) "Non-linear model for secondary circulation and transversal bottom slope in sharp bends." *Proc. 2th-RCEM-congr.*, Obihiro, Japan, 791-800.
- Blanckaert, K. & Graf, W. H. (2002). "Momentum transport in sharp open-channel bends." (*tentatively approved for publication in J. Hydr. Engng., ASCE*).

- Booij, R. (1985). "Eddy viscosity in channel bends." *Int. symp. refined flow mod. turb. meas.*, Iowa, E21,1-10.
- Booij, R. & Tukker, J. (1996). "3-Dimensional laser-Doppler measurements in a curved flume." *Developments in laser techniques and applications to fluid mechanics*, Springer, Berlin, 98-114.
- Bradshaw, P. (1969). "The analogy between streamline curvature and buoyancy in turbulent shear flow." *J. Fluid Mech.*, Cambridge Univ. Press, 36(part I), 177-191.
- Bradshaw, P. (1973). "Effects of streamline curvature on turbulent flow." *AGARDograph No.169*, NATO.
- Cheng, G. C., and Farokhi, S. (1992). "On turbulent flows dominated by curvature effects." *J. Fluids Engng*, Trans. ASME, 114, 52-57.
- de Boor, C. (1978). *A Practical Guide to Splines*, Springer, Berlin.
- Demuren, A. O., and Rodi, W. (1986). "Calculation of flow and pollutant dispersion in meandering channels." *J. Fluid Mech.*, Cambridge Univ. Press, 172, 63-92.
- Dietrich, W. E. (1987). "Mechanics of flow and sediment transport in river bends." *River Channels: environment and process*, K. Richards, ed., Inst. Brit. Geogr. spec. publ., Oxford, 179-227.
- Gibson, M. M., and Rodi, W. (1981). "A Reynolds-stress closure model of turbulence applied to the calculation of a highly curved mixing layer." *J. Fluid Mech.*, Cambridge Univ. Press, 103, 161-182.
- Graf, W. H., and Altinakar, M. (1998). *Fluvial Hydraulics*, Wiley, Chichester, England.
- Hinze, J. O. (1975). *Turbulence*, McGraw-Hill, New York.
- Irwin, H. P. A. H., and Smith, P. A. (1975). "Prediction of the effect of streamline curvature on turbulence." *Physics of Fluids*, AIP, 18(6), 624-630.
- Johannesson, H., and Parker, G. (1989). "Velocity redistribution in meandering rivers." *J. Hydr. Engng*, ASCE, 115(8), 1019-1039.
- Leschziner, M. A., and Rodi, W. (1981). "Calculation of annular and twin parallel jets using various discretization schemes and turbulence-model variations." *J. Fluids Engng*, Trans. ASME, 103, 352-360.
- Muto, Y. (1997). "Turbulent Flow in Two-Stage Meandering Channels," Ph.D., Bradford, Bradford.
- Nezu, I., and Nakagawa, H. (1993). *Turbulence in open-channel flows*, IAHR-monograph, Balkema.
- Odgaard, A. J. (1984). "Bank erosion contribution to stream sediment load." *IIHR Report No. 280*, Iowa Institute of Hydraulic Research, Iowa.
- Piquet, J. (1999). *Turbulent flows: models and physics*, Springer, Berlin.
- Rodi, W., and Scheuerer, G. (1983). "Calculation of curved shear layers with two-equation turbulence models." *Physics of Fluids*, AIP, 26(6), 1422-1436.

- Schwarz, W. R., and Bradshaw, P. (1994). "Turbulence structural changes for a three-dimensional turbulent boundary layer in a 30° bend." *J. Fluid Mech.*, Cambridge Univ. Press, 272, 183-209.
- Shiono, K., and Muto, Y. (1998). "Complex flow mechanisms in compound meandering channels with overbank flow." *J. Fluid Mech.*, Cambridge Univ. Press, 376, 221-261.
- Sudo, K., Sumida, M., and Hibara, H. (2001). "Experimental investigation on turbulent flow in a square-sectioned 90-degree bend." *Exp. in Fluids, Springer*, 30, 246-252.
- Tamai, N., and Ikeya, T. (1985). "Three-dimensional flow over alternating point bars in a meandering channel." *J. Hydrasc. Hydr. Engng*, JSCE, 3(1), 1-13.
- Tennekes, H., and Lumley, J. L. (1972). *A first course in turbulence*, MIT Press, Cambridge, Massachusetts.
- Ye, J., and McCorquodale, J. A. (1998). "Simulation of curved open channel flow by 3D hydrodynamic model." *J. Hydr. Engng*, ASCE, 124(7), 687-698.

APPENDIX II. NOTATION

a_l	=	turbulence structure parameter defined as $a_l = \sqrt{\overline{v_s'v_z'^2} + \overline{v_n'v_z'^2}}$ $2k$
ADVP	=	Acoustic Doppler Velocity Profiler
B	=	channel width
C	=	Chezy roughness coefficient
c_μ	=	coefficient in Eq. (18) for eddy viscosity ν_t
d	=	total derivative operator
d_{50}	=	mean diameter of sand bottom
e_{jk}	=	strain rates, $j, k = s, n, z$
$Fr = U / \sqrt{gH}$	=	Froude number
H	=	reach-averaged flow depth \approx flow depth at centerline in 60°-section
h	=	local flow depth
K	=	mean flow kinetic energy per unit mass
k	=	turbulent kinetic energy per unit mass
k_t	=	instantaneous turbulent kinetic energy per unit mass, Eq. (6)
n	=	transversal reference axis
n^*	=	distance from outer bank
p'	=	turbulent pressure fluctuations
Q	=	discharge
R	=	radius of curvature of channel centerline
R_h	=	hydraulic radius of cross-section
R_f	=	curvature-flux-Richardson number
r_{sn}	=	streamline curvature in horizontal (s, n)-planes
$Re = UH/\nu$	=	Reynolds number
s	=	downstream reference axis
S_s	=	reach-averaged water-surface gradient at centerline
t	=	time
tke	=	turbulent kinetic energy per unit mass

U	=	$Q/(BH)$ = reach-averaged velocity
U_s	=	depth-averaged downstream velocity
$u_* = U\sqrt{g/C}$	=	friction velocity
v_j	=	time-averaged velocity component, $j=s,n,z$
$v_j(t)$	=	instantaneous velocity component, $j=s,n,z$
$v'_j(t)$	=	instantaneous velocity fluctuation, $j=s,n,z$
$\frac{v'_j v'_k}{v_j v_k}$	=	turbulent stress, $j,k=s,n,z$
$\frac{v_j'^a v_k'^b}{v_j v_k}$	=	higher-order turbulent correlation, $j,k=s,n,z$ and a,b =integer
z	=	vertical reference axis; elevation above horizontal (s,n)-plane
z^*	=	distance below water surface

symbols

α_s	=	normalized transversal gradient of downstream velocity, $(\partial v_s / \partial n) / (v_s / R)$
∂	=	partial derivative operator
δ_{jk}	=	Kronecker delta symbol; $\delta_{jk}=1$ if $j=k$ and $\delta_{jk}=0$ if $j \neq k$
ε	=	viscous dissipation of turbulent kinetic energy
κ	=	Karman constant; $\kappa=0.41$
\mathcal{P}	=	production of turbulent kinetic energy in Eq. (5)
ρ	=	density of water; $\rho=998.2$ kg/m ³ at 20 °
ν	=	molecular viscosity of water; $\nu=1.004 \times 10^{-6}$ m ² /s at 20 °
ν_{jk}	=	mixing coefficient defined in Eq. (11); $j,k=s,n,z$
ν_t	=	eddy viscosity
arrow	=	vectorial quantity
overbar	=	time-averaged values
$\langle . \rangle, \langle\langle . \rangle\rangle$	=	values averaged over local flow depth, over measuring grid, resp.
$\ . \ $	=	absolute value (magnitude)
$O(.)$	=	order of magnitude of .

subscripts

b	=	bottom
S	=	water surface
<i>straight</i>	=	corresponding value in straight uniform flow
60	=	value in section at 60°

III.4 Turbulence Structure in Sharp Open-Channel Bends

K. Blanckaert¹ and H.J. de Vriend²

(in preparation for submission to *J. Fluid Mech.*, Cambridge Univ. Press)



Abstract

In spite of its practical relevance, little is known about the turbulence characteristics in sharp open-channel bends. This paper reports on an experimental investigation of the turbulence structure in one cross-section of an open-channel bend. The flow pattern in this section is characterized by a bi-cellular pattern of cross-stream circulation (secondary circulation) and a rather strongly reduced turbulence activity in the outer bend, as compared to straight uniform shear flow. The turbulence structure differs fundamentally from that in straight uniform shear flow. The velocity fluctuations are a-typically coherent over the width, whence they are decomposed into slow width-coherent fluctuations and a fast background signal. The width-coherent fluctuations reflect a bulk spatio-temporal oscillation of the pattern of circulation cells whereas the background signal represents developed turbulence. A spectral analysis shows that the width-coherent fluctuations have the characteristics of a wave-like motion, i.e. they contribute significantly to the turbulent normal stresses but only weakly to the shear stress, whereas the background turbulence is characterized by efficient shear stress generation. The reduced turbulence activity and the tendency of the secondary flow to oscillate are both effects of the streamline curvature. Similar observations on reduced turbulence activity and the tendency to wave-like motion have been reported in literature for flows in curved wind tunnels and density-stratified flows. Our experimental results indicate that these phenomena are potentially important in curved open-channel flows.

1 Introduction

Most natural rivers meander in their alluvial plane. Major points of attention in river management are: (i) bank erosion, especially in the outer bends (ii) transport, spreading and mixing of suspended matter, pollutants and heat, (iii) the transport of sediment and the associated erosion and deposition phenomena. All of these points depend strongly on the turbulence characteristics of the flow.

In spite of this practical relevance, little is known about the turbulence characteristics in open-channel bends. Numerical models of flow in open-channel bends frequently use extensions of turbulence closures that were developed for two-dimensional boundary-layer flow. As these closure models take insufficient account of the curvature effects on the turbulence structure, the results are often disappointing. The almost complete lack of experimental data on the turbulence characteristics in sharply curved open-channel flow hampers the development of improved turbulence models.

¹ Res. Assoc., Lab. d'Hydraulique Environnementale, Ecole Polytechnique Fédérale, CH-1015 Lausanne, Switzerland.

² Professor, Delft University of Technology, POB 5048, 2600 GA Delft, The Netherlands.

In a complementary paper, Blanckaert and de Vriend (2002a) present detailed experimental data on the turbulence characteristics in the outer half of one cross-section of an open-channel bend, in which the cross-stream flow pattern (secondary flow) consisted of two cells rotating in opposite directions. They report a rather strong reduction of the turbulence activity in most of the outer bend, as compared to straight uniform shear flow, and attribute this to differences in the turbulence structure: for the same turbulent kinetic energy level, the efficiency of shear stress generation is less in curved flow. Furthermore, they show the deviations from a straight-uniform-flow turbulence structure to be correlated with a curvature-flux-Richardson number that represents the streamline curvature.

In this paper, the turbulence structure of the same flow field is further investigated. The experiment is briefly described and the main features of the mean flow and the turbulence are presented. The paper further focuses on the analysis of the turbulence. The velocity fluctuations are decomposed into slow large-scale fluctuations and a rapidly varying background signal. The slow fluctuations are shown to represent an overall oscillation in space and time of the pattern of circulation cells, with the characteristics of a wave-like motion. The correlation of this unsteady behaviour with the streamline curvature is investigated. The results are compared with similar findings reported in literature for flows in curved wind tunnels and density-stratified flows. To our knowledge, observations of these phenomena in open-channel flows have not been reported in literature before.

2 The experiment

The experiment was carried out in a laboratory flume with a natural bottom topography, which is in equilibrium with the flow. The initially flat sand bottom was deformed by the flow, leading to the formation of a typical bar-pool topography (Fig. 1a). Since the flow corresponds to clear-water-scour conditions (critical shear stress for sediment movement in the straight uniform flow), a stable bottom topography is ultimately obtained without active sediment transport. The flume is 0.4 m wide and consists of a 2 m long straight approach reach, followed by a 120° bend with a constant radius of curvature of 2 m. The hydraulic conditions are shown in Table 1

The parameter setting $R/B = 5$ and $R/H = 17.9$ corresponds to a rather tight bend with a high aspect ratio ($B/H = 3.6$). The flume is narrower than usual in natural lowland rivers, but these ratios do occur in mountain rivers and man-made channels. Moreover, the flow in bends with a mobile-bottom topography is concentrated in the deepest part of the cross-section near the outer bank, where a significant transversal bottom slope exists (e.g. Odgaard, 1984; Dietrich, 1987). The flow in the outer bend of the experimental flume is expected to be representative of the flow in the deepest part of wider natural bends. By considering a relatively sharp bend, the curvature effects are more pronounced, hence better visible.

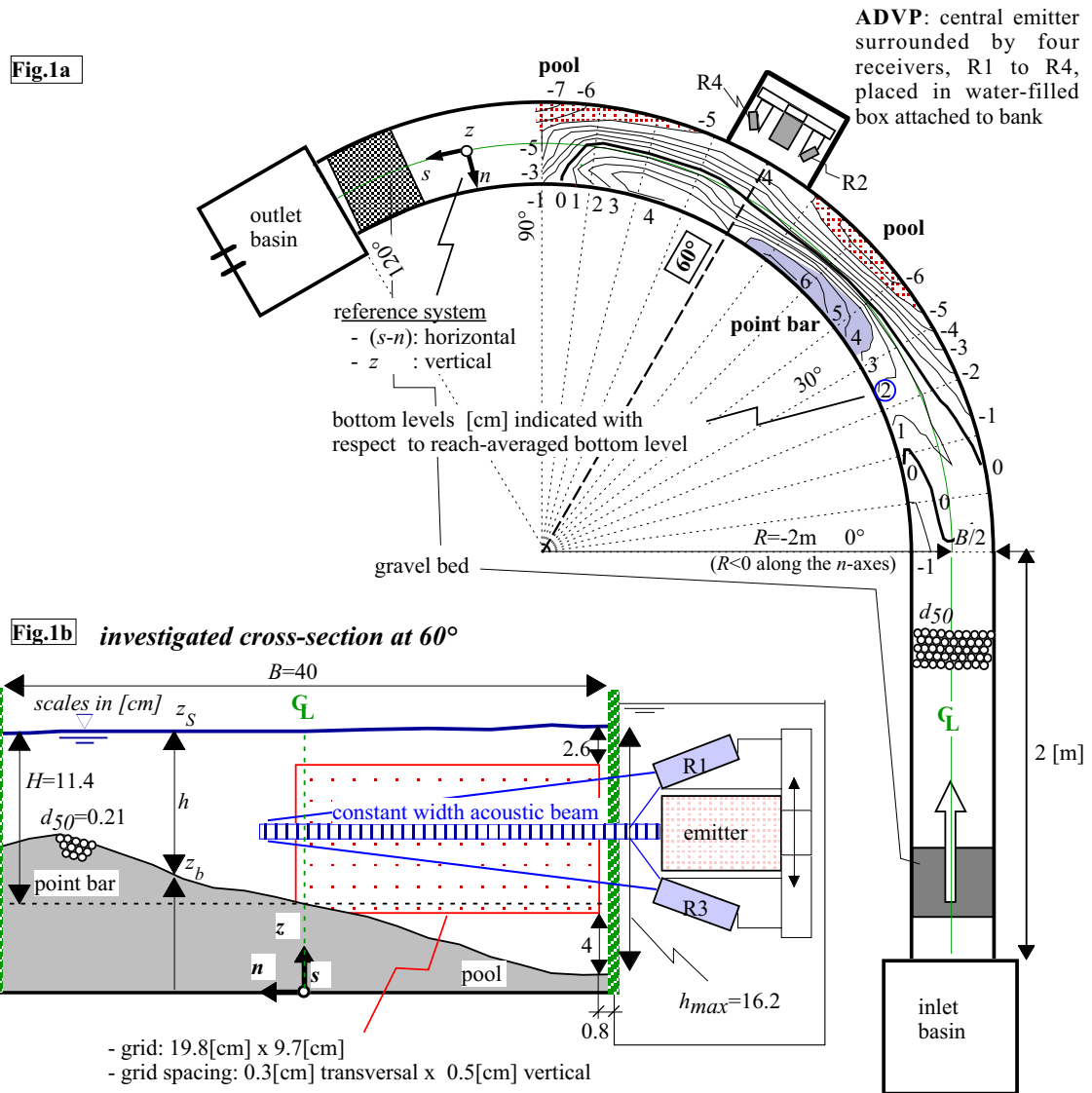


Fig. 1: (a) Experimental set-up, bottom topography and reference system; (b) Measuring section at 60°, Acoustic Doppler Velocity Profiler (ADVP) configuration

R	B	d ₅₀	Q	H	S _s	U	C	Re	Re*	Fr	R/B	R/H	B/H
[m]	[m]	[mm]	[l/s]	[m]	[‰]	[m/s]	[m ^{1/2} /s]	[10 ³]	[/]	[/]	[/]	[/]	[/]
-2.0	0.40	2.1	17	0.11	1.89	0.38	35	42	70	0.36	5	17.9	3.6

R: centreline radius of curvature (negative along the n-axis)
 B: channel width
 d₅₀: median grain size diameter of bed material
 Q: flow discharge
 H: reach-averaged flow depth ≈ flow depth at centreline in section at 60°
 S_s: reach-averaged water-surface gradient at centreline
 u*: friction velocity

U: reach-averaged velocity
 C: Chezy friction factor; C/√g=U/u*
 Fr = U/(gH)^{1/2}: reach-averaged Froude number
 Re = UH/ν: reach-averaged flow Reynolds number
 Re* = u*k_s/ν: reach-averaged particle Reynolds number
 ν: molecular viscosity
 k_s: Nikuradse equivalent sand roughness

Table 1: Hydraulic conditions

Non-intrusive three-dimensional measurements of the mean flow field and the turbulence were made in one cross-section at 60° from the bend entrance. The data are analysed in a reference system with the s -axis pointing downstream along the channel centreline, the transversal n -axis pointing to the inner bank and the vertical z -axis directed upward from the horizontal (s,n) -plane (Figs. 1a,b). The measurements were made with an Acoustic Doppler Velocity Profiler (ADVP), developed in our laboratory at EPFL. This velocity meter simultaneously measures at a high spatial and temporal resolution the instantaneous velocity components. From the measured data, the mean velocity field, $\bar{v}(v_s, v_n, v_z)$, can be derived, as well as the fluctuating velocity field, $\bar{v}'(v'_s, v'_n, v'_z)$, and the turbulent stress tensor, $\overline{v'_j v'_k}$ ($j, k = s, n, z$). Whereas most commercial velocity meters measure point-by-point, our ADVP measures simultaneously all the velocities along the main axis of the measuring device. This profiling capacity will be exploited in the presented analysis. The non-intrusive measurements were made by measuring through the Plexiglas wall forming the outer bank of the flume, with the ADVP mounted in a water-filled box attached to the outside of the wall (Figs. 1a,b). In this configuration, profiles extending over half the channel width were measured every $\Delta z = 0.5\text{cm}$ (Fig. 1b). The sampling frequency was 44.6 Hz and the acquisition time was 180 s. A detailed description of the experimental set-up, the data-treatment procedures and the measuring grid is given in Blanckaert and Graf (2001). More information on the working principle of the ADVP, its experimental accuracy and its comparison with other velocity meters can be found in Lemmin and Rolland (1997), Hurther and Lemmin (1998, 2001), Blanckaert and Graf (2001) and Blanckaert and Lemmin (2002). In summary, the accuracy on the mean-velocities is estimated as better than 4%, that on the turbulent normal stresses as better than 10% and that on the turbulent shear stresses as slightly better than on the turbulent normal stresses. In the lower 20% of the flow depth, however, the accuracy on the turbulence measurements is reduced, due to the important mean-velocity gradients in the measuring volume (effect of spatial averaging).

3 Experimental results

Blanckaert and Graf (2001) gave a detailed presentation of the distributions of all three mean velocity components, as well as all six turbulent stress components. Blanckaert and de Vriend (2002a) present and analyse the kinetic energy distribution of the mean flow and the turbulence. The measured data that are of particular relevance to the present paper are briefly summarized below.

The distribution of the normalized downstream velocity component, v_s/U , in the section investigated is presented in Fig. 2. In a large part of the measuring domain, the downstream velocity is higher than the reach-averaged velocity of 0.38 m/s. Whilst the maximum velocity in straight uniform flow occurs near the water surface, the maximum in this curved flow is found in the lower part of the water column. The mechanisms leading to this distorted velocity distribution have been investigated by Blanckaert and Graf (2002).

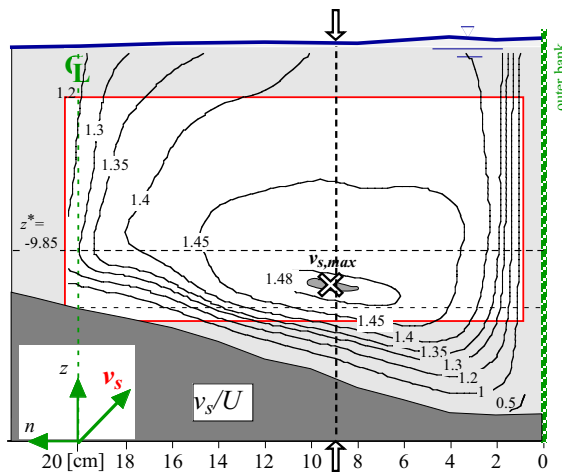


Fig. 2: Isolines of normalized downstream velocity, v_s/U .

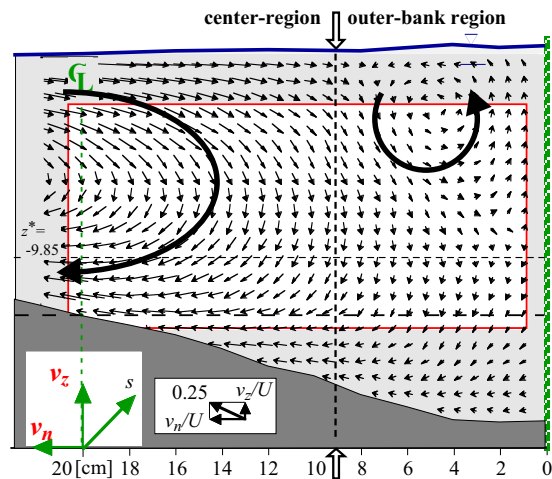


Fig. 3: Vector-representation of normalized cross-stream motion, $(v_n, v_z)/U$.

The vectorial representation of the normalized cross-stream motion, $(v_n, v_z)/U$, in the section investigated is shown in Fig. 3. A circulation cell – termed centre-region cell - with outward velocities near the water surface and inward velocities near the bottom is observed in the centre region. It entails velocities typically of the order of magnitude $0.1U$. This cell represents the well-known helical motion characteristic of flow in bends. A region characterized by weaker cross-stream velocities, typically $O(0.03U)$, is found close to the outer bank. In the upper part of this outer-bank region an additional circulation cell – termed outer-bank cell – occurs, with a sense of rotation opposite to the centre-region cell. The mechanisms underlying this bi-cellular pattern of circulation cells have been investigated by Blanckaert and de Vriend (2002b).

Figs. 4a,b show the normalized distributions of the mean flow kinetic energy, $K/(1/2U^2)$, and the turbulent kinetic energy, $k/(1/2 u_{*,60}^2)$, per unit mass, in which K and k are defined as

$$K = \frac{1}{2}(v_s^2 + v_n^2 + v_z^2) \quad \text{and} \quad k = \frac{1}{2}(\overline{v_s'^2} + \overline{v_n'^2} + \overline{v_z'^2}) \quad (1)$$

respectively. The characteristic shear velocity in the measuring section, $u_{*,60} = \sqrt{gR_h(-\partial z_{s,60}/\partial s)} = 0.045$ m/s, is based on the downstream water-surface gradient at the centreline, $-\partial z_{s,60}/\partial s = 2.89$ ‰, and the hydraulic radius, $R_h = 0.07$ m, in the section at 60° . The contributions of the different components to K and k have been analysed by Blanckaert and Graf (2001). Fig. 4c shows the normalized depth-averaged kinetic energy of the mean flow and the turbulence, $\langle K \rangle/(1/2U^2)$ and $\langle k \rangle/(1/2 u_{*,60}^2)$, respectively, together with the ratio $\langle k \rangle/\langle K \rangle$. Due to the opposite behaviour of K and k , this ratio exhibits a pronounced variation over the width. Blanckaert and de Vriend (2002a) have shown that $\langle k \rangle/\langle K \rangle$ is constant over the width in straight uniform open-channel flow and uniquely depends on the friction factor via

$$\left. \frac{\langle k \rangle}{\langle K \rangle} \right|_{\text{straight}} \approx 4.1 \frac{g}{C^2} \tag{2}$$

which would yield $\langle k \rangle / \langle K \rangle \approx 0.03$ for $C \approx 35 \text{ m}^{1/2}/\text{s}$. In our curved flow, the experimental $\langle k \rangle / \langle K \rangle$ is of the expected order of magnitude near the centreline but it strongly decreases towards the outer bend, down to $O(0.01)$, to increase strongly in the region very close to the outer bank, which is affected by bank friction. Averaged over the cross-section a value of $O(0.03)$ is expected, which means that high $\langle k \rangle / \langle K \rangle$ -values probably exist in the inner part of the cross-section. As compared to straight uniform flow, the turbulence activity is therefore less than average in the outer bend, and it is expected to be higher than average in the inner-bend region.

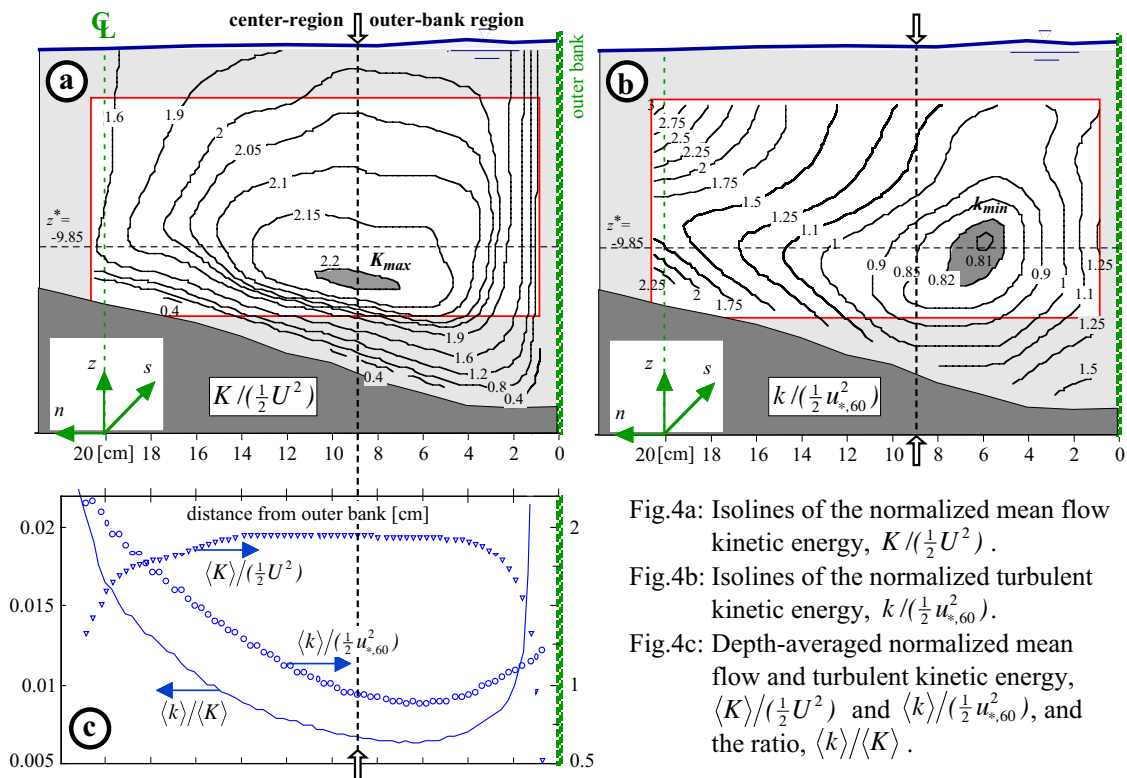


Fig.4a: Isolines of the normalized mean flow kinetic energy, $K / (\frac{1}{2} U^2)$.
 Fig.4b: Isolines of the normalized turbulent kinetic energy, $k / (\frac{1}{2} u_{*,60}^2)$.
 Fig.4c: Depth-averaged normalized mean flow and turbulent kinetic energy, $\langle K \rangle / (\frac{1}{2} U^2)$ and $\langle k \rangle / (\frac{1}{2} u_{*,60}^2)$, and the ratio, $\langle k \rangle / \langle K \rangle$.

The mechanisms leading to this distributions of k and $\langle k \rangle / \langle K \rangle$ are analysed by Blanckaert and de Vriend (2002a). They present some turbulence-structure parameters indicating that curved-flow turbulence is less efficient in producing shear than the straight-flow equivalent with the same amount of turbulent kinetic energy. They show that this change in the turbulence structure is at the basis of the observed distributions of the turbulence properties. In the following, an analysis of the measured velocity fluctuations and the turbulence structure will be made that is complementary to that analysis and will confirm its results.

4 Analysis of velocity fluctuations and of turbulence structure

4.1 Width-coherent velocity fluctuations

As mentioned before, the ADVP has the advantage of measuring simultaneous profiles of the instantaneous velocity components along an entire line (instead of a single point). This line-by-line approach offers the possibility to investigate coherent structures along those lines. In the experiment (see Figs. 1a-b), profiles extending over half the channel width are measured at different vertical levels. They enable investigating the time-behaviour of the system of circulation cells. The time-stack plot in Fig. 5 shows the transversal velocity fluctuations for the profile at 9.85 cm below the water surface. The vertical streaks in this figure indicate that the transversal fluctuations are rather coherent over the width.

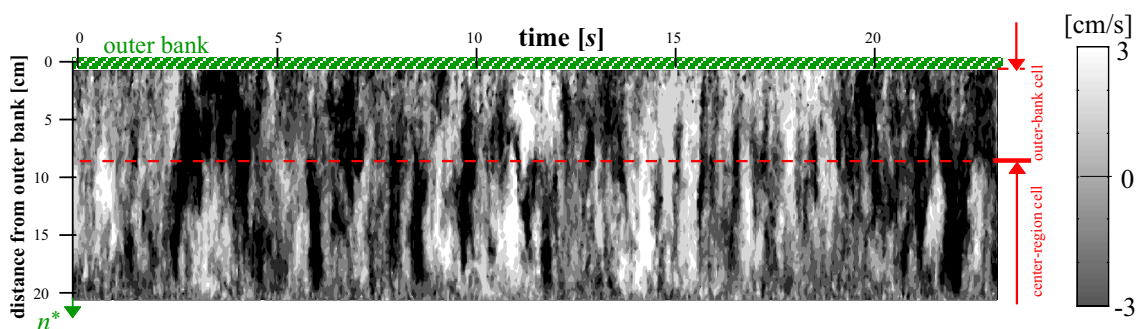


Fig. 5: Time-series of transversal velocity fluctuations for profile at $z^* = 9.5$ cm below water surface.

In order to quantify the coherence of these fluctuations, two-point correlations are evaluated via

$$R_{jj}(-7.5, n; z) = \frac{\overline{v'_j(n = -7.5, z)v'_j(n, z)}}{\sqrt{\overline{v_j'^2(n = -7.5, z)}}\sqrt{\overline{v_j'^2(n, z)}}} \quad (3)$$

The reference point of this correlation is located at $n = -7.5$ cm, i.e. at 12.5 cm from the outer bank. The correlation R_{nn} is shown in Fig. 6a. As the results are rather similar throughout the water column, the vertical mean is representative of the entire vertical. Fig. 6b shows the cross-stream distribution of these vertically averaged values, $\langle R_{jj}(-7.5, n) \rangle$.

Typical two-point correlations of homogeneous turbulence would show an initial steep descent around the reference point, down to values of about 1/3, followed by a tail with $R_{jj} < 1/3$ (Prandtl et al., 1990, Bruns et al., 1999). $\langle R_{zz} \rangle$ in Fig. 6b more or less follows this pattern, but $\langle R_{ss} \rangle$ and $\langle R_{nn} \rangle$ have rather a triangular shape and do not show any initial steep descent. This indicates that the downstream and transversal fluctuations are atypically coherent over the width. In the outer-bank region, $\langle R_{zz} \rangle$ is negative, which indicates that the vertical fluctuations of the outer-bank cell are out of phase with those of the centre-region cell. This phenomenon, however interesting, will not be investigated in further detail. Henceforth, attention will be focused on the downstream and the transversal fluctuations.

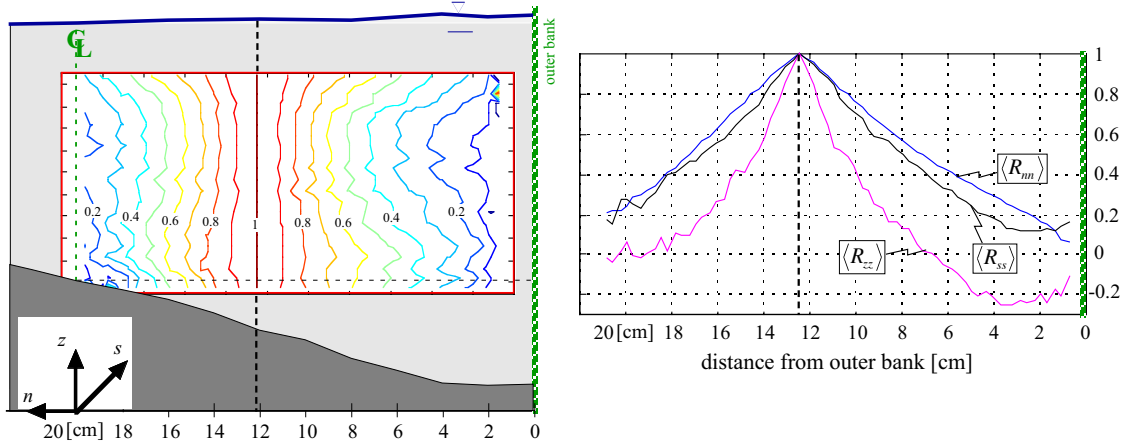


Fig. 6: (a) Two-point correlation $R_m(-7.5, n; z)$ between the transversal velocity fluctuations measured at 12.5 cm from the outer bank and points on the same transversal profile; (b) Vertically-averaged two-point correlations, $\langle R_{ij} \rangle$ ($j=s, n, z$).

4.2 Decomposition of the velocity fluctuations

Following Hussain (1983), the velocity fluctuations, v'_j , can be decomposed into slow and rapid fluctuations. Anticipating the results, we denote the slow fluctuations with the subscript w (wave) and the rapid ones with the subscript b (background turbulence):

$$v'_j(n, z, t) = v'_{j,w}(n, z, t) + v'_{j,b}(n, z, t) \quad (j=s, n) \quad (4)$$

Hussain (1983) and Tamburrino and Gulliver (1999) made the split by taking a moving average over a time period long enough to eliminate the fast fluctuations but short enough not to lose essential information on the slow fluctuations. We exploit the profiling capacity of the ADVP and make use of the observed width-coherence of the downstream and transversal velocity fluctuations (Fig. 6): we assume that the fast fluctuations are not coherent over the width, while the slow ones are. So we assume that, averaged over the width range from $n = -14.7$ cm to $n = 0.9$ cm, i.e. over 53 measuring points,

$$\{v'_{j,b}\}(z, t) \approx 0 \quad \ll \quad \{v'_{j,w}\}(z, t) \approx v'_{j,w}(n, z, t) \quad (5)$$

in which $\{\dots\}$ denotes the width-averaging operation. Together with Eq. (4), this leads to:

$$v'_{j,w}(n, z, t) \approx \{v'_{j,w}\}(z, t) \approx \{v'_j\}(z, t) \quad (6)$$

whence

$$v'_j(n, z, t) = \{v'_j\}(z, t) + v'_{j,b}(n, z, t) \quad (7)$$

This provides an easily applicable method for first-order decomposition of the velocity fluctuations.

4.3 Bulk-oscillation of the pattern of circulation cells

We assume that the slow width-coherent fluctuations represent a bulk-oscillation of the pattern of circulation cells with migration speed $\vec{V}_{osc}(t) = (V_{s,osc}, V_{n,osc})(t)$. In the following, some experimental observations are presented that are in agreement with this assumption.

In an Eulerian framework, a rigid transverse displacement of the pattern of circulation cells over a distance $\Delta n(t)$ replaces the fluid particle at the position n by the particle that originates from the position $n - \Delta n(t)$, thus generating the slow Eulerian velocity variation:

$$\vec{v}^*(n, z, t) = \vec{v}(n - \Delta n(t), z) - \vec{v}(n, z) \quad (8)$$

An illustration for v_n^* is given in Fig. 7. Similar variations induced by the downstream migration are assumed to be small, since the velocity field presumably hardly varies in downstream direction; they are ignored by lack of information (measurements taken in one cross-section only). The slow velocity variations corresponding to such a bulk-oscillation can thus be written as:

$$\vec{v}'_w(n, z, t) = \vec{v}^*(n, z, t) + \vec{V}_{osc}(t) \quad (9)$$

Combining Eq. (6) and Eq. (9) gives:

$$\{\vec{v}'\}(z, t) \approx \{\vec{v}^*\}(z, t) + \vec{V}_{osc}(t) \quad (10)$$

At about mid-depth, v_n and its radial derivative are small (Fig. 7). Accordingly, v_n^* is also small, whence $\{v'_n\} \approx V_{n,osc}$. In the upper part of the water column, v_n^* and $V_{n,osc}$ have the same sign whereas they are of opposite sign in the lower part (see Fig. 7). Thus, if a bulk-oscillation of the pattern of circulation cells exists, $\{v'_n\}$ must have the following property:

$$\overline{\{v'_n\}^2} > \overline{V_{osc}^2} \quad \text{in the upper part of the water column} \quad (11)$$

$$\overline{\{v'_n\}^2} \approx \overline{V_{osc}^2} \quad \text{at about mid-depth} \quad (12)$$

$$\overline{\{v'_n\}^2} < \overline{V_{osc}^2} \quad \text{in the lower part of the water column} \quad (13)$$

In the next section, we will show that the measured profile of $\overline{\{v'_n\}^2}/u_{*,60}^2$ has this property, indeed.

As $\{v_n^*\}(z, t)$, and thus $\{v'_n\}(z, t)$, are mainly generated by the transversal component of the bulk-oscillation, they should have the same skewness $Sk_n = \overline{\{v'_n\}^3} / (\overline{\{v'_n\}^2})^{3/2}$ and kurtosis (also called flatness) $Fl_n = \overline{\{v'_n\}^4} / (\overline{\{v'_n\}^2})^2$ as $V_{n,osc}(t)$, which means that they should be rather uniform over the depth. Fig. 8 shows that this is indeed the case: the skewness of $\{v'_n\}$ is nearly constant at $Sk_n = -0.4$, except near the water surface and the bottom. This indicates that the width-coherent transversal fluctuations are nearly symmetrical. The

kurtosis is nearly constant at $Fl_n=3$, which corresponds to the value for a Gaussian distribution. Fig. 8 also shows the skewness and the kurtosis of the width-coherent downstream oscillations $\{v'_s\}$. The skewness is nearly constant at $Sk_s \approx 0$, indicating symmetrical fluctuations, and the kurtosis is nearly constant at $Fl_s=3$.

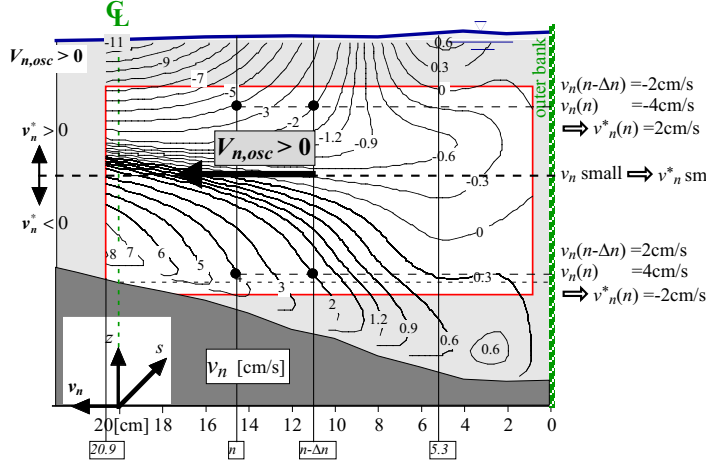


Fig. 7: Slow transversal velocity fluctuations, v_n^* , induced by a transversal bulk displacement Δn of the pattern of circulation cells

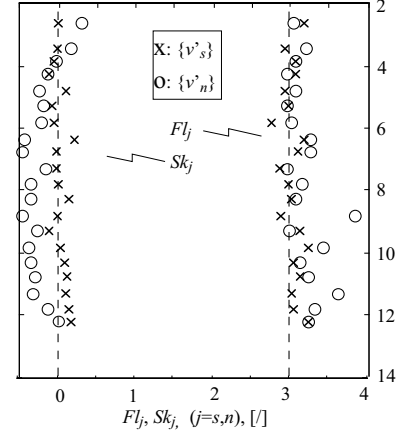


Fig. 8: Skewness, Fl_j , and kurtosis, Sk_j , of the slow width-coherent fluctuations $\{v'_j\}$ ($j=s, n$)

4.4 Decomposition of the turbulent stresses

The kinetic energy content of the width-coherent fluctuations and the background-turbulence is analysed by decomposing the turbulent normal stresses in similar way as the turbulent fluctuations (cf. Eq. 7):

$$\overline{v_j'^2}(n, z) = \overline{\{v'_j\}^2}(z) + \overline{v_{j,b}'^2}(n, z) + 2\overline{\{v'_j\}v'_{j,b}}(n, z) \quad (j=s, n) \quad (14a)$$

Fig. 9 shows the results:

- the turbulent normal stresses due to the total velocity fluctuations, $\overline{v_j'^2}$ (Figs. 9a,b);
- the turbulent normal stress contributions due to the background turbulence, $\overline{v_{j,b}'^2}$ (Figs. 9c,d); both the downstream and the normal component are high in the outer-bank shear layer, decrease to a minimum near the edge of the outer-bank region, and then increase towards the inner bend;
- the turbulent normal stress contributions due to the width-coherent fluctuations, $\overline{\{v'_j\}^2}$ (Fig. 9e), which are of the same order of magnitude as those due to the background turbulence.

Note that the contribution due to the interaction between the background turbulence and the width-coherent fluctuations, $2\overline{\{v'_j\}v'_{j,b}}(n, z)$ (to be evaluated from Eq. 14a and Fig. 9), is not negligible and takes positive as well as negative values on the measuring grid. For further details on the distributions of the total normal stress components $\overline{v_j'^2}$, we refer to Blanckaert and Graf (2001).

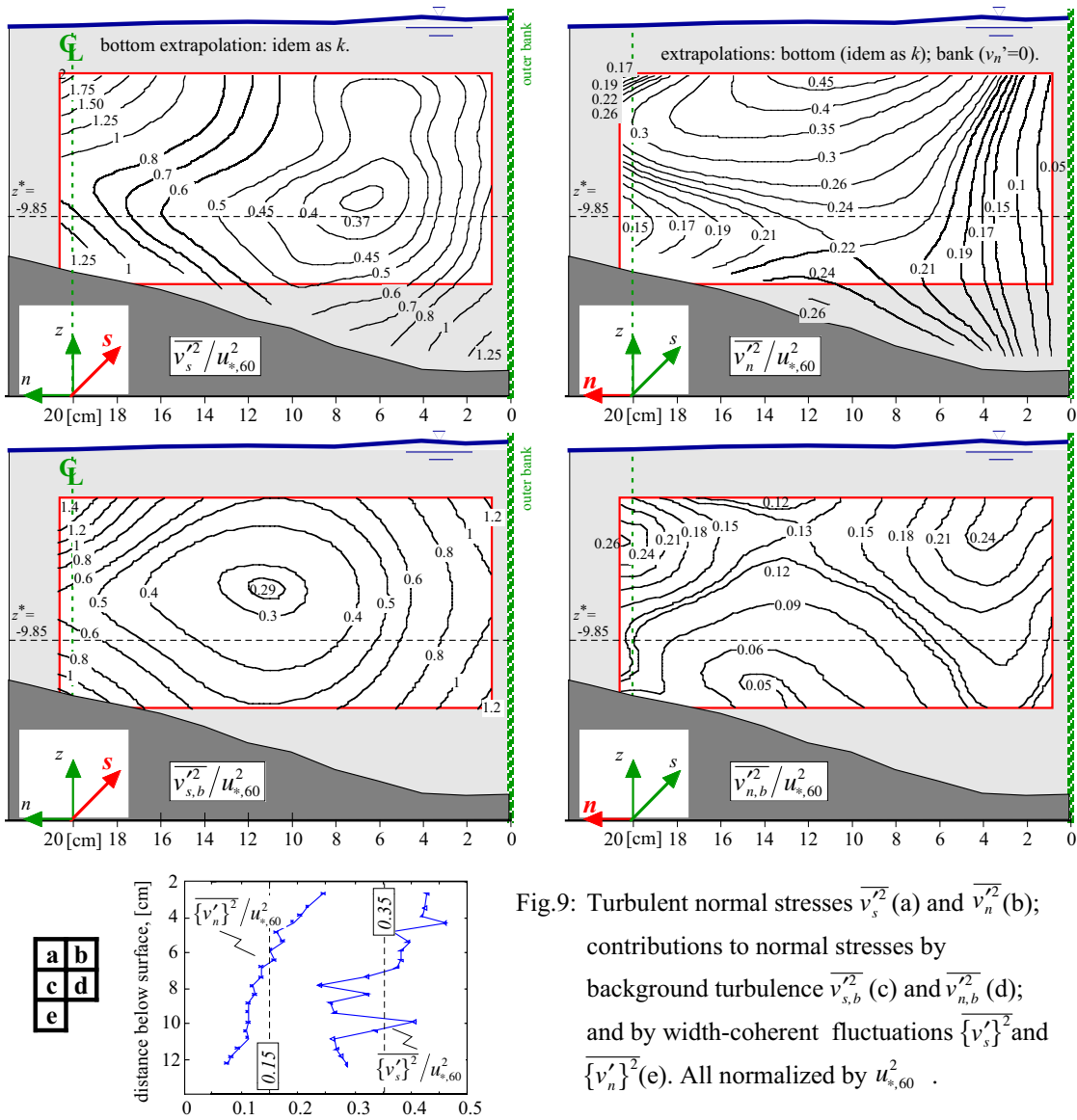


Fig.9: Turbulent normal stresses $\overline{v_s'^2}$ (a) and $\overline{v_n'^2}$ (b); contributions to normal stresses by background turbulence $\overline{v_{s,b}'^2}$ (c) and $\overline{v_{n,b}'^2}$ (d); and by width-coherent fluctuations $\overline{\{v_s'\}^2}$ and $\overline{\{v_n'\}^2}$ (e). All normalized by $u_{*,60}^2$.

As stated before (Eq. 12), the normal stress contribution due to the transversal bulk-oscillation $V_{n,osc}(t)$ at about mid-depth can be approximated by $\sqrt{\overline{V_{n,osc}^2}} u_{*,60} \approx \sqrt{\overline{\{v_n'\}^2}} u_{*,60} \approx 0.4$ (Fig. 9e), i.e. $\sqrt{\overline{V_{n,osc}^2}} \approx \sqrt{\overline{\{v_n'\}^2}} \approx 0.02$ m/s. Fig. 9e shows that the downstream component of the width-coherent fluctuations is considerably larger than the transversal one: $\sqrt{\overline{\{v_s'\}^2}} u_{*,60} \approx 0.6$. This high value suggests that $\overline{\{v_s'\}^2}$ is not primarily induced by the transversal displacement of the pattern of circulation cells, but that the bulk-oscillation has an important downstream component. More extensive measurements, simultaneously covering more than one cross-section, will be needed to investigate this.

The shear stress $\overline{v_s'v_n'}$ is decomposed in line with Eq. (7):

$$\overline{v_s'v_n'}(n, z) = \overline{\{v_s'\}\{v_n'\}}(z) + \overline{v_{s,b}'v_{n,b}'}(n, z) + \overline{\{v_s'\}v_{n,b}'}(n, z) + \overline{v_{s,b}'\{v_n'\}}(n, z) \quad (14b)$$

Fig. 10a shows the normalized total shear stress $-\overline{v'_s v'_n} / u_{*,60}^2$, Fig. 10b the normalized shear stress, $-\overline{\{v'_s\}\{v'_n\}}_{f < 3[\text{Hz}]} / u_{*,60}^2$, generated by the width-coherent velocity fluctuations. In the latter, the high-frequency contributions for $f > 3$ Hz have been filtered out, because they are considered to be parasitic (see below, Fig. 11a). Comparison with the normalized total shear stress shows that the width-coherent fluctuations have a relatively small contribution to the shear stress.

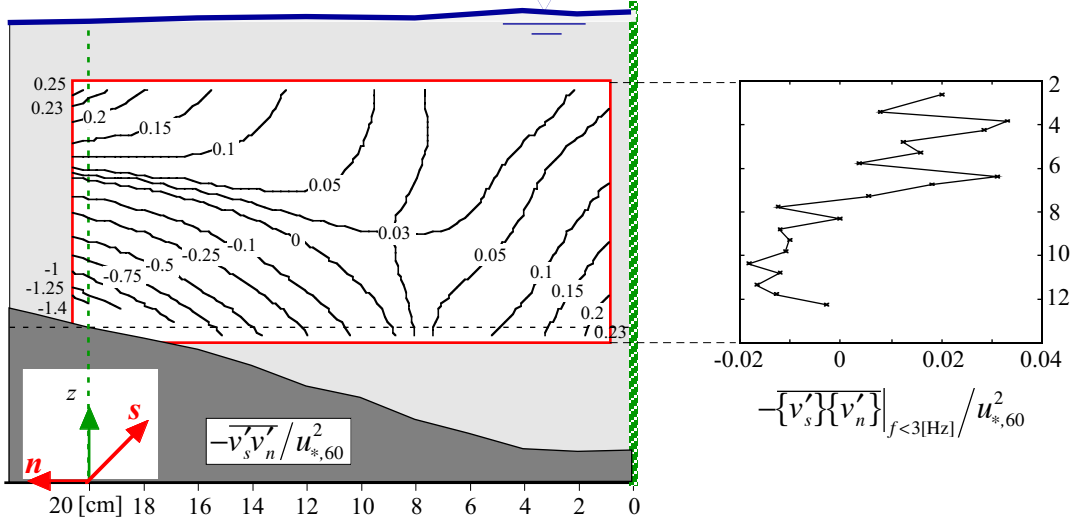


Fig. 10: Normalized shear stress generated by: (a) total velocity fluctuations, $-\overline{v'_s v'_n} / u_{*,60}^2$; (b) width-coherent velocity fluctuations, $-\overline{\{v'_s\}\{v'_n\}}_{f < 3[\text{Hz}]} / u_{*,60}^2$.

In summary, when treated as turbulence, the width-coherent fluctuations contribute significantly to the normal stresses, but much less to the shear stress. Velocity fluctuations that do not generate shear are not representative of developed turbulence, but rather indicate a wave-like motion. This will further be investigated in the following by means of a spectral analysis of the velocity fluctuations.

4.5 Spectral analysis of the structure of turbulence

A spectral analysis of the width-coherent fluctuations $\{v'_j\}$ and of the background turbulence $v'_{j,b}$ is performed to investigate their structure. The fluctuating signals are decomposed into their discrete Fourier-components, as:

$$x'_j(t) = \sum_{\alpha=1}^N a_{j,\alpha} \cos(2\pi f_\alpha t + \phi_{j,\alpha}) \quad (j=s,n) \quad (15)$$

x'_j stands for $\{v'_j\}$ or $v'_{j,b}$, $a_{j,\alpha}$ and $\phi_{j,\alpha}$ are the amplitude and phase of the component with frequency $f_\alpha = \alpha f_l$, f_l is the basic frequency and f_N is the Nyquist frequency, i.e. half the sampling frequency.

The power spectral density function, $F(f)$, and its cumulative power spectral density function, $\mathfrak{S}(f)$, indicate the contribution of each frequency range to the intensity of the fluctuating signal:

$$\mathfrak{S}(f) = \overline{x'^2}(\hat{f} < f) = \int_0^f F(\hat{f}) \cdot d\hat{f} \quad (16)$$

These continuous functions of f are approximated by their discrete Fourier-series counterpart (for simplification of the notation, the same notations have been used for the continuous functions and the discrete approximations):

$$\mathfrak{S}(f_m) = \overline{x'^2}(f < f_m) = \sum_{\alpha=1}^m F(f_\alpha)(f_\alpha - f_{\alpha-1}) \quad (m=1, \dots, N) \quad (17)$$

Equation (16) can also be written as:

$$\mathfrak{S}(f_m) = \int_0^f F(\hat{f}) \cdot d\hat{f} = \int_0^f \hat{f} F(\hat{f}) \cdot d(\ln \hat{f}) \quad (m=1, \dots, N) \quad (18)$$

indicating that in a graphical representation with a logarithmic frequency scale, the contribution of each frequency range is visualized by the area under the graph of $f \cdot F(f)$, or $f_\alpha F(f_\alpha)$ ($\alpha=1, \dots, N$) for the discrete approximation.

Similar F -functions (spectra) of the width-coherent fluctuations were found at each measured elevation. Therefore, and to reduce scatter, only the vertical mean, $f \langle F \rangle$, is shown in Fig. 11a. The main contribution to $\overline{\{v'_s\}^2}$ lies in the frequency range $f < 1$ Hz, with a maximum around $f = 0.1$ Hz, whereas the main contribution to $\overline{\{v'_n\}^2}$ is found around $f = 2$ Hz. This indicates that the pattern of circulation cells does not oscillate with a characteristic dominant frequency, but rather in a range of low frequencies, $0.1 \text{ Hz} < f < 2 \text{ Hz}$. The F -functions of $\{v'_s\}$ and $\{v'_n\}$ both contain a high-frequency tail which does not refer to a low-frequency width-coherent motion. Based on our results (further see Fig. 12b), we assume that frequencies above 3 Hz are parasitical. The \mathfrak{S} -function shows that this parasitical tail represents less than 10% of $\overline{\{v'_s\}^2}$ and less than 20% of $\overline{\{v'_n\}^2}$. This does not alter our previous conclusion that the width-coherent fluctuations contribute significantly to the turbulent normal stresses.

Fig. 11b also shows the F - and \mathfrak{S} -functions of the transversal background-turbulence fluctuations $v'_{n,b}$ for the points at of 8, 12.5 and 17 cm from the outer bank, respectively, at 9.85 cm below the water surface. These points are chosen in regions with low and high level of background-turbulence (see Figs. 9c,d). The maximum contributions to the background-turbulence are found around $f = 4$ Hz. An inertial subrange - corresponding to a slope of $-2/3$ ($-5/3$ in a loglog $F(f)$ -plot) is discernable in Fig. 11b. Towards higher frequencies, a stronger decrease with slope $-4/3$ ($-7/3$ in a loglog $F(f)$ -plot), is observed. The observed F - and \mathfrak{S} -functions of the background-turbulence fluctuations have a form typical of developed turbulence. Similar F - and \mathfrak{S} -functions were found for the downstream background-turbulence fluctuations, $v'_{s,b}$. Especially the F - and \mathfrak{S} -functions of the downstream width-coherent fluctuations, $\{v'_s\}$, are different.

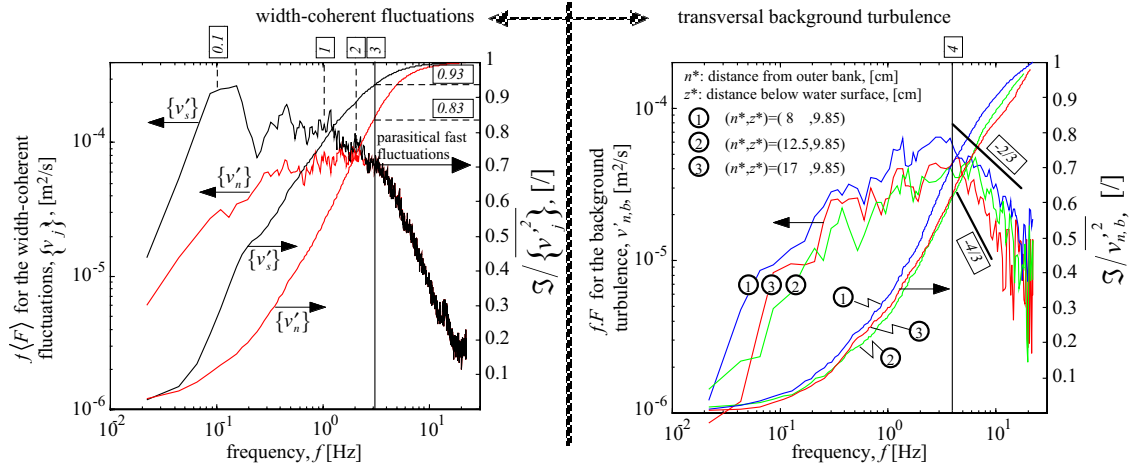


Fig. 11: (a) Frequency x power spectral density, $f\langle F \rangle$ [m²/s], and normalized cumulative power spectral density, $\langle S \rangle / \langle v'_j \rangle^2$ [1], for width-coherent fluctuations, $\{v'_s\}$ and $\{v'_n\}$, averaged over all measured profiles; (b) Frequency x power spectral density, fF [m²/s], and normalized power spectral density, $S / v'_{n,b}{}^2$ [1], for transversal background turbulence, $v'_{n,b}$, in three points.

It was shown in the foregoing that the width-coherent fluctuations significantly contribute to the normal stresses, but generate little shear stress. The efficiency at which fluctuating velocities generate turbulent shear stresses for a given turbulent kinetic energy is an important characteristic of the turbulence structure. In the following, it will be analysed by computing the turbulent shear stresses and the turbulent normal stresses from the Fourier-series representations of the fluctuating velocities, as:

$$\overline{x'_j x'_k} = \frac{1}{T_s} \int_0^{T_s} \left[\sum_{\alpha=1}^N a_{j,\alpha} \cos(2\pi f_\alpha t + \phi_{j,\alpha}) \right] \left[\sum_{\beta=1}^N a_{k,\beta} \cos(2\pi f_\beta t + \phi_{k,\beta}) \right] dt \quad (j,k=s,n) \quad (19)$$

in which T_s is the sampling time. Using the orthogonality characteristic of the Fourier components,

$$\frac{1}{T_s} \int_0^{T_s} \cos(2\pi f_\alpha t + \phi_{s,\alpha}) \cdot \cos(2\pi f_\beta t + \phi_{n,\beta}) \cdot dt = \frac{1}{2} \cos(\phi_{n,\beta} - \phi_{s,\alpha}) \cdot \delta_{\alpha\beta} \quad (20)$$

which is valid for long sampling periods, $T_s \gg \frac{1}{f_\alpha}, \frac{1}{f_\beta}$

the shear stresses and the normal stresses can be expressed as:

$$\overline{x'_s x'_n} = \frac{1}{2} \sum_{\alpha=1}^N a_{s,\alpha} a_{n,\alpha} \cos(\phi_{n,\alpha} - \phi_{s,\alpha}) \quad (21)$$

$$\overline{x'_j{}^2} = \frac{1}{2} \sum_{\alpha=1}^N a_{j,\alpha}^2 \quad (j=s,n) \quad (22)$$

The efficiency by which the turbulent fluctuations at the frequency f_α generate shear stresses can be quantified by the ratio,

$$\frac{\overline{x'_s x'_n}}{\overline{x_s'^2} \overline{x_n'^2}}(f_\alpha) = \cos^2(\phi_{n,\alpha} - \phi_{s,\alpha}) \quad (23)$$

which means that it only depends on the phase lag, $\phi_{n,\alpha} - \phi_{s,\alpha}$. These phase lags enable to distinguish between developed turbulence and wave-like motion (McBean and Miyake, 1972; Komori et al., 1983). The efficiency of shear stress generation is high for developed turbulence, with phase lags typically around $i\pi$ ($i=-1,0,1$), whereas wave-like velocity fluctuations hardly generate shear stresses and have phase lags typically around $\pm \pi/2$.

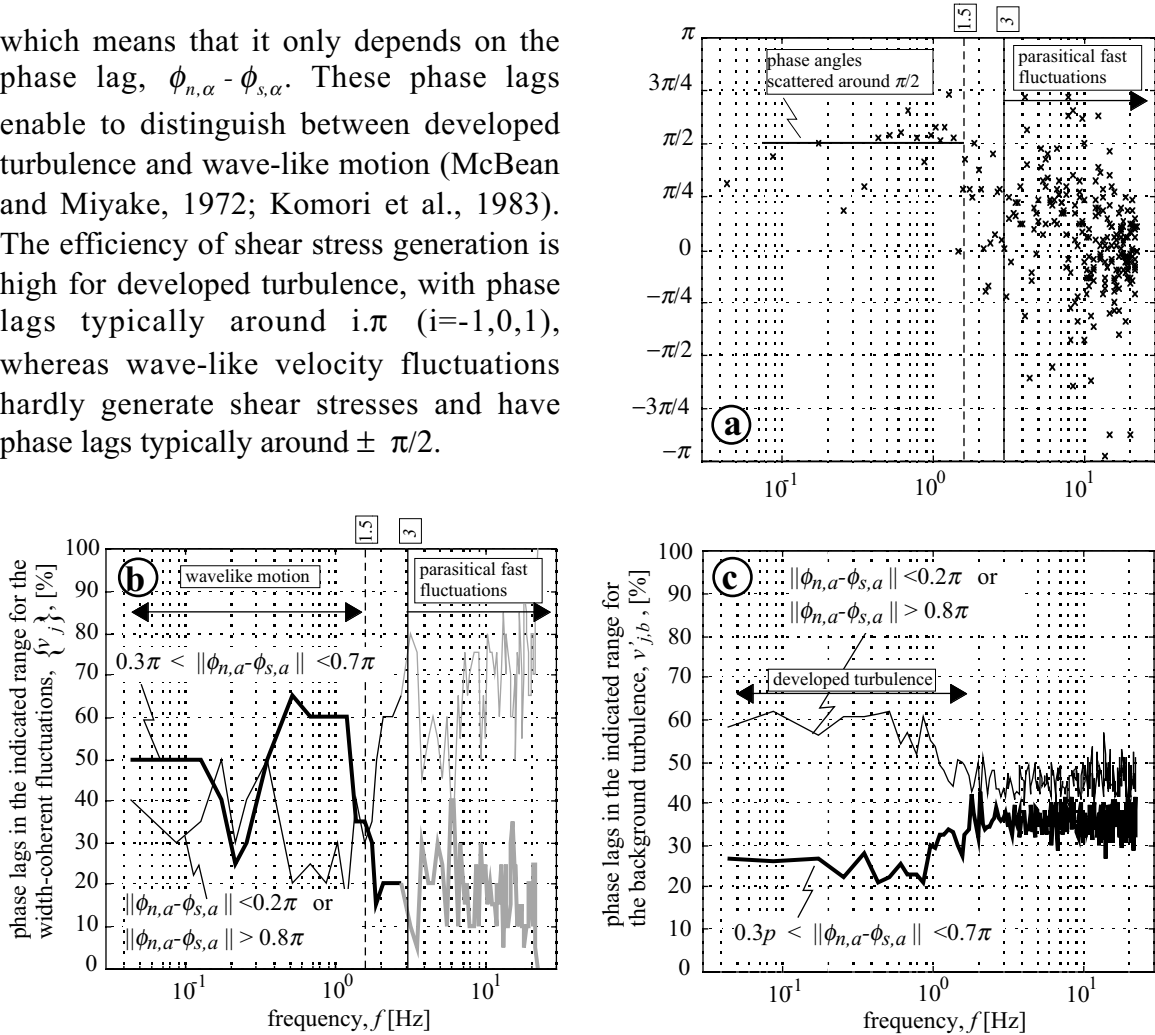


Fig. 12: Phase lags $\phi_{n,\alpha} - \phi_{s,\alpha}$ between (a) width-coherent fluctuations $\{v'_j\}$ and $\{v'_n\}$ for profile at 9.85 [cm] below water surface; (b) width-coherent fluctuations $\{v'_s\}$ and $\{v'_n\}$ averaged over measuring grid; (c) background-turbulence fluctuations $v'_{s,b}$ and $v'_{n,b}$ averaged over measuring grid.

As shown before, the width-coherent velocity fluctuations $\{v'_s\}$ and $\{v'_n\}$ are inefficient in generating shear stress. Fig. 12a shows the phase lags at each frequency between the components of $\{v'_s\}$ and $\{v'_n\}$ for the profile at 9.85cm below the water surface. For $f < 1.5$ Hz, these phase lags are largely scattered around values of $\phi_{n,\alpha} - \phi_{s,\alpha} \approx \pi/2$. Because of the large scatter in this figure, the same data are presented in an alternative way. The phase lags for the width-coherent fluctuations have been calculated at each measured elevation, and those for the background turbulence have been calculated in each measured point. For each frequency, f_α , the percentage of all phase lags found around $\pm\pi/2$ ($0.3\pi \leq \|\phi_{n,\alpha} - \phi_{s,\alpha}\| \leq 0.7\pi$) and around $\pm i\pi$ ($\|\phi_{n,\alpha} - \phi_{s,\alpha}\| \leq 0.2\pi$ or $0.8\pi \leq \|\phi_{n,\alpha} - \phi_{s,\alpha}\|$) is

shown in Figs. 12b and c for the width-coherent fluctuations and the background turbulence, respectively. The phase lags of the width-coherent fluctuations (Fig. 12b) show a different behaviour in the low and high-frequency ranges, separated at about 1.5 Hz. In the low-frequency range, at least in the range that contributes most to the width-coherent normal stresses ($f \approx 0.4 \div 1$ Hz; Fig. 11a), they are mainly found around $\pm \pi/2$. In the high-frequency range they mainly occur around 0 and $\pm\pi$. It is on the basis of this result that we have chosen to consider the contributions with $f > 3$ Hz as fast parasitical fluctuations. The phase lags of the background-turbulence fluctuations (Fig. 12c) are mainly found around 0 and $\pm\pi$ in the low-frequency range and tend to be more randomly distributed at higher frequencies.

Thus, the decomposition of the velocity fluctuations into width-coherent fluctuations and background turbulence seems to be physically meaningful, since they have a fundamentally different turbulence structure. The width-coherent fluctuations seem to represent a bulk-oscillation of the pattern of circulation cells with the characteristics of a wave-like motion, i.e. with a low efficiency in shear generation. The background turbulence has the characteristics of developed turbulence and is much more efficient in shear generation. All departures from the turbulence structure in straight uniform shear flow are directly or indirectly due to the streamline curvature of the mean flow. Blanckaert and de Vriend (2002a) have shown that the departures of the measured turbulence structure from its counterpart in straight uniform shear flow seem to be correlated with a curvature-flux-Richardson number R_f that reflects the streamline curvature. The relation between the experimentally observed turbulence characteristics and the streamline curvature will be further elaborated in the next section.

5 The influence of streamline curvature

Bradshaw (1969, 1973) has shown that the structure of turbulence is sensitive to streamline curvature and stipulated that the influence of streamline curvature is analogous to the influence of buoyancy in a density-stratified flow. The analysis that is generally used to derive buoyancy parameters from the equations of motion can be used to derive equivalent parameters for streamline curvature, such as:

$$\omega_{BV} = \sqrt{2 \frac{v_s}{r^2} \frac{\partial v_s}{\partial n}} \quad [\text{Hz}] \quad (24)$$

$$S = \frac{v_s}{r} \bigg/ \frac{\partial v_s}{\partial n} \quad (25)$$

$$Ri = 2 \frac{v_s}{r^2} \frac{\partial v_s}{\partial n} \bigg/ \left(\frac{\partial v_s}{\partial n} \right)^2 = 2S(1 + S) \quad (26)$$

$$R_f = \frac{2 \overline{v_s' v_n'} \frac{v_s}{r}}{\overline{v_s' v_n'} \frac{1}{r} \frac{\partial v_s}{\partial n}} = \frac{2 \frac{v_s}{r}}{\frac{1}{r} \frac{\partial v_s}{\partial n}} = \frac{2S}{1 + S} \quad (27)$$

with v_s approximating the velocity along the streamline and r the radius of curvature of the streamline. This derivation is limited to two-dimensional flows. The frequency ω_{BV} was first derived by Von Karman (1934) from a simple linear stability analysis. He showed that when an element of fluid is transversally displaced in a plane frictionless curved (or rotating) flow, it will either move further away from its original position or return towards it and oscillate about it. If ω_{BV} is real, it represents the frequency of this oscillation. An imaginary ω_{BV} indicates exponential growth or decay. The frequency ω_{BV} is similar to the Brünt-Väisälä frequency in density-stratified flow. The dimensionless curvature parameter S (Eq. 25) derived by Prandtl (1930) represents the ratio of the curvature-induced extra strain-rate to the inherent strain-rate. Dividing the square of ω_{BV} by $(\partial v_s / \partial n)^2$, which is a typical frequency scale of a shear flow, the curvature-gradient-Richardson number Ri (Eq. 26) is obtained. Whilst ω_{BV} , S and Ri are related to static stability and do not involve turbulence, the curvature-flux-Richardson number R_f (Eq. 27), is derived from the Reynolds stress equations. It is interpreted as minus the ratio of the $\overline{v_n'^2}$ -production due to streamline curvature to the total $\overline{v_s'^2}$ -production. It is positive/negative for stabilizing/destabilizing curvature. According to Eqs. 24-27, S , Ri and R_f are closely related:

$$R_f = Ri / (1 + S)^2 = 2S / (1 + S) \quad \text{whence} \quad R_f \approx Ri \approx 2S \quad \text{for small } S \quad (28)$$

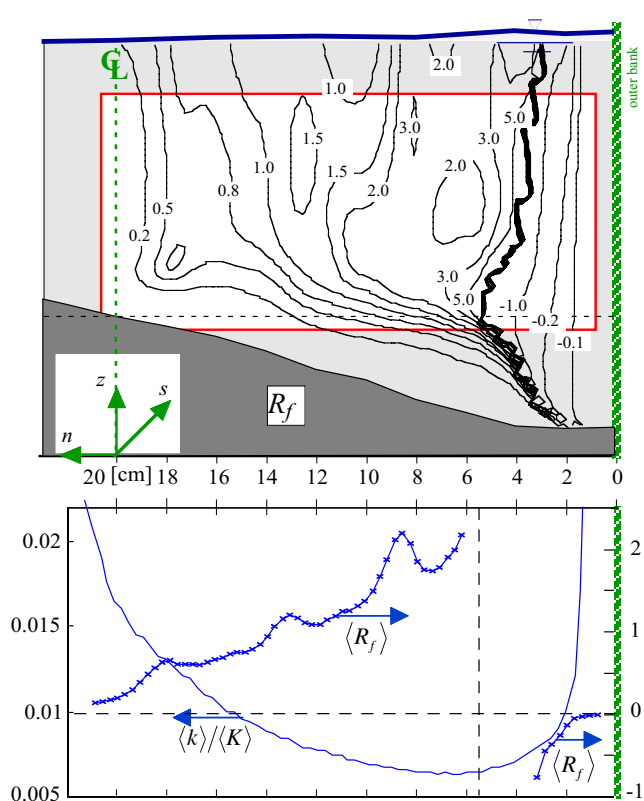


Fig. 13: (a) Flux-curvature-Richardson number, R_f ; (b) Depth-averaged flux-curvature-Richardson number, $\langle R_f \rangle$, and ratio, $\langle k \rangle / \langle K \rangle$ (copied from Fig. 4c).

Blanckaert and de Vriend (2002a) show that in the present strongly three-dimensional flow, the reduction of turbulence activity in the deepest part of the cross-section is correlated with the curvature-flux-Richardson number R_f . Their findings are briefly summarized here. Fig. 13a shows the experimental distributions of R_f and Fig. 13b compares the distributions of its depth-averaged value $\langle R_f \rangle$ with that of $\langle k \rangle / \langle K \rangle$ (copied from Fig. 4c). In most of the area, R_f and $\langle R_f \rangle$ are positive and increase in outward direction from small values near the centreline to maximum values $O(2)$. In the outer-bank shear layer, where R_f and $\langle R_f \rangle$ are negative, the influence of the bank proximity dominates over the influence of the streamline curvature.

There seems to be a rather strong negative correlation between the distributions of $\langle R_f \rangle$ and $\langle k \rangle / \langle K \rangle$. Near the centreline, where $\langle R_f \rangle \sim 0$, $\langle k \rangle / \langle K \rangle$ approaches its straight-uniform-flow value of 0.03. The outward reduction of $\langle k \rangle / \langle K \rangle$ is accompanied by increasing values of $\langle R_f \rangle$, and the maximum of $\langle R_f \rangle$ coincides with the minimum of $\langle k \rangle / \langle K \rangle$. In the outer-bank shear layer, $\langle R_f \rangle < 0$ and $\langle k \rangle / \langle K \rangle$ strongly increases. Like in two-dimensional flows, high positive values of R_f in curved flow goes with a reduction of the turbulent kinetic energy.

Fig.14 shows the distribution of the frequency ω_{BV} (Eq. 24). The calculated values are rather uniform over most of the flow depth, except close to the bottom. Near the outer bank, where the curvature has a destabilising effect, ω_{BV} is imaginary. Values of the order of 0.3 Hz are found in the region where the ratio $\langle k \rangle / \langle K \rangle$ is minimum, and gradually increase to values of about 1 Hz in the innermost part of the measuring section. Near the centreline, where the ratio $\langle k \rangle / \langle K \rangle$ strongly increases, ω_{BV} also shows a stronger increase, up to values of about 1.5 Hz. These frequencies ω_{BV} are of comparable magnitude to the observed dominant frequency ranges of the width-coherent wave-like velocity fluctuations $\{v'_s\}$ and $\{v'_n\}$ shown in Fig.11a.

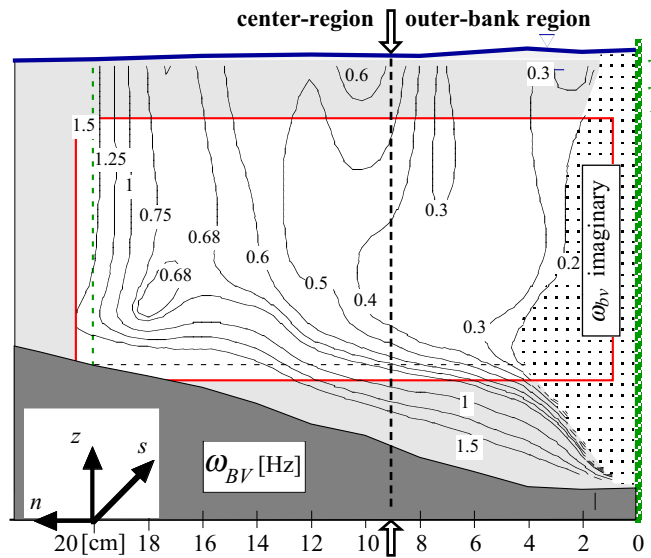


Fig. 14: Theoretical frequency, ω_{bv} [Hz], of a transversally displaced fluid element.

Thus, both the bulk-oscillation of the pattern of circulation cells and the reduction of turbulence activity are correlated with parameters representative of the streamline curvature. The derivation of the curvature parameters ω_{BV} and R_f is based on a linear analysis for small streamline curvatures in two-dimensional curved flow in the s,n -plane (Bradshaw, 1969). Our experiment concerns highly three-dimensional strongly curved flow, with complicating factors such as a relatively strong cross-stream motion, the proximity of the banks and a non-trivial bottom topography. It is remarkable that even in such a complicated flow, the reduction of turbulence and its tendency towards wave-like motion seem to be correlated with simple streamline-curvature parameters such as ω_{BV} and R_f .

Strong turbulence damping and the reduction of low-frequency turbulence to a wave-like motion have been reported in the literature for different configurations. So and Mellor (1973) investigated turbulent boundary layers along a convex surface of varying curvature in a wind tunnel. In a region of stabilizing curvature, $S \approx 0.3$, they measured small turbulent normal stresses and nearly zero shear stresses. They speculate that this represents linear internal waves. Irwin and Smith (1974) derived a model of streamline curvature effects from the simplified Reynolds stress equations, and tested it against experimental data from curved wall jets in still air. The model predicts that turbulence reduces to wave-like motion for $S \approx 0.1$. Holloway and Tavoularis (1992) did experiments on the effects of curvature on sheared turbulence in a wind tunnel, relatively isolated from wall and entrainment effects. They found that turbulence approaches wave-like motion for $S \approx 0.33$. McBean and Miyake (1972) took measurements in density-stratified atmospheric boundary layers and found that the shear stress generation decreases with increasing stability and that internal waves appear. Komori et al. (1983) experimentally investigated stably density-stratified open-channel flow and found that turbulent motion approaches wave-like motion with increasing Richardson number, $Ri \approx 0.3$ to 1. Our observation of a reduced turbulence activity and a tendency to wave-like motion complies qualitatively with these observations.

Blanckaert and de Vriend (2002a) show that for the accurate simulation of turbulence in sharp open-channel bends it is not sufficient for the turbulence closure model to include the transport equation for k . It should also represent the turbulence structure. Turbulence closures based on a scalar eddy viscosity concept are inherently unable to represent this turbulence structure. Yet, their capabilities can probably be improved on the basis of the correlations between the turbulence structure and parameters for the streamline curvature, such as ω_{bv} or R_f . Examples are reported in literature and discussed in Blanckaert and de Vriend (2002a). However, such semi-empirical extensions not derived from first physical principles have to be based on a large amount of detailed experimental data, beyond those presented herein.

6 Discussion and conclusions

Non-intrusive three-dimensional mean flow and turbulence measurements were made in the outer half of one cross-section of an open-channel bend, using an Acoustic Doppler Velocity Profiler (ADVP). This instrument simultaneously measures the three instantaneous velocity components in a line perpendicular to the outer sidewall. This enables to derive the mean velocity vector $\bar{v} = (v_s, v_n, v_z)$, the fluctuating velocity vector $\bar{v}' = (v'_s, v'_n, v'_z)$ and turbulence correlations, such as the six turbulent stress components $\overline{v'_j v'_k}$. In this paper, we exploit the profiling capacity of the ADVP, which enables tracing coherent flow structures.

The downstream mean velocity v_s increases towards the outer bend and the maximum velocities are found in the lower part of the water column. A bi-cellular pattern of cross-

stream circulation exists: besides a centre-region cell (the classical helical motion), a weaker and counter-rotating outer-bank cell occurs near the water surface adjacent to the outer bank. The turbulence activity is rather strongly reduced in most of the outer bend, as compared to straight uniform shear flow.

In a complementary paper, Blanckaert and de Vriend (2002a) present some turbulence-structure parameters indicating that, given the amount of turbulent kinetic energy, turbulent eddies in curved flow are less efficient in producing shear stress than those in straight uniform flow. They show that this change in the turbulence structure is at the basis of the observed turbulence characteristics, especially the reduced turbulence activity in the outer bend, and that it is correlated with the curvature-flux-Richardson number R_f that parameterises streamline curvature.

The analysis presented herein gives more physical insight into the turbulence dynamics, which can speculatively be described as follows. Similar to the influence of buoyancy, streamline curvature leads to turbulence damping. This phenomenon is characterised by parameters such as R_f or ω_{bv} . Whereas increasing Reynolds numbers favour the turbulence activity, increasing streamline curvatures seem to suppress it. This damping occurs basically through a change in the turbulence structure, which goes with a less effective shear production. The velocity fluctuations are a-typically coherent over the width and the decreased shear-efficiency can be explained by decomposing the velocity fluctuations into slow width-coherent fluctuations and rapidly varying background turbulence. The coherent fluctuations seem to represent a bulk-oscillation of the pattern of circulation cells in the downstream and transversal directions, which is significant in magnitude, nearly symmetrical and Gaussian. When treated as turbulence, it contributes significantly to the turbulent normal stresses (and thus also to the turbulent kinetic energy), but it contributes little to the turbulent shear stresses. The structures of the width-coherent velocity fluctuations and of the background turbulence are fundamentally different. The former have the characteristics of a wave-like motion (linear internal waves), with little shear stress generation, whereas the latter has the characteristics of developed turbulence with efficient generation of shear stresses. Obviously, due to the organisation of part of the turbulence into a coherent wave-like motion, the efficiency of shear generation, given the total kinetic energy of the velocity fluctuations, will be reduced.

These results are comparable to the reduced levels of turbulence activity and the tendency to wave-like motion reported in literature for the cases of curved wind tunnels and density-stratified flows. Our measurements show that this suppression of turbulence activity, in favour of a coherent wave-like motion, is a potentially important phenomenon in curved open-channel flows. To our knowledge, observations of this phenomenon in open-channel flows have not been reported before.

Acknowledgements

This research is being sponsored by the Swiss National Science Foundation under grants Nr.2100-052257.97/1 and 2000-059392.99/2. The first author acknowledges his PhD supervisor W.H. Graf.

APPENDIX I. REFERENCES

- Blanckaert, K., and de Vriend, H. J. (2002a). "Turbulence characteristics in sharp open-channel bends." (*submitted for publication*).
- Blanckaert, K., and de Vriend, H. J. (2002b). "Secondary flow in sharp open-channel bends." (*submitted for publication*).
- Blanckaert, K. & Graf, W. H. (2001). "Experiments on flow in an open-channel bend. Mean flow and turbulence." *J. Hydr. Engng, ASCE*, 127(10), 835-847.
- Blanckaert, K. & Graf, W. H. (2002). "Momentum transport in sharp open-channel bends." (*tentatively approved for publication in J. Hydr. Engng., ASCE*).
- Blanckaert, K. & Lemmin, U. (2002). "Improving acoustic turbulence measurements." (*submitted for publication*).
- Bradshaw, P. (1969). "The analogy between streamline curvature and buoyancy in turbulent shear flow." *J. Fluid Mech.*, 36(part I), 177-191.
- Bradshaw, P. (1973). "Effects of streamline curvature on turbulent flow." *AGARDograph No.169*, NATO.
- Bruns, J. M., Fernholz, H. H., and Monkewitz, P. A. (1999). "An experimental investigation of a three-dimensional turbulent boundary layer in an "S"-shaped duct." *J. Fluid Mech.*, 393, 175-213.
- Dietrich, W. E. (1987). "Mechanics of flow and sediment transport in river bends." *River Channels: environment and process*, K. Richards (editor), Inst. Brit. Geogr. spec. publ., Oxford, 391.
- Holloway, A. G. L., and Tavoularis, S. (1992). "The effects of curvature on sheared turbulence." *J. Fluid Mech.*, 237, 569-603.
- Hurther, D. & Lemmin, U. (1998). "A constant beamwidth transducer for three-dimensional Doppler profile measurements in open channel flow." *Meas. Sc. Techn.*, IOP, 9(10), 1706-1714.
- Hurther, D. & Lemmin, U. (2001). "A correction method for turbulence measurements with a 3-D acoustic Doppler velocity profiler." *J. Atm. Oc. Techn.*, AMS, 18, 446-458.
- Hussain, A. K. M. F. (1983). "Coherent structures - reality and myth." *Phys. Fluids*, AIP, 26(10), 2816.
- Irwin, H. P. A. H., and Smith, P. A. (1975). "Prediction of the effect of streamline curvature on turbulence." *Phys. Fluids*, AIP, 18(6), 624-630.

- Komori, S., Ueda, H., Ogino, F., and Mizushima, T. (1983). "Turbulence structure in stably stratified open-channel flow." *J. Fluid Mech.*, 130, 13-26.
- Lemmin, U. & Rolland, T. (1997). "Acoustic velocity profiler for laboratory and field studies." *J. Hydr. Engng*, 123(12), 1089-1098.
- McBean, G. A., and Miyake, M. (1972). "Turbulent transfer mechanisms in the atmospheric surface layer." *Quart. J. Roy. Met. Soc.*, 98, 383-398.
- Odgaard, A. J. (1984). "Bank erosion contribution to stream sediment load." *IIHR Report No. 280*, Iowa Inst. Hydr. Res., Iowa.
- Prandtl, L. (1930). "Reprinted in L. Prandtl gesammelte Abhandlungen 2." , 778, 1961.
- Prandtl, L., Oswatitsch, K. & Wieghardt, K. (1990). "Führer durch die Strömungslehre", 9th Edt., Vieweg, Braunschweig.
- So, R. M. C., and Mellor, G. L. (1973). "Experiment on convex curvature effects in turbulent boundary layers." *J. Fluid Mech.*, 60(1), 43-62.
- Tamburrino, A., and Gulliver, J. S. (1999). "Large flow structures in a turbulent open channel flow." *J. Hydr. Res.*, IAHR, 37(3), 363-380.
- von Karman, T. (1934). "Some aspects of the turbulence problem." *Int. Congr. Appl. Mech.*, Cambridge, 54.

PART III

FUNDAMENTAL RESEARCH

III.5 Conclusions

Valuable information has been obtained on the physical mechanisms and processes underlying the observations reported in part II:

- In **chapter III.1**, it is found that advective momentum transport by the secondary circulation is a dominant mechanism with respect to the downstream velocity distribution. Advective momentum transport by the center-region cell causes the observed increase of v_s in outward direction and the flattening (increasing/decreasing velocities in the lower/upper part of the water column) of the vertical v_s -profiles. Based on these results, chapter IV.1 will propose a non-linear model for the center-region cell and its effect on the downstream velocity distribution. The outer-bank cell prevents this outward increase to persist onto the outer bank. It stabilizes a region in between the outer bank and the center-region cell and thereby keeps the core of high velocity at some distance from the outer bank. The outer-bank cell thus has a protective effect on the stability of the outer bank.
- In **chapter III.2**, it is found that the center-region cell of secondary circulation is mainly generated by the vertical gradient of the centrifugal force, $(\partial/\partial z)(v_s^2/R)$. The non-uniform outward centrifugal force and the nearly-uniform inward pressure gradient, due to the superelevation of the water surface, are on the average in equilibrium. Their local non-equilibrium, however, gives rise to the center-region cell. An important negative feedback exists between the strength of the center-region cell and the vertical profile of v_s . As mentioned above, the v_s -profiles flatten under the influence of the center-region cell. The resulting centrifugal force, v_s^2/R , gets more uniform over the depth, which results in a weaker center-region cell. In chapter IV.1, a non-linear model for the center-region cell and the downstream velocity profile will be proposed that takes due account of this negative feedback. By incorporating the effects of the center-region cell with such a model, reasonably accurate simulations of moderately curved flows can be obtained with depth-integrated flow models. For strong curvatures, however, a fully three-dimensional flow description is required.
- The mechanisms underlying the outer-bank cell of secondary circulation are investigated by means of a term-by-term analysis of the downstream vorticity equation based on the experimental data. Similar outer-bank cells exist in straight turbulent flow as well as in curved laminar flow. In straight turbulent flow, they are induced by the anisotropy of turbulence, and they cannot be simulated with standard $k-\varepsilon$ turbulence closures. In curved laminar flow, they come into existence when the curvature exceeds a critical value: the flattening of the v_s -profiles gets so pronounced that the gradient of the centrifugal force changes sign near the water surface, $(\partial/\partial z)(v_s^2/R) < 0$, provoking the generation of the outer-bank cell. In **chapter III.2**, it is found that both mechanisms have a comparable contribution to the generation of the outer-bank cell in curved turbulent flow and strengthen each other, whence the outer-bank cell is stronger in a curved turbulent flow than in a curved laminar or a

straight turbulent flow. Furthermore, it is found that the restitution of kinetic energy from the turbulence to the mean flow plays an important role in the generation of the outer-bank cell, and that the deficiency of standard $k-\varepsilon$ turbulence closures is due to their inherent incapability to account for such kinetic-energy restitution. A successful numerical simulation of the outer-bank cell with a non-linear $k-\varepsilon$ turbulence closure, based on these indications, will be reported in chapter IV.2.

- In **chapter III.3**, it is found that the reduced turbulence activity in the investigated outer bend may be attributed to a change in turbulence structure as compared to a straight uniform open-channel flow: the a_l turbulence-structure parameter and the mixing coefficients indicate that given the amount of turbulent kinetic energy, there is less shear in a curved flow. The departures from the turbulence structure in straight uniform flow are correlated with a curvature-Richardson number R_f that parameterizes the streamline curvature. Such correlations may help to improve the capabilities of two-equation turbulence closures for three-dimensional curved open-channel flow. In chapter IV.1, it will be shown that the strength of the center-region cell of secondary circulation depends on the same curvature-Richardson number, which must be an important scaling parameter in curved open-channel flow.
- An analysis of the instantaneous behavior of the flow gave more physical insight into the dynamics underlying this change in turbulence structure. The results of **Chapter III.4** suggest that the influence of streamline curvature leads to turbulence damping, similar to the influence of buoyancy, and can be described with similar parameters such as the curvature-Richardson number R_f or the curvature-Brunt-Väisälä frequency ω_{bv} . The streamline curvature imposes a kind of transversal stratification to the turbulence structure. The velocity fluctuations are a-typically coherent over the width and can be decomposed into slow width-coherent fluctuations and a rapidly varying background signal. The slow coherent fluctuations represent a bulk-oscillation of the pattern of circulation cells with the characteristics of a wave-like motion (low shear stress generation) whereas the background signal has the characteristics of developed turbulence (efficient shear stress generation). Obviously, the reduction of part of the turbulence into wave-like motion reduces the efficiency of shear generation. Similar observations on reduced turbulence activity and tendency to wave-like motion have been reported in literature for flow in curved wind tunnels and density-stratified flows. To our knowledge, these potentially important phenomena have not been reported in literature before for the case of open-channel flow. As concluded in chapter III.3, correlations between the turbulence structure and curvature parameters such as R_f and ω_{bv} may help to improve the capabilities of two-equation turbulence closures for three-dimensional curved open-channel flow, although this would require more experimental data.

As mentioned, some of these results will be applied in numerical-simulation techniques in part IV. Note that this part on fundamental research makes uniquely use of the small-flume experiments. Based on these results, the large-flume experiments have been designed, and their analysis will be reported in the future.

PART IV

APPLIED RESEARCH

IV.0	Introduction	
IV.1	Non-Linear Modeling of Secondary Flow and Vertical Flow Structure in Open-Channel Bends	IV.1
IV.2	Simulation of Secondary Flow in Curved Channels	IV.35
IV.3	Conclusions	IV.43

IV.0 Introduction

The knowledge acquired in parts II and III is applied in an engineering sense, mainly by trying to evaluate, improve or develop numerical-simulation techniques.

Due to the integration over the flow depth, all information related to the vertical structure of the flow field, and especially to the secondary circulation, is lost in depth-integrated flow models, and has to be provided. Chapters II.2 and II.3 have shown that linear models for this purpose are inadequate. Chapters III.1 and III.2 indicated as cause their neglect of the feedback between the downstream velocity profile and the secondary circulation. **Chapter IV.1** proposes a non-linear model for the center-region cell of secondary circulation that accounts for this feedback. The non-linear model is derived, validated with experimental data from the large-flume experiments and analyzed. Furthermore, the relevance of the differences between the linear and the non-linear model is estimated for some natural rivers. Previous versions of this non-linear model have been presented in two papers that are not included in this dissertation:

Blanckaert K. (2001) "A model for flow in strongly curved channel bends." *Proc. JF Kennedy student paper comp., 29th-IAHR congr., Beijing, China, 42-50*

Blanckaert, K. & Graf, W. H. (2001) "Non-linear model for secondary circulation and transversal bottom slope in sharp bends." *Proc. 2th RCEM-congr., Obihiro, Japan, 791-800.*

Chapters II.1 and III.1 have shown that the weak outer-bank cell is important since it has a protective effect on the outer bank. Chapter III.2 has indicated that turbulence anisotropy and the restitution of kinetic energy from the turbulence to the mean flow play an important role in the generation of the outer-bank cell, and that the standard $k-\varepsilon$ turbulence closure model cannot account for these underlying physical mechanisms. Based on the acquired knowledge, chapter IV.2 tempts to simulate numerically the outer-bank cell observed in the small-flume experiments with a non-linear $k-\varepsilon$ turbulence closure. These simulations were done in collaboration with the National Center for Computational Hydroscience and Engineering (Univ. Mississippi, Prof. Wang and Prof. Jia).

Part IV ends with a summary of the main **conclusions**.

IV.1 Non-Linear Modeling of Secondary Flow and Vertical Flow Structure in Open-Channel Bends

(in preparation for submission to Water Resources Research, Am. Geoph. Un.)

Abstract

River problems concerning the flow field and the morphology are often investigated by means of depth-integrated flow-sediment models, in which the vertical structure of the flow is accounted for by a closure submodel; this is similar to the turbulence-closure submodels that have to be provided to the Reynolds-averaged flow equations. The required closure for the vertical flow structure mainly has to account for the secondary circulation, which is a characteristic feature of curved open-channel flow that (i) redistributes the flow, the boundary shear stresses and the sediment transport by advecting flow momentum; (ii) causes the direction of the bottom shear stress to deviate from the direction of the depth-averaged velocity and thereby influences the bottom topography; (iii) gives rise to additional friction losses as compared to a straight-uniform flow. The commonly used linear closure models are shown to fail in reproducing essential features, because they neglect the feedback between the downstream velocity and the secondary circulation. A non-linear closure model taking this feedback into account is shown to yield results that compare well with experimental data. The feedback effects turn out to be controlled almost exclusively by a single parameter, which enables their parameterization in a relatively simple way. This control parameter also helps to objectively distinguish weak, moderate and strongly curved flows. This non-linear closure model clearly indicates the relevant flow mechanisms and the sensitivity to the hydraulic parameters. The linear model corresponds to its asymptotic solution for vanishing curvature. An analysis of a velocity-redistribution model for two natural rivers shows that differences between the linear and the non-linear-model closures are relevant with respect to the simulation of the flow and the bottom morphology. The proposed non-linear closure model has the potential of improving the performance of depth-integrated flow-sediment models without much extra computational effort.

Keywords

Open-channel flow, channel bends, meanders, velocity distribution, secondary circulation, helical motion, laboratory experiments, dispersion, flow-sediment modeling

1 Introduction

Rivers typically wind in their alluvial planes through a succession of bends, thereby shaping irregular courses that vary in time. The secondary circulation (cf. Fig. 1, also called helical motion or spiral flow), which is characteristic for flow in bends, is known to play a dominant role in the river mechanics: it redistributes the velocities, the boundary shear stresses and the sediment transport and thereby shapes the river morphology. Furthermore, it plays an important role in the spreading and mixing of dissolved or suspended matter.

IV.2

In the past, numerous river canalization works have been undertaken that confined the river to a given prescribed planform, in order to improve navigation or use the alluvial plane. Recently, there is a tendency to renaturalize rivers, e.g. by giving them more freedom to shape their course in the alluvial plane, which is recognized as a rich biotope and as an important buffer in the flood defense system. Moreover, natural rivers are preferable from a landscape point of view.

The design of river renaturalization works, flood protection schemes or navigation improvement works, as well as the investigation of matter-spreading problems require accurate predictions of the flow field and the river morphology. This is commonly done by means of depth-integrated flow models coupled to sediment-transport models and/or matter-spreading models. The use of more accurate three-dimensional flow models is not always feasible due to limitations in computing capacity. Moreover, given the inaccuracy of the sediment-transport models and the uncertainty in the driving factors (e.g. the discharge hydrograph), it is questionable whether a detailed 3-D flow description adds value to the prediction.

The information related to the vertical structure of the flow field - and especially to the secondary circulation - is lost to a large extent by depth-integrating the flow equations. The remaining information has to be introduced via closure submodels. This is similar to the turbulence-closure submodels that have to be provided to the Reynolds-averaged flow equations. Flokstra (1977), Johannesson & Parker (1989b), Finnie et al. (1999), Blanckaert (2001a) and Blanckaert & Graf (2002) have shown the importance of this closure, especially if it comes to including the feedback effects between the secondary circulation and the main flow. This paper proposes a non-linear model for the vertical structure of the flow field that, contrary to the commonly used linear models, takes due account of the feedback between the secondary circulation and the main flow. Previous versions of this non-linear model have briefly and incompletely been introduced by Blanckaert (2001b) and Blanckaert & Graf (2001b and 2002).

Besides its role as closure model in depth-integrated flow-sediment models, the proposed non-linear model improves the insight in the mechanisms underlying the curvature-induced secondary circulation and its interaction with the flow.

The required closure submodel for the vertical structure of the flow, and its close relation with the secondary circulation, are elaborated in section 2. The approach of the closure submodels is introduced in section 3. Section 4 presents experimental data on strongly-curved open-channel flow that are subsequently used for validation of the linear and non-linear models. Section 5 illustrates the failure of the commonly used linear models and identifies its causes. Section 6 proposes and analyses a non-linear model that compares well with experimental data. Differences between the linear and the non-linear models are discussed in section 7. The relevance of these differences with respect to the flow field and the morphology are discussed and estimations are made for bends on 2 natural rivers in section 8. All mathematics that are non-essential for the comprehension of the paper have been grouped in Annexes at the end of the paper.

2 Mathematical framework

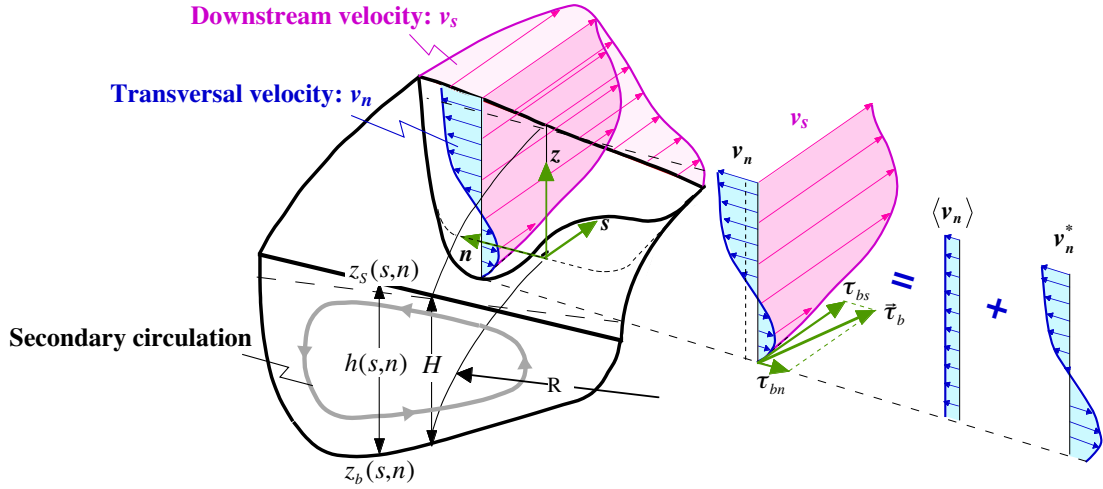


Fig. 1: Definition sketch of curved open-channel flow and decomposition of transversal velocity (cf. Eq. 1).

The main structure of the 3-D flow field in a curved open channel is outlined in Fig. 1. Furthermore, it defines the (s, n, z) -reference system, the centerline radius of curvature, R , the flow depth $h = z_S - z_b$ where z_S and z_b are the elevations of the water surface and the bottom above a horizontal datum, and the bottom shear stress vector $\bar{\tau}_b$ (τ_{bs}, τ_{bn}). The overall mean water depth H can be confounded with the centerline water depth, $h(s, 0)$.

The local instantaneous velocity components are split into a turbulent and a turbulence-averaged part, and the latter into a depth-averaged and a depth-varying part:

$$v_j(t) = \overline{\langle v_j \rangle} + \overline{v_j^*} + v_j'(t) \quad (j=s, n) \quad (1)$$

in which t is time, the overbars indicate turbulence-averaging and the brackets $\langle \rangle$ depth-averaging. Hence, by definition:

$$\overline{v_j'(t)} = 0, \quad \overline{\langle v_j^* \rangle} = 0 \quad \text{and} \quad \overline{\langle v_j \rangle} = U_j \quad (2)$$

in which U_j is the relevant depth-averaged velocity component. Especially for the transversal velocity component, v_n , the decomposition according to Eq. 1 has an important physical meaning: $\overline{\langle v_n \rangle} = U_n$ represents the cross-flow, whereas v_n^* represents the transversal component of the secondary circulation (see Fig. 1). The former is mainly induced by downstream variations in the bottom topography, whereas the latter is a characteristic feature of curved open-channel flow.

The Reynolds and depth-integrated velocity correlations $\overline{\langle v_i(t)v_j(t) \rangle}$ that appear in depth-integrated flow models can be decomposed according to Eq. 1, to yield

$$\overline{\langle v_i(t)v_j(t) \rangle} = U_i U_j + \overline{\langle v_i^* v_j^* \rangle} + \overline{\langle v_i' v_j' \rangle} \quad (3)$$

For simplicity, the overbar is omitted henceforth, except in the instantaneous velocity correlations, such as the last term in Eq. 3, the Reynolds stress.

$$\begin{aligned}
& \text{Mass conservation equation} \\
& \frac{1}{1+n/R} \frac{\partial}{\partial s} (U_s h) + \frac{\partial}{\partial n} (U_n h) + \frac{1}{1+n/R} \frac{U_n h}{R} = 0 \\
& \text{Momentum conservation equations} \\
s: & \frac{1}{1+n/R} \frac{\partial}{\partial s} (U_s^2 h) + \frac{\partial}{\partial n} (U_s U_n h) + \frac{2}{1+n/R} \frac{U_s U_n h}{R} = -\frac{1}{1+n/R} g h \frac{\partial z_s}{\partial s} - \frac{\tau_{bs}}{\rho} \\
& - \frac{1}{1+n/R} \frac{\partial}{\partial s} (\langle v_s'^2 + v_s^{*2} \rangle h) - \frac{\partial}{\partial n} (\langle v_s' v_n' + v_s^* v_n^* \rangle h) - \frac{2}{1+n/R} \frac{h}{R} \langle v_s' v_n' + v_s^* v_n^* \rangle \\
n: & \frac{1}{1+n/R} \frac{\partial}{\partial s} (U_s U_n h) + \frac{\partial}{\partial n} (U_n^2 h) + \frac{1}{1+n/R} \frac{h}{R} (U_n^2 - U_s^2) = -g h \frac{\partial z_s}{\partial n} - \frac{\tau_{bn}}{\rho} \\
& - \frac{1}{1+n/R} \frac{\partial}{\partial s} (\langle v_s' v_n' + v_s^* v_n^* \rangle h) - \frac{\partial}{\partial n} (\langle v_n'^2 + v_n^{*2} \rangle h) - \frac{1}{1+n/R} \frac{h}{R} \langle v_n'^2 - v_s'^2 + v_n^{*2} - v_s^{*2} \rangle
\end{aligned}$$

Panel 1: Depth-integrated flow model; the marked terms require a closure submodel.

Introducing these definitions into the 3-D flow equations and averaging the result over turbulence and depth yields a set of equations like that in Panel 1. In principle, these equations can be solved for the depth-averaged velocities $\bar{U} = (U_s, U_n)$ and the flow depth h after providing appropriate boundary conditions. But first the residual non-linear terms, such as $\langle v_i^* v_j^* \rangle$ and $\langle v_i' v_j' \rangle$, need to be expressed in terms of the turbulence- and depth-averaged dependent variables. The depth-averaged Reynolds stresses, $-\rho \langle v_i' v_j' \rangle$, are related to $\bar{U}(U_s, U_n)$ and h by means of a turbulence closure submodel. Similarly, a closure submodel has to be provided that relates the so-called dispersion stresses, $-\rho \langle v_i^* v_j^* \rangle$, to $\bar{U}(U_s, U_n)$ and h .

Depth-integrated turbulence closure models have amply been published in the literature (Rodi 1984, chapter 2.6.e, Booij 1989, Nezu & Nakagawa 1993, chapters 6.2.2 and 6.5.2, etc.) and will not be discussed herein. The dispersion stresses are typically larger than the depth-averaged Reynolds stresses. Their role has also been investigated extensively (Flokstra 1977, Kalkwijk & de Vriend 1980, Olesen 1987, Johannesson & Parker 1989b, Nezu & Nakagawa 1993, Yulistiyanto et al. 1998, Finnie et al. 1999, Lien et al. 1999, Blanckaert & Graf 2002, etc):

- the velocity correlation $\langle v_s^{*2} \rangle$, which is related to the shape of the downstream velocity profile, does not play an important role (Olesen 1987, p.49), so it will be ignored henceforth;
- the correlation $\langle v_s^* v_n^* \rangle$ is associated with the advective transport of downstream momentum v_s^* by the secondary circulation v_n^* ; this is a dominant mechanism in the (re)distribution of the downstream velocity and boundary shear stress and needs to be modeled accurately in depth-integrated flow models (Johannesson & Parker 1989b, Finnie et al. 1999, Blanckaert & Graf 2002);
- the quantity $\sqrt{\langle v_n^{*2} \rangle}$ is a measure of the strength of the secondary circulation.

Apart from the turbulence- and depth-averaged velocity correlations, also the bottom shear stress vector $\vec{\tau}_b(\tau_{bs}, \tau_{bn})$ appears as an additional unknown in the depth-integrated flow equations and has to be related to $\vec{U}(U_s, U_n)$ and h :

- The bed shear stress direction τ_{bn}/τ_{bs} is determined by the direction of the near-bed velocity vector and thus deviates from the direction U_n/U_s of the depth-averaged velocity vector in the presence of secondary circulation (Olesen, 1987, Eq. 2.42 and Eq. 2.54; see Fig. 1):

$$\frac{\tau_{bn}}{\tau_{bs}} = \frac{U_n}{U_s} + \frac{\tau_{bn}^*}{\tau_{bs}} = \frac{U_n}{U_s} + \alpha_\tau \frac{H}{R} \quad (4)$$

This deviation angle of the bottom shear stress due to the secondary circulation, $\tau_{bn}^*/\tau_{bs} = \alpha_\tau(H/R)$, affects the direction q_{bn}/q_{bs} of the sediment transport vector, and thus has an important influence on the bottom topography. Olesen (1987, Eq. 3.18) explains this as follows:

$$\frac{q_{bn}}{q_{bs}} = \left(\frac{\tau_{bn}}{\tau_{bs}} - G \frac{\partial z_b}{\partial n} \right) = \left(\frac{U_n}{U_s} + \frac{\tau_{bn}^*}{\tau_{bs}} - G \frac{\partial z_b}{\partial n} \right) \quad (5)$$

Over a transversally inclined bottom, $\partial z_b/\partial n$, the sediment-transport direction q_{bn}/q_{bs} deviates from the bottom-shear-stress direction τ_{bn}/τ_{bs} due to the downslope gravitational pull on the sediment particles. Olesen (1987, chapter 3.3) summarized different models for this gravitational pull G , written in general form as $G = G_0(\theta/\theta_0)^{-a}$. θ and θ_0 are the Shields parameter (the non-dimensional bottom shear stress) and its centerline value, respectively; G_0 is a function of θ_0 , and $a=0, 1/2$ or 1 for different models proposed in the literature. For the case of fully-developed curved flow, where the flow and the sediment transport occur parallel to the centerline ($U_n=0$ and $q_{bn}=0$ and indicated by the subscript ∞ ; see Eq. A4 in Annex 1), Eqs. 4-5 indicates that the transversal bottom slope becomes proportional to the deviation angle of the bottom shear stress τ_{bn}^*/τ_{bs} :

$$\left(\frac{\partial z_b}{\partial n} \right)_\infty = S_{T_\infty} \frac{H}{R} = \frac{1}{G} \left(\frac{\tau_{bn}^*}{\tau_{bs}} \right)_\infty = \frac{1}{G} \alpha_{\tau_\infty} \frac{H}{R} \Rightarrow S_{T_\infty} = \frac{\alpha_{\tau_\infty}}{G} \quad (6)$$

The normalized fully-developed transversal bottom slope S_{T_∞} will be named the scour factor further on. Obviously, the transversal bottom slope in the developing reach of the curved flow, $S_T = (\partial z_b/\partial n)/(H/R)$ will also be influenced by the deviation angle of the bottom shear stress, although $S_T \neq \alpha_\tau/G$.

- the magnitude of the bed shear stress, $\|\vec{\tau}_b\|$, is related to the magnitude of the depth-averaged velocity in straight uniform flow through a flow-resistance equation, such as $\tau_{bs}/\rho U_s^2 = C_{f0}$, (the subscript 0 refers to straight uniform flow). The friction factor C_{f0} relates to the Chezy coefficient C via $C_f = g/C^2$. Given the depth-averaged velocity, the bottom shear stress in a curved flow is higher than in the equivalent straight uniform flow. Firstly, there is an additional transversal bottom shear stress component, τ_{bn}^* , due to the secondary circulation. Secondly, due to the advective momentum transport by the secondary circulation, the velocity profiles in a curved flow are typically flatter than in a straight flow (Blanckaert & Graf 2002). Since the bottom shear stress is

IV.6

determined by the near-bed velocity gradients, this will cause an increase of $\|\vec{\tau}_b\|$ for the same depth-averaged velocity $\|\vec{U}\|$. This is expressed by multiplying the flow resistance as in straight uniform flow by the amplification factor ψ , yielding:

$$\|\vec{\tau}_b\| = C_f \rho \|\vec{U}\|^2 = \psi C_{f0} \rho \|\vec{U}\|^2 \quad \text{or} \quad \psi = \frac{\|\vec{\tau}_b\|}{\|\vec{\tau}_b\|_0} = \frac{C_f}{C_{f0}} = \frac{1}{C_{f0}} \frac{\sqrt{\tau_{bs}^2 + \tau_{bn}^2}}{\rho \|\vec{U}\|^2} \quad (7)$$

The remainder of this paper focuses on the closure submodels for the dispersion stresses, the bed shear stress direction and the shear stress amplification factor. Note that these quantities are all closely related to the secondary circulation, which underlines the dominant role of the secondary circulation in the river mechanics and underscores the importance of accurately modeling the secondary-circulation effects in the depth-integrated flow equations.

3 Approaches of model closure

The flow field in a bend is described rather well by the three-dimensional hydrostatic flow equations, Eqs. A1-3 in Annex 1. From the 3-D solutions for v_s and v_n , the normalized dispersion terms

$$\langle f_s f_n \rangle = \langle v_s^* v_n^* \rangle / U^2 \frac{H}{R} \quad \text{and} \quad \sqrt{\langle f_n^2 \rangle} = \sqrt{\langle v_n^{*2} \rangle} / U \frac{H}{R} \quad (8)$$

could be evaluated. $U=Q/(BH)$ is the overall mean velocity and $f_s=v_s/U$ and $f_n= v_n^*/(UH/R)$ represent the form of the vertical profiles of v_s and v_n^* , respectively. Similarly, the 3-D solution defines the relation between the bottom shear stress vector $\vec{\tau}_b(\tau_{bs}, \tau_{bn})$ and the dependent variables $\vec{U}(U_s, U_n)$ and h of the depth-integrated flow model. It is therefore logical to derive a closure model for these quantities from the 3-D hydrostatic flow equations. This can be done in a number of steps:

- (1) The 3-D hydrostatic flow equations are simplified to the simplest form that still represents all essential mechanisms. This simplification is briefly described below, but explained in detail in Annex 1. Firstly, fully-developed curved flow - defined by $\partial/\partial s=0$, $U_n=0$ - is considered at the centerline of the river, where $n=0$, $h \approx H$, $U_s \approx U$ and $v_z \approx 0$. Subsequently, an order-of-magnitude analysis is made by means of a normalization in order to identify the dominant terms/mechanisms in the flow equations (see Panel A1 in Annex 1).
- (2) Various approaches can be taken to simplify the normalized flow equation in order to derive the vertical structure of the velocity components in fully-developed curved flow. A formal first-order perturbation approach with H/R as a perturbation parameter leads to the commonly used linear model approach (see Section 5). This will be compared with a more physics-based non-linear approach that includes the feedback between the secondary flow and the main flow (see Section 6).
- (3) The closure model needs to provide the vertical structure of the flow all around bends of varying curvature, not only in fully-developed curved flow. Therefore, a semi-

heuristic relaxation model is adopted that describes the inertial adaptation of the vertical flow structure to curvature changes:

$$\lambda \frac{\partial Y}{\partial \phi} + Y = \begin{cases} Y_\infty & \text{in bend} \\ 0 & \text{in straight outflow} \end{cases} \quad (9)$$

where $Y = \langle f_s f_n \rangle, \langle f_n^2 \rangle, \psi$ or α_τ and $\phi = s/R$ (bend) or s/B (straight) is the normalized downstream coordinate. This relaxation model expresses that the solution Y in the developing region of the flow lags behind its target value (Y_∞ in a bend, 0 in a straight reach). The relaxation factor λ indicates how strong this inertial lag effect is in terms of normalized downstream distance. Various models have been proposed in the literature (Rozovskii 1957, Yen 1965, de Vriend 1981a, Kitanidis & Kennedy 1984, Kalkwijk & Booij 1986, Odgaard 1986; Ikeda & Nishimura 1986, Olesen 1987; Johannesson & Parker 1989a, etc.). Their main differences lie in the definition of the relaxation factor. Although $\langle f_n^2 \rangle$ and α_τ have different relaxation factors according to de Vriend (1981a) and Kalkwijk & Booij (1986), hereafter the relaxation factor proposed by Johannesson & Parker (1989a) will be adopted:

$$\lambda = \begin{cases} \frac{H/R}{\delta C_f} & \text{in bend} \\ \frac{H/B}{\delta C_f} & \text{in straight outflow} \end{cases} \quad \text{with } \delta = \frac{(13\sqrt{C_f})^{-2} \left((13\sqrt{C_f})^{-1} - \frac{1}{12} \right)}{\frac{(13\sqrt{C_f})^{-2}}{12} - \frac{(13\sqrt{C_f})^{-1}}{40} + \frac{1}{945}} \quad (10)$$

- (4) The closure model is now defined at the centerline of rivers of varying curvature. However, the closure models need to provide the vertical structure of the flow throughout the flow domain. Ikeda et al. (1990) propose a semi-heuristic width-extension, but measured distributions over the width remain to be published. This paper will therefore abstain from any width-extension.

4 The experiments

Further on in this paper, the linear and non-linear model results will be compared to experimental data gathered in the laboratory flume shown in Fig. 2. This section uniquely aims at introducing the data that will be used for validation further in the paper.

The laboratory flume has a 9 m long straight inflow reach followed by a 193° bend with a constant centerline radius of curvature of $R=1.7\text{m}$ and a 5m long straight outflow reach. The width is $B=1.3\text{m}$ and the vertical banks are made of Plexiglas. The horizontal bottom was covered by nearly uniform sand with diameters in the range, $1.6\text{mm} < d < 2.2\text{mm}$; it was fixed by spraying a paint on it, thus preserving the grain roughness.

Measurements were made for 3 subcritical hydraulic conditions, summarized in Fig. 2. Increasing the discharge Q mainly resulted in an increasing water depth H and curvature ratio H/R , whereby the friction factor varied between $10.2 < 1/\sqrt{C_f} = 1/\sqrt{\psi C_{f0}} < 11.2$. The curvature ratios indicate very sharp bends that will rarely be encountered in natural open-channel flows. These experimental conditions are a severe test for the proposed non-linear model.

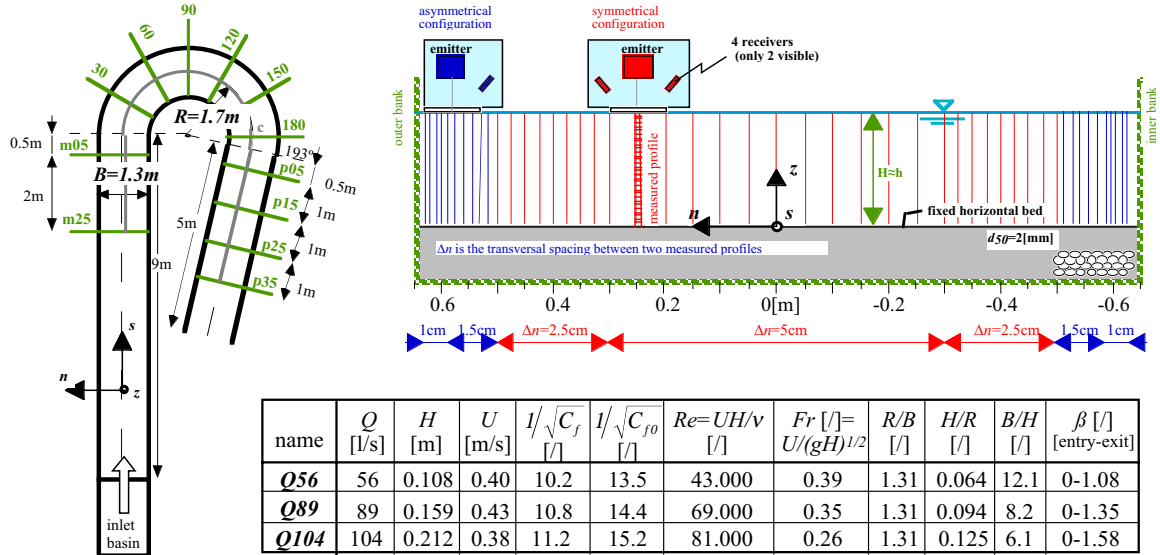


Fig. 2: Laboratory flume, measuring sections and grid, Acoustic Doppler Velocity Profiler (ADVP) and hydraulic conditions.

The linear and non-linear models depend on the equivalent-straight-uniform-flow roughness factor C_{f0} . The equivalent-straight-uniform flow is defined as the straight-uniform flow that would exist for vanishing curvature, with the same velocity U and the same water depth H and over a bottom with the same granulometry. The bottom-friction characteristics are determined by the equivalent sand roughness, which has been estimated as $k_s=3d\approx 0.006\text{m}$ (van Rijn 1984), and C_{f0} is estimated from (Graf & Altinakar 1998, Eq. 2.64):

$$\frac{1}{\sqrt{C_{f0}}} = \frac{1}{\kappa} \ln\left(\frac{H}{k_s}\right) + 6.25 \quad (11)$$

where $\kappa=0.4$ is the Karman constant. In hydraulic engineering, often use is made of the Manning friction factor, $n=H^{1/6}(C_f/g)^{1/2}$, which is nearly constant at $n_0=1/61$. This agrees well with the Strickler formula (Graf & Altinakar 1998, Eq.3.18), $n_0=d^{1/6}/21.1\approx 1/59.5$.

Measurements with high spatial and temporal resolution of the three-dimensional flow and turbulence fields were made with an Acoustic Doppler Velocity Profiler (ADVP), developed in our laboratory (Lemmin & Rolland 1997, Hurther & Lemmin 1998 and 2001, Blanckaert & Graf 2001a). Vertical profiles were first measured at the centerline every 15° in the bend and every 0.25m in the straight reaches. Subsequently, measurements on the fine grid shown in Fig. 2 were made in the reference-straight-flow cross-section 2.5m upstream of the bend as well as in the bend cross-section characterized by the strongest secondary circulation, which was found at 135° for $Q56$, at 90° for $Q89$ and at 75° for $Q104$ (cf. Fig. 5). For the $Q89$ -experiment, the 12 cross-sections along the flume, indicated in Fig. 2, were measured in detail.

The centerline evolutions of $\langle f_n^2 \rangle$ and $\langle f_s f_n \rangle$ are shown in Fig. 5 and will be discussed further in the paper. Fig. 3a compares some vertical $f_s(\eta)$ -profiles (averages of the profiles measured from 0-60°, 60-120° and 120-193° in the bend; $\eta=z/h$) measured at the centerline in the *Q89*-experiment with a logarithmic straight-flow profile based on $1/\sqrt{C_f}=10.8$ (cf. Fig. 2). Near the bend entrance, the measured profiles agree rather well with the logarithmic profile. As the flow proceeds through the bend, f_s gradually flattens by decreasing/increasing in the upper/lower part of the water column and it attains a non-monotonic form ($\partial f_s/\partial \eta < 0$ in the upper part of the water column) that is typical for strongly-curved open-channel flow.

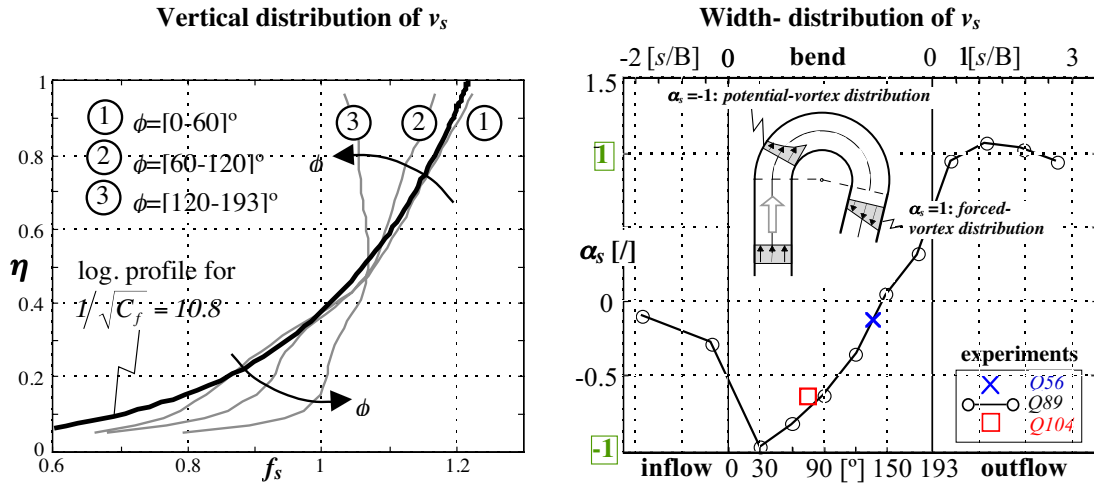


Fig. 3 (a) Vertical profiles of downstream velocity, $f_s = v_s/U$, on centerline for *Q89*-experiment; (b) Width distribution of downstream velocity around the bend, parameterized by α_s (cf. Eq. 12).

In section 6, it will be shown that the width-distribution of the downstream velocity plays an important role in the non-linear model and especially with respect to this flattening of the f_s -profiles. It will be parameterized by the normalized transversal gradient at the centerline of the depth-averaged downstream velocity:

$$\alpha_s = \left[\frac{\partial U_s}{\partial n} / \frac{1}{1 + \eta/R} \frac{U_s}{R} \right]_{n=0} \quad (12)$$

which has been proposed by Einstein & Harder (1954). According to Bradshaw (1969), Prandtl (1930) already proposed this parameter to investigate the influence of curvature on turbulent flows. The measured values of α_s for the 3 experimental conditions are shown in Fig. 3b. For the *Q89*-experiment, it could be estimated in all 12 cross-sections along the flume, whereas it could only be estimated in the cross-sections with the strongest secondary circulation at 135° for *Q56* and at 75° for *Q104*. For *Q89*, the experimental α_s -values sharply decrease from 0 in the straight inflow reach to about -1 near the bend entry. Around the bend, α_s gradually increases onto about 0.5. Near the bend exit, it sharply increases to about 1 before recovering slowly to 0 far downstream of the bend. The experimental points for *Q56* and *Q104* indicate a similar evolution.

Authors like de Vriend (1981, p29-30, p213), Steffler (1984, p30-33) or Odgaard (1986, Eq. 18) state that for flow over a horizontal bed, the transversal velocity distributions are often approximated by a “free-vortex” or “potential-vortex”-distribution near the bend entry and by a “forced-vortex”-distribution near the bend exit. In the adopted reference system, the “potential-vortex” distribution is defined by, $U_s(n) = U_s(n=0)(1+n/R)^{-1}$, giving $\alpha_s = (\partial U_s / \partial n) / (U_s / R) = -1$, whereas the “forced-vortex” distribution is defined by, $U_s(n) = U_s(n=0)(1+n/R)$, giving $\alpha_s = (\partial U_s / \partial n) / (U_s / R) = 1$. Our experimental data thus confirm these approximations, as used in the literature. The two types of vortices are schematically illustrated in Fig. 3b. In section 6, it will be shown that the parameter $\alpha_s + 1$ plays an important role in the non-linear model; it can be interpreted as the deviation from the “potential-vortex” velocity distribution. In nature, the change in curvature is gradual and α_s will rarely attain values as low as -1 . Furthermore, over a developed bar-pool bottom topography α_s will be larger than over a horizontal bottom due to the increasing flow depth in outward direction (see Eq. 24 and field examples in section 8). $\alpha_s = -1$ is thus a reasonable lower bound of the α_s -range. A reasonable upper bound is $\alpha_s = 2R/B$, where B is the channel width: this corresponds to a linear velocity increase from 0 at the inner bank to twice the centerline velocity, $2U_s(n=0)$, at the outer bank.

5 Linear approach of closure

The linear approach of the closure problem is summarized in Panel 2. It is based on the normalized equations for fully-developed curved flow at the centerline and a formal perturbation analysis with the curvature ratio, H/R , as a perturbation parameter. The equations shown in Panel 2 correspond to the zero-order system of equations, which includes only the terms in Panel A1 (Annex 1) that remain if $H/R \downarrow 0$. The solutions of this linear closure submodel will be given the suffix 0.

$0 = -C_{f0} - \sqrt{C_{f0}} \frac{\partial}{\partial \eta} \left(f_{v0} \frac{\partial f_{s0}}{\partial \eta} \right) \quad \text{and} \quad \langle f_{s0} \rangle = 1 \quad (13a)$
$-f_{s0}^2 = -S_{n0} - \sqrt{C_{f0}} \frac{\partial}{\partial \eta} \left(f_{v0} \frac{\partial f_{n0}}{\partial \eta} \right) \quad \text{and} \quad \langle f_{n0} \rangle = 0 \quad (14a)$
$\frac{\tau_{bs0}}{\rho U^2} = -C_{f0} \quad (15a)$
$\frac{\tau_{bn0}^*}{\rho U^2} = \left(\frac{H}{R} \right) (-S_{n0} + \langle f_{s0}^2 \rangle) \quad (16a)$
$S_{s0} = 1 \quad \text{and} \quad \psi_0 = 1$

Panel 2: Linear model equations for fully-developed flow. Inertia effects are included by means of Eq. 9.

The linear model consists of six coupled equations, including the two integral conditions $\langle f_{s0} \rangle = 1$ and $\langle f_{n0} \rangle = 0$. They can be solved for the six variables, $f_{s0}, f_{n0}, S_{s0}, S_{n0}, \alpha_{\tau 0}$ and ψ_0 . The downstream momentum equation, Eq. 13a, is identical to the one in straight uniform flow and will yield the corresponding profile of the downstream velocity, $f_{s0}(\eta; C_{f0})$, in which C_{f0} is the only control parameter. The additional condition $\langle f_{s0} \rangle = 1$ determines the normalized downstream water surface slope as $S_s=1$, due to the chosen normalization. The transversal momentum equation, Eq. 14a, expresses the local imbalance between the centrifugal force and the transversal pressure gradient that is known to give rise to the curvature-induced secondary circulation. The solution of the normalized horizontal component of the secondary flow velocity, f_n , is completely determined by the downstream velocity profile, f_s , and the corresponding eddy viscosity profile f_{v0} : inserting f_{s0} and f_{v0} and applying the condition $\langle f_{n0} \rangle = 0$ yields the solutions for $f_{n0}(\eta; C_{f0})$ and S_{n0} .

Since f_{s0} and f_{v0} depend uniquely on C_{f0} , this will also be the only control parameter in $f_{n0}, S_{n0}, \langle f_n^2 \rangle_0$ and $\langle f_s f_n \rangle_0$. The deviation angle τ_{bn}^*/τ_{bs} of the bottom shear stress is proportional to the curvature ratio, with the factor of proportionality, $\alpha_{\tau 0}$, also depending uniquely on C_{f0} . Furthermore, at zeroth-order, $\psi_0=1$.

This closure submodel is called linear, because all resulting (dimensional) variables, viz. $\langle v_s^* v_n^* \rangle, \sqrt{\langle v_n^{*2} \rangle}, \alpha_{\tau}$, increase linearly with the curvature ratio H/R .

Various linear-model solutions have been proposed in the literature (e.g. Engelund 1974, Kikkawa et al. 1976, de Vriend 1977, Odgaard 1986, Johannesson & Parker 1989a, etc.). They mainly differ in the choice of the eddy viscosity profile, f_{v0} , and the resulting downstream velocity profile, f_{s0} . Here we adopt the model proposed by de Vriend (1977), which is based on a parabolic eddy viscosity profile, $f_{v0} = \kappa v(1-\eta)$, resulting in a logarithmic f_{s0} ; the solutions for $\sqrt{\langle f_n^2 \rangle_0}, \langle f_s f_n \rangle_0$ and $\alpha_{\tau 0}$ are shown in Fig. 4.

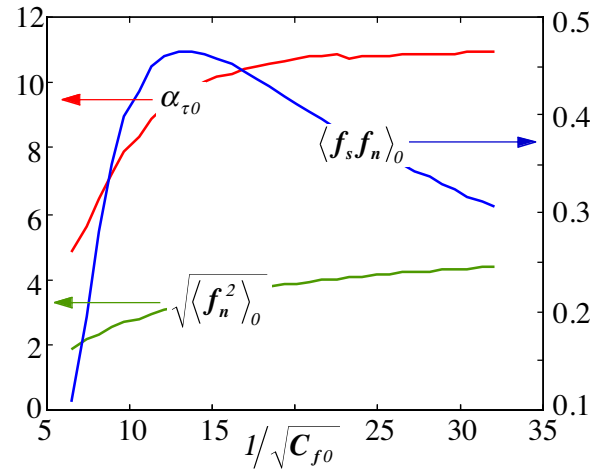
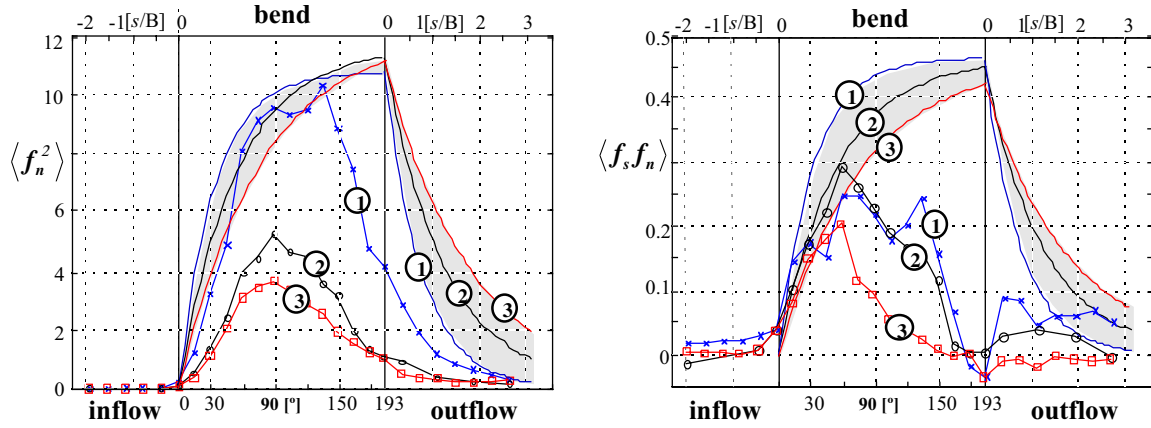


Fig. 4: Normalized linear model solutions.

These fully-developed solutions are extended in the developing flow region according to Eq. 9, and compared in Fig. 5 with the measured centerline evolution of $\langle f_n^2 \rangle$ and $\langle f_s f_n \rangle$.



Averaged values in bend reach [0-193°]

Code				Experiment		Linear model		Ratio exp./model	
	Q [l/s]	H/R	$1/\sqrt{C_{f0}}$	$\langle f_n^2 \rangle$	$\langle f_s f_n \rangle$	$\langle f_n^2 \rangle_0$	$\langle f_s f_n \rangle_0$	$\langle f_n^2 \rangle$	$\langle f_s f_n \rangle$
1	56	0.064	13.5	6.90	0.156	8.98	0.388	0.77	0.4
2	89	0.094	14.4	2.94	0.152	8.47	0.340	0.35	0.45
3	104	0.125	15.2	2.16	0.075	7.72	0.293	0.28	0.26

Fig. 5: Comparison of linear-model results (full lines) with data (symbols) measured at the centerline.

The graphs and the table included in Fig. 5 show that the linear model fails to represent the observed behavior at various points:

- according to the model, the non-dimensional quantities only depend on C_{f0} , not on H/R , whereas the experimental data show a decreasing tendency with H/R ;
- the model generally overestimates the experimental data;
- the model results increase monotonically towards their fully-developed values and remain constant after having reached those, only to decrease in the straight reach downstream of the bend, whereas the experimental data reach a maximum in the bend and then decrease considerably in the second part of the bend.

As stated above, the linear model solution is completely determined by the assumed eddy viscosity profile and the corresponding downstream velocity profile. De Vriend (1981a) already indicated that the neglected feedback between f_s and f_n might be responsible of the poor linear-model predictions. His three-dimensional simulations for laminar curved flow indicate that advective momentum transport by the secondary circulation, $f_s f_n$, reduces f_s near the water surface and increases it near the bottom. These flattened f_s -profiles lead to a reduction of the force imbalance that drives the secondary circulation. The mechanisms for the flattening of the f_s -profile and the subsequent reduction of $\langle f_n^2 \rangle$ have been investigated experimentally by Blanckaert & Graf (2002) and Blanckaert & de Vriend (2002), respectively, for turbulent curved flow.

Yet, this feedback mechanism between f_s and f_n has not been quantified before and it is not clear to what extent it is responsible of the poor performance of the linear model. These questions will be addressed in the next section, where a non-linear model will be proposed that accounts for this feedback mechanism.

6 Non-linear approach of closure

6.1 Existing non-linear models

Closure submodels that account for the feedback between f_s and f_n are called non-linear. Non-linear submodels have been proposed by Jin & Steffler (1993) and Yeh & Kennedy (1993). They adopt predefined profiles of the downstream velocity and the secondary circulation, both with one degree of freedom representing their modification due to curvature influences. This degree of freedom is determined from two equations expressing the depth-integrated conservation of moment-of-momentum, which are added to the system of depth-integrated flow equations. These models simulate the flattening of the f_s -profiles and the reduction of the secondary circulation in the second part of the bend. Moreover, they partially account for the bed shear stress amplification factor, ψ .

However, these models are not quite transparent, as they do not clearly indicate the relative importance of the various mechanisms, nor the sensitivity to certain parameters. For example, the influences of the friction factor C_f , the curvature ratio H/R and the transversal velocity distribution α_s (cf. Eq. 12), are accounted for in these models, but are not discernable in the sophisticated mathematical formulation. In the following, a non-linear closure model is proposed that aims at improving and extending these models. Instead of using predefined velocity profiles with one degree of freedom, it will calculate the entire vertical profiles of the downstream velocity and the secondary circulation.

6.2 Non-linear-model equations

The proposed non-linear model is based on the flow equations for fully-developed flow at the centerline, brought to their simplest form that still includes all essential mechanisms (Panel 3). Whereas in the linear model a formal perturbation approach was taken and all terms multiplied by a power of H/R in Panel A1 (Annex 1) were neglected, the non-linear model equations are based on a more physical approach. Although formally of the order $(H/R)^2$, the terms representing the advective transport of downstream momentum by the secondary circulation are retained in the downstream momentum equations, for the following reasons:

- The ratio of the advective momentum transport terms and the driving gravity term is of order $(H/R)^2/C_{f0}$, and thus increasing with increasing curvature and decreasing roughness. Whereas it is negligible for weak curvatures and rough boundaries, $(H/R)^2/C_{f0} \sim (1/100)^2/(0.01) \sim 0.01$, it cannot be neglected anymore for sharp bends and/or smooth boundaries, $(H/R)^2/C_{f0} \sim (1/20)^2/(0.0025) \sim 1$.
- Blanckaert & Graf (2002) made a term-by-term analysis of the downstream momentum equations (three dimensional as well as depth-integrated), based on experimental data for flow in an open-channel bend with $(H/R)^2/C_{f0} \sim (0.11/2)^2/0.008 \sim 0.38$. They found that, when averaged over the flow depth, the advective momentum transport terms were of the same order of magnitude as the driving gravity term. Locally, however, they were an order of magnitude larger, especially near the center of the secondary circulation cell. This shows that the

advective-momentum-transport terms are more important than indicated by an order-of-magnitude analysis, and that they might even play an important role in weakly curved flows with $(H/R)^2/C_{f0} \ll 1$. Furthermore, Blanckaert & Graf (2002) demonstrated that the advective transport of momentum by the secondary flow is the main cause of the flattening of the f_s -profiles.

$$\left(\frac{H}{R}\right)^2 \left(f_n \frac{\partial f_s}{\partial \xi} + f_n f_s \right) = -C_{f0} S_s - \sqrt{\psi} \sqrt{C_{f0}} \frac{\partial}{\partial \eta} \left(f_{v0} \frac{\partial f_s}{\partial \eta} \right) \quad \text{and} \quad \langle f_s \rangle = 1 \quad (9b)$$

$$-f_s^2 = -S_n - \sqrt{\psi} \sqrt{C_{f0}} \frac{\partial}{\partial \eta} \left(f_{v0} \frac{\partial f_n}{\partial \eta} \right) \quad \text{and} \quad \langle f_n \rangle = 0 \quad (10b)$$

$$\frac{\tau_{bs}}{\rho U^2} = -C_{f0} S_s - \left(\frac{H}{R}\right)^2 \frac{\partial}{\partial \xi} (\langle f_s f_n \rangle \hat{h}) - 2 \left(\frac{H}{R}\right)^2 \langle f_s f_n \rangle \hat{h} \quad (11b)$$

$$\frac{\tau_{bn}^*}{\rho U^2} = \left(\frac{H}{R}\right) (-S_n + \langle f_s^2 \rangle) \quad (12b)$$

Panel 3: Non-linear model equations for fully-developed flow. Inertia effects are included by means of Eq. 9.

The simple eddy-viscosity concept that underlies the linear model is maintained: the shape is kept parabolic throughout the bend, and the magnitude is taken proportional to the local shear velocity, $\sqrt{\|\bar{\tau}_b(n)/\rho\|}$ and local water depth, $h(n)$. At the centerline, this leads to (also see Eq. A5 in Annex 1):

$$v_t = \sqrt{\|\bar{\tau}_b/\rho\|} H f_{v0} = \sqrt{\psi} \sqrt{C_{f0}} U H f_{v0} \quad (17)$$

Since the non-linear model equations are applied at the centerline, they cannot solve for the transversal gradients (the shaded $\partial/\partial \xi$ -terms in Panel 3), which therefore have to be modeled. The effect of these transversal gradients is incorporated as follows:

Since the non-linear model will serve as a closure submodel in the depth-integrated flow equations, information on transversal gradients of depth-averaged quantities becomes available when solving the combined model. Since the transversal gradients in the closure model are somehow related to the transversal gradients of the depth-averaged quantities, the closure model and the depth-integrated flow model get intrinsically coupled. This is similar to most turbulence closures, where the turbulent stresses are related to gradients of the to-be-computed mean flow field.

The transversal gradient of the depth-averaged downstream velocity at the centerline is represented by the non-dimensional parameter α_s (cf. Eq. 12). Annex 2 shows that the transversal gradients in the non-linear model can be expressed in terms of α_s via:

$$\frac{\partial f_s}{\partial \xi} = \alpha_s f_s \quad \text{and} \quad \frac{\partial}{\partial \xi} (\langle f_s f_n \rangle \hat{h}) = (\alpha_s - 1) \langle f_s f_n \rangle \hat{h} \quad (18)$$

This yields the non-linear closure model summarized in Panel 4, where the transversal momentum equation is given in its integral form. Like in the linear model, the inertial lag effects in zones of varying curvature are included using a linear relaxation model (Eq. 9). Note that by parameterizing the transversal gradients, the original partial differential equations reduce to ordinary differential equations.

$$\left(\frac{H}{R}\right)^2 (\alpha_s + 1) f_s f_n = -C_{f0} S_s - \sqrt{\psi} \sqrt{C_{f0}} \frac{d}{d\eta} \left(f_{v0} \frac{df_s}{d\eta} \right) \quad \text{and } \langle f_s \rangle = 1 \quad (13c)$$

$$f_n(\eta) = \frac{1}{\sqrt{\psi} \sqrt{C_{f0}}} \left[\int_{\eta_0}^{\eta} \frac{1}{f_{v0}(\eta')} \left(\int_{\eta'}^{\eta} f_s^2(\eta'') d\eta'' \right) d\eta' - S_n \int_{\eta_0}^{\eta} \frac{1-\eta'}{f_{v0}(\eta')} d\eta' \right] \quad \text{and } \langle f_n \rangle = 0 \quad (14c)$$

$$\frac{\tau_{bs}}{\rho U^2} = -C_{f0} S_s - \left(\frac{H}{R}\right)^2 (\alpha_s + 1) \langle f_s f_n \rangle \quad (15c)$$

$$\frac{\tau_{bn}^*}{\rho U^2} = \left(\frac{H}{R}\right) \left(-S_n + \langle f_s^2 \rangle \right) \quad (16c)$$

$$\Rightarrow \left\{ \begin{array}{l} \frac{\tau_{bn}^*}{\tau_{bs}} = \frac{-S_n + \langle f_s^2 \rangle}{-C_{f0} S_s - \left(\frac{H}{R}\right)^2 (\alpha_s + 1) \langle f_s f_n \rangle} \frac{H}{R} = \alpha_\tau \frac{H}{R} \\ \psi = \left[S_s + \left(\frac{1}{\sqrt{C_{f0}}} \frac{H}{R} \right)^2 (\alpha_s + 1) \langle f_s f_n \rangle \right]^2 + \left[\left(\frac{1}{C_{f0}} \frac{H}{R} \right) \left(-S_n + \langle f_s^2 \rangle \right) \right]^2 \right]^{1/2} \end{array} \right. \quad (19)$$

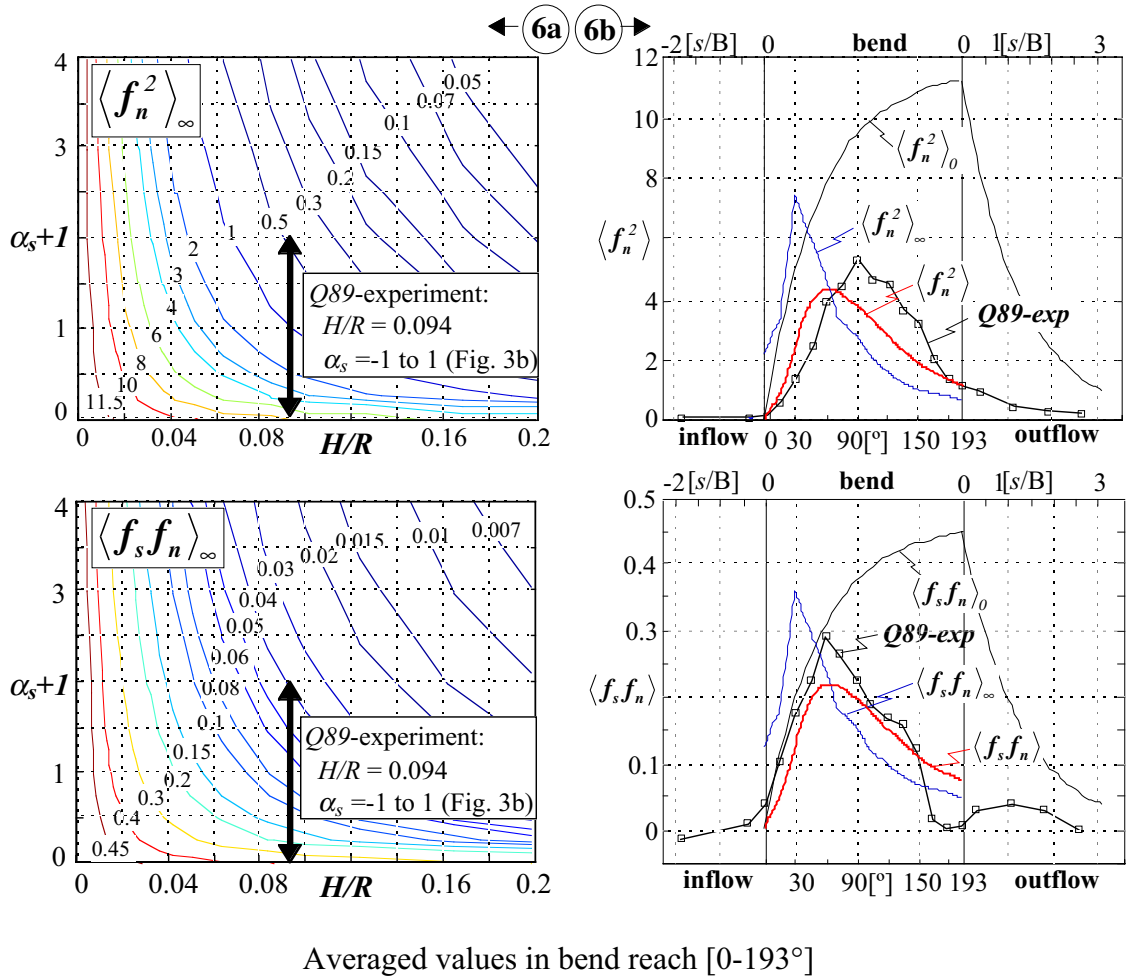
$$\psi = \left[S_s + \left(\frac{1}{\sqrt{C_{f0}}} \frac{H}{R} \right)^2 (\alpha_s + 1) \langle f_s f_n \rangle \right]^2 + \left[\left(\frac{1}{C_{f0}} \frac{H}{R} \right) \left(-S_n + \langle f_s^2 \rangle \right) \right]^2 \quad (20)$$

Panel 4 : Modeled non-linear model equations for fully-developed flow. For $H/R \downarrow 0$, the linear-model equations are found. Inertia effects are included by means of Eq. 9.

The non-linear model consists of six coupled equations, including the two integral conditions $\langle f_s \rangle = 1$ and $\langle f_n \rangle = 0$. They can be solved for the six variables, $f_s, f_n, S_s, S_n, \alpha_\tau$ and ψ . These variables are strongly coupled, as illustrated schematically by Figure 10, which makes the solution procedure rather intricate, as discussed briefly in Annex 3. The solution depends on three parameters (marked gray in Panel 4): the friction factor, C_{f0} , the curvature ratio, H/R , and the deviation from the potential-vortex distribution, $\alpha_s + 1$. Note that for vanishing curvature ratio, $H/R \downarrow 0$, the dependence on $\alpha_s + 1$ vanishes, as well, and the linear model equations emerge. For $\alpha_s + 1 = 0$, the advective momentum transport terms vanish; however, the non-linear model differs (slightly) from the linear one through the bend friction factor, $\psi > 1$.

6.3 Validation

Before further elaborating the non-linear model, it will first be checked against measured data from the very-strongly-curved $Q89$ -experiment. The fully-developed non-linear model solutions $\langle f_n^2 \rangle$ and $\langle f_s f_n \rangle$ for the estimated straight-uniform-flow friction factor $1/\sqrt{C_{f0}} = 14.4$ (cf. Fig. 2) are shown in Fig. 6a as a function of the two remaining non-linear-model parameters H/R and $\alpha_s + 1$. The non-linear-model solutions for the experimental curvature ratio $H/R = 0.094$ and for the experimental centerline evolution of $\alpha_s + 1$ (cf. Fig. 3b) are read from Fig. 6a and indicated in Fig. 6b by the subscript ∞ . The final non-linear-model solutions, shown in Fig. 6b, are found after applying the inertia-extension, Eq. 9. The linear model solutions $\langle f_n^2 \rangle_0$ and $\langle f_s f_n \rangle_0$ are also shown for comparison.



			Experiment		Linear model		Non-linear model	
Q [l/s]	H/R	$1/\sqrt{C_{f0}}$	$\langle f_n^2 \rangle$	$\langle f_s f_n \rangle$	$\langle f_n^2 \rangle_0$	$\langle f_s f_n \rangle_0$	$\langle f_n^2 \rangle_\infty$	$\langle f_s f_n \rangle_\infty$
89	0.094	14.4	2.94	0.152	8.47	0.340	2.58	0.138

Fig. 6: (a) Non-linear-model solution for $1/\sqrt{C_{f0}}=14.4$ as a function of H/R and α_s ; (b) Comparison of data measured at the centreline (symbols) with the linear model solution (0), non-linear model solution for fully-developed flow (∞), and non-linear model solution.

The non-linear model performs considerably better than the linear one at various points:

- The linear-model's overestimations and its failure to account for the decrease of $\langle f_n^2 \rangle$ and $\langle f_s f_n \rangle$ with H/R (cf. Fig. 5) are explained by the fact that the linear model is an asymptotic solution of the non-linear one for vanishing curvature. The non-linear model solution shows a significant decrease with increasing H/R and predicts the correct order of magnitude.
- The linear model failed to account for the decreasing tendencies of $\langle f_n^2 \rangle$ and $\langle f_s f_n \rangle$ in the second part of the bend, since it exclusively depends on C_{f0} , which does not vary around the bend. The non-linear model includes the interaction between the main and the secondary flow and therefore reproduces the decrease, via its dependence on $\alpha_s + 1$, the only non-linear model parameter that varies around the bend. The importance of $\alpha_s + 1$ will be discussed in further depth in Section 7.

Note also that the experimental data lag behind the fully developed non-linear-model solution (subscript ∞) and reach a lower maximum. If inertial lag effects are included, however, the agreement between model results and data is rather good (cf. Fig. 6b). This indicates that the linear relaxation model for the inertial lag effects is adequate.

- When averaged over the bend reach, the shear stress amplification factor, ψ , has a value of 1.56 (not shown), yielding $1/\sqrt{C_f} = 1/\sqrt{\psi C_{f0}} = 11.55$, which compares rather well with the experimental value of 10.8.

In general, the agreement between the non-linear-model results and the measured data is good, given that the experiment concerns a very strongly curved channel ($H/R=0.094$ will rarely occur in natural open-channel bends) and that no calibration parameters are used in the model. Blanckaert & Graf (2002) reported that the non-linear model also agrees fairly well with experimental data in one cross-section of a curved flow over a developed bottom topography, that deviate strongly from linear-model predictions.

6.4 Parameter reduction

In its present form, the fully-developed non-linear closure model presented above is not quite convenient for practical use. The model requires the solution of six coupled equations and the results depend on three parameters, viz. C_{f0} , H/R and α_s+1 . In the following, the solutions of $\langle f_n^2 \rangle$, $\langle f_s f_n \rangle$ and α_τ will be approximated as functions of the combined parameter $\beta = (C_f)^{-0.275} (H/R)^{0.5} (\alpha_s+1)^{0.25}$. These approximate solutions can be brought into a tabular or graphical form that is convenient to use. The subsequent extension for the developing region, Eq. 9, is not modified.

The parameters H/R and α_s+1 mostly occur in the combination $(H/R)^2(\alpha_s+1)$ (cf. Panel 4). Only the magnitude of the eddy viscosity, parameterized by ψ , contains a contribution that depends on the curvature ratio H/R alone. Fig. 7a shows the solutions for $\langle f_n^2 \rangle_\infty$, $\langle f_s f_n \rangle_\infty$, α_τ and $\sqrt{\psi_\infty}$, normalized by the linear-model solution, as functions of the combined parameter $[(H/R)^2(\alpha_s+1)]^{0.25}$, all for $1/\sqrt{C_{f0}}=14.4$. Each of the solutions for $\langle f_n^2 \rangle_\infty$, $\langle f_s f_n \rangle_\infty$ and α_τ show very little scatter around a single curve, whereas the solution for $\sqrt{\psi_\infty}$ shows a somewhat larger scatter, which was to be expected since ψ also depends on H/R only. Yet, most points fall close to a single curve and scatter mainly increases at very high H/R -values, which are rare in nature. These single curves therefore provide a good approximation of the non-linear model solution as a function of the combined parameter $[(H/R)^2(\alpha_s+1)]^{0.25}$, given the value of C_{f0} .

It is more convenient, however, to have the non-linear-model solution as a function of the bend friction factor $C_f = \psi C_{f0}$. Since the solution of ψ is known as a function of $[(H/R)^2(\alpha_s+1)]^{0.25}$ and C_{f0} , it is straightforward to substitute C_{f0} by $C_f = \psi C_{f0}$. The normalized non-linear model solutions for $\langle f_n^2 \rangle_\infty$, $\langle f_s f_n \rangle_\infty$, α_τ and $\sqrt{\psi_\infty}$, as a function of $[(H/R)^2(\alpha_s+1)]^{0.25}$ and C_f , are given in Fig. 7b.

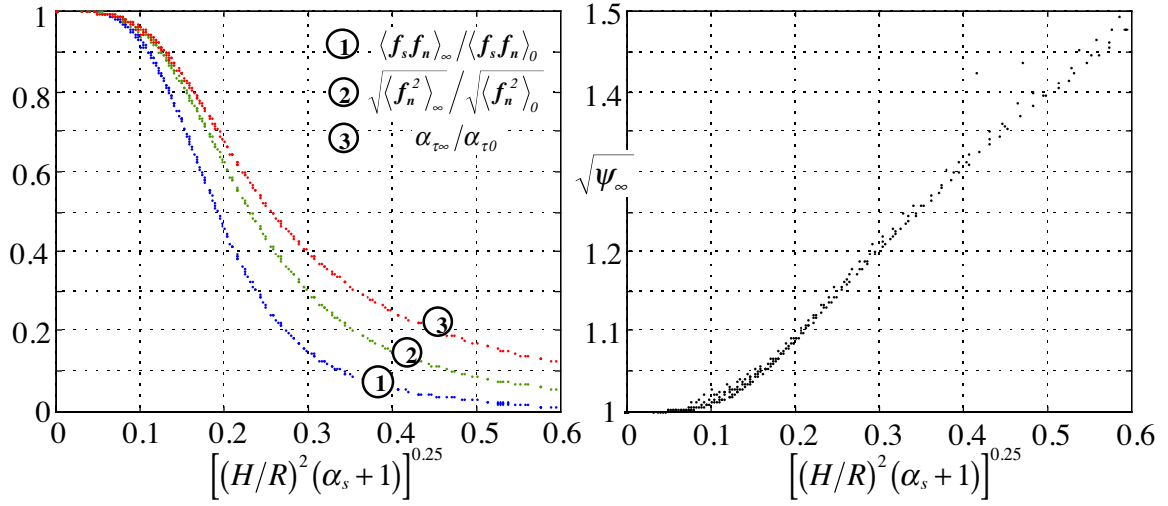


Fig. 7a: Non-linear-model solution for fully-developed flow, normalized with the linear-model solution (cf. Fig. 4) for $1/\sqrt{C_{f0}} = 14.4$. The abscise is taken to the power 0.25 in order to stretch the low-value range.

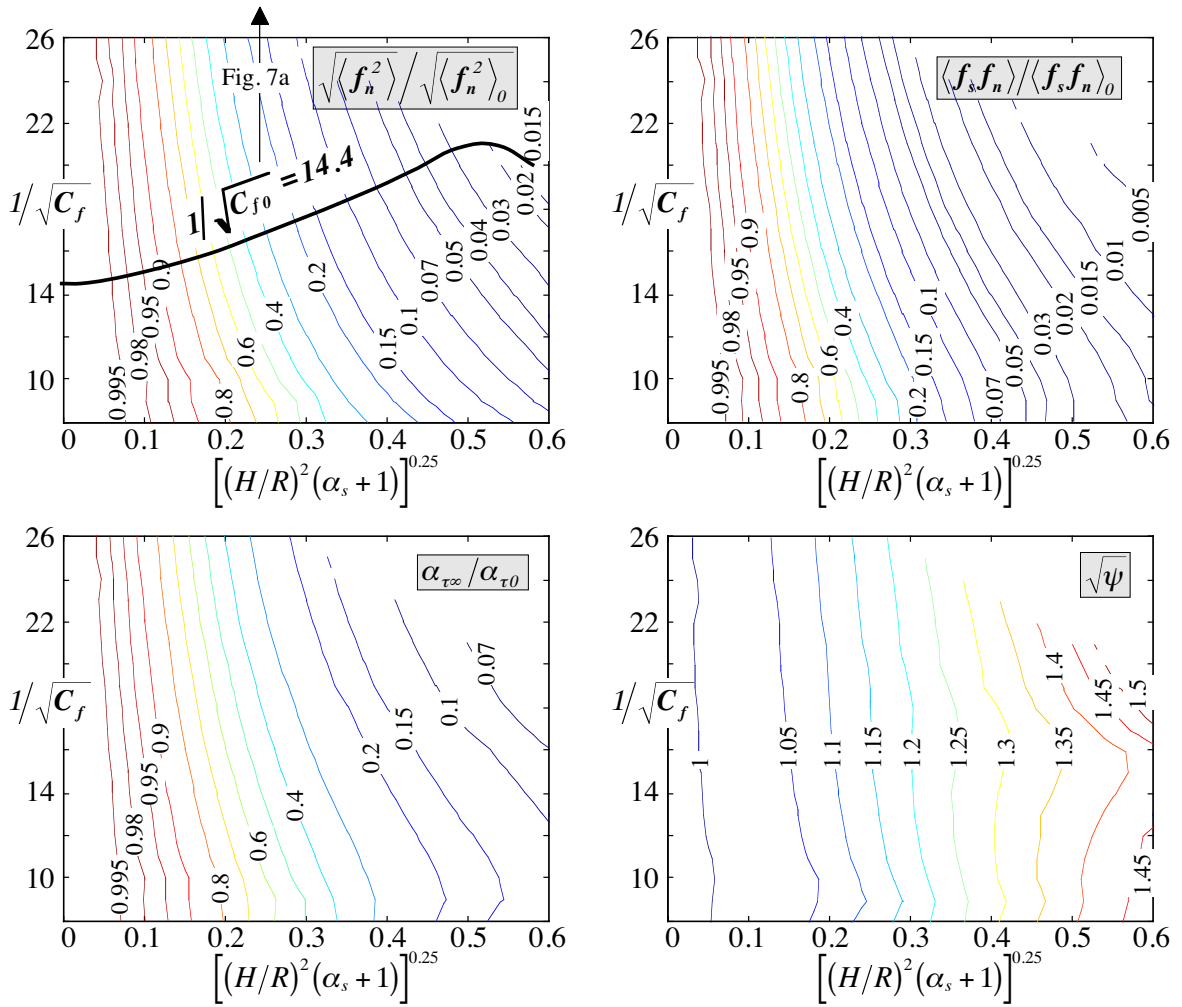


Fig. 7b: Fully-developed non-linear model solution as a function of $1/\sqrt{C_f}$ and $[(H/R)^2(\alpha_s + 1)]^{0.25}$. The solutions are normalized by the fully-developed linear-model solution, shown in Fig. 4.

Closer inspection of the solutions for $\langle f_n^2 \rangle_\infty$, $\langle f_s f_n \rangle_\infty$ and $\alpha_{\tau\infty}$, and to a lesser extent that of $\sqrt{\psi_\infty}$, suggests that the parameters $[(H/R)^2(\alpha_s+1)]^{0.25}$ and C_f be correlated. In fact, Fig. 8 shows that, when plotted against the parameter $(C_f)^{-0.275}(H/R)^{0.5}(\alpha_s+1)^{0.25}$, the solutions for $\langle f_n^2 \rangle_\infty$, $\langle f_s f_n \rangle_\infty$ and $\alpha_{\tau\infty}$ each almost collapse on a single curve. The solution for $\sqrt{\psi_\infty}$ shows a somewhat larger, but still acceptable scatter around a single curve when plotted against the parameter $(C_f)^{-0.125}(H/R)^{0.5}(\alpha_s+1)^{0.25}$. Thus the parameter $\beta = (C_f)^{-0.275}(H/R)^{0.5}(\alpha_s+1)^{0.25}$ is identified as a control parameter in curved open-channel flow. It will henceforth be named the bend parameter. Note that it differs from the turbulent Dean number, $De = 13(C_f)^{-0.5}(H/R)^{0.5}$, that has been used before (de Vriend 1981b) to indicate the stability of curved channel flow.

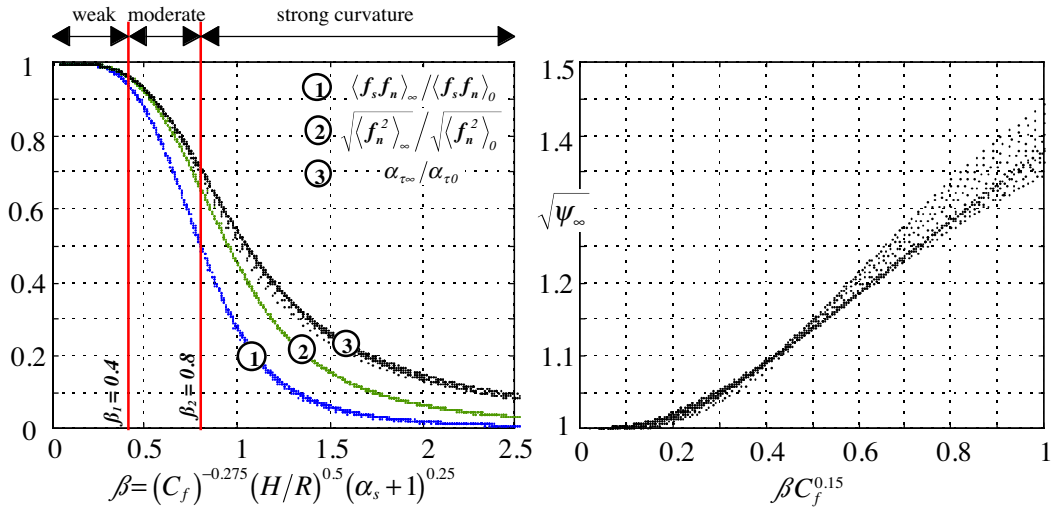


Fig. 8: General solution of the non-linear model for fully-developed flow, normalized with the linear-model solution (cf. Fig. 4), as a function of the bend parameter β .

The non-linear model accounts for the feedback between the main and the secondary flow, which – via the reduced imbalance between the centrifugal force and the transversal pressure gradient - will also affect the secondary flow intensity. Since the linear-model profiles depend on C_{f0} only, the non-linear-model profiles will not depend exclusively on β , but also on C_f . Fig. 9 shows the simulated flattening of the f_s -profiles and the reduction of f_n for flow over a rough bottom ($1/\sqrt{C_f}=10$) and a smooth one ($1/\sqrt{C_f}=20$) for values of the bend parameter $\beta=0, 0.5, 0.65, 0.85, 1$ and 1.3 .

With increasing β , the f_s -profiles flatten by decreasing/increasing in the upper/lower part of the water column. For high values of β , non-monotonic f_s -profiles are found (i.e. with $\partial f_s / \partial \eta < 0$ in the upper part of the water column), leading to a considerable reduction of f_n .

Note that Fig. 8 represents the general fully-developed solution of the non-linear model. This solution remains to be extended to the developing flow regions by means of the relaxation equation (Eq. 9). After that operation, the results can be conveniently used as a closure submodel (e.g. using look-up tables or analytical functions) in depth-integrated flow models. Moreover, they clearly reflect the relevant flow mechanisms and the sensitivity to the various model parameters. A discussion of the relevance of the non-linear-model closure and application examples for two river bends are given in section 8.

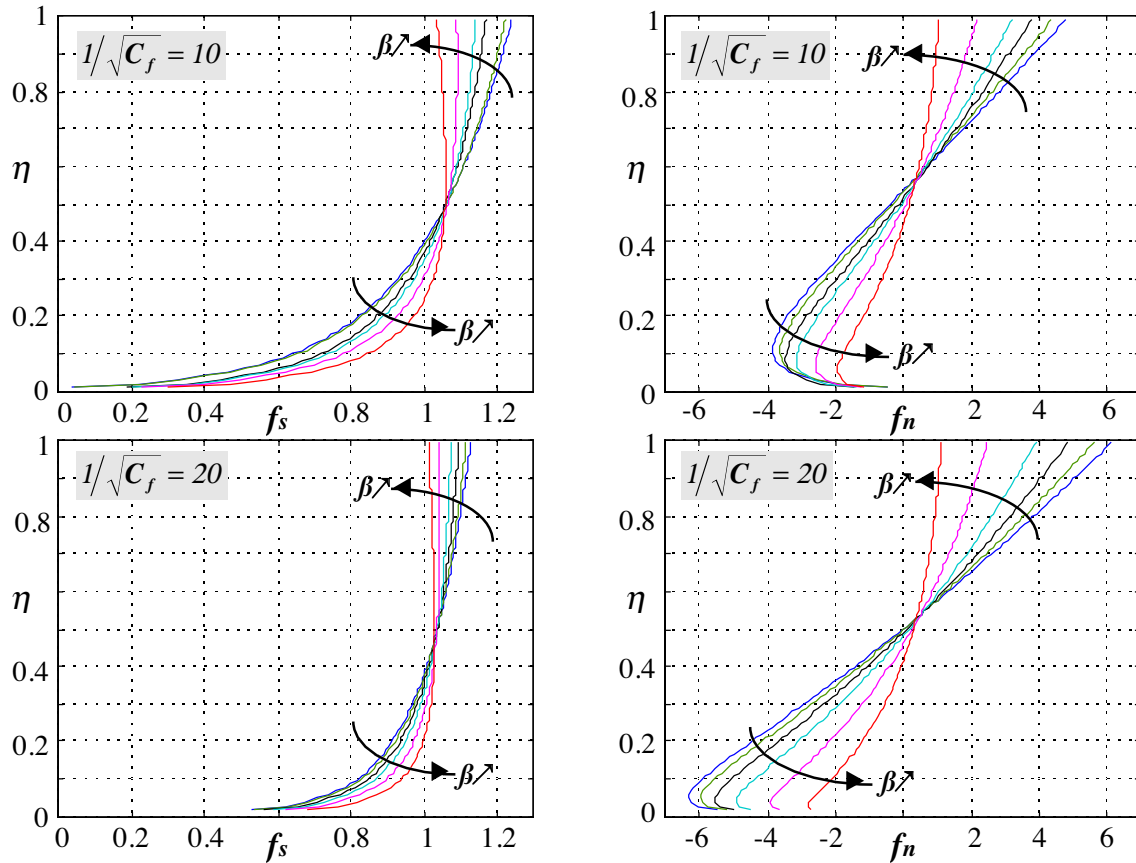


Fig. 9: Non-linear model solution for the f_s and f_n -profiles for values of the bend parameter of $\beta = 0; 0.5; 0.65; 0.8$ and 1.3 for a rough ($1/\sqrt{C_f}=10$) and a smooth ($1/\sqrt{C_f}=20$) bottom.

7 Linear vs. non-linear model

De Vriend (1981a) already indicated that the validity of the linear model is limited to weak curvatures. Neither the range of validity, however, nor the discrepancies in case of strong curvatures could be quantified. With the non-linear model, which encompasses the linear model as a limit case for $H/R \downarrow 0$, this is possible now. Three regions can be distinguished in the solution domain (see Fig. 8), which can be objectively related to the notions of weak, moderate and strong curvature:

- for $\beta < 0.4$, the linear model solution is acceptable;
- for $0.4 < \beta < 0.8$, the ratio of the non-linear to the linear-model solution decreases strongly and almost linearly;
- for $\beta > 0.8$, the non-linear model solution for $\langle f_s f_n \rangle$, which is the dominant parameter with respect to the velocity redistribution, is reduced to less than half the linear one. Although the ratios still show a pronounced decrease, we have not chosen a higher discriminator because: (i) the hypothesis at the origin of the non-linear model may no longer be justified for larger β values; (ii) otherwise no natural rivers would qualify as strongly curved.

The notions of weak, moderate and strong curvature used to be defined in a rather arbitrary way, mostly in terms of the H/R or B/R -ratio or by means of the Dean number, $De = 13(C_f)^{-0.5}(H/R)^{0.5}$. According to the objective measure provided by the bend parameter, the degree of the curvature depends on the curvature ratio H/R , the friction factor C_f and the parameter α_s , and via the latter implicitly on the arc-length of the bend, the channel width B and the bottom topography.

The non-linear model solution (cf. Fig. 8a) clearly indicates that the secondary circulation becomes self-limited for sharp bends. This idea is not completely new, but the non-linear model establishes this phenomena clearly and quantifies it.

Although the linear and the non-linear models compute the secondary circulation f_n from the same simplified transversal momentum equation (Eqs. 14a/b in Panels 2/3), the linear model does not capture all essential mechanisms. In Fig. 10, the mechanisms included in the linear model are indicated by fine arrows. A given straight-flow f_{s0} -profile yields the secondary circulation f_{n0} ; from the f_{s0} and f_{n0} -profiles, the depth-averaged advective momentum transport by the secondary circulation $\langle f_s f_n \rangle_0$ is computed. Over a mobile bottom, $\langle f_s^2 \rangle_0$ and S_{n0} influence the normalized fully developed transversal bottom slope $S_{T\infty 0}$. Both $\langle f_s f_n \rangle$ and $S_{T\infty}$ are important contributors to the distribution of the downstream velocity over the width, which is parameterized by α_s (see further Eq. 24). The normalized linear-model solution depends on C_{f0} only and is independent of H/R and α_s . Closure models based on the linear approach are therefore static, in that they are independent of the solution of the depth-averaged flow model. This is equivalent to saying that the vertical flow structure is imposed, i.e. independent of the depth-averaged model solution.

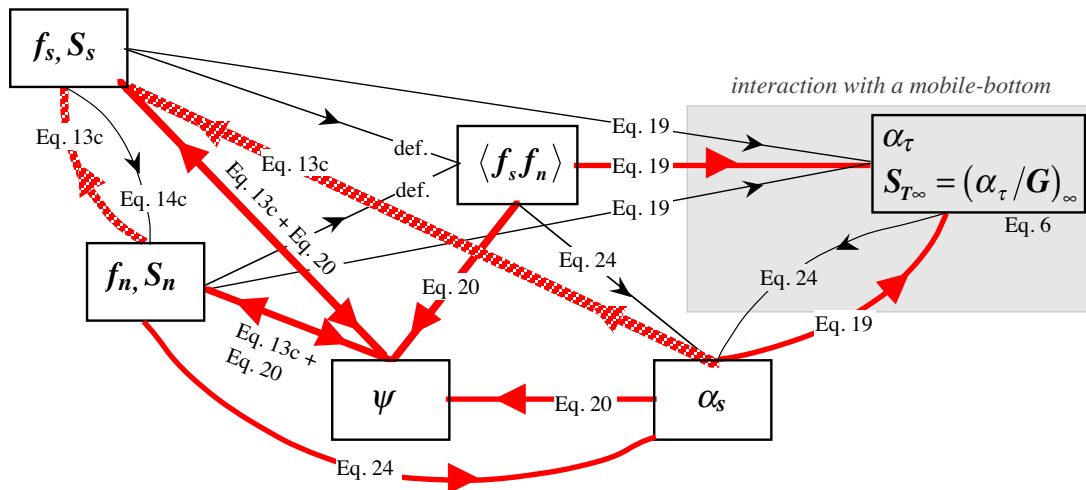


Fig. 10: Schematic representation of the interaction between the components in the linear model (fine arrows) as well as in the non-linear model (all arrows), based on the equations in Panel 4.

In Fig. 10, the extra mechanisms that are included in the non-linear model are indicated by bold arrows. Contrary to the linear model, the various components are now intricately coupled, as is indicated by the two-way arrows and the multiple loops. Especially important are the two feedback mechanisms on f_s , indicated by the shaded arrows:

- (1) f_n flattens the f_s -profiles by advecting main flow momentum, $f_s f_n$, thus yielding a decrease of f_n .
- (2) the vertical distribution of v_s , represented by f_s , is coupled to its distribution over the width, represented by α_s ; the larger α_s gets, the flatter the f_s -profile and the smaller f_n ; this leads to a decrease of $\langle f_s f_n \rangle$ and $S_{T\infty}$, and finally to a reduction of α_s .

Note that both feedbacks are negative and thus tend to stabilize their effects. Due to these feedbacks, the non-linear model depends mainly on the parameter combination $\beta = (C_f)^{-0.275} (H/R)^{0.5} (\alpha_s + 1)^{0.25}$, rather than on C_f only.

Especially $\alpha_s + 1$, parameterizing the width-distribution of v_s , plays an important role:

- it accounts for the coupling between the vertical (f_s) and the horizontal (α_s) distributions of v_s . Closure models based on the non-linear approach are therefore dynamic, in that they are dependent of the solution of the depth-averaged flow model. This is equivalent to saying that the vertical flow structure is not imposed, but computed as part of the solution.
- the α_s -dependence explains the decreasing tendencies of $\langle f_n^2 \rangle$ and $\langle f_s f_n \rangle$ in the second part of the bend.
- Bends with a horizontal bottom, with α_s usually varying between -1 and $+1$, are atypical of natural rivers, in which α_s can reach significantly higher values. The vertical flow structure expressed by the non-linear model depends on α_s and must therefore be different in either case. This implies that laboratory experiments with a horizontal bottom may not be representative of the flow in natural river bends.

Thus, the non-linear closure submodel accurately represents the vertical flow structure, including feedback mechanisms between the main flow and the secondary circulation. It encompasses the linear model as a limit case for $H/R \downarrow 0$, but remains valid for strong curvatures. Furthermore, it identifies α_s as an important parameter in curved flows and defines the bend parameter $\beta = (C_f)^{-0.275} (H/R)^{0.5} (\alpha_s + 1)^{0.25}$ as a major control parameter in a curved flow.

8 Relevance of non-linear model and practical application

This section tries to estimate the relevance of differences between the linear and the non-linear closure submodels with respect to the simulation of the flow field and the river morphology. The estimations are based on an analytical velocity redistribution model proposed by Johannesson & Parker (1989b).

8.1 Theoretical background

Johannesson & Parker (1989b) applied a first-order perturbation approach and a moment-method to derive a differential equation for the evolution α_s around the bend. In the notations of the present paper, their equation (39) reads:

$$\left(\frac{H}{R}/C_f\right)\frac{d\alpha_s}{d\phi} + 2\alpha_s = S_n\left(\frac{H}{R}/C_f\right)\frac{1}{\sigma}\frac{d\sigma}{d\phi} + (S_n Fr^2 - 1)\sigma + (S_{T_\infty} + A_s)\sigma_s \quad (21)$$

where $\phi = s/R$ and $0 < \sigma = R_{min}/R(s) < 1$ represents the variation of the centerline radius of curvature around the bend. σ_s quantifies the strength of, and the phase shift in, the secondary circulation due to the changing curvature, whence $\sigma \sim \sigma_s = O(1)$. The scour factor $S_{T_\infty} = \alpha_{\tau_\infty}/G$ (cf. Eq. 6), characterizes the fully-developed transversal bottom slope over a mobile bottom. The factor A_s represents momentum redistribution by the secondary circulation and is defined as:

$$A_s = 12 \frac{1}{C_f} \left(\frac{H}{B}\right)^2 \langle f_s f_n \rangle \quad (22)$$

In Eq. 21, four mechanisms contribute to the width-distribution of v_s . $S_n Fr^2$ represents the superelevation (tilting) of the water surface, the factor -1 would lead to a potential-vortex distribution, S_{T_∞} represents the scour effect (tilting of the bottom) and A_s represents advective momentum transport by the secondary circulation. The second of these impels the locus of high velocity towards the inside of the bend; the remaining three impel the locus to the outside. Johannesson & Parker identify S_{T_∞} and A_s as the dominant mechanisms: $S_n Fr^2 = O(Fr^2) \ll 1$ whereas S_{T_∞} is typically in the range 2.5~6 for natural streams (e.g. Odgaard 1981) and A_s is of comparable magnitude.

An estimation of the relevance of the differences between the linear and the non-linear-model closures is obtained by replacing the linear-model values for S_n , S_{T_∞} and A_s (indicated by the index 0) by their non-linear-model counterparts in Eqs. 6 and 21:

$$S_{T_\infty} = \left(\frac{\alpha_\tau}{\alpha_{\tau 0}}\right) S_{T_\infty 0} \quad (23)$$

$$\left(\frac{H}{R}/C_f\right)\frac{d\alpha_s}{d\phi} + 2\alpha_s = \frac{S_n}{S_{n0}} S_{n0} \left(\frac{H}{R}/C_f\right)\frac{1}{\sigma}\frac{d\sigma}{d\phi} + \left(\frac{S_n}{S_{n0}} S_{n0} Fr^2 - 1\right)\sigma + \left(\frac{\alpha_\tau}{\alpha_{\tau 0}} S_{T_\infty 0} + \frac{\langle f_s f_n \rangle}{\langle f_s f_n \rangle_0} A_{s0}\right)\sigma_s \quad (24)$$

The fully-developed transversal bottom slope S_{T_∞} is reduced by a factor $(\alpha_\tau/\alpha_{\tau 0})_\infty$, which will obviously also affect the river morphology in the developing zone of the bend. The velocity distribution will mainly be affected through the reduction of the transversal bottom slope with a factor $\alpha_\tau/\alpha_{\tau 0}$ and the advective momentum transport with a factor $\langle f_s f_n \rangle / \langle f_s f_n \rangle_0$.

Eq. 24 is schematized in Fig. 10 by the arrows that represent the dependence of α_s on $\langle f_s f_n \rangle$ and on α_τ . These arrows close the $(f_s - \langle f_s f_n \rangle - \alpha_s)$ and the $(f_s - \alpha_\tau - \alpha_s)$ loops and thus provide for the feedback between the horizontal (α_s) and the vertical (f_s) distribution of v_s : an increase of α_s leads to a decrease of $\alpha_\tau/\alpha_{\tau 0}$ and $\langle f_s f_n \rangle / \langle f_s f_n \rangle_0$ (cf. Fig. 8), which according to Eq. 24 provokes a reduction in α_s .

8.2 Practical application

The non-linear model effects are estimated for two strongly curved rivers, characterized by a bend factor of about $\beta \approx 0.55$ on the average. The Desna (Russia, Rozovskii 1957) is a rather smooth ($1/\sqrt{C_f} = 14.4$) meandering river of medium size, where the curvature ratio in the considered bend is nearly constant at $H/R = 1/100$. The Dommel (The Netherlands, de Vriend & Geldof 1983) is a rather rough ($1/\sqrt{C_f} = 9.5$) small river with a varying curvature ratio in the considered bend that attains maximum values of $H/R = 1/18$.

The river's planforms, the measuring sections and the relevant geometric and hydraulic parameters are indicated in Fig. 11. The evolution around the bend of H , R , B and α_s has been estimated from the reported distributions of the velocity and the flow depth in the measuring sections. From the centerline evolution of the bend factor $\beta = (C_f)^{-0.275} (H/R)^{0.5} (\alpha_s + 1)^{0.25}$, the fully-developed non-linear-model solution is derived and inertia effects are subsequently accounted for by applying the relaxation model, Eq. 9. The results for α_τ and $\langle f_s f_n \rangle$ are shown in Fig. 11.

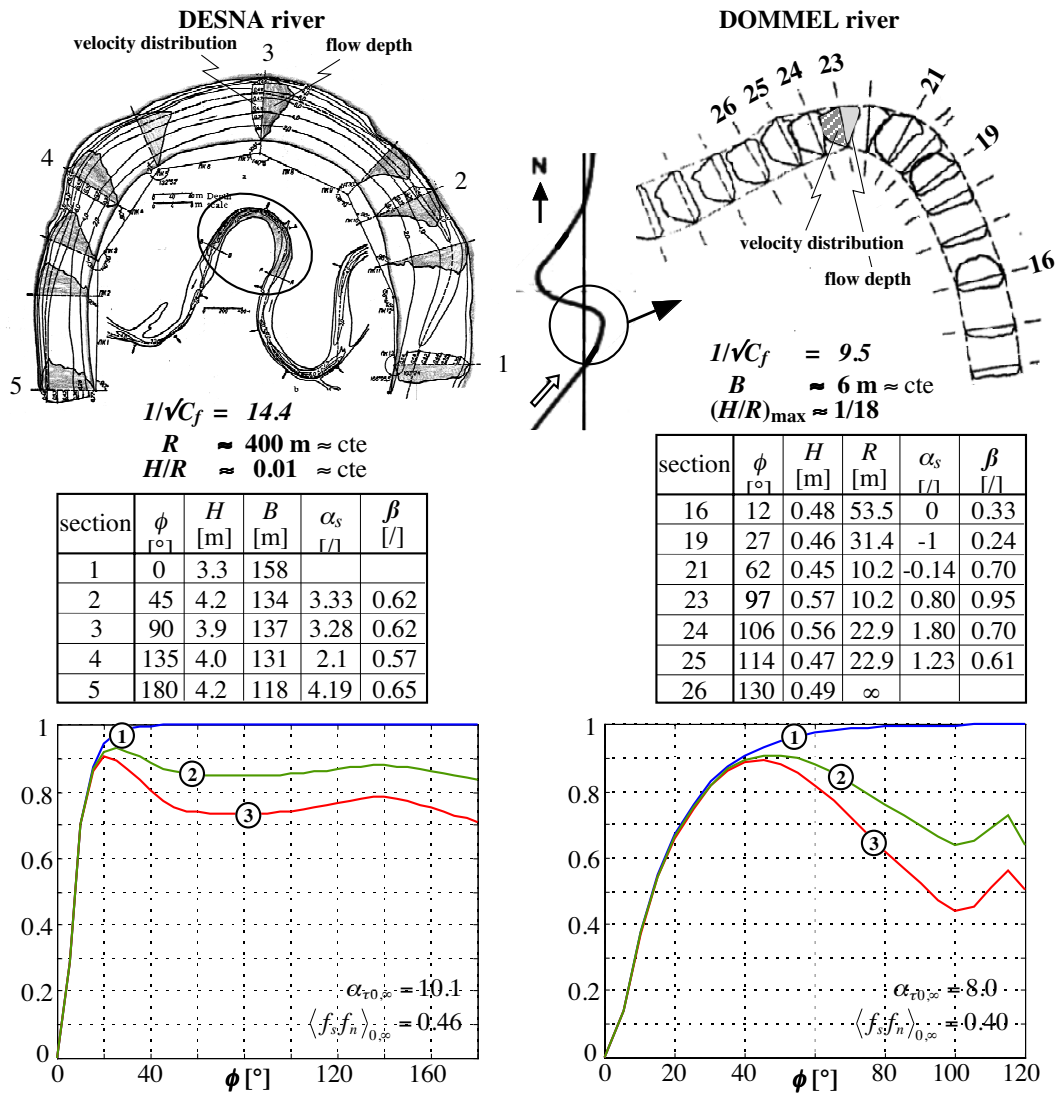


Fig. 11: Geometric and hydraulic characteristics of the Desna and the Dommel rivers. Linear model solutions $\alpha_{\tau 0}/\alpha_{\tau 0, \infty}$ and $\langle f_s f_n \rangle_0/\langle f_s f_n \rangle_{0, \infty}$ (curve 1) and non-linear model solutions $\alpha_\tau/\alpha_{\tau 0, \infty}$ (curve 2) and $\langle f_s f_n \rangle/\langle f_s f_n \rangle_{0, \infty}$ (curve 3).

The linear-model solutions, $\alpha_{\tau 0}/\alpha_{\tau 0,\infty}$ and $\langle f_s f_n \rangle_0 / \langle f_s f_n \rangle_{0,\infty}$, increase monotonically in the developing reach of the bend before remaining constant at their fully-developed value. The non-linear-model solutions, $\alpha_{\tau}/\alpha_{\tau 0,\infty}$ and $\langle f_s f_n \rangle / \langle f_s f_n \rangle_{0,\infty}$, hardly deviate from the linear ones in the developing reach. The flow redistribution is quickly accomplished in the Desna, as indicated by the nearly constant values of $\alpha_s \approx 3$, $\alpha_{\tau}/\alpha_{\tau 0,\infty} \approx 0.85$ and $\langle f_s f_n \rangle / \langle f_s f_n \rangle_{0,\infty} \approx 0.75$ through the bend. The flow redistributes more gradually in the Dommel, as indicated by the gradual increase of α_s and the corresponding gradual decrease of $\alpha_{\tau}/\alpha_{\tau 0,\infty}$ and $\langle f_s f_n \rangle / \langle f_s f_n \rangle_{0,\infty}$ from about 0.9 to about 0.7 and 0.5, respectively, near the bend exit. The non-linear-model reductions $\alpha_{\tau}/\alpha_{\tau 0}$ and $\langle f_s f_n \rangle / \langle f_s f_n \rangle_0$ have bend-averaged values of about 0.87 and 0.78 for the Desna and about 0.83 and 0.74 for the Dommel, respectively.

Both examples indicate that the reductions due to the non-linear model might be minor for short bends, but become more important with increasing bend length, because the velocity redistribution can get further accomplished, resulting in higher α_s -values.

The effect of both non-linear model reductions on the velocity-redistribution, is estimated from Eq. 24, which reduces for fully-developed flow to:

$$\alpha_{s\infty} \sim \frac{1}{2} \left[\left(\frac{S_n}{S_{n0}} S_{n0} Fr^2 - 1 \right) + \left(\frac{\alpha_{\tau}}{\alpha_{\tau 0}} S_T + \frac{\langle f_s f_n \rangle}{\langle f_s f_n \rangle_0} A_s \right) \right] \quad (25)$$

	Fr^2	$S_{T\infty}$ exp.	A_s	$\left(\frac{\alpha_{\tau}}{\alpha_{\tau 0}} \right)_{avgd}$	$\left(\frac{\langle f_s f_n \rangle}{\langle f_s f_n \rangle_0} \right)_{avgd}$	$\alpha_{s\infty}$ linear model	$\alpha_{s\infty}$ non-linear model	$\Delta\alpha_{s\infty}$	$\alpha_{s\infty}$ exp.
Desna	0.005	5.5	1	0.87	0.78	2.75	2.25	0.5	3.0
Dommel	0.05	3.45	3.03	0.83	0.74	2.7	2.0	0.75	2.0

Table 1. Estimation of the influence of differences between the linear and non-linear closure models on the velocity distribution in two natural rivers.

Table 1 summarizes linear and non-linear model estimates of the contributions in the right-hand-side, and compares the corresponding values of $\alpha_{s\infty}$ with an experimental estimation. The scour factor $S_{T\infty} = (\alpha_{\tau}/\alpha_{\tau 0})_{\infty} S_{T\infty 0}$ is estimated from the experimental data and the factor A_s is computed from the linear-model solution $\langle f_s f_n \rangle_{0,\infty}$ (cf. Eq. 22). For both rivers, the differences between the linear and the non-linear-model estimations are relevant. For the Desna, the difference amounts to $\Delta\alpha_{s\infty} \sim 0.5$, which is about 17% of $\alpha_{s\infty} \sim 3$. The difference is almost entirely due to the reduction in the transversal bottom slope. For the Dommel, $\Delta\alpha_{s\infty} \sim 0.75$, which is about 37% of $\alpha_{s\infty} \sim 2$. Here, the difference is equally due to the reductions in the transversal bottom slope and the advective momentum transport by the secondary circulation.

These examples indicate that the differences between the linear and the non-linear-model closures are relevant with respect to the river morphology and the velocity distribution. The differences might be minor for short bends but grow in importance with bend length. Both the linear and non-linear-model closures are presently being implemented in a depth-integrated flow-sediment model in order to confirm univocally the above indications.

9 Conclusions

In depth-integrated flow-sediment models of winding rivers, the influence of the vertical structure of the flow field has to be accounted for by a closure submodel. A non-linear approach of this closure problem is proposed, which is shown to perform better than the commonly used linear one.

The required closure mainly has to account for the secondary circulation, which is a characteristic of curved open-channel flow and has the following effects:

- (i) it redistributes the flow, the boundary shear stresses and the sediment transport by advecting flow momentum, represented by $\langle f_s f_n \rangle$;
- (ii) it causes the direction of the bottom shear stress to deviate from the direction of the depth-averaged velocity, given by α_τ ;
- (iii) it causes additional friction losses in a bend, parameterized by ψ .

A non-linear closure submodel representing these effects is derived from the three-dimensional flow equations, by reducing them to the simplest form that still includes all essential mechanisms. As a first step, a closure model is derived for the river centerline in fully developed curved flow. In a subsequent step, the closure model is extended to regions of varying curvature by applying a linear relaxation model that expresses the inertial lag effects in the response of the closure variables to the curvature variation. A last step would be to extend the closure model over the entire river width, but this remains to be investigated.

The commonly used linear closure models are derived from the 3-D flow equations via a formal first-order perturbation approach, with the curvature ratio H/R as a perturbation parameter. They are based on the main flow profile f_{s0} , that follows directly from the assumed eddy viscosity profile. The results for the strength of the secondary circulation $\langle f_s f_n \rangle_0$, $\alpha_{\tau 0}$, and $\langle f_n^2 \rangle_0$ depend exclusively on the friction factor C_{f0} in the equivalent straight uniform flow, whereas ψ_0 is identically equal to 1. These linear models fail to represent the behavior observed in strongly curved flow: they overpredict the secondary flow and its effects and do not represent any decreasing tendency with increasing H/R , or a gradual decrease beyond the first part of the bend.

Based on physical arguments, the proposed non-linear model retains the advective momentum terms in the 3-D flow equations, even though they are of order $(H/R)^2$. Its results depend on the straight-uniform flow friction factor C_{f0} , the curvature ratio H/R and the distribution of the downstream velocity over the width, parameterized by $\alpha_s = [(\partial U_s / \partial n) / (U_s / R)]_{n=0}$. The linear model is found to be the asymptotic case for vanishing curvature ratio. The non-linear models solution agree well with experimental data: they are of the correct order of magnitude, correctly represent the decrease with increasing H/R and the α_s -dependence accounts for the occurrence of a maximum in the first part of the bend.

The non-linear model solution can be expressed in a good approximation as functions of a single parameter. For the quantities $\langle f_s f_n \rangle$, $\langle f_n^2 \rangle$ and α_τ this is the so-called bend parameter $\beta = (C_f)^{-0.275} (H/R)^{0.5} (\alpha_s + 1)^{0.25}$, whereas ψ shows the least scatter against the parameter $\beta C_f^{0.15}$. This allows for convenient and computationally cheap ways (e.g. using

look-up tables or analytical functions) to include this closure submodel into a depth-integrated flow-sediment model. Furthermore, this identifies β as an important control parameter in curved open-channel flow. It indicates the validity of the commonly used linear models and helps to distinguish between weak, moderate and strong curvatures.

As the non-linear model accounts for the feedback between the secondary circulation, f_n , the vertical distribution of the downstream velocity, f_s , and its width-distribution, α_s , it is able to reproduce the flattening of the f_s -profiles that is typical of curved-channel flow. Closure models based on the non-linear model are dynamic, in that the vertical flow-structure is not imposed but computed as part of the solution.

An analysis of two strongly curved natural rivers indicates that the differences between the linear and the non-linear closure submodels are significant with respect to the bottom morphology and the flow distribution.

The above conclusions indicate that the proposed non-linear-model closure for the vertical structure of the flow field, and especially for the effects of the secondary circulation, has the potential to effectively and efficiently improve the capabilities of depth-integrated flow-sediment models.

Acknowledgements

This research is being sponsored by the Swiss National Science Foundation under grants 2100-052257.97 and 2000-059392.99. The author wishes to acknowledge his PhD supervisor, Prof. W.H. Graf, for his support, and Prof. H.J. de Vriend for fruitful discussions during his stays as visiting Professor at EPFL.

REFERENCES

- Blanckaert, K. (2001a). "discussion on: Bend-flow simulation using 2D depth-averaged model, by." *J. Hydr. Engng*, ASCE, 127(2), 167-170.
- Blanckaert, K. (2001b) "A model for flow in strongly curved channel bends." *Proc. JF Kennedy student paper comp., 29th-IAHR congr.*, Beijing, China, 42-50.
- Blanckaert, K. & de Vriend, H. J. (2002). "Secondary flow in sharp open-channel bends." (*submitted for publication*).
- Blanckaert, K. & Graf, W. H. (2001a). "Mean Flow and Turbulence in an Open-Channel Bend." *J. Hydr. Engng*, ASCE, 127(10), 835-847.
- Blanckaert, K. & Graf, W. H. (2001b) "Non-linear model for secondary circulation and transversal bottom slope in sharp bends." *Proc. 2th RCEM-congr.*, Obihiro, Japan, 791-800.
- Blanckaert, K. & Graf, W. H. (2002). "Momentum transport in sharp open-channel bends." (*tentatively approved for publication in J. Hydr. Engng*, ASCE).
- Booij, R. (1989). "Depth-averaged K- ϵ modelling." *Proc. 13th IAHR-congress*, Ottawa, Canada, 199-206.
- Bradshaw, P. (1969). "The analogy between streamline curvature and buoyancy in turbulent shear flow." *J. Fluid Mech.*, Cambridge Univ. Press, 36(part I), 177-191.

- de Vriend, H. J. (1977). "A mathematical model of steady flow in curved shallow channels." *J. Hydr. Res.*, IAHR, 15(1), 37-54.
- de Vriend, H. J. (1981a). "Steady flow in shallow channel bends." Report No. 81-3, Lab. Fl. Mech., Dept. Civ. Eng., Delft Univ. Techn., Delft.
- de Vriend, H. J. (1981b). "Velocity redistribution in curved rectangular channels." *J. Fluid Mech.*, Cambridge Univ. Press, 107, 423-439.
- de Vriend, H. J. & Geldof, H. J. (1983). "Main flow velocity in short and sharply curved river bends." Report No. 83-6, Lab. Fl. Mech., Dept. Civ. Eng., Delft Univ. Techn., Delft.
- Dietrich, W. E. & Whiting, P. (1989). "Boundary shear stress and sediment transport in river meanders of sand and gravel." *River Meandering*, S. Ikeda and G. Parker, eds., AGU, Washington, 1-50.
- Einstein, H. A. & Harder, J. A. (1954). "Velocity distribution and the boundary layer at channel bends." *Transactions, American Geophysical Union*, 35(1), 114-120.
- Engelund, F. (1974). "Flow and bed topography in channel bends." *J. Hydr. Div.*, ASCE, 100(HY11), 1631-1648.
- Finnie, J., Donnell, B., Letter, J. & Bernard, R. S. (1999). "Secondary flow correction for depth-averaged flow calculations." *J. Engng. Mech.*, ASCE, 125(7), 848-863.
- Flokstra, C (1977). "The closure problem for depth-averaged two-dimensional flow." *Proc. 17th IAHR congress*, Vol. 2, Baden-Baden, 247-256.
- Graf, W. H. & Altinakar, M. (1998). *Fluvial Hydraulics*, Wiley, Chichester, England.
- Hurther, D. & Lemmin, U. (1998). "A constant beamwidth transducer for three-dimensional Doppler profile measurements in open channel flow." *Meas. Sciences and Techn.*, IOP, 9(10), 1706-1714.
- Hurther, D. & Lemmin, U. (2001). "A correction method for turbulence measurements with a 3-D acoustic Doppler velocity profiler." *J. Atm. Oc. Techn.*, AMS, 18, 446-458.
- Ikeda, S. & Nishimura, T. (1986). "Flow and bed profile in meandering sand-silt rivers." *J. Hydr. Engng*, ASCE, 112(7), 562-579.
- Ikeda, S., Yamasaka, M. & Kennedy, J. F. (1990). "Three-dimensional fully developed shallow-water flow in mildly curved bends." *Fluid Dynamics Research 6*, JSFM, ed., Noth-Holland, 155-173.
- Jin, Y.-C. & Steffler, P. M. (1993). "Predicting flow in curved open channels by depth-averaged method." *J. Hydr. Engng*, ASCE, 119(1), 109-124.
- Johannesson, H. & Parker, G. (1989a). "Secondary flow in mildly sinuous channel." *J. Hydr. Engng*, ASCE, 115(3), 289-308.
- Johannesson, H. & Parker, G. (1989b). "Velocity redistribution in meandering rivers." *J. Hydr. Engng*, ASCE, 115(8), 1019-1039.
- Kalkwijk, J. P. T. & Booij, R. (1986). "Adaptation of secondary flow in nearly-horizontal flow." *J. Hydr. Res.*, IAHR, 24(1), 19-37.
- Kalkwijk, J. P. T. & de Vriend, H. J. (1980). "Computation of the flow in shallow river bends." *J. Hydr. Res.*, IAHR, 18(4), 327-342.
- Kikkawa, H., Ikeda, S. & Kitagawa, A. (1976). "Flow and bed topography in curved open channels." *J. Hydr. Div.*, ASCE, 102(HY9), 1327-1342.
- Kitanidis, P. K. & Kennedy, J. F. (1984). "Secondary current and river-meander formation." *J. Fluid Mech.*, Cambridge Univ. Press, 144, 217-229.
- Lemmin, U. & Rolland, T. (1997). "Acoustic velocity profiler for laboratory and field studies." *J. Hydr. Engng*, ASCE, 123(12), 1089-1098.

- Lien, H. C., Hsieh, T. Y., Yang, Y. C. & Yeh, K. C. (1999). "Bend-Flow Simulation Using 2D Depth-Averaged Model." *J. Hydr. Engng*, ASCE, 125(10), 1097-1108.
- Nezu, I. & Nakagawa, H. (1993). *Turbulence in open-channel flows*, IAHR-monograph, Balkema.
- Odgaard, J. A. (1981). "Transverse bed slope in alluvial channel bends." *J. Hydr. Div.*, ASCE, 107(HY12), 1677-1693.
- Odgaard, J. A. (1986). "Meander flow model. I: Development." *J. Hydr. Engng*, ASCE, 112(12), 1117-1136.
- Olesen, K. W. (1987). "Bed topography in shallow river bends." Report No. 87-1, Dept. Civ. Eng., Delft Univ. Techn., Delft.
- Prandtl, L. (1930). Reprinted in L. Prandtl: gesammelte Abhandlungen zur angewandten Mechanik, Hydro- und Aerodynamic. II. , 1961, 778, Springer, Berlin.
- Rodi, W. (1984). *Turbulence models and their applications in hydraulics - A state-of-the-art review*. IAHR-monograph, Balkema.
- Rozovskii, I. L. (1957). *Flow of Water in Bends of Open Channels*, Ac. Sc. Ukr. SSR, Isr. Progr. Sc. Transl., Jerusalem, 1961.
- Schlichting, H. & Gersten, K. (2000). *Boundary-Layer Theory*, 8th ed, Springer, Berlin.
- van Rijn, L. C. (1984). "Sediment transport, Part I: Bed load transport." *J. Hydr. Engng*, ASCE, 110(10), 1431-1456.
- Yeh, K. C. & Kennedy, J. F. (1993). "Moment model of nonuniform channel-bend flow. I: Fixed beds." *J. Hydr. Engng*, ASCE, 119(7), 776-795.
- Yen, B. C. (1965). "Characteristics of subcritical flow in a meandering channel." , Report, Iowa Institute of Hydraulic Research, Iowa.
- Yulistiyanto, B., Zech, Y. & Graf, W. H. (1998). "Flow around a cylinder: shallow-water modeling with diffusion-dispersion." *J. Hydr. Engng*, ASCE, 124(4), 419-429.

ANNEX 1: Derivation of linear and non-linear-model equations

The three-dimensional Reynolds-averaged conservation equations for mass and momentum in cylindrical co-ordinates are reported in Schlichting & Gersten (2000). Distinguishing between the cross-flow U_n and the secondary circulation v_n^* according to Eq. 1, they can be written as:

$$\left[\frac{1}{1+n/R} \frac{\partial v_s}{\partial s} + \left(\frac{\partial U_n}{\partial n} + \frac{1}{1+n/R} \frac{U_n}{R} \right) \right] + \left(\frac{\partial v_n^*}{\partial n} + \frac{1}{1+n/R} \frac{v_n^*}{R} \right) + \frac{\partial v_z}{\partial z} = 0 \quad (\text{A1})$$

$$\begin{aligned} \frac{\partial v_s}{\partial t} + \left[\frac{1}{1+n/R} v_s \frac{\partial v_s}{\partial s} + U_n \frac{\partial v_s}{\partial n} + \frac{1}{1+n/R} \frac{v_s U_n}{R} \right] + \left(v_n^* \frac{\partial v_s}{\partial n} + v_z \frac{\partial v_s}{\partial z} + \frac{1}{1+n/R} \frac{v_s v_n^*}{R} \right) = -\frac{1}{1+n/R} g \frac{\partial z_s}{\partial s} \\ - \frac{1}{1+n/R} \frac{\partial}{\partial s} \left[2v_t \left(\frac{1}{1+n/R} \frac{\partial v_s}{\partial s} + \frac{1}{1+n/R} \frac{v_n}{R} \right) \right] - \frac{\partial}{\partial n} \left(v_t \left(\frac{1}{1+n/R} \frac{\partial v_n}{\partial s} + \frac{\partial v_s}{\partial n} - \frac{1}{1+n/R} \frac{v_s}{R} \right) \right) \\ - \frac{\partial}{\partial z} \left(v_t \left(\frac{1}{1+n/R} \frac{\partial v_z}{\partial s} + \frac{\partial v_s}{\partial z} \right) \right) - \frac{2}{1+n/R} \frac{v_t}{R} \left(\frac{1}{1+n/R} \frac{\partial v_n}{\partial s} + \frac{\partial v_s}{\partial n} - \frac{1}{1+n/R} \frac{v_s}{R} \right) \end{aligned} \quad (\text{A2})$$

$$\begin{aligned} \frac{\partial v_n}{\partial t} + \left[\frac{1}{1+n/R} v_s \frac{\partial v_n}{\partial s} + U_n \frac{\partial U_n}{\partial n} + U_n \frac{\partial v_n^*}{\partial n} + v_n^* \frac{\partial U_n}{\partial n} + v_z \frac{\partial U_n}{\partial z} \right] \\ + \left(v_n^* \frac{\partial v_n^*}{\partial n} + v_z \frac{\partial v_n^*}{\partial z} - \frac{1}{1+n/R} \frac{v_s^2}{R} \right) = -g \frac{\partial z_s}{\partial n} \\ - \frac{1}{1+n/R} \frac{\partial}{\partial s} \left[v_t \left(\frac{1}{1+n/R} \frac{\partial v_n}{\partial s} + \frac{\partial v_s}{\partial n} - \frac{1}{1+n/R} \frac{v_s}{R} \right) \right] \\ - \frac{\partial}{\partial n} \left(2v_t \frac{\partial v_n}{\partial n} \right) - \frac{\partial}{\partial z} \left[v_t \left(\frac{\partial v_z}{\partial n} + \frac{\partial v_n}{\partial z} \right) \right] - \frac{1}{1+n/R} \frac{2v_t}{R} \left(\frac{\partial v_n}{\partial n} - \frac{1}{1+n/R} \frac{\partial v_s}{\partial s} - \frac{1}{1+n/R} \frac{v_n}{R} \right) \end{aligned} \quad (\text{A3})$$

The hydrostatic pressure assumption, $p = \rho g(z_s - z)$, replaces the momentum-conservation equation for the vertical velocity component v_z . The Reynolds stresses are expressed in terms of the mean velocity components using the eddy viscosity concept $-\overline{v_i v_j} = 2v_t e_{ij}$ ($i, j = s, n, z$), where v_t is the eddy viscosity and e_{ij} are the strain rates. The horizontal s -axis lies along the channel centerline, the horizontal n -axis is perpendicular to the centerline and points to the left, and the z -axis is vertically upward (cf. Fig. 1). R is the centerline radius of curvature (positive/negative for bends turning to the right/left); ρ is the fluid density; $(1+n/R)$ is a metric factor.

Eqs. A1 to A3 are now simplified by:

- 1) considering steady and fully-developed curved flow. If a straight channel is followed by a bend, the flow field and the bottom topography gradually adjust to the change in curvature. The flow in this adaptation zone is called developing curved flow. After some distance in the bend, the flow field and the transversal bottom slope will have adapted to the curvature and no longer vary in the downstream direction. In this so-

called fully-developed curved flow situation, which will be indicated by the subscript ∞ , we have:

$$\partial/\partial s=0 \text{ (except for gravity term } \partial z_s/\partial s) \rightarrow U_n=0 \text{ and } v_n=v_n^* \quad (\text{A.4})$$

whence all terms between square brackets vanish;

- 2) concentrating on the river centerline, where $n=0$;
- 3) assuming that the centerline falls within the central part of the secondary circulation cell, where $v_z \ll v_n$. We have verified that v_z has a negligible effect on the solution of the non-linear model, even near important transversal bottom slopes where $v_z = -v_n \partial z_b / \partial n$, and can therefore be neglected;
- 4) normalizing them in order to identify the dominant terms/mechanisms:

$$\begin{aligned} s &= R\phi; \quad n = R\xi; \quad z = H\hat{h}\eta, \quad h(n) = H\hat{h}(\xi) \quad \text{with } \hat{h}(0) = 1 \\ v_s(n, z) &= U f_s(\xi, \eta) \quad \text{with } \langle f_s(0) \rangle = 1 \\ v_n^*(n, z) &= 0 + U \frac{H}{R} f_n(\xi, \eta) \quad \text{with } \langle f_n \rangle = 0 \\ v_r(n, z) &= \sqrt{\psi(\xi)} \langle f_s(\xi) \rangle \hat{h}(\xi) \sqrt{C_{f0}} U H f_{v0}(\eta) \quad \text{with } \sqrt{\psi} = 1 + O(H/R) \\ \frac{\partial z_s(n)}{\partial s} &= \frac{U^2}{gH} C_{f0} S_s(\xi) \quad \text{with } S_s = 1 + O(H/R) \\ \frac{\partial z_s(n)}{\partial n} &= 0 + \frac{U^2}{gH} \frac{H}{R} S_n(\xi) \quad \text{and} \quad \frac{\partial z_b(n)}{\partial n} = 0 + \frac{H}{R} S_r(\xi) \end{aligned} \quad (\text{A5})$$

H and U are the overall mean values of $h(s, n)$ and $U_s(s, n)$. We assume that H and U can be confounded with the centerline values $h(s, 0)$ and $U_s(s, 0)$. The horizontal coordinates s and n are normalized with the centerline radius of curvature R , which is of the same order of magnitude as the channel width B for sharp bends. The velocities are normalized with U ; the transversal component of the secondary circulation v_n^* is furthermore scaled with the curvature ratio H/R .

A simple eddy-viscosity model is adopted, with the same profile shape, $f_{v0}(\eta)$, throughout the model domain. Its magnitude is taken proportional to the local water depth $h(n)$ and the local shear velocity, $\sqrt{\|\tau_b(n)\|/\rho} = \sqrt{\psi(n)} \sqrt{C_{f0}} U_s(n)$.

The downstream and transversal water-surface gradients scale with the square of the straight-uniform-flow Froude number, $Fr^2 = U^2/(gH)$. They furthermore scale with the friction factor C_{f0} and the curvature ratio H/R , respectively. The downstream momentum equation dictates that $S_s = 1$ for straight-uniform flow whereas $S_s = 1 + O(H/R)$ in curved flow. The scaling of the transversal water-surface gradients expresses the near-equilibrium between the inward pressure gradient, $g \partial z_s / \partial n$, and the outward centrifugal force, U^2/R , whence $S_n = O(1)$.

The normalizations of v_n^* , $\partial z_s / \partial n$ and $\partial z_b / \partial n$ can be interpreted as perturbation developments in the small parameter H/R .

Panel A1 gives the resulting momentum-conservation equations, whereby Eqs. A8 and A9 are the corresponding depth-integrated equations (also see Dietrich & Whiting 1989 or Blanckaert & Graf 2001b).

Three-dimensional downstream and transversal momentum equations:

$$\mathbf{s}: \left(\frac{H}{R}\right)^2 \left(f_n \frac{\partial f_s}{\partial \xi} + f_n f_s \right) = -C_{f0} S_s - \sqrt{\psi} \sqrt{C_{f0}} \left\{ \left(\frac{H}{R}\right)^2 \frac{\partial}{\partial \xi} \left[f_{v0} \left(\frac{\partial f_s}{\partial \xi} - f_s \right) \right] + \frac{\partial}{\partial \eta} \left(f_{v0} \frac{\partial f_s}{\partial \eta} \right) + 2 \left(\frac{H}{R}\right)^2 f_{v0} \left(\frac{\partial f_s}{\partial \xi} - f_s \right) \right\} \quad (\text{A6})$$

$$\mathbf{n}: \left(\frac{H}{R}\right)^2 f_n \frac{\partial f_n}{\partial \xi} - f_n^2 = -S_n - \sqrt{\psi} \sqrt{C_{f0}} \left\{ \left(\frac{H}{R}\right)^2 2 \frac{\partial}{\partial \xi} \left(f_{v0} \frac{\partial f_n}{\partial \xi} \right) + \frac{\partial}{\partial \eta} \left(f_{v0} \frac{\partial f_n}{\partial \eta} \right) + \left(\frac{H}{R}\right)^2 2 f_{v0} \left(\frac{\partial f_n}{\partial \xi} - f_n \right) \right\} \quad (\text{A7})$$

Depth-integrated downstream and transversal momentum equations:

$$\frac{\tau_{bs}}{\rho U^2} = -C_{f0} S_s - \left(\frac{H}{R}\right)^2 \frac{\partial}{\partial \xi} \left\{ \sqrt{\psi} \sqrt{C_{f0}} f_{v0} \left(\frac{\partial f_s}{\partial \xi} - f_s \right) + f_s f_n \right\} \hat{h} - 2 \left(\frac{H}{R}\right)^2 \sqrt{\psi} \sqrt{C_{f0}} f_{v0} \left(\frac{\partial f_s}{\partial \xi} - f_s \right) + f_s f_n \quad (\text{A8})$$

$$\frac{\tau_{bn}^*}{\rho U^2} \left(\frac{H}{R}\right)^{-1} = -S_n - \left(\frac{H}{R}\right)^2 \frac{\partial}{\partial \xi} \left\{ 2 \sqrt{\psi} \sqrt{C_{f0}} f_{v0} \frac{\partial f_n}{\partial \xi} + f_n^2 \right\} \hat{h} - \left(\frac{H}{R}\right)^2 \left\{ 2 \sqrt{\psi} \sqrt{C_{f0}} f_{v0} \left(\frac{\partial f_n}{\partial \xi} - f_n \right) + f_n^2 - \left(\frac{H}{R}\right)^2 f_n^2 \right\} \quad (\text{A9})$$

Panel A1: Normalized hydrostatic momentum-conservation equations for steady fully-developed flow at the centerline.

ANNEX 2: Transversal gradients in non-linear model

Since the non-linear model equations are applied only at the centerline, the transversal gradients have to be provided. In the following, they will be related to the transversal gradient of the downstream velocity, parameterized by α_s (see Eq. 12).

Definitions

A similarity hypothesis is adopted for the vertical distributions of f_s and f_n ,

$$f_j(\xi, \eta) = \hat{f}_j(\eta) g_j(\xi) \quad (j=s, n) \quad (\text{A10})$$

in which \hat{f}_j represents the shape of the vertical distribution and g_j a gain factor that may vary over the width. Coefficients are now defined as:

$$\alpha_s \stackrel{\text{Eq. 12}}{=} \left[(\partial U_s / \partial n) / (U_s / R) \right]_{n=0} = \left[(\partial g_s / \partial \xi) / g_s \right]_{\xi=0} \quad (\text{A11})$$

$$\alpha_n = \left[(\partial g_n / \partial \xi) / g_n \right]_{\xi=0} \quad (\text{A12})$$

where α_n represents the transversal gradient of the magnitude of the secondary circulation. According to Eq. A5, the transversal gradient of the flow depth, which is due to the tilting of the water surface and the bottom slope, can be written in a similar form:

$$\alpha_H = \left[(\partial \hat{h} / \partial \xi) / \hat{h} \right]_{\xi=0} = Fr^2 S_n + S_T \quad (\text{A13})$$

If the water depth varies over the width, ξ and η are not mutually orthogonal:

$$\frac{\partial \eta}{\partial \xi} = \frac{z}{H} \frac{\partial}{\partial \xi} \left(\frac{1}{\hat{h}} \right) = -\frac{z}{H} \frac{1}{\hat{h}^2} \frac{\partial \hat{h}}{\partial \xi} = -\frac{\eta}{\hat{h}} \frac{\partial \hat{h}}{\partial \xi} = -\alpha_H \eta \quad (\text{A14})$$

The transversal gradients of f_s and f_n can now be parameterized as:

$$\begin{aligned} \frac{\partial f_j(\xi, \eta)}{\partial \xi} &= \frac{\partial \hat{f}_j(\eta)}{\partial \eta} \frac{\partial \eta}{\partial \xi} g_j(\xi) + \hat{f}_j(\eta) \frac{\partial g_j(\xi)}{\partial \xi} \\ &= \left(-\frac{1}{\hat{f}_j} \frac{\partial \hat{f}_j(\eta)}{\partial \eta} \alpha_H \eta + \alpha_j \right) \hat{f}_j(\eta) g_j(\xi) = \alpha_{j,3D} f_j(\xi, \eta) \approx \alpha_j f_j(\xi, \eta) \quad (\text{A15}) \end{aligned}$$

It has been verified that the depth-varying contribution $\alpha_{j,3D}$ has negligible effect on the solution of the non-linear model, even for important transversal bottom slopes, whence it is neglected further on. This simplification eliminates the explicit dependence of the non-linear model on the transversal bottom slope S_T , which occurs in α_H (cf. Eq. A13).

The transversal-gradient term in the depth-integrated momentum equations can now be parameterized as:

$$\begin{aligned} \frac{\partial}{\partial \xi} (\langle f_s(\xi, \eta) f_n(\xi, \eta) \rangle \hat{h}(\xi)) &= \langle \hat{f}_s(\eta) \hat{f}_n(\eta) \rangle \frac{\partial}{\partial \xi} (g_s(\xi) g_n(\xi) \hat{h}(\xi)) \\ &= \langle \hat{f}_s \hat{f}_n \rangle \left(\frac{\partial g_s(\xi)}{\partial \xi} g_n(\xi) \hat{h}(\xi) + \frac{\partial g_n(\xi)}{\partial \xi} g_s(\xi) \hat{h}(\xi) + \frac{\partial \hat{h}(\xi)}{\partial \xi} g_s(\xi) g_n(\xi) \right) \\ &= (\alpha_s + \alpha_n + \alpha_H) \langle f_s(\xi, \eta) f_n(\xi, \eta) \rangle \hat{h}(\xi) \end{aligned} \quad (\text{A16})$$

Determination of α_n

The principle of mass-conservation underlies the determination of α_n . Since depth-integration of the 3-D mass-conservation equation (Eq. A1) removes f_n , the following indirect method is proposed:

The curvilinear control volume, indicated in Fig. A1, covering the upper half of the water column in the central part of the circulation cell is considered. It is assumed that the f_n -profiles are linear and that the vertical velocity is negligible. The value of α_n is now found by expressing the equality of the incoming and outgoing mass flux due to the secondary circulation.

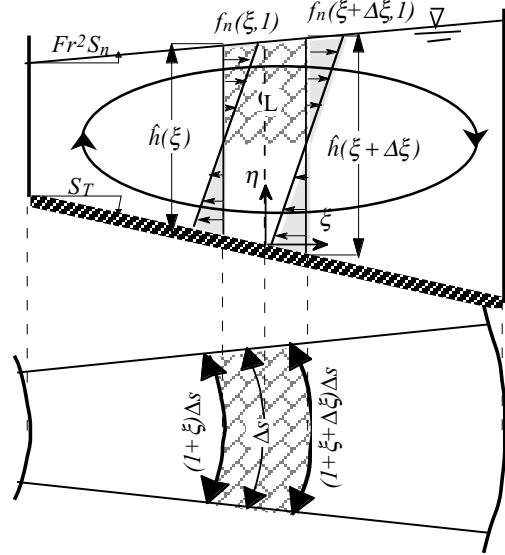


Fig. A1: Definition sketch of normalized quantities and derivation of α_n

$$\frac{1}{4} f_n(\xi, 1) \hat{h}(\xi) (1 + \xi) \Delta s = \frac{1}{4} f_n(\xi + \Delta \xi, 1) \hat{h}(\xi + \Delta \xi) (1 + \xi + \Delta \xi) \Delta s$$

Substituting $f_n(\xi, 1) = \hat{f}_n(1) g_n(\xi)$ gives:

$$g_n(\xi) \hat{h}(\xi) (1 + \xi) = \left(g_n(\xi) + \Delta \xi \frac{\partial g_n(\xi)}{\partial \xi} \right) \left(\hat{h}(\xi) + \Delta \xi \frac{\partial \hat{h}(\xi)}{\partial \xi} \right) (1 + \xi + \Delta \xi) + O(\Delta \xi^2)$$

$$0 = \Delta \xi \left[\frac{\partial g_n(\xi)}{\partial \xi} \hat{h}(\xi) (1 + \xi) + g_n(\xi) \frac{\partial \hat{h}(\xi)}{\partial \xi} (1 + \xi) + g_n(\xi) \hat{h}(\xi) \right] + O(\Delta \xi^2)$$

$$0 = \Delta \xi (\alpha_n + \alpha_H + 1) g_n(\xi) \hat{h}(\xi) + O(\Delta \xi^2)$$

$$\alpha_n + \alpha_H + 1 \approx 0 \quad (\text{A17})$$

The transversal gradients in the non-linear model equations (cf. Panel 3) are now uniquely parameterized by α_s :

$$\frac{\partial f_s}{\partial \xi} = \alpha_s f_s \quad \text{and} \quad \frac{\partial}{\partial \xi} (\langle f_s f_n \rangle \hat{h}) \stackrel{(\text{cf. Eq. A16})}{=} (\alpha_s - 1) \langle f_s f_n \rangle \hat{h} \quad (\text{A18})$$

ANNEX 3: Solution procedure of the non-linear closure submodel

The non-linear model, summarized in Panel 4, consists of six coupled equations in six dependent variables, viz. $f_s, f_n, S_s, S_n, \alpha_\tau$ and ψ . The interdependencies between these six variables are schematized in Fig. 10. The following summarizes the iterative solution procedure of the non-linear model.

The first step in the solution procedure for given parameters $C_{f0}, H/R$ and α_s is to compute the linear-model solution, corresponding to $H/R=0$ (see section 5) and indicated by $f_s^{(0)}, f_n^{(0)}, S_s^{(0)}=1, S_n^{(0)}, \alpha_\tau^{(0)}$ and $\psi^{(0)}=1$. This solution defines the parameters to be used in the law-of-the-wall bottom-boundary conditions, viz. the equivalent sand roughness and a constant for the case of a logarithmic $f_s^{(0)}$ -profile (cf. Eq. 11). Subsequently, an iterative procedure is adopted to compute the solution for the given value of H/R :

- 1) $f_s^{(i+1/2)}$ is computed from the downstream momentum equation (Eq. 13c) in which $f_n^{(i)}$ and $\psi^{(i)}$ are substituted, and which is supplemented by the law-of-the-wall bottom-boundary condition and the no-shear condition at the water surface. Furthermore, $S_s^{(i+1)}$ is chosen (by iteration) so that $\langle f_s^{(i+1/2)} \rangle = 1$. For convergence, an under-relaxation had to be applied:

$$f_s^{(i+1)} = \theta f_s^{(i)} + (1-\theta) f_s^{(i+1/2)} \quad (\text{A21})$$

The feedback between f_s and f_n is known to be very sensitive. This may explain why under-relaxation factors as high as $\theta=0.975$ are required.

- 2) $f_n^{(i+1)}$ is computed from the transversal momentum equation (Eq. 14c), in which $f_s^{(i+1)}$ and $\psi^{(i)}$ are substituted, and which is supplemented by the law-of-the-wall bottom-boundary condition and by the no-shear condition at the water surface. Furthermore, $S_n^{(i+1)}$ is chosen so that $\langle f_n^{(i+1)} \rangle = 0$.
- 3) $\tau_{bs}^{(i+1)}, \tau_{bn}^{*(i+1)}$ and $\psi^{(i+1)}$ are computed by substituting $f_s^{(i+1)}, f_n^{(i+1)}, S_s^{(i+1)}$ and $S_n^{(i+1)}$ into Eqs. 15c, 16c and 20.

Since the solution of the non-linear model is completely determined by the solution for f_s , steps 1-3 are repeated until $\langle (f_s^{(i+1)} - f_s^{(i)})^2 \rangle$ is smaller than a given tolerance.

In the above solution procedure, it is assumed that the depth-averaged centerline velocity remains constant: $U_s(n=0)=U$, whence $\langle f_s \rangle = 1$. Due to the increased friction in a bend as compared to the equivalent straight uniform flow, a greater downstream water-surface gradient $S_s > 1$ is required to maintain U . An alternative solution procedure would be to maintain $S_s=1$, which would result in a reduction of the centerline velocity, $U_s(n=0) < U$, or $\langle f_s \rangle < 1$. The real situation is probably in between both extremes: the centerline velocity somewhat decreases and the water-surface gradient somewhat increases. It has been verified that both solution procedures yield negligible differences in non-linear-model results, whence the first procedure has been adopted in the paper.

IV.2 Simulation of Secondary Flow in Curved Channels

Proc. 8th Int. Symposium on Flow Modeling and Turbulence Measurements, FMTM2001, Tokyo, Japan, Dec. 2001

YAFEI JIA

*National Center for Computational Hydroscience and Engineering,
University of Mississippi, Carrier Hall 102, MS 38677, USA
E-mail: jia@ncche.olemiss.edu*

KOEN BLANCKAERT

*Laboratoire de Recherches Hydrauliques
LRH-DGC-EPFL, 1015 Lausanne, Switzerland
E-mail: koen.blanckaert@epfl.ch*

SAM, S.Y. WANG

*National Center for Computational Hydroscience and Engineering,
University of Mississippi, Carrier Hall 102, MS 38677, USA
E-mail: wang@ncche.olemiss.edu*

Besides the center-region cell (helical motion), a weaker counter-rotating outer-bank cell is often observed in open-channel bends. It could play an important role in the outer bank erosion process because the near bank sediment transport is related to the flow structure. This outer-bank cell cannot be simulated with turbulence closures, such as the standard $k-\varepsilon$ model, since they fail to generate the cross-stream turbulence anisotropy. This paper reports simulations of both circulation cells with a non-linear $k-\varepsilon$ closure that compare reasonably well with two sets of experimental data.

1 Introduction

The flow in river bends is characterized by cross-stream circulation cells (secondary flow). The main flow velocity and the boundary shear stress distribution over the cross-section, the intensity and the direction of the sediment transport, and the river morphology are strongly related to the secondary flow.

Besides the classical helical motion – termed here center-region cell – often a smaller and weaker counter-rotating outer-bank cell is observed in the corner formed by the water surface and the outer-bank. The well-known *center-region cell* is attributed to the local imbalance between the outward centrifugal force and the inward pressure force due to the super-elevation of the water surface. It has been successfully simulated, even with a zero equation turbulence closure (Jia and Wang 1992) and a $k-\varepsilon$ model (Wu, et al 2000). The *outer-bank cell* is known to play an important role with respect to the stability of the outer bank (Blanckaert and Graf 2001a, Christensen et al. 1999, Bathurst et al. 1979). Although it has often been observed in the laboratory (among others by Rozovskii 1957, de Vriend 1979, Blanckaert and Graf 2001a and Tominaga and Nagao 2000) as well as in the field (among others by Bathurst et al. 1979, Dietrich and Smith 1983 and de Vriend and Geldof 1983), the mechanism underlying the generation of this cell are not fully understood. This is partially due to lack of available detailed experimental data on all mean velocity components and all turbulent stresses (see Blanckaert and Graf 2001a, Table1).

Blanckaert and de Vriend (2001) analyzed the mechanics underlying both circulation cells and concluded that the outer-bank cell is generated by the interplay between two mechanisms: the anisotropy of the cross-stream turbulence and the deformation of the vertical profiles of the downstream velocity, which have maximum values well below the water surface. The anisotropy of the cross-stream turbulence is known to generate the similar near-bank circulation cells found in straight uniform flow (Nezu and Nakagawa 1993).

Christensen et al. (1999) succeeded in simulating the outer-bank cell in a channel bend of constant curvature with the standard $k-\varepsilon$ turbulence closure as well as the Reynolds Stress Model (RSM). The RSM model is known to be capable of simulating the cross-stream turbulence anisotropy. However, reproducing the outer-bank cell with a standard $k-\varepsilon$ model is inconsistent with previous studies (Wu, et al 2000).

Circulation cells induced by the cross-stream turbulence anisotropy have been simulated successfully with the non-linear $k-\varepsilon$ turbulence closure proposed by Speziale (1987) for the cases of straight uniform flow (Speziale 1987) and flow in straight compound channels (Pezzinga 1994, Jia and Wang 1998). Such non-linear $k-\varepsilon$ turbulence closures are computationally more efficient than the RSM model.

This paper reports numerical simulations of curved channel flows with a free-surface three-dimensional model, CCHE3D. This model has been validated extensively for many different types of open-channel flow with numerous experimental data sets (for instance Jia and Wang 1992 and 1998). In order to simulate both circulation cells in open-channel bends, the non-linear $k-\varepsilon$ turbulence closure has been adopted. The simulated results are compared with experimental data for strongly curved flow over a developed bed topography as well as over a fixed horizontal bed.

2 The mathematical model

The CCHE3D model solves the Reynolds-averaged momentum equations, Eq. (1), and the incompressible continuity equation, Eq. (2), in a Cartesian coordinate system (x_i or x,y,z),

$$\frac{\partial u_i}{\partial t} + u_j \frac{\partial u_i}{\partial x_j} - \frac{\partial}{\partial x_j} \overline{(u'_i u'_j)} + \frac{1}{\rho} \frac{\partial p}{\partial x_i} + f_{x_i} = 0 \quad (i,j=1,2,3) \quad (1)$$

$$\frac{\partial u_j}{\partial x_j} = 0 \quad (2)$$

using the Efficient Element Method, a collocation approach of the classic weighted residual method. u_i , u'_i and f_{xi} are the components of the mean velocity, the velocity fluctuation, and the external force along the i -reference axis, respectively; t is time; p is pressure; ρ is the water density; the overbar denotes time-averaged values. The elevation η of the free surface is computed using the free surface kinematic equation:

$$\frac{\partial \eta}{\partial t} + u_{1(z=\eta)} \frac{\partial \eta}{\partial x_1} + u_{2(z=\eta)} \frac{\partial \eta}{\partial x_2} - u_{3(z=\eta)} = 0 \quad (3)$$

The non-linear k - ε turbulence closure proposed by Speziale (1987) is adopted:

$$-\overline{u'_i u'_j} = -\frac{2}{3} k \delta_{ij} + 2\nu_t S_{ij} + 4C_D c_\mu^2 \frac{k^3}{\varepsilon^2} \left(S_{im} S_{mj} - \frac{1}{3} S_{mn} S_{mn} \delta_{ij} \right) + 4C_\varepsilon c_\mu^2 \frac{k^3}{\varepsilon^2} \left(\overset{\circ}{S}_{ij} - \frac{1}{3} \overset{\circ}{S}_{mn} \delta_{ij} \right) \quad (4)$$

where

$$\overset{\circ}{S}_{ij} = \frac{\partial S_{ij}}{\partial t} + \bar{u} \cdot \nabla S_{ij} - \frac{\partial u_i}{\partial x_k} S_{kj} - \frac{\partial u_j}{\partial x_k} S_{ki} \quad (5)$$

in which the strain rate tensor S_{ij} , the turbulent kinetic energy k , and the eddy viscosity ν_t are defined as:

$$S_{ij} = \frac{1}{2} \left(\frac{\partial u_i}{\partial x_j} + \frac{\partial u_j}{\partial x_i} \right); \quad k = \frac{1}{2} \overline{u_i'^2} \quad \text{and} \quad \nu_t = c_\mu \frac{k^2}{\varepsilon} \quad (6)$$

respectively. δ_{ij} is the Kronecker delta symbol and ε is the dissipation of turbulent kinetic energy. k and ε are computed from their transport equations:

$$\frac{\partial k}{\partial t} + u_j \frac{\partial k}{\partial x_j} - \frac{\partial}{\partial x_j} \left(\nu_t \frac{\partial k}{\partial x_j} \right) = P - \varepsilon \quad (7)$$

$$\frac{\partial \varepsilon}{\partial t} + u_j \frac{\partial \varepsilon}{\partial x_j} - \frac{\partial}{\partial x_j} \left(\frac{\nu_t}{\sigma_\varepsilon} \frac{\partial \varepsilon}{\partial x_j} \right) = c_{\varepsilon 1} P \frac{\varepsilon}{k} - c_{\varepsilon 2} \frac{\varepsilon^2}{k} \quad (8)$$

where the production of turbulent kinetic energy, P , is defined as:

$$P = -\overline{u'_i u'_j} \frac{\partial u_i}{\partial x_j} \quad (9)$$

The constants in Eqs. 4-8 take the values: $c_\mu=0.09$, $\sigma_k=1.0$, $\sigma_\varepsilon=1.3$, $c_{\varepsilon 1}=1.44$, $c_{\varepsilon 2}=1.92$, $C_D=C_\varepsilon=1.67$.

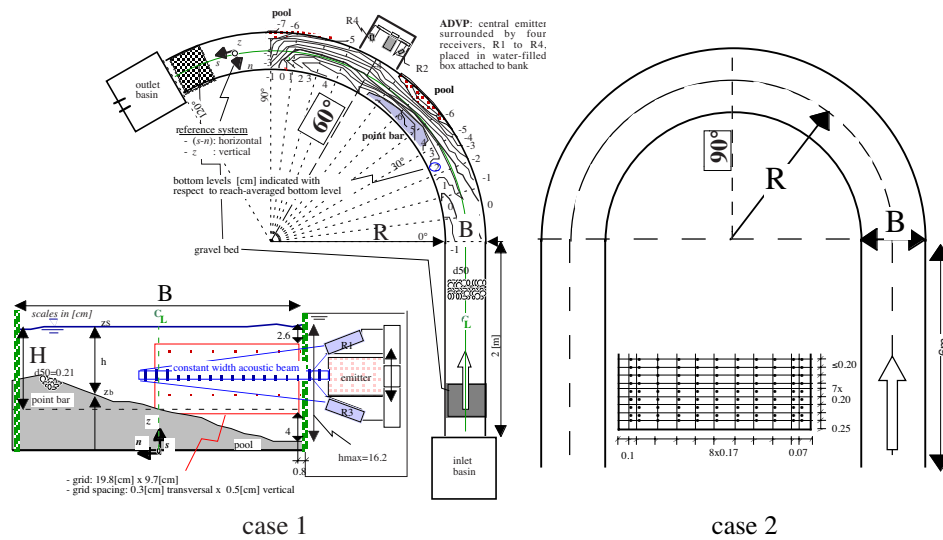
The dynamic pressure, which is important in three-dimensional flows with strong vertical currents, is computed by using a velocity correction method. A Poisson equation is formulated with the provisional velocities, and the final velocity, satisfying the divergence-free condition, is obtained via a velocity correction procedure using the computed pressure. The Eqs. (1), (3), (7) and (8), are integrated in time with a first order Euler scheme and the system of equations is solved implicitly by using the SIP method. Wall boundary conditions are used for the momentum equations and the k - ε model. The boundary condition for the ε equation at the water surface proposed by Naot and Rodi (1982) is modified slightly as follows:

$$\varepsilon_{(z=\eta)} = \frac{c_\mu^{3/4} k^{3/2}}{\kappa} \left(\frac{1}{0.07h} + \frac{1}{d_w} \right) \quad \text{replaced by} \quad \varepsilon_{(z=\eta)} = \frac{c_\mu^{3/4} k^{3/2}}{0.07\kappa} \left(\frac{1}{h} + \frac{1}{d_w} \right) \quad (10)$$

$\kappa=0.41$ is the Karman constant, h is the local flow depth and d_w is the distance to the wall. It is found in this study that the numerical simulation is not stable unless the convection term for the strain rates, $\bar{u} \cdot \nabla S_{ij}$, in equation (5) is eliminated. The simulations in this study are therefore conducted without this term.

3 Physical model data

This paper reports the simulation of two experiments on strongly curved flow: Case 1 is over an irregular bed topography preformed by erosion on a mobile bed (Blanckaert and Graf 2001a) while Case 2 is over a fixed horizontal bottom (de Vriend 1979). Their experimental set-up and hydraulic conditions are shown in Fig. 1. Blanckaert and Graf (2001a) only measured in one outer half-section at 60° in the bend (Fig. 1). Their measurements are very detailed and they reported distributions of all mean velocity components and all Reynolds stresses measured with high temporal (44.6 Hz) and spatial (1360 measuring points) resolution. De Vriend (1979) measured the flow field all along the flume in 21 different cross-sections. He only measured the downstream and the transversal components of the mean velocity and used a rather coarse grid (11 verticals and 9 points per vertical, see Fig. 1). Both experiments clearly show the existence of a bi-cellular pattern of cross-stream circulation cells (Fig. 2a, Fig. 3a).



Hydraulic conditions (flume-averaged values)

	Q (m ³ /s)	B (m)	H (m)	U (m/s)	Fr	R (m)	θ (°)	C (m ^{1/2} /s)	d_{50} (mm)
	discharge	width	depth	velocity	Froude	radius	angle	Chezy	sediment
Case 1	0.017	0.4	0.11	0.38	0.36	2.0	120	1.89	2.1
Case 2	0.12	1.7	0.21	0.35	0.25	4.25	180		1

Fig. 1: Experimental set-up and hydraulic conditions

4 Comparison of measured with computed flow field

The measured and simulated flow fields are compared in a cylindrical reference system with the s -axis downstream along the centerline, the n -axis perpendicular to it and the upward z -axis perpendicular to the horizontal (s,n)-plane. Figs. 2a,b show the measured cross-stream motion (v_n, v_z) and downstream velocity v_s in the investigated outer-half section at 60° for case 1, whereas Figs. 2c,d show their simulated counterparts in the entire cross-section. They have been normalized by the overall mean velocity, $U=Q/(BH)=0.38$ m/s. The frames indicate the measured zones; the velocities outside it near the boundaries were extrapolated. Before the non-linear $k-\varepsilon$ model is activated, the linear $k-\varepsilon$ model was applied to prepare the initial flow field. This reconfirmed the failure of the linear $k-\varepsilon$ model to reproduce the outer bank cell for both cases.

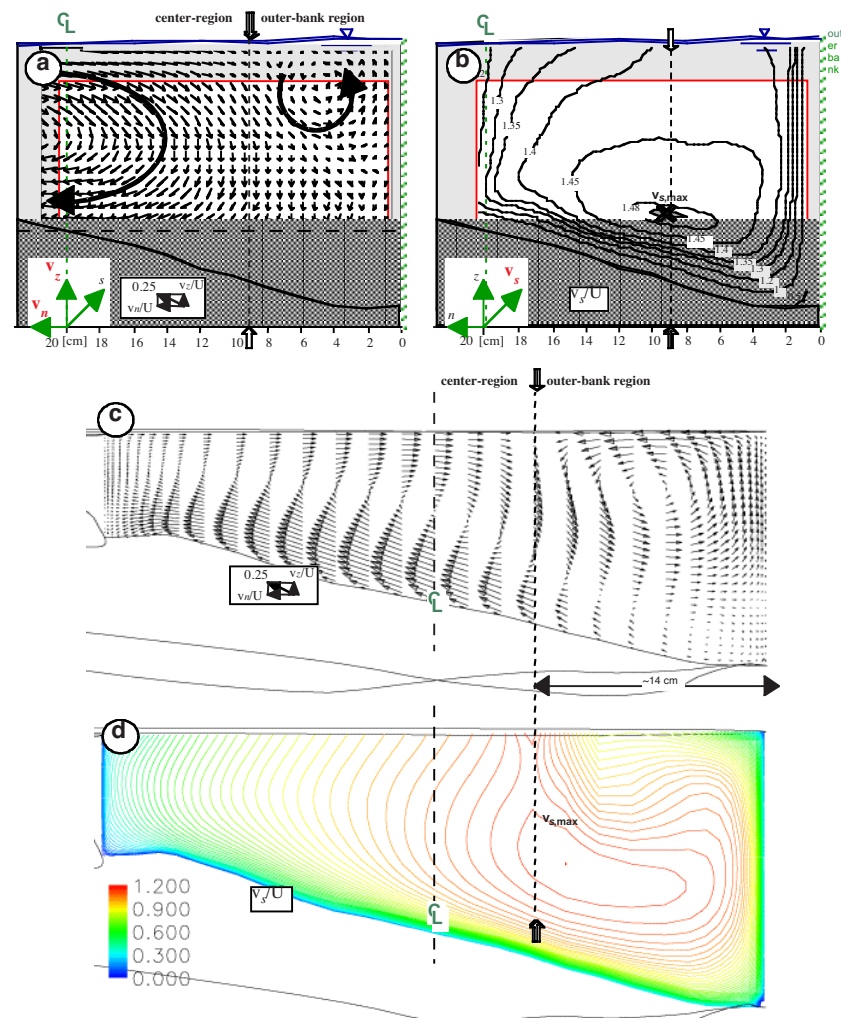


Fig. 2: Measured cross-stream motion, $(v_n, v_z)/U$ (a), and downstream velocity, v_s/U (b) and their simulated counterparts (c) and (d), normalized by the overall mean velocity $U=0.38$ m/s for case 1.

The main features of the flow field are captured by the simulation. The simulated cross-stream motion contains both circulation cells and the downstream velocity increases in outward direction: $v_s/U < 1$ in the inner bend and $v_s/U > 1$ in the outer bend. The core of maximum velocities, $v_{s,max}/U$, is found at the separation between both circulation cells. The vertical v_s -profiles deviate from the logarithmic profile that is typical for straight uniform flow: the maximum velocity is found in the lower part of the water column and $\partial v_s/\partial z < 0$ in the upper part.

Although the flow field is qualitatively well simulated, there are some important quantitative discrepancies between the measurements and the simulation. The simulation underestimates the strength of the center-region cell and rather strongly overestimates the strength of the outer-bank cell, as shown by the maximum transversal velocities in both cells:

$$\left[\frac{v_s}{U} \right]_{center-region\ cell}^{simulated} \approx 0.15 < \left[\frac{v_s}{U} \right]_{center-region\ cell}^{measured} \approx 0.25 \quad (11a)$$

$$\left[\frac{v_s}{U} \right]_{outer-bank\ cell}^{simulated} \approx 0.10 > \left[\frac{v_s}{U} \right]_{outer-bank\ cell}^{measured} \approx 0.025 \quad (11b)$$

The simulated width of the outer-bank cell (~ 14 cm) also overestimates the measured one (~ 10 cm). The outward increase of the downstream velocity is underestimated and the maximum simulated velocity of $v_{s,max}/U \approx 1.2$ is considerably smaller than the measured one of $v_{s,max}/U \approx 1.5$. Furthermore, the simulation rather strongly exaggerates the deformation of the v_s -profiles in the zone covered by the outer-bank cell: the measured v_s only slightly decreases from its maximum in the lower part of the water column towards the water surface, whereas the simulated ones show a steep descent from their maximum towards the water surface.

Blanckaert and Graf (2002) have shown that the outward increase of v_s and the deformations of its vertical profiles are mainly the result of advective momentum transport by the circulation cells. The underestimation of the outward increase of v_s is thus explained by the underestimation of the strength of the center-region cell. More research is needed to identify the reasons for this inaccurately simulated circulation strength. The exaggerated deformation of the vertical v_s -profiles and the overestimated strength of the outer-bank cell are closely interrelated because the outer-bank cell advects low momentum fluid from the near-bank area in inward direction at the water surface. Blanckaert and de Vriend (2001) have shown that the resulting decreasing velocities towards the water surface, $\partial v_s/\partial z < 0$, are an important generation mechanism for the outer-bank cell. This leads to the following feedback mechanism: the overestimated strength of the outer-bank cell causes an exaggerated gradient $\partial v_s/\partial z < 0$, which in turn further strengthens the outer-bank cell. More research is needed to improve our understanding of this mechanism and its modeling. Furthermore, there is need for better experimental data near the free surface and the walls.

Figs. 3a,b show the measured transversal velocity v_n and simulated secondary current vector field in the cross-section at 90° for case 2. The simulated strength of the center-region cell agrees reasonably well with the measured one. The two measured profiles on the right side (outer bank) indicate the existence of an outer-bank cell. In approaching the outer bank, the flow of the center cell is forced to dive under this outer-bank cell. The distance of these two profiles to the outer bank is 0.1m and 0.17m. Thus the width of the outer bank cell is of the order of the flow depth ($H=0.2\text{m}$). The width of the outer bank cell in the simulation is found to be almost constant from where this cell appears (0° section) to the outlet section. The simulated secondary flow velocities are very close to the observed ones. The simulated outer-bank cell has a width of about $0.75H$, very close to the measured one. In the upstream straight reach, the simulated cell develops similar to those in the straight channels. In the curved part of the channel, the width of the simulated cell remains nearly constant and subsequently increases a little in the downstream straight reach. Its strength, however, decreases gradually towards the outlet section.

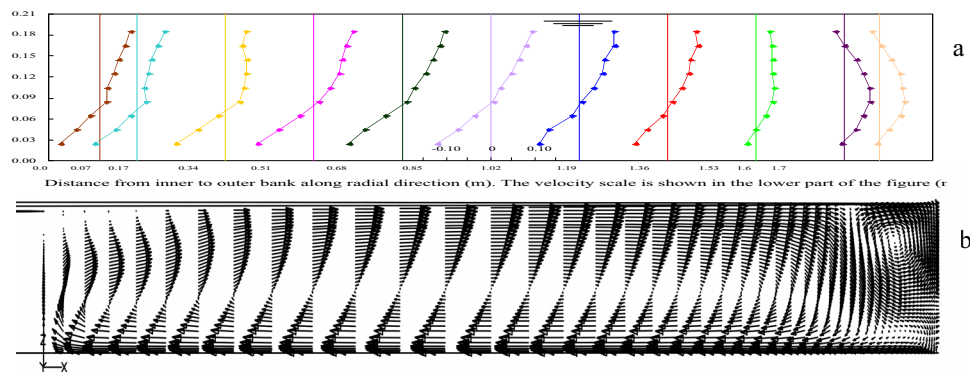


Fig. 3: measured (a) transversal velocity (v_n) and simulated (b) transversal vector field ($v_n - v_s$) in the cross-section at 90° for case 2

5 Conclusions

Flow in open-channel bends is characterized by cross-stream circulation cells which strongly influence the flow field and the river morphology. Besides the classical center-region cell, often a smaller and weaker counter-rotating outer-bank cell occurs. Whereas the standard $k-\varepsilon$ turbulence closure is inherently unable to simulate the bi-cellular pattern of cross-stream circulation cells in open-channel bends, this paper reports on successful simulations with a computationally inexpensive non-linear $k-\varepsilon$ closure. Both flow over a mobile-bed topography and over a fixed horizontal bed are simulated. The main features of the flow field are simulated reasonably well although some discrepancies appear. The preliminary simulations reported indicate the importance of the anisotropy of turbulence in generating the outer bank cell. Furthermore, they indicate that the non-linear $k-\varepsilon$ turbulence closure has the potential to simulate accurately the complex flow in open-channel bends. More research, both numerically as well as experimentally, is presently undertaken in order to further improve the simulations.

Acknowledgements

The measurements by the second author were sponsored by the Swiss National Science Foundation under grants Nr.2100-052257.97/1 and 2000-059392.99/2. The second author gratefully acknowledges his PhD supervisor, Prof. W.H. Graf, for his support. The work of the first and last author is a result of research supported in part by the USDA Agriculture Research Service under Specific Research Agreement No. 58-6408-7-035 (monitored by the USDA-ARS National Sedimentation Laboratory) and The University of Mississippi.

References

- Bathurst, J. C., Thorne, C. R. & Hey, R. D. (1979). "Secondary flow and shear stress at river bends." *J. Hydr. Div.*, ASCE, 105(10), 1277-1295.
- Blankaert, K. & Graf, W.H. (2001a). "Mean flow and turbulence in an open channel bend". *J. Hydr. Engng.*, ASCE, 127(10), 835-847.
- Blankaert, K. & Graf, W.H. (2002). "Momentum transport in sharp open-channel bends". (*tentatively approved for publication in J. Hydr. Engng.*, ASCE).
- Blankaert, K. & de Vriend, H.J. (2001). "Secondary flow in sharp open-channel bends". (*submitted for publication*).
- Christensen, B., Gislason, K. & Fredsoe, J. (1999). "Secondary turbulent flow in an infinite bend." *1st-RCEM symp.*, Genova, Italy, Vol.1, 543-553.
- de Vriend, H. J. (1979). "Flow measurements in a Curved Rectangular Channel." Report No. 79-9, Lab. Fl. Mech., Dept. Civ. Eng., Delft Univ. Techn., Delft, Netherlands.
- de Vriend, H. J. & Geldof, H. J. (1983). "Main flow velocity in short and sharply curved river bends." Report No. 83-6, Lab. Fl. Mech., Dept. Civ. Eng., Delft Univ. Techn., Delft, Netherlands.
- Dietrich, W. E. & Smith, J. D. (1983). "Influence of the point bar on flow through curved channels." *Water Resourc. Res.*, AGU, 19(5), 1173-1192.
- Jia, Y. & Wang, S.S.Y. (1992). "Computational Model Verification Test Case using Flume Data". ASCE Water Forum, Baltimore, MD, August 1992, 436-441.
- Jia, Y. & Wang, S.S.Y. (1998). "Numerical modeling of secondary motion of turbulent flows in compound channels". ASCE, Proc. Int. Water Res. Engng. Conf., 1038-1043.
- Naot, D. & Rodi, W. (1982). "Calculations of secondary currents in channel flow". *J. Hydr. Div.*, ASCE, 108(8), 948-968.
- Nezu, I. & Nakagawa, H. (1993). *Turbulence in Open Channel Flows*. IAHR/AIRH Monograph, A.A.Balkema, Rotterdam, Netherlands.
- Pezzinga, G. (1994). "Velocity distribution in compound channel flows by numerical modeling", *J. Hydr. Engng.*, ASCE, 120(10), 1176-1198.
- Rozovskii, I. L. (1957). *Flow of Water in Bends of Open Channels*, Ac. Sc. Ukr. SSR, Isr. Progr. Sc. Transl., Jerusalem, 1961.
- Speziale, C. G. (1987). "On nonlinear K-1 and K-e models of turbulence." *J. Fluid Mech.*, 178, 459-475.
- Tominaga, A. & Nagao, M. (2000) "Secondary flows in bends of open channels with various cross sections". Proc. Int. Conf. Hydrosc. and Engng., Seoul, Korea.
- Wu, W.M., Rodi, W., and Wenka, T., 2000, "3D numerical model of flow and sediment transport in open channels", ASCE, Journal of Hydraulic Engineering, Vol. 126, No. 1, p4-15.

PART IV**APPLIED RESEARCH****IV.3 Conclusions**

Some improvements to numerical-simulation techniques were made based on the knowledge acquired in parts II and III.

Due to the integration over the flow depth, all information related to the vertical structure of the flow field, and especially to the secondary circulation, is lost in depth-integrated flow models, and has to be provided. Chapters II.2 and II.3 have shown that linear models for this purpose are inadequate for moderate to strong curvatures. Chapter IV.1 proposes a non-linear model that accounts for the feedback between the downstream velocity profile and the center-region cell of secondary circulation: it simulates the flattening of the downstream velocity profiles and the corresponding weakening of the center-region cell with increasing curvature. The non-linear model depends on the curvature ratio H/R , the flow friction factor and the spanwise-distribution of the downstream velocity, which can be combined with good approximation into one single newly-defined parameter, called bend parameter, that allows to distinguish objectively between weak, moderate and strong curvatures. The commonly used linear models are found as the asymptotic solution for vanishing curvature. The non-linear model agrees fairly well with experimental data for strongly curved flow from both the small flume (chapter III.1) and the large flume (chapter IV.1). Estimations for natural rivers show that differences between the linear and the non-linear model are relevant. The non-linear model has the potential to improve the capabilities of depth-integrated flow models at low computational cost: a quasi three-dimensional flow field is obtained by extending such depth-integrated models with this non-linear model.

Chapter III.2 has shown that the outer-bank cell of secondary circulation, which has a protective effect on the outer bank, cannot be simulated with the standard $k-\varepsilon$ turbulence closure model. Chapter IV.2 succeeds in simulating the outer-bank cell observed in the small-flume experiments with a non-linear $k-\varepsilon$ turbulence closure model. These simulations were done in collaboration with the National Center for Computational Hydroscience and Engineering (Univ. Mississippi, Prof. Wang and Prof. Jia). Chapter IV.2 reports the first results of this collaborations that is presently being intensified.

PART V

WORK IN PROGRESS

V.1 Experimental observations and fundamental research
V.2 Applied research

V.1
V.2

Due to results beyond all expectations, our research project could not be accomplished within the framework of this PhD-thesis, and a lot of research is currently still in progress.

V.1 Experimental observations and fundamental research

The limited series of small-flume experiments yielded results beyond all expectations that form the core of this dissertation. As a side-effect, the extended series of large-flume experiments were somewhat postponed. At present, the analysis of the small-flume experiments is accomplished, but only a basic data analysis has been performed on the series of large-flume experiments over a horizontal bottom topography – some data are presented in chapters II.3 and II.4 and exploited in chapter IV.1 – whereas the series of large-flume experiments over a mobile-bottom topography is only now in its final phase. The analysis of the large-flume experiments is similar to that of the small-flume experiments.

First of all, the enormous amount of data from these large-flume experiments will be reduced into a convenient format. This will constitute an important database for the validation of numerical models, with the unique property of containing all three mean velocity components, all six Reynolds stresses and even the higher-order turbulent correlations. This responds to a need for detailed data on three-dimensional open-channel flow, which are at present very scarce. Furthermore, the most relevant observations on the behavior of the flow and the turbulence will be highlighted.

Subsequently, a detailed analysis of the physical mechanisms and processes underlying these observations will be made, with the aim of confirming the results of the small-flume experiments and acquiring new knowledge concerning:

- the flow behavior in entire cross-sections instead of only the outer half of the cross-section.
- the evolution of the flow as it proceeds through the bend.
- the flow behavior as a function of the degree of curvature, parameterized by the curvature ratio H/R .
- differences between the flow over a horizontal and a mobile-bottom topography.

Finally, some aspects of the flow that have not been considered in the small-flume experiments will be investigated in the large-flume experiments, such as coherent structures in the turbulent flow field (sweeps, ejections, etc.). This has been done with our ADV-instrument for straight uniform flow, but to our knowledge no analysis of coherent structures in three-dimensional open-channel flows has been reported in literature before. These coherent structures are important with respect to the shear stresses on the boundaries and the transport of sediments as bedload and in suspension.

Besides, the next phase of experimental research on open-channel bends has been launched, intending to investigate the dynamics of suspended sediment transport.

At the end of this PhD, a rich amount of experimental data is available that is far from being exhausted. It is beyond all doubt that its analysis will shed new light on the dynamics of the mean flow and the turbulence in open-channel bends.

V.2 Applied research

Also the applied research, reported in part IV, with the aim of evaluating, improving and developing numerical simulation techniques, is far from being accomplished.

Chapter IV.1 presented a non-linear model for the vertical flow structure that, unlike commonly used linear models, accounts for the feedback between the downstream velocity profile and the secondary circulation.

- Predictions by this non-linear model of important differences between the secondary circulation over a horizontal and a mobile-bottom topography led to the design of the two series of large-flume experiments over different bottom topographies. Experimental data from both series will serve to further evaluate, and hopefully validate, the non-linear model. A companion paper to chapter IV.1 that highlights the differences between the flow over both bottom topographies and that evaluates the non-linear model is in preparation.
- A simplified implementation of this non-linear model into the depth-integrated flow-sediment model developed by WLIDelft Hydraulics (The Netherlands, Prof. de Vriend) has given promising results. It greatly enhanced the capacity of the depth-integrated flow-sediment model at low computational cost. Simulations of the flow over a horizontal bottom topography and simulations of the development of the bottom topography have already been reported in two congress papers:
 - Blanckaert K., Glasson L., Altinakar M., Jagers H. R. A. & Sloff C. J. (2003). 'A quasi-3D model for flow in sharp open-channel bends'. *Proc. 30th IAHR Congr.*, Thessaloniki, Greece (*in press*).
 - Blanckaert K., Glasson L., Jagers H. R. A. & Sloff C. J. (2003). 'Quasi-3D simulation of the morphology in sharp open-channel bends'. *Proc. Int. Symp. Shallow Flows*, Techn. Univ. Delft, Delft, The Netherlands. (*in press*).
- This non-linear model will now be fully implemented into the depth-integrated flow-sediment model developed by WLIDelft Hydraulics. The thus obtained quasi-3D model will be used as a tool for the investigation of river morphodynamics, and especially for the simulation of meander dynamics in the high-curvature range.

Chapter IV.2 reported simulations of the three-dimensional flow field, including the outer-bank cell of secondary circulation, with a non-linear $k-\varepsilon$ turbulence closure, which were done in collaboration with the National Center for Computational Hydroscience and Engineering (Univ. Mississippi, Prof. Wang and Prof. Jia). This collaboration is being intensified. The question that we aim to address is: "what kind of turbulence closure is required to simulate a specific phenomenon, such as the outer-bank cell of secondary circulation or the reduction of turbulence activity under the effect of streamline curvature" ? Simulations of both the small and large-flume experiments will be done in order to evaluate different non-standard turbulence closure models. Furthermore, the numerical simulations will allow to extend our research to a wider range of geometric and hydraulic parameters. The behavior of the cells of secondary circulation, for example, can be investigated numerically as a function of the curvature ratio, the aspect ratio, the river roughness, etc.

Finally, also the turbulence characteristics will further be investigated by means of numerical simulation techniques. Collaborations have been launched with the Technical University Delft (The Netherlands, Dr. Booij) and with the University of Karlsruhe (Prof. Rodi, Dr. Stoesser) with the aim of simulating the flow and the turbulence in open-channel bends by using Large-Eddy-Simulation (LES) techniques.

PART VI

CONCLUSIONS

VI.1	Introduction and objectives	VI.1
VI.2	Conclusions	VI.1

VI.1 Introduction and objectives

Rivers are the arteries of our planet: they shape our landscapes, irrigate our lands, supply us with drinking water and food and constitute important connecting links. But rivers also frequently cause devastation: they erode fertile land and endanger property, inundate vast areas of land and spread disease.

At present, the term “sustainable development” is in vogue. Applied to the river environment, this means attempting to exploit the river’s resources and to seek protection against its threats, by preserving its ecological and biological richness.

“Sustainable-development” river projects, such as renaturalization works, flood protection schemes, navigation improvement works or water quality improvement measures, require an understanding of the three-dimensional flow and turbulence in complex geometries.

However, hardly any experimental data exists on three-dimensional flow and turbulence in complex geometries. Furthermore, three-dimensional numerical simulations are mostly based on “straight-uniform-flow” knowledge.

This PhD investigates, mainly experimentally, the flow and turbulence in open-channel bends, as a generic case of highly three-dimensional flow, with as principal objectives:

- To provide a high-quality data base on three-dimensional open-channel flow, including all three mean velocity components and all six Reynolds stresses on a fine grid.
- To document interesting features of the flow field and the turbulence, such as the multi-cellular pattern of secondary circulation, the curvature influence on the turbulence, etc.
- To gain insight in the relevant physical mechanisms and processes underlying these features.
- To apply the acquired knowledge in an engineering sense, mainly by evaluating, improving and developing numerical simulation techniques.

The experimental research is rendered feasible by the availability of a powerful Acoustic Doppler Velocity Profiler (ADVP), developed in our laboratory. Within the framework of this PhD, techniques have been developed to improve acoustic turbulence measurements, mainly by optimizing the ADVP-configuration and by supplying acoustic targets to the flow in order to increase the signal-noise ratio.

VI.2 Conclusions

The core of this dissertation is structured into three parts, corresponding to the above defined objectives: Part II “Experimental observations”, Part III “Fundamental research” and Part IV “Applied research”. At the end of each part, the main conclusions are summarized. Regrouping these leads to the following main conclusions of this dissertation:

Downstream velocity, v_s

(chapters II.1 and III.1)

The distribution of the downstream velocity v_s is strongly determined by the secondary circulation (see next point). The center-region cell of secondary circulation redistributes the velocity by advecting flow momentum in outward direction, thereby causing the observed outward increase of v_s . Furthermore, it causes a flattening of the vertical profile of v_s , by increasing/decreasing the velocities in the lower/upper part of the water column. For strong curvatures, the v_s -profile gets non-monotonic, with maximum velocities occurring in the lower part of the water column.

Although small and weak, the outer-bank cell of secondary circulation plays an important role. It stabilizes a buffer region that protects the outer-bank against influences of the center-region cell. Most important, the outward increase of v_s does not continue onto the outer bank, but the core of maximum v_s is found at the separation of both circulation cells.

A precise description of the secondary circulation is a prerequisite for the accurate simulation of the flow field.

Pattern of secondary circulation cells

Besides the classical center-region cell (helical motion), a weaker and smaller counter-rotating outer-bank cell of secondary circulation is observed in the corner formed by the outer bank and the water surface. As mentioned above, this outer-bank cell has a protective effect on the erosional stability of the outer bank and the adjacent bottom.

Center-region cell

(chapters II.1, II.4, III.2 and IV.1)

The center-region cell is mainly generated by the vertical gradient of the centrifugal force, $(\partial/\partial z)(v_s^2/R)$. The non-uniform outward centrifugal force and the nearly-uniform inward pressure gradient, due to the super-elevation of the water surface, are on the average in equilibrium. Their local non-equilibrium, however, gives rise to the center-region cell.

An important negative feedback exists between the strength of the center-region cell and the vertical profile of v_s . As mentioned above, the v_s -profile flattens under the influence of the center-region cell. The resulting centrifugal force, v_s^2/R , gets more uniform over the depth, which results in a weaker center-region cell.

In engineering problems concerning the flow and the bottom morphology, often depth-integrated flow models are used, to which a closure model for the vertical structure of the flow, and especially for the secondary circulation, has to be provided. Commonly-used linear closure models that neglect this negative feedback between the downstream velocity profile and the center-region cell are inaccurate for moderate to strong curvatures. A non-linear closure model is proposed that accounts for this feedback and agrees well with experimental data for strongly curved flow. It depends on the ratio between the flow depth and the bend radius, the flow friction factor and the spanwise distribution of the downstream velocity, which can be combined with good approximation into one single newly-defined parameter, called bend-parameter, that allows to distinguish objectively between weak, moderate and strong curvatures. The commonly used linear

models are found as the asymptotic solution for vanishing curvature. Evaluations for natural rivers show that differences between the linear and non-linear models are relevant. The non-linear model has the potential to improve the capabilities of depth-integrated flow models at low computational cost: a quasi three-dimensional flow field is obtained by extending such depth-integrated models with this non-linear model.

Outer-bank cell

(chapters II.1-4, III.2 and IV.2)

In all of the small and large-flume experiments, outer-bank cells occurred. They seem to widen and strengthen considerably with increasing curvature.

Similar outer-bank cells exist in straight turbulent flow as well as in curved laminar flow. In straight turbulent flow, they are induced by the anisotropy of turbulence, and they cannot be simulated with the standard $k-\varepsilon$ turbulence closure. In curved laminar flow, they come into existence when the curvature exceeds a critical value. As described above, the v_s -profile flattens under the effect of the center-region cell. At the critical curvature, the v_s -profile gets non-monotonic, the gradient of the centrifugal force, $(\partial/\partial z)(v_s^2/R)$, changes sign near the water surface, and the outer-bank cell comes into existence.

A term-by-term evaluation of the downstream vorticity equation based on the experimental data indicates that both mechanisms have a comparable contribution to the generation of the outer-bank cell in curved turbulent flow. Furthermore, both mechanisms seem to strengthen each other, whence the outer-bank cell is stronger in a curved turbulent flow than in a curved laminar or a straight turbulent flow.

The restitution of kinetic energy from the turbulence to the mean flow plays an important role in the generation of the outer-bank cell. The deficiency of the standard $k-\varepsilon$ turbulence closure is due to its inherent incapability to account for such kinetic-energy restitution. Based on these indications, successful numerical simulations of the outer-bank cell have been done with a non-linear $k-\varepsilon$ turbulence closure.

Turbulence

(chapters II.1 and III.3-4)

The turbulence characteristics are of engineering relevance. The turbulence anisotropy plays an important role in the generation of the outer-bank cell, which on its turn affects the velocity distribution, the distribution of the boundary shear stresses, the sediment transport and ultimately the river morphology. Furthermore, the turbulence characteristics determine the spreading and mixing of matter, such as pollutants or suspended sediment, and heat.

The Reynolds stresses have pronounced spatial distributions in curved flow that considerably differ from their counterparts in straight uniform open-channel flow. Moreover, the turbulence activity, represented by the ratio of turbulent to mean-flow kinetic energy, is reduced in the outer half of the cross-section in the investigated open-channel bend, and presumably increased in the inner half. This reduced turbulence in the outer bend is attributed to a change in the turbulence structure: given the amount of turbulent kinetic energy, there is less shear in a curved flow.

The underlying turbulence dynamics can, speculatively, be described as follows. Similar to the influence of buoyancy, streamline curvature leads to turbulence damping, and it can be described by similar parameters such as the curvature-Richardson number R_f or the curvature-Brunt-Väisälä frequency ω_{bv} . The influence of the streamline curvature acts primarily in the horizontal and imposes a kind of spanwise stratification to the turbulence structure. The damping occurs basically through a change in the turbulence structure: the velocity fluctuations are a-typically coherent over the width and can be decomposed into slow width-coherent fluctuations and rapidly varying background turbulence. The coherent fluctuations represent a bulk-oscillation of the pattern of circulation cells with the characteristics of a wave-like motion: when treated as turbulence, they contribute significantly to the turbulent kinetic energy, but little to the turbulent shear stresses. The background turbulence is characterized by an efficient shear stress generation. Obviously, the reduction of part of the turbulence into wave-like motion reduces the efficiency of shear generation. Similar observations on reduced turbulence activity and tendency to wave-like motion have been reported in literature for flow in curved wind tunnels and density-stratified flows. To our knowledge, these potentially important phenomena have not been reported before in literature for the case of open-channel flow.

Consequently, in order to simulate numerically the observed reduced turbulence activity, it is not sufficient for turbulence closures to incorporate the transport equation for the turbulent kinetic energy, but they also have to represent the turbulence structure. Two-equation turbulence models, such as the commonly used k - ε -model, are inherently unable to do so. Semi-empirical extensions, based on the observed correlations between the turbulence structure and curvature parameters such as R_f and ω_{bv} , may be used to improve the capabilities of two-equation turbulence closures for three-dimensional curved flows, but this requires more experimental data, with a larger spatial coverage and for a wider range of hydraulic and geometric conditions.

Since the strength of the center-region cell of secondary circulation depends on the same curvature-Richardson number (it parameterizes the spanwise-distribution of the downstream velocity, see above), R_f must be an important scaling parameter in curved open-channel flow.

Our research on flow and turbulence in open-channel bends is not accomplished with this dissertation. The **work in progress**, as well as the continuation of the research are described in Part V “Work in progress”.

The experimental data presented in this dissertation are obtainable from the author.

Refereed journals

- [1] Altinakar M., Blanckaert K. & Graf W. H. (1999). 'Book review of : Erosion and sedimentation by P. Julien, Cambridge Univ. Press, UK.' *J. Hydr. Engng.*, ASCE, 125(5), 554-555.
- [2] Blanckaert K. (2001). 'Discussion on: Bend-flow simulation using 2D depth-averaged model, by Lien H.C. et al.' *J. Hydr. Engng.*, ASCE, 127(2), 167-170. (ch. II.2)
- [3] Blanckaert K. & Graf W. H. (2001). 'Mean flow and turbulence in open-channel bend.' *J. Hydr. Engng.*, ASCE, 127(10), 835-847. (ch. II.1)
- [4] Blanckaert K. & Graf W. H. (2002). 'Momentum transport in sharp open-channel bends.' (tentatively approved for publication in *J. Hydr. Engng.*, ASCE). (ch. III.1)
-
- [5] Blanckaert K. & de Vriend H. J. (2002). 'Secondary flow in sharp open-channel bends.' (submitted for publication). (ch. III.2)
- [6] Blanckaert K. & Lemmin U. (2002). 'Improving acoustic turbulence measurements.' (submitted for publication). (ch. I.2)
-
- [7] Blanckaert K. & de Vriend H. J. (2003). 'Turbulence characteristics in sharp open-channel bends.' (in preparation for submission). (ch. III.3)
- [8] Blanckaert K. & de Vriend H. J. (2003). 'Turbulence structure in sharp open-channel bends.' (in preparation for submission). (ch. III.4)
- [9] Blanckaert K. & de Vriend H. J. (2003). 'A natural limit to meander curvature.' (in preparation for submission).
- [10] Blanckaert K. & de Vriend H. J. (2003). 'Mean flow redistribution in curved open-channels. Part II: Experiments and non-linear model validation.' (in preparation for submission).
- [11] Blanckaert K. (2003). 'Mean flow redistribution in curved open-channels. Part I: Non-linear modelling.' (in preparation for submission). (ch. IV.1)

Conference proceedings

- [12] Blanckaert K. & Graf W. H. (1999). 'Experiments on flow in open-channel bends.' *Proc. 28th IAHR Congr.*, Techn. Univ. Graz, Graz, Austria, CD-ROM.
- [13] Blanckaert K. & Graf W. H. (1999). 'Outer-bank cell of secondary circulation and boundary shear stress in open-channel bends.' *Proc. 1st RCEM symp.*, Genova, Italy, Vol. I, 533-542.
- [14] Blanckaert K. (2001). 'A model for flow in strongly curved channel bends.' *Proc. 29th IAHR Congr.*, J.F. Kennedy Student Paper, Beijing, China, 42-50.
- [15] Blanckaert K. & Graf W. H. (2001). 'Experiments on flow in a strongly curved channel bend.' *Proc. 29th IAHR Congr.*, Beijing, China, Vol. D (I), 371-377. (ch. II.3)
- [16] Blanckaert K. & Graf W. H. (2001). 'Non-linear model for secondary circulation and transversal bottom slope in sharp bends.' *Proc. 2nd RCEM symp.*, Obihiro, Japan, 791-800.
- [17] Jia Y., Blanckaert K. & Wang S. S. Y. (2001). 'Simulation of secondary currents in curved channels.' *Proc. 8th FMTM Congr.*, Tokyo, Japan. (ch. IV.2)
- [18] Blanckaert K. (2002). 'Analysis of coherent flow structures based on instantaneous-velocity profiling.' *Proc. 3th Int. Symp. Ultrasonic Doppler Meth. for Fluid Mech. and Fluid Engng.*, Lausanne, Switzerland, 51-58.
- [19] Blanckaert K. (2002). 'Secondary currents measured in sharp open-channel bends.' *Proc. River Flow 2002*, Louvain, Belgium, Vol. I, 117-125. (ch. II.4)
- [20] Graf W. H. & Blanckaert K. (2002). 'Flow around bends in rivers.' *Proc. 2nd Int. Congr. New Trends in Water and Env. Engng.*, Capri, Italy, CD-ROM.
- [21] Hurther D., Lemmin U. & Blanckaert K. (2002). 'A field study of transport and mixing in a river, using an acoustic Doppler velocity profiler.' *Proc. River Flow 2002*, Louvain, Belgium, Vol. II, 1205-1210.
- [22] Blanckaert K., Glasson L., Altinakar M., Jagers H. R. A. & Sloff C. J. (2003). 'A quasi-3D model for flow in sharp open-channel bends'. *Proc. 30th IAHR Congr.*, Thessaloniki, Greece (in press).
- [23] Blanckaert K., Glasson L., Jagers H. R. A. & Sloff C. J. (2003). 'Quasi-3D simulation of the morphology in sharp open-channel bends'. *Proc. Int. Symp. Shallow Flows*, Techn. Univ. Delft, Delft, The Netherlands. (in press).

CURRICULUM VITAE

BLANCKAERT Koen

Belgian
Born in Ghent, Belgium
on 28.08.1972
Unmarried

Private :

Chemin des Triaudes, 12/22
CH-1024 Ecublens
Switzerland
Tél: +41/21/691.46.33
Gsm: +41/79/795.23.65

Professional:

Dr. ès Sciences
Research associate and lecturer
Environmental Hydraulics Laboratory (LHE)¹
Civil Engineering Department
Ecole Polytechnique Fédérale Lausanne (EPFL)
CH-1015 Lausanne
Switzerland
Tél. ++41/21/693.23.78
Fax. ++41/21/693.67.67
Koen.Blanckaert@epfl.ch



EDUCATION

- 2002-2003 Postdoc research on 'Flow and bed topography in open-channel bends' at LHE, EPFL.
1998-2002 PhD thesis on 'Flow and turbulence in sharp open-channel bends' under supervision of Prof. W.H. Graf and Prof. H.J. de Vriend at LHE, EPFL.
1997 Diplôme d'Etudes Approfondies de Mécanique² at Ecole Centrale Lyon, France.
Certificate of third cycle studies in fluid dynamiques, Mechanical Engng. Dept., EPFL.
1996 Research assistant at Hydraulics Laboratory, Civil Engng. Dept., University Ghent, Belgium (Prof. R. Verhoeven).
1991-1995 Civil Engineering at University Ghent, Belgium. Fifth year and student thesis at Civil Engng. Dept., EPFL (Erasmus European Exchange programme).

DISTINCTIONS

- 1997 Diplôme d'Etudes Approfondies de Mécanique at Ecole Centrale Lyon, France: first rank and high distinction ('mention très bien').
1995 Civil Engineering Degree at University Ghent, Belgium: high distinction ('mention très bien').

LANGUAGES

English, French, German: fluent
Dutch: mother tongue

PROFESSIONAL EXPERIENCES

- 2002-2003 Research associate and lecturer at EPFL in replacement of Prof. Graf for the courses³: Fluid mechanics I, Fluid mechanics II, Fluvial hydraulics and river development.
1997-2002 Research associate and teaching assistant at LHE, EPFL.
1997 Research project on 'Flow in open channel bends' in framework of Diplôme d'Etudes Approfondies de Mécanique at Ecole Centrale Lyon, France.
1996 Research project on 'Protection of the Belgian sand coast against erosion' at Hydraulics Laboratory, Civil Engng. Dept., University Ghent, Belgium.
1994-1995 Student thesis on 'Migration of dredged trenches in alluvial rivers' at Hydraulic Structures Laboratory, Civil Engng. Dept., EPFL.

¹ Laboratoire d'Hydraulique Environnementale. Formerly: Laboratoire de Recherches Hydrauliques (LRH).

² Similar to M.Sc. in Mechanical Engineering.

³ Mécanique des fluides I, Mécanique des fluides II, Hydraulique fluviale et aménagements des cours d'eau.